ADVANCES IN INORGANIC CHEMISTRY

Volume 47

A. G. Sykes

Advances in

INORGANIC CHEMISTRY

Volume 47

ADVISORY BOARD

I. Bertini
Università degli Studi di Firenze
Florence, Italy

A. H. Cowley, FRS
University of Texas
Austin, Texas, USA

H. B. Gray
California Institute of Technology
Pasadena, California, USA

M. L. H. Green, FRS
University of Oxford
Oxford, United Kingdom

O. Kahn
Institut de Chimie de la Matière Condensée de Bordeaux
Pessac, France

André E. Merbach
Institut de Chimie Minérale et Analytique
Université de Lausanne
Lausanne, Switzerland

D. M. P. Mingos, FRS
Imperial College of Science, Technology, and Medicine
London, United Kingdom

J. Reedijk
Leiden University
Leiden, The Netherlands

A. M. Sargeson, FRS
The Australian National University
Canberra, Australia

Y. Sasaki
Hokkaido University
Sapporo, Japan

D. F. Shriver
Northwestern University
Evanston, Illinois, USA

R. van Eldik
Universität Erlangen-Nürnberg
Erlangen, Germany

K. Wieghardt
Max-Planck Institut
Mülheim, Germany

Advances in
INORGANIC CHEMISTRY

Iron–Sulfur Proteins

EDITED BY

A. G. Sykes

Department of Chemistry
The University
Newcastle upon Tyne, England

CO-EDITED BY

Richard Cammack

Department of Biochemistry
King's College
London, England

VOLUME 47

ACADEMIC PRESS

San Diego New York Boston
London Sydney Tokyo Toronto

This book is printed on acid-free paper. ♾

Copyright © 1999 by ACADEMIC PRESS

All Rights Reserved.
No part of this publication may be reproduced or transmitted in any form or by any means, electronic or mechanical, including photocopy, recording, or any information storage and retrieval system, without permission in writing from the Publisher.
The appearance of the code at the bottom of the first page of a chapter in this book indicates the Publisher's consent that copies of the chapter may be made for personal or internal use of specific clients. This consent is given on the condition, however, that the copier pay the stated per copy fee through the Copyright Clearance Center, Inc. (222 Rosewood Drive, Danvers, Massachusetts 01923), for copying beyond that permitted by Sections 107 or 108 of the U.S. Copyright Law. This consent does not extend to other kinds of copying, such as copying for general distribution, for advertising or promotional purposes, for creating new collective works, or for resale. Copy fees for pre-1999 chapters are as shown on the title pages. If no fee code appears on the title page, the copy fee is the same as for current chapters.
0898-8838/99 $30.00

Academic Press
a division of Harcourt Brace & Company
525 B Street, Suite 1900, San Diego, California 92101-4495, USA
http://www.apnet.com

Academic Press
24-28 Oval Road, London NW1 7DX, UK
http://www.hbuk.co.uk/ap/

International Standard Book Number: 0-12-023647-8

PRINTED IN THE UNITED STATES OF AMERICA
99 00 01 02 03 04 QW 9 8 7 6 5 4 3 2 1

CONTENTS

Biological and Synthetic [Fe_3S_4] Clusters

MICHAEL K. JOHNSON, RANDALL E. DUDERSTADT, AND EVERT C. DUIN

I. Introduction 1
II. Historical Perspective 2
III. Occurrence and Function 5
IV. Structures 17
V. Electronic, Magnetic, and Vibrational Properties 21
VI. Cluster Conversions 55
VII. Synthetic Model Compounds 58
VIII. Mixed Metal Clusters 63
IX. Future Directions 72
References 73

The Structures of Rieske and Rieske-Type Proteins

THOMAS A. LINK

I. Introduction 83
II. Historical Background 84
III. Structural Aspects 85
IV. Spectroscopy 113
V. Electrochemistry 137
VI. Biosynthesis 144
VII. Function. 146
VIII. Outlook 151
References 152

Structure, Function, and Biosynthesis of the Metallosulfur Clusters in Nitrogenases

BARRY E. SMITH

I. Introduction 160
II. The Fe Proteins of Molybdenum Nitrogenase 162
III. The MoFe Proteins 166
IV. Biosynthesis of Molybdenum Nitrogenase 174
V. The Mechanism of Molybdenum Nitrogenase 183
VI. The Alternative Nitrogenases 202

VII. Conclusions and Outlook 211
References 212

The Search for a "Prismane" Fe–S Protein

ALEXANDER F. ARENDSEN AND PETER F. LINDLEY

I. Introduction 219
II. Historical Discovery of "Prismane" Protein (Now Termed Feps) . . 221
III. Crystallographic Studies 232
IV. Conclusion and Future Studies 245
References 247

NMR Spectra of Iron–Sulfur Proteins

IVANO BERTINI, CLAUDIO LUCHINAT, AND ANTONIO ROSATO

I. Introduction 251
II. Electron Relaxation Times 252
III. Valence Delocalization 257
IV. Considerations on the Reduction Potential 265
V. Solution Structure 266
VI. Folding 271
VII. Perspectives 276
References 277

Nickel–Iron–Sulfur Active Sites: Hydrogenase and CO Dehydrogenase

JUAN C. FONTECILLA-CAMPS AND STEPHEN W. RAGSDALE

I. Introduction 283
II. General Concepts Regarding Nickel and Iron–Sulfur . . . 285
III. Hydrogenase 286
IV. CODH/ACS 305
V. Conclusions 326
References 326

FeS Centers Involved in Photosynthetic Light Reactions

BARBARA SCHOEPP, MYRIAM BRUGNA, EVELYNE LEBRUN, AND WOLFGANG NITSCHKE

I. Introduction 335
II. 2[4Fe–4S] Proteins 338

III. The Bridging Cluster F_X 344
IV. [2Fe–2S] Ferredoxins 344
V. High-Potential Iron–Sulfur Proteins 345
VI. The Rieske Protein 347
VII. Evolutionary Remarks 355
References 356

Simple and Complex Iron–Sulfur Proteins in Sulfate Reducing Bacteria

ISABEL MOURA, ALICE S. PEREIRA, PEDRO TAVARES, AND JOSÉ J. G. MOURA

I. Introduction 361
II. Rubredoxin and Desulforedoxin 362
III. Desulfoferrodoxin 366
IV. Rubrerythrin 367
V. Ferredoxins 370
VI. Fuscoredoxin (Novel Fe–S Cluster) 378
VII. APS Reductase 382
VIII. Pyruvate–Ferredoxin Oxidoreductase 385
IX. Sulfite Reductase 386
X. Hydrogenase 388
XI. Molybdopterin-Containing Enzymes in SRB 395
XII. Concluding Remarks 405
References 410

Application of EPR Spectroscopy to the Structural and Functional Study of Iron–Sulfur Proteins

BRUNO GUIGLIARELLI AND PATRICK BERTRAND

I. Introduction 421
II. EPR Characteristics and Relaxation Properties of the Centers . . 423
III. Application of EPR to the Structural Study of Iron–Sulfur Proteins . 450
IV. Application of EPR to the Functional Study of Iron–Sulfur Centers . 474
V. Conclusion 484
Appendix: Spin–Lattice Relaxation Processes 486
References 487

INDEX 499
CONTENTS OF PREVIOUS VOLUMES 511

This Page Intentionally Left Blank

BIOLOGICAL AND SYNTHETIC $[Fe_3S_4]$ CLUSTERS

MICHAEL K. JOHNSON, RANDALL E. DUDERSTADT, and EVERT C. DUIN

Department of Chemistry and Center for Metalloenzyme Studies, University of Georgia, Athens, Georgia 30602

I. Introduction
II. Historical Perspective
III. Occurrence and Function
A. Ferredoxins
B. Succinate Dehydrogenase and Fumarate Reductase
C. Nitrate Reductase
D. Glutamate Synthase
E. NiFe-Hydrogenase
IV. Structures
V. Electronic, Magnetic, and Vibrational Properties
A. $[Fe_3S_4]^+$ Clusters
B. $[Fe_3S_4]^0$ Clusters
C. $[Fe_3S_4]^-$ Clusters and Cluster Fragments
D. $[Fe_3S_4]^{2-}$ Clusters
VI. Cluster Conversions
VII. Synthetic Model Compounds
VIII. Mixed Metal Clusters
A. Protein-Bound $[MFe_3S_4]$ Clusters
B. Synthetic $[MFe_3S_4]$ Clusters
IX. Future Directions
References

I. Introduction

Over the past two decades, clusters containing cubane-derived $[Fe_3S_4]$ cores have become established as a distinct class of physiologically relevant iron–sulfur centers. During this period, our understanding of the diverse roles and properties of biological iron–sulfur clusters has greatly proliferated (*1–4*) and the rich cluster conversion chemistry, redox, and electronic properties of $[Fe_3S_4]$ clusters have become a paradigm for understanding the properties of iron–sulfur clus-

Copyright 1999 by Academic Press.
All rights of reproduction in any form reserved.
0898-8838/99 $30.00

ters in general. In many ways the discovery and characterization of $[Fe_3S_4]$ clusters is one of the classic stories in bioinorganic chemistry and an excellent case study for students new to this area. In particular it serves to demonstrate the power of a multidisciplinary approach incorporating X-ray crystallography, the full armory of biophysical spectroscopic methods, molecular biology, and synthetic inorganic chemistry.

The class of Fe–S proteins containing 3Fe clusters was reviewed (*5*) soon after their discovery, and before the structure and physiological relevance had been definitively established. However, this excellent review posed the right questions and stimulated much of the research described herein. The objective of this review is to summarize the current understanding of the structural, electronic, and redox properties of biological and synthetic $[Fe_3S_4]$ and heterometallic $[MFe_3S_4]$ clusters. Throughout, the relevance to structure–function relations of iron–sulfur clusters, in general, and the major unresolved issues concerning $[Fe_3S_4]$ clusters, in particular, are emphasized. If this review stimulates anything like the level of interest and research that resulted from the Beinert and Thomson review (*5*), it will have served its purpose.

II. Historical Perspective

The discovery of Fe–S clusters containing 3Fe atoms in 1980 resulted from Mössbauer studies of *Azotobacter vinelandii* 7Fe ferredoxin (FdI) (*6*) and *Desulfovibrio gigas* FdII (*7*) and the X-ray crystallographic studies of *A. vinelandii* FdI (*8*). Although the Mössbauer data and analysis have withstood the test of time, the same cannot be said for the initial interpretation of the structure of the cluster in *A. vinelandii* FdI at 2.5 Å resolution. One of the clusters was correctly modeled as a cubane $[Fe_4S_4]$ center, whereas the other was erroneously modeled as containing an almost planar cyclic $[Fe_3S_3]$ core with Fe–Fe distances of 4.1 Å (*8*, *9*). The first clue as to the correct structure came from variable-temperature magnetic circular dichroism (VTMCD) studies which revealed that 3Fe clusters can be formed via oxidative degradation of cubane-type $[Fe_4S_4]$ clusters in a bacterial 8Fe ferredoxin (Fd) (*10*). This result was subsequently confirmed by resonance Raman (*11*) and Mössbauer (*12*) studies of bacterial 8Fe and 4Fe Fds and lead to speculation that some or all of the 3Fe clusters found in proteins were artifacts of oxidative degradation of $[Fe_4S_4]$ clusters (*5*). Taken together with the reports that the 3Fe clus-

ter in aerobically purified aconitase could be reductively converted to [Fe_4S_4] clusters by addition of ferrous ion (*13*) and of interconversion between 3Fe and [Fe_4S_4] clusters in *D. gigas* FdII (*14*), this suggested a structure derived from and closely related to a cubane-type [Fe_4S_4] cluster.

More direct challenges to the crystallographically deduced structure came from analytical and spectroscopic studies of proteins containing a single 3Fe cluster as the sole prosthetic group. Careful iron and inorganic sulfide analysis of the aerobically purified, inactive form of aconitase indicated a [Fe_3S_4] core stoichiometry (*15*). X-ray absorption fine structure (EXAFS) studies of *D. gigas* FdII (*16*) and inactive aconitase (*15*) showed average Fe–Fe distances of 2.7 Å, that is 1.4 Å shorter than in the crystallographically deduced structure. Resonance Raman studies of a range of 3Fe-containing Fds including *D. gigas* FdII and *A. vinelandii* FdI pointed to a common [Fe_3S_4] core in both the solution and crystalline states (*17*). The uncertainty over the cluster stoichiometry and structure was reflected by the use of [3Fe–xS] or [Fe_3S_x] in many publications during the 1980s. Resolution of the conflicting structural information on 3Fe clusters finally came in 1988 with the reinvestigation of *A. vinelandii* FdI crystal structure (*18*) and the publication of the *D. gigas* FdII crystal structure at 1.7 Å resolution (*19*). Both structures indicated a [Fe_3S_4] core stoichiometry with a $Fe_3(\mu_3\text{-}S)(\mu_2\text{-}S)_3$ structure that is best visualized as a cubane cluster minus one Fe.

In the early 1980s, the combination of EPR, Mössbauer, and VTMCD studies demonstrated that biological 3Fe clusters undergo one-electron redox cycling between $S = 1/2$ $[Fe_3S_4]^+$ and $S = 2$ $[Fe_3S_4]^0$ states (*6*, *7*, *10*, *13*, *20*, *21*). The unique magnetic and electronic properties in both oxidation states facilitated spectroscopic identification of analogous clusters in a wide range of enzymes and proteins. In addition to numerous ferredoxins, stoichiometric amounts of $[Fe_3S_4]^{+,0}$ clusters were identified in several enzymes: succinate dehydrogenase (*22*), fumarate reductase (*23*), nitrate reductase (*24*), glutamate synthase (*25*), and NiFe-hydrogenases (*26*, *27*). Since it was clear that the [Fe_3S_4] clusters in aconitase and many ferredoxins were artifacts of oxidative degradation of [Fe_4S_4] clusters, the physiological relevance of these clusters became a major issue. This question was first addressed by EPR studies of whole cells of *Escherichia coli* with amplified expression of fumarate reductase that showed that the $[Fe_3S_4]^{+,0}$ cluster is indeed an intrinsic component of the enzyme *in vivo* (*28*). On the basis of primary sequence data, inability to effect [Fe_3S_4] to [Fe_4S_4] cluster conversions and/or crystallographic and

whole cell EPR data, $[Fe_3S_4]^{+,0}$ clusters are now considered to be intrinsic redox components of each of these enzymes and of many 3Fe and 7Fe Fds.

The electronic and magnetic properties of $[Fe_3S_4]^{+,0}$ clusters have also provided the groundwork for understanding intracluster spin coupling and valence delocalization in Fe–S clusters in general. Mössbauer spectroscopy played the crucial role in this endeavor by revealing a valence delocalized $Fe^{2.5+}Fe^{2.5+}$ pair in $[Fe_3S_4]^0$ clusters (*7*, *29*). This led to the recognition that spin-dependent delocalization (SDD), in addition to the conventional Heisenberg–Dirac–van Vleck (HDvV) exchange, is required to explain the complex ground- and excited-state properties of Fe–S clusters and the development of spin coupling models to explain the $S = 1/2$ and 2 ground states of the oxidized and reduced $[Fe_3S_4]^{+,0}$ clusters, respectively (*29*, *30*). Further insight into the electronic, magnetic, and redox properties of Fe–S clusters, as well as information on the site-specific properties of cubane clusters, has come from the preparation of heterometallic cubane clusters $[MFe_3S_4]$ by incorporation of the heterometal, M, in the vacant coordination site of a $[Fe_3S_4]$ cluster. Following the pioneering work of Münck, Moura, and co-workers to form heterometallic $[ZnFe_3S_4]$, $[CdFe_3S_4]$ and $[CoFe_3S_4]$ clusters in *D. gigas* FdII (*31–33*), a wide range of heterometallic $[MFe_3S_4]$ clusters (M = Zn, Cd, Co, Cr, Mn, Ni, Cu, Tl) have now been prepared and characterized in bacterial and archaeal Fds (*34–41*).

Proteins containing 3Fe clusters have proven to be a particularly fertile area for studying cluster conversions. In addition to the well-established $[Fe_3S_4] \leftrightarrow [Fe_4S_4]$ interconversions, which occur particularly readily in proteins such as aconitase, *Pyrococcus furiosus* Fd, and *Desulfovibrio africanus* FdIII that contain site-differentiated $[Fe_4S_4]$ clusters (*13*, *42*, *43*), inactive aconitase has also been shown to undergo an irreversible alkaline transition to yield a protein containing a linear $[Fe_3S_4]^+$ cluster with an $S = 5/2$ ground state (*44*, *45*). More recently, a new type of reversible cluster conversion between $S = 1/2$ and 5/2 $[Fe_3S_4]^+$ clusters has been proposed in a variant form of *P. furiosus* Fd containing an additional cysteine residue in close proximity to the cluster (*46*).

Synthetic analog clusters have played a pivotal role in development of Fe–S cluster biochemistry. Indeed, the synthesis and characterization of clusters with $[Fe_2(\mu_2\text{-}S)_2]$, $[Fe_4(\mu_3\text{-}S)_4]$, and linear $[Fe_3(\mu_2\text{-}S)_4]$ cores by Holm and co-workers (*47*, *48*) were crucial in establishing the properties of these clusters and identifying these types of centers in biological systems. However, the synthesis of a cluster with the physi-

ologically relevant cuboidal $[Fe_3S_4]$ core proved to be particularly challenging. Holm and co-workers were finally successful in 1995 (*49*), and detailed accounts of the structure and properties of a synthetic cluster with a $[Fe_3S_4]^0$ core (*50*) and the metal ion incorporation reactions (*51*) appeared shortly thereafter. In addition to providing the first detailed metrical assessment of this type of cluster, the valence delocalization scheme and $S = 2$ ground state were shown to be an intrinsic property of a $[Fe_3S_4]^0$ cluster as opposed to being a consequence of the protein environment.

III. Occurrence and Function

The enzymes and proteins containing $[Fe_3S_4]$ clusters as intrinsic prosthetic groups are summarized in Table I, along with the prosthetic group composition and range of redox potentials for the $[Fe_3S_4]^{+,0}$ couple. This tabulation illustrates that $[Fe_3S_4]$ clusters are

TABLE I

ENZYMES AND PROTEINS CONTAINING INDIGENOUS $[Fe_3S_4]$ CLUSTERS

Protein/Enzyme	Source	Function	Prosthetic groups	$E_m([Fe_3S_4]^{+,0})$ (mV)[a]	Refs.
Ferredoxin					
3Fe	Bacteria/Archaea	Electron transport	$[Fe_3S_4]^{+,0}$	−130 to −200	*52*
7Fe	Bacteria/Archaea	Electron transport/ Redox sensing	$[Fe_3S_4]^{+,0}$; $[Fe_4S_4]^{2+,+}$	−140 to −460	*52*
Succinate dehydrogenase (Succinate:Q oxidoreductase)	Mitochondria and aerobic bacteria	Succinate + Q → Fumarate + QH_2	$[Fe_2S_2]^{2+,+}$; $[Fe_3S_4]^{+,0}$; $[Fe_4S_4]^{2+,+}$; FAD; 1-2Cyt *b*	+90 to −30	*53*, *54*
Fumarate reductase (MQH_2:fumarate reductase)	Anaerobic bacteria	Fumarate + MQH_2 → Succinate + MQ	$[Fe_2S_2]^{2+,+}$; $[Fe_3S_4]^{+,0}$; $[Fe_4S_4]^{2+,+}$; FAD; (Cyt *b*)	−20 to −70	*53*, *54*
Nitrate reductase (respiratory) (QH_2:nitrate reductase)	Aerobic bacteria	NO_3^- + QH_2 → NO_2^- + Q	$3[Fe_4S_4]^{2+,+}$; $[Fe_3S_4]^{+,0}$; Mo-cofactor	+60	*24*, *55*
Glutamate synthase					
NAD(P)H-dependent	Plants, bacteria	Glutamine + 2-oxoglutarate + NAD(P)H → 2 glutamate + NAD(P)	$[Fe_3S_4]^{+,0}$; $2[Fe_4S_4]^{2+,+}$; FMN; FAD	n.d.	*56*
Ferredoxin-dependent	Chloroplasts	Glutamine + 2-oxoglutarate + $2Fd_{ox}$ → 2 glutamate + $2Fd_{red}$	$[Fe_3S_4]^{+,0}$; FMN	−170 to −225	*25*, *57*, *58*
NiFe-hydrogenase	Bacteria	$H_2 \rightarrow 2H^+ + 2e^-$	$[Fe_3S_4]^{+,0}$; $2[Fe_4S_4]^{2+,+}$; NiFe center	−70	*59*

[a] Versus NHE at pH 7; n.d., not determined.

found as electron transfer catalysts in each of the three kingdoms of life, eukarya, archaea, and bacteria. However, in contrast to the more ubiquitous $[Fe_2S_2]$ and $[Fe_4S_4]$ clusters (*1–4*), all the available evidence indicates that biological $[Fe_3S_4]$ clusters are ligated exclusively by cysteine residues and function in electron transfer and/or redox sensing regulatory roles.

A. Ferredoxins

On the basis of the available structural data, evidence has accumulated for a common ancestral 8Fd with two $[Fe_4S_4]$ clusters for both monocluster (3Fe and 4Fe) and dicluster (7Fe and 8Fe) Fds. The evolutionary aspects of Fds have been discussed in detail in several reviews (*52*, *60*) and the arguments will not be repeated here. It is worth noting, however, that the higher potential $[Fe_3S_4]^{+,0}$ clusters are believed to have evolved from their low potential $[Fe_4S_4]^{2+,+}$ counterparts in order to facilitate higher potential electron transport processes.

1. 3Fe Ferredoxins

There are only a handful of examples of Fds containing a single $[Fe_3S_4]$ cluster and in each case the cluster is coordinated by two cystines in a -C–X_2–$\underline{X}$–X_2–C- arrangement with a more remote -CP- providing the third cysteine ligand (*52*). In the two best-characterized examples, *D. gigas* FdII (*19*, *61*) and *P. furiosus* Fd (*42*), $\underline{X}$ is C and D, respectively, and these residues coordinate the removable Fe in the $[Fe_4S_4]$ forms of these Fds (*62*, *63*). Indeed, *D. gigas* is remarkable in that different oligomeric forms of the same ferredoxin polypeptide accommodate different Fe–S clusters; FdI is a trimer with one $[Fe_4S_4]^{2+,+}$ per subunit (E_m = −450 mV), whereas FdII is a tetramer with one $[Fe_3S_4]^{+,0}$ per subunit (E_m = −130 mV) (*60*, *64*). The physiological significance of the 3Fe form and of the interconversion between FdII and FdI in *D. gigas* have been the subject of much debate (*60*), but are still unresolved issues. Anaerobically purified *P. furiosus* Fd is a monomer (M_r = 7,500) containing a single $[Fe_4S_4]^{2+,+}$ cluster (E_m = −370 mV), but the aspartyl-coordinated Fe is readily removed by chemical oxidation with ferricyanide to yield a $[Fe_3S_4]^{+,0}$ cluster (E_m = −200 mV) (*42*, *65*). Kinetic analyses indicate that the $[Fe_4S_4]$-containing form is optimal for accepting electrons from pyruvate oxidoreductase and donating electrons to ferredoxin : NADP oxidoreductase in *P. furiosus* (*65*). Hence, the possibility of a physiological role for the $[Fe_3S_4]$ form of *P. furiosus* Fd seems remote at this point in time. It is, however, interesting to note that both *P. furiosus* Fd and *D. gigas* FdII

have redox active disulfides (*66*, *67*), and the possibility that the [Fe_3S_4] clusters are involved in some hitherto undefined redox function involving these disulfides cannot be excluded at this stage.

The only clearcut examples of 3Fe Fds that are likely to be physiologically relevant are those associated with the sulfonylurea herbicide-inducible monooxygenase system of *Streptomyces griseolus* (*68*). Two ferredoxins, Fd-1 and Fd-2 (both $M_r \sim 7$ kDa), have been purified from sulfonylurea herbicide-induced *S. griseolus,* and each was shown to contain a single $[Fe_3S_4]^{+,0}$ cluster on the basis of analytical and spectroscopic studies. The genes for these ferredoxins were located just downstream from each of the two inducible cytochrome P450 enzymes, and either protein was found to restore sulfonylurea monooxygenase activity to an aerobic mixture of NADPH, spinach ferredoxin : NADP oxidoreductase, the purified cytochrome P450, and the herbicide substrate. One of the ferredoxins, Fd-1, has only three cysteines, and both ferredoxins have the customary cysteine motif for ligation of a [Fe_3S_4] cluster with alanine in place of the cysteine or aspartate that ligates the fourth iron ($\underline{X}$ = A), that is, -C–X_2–A–X_2–C---CP- for Fd-1 and -C–C–X–A–X_2–C---CP- for Fd-2.

2. 7Fe Ferredoxins

Approximately 20 7Fe Fds have been purified to homogeneity, and a summary of the redox properties, sequence type, and key characterization or sequence references is presented in Table II. Although specific electron transfer functions are known in only a few cases, sequence data and/or whole cell EPR studies suggest that these Fds contain $[Fe_3S_4]^{+,0}$ and $[Fe_4S_4]^{2+,+}$ clusters *in vivo.* The redox potential of each cluster varies over a wide range ($E_m = -140$ to -460 mV for the $[Fe_3S_4]^{+,0}$ couple and $E_m = -410$ to -715 mV for the $[Fe_4S_4]^{2+,+}$ couple), with the tetranuclear cluster invariably having the lower potential. In cases where a specific redox function has been identified, only the $[Fe_3S_4]^{+,0}$ cluster undergoes redox cycling under physiological conditions.

On the basis of primary sequence considerations, 7Fe Fds can be subdivided into at least two major classes. The first class (*Azotobacter*-type) is typified by the structurally characterized *A. vinelandii* FdI (*18*, *69*, *123*, *124*) and has two groups of coordinating cysteine residues with consensus sequences of -$\underline{C}$–X_2–$\underline{X}$–K–X_3–$\underline{C}$–X_3–$\underline{C}$–P–V- and -$\underline{\underline{C}}$–$X_2$–$\underline{\underline{C}}$–$X_2$–$\underline{\underline{C}}$–$X_3$–$\underline{C}$–P- for the first and second groupings, respectively. The $\underline{C}$ and $\underline{\underline{C}}$ residues ligate the [Fe_3S_4] and [Fe_4S_4] clusters, respectively, and the $\underline{X}$ residue is C, V, T, or E; see Table II. In addition to the anomalous arrangement of cysteine resi-

TABLE II

PROPERTIES OF 7Fe FERREDOXINS

Source/name	Sequence type[a]	$E_m[Fe_3S_4]^{+,0}$ (mV vs NHE)	$E_m[Fe_4S_4]^{2+,+}$ (mV vs NHE)	Refs.
Azotobacter vinelandii FdI	A-type ($\underline{X}$ = C)	−425 (pH 7.8)	−650 (pH 7.8)	*6*, *69–74*
Azotobacter chroococcum FdI	A-type ($\underline{X}$ = C)	−460 (pH 8.3)	−645 (pH 8.3)	*75*, *76*
Pseudomonas stutzeri 7Fe Fd	A-type ($\underline{X}$ = C)			*77*
Pseudomonas ovalis 7Fe Fd	A-type ($\underline{X}$ = C)			*78–81*
Pseudomonas nautica 7Fe Fd	A-type ($\underline{X}$ = C)	−175 (pH 7.6)	−715 (pH 7.6)	*82*
Rhodobacter capsulatus FdII	A-type ($\underline{X}$ = C)			*83–87*
Rhodospirillum rubrum FdII	A-type ($\underline{X}$ = C)			*88*
Rhodopseudomonas palustris 7Fe Fd	Unknown	−260 (pH 8.0)	−560 (pH 8.0)	*89*, *90*
Thermus thermophilus 7Fe Fd	A-type ($\underline{X}$ = V)	−250 (pH 9.0)	−530 (pH 9.0)	*70*, *79*, *81*, *91–94*
Mycobacterium smegmatis 7Fe Fd	A-type ($\underline{X}$ = V)	−435		*95–98*
Streptomyces griseus 7Fe Fd	A-type ($\underline{X}$ = V)	< −400	< −500	*99*, *100*
Bacillus schlegelii 7Fe Fd	A-type ($\underline{X}$ = T)			*101–105*
Bacillus acidocaldarius 7Fe Fd	A-type ($\underline{X}$ = E)			*106*
Desulfovibrio africanus FdIII	D-type ($\underline{X}$ = E)	−140 (pH 7.5)	−410 (pH 7.5)	*43*, *107*, *108*
Desulfovibrio vulgaris Miyazaki FdI	D-type ($\underline{X}$ = E)	+40, −140, −310 (pH 7.7)[b]	−440 (pH 7.7)	*109–111*
Sulfolobus sp. Strain 7 7Fe Fd	D-type ($\underline{X}$ = P)	−280 (pH 7.0)	−530 (pH 7.0)	*112–115*
Thermoplasma acidophilum 7Fe Fd	D-type ($\underline{X}$ = P)			*116*
Sulfolobus acidocaldarius 7Fe Fd	D-type ($\underline{X}$ = P)	−275 (pH 6.4)	−529 (pH 6.4)	*117–119*
Desulfurolobus ambivalens 7Fe Fd	D-type ($\underline{X}$ = P)	−270 (pH 7.5)	−540 (pH 7.0)	*120*, *121*
Pyrobaculum islandicum 7Fe Fd	P-type			*122*

[a] A-type = *Azotobacter*-type; –$\underline{C}$–X_2–$\underline{X}$–K–X_3–$\underline{C}$–X_3–$\underline{\underline{C}}$–P–V– and –$\underline{\underline{C}}$–$X_2$–$\underline{\underline{C}}$–$X_2$–$\underline{C}$–$X_3$–$\underline{C}$–P– consensus sequence in regions of cluster coordinating residues; D-type = *Desulfovibrio*-type; –$\underline{C}$–X_2–D–X_2–$\underline{C}$–X_3–$\underline{\underline{C}}$–P–V– and –$\underline{\underline{C}}$–$X_2$–$\underline{\underline{C}}$–$X_2$–$\underline{\underline{C}}$–$X_3$–$\underline{C}$–$\underline{X}$– consensus sequence in region of cluster coordinating residues $\underline{C}$ and $\underline{\underline{C}}$ residues ligate the $[Fe_3S_4]$ and $[Fe_4S_4]$ clusters, respectively, for A-type and D-type); P-type = *Pyrobaculum*-type; –C–X_2–C–X_2–$\underline{\underline{C}}$–$X_3$–C–P– and –C–$X_2$–D–$X_2$–C–$X_3$–C–P–V– arrangement of cysteines, but the specific cysteines ligating each cluster have still to be determined.

[b] EPR redox titrations indicate heterogeneity in the $[Fe_3S_4]$ center.

dues, *Azotobacter*-type 7Fe Fds have a 30- to 50-residue C-terminal extension compared to clostridial 8Fe Fds, resulting in M_r of approximately 12,700.

Ferricyanide oxidation of *Azotobacter*-type 7Fe Fds generally leads to degradation of the $[Fe_4S_4]$ cluster, with an $[Fe_3S_4]$ intermediate being observed in some cases, such as *Pseudomonas ovalis* (*79*), *Thermus thermophilus* (*79*), and *Mycobacterium smegmatis* (*79*, *97*). Since the $[Fe_3S_4]$ cluster does not undergo facile $[Fe_3S_4]$ to $[Fe_4S_4]$ cluster conversion under reducing conditions, it is generally considered to be an intrinsic redox active component rather than artifact of aerobic isolation. Moreover, in the X-ray crystal structure of *A. vinelandii* FdI (*18*, *69*), the nonconserved cysteine, $\underline{X}$, is moved out of range for ligating a fourth Fe site by the insertion of two additional residues between the second and third cysteines of the -C–X_2–C–X_2–C- motif that customarily ligates $[Fe_4S_4]$ clusters in 4Fe and 8Fe Fds (*52*). Nevertheless, for *Azotobacter*-type 7Fe Fds with $\underline{X}$ = C, conditions have been found to effect at least partial $[Fe_3S_4]$ to $[Fe_4S_4]$ conversion under re-

ducing conditions in the presence of Fe(II) ion, such as in *A. vinelandii* (*125*) and in *Azotobacter chroococcum* (*75*), and there is an unconfirmed report that *A. vinelandii* FdI can be reconstituted from apoprotein as an 8Fe Fd (*126*).

Relatively little is known about the physiological function of *Azotobacter*-type Fds. The most clearcut case for a specific function can be made for *S. griseus* 7Fe Fd (*99*). This 7Fe Fd is induced along with cytochrome P450 by adding soybean flour to the medium and can act as an electron donor to the inducible cytochrome P450 *in vitro.* The $[Fe_3S_4]^{+,0}$ couple in the 7Fe Fd from the thermophilic hydrogen-oxidizing bacterium *Bacillus schlegelii* has been shown to be functional in mediating electron transfer to cytochrome *c* from NADPH : ferredoxin reductase (*103*). The roles of the 7Fe Fds in nitrogen-fixing and photosynthetic bacteria have been addressed by assessing the consequences of disrupting the genes encoding for these proteins in *A. vinelandii* (*127*) and *Rhodobacter capsulatus* (*83*). The resulting *A. vinelandii* strain had no obvious phenotype with respect to cell growth, but a regulatory role for FdI was implicated by the observation of dramatically elevated levels of NADPH : ferredoxin reductase (*128*). Since this enzyme specifically binds FdI, they are likely to be redox partners *in vivo* (*129*). Moreover, the most recent results strongly suggest that the specific function of FdI is to serve as a redox sensor that regulates the expression of of NADPH : ferredoxin reductase via inactivation of an oxidative stress response system (*128*, *130*). In contrast to *A. vinelandii,* disruption of the gene encoding for FdII in *R. capsulatus* resulted in no growth even under conditions that derepress the expression of the other three Fd genes (*83*), indicating some type of specialized physiological function that is indispensable for the bacterium.

The second class (*Desulfovibrio*-type) is typified by *Desulfovibrio africanus* FdIII and has two groupings of cysteine residues with consensus sequence -$\underline{C}$–X_2–D–X_2–$\underline{C}$–X_3–$\underline{\underline{C}}$–P–V- and -$\underline{C}$–$X_2$–$\underline{\underline{C}}$–$X_2$–$\underline{C}$–$X_3$–$\underline{C}$–$\underline{X}$-. Once again the $\underline{C}$ and $\underline{\underline{C}}$ residues ligate the $[Fe_3S_4]$ and $[Fe_4S_4]$ clusters, respectively, and the $\underline{X}$ residue is E for the examples from sulfate-reducing bacteria and P in the examples from thermoacidophilic archaea; see Table II. The two examples from sulfate-reducing bacteria, that is, *D. africanus* FdIII and *Desulfovibrio vulgaris* Miyazaki FdI, have $M_r \sim 6{,}600$ and primary sequences similar to those of clostridial type 8Fe Fds (*107*, *110*). However, the primary structures of 7Fe Fds from the thermophilic archaea *Sulfolobus* sp. strain 7, *Sulfolobus acidocaldarius, Desulfolobus ambivalens,* and *Thermoplasma acidophilum* are distinct for those of the sulfate-reducing bacteria in

two regions. They each have an ~40-residue N-terminal extension that contains a Zn(II) ion tetrahedrally coordinated by three histidines and one aspartate and an ~10-residue insertion in the middle of the polypeptide chain, resulting in $M_r \sim 11{,}500$ (*131*). On the basis of the crystal structure of a 6Fe (2x[Fe_3S_4]) form of *Sulfolobus* sp. strain 7 (*114*, *131*), it seems likely that the zinc ion plays an important role in stabilizing the structure by connecting the N-terminal extension and the core fold.

The [Fe_3S_4] clusters in *D. africanus* FdII and *D. vulgaris* FdI both undergo facile conversion to [Fe_4S_4] clusters on addition of Fe(II) ion under reducing conditions (*43*, *111*). The resulting $S = 3/2$ [Fe_4S_4]$^+$ clusters have properties very similar to those of the [Fe_4S_4] cluster in *P. furiosus* Fd (*42*, *63*), suggesting that the incorporated Fe is ligated by the aspartate that replaces the cysteine in the conventional 4Fe and 7Fe Fd sequences. There have been no reports thus far of analogous reductive [Fe_3S_4] → [Fe_4S_4] cluster conversion for any of the 7Fe Fds from thermophilic archaea. However, on the basis of results obtained with *Sulfolobus* 7Fe Fd (*114*, *115*), this group of 7Fe Fds is likely to readily undergo aerial oxidative [Fe_4S_4] → [Fe_3S_4] degradation at pH 5 to yield stable 6Fe Fds containing 2 [Fe_3S_4] clusters.

In vitro studies suggest that *D. vulgaris* Miyazaki FdI is an electron carrier in the phosphoroclastic reaction involving pyruvate dehydrogenase and the hydrogenase–cytochrome c_3 system (*109*). No specific role has been proposed for *D. africanus* FdIII, and there is no direct evidence that the [Fe_3S_4]-containing form is the physiologically relevant form of either of the 7Fe Fds isolated from sulfate-reducing bacteria. Strong evidence that [Fe_3S_4]-containing forms of the 7Fe Fds from thermophilic archaea are present *in vivo* has come from whole-cell EPR studies of protein from *D. ambivalens* (*120*). Moreover, the [Fe_3S_4]$^+$ cluster of purified *D. ambivalens* Fd is able to accept electrons from the pyruvate oxidase and NADH oxidase isolated from this organism. A role in 2-oxoacid oxidation for the 7Fe Fds of thermophilic archaea was first proposed based on studies of *Sulfolobus* 7Fe Fd (*132*) and subsequent studies have shown that only the higher potential [Fe_3S_4]$^{+,0}$ cluster is reduced at the physiological pH during steady-state turnover of the purified 2-oxoacid : ferredoxin oxidoreductase at 50°C (*112*).

Very recently a new type of 7Fe Fd ($M_r \sim 12{,}000$) has been purified from the hyperthermophilic archaeon *Pyrobaculum islandicum* (*122*). The protein has a C-terminal extension, as in *A. vinelandii* FdI, but the overall sequence homology between these two Fds is low, and the

arrangement of cysteines -C–X_2–C–X_2–C–X_3–C–P- and -C–X_2–D–X_2–C–X_3–C–P–V- (P-type, see Table II) suggests that the [Fe_3S_4] cluster is ligated by the last cysteine of the first motif and the first and second cysteines of the second motif, that is, the opposite arrangement to that encountered in all 7Fe Fds investigated thus far. The Fd was rapidly reduced by the 2-oxoglutarate : ferredoxin oxidoreductase isolated from the same organism, indicating a role as an electron acceptor for redox enzymes involved with glycolytic metabolism.

B. Succinate Dehydrogenase and Fumarate Reductase

Succinate dehydrogenases and fumarate reductases constitute a large group of iron–sulfur flavoenzymes with very similar catalytic and physical properties (*53*, *54*, *133*). Succinate dehydrogenase is present in aerobic organisms as a membrane-bound component of the respiratory chain (Complex II of the mitochondrial respiratory chain). As a tricarboxylic cycle enzyme, it catalyzes the oxidation of succinate to fumarate and transfers electrons to the quinone pool for oxygen reduction and energy transduction. Fumarate reductase catalyzes the reverse reaction in anaerobic organisms and is the terminal enzyme in the anaerobic electron transport chain when fumarate is utilized as the respiratory oxidant. Both enzymes have a hydrophilic catalytic domain that consists of a flavoprotein ($M_r \sim 70{,}000$) containing covalently bound FAD and iron-sulfur protein ($M_r \sim 27{,}000$) containing $[Fe_2S_2]^{2+,+}$, $[Fe_4S_4]^{2+,+}$, $[Fe_3S_4]^{+,0}$ clusters (Centers 1, 2, and 3, respectively). The catalytic domain is attached to the membrane by one or two hydrophobic subunits that usually contain one or two *b*-type cytochromes.

The first suggestion that succinate dehydrogenase contained a [Fe_3S_4] cluster came from the magnetic field dependence of the linear electric field on the EPR spectrum of air-oxidized bovine heart Complex II (*134*). This was confirmed by identification of the unique VTMCD properties of the $[Fe_3S_4]^0$ clusters in dithionite-reduced soluble succinate dehydrogenase preparations from bovine heart mitochondria (*22*) and in dithionite-reduced samples of the cytochrome *b* deficient four-subunit complex and soluble form of fumarate reductase from *E. coli* (*23*). The inability to effect [Fe_3S_4] to [Fe_4S_4] cluster conversion under reducing conditions by addition of Fe(II) ion (*22*, *23*), coupled with observation of the characteristic EPR signal of the $[Fe_3S_4]^+$ cluster in whole cells of *E. coli* with amplified expression of fumarate reductase (*28*), provided strong evidence that the $[Fe_3S_4]^{+,0}$ cluster in these enzymes was an intrinsic redox active component

rather than an isolation artifact. As indicated later, this conclusion has subsequently been confirmed by primary sequence and mutagenesis data and the $[Fe_3S_4]^{+,0}$ cluster has been shown to play an intrinsic role in mediating electron transfer to or from the quinone/quinol.

Mutagenesis studies of *E. coli* fumarate reductase have identified the cysteines ligating each of the three clusters in the iron–sulfur protein subunit (*135–137*), and the three cysteines involved with ligating the $[Fe_3S_4]$ cluster are conserved in all fumarate reductases and succinate dehydrogenases sequenced thus far. The primary sequences of the iron–sulfur protein subunit of 14 succinate dehydrogenases and 6 fumarate reductases from a variety of eukarya and bacteria are currently available in the Swiss Protein data base, and the $[Fe_3S_4]$ and $[Fe_4S_4]$ clusters are ligated by the second and third groups of cysteines in an arrangement similar to that found in 7Fe Fds, that is, -$\underline{\underline{C}}$–$X_2$–$\underline{\underline{C}}$–$X_2$–$\underline{\underline{C}}$–$X_3$–$\underline{C}$–P- and -$\underline{C}$–$X_2$–$\underline{X}$–$X_2$–$\underline{C}$–$X_3$–$\underline{\underline{C}}$–P- with the $\underline{C}$ and $\underline{\underline{C}}$ residues ligating the $[Fe_3S_4]$ and $[Fe_4S_4]$ clusters, respectively. Support for the proposal that the $[Fe_3S_4]$ cluster is not an isolation artifact comes from the observation that the residue capable of ligating a removable Fe by analogy with 4Fe and 8Fe Fds, $\underline{X}$, is usually a noncoordinating residue such as I, V, L or A. Three lines of evidence point to a direct role for the $[Fe_3S_4]^{+,0}$ cluster in mediating electron transfer to or from the quinone/quinol pool. First, the redox potential of the $[Fe_3S_4]^{+,0}$ couple is commensurate with a role as a ubiquinone/menaquinone oxidoreductase. In succinate dehydrogenases using ubiquinone (E_m = +65 mV) as the electron acceptor, the $[Fe_3S_4]^{+,0}$ cluster has a midpoint potential between +60 and +90 mV, whereas in fumarate reductases using menaquinol (E_m = −74 mV) as the electron donor, the midpoint potential is between −70 and −20 mV; see Table I. Second, soluble preparations of succinate dehydrogenase that are deficient in the $[Fe_3S_4]$ cluster are not able to mediate electron transfer to ubiquinone in reconstitution experiments (*22*). Third, conversion of the $[Fe_3S_4]^{+,0}$ cluster (E_m = −70 mV) to a lower potential $[Fe_4S_4]^{2+,+}$ cluster (E_m = −350 mV) in *E. coli* fumarate reductase, via $\underline{X}$ = V to C site-directed mutagenesis, results in a marked decrease in both the growth rate under conditions requiring a functional fumarate reductase and the catalytic activity using menaquinol as electron donor (*137*). A related study with *B. subtilis* succinate dehydrogenase showed that the $\underline{X}$ = S to C mutation did not effect $[Fe_3S_4]$ to $[Fe_4S_4]$ conversion in this enzyme (*138*), but did result in substantially impaired quinone reductase activity, adding further support to a role for the $[Fe_3S_4]^{+,0}$ cluster in mediating electron transfer to quinone. Furthermore, there is now an example of an archaeal

succinate dehydrogenase complex from *Sulfolobus acidocaldarius* with $\underline{X}$ = C that appears to have a [Fe_4S_4] cluster in place of the [Fe_3S_4] cluster on the basis of EPR studies and has poor activity with the caldariella quinone, the physiological acceptor (*139*).

C. Nitrate Reductase

When *E. coli* is grown anaerobically with nitrate as the respiratory oxidant, it develops a respiratory chain terminated by a membrane-bound quinol : nitrate oxidoreductase (NarGHI) that reduces nitrate to nitrite. The enzyme is a heterotrimer comprising a Mo-cofactor-containing catalytic subunit (NarG; 139 kDa), an Fe–S cluster-containing electron transfer subunit (NarH; 58 kDa), and a heme-containing membrane anchor subunit (NarI; 26 kDa) (*140*). The presence of a single $[Fe_3S_4]^{+,0}$ cluster in addition to multiple $[Fe_4S_4]^{2+,+}$ clusters was first established on the basis of EPR and VTMCD studies of the oxidized and reduced forms of the two subunit (NarGH) soluble enzyme (*24*). More detailed EPR studies coupled with extensive mutagenesis experiments have identified the redox properties, subunit location, and ligation of the $[Fe_3S_4]^{+,0}$ cluster (E_m = +60 mV) and the three $[Fe_4S_4]^{2+,+}$ clusters (E_m = +80, −200, and −400 mV) (*55*, *141*). All four clusters are located in the NarH subunit and coordinated by cysteine residues in Fd-like arrangements, that is, -C–X_2–C–X_2–C–X_3–C-, except that the third group of cysteines, which is responsible for two of the ligands to the [Fe_3S_4] cluster, has W in place of the second C. Hence, the sequence data argues strongly in favor of the $[Fe_3S_4]^{+,0}$ center being an intrinsic redox component of the enzyme *in vivo,* and it has not been possible to assemble a [Fe_4S_4] cluster in this site even in the W to C mutant (*142*). Rather, mutagenesis experiments involving selective removal of individual centers point to a crucial role for the two high-potential clusters in mediating electron transfer from the quinol to the Mo cofactor active site (*141–144*). Although *E. coli* nitrate reductase is closely related to several other Mo-containing oxidoreductases, such as *E. coli* formate dehydrogenase (FdnGHI) (*145*), *Wolinella succinogenes* polysulfide reductase (PsrABC) (*146*), and *E. coli* dimethyl sulfoxide reductase (DmsABC) (*147*), each of these enzymes has four [Fe_4S_4] clusters with complete cysteinyl ligation, in the Fe–S containing electron transfer subunit. Since the nitrate/nitrite couple (E'_m = +420 mV) has by far the highest redox potential of any of the reactions catalyzed by this class of enzymes, it seems reasonable to speculate that the $[Fe_3S_4]^{+,0}$ cluster in nitrate reductase has evolved

in order to facilitate high-potential electron transfer to the Mo active site.

D. Glutamate Synthase

Glutamate synthase, a key enzyme in the nitrogen assimilation pathway in plants and microorganisms, catalyzes the reductive transfer of the amide group from the side chain of glutamine to 2-oxoglutarate to form glutamate; see Table I. The reducing equivalents are provided by NAD(P)H in bacterial enzymes and by ferredoxin in photosynthetic tissues. Both classes of enzyme have a common, highly conserved catalytic subunit (~160 kDa) with FMN as the active site and a single $[Fe_3S_4]^{+,0}$ cluster to mediate electron transfer (*25*, *56*, *58*, *148*). In the case of the NAD(P)H-dependent enzymes, there is an additional subunit (~53 kDa) containing two $[Fe_4S_4]^{2+,+}$ clusters and a FAD which is the site of NAD(P)H oxidation (*149*).

The first suggestion that glutamate synthase contained a $[Fe_3S_4]^{+,0}$ cluster came from EPR and Mössbauer studies of the oxidized and reduced forms of the NAD(P)H-dependent enzyme purified from *A. vinelandii* (*6*, *150*). Definitive evidence for a single $S = 1/2$ $[Fe_3S_4]^+$ cluster in oxidized samples and an $S = 2$ $[Fe_3S_4]^0$ cluster in the dithionite reduced samples came from EPR and VTMCD studies of the Fd-dependent spinach glutamate synthase (*25*). Moreover, addition of Fe(II) ion to spinach glutamate synthase under reducing conditions did not effect conversion to $[Fe_4S_4]$ cluster, indicating that the $[Fe_3S_4]^{+,0}$ cluster was unlikely to be an artifact of oxidative degradation during purification. The specific ligands to the $[Fe_3S_4]$ cluster have yet to be determined, but each of the five Fd-dependent and six NAD(P)H-dependent enzymes in the Swiss Protein data base has a conserved group of closely spaced cysteines, $-C-X_5-C-X_4-C-P-$. By analogy with $[Fe_3S_4]$ clusters in Fds, succinate dehydrogenases, fumarate reductases, and nitrate reductase, it is likely that at least the first two cysteines in this grouping are involved with ligation of the $[Fe_3S_4]$ cluster in glutamate synthases (*25*). The redox potentials of the FMN and $[Fe_3S_4]^{+,0}$ centers in the Fd-dependent spinach enzyme were determined to be -180 and -170 mV, respectively, on the basis of optical and EPR monitored redox titrations (*57*), and to be isopotential with $E_m = -225$ mV by cyclic voltammetry (*58*). While the 50-mV discrepancy in the redox potential of the $[Fe_3S_4]^{+,0}$ couple by these two methods has yet to be resolved, the choice of a $[Fe_3S_4]$ cluster to mediate electron transfer to the FMN active site is probably dictated by

the higher redox potentials generally associated with $[Fe_3S_4]^{+,0}$ couples compared to $[Fe_2S_2]^{2+,+}$ or $[Fe_4S_4]^{2+,+}$ couples.

E. NiFe-Hydrogenase

NiFe-hydrogenases enable microorganisms to use H_2 as an energy source by catalyzing the oxidative cleavage of H_2 to $2H^+$, thereby providing a source of electrons for substrate reduction and ultimately ATP synthesis. All have a common, highly conserved large subunit (~60 kDa) which contains the binuclear NiFe hydrogen activating center and a smaller, more variable Fe–S cluster subunit, containing one $[Fe_4S_4]$ cluster, or three $[Fe_4S_4]$ clusters, or two $[Fe_4S_4]$ clusters and one $[Fe_3S_4]$ cluster, which mediates electron transfer to the electron acceptor (*151*, *152*). Definitive spectroscopic evidence for a $[Fe_3S_4]^{+,0}$ cluster that could not be converted to a $[Fe_4S_4]$ cluster by addition of Fe(II) ion under reducing conditions initially came from EPR, Mössbauer, and VTMCD studies of the NiFe-hydrogenase from *D. gigas* (*26*, *27*, *59*, *153*) and *Chromatium vinosum* (*154*, *155*). Moreover, on the basis of EPR studies and primary sequence considerations, $[Fe_3S_4]$ clusters are likely to be intrinsic components of many of the NiFe-hydrogenases from sulfate-reducing and photosynthetic bacteria (*151*, *156*).

The structure of the novel binuclear NiFe active site and the identity of the diatomic ligands at the Fe site as one CO and two CN^- has been determined by the combination of crystallographic and FTIR studies (*157–161*). The crystallographic results for *D. gigas* NiFe hydrogenase (*157*) also revealed the electron transport pathway to the active site, the ligation of the Fe–S clusters in the small subunit, the origin of the variability in the sequence, and Fe–S cluster content among NiFe-hydrogenases in general. The Fe–S subunit invariably contains an N-terminal domain with four conserved cysteines in a unique arrangement that ligate the $[Fe_4S_4]^{2+,+}$ cluster proximal to the NiFe center. Variability occurs in the C-terminal domain, which is absent, or has an arrangement of eight cysteines analogous to that of an 8Fe–Fd, or has a novel fold with six or seven cysteines that ligate two $[Fe_4S_4]^{2+,+}$ clusters or one $[Fe_4S_4]^{2+,+}$ and one $[Fe_3S_4]^{+,0}$ cluster. This C-terminal domain has -H–X_2–C–$X_{\sim 26}$–C–X_5–C–X_8–C–X_{10}–$\underline{X}$–X_6–C–X_2–C- with $\underline{X}$ = C for domains containing two $[Fe_4S_4]$ clusters and $\underline{X}$ = P for domains containing one $[Fe_3S_4]$ and one $[Fe_4S_4]$ cluster. The crystallographically characterized enzymes from *D. gigas* (*157*) and *Desulfovibrio vulgaris* Miyazaki (*162*) both have $\underline{X}$ = P, and the structures show that the histidine and the first three cysteine resi-

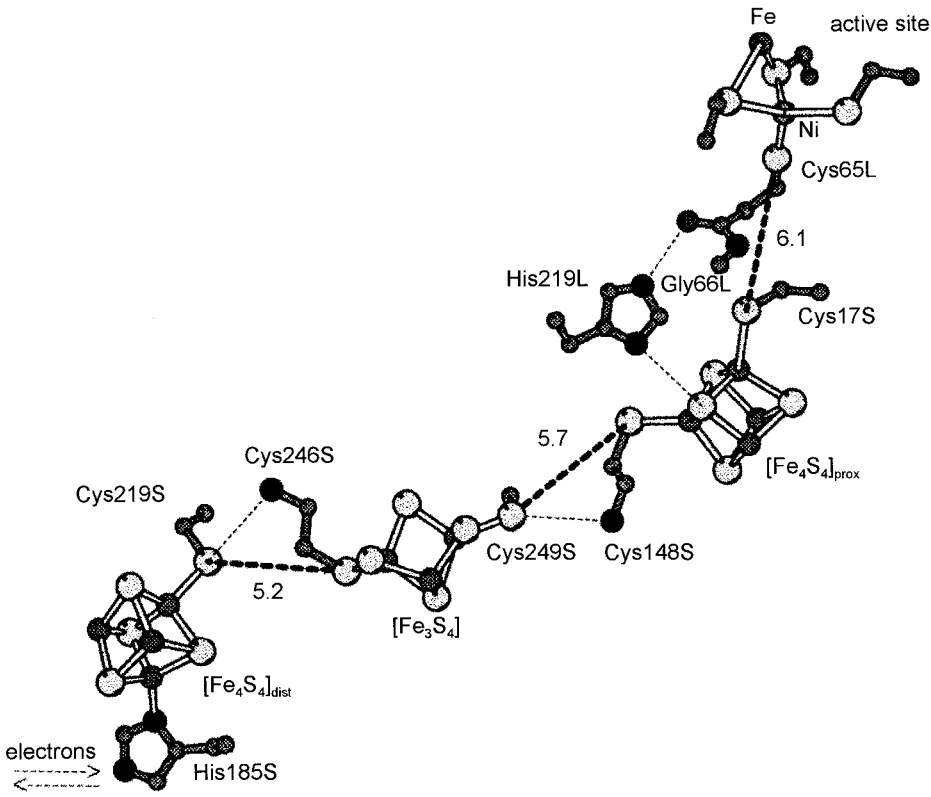

FIG. 1. Proposed electron transport pathway in *D. gigas* NiFe-hydrogenase. Selected distances are given in angstroms. Modified with permission from Ref. (*157*).

dues ligate a distal $[Fe_4S_4]$ cluster and that the last three cysteine residues ligate the $[Fe_3S_4]$ with the proline residue occupying the position of a cysteine that would ligate a potential fourth Fe site. Indeed, in NiFe-hydrogenases such as that from *Desulfovibrio baculatus*, which have $\underline{X}$ = C, EPR and Mössbauer studies have shown that the $[Fe_3S_4]$ cluster has been replaced by a $[Fe_4S_4]$ cluster (*163*). Hence, the structural/sequence data indicate that the $[Fe_3S_4]$ clusters in NiFe-hydrogenases are intrinsic components of the functional enzymes and are ligated by a unique arrangement of cysteines compared to other indigenous $[Fe_3S_4]$ clusters.

The spatial arrangement of the Fe–S clusters in *D. gigas* NiFe-hydrogenase (see Fig. 1) suggests an active role for the $[Fe_3S_4]^{+,0}$ cluster in mediating electron transfer from the NiFe active site to the

distal cluster, which has an exposed histidine ligand. However, the high redox potential of the $[Fe_3S_4]^{+,0}$ cluster (−70 mV) compared to those of the two flanking $[Fe_4S_4]^{2+,+}$ clusters (−290 and −340 mV at pH 7) (*59*) and the reaction being catalyzed (−413 mV at pH 7), coupled with the absence of this cluster in some NiFe-hydrogenases, raises doubts about its involvement in electron transfer. Morevoer, conversion of the $[Fe_3S_4]^{+,0}$ cluster to a $[Fe_4S_4]^{2+,+}$ cluster in *Desulfovibrio fructosovorans* NiFe-hydrogenase via a P238C mutation resulted in a 300-mV decrease in the midpoint potential, but had only a slight effect on the enzymatic activity (*164*). The implication is that the $[Fe_3S_4]^{+,0}$ cluster is not required for efficient electron transfer through the Fe–S subunit, and the role of this cluster in NiFe-hydrogenases remains an enigma.

IV. Structures

X-ray crystal structures are now available for six proteins containing $[Fe_3S_4]$ clusters: *A. vinelandii* FdI (*124*, *165*); *D. gigas* FdII (*19*, *61*, *166*); *Sulfolobus* 7Fe Fd (*114*); mitochondrial aconitase (*167*); and NiFe-hydrogenases from *D. gigas* (*157*, *158*) and *D. vulgaris* Miyazaki (*162*). In each case the structure has been determined for the oxidized protein containing a $[Fe_3S_4]^+$ cluster, and *A. vinelandii* FdI is currently the only protein for which the structure has been obtained for both oxidized and reduced forms containing $[Fe_3S_4]^+$ and $[Fe_3S_4]^0$ clusters, respectively (*124*). However, average Fe–Fe and Fe–S distances have been determined by EXAFS for the $[Fe_3S_4]^+$ and $[Fe_3S_4]^0$ clusters in *P. furiosus* Fd (G. N. George, R. C. Prince, S. J. George, Z. H. Zhou, M. W. W. Adams, and I. J. Pickering, unpublished results) and *D. gigas* FdII (*16*), as well as for the $[Fe_3S_4]^+$ cluster in mitochondrial aconitase (*16*). These EXAFS studies and the crystallographic data for *A. vinelandii* FdI were important in demonstrating that the overall $Fe_3(\mu_3\text{–}S)(\mu_2\text{–}S)_3(S(Cys))_3$ structure of the oxidized cluster (best visualized as a cubane-type $[Fe_4S_4]$ center minus one Fe atom) is preserved on one-electron reduction. This has been confirmed by the synthesis of a model complex, $[Fe_3S_4(LS_3)]^{3-}$ (LS_3 is a trithiolate cavitand ligand), which has a $[Fe_3S_4]^0$ core with properties analogous to those of the protein counterparts (*49*).

A summary of the Fe–Fe and Fe–S distances in cuboidal $[Fe_3S_4]^{+,0}$ centers as deduced by X-ray crystallography and EXAFS, is given in

TABLE III

METRIC DATA FOR CUBOIDAL $[Fe_3S_4]$ CLUSTERS AS DETERMINED BY CRYSTALLOGRAPHIC STUDIES[a]

Protein/model	Resolution (Å)	Oxidation state	Fe–Fe (Å)		Fe–μ_3S (Å)		Fe–μ_2S (Å)		Fe–S(Cys/L) (Å)		Ref.
			Values	Ave.	Range	Ave.	Range	Ave.	Range	Ave.	
$[Fe_3S_4(LS_3)]^{3-}$		$[Fe_3S_4]^0$	2.67, 2.71, 2.73	2.70	2.27–2.33	2.31	2.24–2.28	2.26	2.31–2.33	2.32	*50*[b]
A. vinelandii FdI											
pH 7.8	1.35	$[Fe_3S_4]^+$	2.64, 2.67, 2.73	2.68	2.27–2.33	2.31	2.21–2.29	2.25	2.29–2.32	2.31	*165*
pH 8	1.9	$[Fe_3S_4]^+$	2.64, 2.65, 2.71	2.67	2.26–2.29	2.27	2.25–2.30	2.28	2.27–2.31	2.29	*124*
pH 6	2.1	$[Fe_3S_4]^+$	2.60, 2.61, 2.71	2.64	2.25–2.28	2.27	2.27–2.32	2.29	2.27–2.31	2.29	*124*
pH 8	2.1	$[Fe_3S_4]^0$	2.54, 2.62, 2.65	2.60	2.23–2.26	2.24	2.27–2.33	2.29	2.28–2.35	2.31	*124*
pH 6	2.2	$[Fe_3S_4]^0$	2.57, 2.60, 2.65	2.61	2.28–2.29	2.28	2.25–2.30	2.28	2.27–2.28	2.28	*124*
D. gigas FdII	1.7	$[Fe_3S_4]^+$	2.70, 2.76, 2.79	2.75	2.31–2.32	2.32	2.22–2.33	2.27	2.22–2.29	2.26	*61*
Sulfolobus 6Fe Fd											
Cluster I	2.0	$[Fe_3S_4]^+$	2.63, 2.66, 2.71	2.67	2.32–2.33	2.32	2.31–2.43	2.33	2.31–2.31	2.31	*114*
Cluster II	2.0	$[Fe_3S_4]^+$	2.58, 2.61, 2.62	2.60	2.29–2.32	2.31	2.26–2.30	2.28	2.28–2.30	2.29	*114*
Aconitase	2.1	$[Fe_3S_4]^+$	2.53, 2.58, 2.65	2.59	2.27–2.31	2.28	2.28–2.36	2.33	2.26–2.29	2.28	*167*[c]
D. gigas NiFe H_2ase	2.5	$[Fe_3S_4]^+$	2.69, 2.75, 2.77	2.74	2.25–2.29	2.27	2.21–2.35	2.26	2.25–2.35	2.29	*158*

[a] All metric data for proteins are taken from the structures deposited in the Brookhaven Protein Data Bank.

[b] LS_3 is the trithiolate cavitand ligand, 1,3,5-tris((4,6-dimethyl-3-mercaptophenyl)thio)-2,4,6-tris(*p*-tolylthio)benzene(3-).

[c] The Fe–Fe distances in the published article, 2.64, 2.71, 2.73 Å, differ significantly from those deduced from the structure deposited in the Protein Data Bank.

Tables III and IV, respectively. Overall, the crystallographic data indicate Fe–Fe distances ranging from 2.53 to 2.79 Å (average = 2.67 Å) and Fe–S distances ranging from 2.21 to 2.36 Å (average = 2.29 Å). At first sight, the large variation in Fe–Fe distances, in particular, suggests significant variations in core structure. However, the variance in the interatomic distances is within the limits of experimental error for the protein crystal structures refined at resolutions ≥2 Å (*168*). Hence, meaningful assessment of the variability and distortions in the core structures of $[Fe_3S_4]^{+,0}$ clusters, must be confined to a comparison of the two high-resolution protein structures (*A. vinelandii* FdI at 1.35 Å resolution and *D. gigas* FdII at 1.7 Å resolution),

TABLE IV

AVERAGE Fe–Fe AND Fe–S DISTANCES FOR $[Fe_3S_4]$ CLUSTERS AS DETERMINED BY EXAFS

Protein	Oxidation state	Fe–Fe (Å)	Fe–S (Å)	Ref.
D. gigas FdII	$[Fe_3S_4]^+$	2.70	2.25	*16*
	$[Fe_3S_4]^0$	2.67	2.27	*16*
Aconitase	$[Fe_3S_4]^+$	2.71	2.24	*15*
P. furiosus Fd	$[Fe_3S_4]^+$	2.67	2.24	*a*
	$[Fe_3S_4]^0$	2.67	2.27	*a*

[a] George, G. N., Prince, R. C., George, S. J., Zhou, Z. H., Adams, M. W. W., and Pickering, I. J., unpublished results.

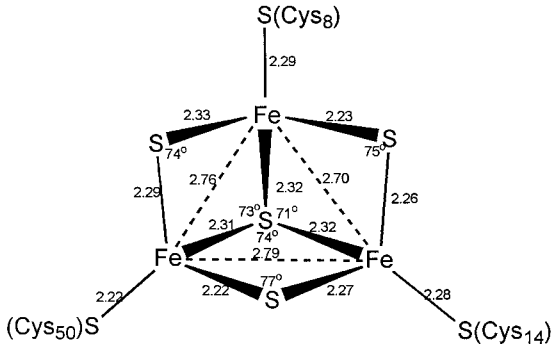

Dg FdII
$[Fe_3S_4]^+$

Bond angles	Ave	Range
∠(μ_2S-Fe-μ_2S)	107°	105-109°
∠(μ_2S-Fe-μ_3S)	103°	101-105°
∠(S-Fe-S(Cys))	114°	106-121°

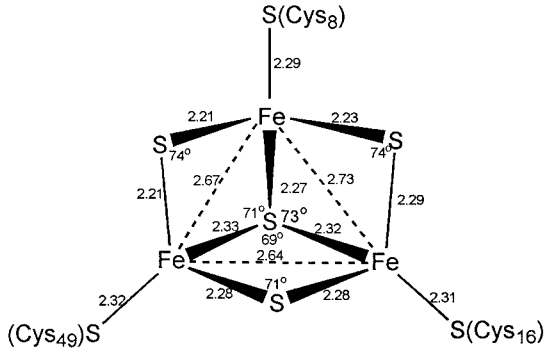

Av FdI
$[Fe_3S_4]^+$

Bond angles	Ave	Range
∠(μ_2S-Fe-μ_2S)	113°	111-115°
∠(μ_2S-Fe-μ_3S)	104°	100-106°
∠(S-Fe-S(Cys))	112°	107-116°

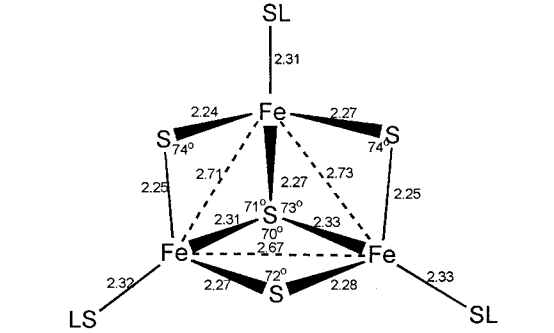

$[Fe_3S_4(LS_3)]^{3-}$
$[Fe_3S_4]^0$

Bond angles	Ave	Range
∠(μ_2S-Fe-μ_2S)	113°	112-114°
∠(μ_2S-Fe-μ_3S)	104°	102-106°

FIG. 2. Metrical data for [Fe_3S_4] clusters taken from the high-resolution crystal structures of *D. gigas* FdII (1.7 Å resolution) (*19*, *61*, *166*), *A. vinelandii* FdI (1.35 Å resolution) (*165*), and the model complex $(Et_4N)_3[Fe_3S_4(LS_3)]$ (*50*).

together with the structure of the synthetic complex and the EXAFS data. Bond angles and interatomic distances for the three high-resolution crystal structures are compared in Fig. 2.

Metrical parameters for the $[Fe_3S_4]^+$ cluster in *A. vinelandii* FdI and the $[Fe_3S_4]^0$ in the model complex have been determined to an accu-

racy of at least 0.01 Å or 1° and the close correspondence is particularly striking (*165*). The average Fe–S bond lengths are the same within experimental error, and the Fe–μ_2S bonds are on average 0.05 Å shorter than the Fe–μ_3S and Fe–S(Cys/L) bonds. The average Fe–Fe distances are very close (2.68 and 2.70 Å) and lie within the range established by EXAFS studies of protein-bound $[Fe_3S_4]^{+,0}$ clusters (2.67–2.71 Å). The average μ_2S–Fe–μ_2S bond angles (113° in both) are 9° larger than the average μ_2S–Fe–μ_3S bond angles (104° in both), consistent with a more open or splayed configuration compared to a cubane $[Fe_4S_4]$ cluster as a result of the removal of an Fe (*50*). Perhaps the most significant difference lies in the distribution of the Fe–Fe distances: one short (2.67 Å) and two long (2.71 and 2.73 Å) for the $[Fe_3S_4]^0$ cluster in the model complex, compared to one long (2.73 Å) and two short (2.64 and 2.67 Å) for the $[Fe_3S_4]^+$ cluster in *A. vinelandii* FdI. Although it has yet to be proven, it is tempting to speculate that the pseudomirror symmetry that is apparent in the model complex is a consequence of the short Fe–Fe interaction corresponding to the valance-delocalized $Fe^{2.5+}$–$Fe^{2.5+}$ pair (*50*); see later discussion.

The structure of *D. gigas* FdII has been refined at 1.7 Å resolution, and the estimated variance in the cluster interatomic distances is $\leq$0.05 Å (*19*, *61*). Bearing this limit of accuracy in mind, there do appear to be some significant differences in the structures of the $[Fe_3S_4]^+$ centers in *D. gigas* FdII and *A. vinelandii* FdI (*165*); see Fig. 2 and Table III. The Fe–Fe distances are longer in FdII (range 2.70–2.79 Å, average 2.75 Å, vs range 2.64–2.73 Å, average 2.68 Å in FdI) and the Fe–S(Cys) distances are shorter in FdII (range 2.22–2.29 Å, average 2.26 Å, vs range 2.29–2.32 Å, average 2.31 Å in FdI). Furthermore, the splayed configuration is much less pronounced in FdII as judged by the difference in the average μ_2S–Fe–μ_2S and μ_2S–Fe–μ_3 S bond angles (4° vs 9° in FdI), and the shortest Fe–Fe distance occurs between the Fe atoms ligated by the N-terminal and middle cysteines (Cys8 and Cys14) in FdII as opposed to middle and C-terminal cysteines (Cys16 and Cys49) in FdI. Therefore, it seems likely that the $[Fe_3S_4]^+$ clusters have somewhat different distortions in the crystalline forms of these two proteins. However, the possibility that these structures are not maintained in frozen solution is raised by EXAFS studies of oxidized *D. gigas* FdII, which indicate a significantly shorter average Fe–Fe distance (2.70 Å) than the crystallographic data (2.75 Å); see Tables III and IV.

Unfortunately, the question of the core structural changes accompa-

nying reduction are poorly addressed by the available structures. What is required are high-resolution crystal structures of a protein or the model complex with the cluster in each of the accessible redox states. EXAFS studies of *D. gigas* FdII and *P. furiosus* Fd indicate that the structural changes accompanying one-electron reduction are likely to be small; see Table IV. The average Fe–Fe distance in the $[Fe_3S_4]^0$ clusters (2.67 Å) was unchanged and showed a 0.03-Å increase on one-electron oxidation of *P. furiosus* Fd and *D. gigas* FdII, respectively. In accord with the increase in formal oxidation state of the Fe from +2.67 to +3.0, the average Fe–S distance (2.67 Å) decreased by 0.03 and 0.02 Å on one-electron oxidation of *P. furiosus* Fd and *D. gigas* FdII, respectively. X-ray crystal structures have been refined at 1.9–2.2 Å resolution for oxidized and reduced forms of *A. vinelandii* FdI at pH 8 and 6 (*124*). The results added support to mutagenesis studies that indicated that a nearby aspartate residue (Asp15) participates in the protonation of the $[Fe_3S_4]^0$ cluster (pK_a = 7.7) (*169*) and showed that no major structural changes in the [Fe_3S_4] center accompany reduction and/or protonation. However, the resolution was not sufficient to address in detail the structural changes in the [Fe_3S_4] core. Indeed, in contrast to the EXAFS data for *D. gigas* FdII and *P. furiosus* Fd, the crystallographic data, taken at face value, for the unprotonated form (pH 8), would indicate that one-electron reduction is accompanied by a 0.07-Å decrease in the average Fe–Fe distance and no change in the average Fe–S distance; see Table III.

V. Electronic, Magnetic, and Vibrational Properties

Many techniques have contributed to the current understanding of the electronic properties and intracluster magnetic interactions of biological [Fe_3S_4] clusters. EPR, ENDOR, Mössbauer, VTMCD, saturation magnetization, and resonance Raman studies have been used to elucidate ground-state magnetic and vibrational properties, and excited-state electronic structure has been assessed by absorption, CD, VTMCD, and resonance Raman. Mössbauer has played a particularly crucial role by demonstrating the presence of valence delocalized $Fe^{2.5+}Fe^{2.5+}$ pairs in both $[Fe_3S_4]^0$ clusters and $[Fe_3S_4]^-$ cluster fragments. Hence, valence delocalized pairs are crucial for understanding both the redox and electronic properties of [Fe_3S_4] clusters, and the past few years have witnessed major new insights into the properties and factors responsible for the generation of these units. A summary of the current picture of the valence delocalization schemes in each

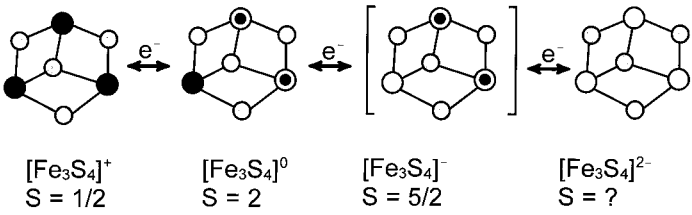

FIG. 3. Ground state spin (S) and valence delocalization schemes for the known oxidation states of $[Fe_3S_4]$ clusters. Discrete $[Fe_3S_4]^-$ clusters have not been observed in any protein, but they have been identified as fragments in heterometallic cubane clusters. Reduction of the $[Fe_3S_4]^+$ cluster by three electrons, to yield a putative all-ferrous cluster, occurs with the concomitant addition of three protons. Key: S^{2-}, grey; Fe^{3+}, black; Fe^{2+}, white; $Fe^{2.5+}$, white with central black dot.

for the known oxidation states of $[Fe_3S_4]$ clusters is presented in Fig. 3. The objective of this section is to summarize the electronic, magnetic, and vibrational properties of $[Fe_3S_4]$ clusters in each of these four redox states in light of the structural data discussed previously.

A. $[Fe_3S_4]^+$ CLUSTERS

1. Ground-State Properties

The fundamental ground-state properties of $[Fe_3S_4]^+$ clusters were revealed in the original EPR and Mössbauer studies of *A. vinelandii* FdI (*6*) and *D. gigas* FdII (*7*). These studies showed an $S = \frac{1}{2}$ ground state with an EPR signal centered around $g = 2.01$, which results from magnetic interaction between three high-spin ($S = \frac{5}{2}$) Fe^{3+} centers with rubredoxin-like isomer shift and quadrupole splitting parameters ($\delta \sim 0.3$ mm/s and $\Delta E_Q \sim 0.6$ mm/s), that is, tetrahedral sulfur coordination; see Table V. Three magnetically inequivalent Fe sites with substantially different ^{57}Fe coupling constants were apparent in Mössbauer spectra recorded in applied magnetic fields up to 6 T at 1.5 K; $A_1 = -38$ MHz, $A_2 = +22$ MHz, $A_3 = -2$ MHz for *D. gigas* FdII (*7,66*); $A_1 = -42$ MHz, $A_2 = +17$ MHz, $A_3 = +2$ MHz for *A. vinelandii* FdI (*6*, *72*). Similar values have been established by Mössbauer and/or ^{57}Fe-ENDOR in all the $[Fe_3S_4]^+$ clusters investigated thus far; see Table V. These coupling constants and the $S = \frac{1}{2}$ ground state were successfully rationalized in terms of a simple spin coupling model for three sites having intrinsic hyperfine interactions similar to those of ferric rubredoxin (*30*). A simple HDvV exchange Hamiltonian of the form $\mathcal{H} = J_{12}S_1 \cdot S_2 + J_{23}S_2 \cdot S_3 + J_{13}S_1 \cdot S_3$ involving three high-spin Fe^{3+} ions ($S_1 = S_2 = S_3 = \frac{5}{2}$) predicts an $S = \frac{1}{2}$

TABLE V

SUMMARY OF EPR *g*-VALUES, ^{57}Fe-HYPERFINE COUPLING CONSTANTS, ISOMER SHIFTS, AND QUADRUPOLE SPLITTINGS FOR SOME REPRESENTATIVE $[Fe_3S_4]^+$ CLUSTERS

Protein	*g*-values[a]	*A*-values (MHz)[b]	δ (mm/s)	ΔE_Q (mm/s)	Refs.
D. gigas FdII	2.02, 2.00, 1.97	−39, +22, −2	0.28	0.54	*7*, *66*
P. furiosus Fd	2.30, 1.95, ~1.87	−38, +26, −11			*42*, *170*
A. vinelandii FdI	2.02, 2.01, ~1.99	−42, +17, +2	0.30	0.63	*6*, *72*, *171*
T. thermophilus 7Fe Fd	2.024, 1.992, 1.936	(−37, +26, +5)[c]	0.28	0.53	*93*, *94*
D. gigas hydrogenase	2.032, 2.024, 2.016	−44, +20, ~+3	0.33	0.70	*59*, *153*, *172*
	2.029, 2.017, 2.003	−39, +23, ud[d]			
C. vinosum hydrogenase	2.018, 2.016, 2.002	−44, +12, ud[d]	0.26	0.65	*155*, *173*
Bovine heart aconitase					
$[Fe_3S_4]^+$	2.024, 2.016, 2.004	−31, +28, −11	0.27	0.72	*13*, *174*, *175*
$[Fe_3Se_4]^+$	2.04, 1.985, 1.92	−32, +26, ud[d]	0.30	0.66	*174*
Bovine heart succinate dehydrogenase	2.018, 2.011, 1.990				*171*
E. coli fumarate reductase	2.02, 1.98, ~1.93				*23*
E. coli nitrate reductase	2.02, 2.00, ~1.94				*24*
Spinach glutamate synthase	2.02, 1.94, ~1.86				*25*

[a] *g*-values are based on published and unpublished (M. K. Johnson and co-workers) simulations of the resonances and may not accurately reflect the principal components of the *g*-tensor as explained in the text.

[b] Average *A*-values for each Fe as determined by Mössbauer and/or ^{57}Fe-ENDOR.

[c] Approximate values.

[d] Undetermined.

ground state, provided all the coupling constants are greater than zero, $J_{ij} > 0$, that is, antiferromagnetic interaction, and $0.5 < J_{13}/J_{23} < 1$, $0.6 < J_{12}/J_{23} < 1$, and $|J_{12} - J_{13}|/J_{12} < 0.2$, that is, asymmetric coupling with $J_{12} \approx J_{13} < J_{23}$, but with comparable values for all three coupling constants. Such a model predicts that the first excited state will also have $S = \frac{1}{2}$, provided $0.8 < J_{12}/J_{23} < 1$, with the ground state corresponding to the more strongly coupled pair having $S_{23} = 2$ ($S_{23} = S_2 + S_3$) and the first excited state corresponding to $S_{23} = 3$. Population of the low-lying $S = \frac{1}{2}$ excited state has been invoked to explain the EPR relaxation properties and the anomalous temperature dependence of the EPR lineshape exhibited by $[Fe_3S_4]^+$ clusters in some bacterial Fds, such as *D. gigas* FdII (*176*). However, this analysis leads to an estimate of J of around 40 cm^{-1}, which is much lower than the lower limit of 200 cm^{-1} for J determined in subsequent saturation magnetization studies of oxidized *D. gigas* FdII (*177*) and the value estimated based on NMR studies of the β-CH_2 cysteinate protons of the $[Fe_3S_4]^+$ cluster in the same protein, $J = 300$ cm^{-1} (*178*). Strong support for the values based on the saturation magnetization and NMR analyses comes from the determination of the exchange cou-

pling constant of an Fe^{3+}–Fe^{3+} pair in a cubane-type $[Fe_4S_4]$ cluster, $J \approx 300$ cm^{-1} (*179*).

Initial identification of an $[Fe_3S_4]$ cluster in a metalloprotein is usually based on a fast-relaxing EPR resonance centered around $g = 2.01$ in the oxidized protein, that is only observed at temperatures below 30 K. However, these resonances frequently differ significantly in terms of both lineshape and apparent g-value anisotropy in different proteins; see Table V. In general they exhibit a well-defined low-field g-value at $g \sim 2.02$, but frequently have poorly resolved high-field components due to conformational microheterogeneity in the cluster structure (*180*), which results from a distribution in the single Fe^{3+} ion zero-field splitting (D) and exchange coupling parameters (J) in frozen samples (*172*, *181*, *182*); see Table V. This can be viewed as a type of "g-strain" (*183*) that can qualitatively alter the observed spectrum rather than being apparent solely in terms of linewidth contributions. Hence, the g-values obtained for spectral simulations do not necessarily correspond to the principal components of the g-tensor.

The importance of the cluster environment in determining the EPR properties of $[Fe_3S_4]^+$ clusters has been demonstrated by mutagenesis studies of *P. furiosus* 3Fe Fd (*184*). EPR spectra spanning the entire range of those observed for $[Fe_3S_4]^+$ clusters in Fds were observed by varying the residue proximal to the tri(μ_2-S) face of the cluster (D14 in the wild type); see Fig. 4. To a first approximation, the spectra fall into two types with D14, D14H, D14S, and D14N displaying particularly broad spectra, indicative of severe protein conformational distribution, compared to those of D14Y, D14C, and D14V. On the basis of VTMCD studies of the reduced samples (see later discussion) and the two distinct types of sequence-specific assignments that have been deduced via NMR studies of oxidized 3Fe Fds (see later discussion), we have proposed that these two types of EPR characteristics reflect different pairings for the more strongly coupled irons (*184*). A detailed analysis of the ^{57}Fe hyperfine coupling constants of the $[Fe_3S_4]^+$ cluster in wild-type *P. furiosus* Fd, as deduced by ^{57}Fe-ENDOR (see Table V), indicated that the ground state corresponds to the more strongly coupled pair having $S_{23} = 2$, as in other Fds (*170*). However, the ground state has more mixing of the low-lying $S = \frac{1}{2}$ state with $S_{23} = 3$ than other 3Fe Fds, as a result of less symmetrical coupling, and this presumably accounts for the extremely broad g distribution associated with this conformation.

NMR is the only technique capable of assigning the cysteines ligating specific Fe atoms, since the asymmetric coupling of the three Fe^{3+} ions results in different temperature dependence for the contact shifts

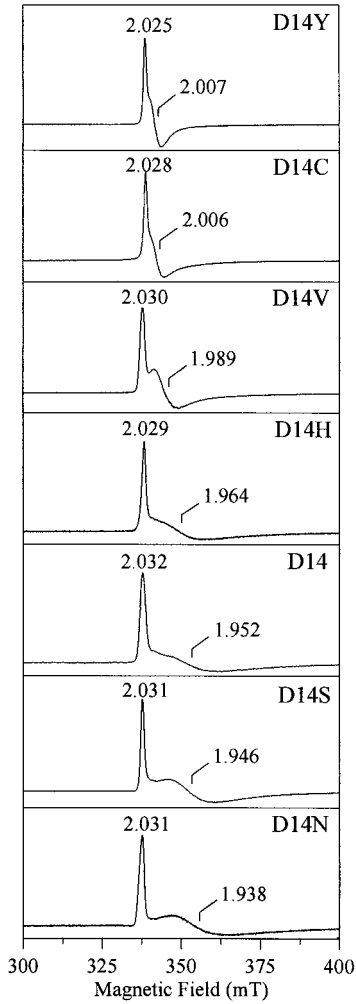

FIG. 4. X-band EPR spectra of $[Fe_3S_4]^+$ clusters in wild type and mutant forms of *P. furiosus* Fd. All spectra were recorded at 4.2 K; microwave power, 1 mW; microwave frequency, 9.60 GHz; modulation amplitude, 0.63 mT. All samples were in 100 mM Tris-HCl buffer, pH 7.8.

of the β-CH_2 protons of coordinating cysteine residues. This approach has thus far been applied to three 3Fe Fds and two distinct types of sequence-specific assignments have been observed. The unique Fe site in the preceding coupling scheme (S_1) was found to be ligated by the N-terminal cysteine in *P. furiosus* Fd (*185*) and by the C-terminal

cysteine in *D. gigas* FdII (*178*) and *Thermococcus litoralis* Fd (*186*). *D. gigas* FdII and *T. litoralis* Fd have a cysteine in the position equivalent to residue 14 in *P. furiosus* Fd and have EPR spectra identical to that of the D14C mutant of *P. furiosus* Fd. Hence, the very broad type of EPR spectra (typified by wild-type *P. furiosus* Fd) and the more narrow type of EPR spectra (typified by *D. gigas* FdII) are tentatively attributed to the more unique Fe site being ligated by the N-terminal and C-terminal cysteines, respectively. Sequence-specific NMR assignments of the β-CH_2 protons of the cysteines ligating the $[Fe_3S_4]^+$ clusters in numerous *Azotobacter*-type 7Fe Fds (*74*, *81*, *90*, *102*) and one *Defulfovibrio*-type 7Fe Fd (*121*) have also been reported. These data have been reinterpreted on the basis of an NMR study of the *Azotobacter*-type 7Fe Fd from *R. palustris* (90), and in each case the unique Fe sites is believed to be ligated by the C-terminal cysteine. At present it is difficult to see how this coupling scheme relates to the crystal structures, since the more strongly coupled pair corresponds to the shortest Fe–Fe distance in *D. gigas* FdII and the longest Fe–Fe distance in *A. vinelandii* FdII, see Fig. 2.

This analysis raises the possibility that different conformations, possibly with distinct pairwise Fe interactions, might be present in frozen solution samples of some protein-bound $[Fe_3S_4]^+$ clusters. Indeed, this might provide an alternative explanation for the anomalous temperature dependence of the EPR lineshape exhibited by $[Fe_3S_4]^+$ clusters in some bacterial Fds, such as *D. gigas* FdII (*176*). The first direct evidence for this type of behavior was provided by EPR and ^{57}Fe-ENDOR studies of the $[Fe_3S_4]^+$ cluster in *D. gigas* NiFe-hydrogenase (*172*). The EPR resonance is much narrower than those associated with $[Fe_3S_4]^+$ clusters in Fds, presumably because of the different arrangement of coordinating cysteine residues. As a result, X-band and Q-band EPR studies were able to resolve two resonances, g = 2.032, 2.024, 2.016 (70%) and g = 2.029, 2.017, 2.003 (30%), with similar although not identical ^{57}Fe coupling constants as determined by ENDOR (*172*) and Mössbauer (*59*, *153*); see Table V. On the basis of the 3Fe Fd data, these forms are likely to reflect different pairwise Fe interactions, but there is as yet no direct evidence for this interpretation.

The multifrequency EPR and Mössbauer properties of the $[Fe_3S_4]^+$ in *C. vinosum* NiFe-hydrogenase are particularly interesting since they provide evidence of magnetic interactions with nearby paramagnetic species (*151*, *154*, *155*). The magnetically isolated form exhibits a well-resolved, almost axial EPR signal, g = 2.018, 2.016, 2.002, indicative of minimal conformational heterogeneity. However, a com-

plex resonance corresponding to up to 50% of the [Fe_3S_4] clusters appears at potentials $> +150$ mV and has been shown to result from weak magnetic interactions involving the $S = \frac{1}{2}$ Ni^{3+} center, the $S = \frac{1}{2}$[Fe_3S_4]$^+$ cluster, and an as yet unidentified $S = \frac{1}{2}$ species. By clamping the Ni in the diamagnetic Ni^{2+}–CO form, the interaction signal from the [Fe_3S_4]$^+$ cluster and the unidentified $S = \frac{1}{2}$ species can be observed in isolation, $g = 2.01$, 1.974, and 1.963 at X-band. This resonance has been tentatively interpreted in terms of an $S = 1$ species resulting from ferromagnetic interaction between two $S = \frac{1}{2}$ species, on the basis of Mössbauer (*155*) and EPR (*187*) studies. However, the nature of the unidentified $S = \frac{1}{2}$ species still remains elusive. A radical species resulting from oxidation of a cluster ligand or nearby residue now seems more likely than the original suggestion of a nearby low-spin Fe^{3+} center (*155*), in light of the available crystallographic data for NiFe-hydrogenases (*157*, *158*, *162*). However, it should be borne in mind that although this magnetic interaction is apparent in several NiFe-hydrogenases (*151*), it has not been observed in either of the two crystallographically defined NiFe-hydrogenases.

The ground-state properties of the [Fe_3S_4]$^+$ cluster in inactive aconitase have been extensively characterized by EPR and Mössbauer (*13*, *175*); see Table V. Overall, the EPR resonance, $g = 2.024$, 2.016, 2.004, is more isotropic than in Fds and similar to those observed in NiFe-hydrogenases, albeit with increased linewidths. This may be a consequence of the more "hydrogenase-like" arrangement of the coordinating cysteine residues (Cys358, Cys421, and Cys424 in mitochondrial aconitase (*167*, *175*)). Aconitase has also provided the only example of [Fe_3S_4]$^+$ suitable for spectroscopic investigation (*174*, *188*). Reconstitution of aconitase apoenzyme with selenide and iron to form a [Fe_3S_4]$^{2+,+}$ cluster followed by oxidative degradation with ferricyanide yielded a route to a stable protein-bound [Fe_3S_4]$^{+,0}$ cluster. The ground-state properties of the [Fe_3S_4]$^+$ cluster are largely unperturbed compared to those of the [Fe_3S_4]$^+$ cluster. However, while the overall EPR lineshape is maintained, the resonance is substantially more anisotropic, $g = 2.04$, 1.99, 1.92; see Table V. This is presumably a consequence of the fourfold larger spin–orbit coupling for Se compared to S.

2. *Excited-State Properties*

The relatively broad and featureless absorption spectra of [Fe_3S_4]$^+$ clusters belies their complex excited-state electronic structure. This is illustrated in Fig. 5 using *P. furiosus* 3Fe Fd as an example (42). In addition to the protein band centered at 280 nm, the UV-visible

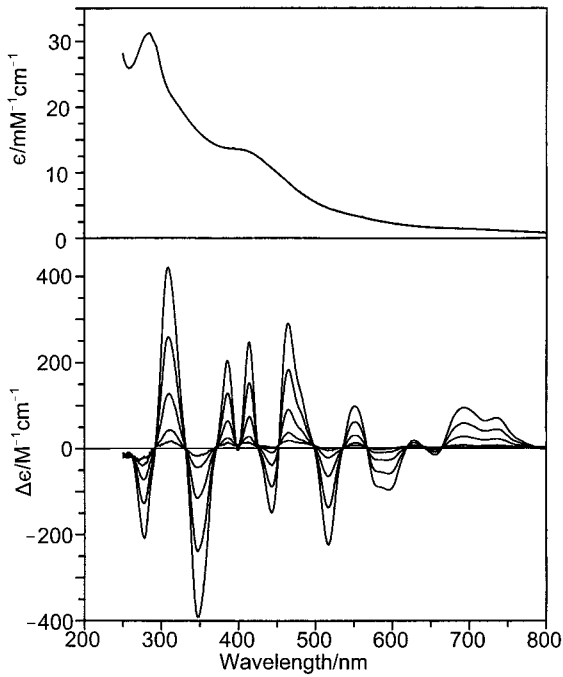

FIG. 5. UV-visible absorption and VTMCD spectra of the $[Fe_3S_4]^+$ cluster in wild-type *P. furiosus* Fd. The absorption spectrum was recorded at room temperature, and the MCD spectra were recorded at 1.59, 4.22, 9.9, 17.6, and 53.0 K (all transitions increase in intensity with decreasing temperature) with an applied magnetic field of 4.5 T.

absorption spectrum extends out to at least 800 nm and comprises broad unresolved shoulders centered at ~340 nm, ~410 nm (ε = 12–15 mM^{-1} cm^{-1} per cluster), ~460 nm, and ~550 nm. These absorption characteristics are qualitatively similar to those of diamagnetic $[Fe_4S_4]^{2+}$ clusters, rendering absorption spectra alone useless for identifying cluster type.

The origin of the broad absorption spectrum and the true complexity of the excited-state electronic structure is only revealed in the VTMCD spectra (*189*). Since only paramagnetic metal chromophores exhibit MCD bands that increase in intensity with decreasing temperature, this technique can be used to investigate the electronic structure of $[Fe_3S_4]^+$ clusters in the presence of additional diamagnetic clusters, metal centers, or other types of prosthetic groups. Bearing in mind that each positive or negative absorption-shaped band corresponds to a discrete electronic transition, at least 17 overlapping elec-

tronic transitions associated with the $[Fe_3S_4]^+$ center are resolved in the VTMCD spectrum in the 200–800 nm region; see Fig. 5. MCD magnetization studies at discrete wavelengths confirm that all transitions originate from the EPR-detectable $S = \frac{1}{2}$ ground state.

The overall pattern of VTMCD bands is highly conserved among biological $[Fe_3S_4]^+$ clusters, making VTMCD a useful adjunct to EPR and/or Mössbauer for assessing or confirming Fe-S cluster type. This is illustrated by the qualitative comparison of the VTMCD spectra of representative examples of biological $[Fe_3S_4]^+$ clusters shown in Fig. 6. Each of the spectra can be resolved into an equivalent series of positive or negative, temperature-dependent Gaussian-shaped bands, and the spectral differences result primarily from minor changes in the relative intensities and/or energies of the discrete MCD transitions. A further illustration of how the excited-state electronic structure of biological $[Fe_3S_4]^+$ clusters is relatively independent of the protein environment has come from mutagenesis studies of *P. furiosus* 3Fe Fd. Except for minor changes in the weak bands in the 600–800 nm region, the VTMCD spectra were found to be almost invariant to changes in the residue occupying the position proximal to the tri(μ_2-S) face of the cluster (i.e., in D14, D14H, D14S, D14N, D14Y, D14C, and D14V) (*184*).

As yet there are no detailed assignments for the electronic transitions associated with $[Fe_3S_4]^+$ clusters. The only direct information comes from VTMCD studies of the $[Fe_3S_4]^+$ cluster in aconitase (*188*). The higher energy transitions in the region 300–420 nm have been attributed primarily to bridging-S^{2-}-to-Fe^{3+} change transfer on the basis of large red shifts in the Se-substituted form. The lower energy bands exhibit less pronounced red and blue shifts in the Se-substituted form and are therefore considered to result primarily from cysteinyl-S-to-Fe^{3+} charge transfer and *d–d* transitions associated with the Fe core.

3. Vibrational Properties

Resonance Raman has been used to investigate the Fe–S stretching frequencies and/or establish the existence of $[Fe_3S_4]^+$ centers in a wide variety of enzymes and proteins: 3Fe Fds from *D. gigas* (*17*, *190*) and *P. furiosus* (*37*, *42*, *191*); 7Fe Fds from *A. vinelandii* (*17*, *192*), *T. thermophilus* (*17*), *P. ovalis* (*193*), and *M. smegmatis* (*98*, *193*); ferricyanide-treated *C. pasteurianum* 8Fe Fd (*11*, *17*); bovine heart aconitase (*194*, *195*); spinach glutamate synthase (*25*); and NiFe-hydrogenases from *D. gigas* (*196*) and *D. desulfuricans* (*194*). The resonant enhancements of Fe–S stretching modes with blue/green excita-

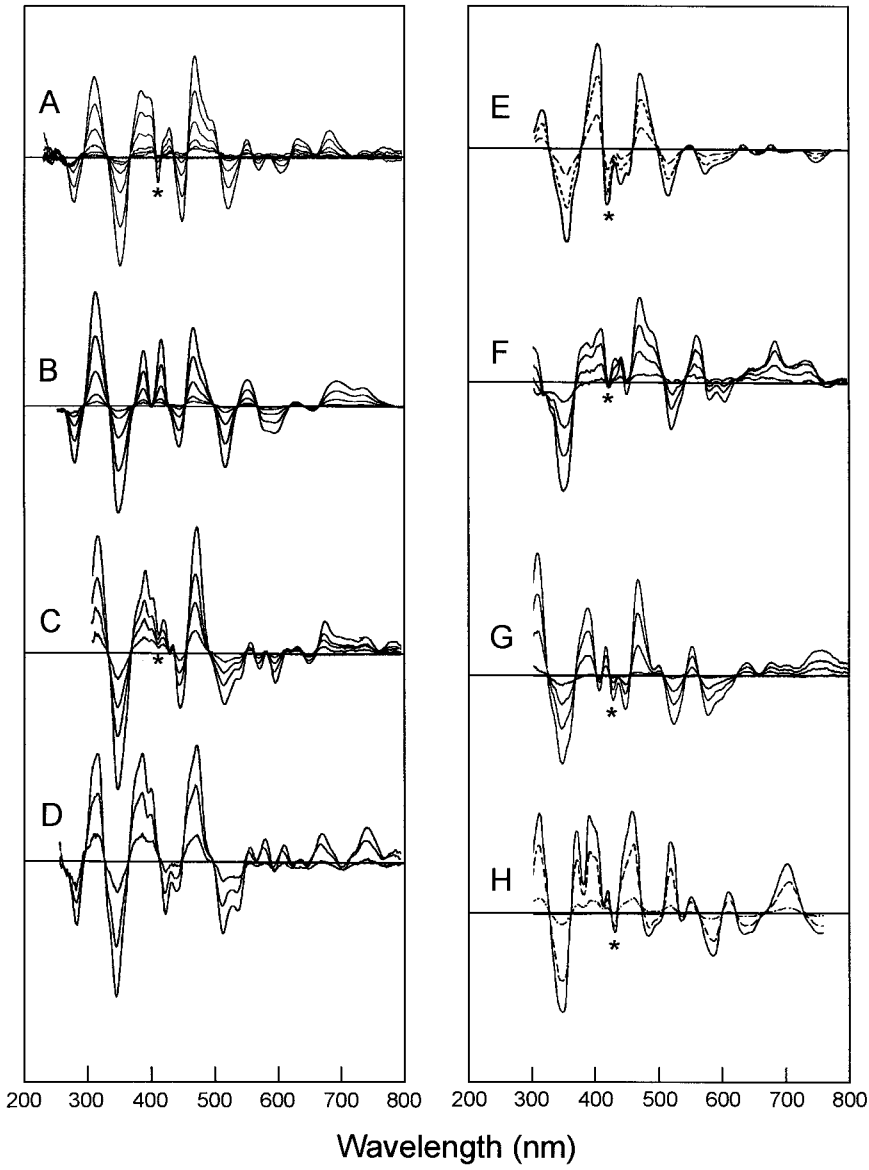

FIG. 6. Comparison of VTMCD spectra for biological $[Fe_3S_4]^+$ clusters. (A) *D. gigas* FdII (*20*); (B) *P. furiosus* 3Fe Fd (*42*); (C) *A. vinelandii* FdI (*70*); (D) *T. thermophilus* 7Fe Fd (*70*); (E) *E. coli* nitrate reductase (*24*); (F) *E. coli* fumarate reductase (*53*); (G) spinach glutamate synthase (*25*); (H) beef heart aconitase (*21*). Spectra were recorded at temperatures between 1.5 and 70 K with an applied magnetic field of 4.5 T (all transitions increase in intensity with decreasing temperature). Bands originating from minor heme contaminants are indicated by an asterisk.

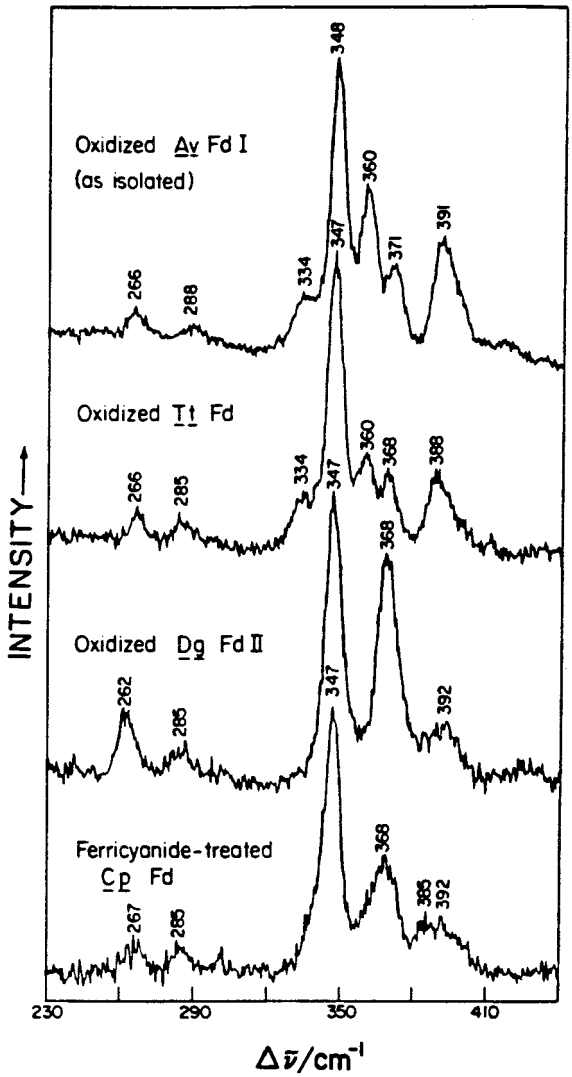

FIG. 7. Low-temperature (77 K) resonance Raman spectra for *A. vinelandii* FdI, *T. thermophilus* Fd, *D. gigas* FdII, and ferricyanide-treated *C. pasteurianum* Fd obtained with 488.0-nm excitation. Taken with permission from Ref. (*17*).

tion are up to five times greater than for $[Fe_3S_4]^{2+}$ clusters. Hence, the resonance Raman spectra of multicluster proteins such as 7Fe Fds and NiFe-hydrogenases are generally dominated by bands from the $[Fe_3S_4]^{+}$ center. This is illustrated in Fig. 7, which compares reso-

nance Raman spectra for the oxidized 7Fe Fds from *A. vinelandii* and *T. thermophilus* with those of two proteins containing a single $[Fe_3S_4]^+$ cluster, that is, *D. gigas* FdII and ferricyanide-treated *C. pasteurianum* Fd (*17*). Since the dominant band in the resonance Raman spectrum of biological $[Fe_3S_4]^{2+}$ clusters using 488.0-nm excitation is the totally symmetric breathing mode of the cubane core, which occurs near 334 cm^{-1}, all bands are attributed to Fe–S stretching modes of the $[Fe_3S_4]^+$ cluster, with the exception of the shoulder at 334 cm^{-1}. The similarity among the spectra is striking. All have resolved bands centered near 265, 290, and 345 cm^{-1}, and a broad ill-defined feature near 390 cm^{-1} corresponding to at least two overlapping bands. The major difference lies in the presence of one or two bands in the 350–380 cm^{-1} region. However these bands were assigned primarily to Fe–S(Cys) modes on the basis on negligible ^{34}S-isotope shifts in samples of ferricyanide-treated *C. pasteurianum* Fd reconstituted with $^{34}S^{2-}$ (*17*); see Table VI. Hence the differences were interpreted in terms of changes in the Fe–S–C–C dihedral angles and/or Fe–S force con-

TABLE VI

VIBRATIONAL FREQUENCIES (cm^{-1}), $^{34}S^b$ ISOTOPE DOWNSHIFTS (cm^{-1} IN PARENTHESES), AND ASSIGNMENTS FOR THE Fe–S STRETCHING MODES OF OXIDIZED $Fe_3S_4^bS_3^t$ CENTERS IN BEEF HEART ACONITASE, *A. vinelandii* FdI, *T. thermophilus* Fd, *P. furiosus* Fd, *D. gigas* FdII, AND *C. pasteurianum* Fd

Assignment C_{3v} symmetry	Calculated[a] $Fe_3S_4(SEt)_3$	Aconitase[a]	*Av* FdI[b]	*Tt* Fd[b]	*Pf* Fd[c]	*Cp* Fd[b]	*Dg* FdII[b]
			Mainly Fe–S^t stretching				
A_1	375(2)	372(1)	371	368	386(2)	385(0)	~392
E	353(2)	359(0)	360	360	367(1)	368(0)	368
			Mainly Fe–S^b stretching				
A_1	402(7)	400(4)	391	388	405(5)	392(0)[d]	~392
E	373(5)				397(6)		
A_1	345(8)	342(8)	348	347	347(7)	347(7)	347
A_2	291(4)				305(4)		
E	274(4)	293(4)	288	285	290(6)	285(4)	285
E	268(3)	264(5)	266	266	265(4)	267(6)	262

[a] Taken from Ref. (*195*).

[b] Frequencies taken from Ref. (*17*).

[c] Taken from Ref. (*191*). Isotope shifts are the average of data collected with 457.9-, 488.0-, and 514.5-nm excitation.

[d] The $^{34}S^b$ isotope shifts was reported as zero (*17*), but the data are of poor quality and the band is not well resolved. The isotope shift needs to be reinvestigated in light of isotope shifts observed for the equivalent band in the high-quality data obtained for aconitase and *Pf* Fd.

stants of the coordinated cysteines rather than structural differences in the [Fe_3S_4] core.

In the 1980s, the distinctive resonance Raman spectrum proved effective in establishing oxidative [Fe_3S_4] to [Fe_3S_4] cluster conversion in bacterial Fds (*11*), identifying [Fe_3S_4]$^+$ clusters in several enzymes and proteins (*197*), and providing some of the most persuasive early evidence for a common [Fe_3S_4] core for biological 3Fe clusters (*17*). However, although the vibrational data were shown to favor a cuboidal [Fe_3S_4] structure, detailed assignments were not attempted at that time because of uncertainty in the core structure. Vibrational assignments for the cuboidal $Fe_3S_4^bS_3^t$ units (S^b bridging or inorganic S; S^t = terminal or cysteinyl S) in aconitase have since been made under effective C_{3v} symmetry based on normal mode calculations and $^{34}S^b$ isotope shifts (*195*); see Table VI. While there is substantial mixing, the two symmetric (A_1) Fe–S^b modes at ~400 cm^{-1} and ~345 cm^{-1} can be considered, to a first approximation, as involving vibrations of μ_2S^b and μ_3S^b types of bridging sulfide. The calculated frequencies were based on the force field used for cubane [Fe_3S_4] clusters, except that one Fe was removed, the FeS–CC dihedral angles were adjusted to those reported in the crystal structure of aconitase, and the six Fe–μ_2S^b force constants were increased by 17% compared to the three Fe–μ_3S^b force constants. The last change would be expected to result in a contraction of 0.07 Å in the Fe–μ_2S^b bonds on the basis of Badger's rule, which is in excellent agreement with the 0.05–0.06 Å contraction reported in the high-resolution crystallographic data for *D. gigas* Fd II, *A. vinelandii* FdI, and the synthetic model compound; see Table III.

High-quality resonance Raman spectra and reliable $^{34}S^b$ isotopes have also been reported for the [Fe_3S_4] cluster in *P. furiosus* 3Fe Fd (*37*, *191*); see Fig. 8 and Table VI. The major difference compared to aconitase lies in the frequencies of the Fe–S^t (Fe–S(Cys)) modes that occur at higher frequencies for the [Fe_3S_4]$^+$ center in *P. furiosus* Fd (12 cm^{-1} higher on average). In general, the resonance Raman spectra of [Fe_3S_4]$^+$ clusters can be subdivided into two groups on the basis of the frequencies of the Fe–S^t modes, with *A. vinelandii* and *T. thermophilus* 7Fe Fds similar to aconitase and *D. gigas* FdII and ferricyanide-treated *C. pasteurianum* Fd corresponding to *P. furiosus* 3Fe Fd; see Table VI. The difference in the Fe–S^t frequencies between the two groups is unlikely to relate to the Fe–S–C–C dihedral angles, since very similar dihedral angles (80° ± 10°, 90° ± 10°, and 115° ± 15°) are observed for the equivalent cysteines in the three crystallographically defined proteins, that is, aconitase (*167*), *A. vinelandii* FdI

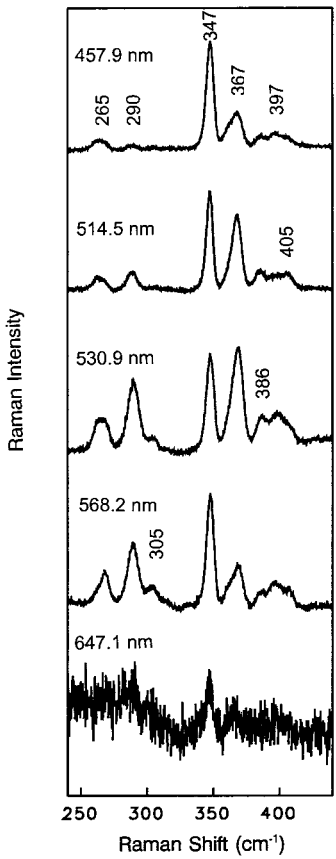

FIG. 8. Low-temperature (20 K) resonance Raman spectra of oxidized *P. furiosus* 3Fe Fd as a function of excitation wavelength (*191*).

(*124*, *165*), and *D. gigas* FdII (*61*). Hence, the difference must reflect differences in Fe–S^t bond strength, with stronger and therefore shorter bonds in the 3Fe Fds. This is in accord with the high-resolution crystal structures that show Fe–S(Cys) bonds shorter by 0.05 Å, on average, in *D. gigas* FdII compared to *A. vinelandii* FdI; see Table III.

As illustrated by the spectra of *P. furiosus* 3Fe Fd shown in Fig. 8, the relative intensities of the Raman bands for $[Fe_3S_4]^+$ clusters vary considerably with excitation wavelength. However, because of the extensive mixing of Fe–S^t and Fe–S^b modes, excitation profiles in the region 400–650 nm appear to be of little use in effecting electronic

assignments in terms of cysteinyl-S-to-Fe^{3+} or bridging-S-to-Fe^{3+} charge transfer. Excitation profiles for discrete bands in *D. gigas* FdII and *T. thermophilus* Fd were reported to fall into two sets with maxima at 470 and 500 nm (*17*), and this is now supported by data for *P. furiosus* 3Fe Fd (*191*). However, these different maxima correlate better with A_1 and E assignments, respectively, as opposed to predominantly Fe–S^b and Fe–S^t vibrational modes. This most likely reflects the fact that non–totally symmetric modes can only be enhanced via a vibronic mixing mechanism involving two electronic transitions, one of which occurs near 500 nm. Hence, the enhancement profiles are more useful in effecting vibrational assignments than in identifying specific types of electronic transition.

B. [Fe_3S_4]^0 Clusters

1. Ground-State Properties

The Mössbauer-determined ground-state properties of the one-electron reduced [Fe_3S_4]^0 clusters in *D. gigas* FdII (*29*), *P. furiosus* Fd (*198*), *A. vinelandii* FdI (*72*), aconitase (*174*), *C. vinosum* NiFe hydrogenase (*155*), *D. gigas* NiFe hydrogenase (*59*), and the synthetic analog complex [$Fe_3S_4(LS_3)$]$^{3+}$ (*50*) have been summarized; see Table 6 of Ref. (*50*). This tabulation will not be repeated herein, since the ground-state properties have been found to be remarkably invariant and therefore an intrinsic property of the cluster core (*50*). Moreover, the ground-state properties are maintained for [Fe_3Se_4]^0 clusters as judged by Mössbauer studies of Se-reconstituted aconitase (*174*) and the [$Fe_3Se_4(LS_3)$]$^{3-}$ analog complex (*50*). Mössbauer spectra recorded in the absence of an applied field consist of two quadrupole doublets with intensity ratio 2 : 1. The minor doublet has quadrupole splitting ΔE_Q = 0.38–0.59 mm/s and an isomer shift δ = 0.30–0.35 mm/s, slightly larger than those for a Fe^{3+} site with tetrahedral sulfur coordination. The major doublet has ΔE_Q = 1.2–1.67 mm/s and δ = 0.46–0.49 mm/s, and the isomer shift is about the mean of the values for Fe^{3+} and Fe^{2+} sites with tetrahedral sulfur coordination, indicating a valence delocalized $Fe^{2.5+}Fe^{2.5+}$ pair. The S = 2 ground state, identified initially via MCD magnetization studies (*20*), results in well-resolved magnetic splittings in Mössbauer spectra recorded at low temperatures in the presence of strong applied fields. Detailed analysis showed that the components of the valence delocalized pairs have almost indistinguishable ^{57}Fe-hyperfine tensors (A_{av} = −17.0 to −20.9 MHz) that are opposite in sign to those of the localized Fe^{3+} sites

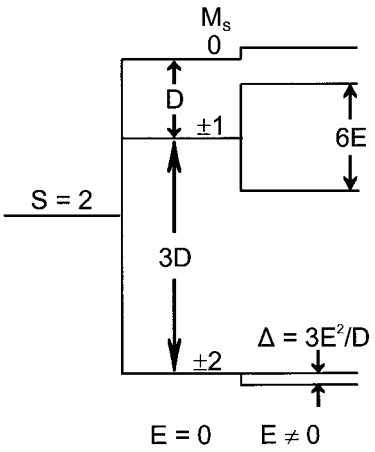

FIG. 9. Zero-field splitting of the $S = 2$ ground state of $[Fe_3S_4]^0$ clusters. Constructed for $D = -2.5$ cm^{-1} and $E/D = 0.23$, where D and E are the axial and rhombic zero-field splitting parameters, respectively.

(A_{av} = 14.8 to 17.3 MHz). Overall, the Mössbauer data were shown to be consistent with an $S = 2$ ground state, with $D \approx -2.5$ cm^{-1} and $E/D = 0.20$–0.25, where D and E are the axial and rhombic zero-field splitting parameters, respectively, that arises from antiferromagnetic exchange interaction between an $S = \frac{9}{2}$ valence-delocalized pair and the $S = \frac{5}{2}$ high-spin Fe^{3+} site (*29*, *33*); see Fig. 3. Similar axial zero-field splitting parameters for the $S = 2$ ground state have been deduced from analysis of the temperature dependence of the MCD spectra in weak applied fields (*70*, *71*) and from saturation magnetization studies (*177*). The ground-state zero-field splitting of the $S = 2$ ground state of $[Fe_3S_4]^0$ clusters is shown in Fig. 9.

The two lowest levels of the $S = 2$ manifold ($M_S = \pm 2$ in the limit of $E = 0$) are split in zero-field by an energy $\Delta = 3E^2/D$; see Fig. 9. Using the spin Hamiltonian parameters derived from the Mössbauer analysis, this rhombic zero-field splitting in the lowest doublet is approximately 0.4 cm^{-1}, which is comparable with the microwave quantum for X-band EPR. Hence, a broad integer spin EPR resonance (i.e., one that increases in intensity and is sharper in parallel mode ($\Delta M_S = 0$ selection rule) than in perpendicular mode ($\Delta M_S = \pm 1$ selection rule)), can usually be observed in the low-field region of the X-band EPR spectrum, for example, in *T. thermophilus* 7Fe Fd (*94*), *D. gigas* FdII (*29*), *P. furiosus* 3Fe Fd (*42*, *184*), *B. schlegelii* 7Fe Fd (*104*), *D. ambivalens* 7Fe Fd (*120*), *S. acidocaldarius* (*118*), spinach glutamate synthase (*25*), *D. gigas* NiFe-hydrogenase (*59*), *C. vinosum*

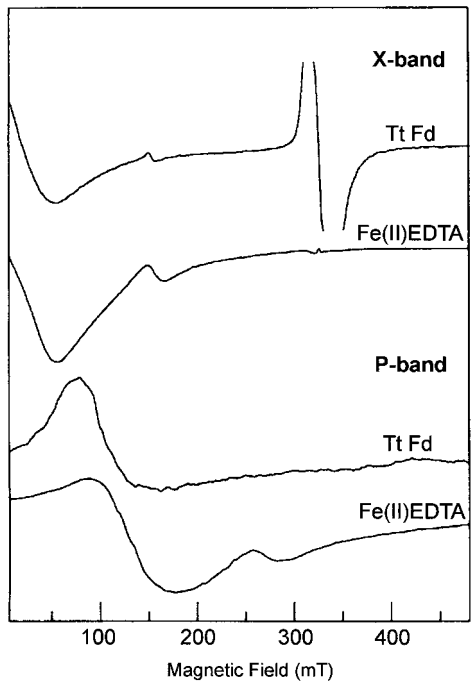

FIG. 10. X-band and P-band perpendicular mode EPR spectra of partially reduced *T. thermophilus* 7Fe Fd and Fe^{2+}-EDTA. The signal around $g = 2$ in *T. thermophilus* Fd arises from approximately 1% of $S = 1/2$ $[Fe_3S_4]^+$ clusters in the partially reduced sample. Taken from Ref. (*94*).

NiFe-hydrogenase (*187*), *T. acidophilum* succinate dehydrogenase (*190*), and the synthetic analog complex $[Fe_3S_4(LS_3)]^{3-}$ (*50*). The breadth results from a distribution of E/D values in frozen solution, and it is important to realize that only the fraction of molecules with $\Delta \leq 0.3$ cm^{-1} contribute to the observed resonance at X-band. The complete resonance is often only visible at higher frequencies, and this is well illustrated by the X-band (~9 GHz) and P-band (~15 GHz) perpendicular mode EPR spectra of partially reduced *T. thermophilus* 7Fe Fd ($[Fe_3S_4]^0$ and $[Fe_4S_4]^{2+}$) (*94*); see Fig. 10. Even if EPR signals from $S = 2$ $[Fe_3S_4]^0$ clusters are not readily observable, their presence is sometimes evident by enhanced relaxation and/or broadening of $S = \frac{1}{2}$ resonances of nearby $[Fe_4S_4]^+$ or $[Fe_2S_2]^+$ clusters as a result of weak intercluster spin–spin interactions, such as in 7Fe Fds (*94*) and in fumarate reductases and succinate dehydrogenases (*53*, *137*).

Studies of mutant forms of *P. furiosus* 3Fe Fd have shown that the $[Fe_3S_4]^{+,0}$ redox potential is strongly dependent on the protein environment. For example, changing the nonligating residue proximal to the tri(μ_2–S) face of the cluster from aspartate to serine results in a 120-mV increase in the midpoint potential (*65*). However, any detailed understanding of how the protein environment controls the redox potential will clearly require assignment of the specific cysteines ligating the valence delocalized pair and assessment of whether or not the pairwise interactions established by NMR in the $[Fe_3S_4]^+$ clusters are maintained on reduction. Unfortunately, despite numerous NMR studies of Fds containing $[Fe_3S_4]^0$ clusters (*74*, *81*, *90*, *102*, *121*, *178*, *185*, *192*, *199*), resonances from the β-CH_2 protons of the coordinating cysteines have never been reported. The NMR linewidths are considered to be too broad as a result of an abnormally long electronic relaxation time or exchange broadening. Since dipolar line broadening is much less for ^2H signals relative to ^1H signals (because of the smaller magnetic moment of ^2H), the most recent attempt to use NMR to make sequence-specific assignments of coordinating cysteine residues, utilized the 7Fe Fd from *B. schlegelii* in which the protein cysteines had been deuterated at the β position (*105*). Although sharp ^2H NMR signals were observed for the cysteines ligating the $[Fe_3S_4]^+$ cluster, none were detected for the $[Fe_3S_4]^0$ cluster. Since theoretical considerations predict that these signals should be observable, it was concluded that the resonances coalesce because the Fe sites exchange valencies faster than the NMR time scale.

Thus far the discussion of ground-state properties has been confined to the unprotonated form of biological $[Fe_3S_4]^0$ clusters. The initial discovery that $[Fe_3S_4]^0$ clusters can undergo a reversible protonation equilibrium came from VTMCD and direct electrochemical studies of *A. chroococcum* 7Fe Fd, pK_a = 7.8 (*75*, *76*). Subsequent VTMCD and direct electrochemistry studies of the 7Fe Fds from *A. vinelandii* (*70*, *71*, *169*) and *S. acidocaldarius* (*118*) have demonstrated a one-proton uptake with pK_as of 7.7 and 5.8, respectively. Direct electrochemistry studies of wild-type and D14H, D14S, D14N, D14Y, D14C and D14V mutant forms of *P. furiosus* 3Fe Fd as a function of pH have also found evidence for protonation with pK_a values in the range 3.3–4.7 (*65*). Hence, this is likely to be a general property of biological $[Fe_3S_4]^0$, although for the majority of clusters it is not apparent in the physiological pH range. Mutagenesis studies of *A. vinelandii* FdI have shown that Asp15, a residue immediately adjacent to the cluster, participates in the proton transfer (*169*, *193*). However, the dramatic change in the VTMCD spectrum as a function of pH was

shown to be a consequence of protonation of the cluster rather than this proximal aspartate (*169*). Although the excited state properties of $[Fe_3S_4]^0$ clusters are dramatically altered on protonation (see later discussion), there is relatively little change in the ground-state properties and crystallographic studies of *A. vinelandii* FdI at pH 6.0 and 8.5 show that the cuboidal $[Fe_3S_4]$ structure is preserved (*124*); see Table III. As in the unprotonated form, the protonated $[Fe_3S_4]^0$ clusters have $S = 2$ ground states with $D = -2.5 \pm 0.5$ cm^{-1}, as evidenced by VTMCD and Mössbauer studies (*70–72*, *75*, *118*). Moreover, Mössbauer studies indicate that the protonation-induced changes are confined to relatively minor perturbation of the magnetic hyperfine tensor of one of the Fe sites of the valence delocalized pair (*72*). Taken together, the Mössbauer and VTMCD data are consistent with protonation of a doubly bridging sulfide, but the possibility that a cysteinyl S is the protonation site cannot be excluded on the basis of the available data.

The discovery of an $S = \frac{9}{2}$ valence-delocalized $Fe^{2.5+}Fe^{2.5+}$ pair in $[Fe_3S_4]^0$ clusters led to the recognition that spin-dependent delocalization (SDD), in addition to the more commonly observed HDvV exchange, is required to understand the electronic and magnetic properties of Fe–S clusters (*29*). The basic idea of SDD (termed double exchange in the original theory developed by Zener (*194*) and Anderson and Hasegawa (*200*)) is illustrated by the energy level diagram for a symmetric $Fe^{2+}Fe^{3+}$ dimer shown in Fig. 11. Spin coupling of high-spin Fe^{2+} (d^6, $S = 2$) and Fe^{3+} (d^5, $S = \frac{5}{2}$) by HDvV exchange leads to a ladder of states with energies $JS(S+1)/2$ and the $S = \frac{1}{2}$ state lowest for antiferromagnetic exchange ($J > 0$). Each spin multiplet occurs twice since the extra (sixth) electron can be on either Fe and both arrangements are assumed to be degenerate in this simplified view. Resonance delocalization of the extra electron via a direct Fe–Fe interaction mixes the degenerate $Fe^{2+}Fe^{3+}$ and $Fe^{3+}Fe^{2+}$ configurations and results in an additional splitting, $\pm B(S + \frac{1}{2})$, where B is the SDD or double exchange parameter. It is intuitively obvious that delocalization is favored by the ferromagnetic alignment, since the extra electron is then free to visit both Fe sites without changing spin orientation. Accordingly, as B/J increases the ground-state spin switches from $S = \frac{1}{2}$ to $\frac{9}{2}$ and the energy separation between the $S = \frac{9}{2}$ bonding and antibonding components corresponds to $10B$ or 2β, where β corresponds to the resonance energy of a Hückel molecular orbital treatment. Inclusion of the factors responsible for valence delocalization, that is, vibronic coupling (*201–203*) and inequivalence in the energies of the $Fe^{2+}Fe^{3+}$ and $Fe^{3+}Fe^{2+}$ configurations (*204*), decreases

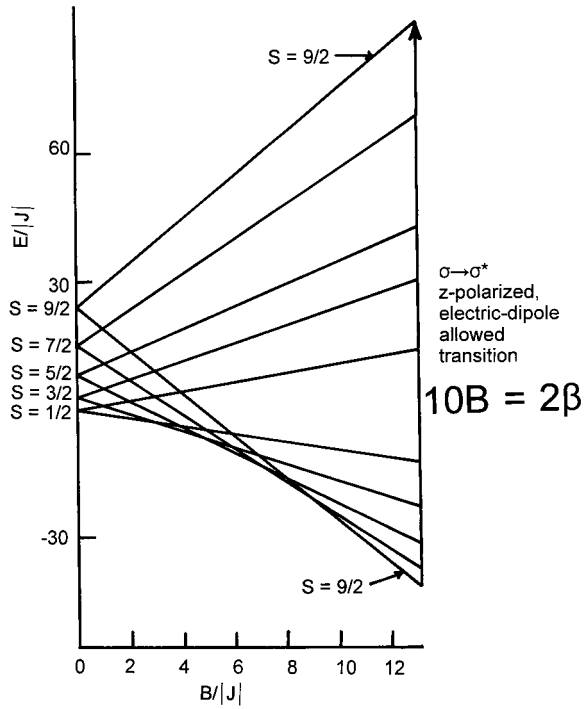

FIG. 11. Energy level diagram for a symmetric, exchange-coupled $Fe^{2+}Fe^{3+}$ dimer as a function of increasing spin-dependent delocalization. Taken with permission from Ref. (*207*).

the B/J range in which the ground state has $\frac{3}{2} \leq S \leq \frac{7}{2}$ and hence decreases the likelihood of having valence delocalized pairs with intermediate-spin ground states. As discussed in the next section, the discovery of valence delocalized $S = \frac{9}{2}$ $[Fe_2S_2]^+$ clusters in mutant 2Fe Fds (*205–207*) has led to the direct determination of B ($\approx$900 cm^{-1}) in both $[Fe_2S_2]^+$ and $[Fe_3S_4]^0$ clusters, via the identification of the z-polarized, electric dipole allowed, $\sigma \rightarrow \sigma^*$ "intervalence" transition depicted in Fig. 11.

2. *Excited-State Properties*

One-electron reduction to the $[Fe_3S_4]^0$ state results in partial bleaching of the visible absorption. As illustrated by *P. furiosus* 3Fe Fd in Fig. 12, the resulting absorption spectrum is relatively featureless, gradually increasing with increasing energy, except for a pronounced shoulder at ~430 nm and a weak shoulder at ~660 nm. The

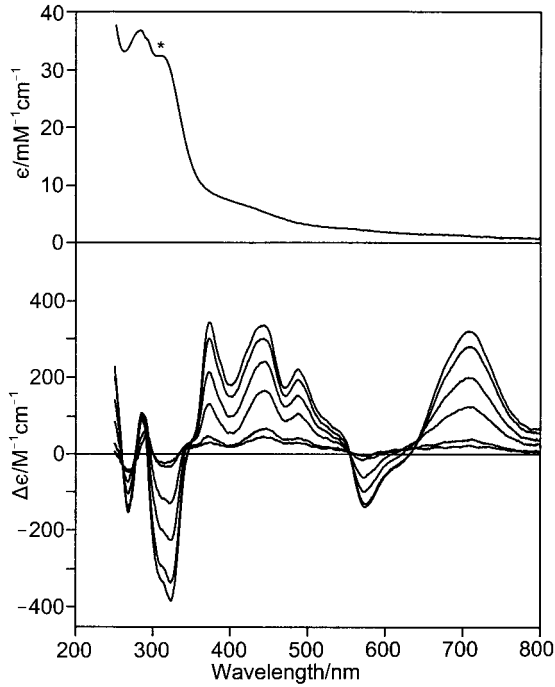

FIG. 12. UV-visible absorption and VTMCD spectra of the $[Fe_3S_4]^0$ cluster in wild-type *P. furiosus* Fd. The absorption spectrum was recorded at room temperature and the MCD spectra were recorded at 1.67, 4.22, 9.0, 15.8, and 51.0 K (all transitions increasing in intensity with decreasing temperature) with an applied magnetic field of 4.5 T. The band at 314 nm in the absorption spectrum (marked with an asterisk) is due to excess dithionite.

latter is better resolved in spectra recorded at 4.2 K (*20*). Once again the complexity of the excited-state electronic structure is only revealed in the VTMCD spectrum, which comprises at least 14 overlapping positive or negative bands in the 200–800 nm region, each corresponding to an electronic transition; see Fig. 12. The VTMCD spectrum is remarkably conserved among $[Fe_3S_4]^0$ clusters in different enzymes and proteins and more intense (by a factor of between 2 and 6) than those exhibited by other types of paramagnetic Fe–S clusters, that is, $S = \frac{1}{2}$ $[Fe_4S_4]^{3+,+}$ and $[Fe_2S_2]^+$ clusters, under comparable conditions of measurement (*189*). In addition, the intense band centered around 700 nm that is common to all $[Fe_3S_4]^0$ centers has characteristic MCD magnetization behavior (*20*). The field-dependent saturation curve at a fixed temperature below 2 K is invariably fit to a good

approximation by a purely *xy*-polarized transition originating from a doublet state with $g_{\|} = 8.0$ and $g_{\perp} = 0.0$, that is, the effective *g*-values in the axial limit of the lowest $M_S = \pm 2$ doublet of an $S = 2$ ground state with $D < 0$. Taken together, the characteristic MCD spectrum and magnetization data provide a convenient, semiquantitative method for establishing the presence of $[Fe_3S_4]^0$ clusters in proteins. Indeed, this approach has proven particularly effective in multicluster enzymes such as succinate dehydrogenase (*22*), fumarate reductase (*23*), nitrate reductase (*24*), and NiFe-hydrogenases (*27*).

To illustrate the range of VTMCD spectra exhibited by biological $[Fe_3S_4]^0$ centers and how the protein environment determines the location of the valence delocalized pair, we have chosen to show data for mutant forms of reduced *P. furiosus* 3Fe Fd that differ only in the residue at position 14, that is, the non-ligating residue proximal to the tri(μ_2–S) fact of the cluster; see Fig. 13. Each of these spectra can be viewed as the sum of two distinct types, with the D14Y and D14N mutants corresponding to almost homogeneous examples of type 1 and type 2, respectively (*184*). To a good approximation, the spectra of the other mutants and wild type can be simulated by adding different proportions of the D14Y and D14N spectra. By analogy with the EPR analysis for the equivalent oxidized clusters (see earlier discussion) and in light of the observation that the VTMCD spectra are dominated by transitions associated with the valence-delocalized pair (see later discussion), we have tentatively attributed the two distinct types of VTMCD spectra to different locations of the valence-delocalized pair. Since both types of spectra contribute to the VTMCD of the wild-type, D14S, D14C, and D14H samples in frozen solution, it seems likely these two distinct valence isomers are in dynamic equilibrium at room temperature. Such an interpretation is clearly in accord with the NMR data discussed previously. On surveying the published VTMCD spectra for $[Fe_3S_4]^0$ clusters in different proteins, it is particularly striking that each can be classified as predominantly type 1, for example, *D. africanus* FdIII (*108*), *S. acidocaldarius* 7Fe Fd (high pH form) (*118*), and spinach glutamate synthase (*25*), or predominantly type 2, for example, *D. gigas* FdII (*20*), *P. furiosus* 3Fe Fd (*42*), *A. vinelandii* FdI (high pH form) (*70*), *A. chroococcum* 7Fe Fd (high pH form) (*75*), *T. thermophilus* 7Fe Fd (*70*), and aconitase (*21*). In other enzymes, it is difficult to classify the spectral type because of interference from other paramagnetic clusters.

A major breakthrough in assigning the VTMCD spectra of $[Fe_3S_4]^0$ clusters came with the discovery of $S = \frac{9}{2}$ valence-delocalized $[Fe_2S_2]^+$ clusters in the alkaline forms of the C56S and C60S mutants of *C.*

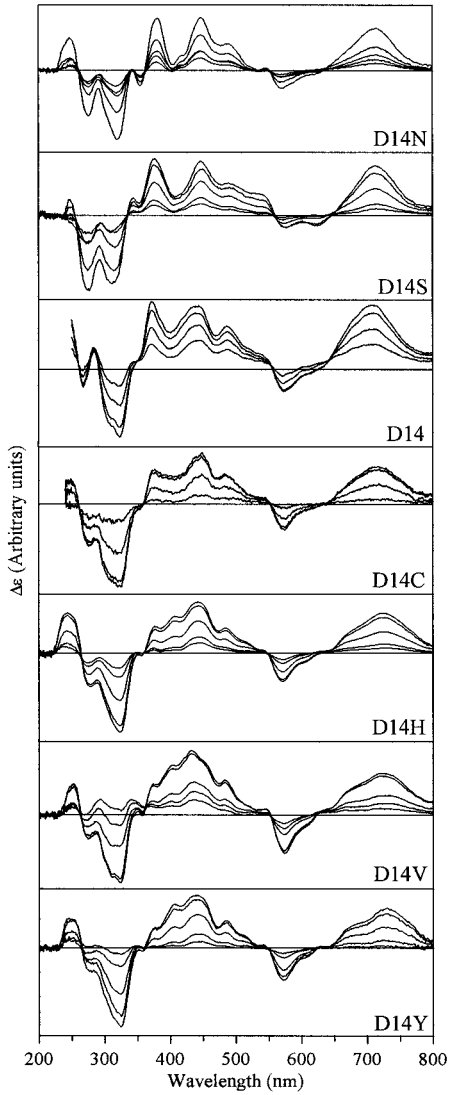

FIG. 13. VTMCD spectra of $[Fe_3S_4]^0$ clusters in wild type and mutant forms of *P. furiosus* Fd. In each case the spectra shown were recorded at temperatures between 1.5 and 50 K with an applied magnetic field of 4.5 or 6 T (all transitions increase in intensity with decreasing temperature).

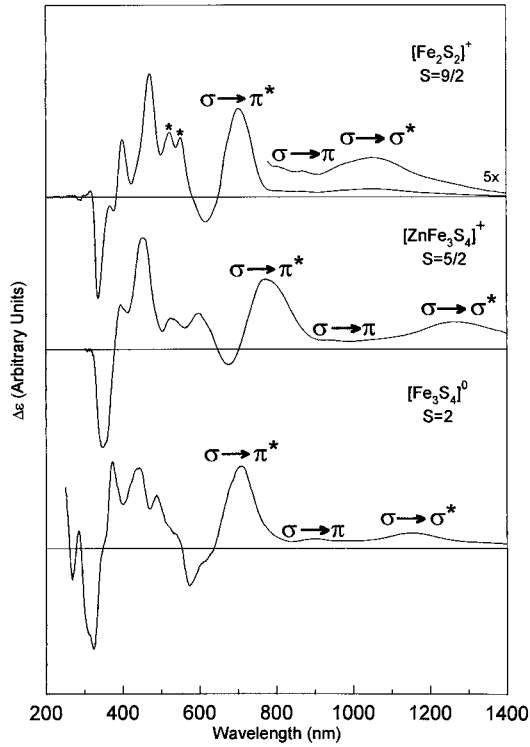

FIG. 14. Comparison of the VTMCD spectra (~1.6 K and 6 T) of the valence-delocalized $S = 9/2$ $[Fe_2S_2]^+$ cluster in the alkaline form of the C60S mutant of *C. pasteurianum* 2Fe Fd with those of the $[ZnFe_3S_4]^+$ and $[Fe_3S_4]^0$ clusters in *P. furiosus* Fd. Magnetization and temperature dependence studies show that the bands marked with an asterisk in the valence-delocalized $S = 9/2$ $[Fe_2S_2]^+$ spectra result from a valence-localized $S = 1/2$ component.

pasteurianum 2Fe Fd via the combination of VTMCD, EPR, and Mössbauer studies (*205–207*). The $[Fe_2S_2]^+$ clusters in these mutants reversibly interconvert between valence-localized $S = \frac{1}{2}$ and valence-delocalized $S = \frac{9}{2}$ forms as a function of pH with a $pK_a \approx 9$ (*207*). Comparison of the VTMCD spectrum of the valence-delocalized $S = \frac{9}{2}$ $[Fe_2S_2]^+$ with that of a $[Fe_3S_4]^0$ cluster shows that the latter is dominated by electronic transitions from the valence-delocalized pair; see Fig. 14. Tentative assignments of the higher energy bands (<500 nm) for the valence-delocalized $[Fe_2S_2]^+$ cluster have been made by analogy with the valance-localized form (*207*). Hence, the dominant positive band at 480 nm is assigned primarily to $\mu_2S^{2-} \rightarrow Fe^{2.5+}$ charge

transfer (blue-shifted from the $\mu_2S^{2-} \rightarrow Fe^{3+}$ charge transfer band at 540 nm in the localized valence form) and the higher energy bands are assigned primarily to $CysS^- \rightarrow Fe^{2.5+}$ charge transfer (again blue-shifted compared to the equivalent bands in the localized valence form). However, there are no counterparts in the valence-localized $[Fe_2S_2]^+$ VTMCD spectrum for the near-IR bands in the valance-delocalized $[Fe_2S_2]^+$ spectrum, that is, the negative band at 610 nm, the positive band at 705 nm, and the weak positive bands at ~850 and 1070 nm. Hence, these bands have been attributed to the Fe–Fe interactions that lead to spin-dependent valence delocalization; an assignment that is supported by the enhancement of vibrational modes involving Fe–Fe displacement in the resonance Raman spectrum of the alkaline form of C56S *C. pasteurianum* 2Fe Fd, using 676-nm excitation (*207*).

A schematic molecular orbital diagram for the Fe–Fe interaction in an $S = \frac{9}{2}$ valence-delocalized $Fe^{2.5+}Fe^{2.5+}$ pair based on effective C_{2v} symmetry at the Fe sites and the observed electronic transitions for the valance-delocalized $[Fe_2S_2]^+$ cluster is shown in Fig. 15. The dominant interaction (responsible for the $S = \frac{9}{2}$ ground state) is the σ overlap between the pair of d_{z^2} orbitals, with progressively smaller π interactions between pairs of d_{xz} and d_{yz} orbitals and δ interactions between pairs of d_{xy} and $d_{x^2-y^2}$ orbitals. The three highest energy transitions are predicted to be $\sigma \rightarrow \sigma^*$ (electric-dipole allowed, but z-polarized, resulting in weak VTMCD intensity), $\sigma \rightarrow \pi$ (xy-polarized, but electric-dipole forbidden, resulting in weak VTMCD intensity), and $\sigma \rightarrow \pi^*$ (xy-polarized and electric-dipole allowed, resulting in strong VTMCD intensity). The latter two transitions are expected to be derivative-shaped (pseudo A-terms) and are likely to be split in low-symmetry biological environments. The assignments of these three transitions for the $S = \frac{9}{2}$ valence-delocalized $[Fe_2S_2]^+$ cluster are shown in Fig. 15. Hence, the intense derivative-shaped feature centered at 660 nm (negative band at 610 nm and positive band 705 nm) is assigned to the $\sigma \rightarrow \pi^*$ transition. Assignment of the 1070-nm band as a z-polarized transition has been confirmed by MCD magnetization data (*207*). The energy of this $\sigma \rightarrow \sigma^*$ transition is particularly important since it corresponds to 2β ($=10B$), and thereby provides a direct measurement of $\beta = 4650$ cm^{-1}) in a valence-delocalized $[Fe_2S_2]^+$ cluster. This agrees well with the estimates based on density functional calculations for $[Fe_4S_4]$ clusters, $B = 700$–900 cm^{-1} (*208*), and extrapolation of the analysis for structurally characterized valence-delocalized $S = \frac{9}{2}$ diiron centers to $[Fe_2S_2]^+$ clusters, $B \sim 965$ cm^{-1} (*209*). A comprehensive discussion of electron delocalization in mixed-valence

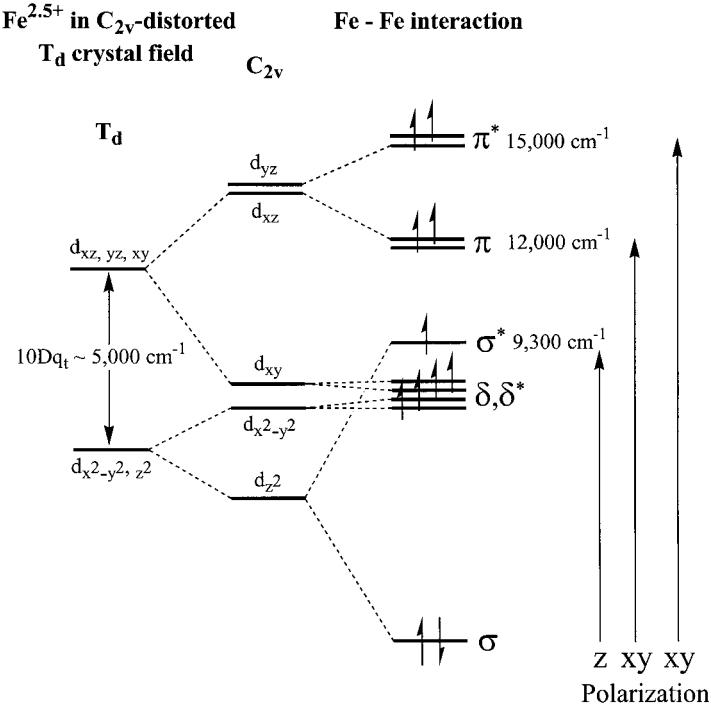

FIG. 15. Schematic MO diagram and proposed electronic assignments for the Fe–Fe interaction in a valence-delocalized $S = 9/2$ $[Fe_2S_2]^+$ unit. Modified with permission from Ref. (*207*).

Fe–S clusters can be found in a set of commentaries in the *Journal of Biological Inorganic Chemistry* (*204*, *210–213*).

In order to confirm analogous assignments for $[Fe_3S_4]^0$ clusters and hence quantify the resonance energy for the $S = \frac{9}{2}$ valence-delocalized pairs in each of the two distinct types of VTMCD spectra, MCD magnetization data have been collected for bands centered around at 710 nm and 1150 nm; see Fig. 16. Uniaxial transitions such as the $\sigma \rightarrow \sigma^*$ transition of an Fe–Fe interaction are predicted to have anomalous MCD magnetization properties for transitions originating from a highly anisotropic doublet (*70*, *214*). Completely different MCD magnetization data are observed for the bands centered at 713 and 1148 nm. The lowest temperature data at 713 nm is well fit by theoretical data constructed for a *xy*-polarized transition arising from a doublet with $g_{\|} = 8.0$ and $g_{\perp} = 0.0$. In contrast, the anomalous magnetization behavior at 1148 nm, that is, increasing to a maximum and then de-

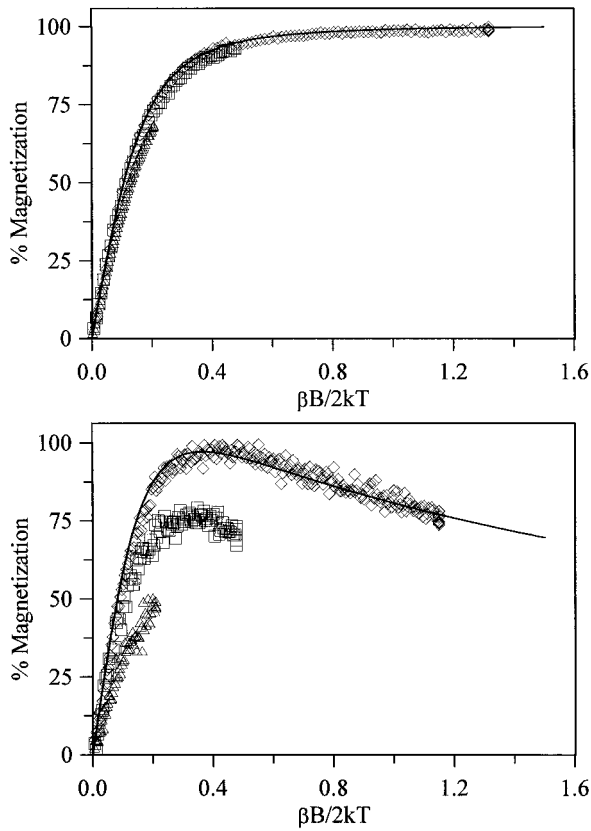

FIG. 16. MCD magnetization data for the $[Fe_3S_4]^0$ cluster in the D14S mutant of dithionite-reduced *P. furiosus* Fd. Upper panel: Magnetization data collected at 713 nm; magnetic fields between 0 and 6.0 T; temperatures, (◇) 1.68 K, (□) 4.22 K, (△) 9.7 K. The solid line is theoretical magnetization data constructed according to Ref. (*214*) for a *xy*-polarized transition originating from the $M_s = \pm 2$ doublet of an axial $S = 2$ ground state, with $g_\parallel = 8.0$ and $g_\perp = 0.0$. Lower panel: Magnetization data collected at 1148 nm; magnetic fields between 0 and 6.0 T; temperatures, (◇) 1.75 K, (□) 4.22 K, (△) 9.62 K. The solid line is theoretical magnetization data constructed according to Ref. (*214*) for a predominantly *z*-polarized transition originating from the $M_s = \pm 2$ doublet of an $S = 2$ ground state, with $g_\parallel = 8.0$ and $g_\perp = 0.1$, and $m_z/m_{xy} = 55$.

creasing as a function of $\beta B/2kT$, is predicted only for a predominantly *z*-polarized transition, when both the *z*-polarized and *xy*-polarized transition dipole moments (m_z and m_{xy}, respectively) have the same sign (*214*). For example, the lowest temperature data at 1148 nm is fit by a theoretical curve constructed of a *z*-polarized transition ($m_z/m_{xy} = 55$) with $g_\parallel = 8.0$ and $g_\perp = 0.1$. The lowest energy near-

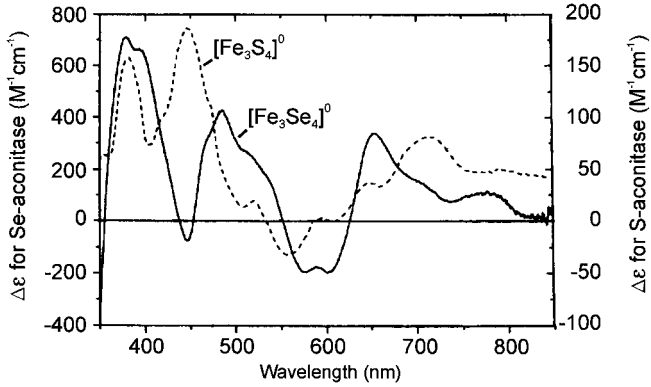

FIG. 17. Comparison of the VTMCD spectra (4.5 K and 5 T) of the $[Fe_3S_4]^0$ and $[Fe_3Se_4]^0$ centers in bovine heart aconitase. Taken from Ref. (*188*).

IR VTMCD band in each of the $[Fe_3S_4]^0$ spectra, therefore, corresponds to the uniaxial $\sigma \rightarrow \sigma^*$ transition of Fe–Fe interaction and the resonance delocalization energy, β, is determined to be 4290 $\pm$ 25 cm^{-1} for Type 1 clusters and 4350 $\pm$ 25 cm^{-1} for Type 2 clusters. Hence, the Fe–Fe interactions within the valence-delocalized pair are very similar in both locations.

The close similarity in the VTMCD spectra of $[Fe_3S_4]^0$ and valence-delocalized $[Fe_2S_2]^+$ clusters suggests that the majority of the bands can be assigned to transitions associated with the valence-delocalized pair. Hence, by analogy to the valence-delocalized $[Fe_2S_2]^+$ clusters, the positive band at 450 nm is assigned to a $\mu_2S^{2-} \rightarrow Fe^{2.5+}$ charge transfer transition and bands to higher energy are likely to have a large component of $CysS^- \rightarrow Fe^{2.5+}$ charge transfer. The only bands attributable to $S \rightarrow Fe^{3+}$ transitions at the localized-valence Fe^{3+} site are the relatively weak positive and negative features in the 480–600 nm region. This assignment is further supported by the comparison of the VTMCD spectra of the $[Fe_3S_4]^0$ and $[Fe_3Se_4]^0$ clusters in aconitase (*188*); see Fig. 17. The Se-induced red shifts of the bands in the 400–600 nm region are consistent with charge transfer transitions involving primarily inorganic sulfide/selenide, and the Se-induced blue shifts in the $\sigma \rightarrow \pi$ and $\sigma \rightarrow \pi^*$ transitions are consistent with larger Fe *d*-orbital splitting in the Se-substituted form. Near-IR MCD studies to longer wavelengths will be required to locate the $\sigma \rightarrow \sigma^*$ transition and thereby assess the resonance energy for the delocalized pair in the Se-substituted cluster. VTMCD studies of the

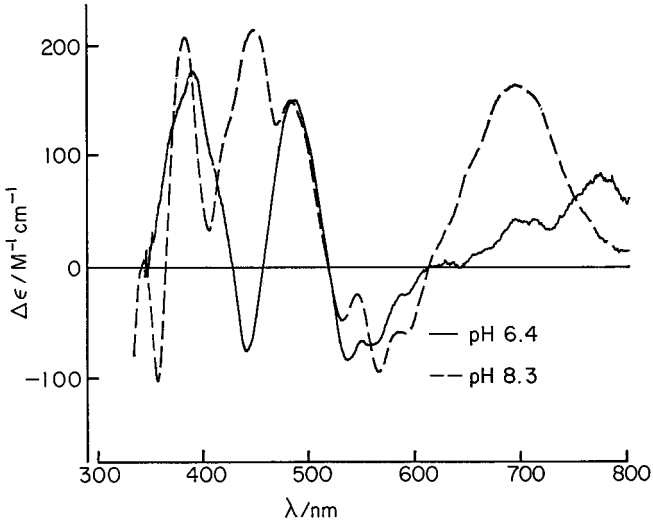

FIG. 18. VTMCD spectra (4.2 K and 4.5 T) of partially reduced (i.e., $[Fe_3S_4]^0$ and $[Fe_4S_4]^{2+}$) *A. vinelandii* FdI at pH 8.3 and 6.4. Taken from Ref. (*70*).

$[Fe_3S_4(LS_3)]^{3-}$ and $[Fe_3Se_4(LS_3)]^{3-}$ synthetic analog complexes (*50*) would also be very useful in testing these assignments.

Protonation of the $[Fe_3S_4]^0$ clusters in *A. chroococcum* 7Fe Fd, *A. vinelandii* FdI, and *S. acidocaldarius* 7Fe Fd was discovered as a result of the dramatic changes in VTMCD spectra as a function of pH (*70*, *71*, *75*, *118*). VTMCD spectra for the protonated and unprotonated forms of *A. vinelandii* FdI are shown in Fig. 18. On the basis of these assignments, the changes primarily involve the $\mu_2S^{2-} \rightarrow Fe^{2.5+}$ charge transfer transition at 450 nm and the $\sigma \rightarrow \pi^*$ Fe–Fe transition of the valance-delocalized pair at 700 nm. This strongly suggests a μ_2S^{2-} as the protonation site. Near-IR MCD studies to longer wavelengths are required to locate the $\sigma \rightarrow \sigma^*$ transition in the protonated form and thereby directly address the protonation-induced changes at the valence delocalized pair.

A major discrepancy that remains unresolved in the excited-state properties of the $[Fe_3S_4]^0$ cluster in *D. gigas* FdII concerns the existence of a low-lying, fully valence-delocalized state that becomes populated at temperatures above 25 K. Such a state is clearly apparent in the temperature-dependent Mössbauer studies of reduced *D. gigas* FdII (*29*) and *P. furiosus* 3Fe Fd (*198*) and is represented by one quadrupole doublet with $\Delta E_Q \approx 0.9$ mm/s and $\delta = 0.45$ mm/s. Such a

state would not be expected to exhibit an $S = 2$ ground state, since delocalization has a direct effect on the ground-state spin. However, saturation magnetization data for reduced *D. gigas* FdII was found to obey the Curie law from 4 to 200 K indicating that any excited state populated over this temperature range must have the same spin as the ground state $S = 2$ state (*177*). One possible explanation that does not appear to have been considered explicitly is that the "fully delocalized" form is due to a conformation in which the energy barrier between configurations with different valence delocalized pairs is very low, such that the Fe sites undergo rapid interchange compared to the Mössbauer time scale even at temperatures as low as 25 K. As detailed earlier, such rapid interchange between conformations has been invoked to explain the absence of well-defined β-CH_2 resonances from the ligated cysteines in near-room-temperature NMR studies of proteins containing $[Fe_3S_4]^0$ clusters (*105*), and VTMCD studies indicate that the majority of $[Fe_3S_4]^0$ clusters exist as a mixture of two conformations in frozen solutions that differ in the location of the valence-delocalized pair (*184*).

3. *Vibrational Properties*

Published resonance Raman data of $[Fe_3S_4]^0$ centers are limited to a poor-quality room-temperature spectrum of *D. gigas* FdII (*215*) and a low-temperature spectrum of *P. furiosus* 3Fe Fd obtained with 457.9-nm excitation (*37*). In part, the paucity of the available data is a consequence of the weak resonance enhancement compared to $[Fe_3S_4]^+$ centers. Nevertheless, high-quality resonance Raman spectra have been obtained for *P. furiosus* using excitation wavelengths in the range 457.9–514.5 nm (see Fig. 19), and the bands have been categorized as involving predominantly Fe–S^b and Fe–S^t stretching on the basis of $^{34}S^b$ isotope shifts; see Fig. 20 (*191*). The strongly enhanced bands at 245, 271, 287, 368 and 379 cm^{-1} predominantly involve Fe–S^b stretching, since all have $^{34}S^b$ downshifts ≥ 5 cm^{-1}. In contrast, the weakly enhanced bands at 319, 334, and 349 cm^{-1} are assigned primarily to Fe–S^t stretching on the basis of $^{34}S^b$ downshifts ≤ 3 cm^{-1}. The spectra are completely different from those of the $[Fe_3S_4]^+$ clusters discussed earlier, and this has impeded more detailed assignments. However, the spectra are very similar to those we have obtained for the valance-delocalized $[Fe_2S_2]^+$ clusters in alkaline samples of the C56S and C60S mutants of *C. pasteurianum* 2Fe Fd (Duin, E. C., Crouse, B. R., Meyer, J., and Johnson, M. K., unpublished results). This is, of course, in accord with the VTMCD studies of $[Fe_3S_4]^0$ centers discussed previously, which indicate that the elec-

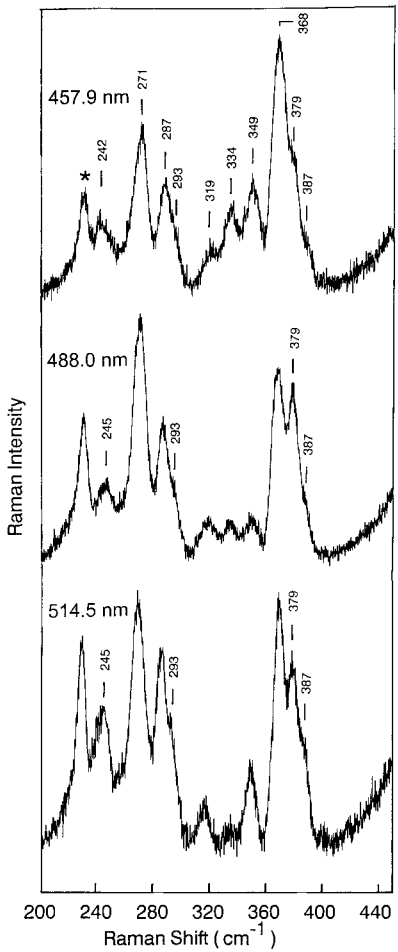

FIG. 19. Low-temperature (20 K) resonance Raman spectra of dithionite-reduced *P. furiosus* 3Fe Fd as a function of excitation wavelength (*191*). The asterisk indicates a lattice mode of ice.

tronic absorption spectrum in the visible region is dominated by transitions localized on the valance-delocalized pair. The dominant enhancement of Fe–S^b modes with excitation wavelengths >450 cm^{-1} is also in excellent agreement with the electronic assignments present in the previous section. Hence, the dramatic difference in the resonance Raman of the oxidized and reduced $[Fe_3S_4]^{+,0}$ clusters appears to be a consequence of selective resonance enhancement of the valence-delocalized pair of the reduced cluster. We are in the process

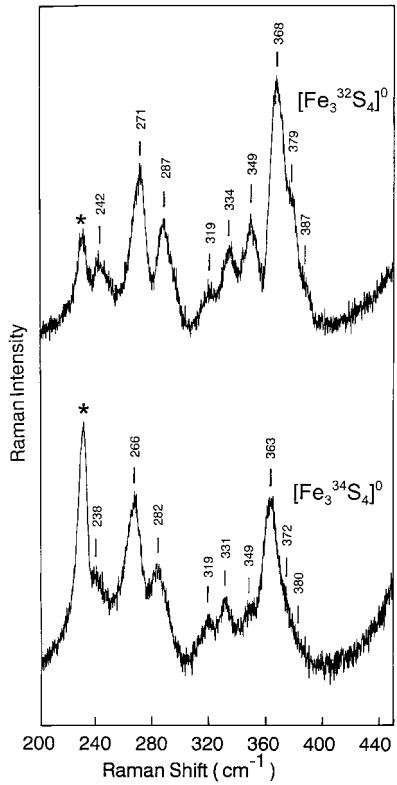

FIG. 20. Low-temperature (20 K) resonance Raman spectra of natural-abundance and $^{34}S^{b}$-enriched samples of dithionite-reduced *P. furiosus* 3Fe Fd with 457.9-nm excitation (*191*). The asterisk indicates a lattice mode of ice.

of effecting detailed assignments for valence-delocalized $[Fe_2S_2]^{+}$ clusters and $[Fe_3S_4]^{0}$ clusters based on isotope shifts and normal mode analysis, and these results will be presented elsewhere.

C. $[Fe_3S_4]^{-}$ Clusters and Cluster Fragments

As yet there has been no spectroscopic or electrochemical evidence for discrete $[Fe_3S_4]^{-}$ clusters in any biological sample. In contrast, there is electrochemical evidence for a reversible three-membered electron transfer series encompassing the $[Fe_3S_4]^{+,0,-}$ core oxidation states for the synthetic analog complex $[Fe_3S_4(LS_3)]^{3-}$ (*50*). However, since the $[Fe_3S_4]^{0,-}$ potential (-1.72 V in acetonitrile) is very negative and 0.93 V lower than the $[Fe_3S_4]^{+,0}$ potential (-0.79 V in acetoni-

trile), the $[Fe_3S_4]^-$ state in a protein is likely to be inaccessible under physiological conditions without protonation or binding of a positively charged transition-metal ion. Accordingly, the properties of a putative $[Fe_3S_4]^-$ cluster have been deduced from studies of heterometallic cubanes $[MFe_3S_4]^+$ where M is a redox-inactive and diamagnetic d^{10} transition-metal ion such as Zn^{2+} or Cd^{2+}, that is, in *D. gigas* FdII (*32*, *33*, *64*), *D. africanus* FdIII (*38*, *41*), and *P. furiosus* Fd (*35*, *36*, *198*).

The combination of EPR, Mössbauer, and/or VTMCD has revealed an $S = \frac{5}{2}$ ground state for the $[Fe_3S_4]^-$ fragment in $[ZnFe_3S_4]^+$ and $[CdFe_3S_4]^+$ clusters. On the basis of the Mössbauer studies of the $[ZnFe_3S_4]^+$ clusters in *D. gigas* FdII (*32*, *33*) and *P. furiosus* Fd (*198*), the $S = \frac{5}{2}$ ground state has been rationalized in terms of antiferromagnetic exchange interaction between a valence-localized high-spin Fe^{2+} site ($S = 2$) and a valence-delocalized $Fe^{2.5+}Fe^{2.5+}$ pair ($S = \frac{1}{2}$). At all temperatures, the Mössbauer spectra were analyzed as the sum of two components in a 2:1 ratio, with the minor component having $\Delta E_Q = 2.7–3.1$ mm/s and $\delta = 0.62$ mm/s (slightly smaller than those for a Fe^{2+} site with tetrahedral sulfur coordination) and the major component having $\Delta E_Q = 1.5–1.6$ mm/s and $\delta = 0.51–0.54$ mm/s (slightly higher than the valence-delocalized $Fe^{2.5+}Fe^{2.5+}$ pair in the $[Fe_3S_4]^0$ cluster). The components of the valence-delocalized pairs have very similar ^{57}Fe-hyperfine tensors ($A_{av} = -14$ to -15 MHz), whereas that of the localized Fe^{2+} site is not uniquely defined ($|A_{av}| < 7$ MHz). The presence of an $S = 9/2$ valence-delocalized pair is strongly supported by the VTMCD studies of the $[ZnFe_3S_4]^+$ clusters in *P. furiosus* Fd and *D. gigas* FdII (*35*) and the $[CdFe_3S_4]^+$ cluster in *P. furiosus* Fd (*36*). As illustrated by the $[ZnFe_3S_4]^+$ cluster in *P. furiosus* Fd (see Fig. 14), the VTMCD is very similar to that of the $S = 9/2$ valence-delocalized $[Fe_2S_2]^+$ cluster and can be assigned accordingly. The major difference is that the transitions associated with Fe–Fe interaction are all shifted to lower energy, indicative of a longer Fe–Fe distance and smaller resonance delocalization energy. As in the case of the valence-delocalized $[Fe_2S_2]^+$ clusters and $[Fe_3S_4]^0$ clusters, the uniaxial $\sigma \rightarrow \sigma^*$ transition has been identified by its anomalous MCD magnetization behavior, since the lowest doublet of the ground-state manifold is highly anisotropic (Duderstadt R. E., Duin, E. C., and Johnson, M. K., unpublished results). In $[ZnFe_3S_4]^+$ clusters, this transition occurs at 1265 nm, indicating significantly smaller resonance delocalization energy, $\beta = 3950$ cm^{-1}, compared to the valence-delocalized pairs in $[Fe_3S_4]^0$ clusters ($\beta = 4290–4350$ cm^{-1}).

The ground-state properties of the $[ZnFe_3S_4]^+$ and $[CdFe_3S_4]^+$ clus-

ters have been found to be identical in a given protein. However, although it was not noted in the original publications (*35*, *36*, *38*), the Cd and Zn heterometallic clusters in *P. furiosus* Fd and *D. africanus* FdIII appear to exist as a mixture of two analogous forms with distinctive EPR signals. The dominant form in *P. furiosus* Fd has $D = -2.3$ cm^{-1} and $E/D = 0.18$, and the minor form is more rhombic with $E/D \approx 0.3$. The minor species is responsible for the low-field resonance at $g = 9.7$, and a broad feature centered at $g = 4.3$ is predicted, but obscured by overlap with the dominant more axial species. The situation is reversed in *D. africanus* FdIII, with the dominant species being a rhombic component with $E/D \approx 0.3$ that gives rise to a broad ill-defined resonance centered at $g = 4.3$. The evidence for a minor species with $D < 0$ and $E/D = 0.18$ is the appearance of a resonance at $g = 8.8$ that increases with increasing temperature. In contrast, the $[ZnFe_3S_4]^+$ cluster in *D. gigas* FdII is more homogeneous, with ground-state properties intermediate between these two extremes, that is, $D \approx -2.7$ cm^{-1} and $E/D = 0.25$. This difference in ground-state properties is likely to be a consequence of thiolate as opposed to carboxylate coordination at the Zn site, since the residue ligating the fourth site is cysteine in *D. gigas* FdII and aspartate in *P. furiosus* Fd and *D. africanus* FdIII. Moreover, the addition of a large excess of exogenous thiolate to the $[ZnFe_3S_4]^+$ cluster in *P. furiosus* Fd results in EPR properties analogous to those of the $[ZnFe_3S_4]^+$ cluster in *D. gigas* FdII. Whether the observed heterogeneity in $[ZnFe_3S_4]^+$ and $[CdFe_3S_4]^+$ clusters in *P. furiosus* Fd and *D. africanus* FdIII results from monodentate/bidentate aspartate ligation at the Zn site and/or conformations with different locations for the valence-delocalized pair remains to be determined.

D. $[Fe_3S_4]^{2-}$ Clusters

Following the pioneering electrochemical studies of *D. africanus* FdIII coadsorbed on the electrode surface as an electroactive film (*196*), protonation-assisted reduction of adsorbed $[Fe_3S_4]^0$ proteins in a cooperative two-electron process to yield a formal $[Fe_3S_4]^{2-}$ cluster has emerged as a general property of all 3Fe-containing proteins investigated thus far (*118*). These include *A. vinelandii* FdI (*169*), *S. acidocaldarius* 7Fe Fd (*118*, *119*), *Sulfolobus* sp7 7Fe Fd (*112*), *D. gigas* FdII (*64*), *P. furiosus* Fd (*216*), bovine heart aconitase (*217*), and *E. coli* fumarate reductase (*218*). In each case, the reaction is chemically reversible, the product is surprisingly inert, and the pH-dependent redox potential is ~ -700 mV at pH 7. Voltammetry stud-

ies of the pH dependence of three 7Fe Fds as coadsorbed films indicate that reduction to the $[Fe_3S_4]^{2-}$ state involves the net uptake of three protons relative to the $[Fe_3S_4]^{+}$ state (*119*). This protonation presumably facilitates multielectron reduction by counteracting the accumulation of negative charge and the insensitivity to the protein host suggests that the cluster itself is the site of protonation. In light of the analysis presented earlier for the protonation site of the $[Fe_3S_4]^{0}$ cluster, the three μ_2-S atoms are clearly the most likely sites for protonation. However, there is as yet no direct evidence to support this proposal.

The ability to reversibly produce the $[Fe_3S_4]^{2-}$ redox state in *S. acidocaldarius* 7Fe Fd by bulk electrochemical reduction in solution has afforded the opportunity to investigate the ground- and excited-state properties using absorption, VTMCD, and EPR spectroscopies (*119*). The absence of an EPR signal in parallel or perpendicular mode, coupled with the lack of significant visible absorption and a MCD spectrum that most closely resembles that of reduced rubredoxin, support the notion of an all-Fe^{2+} cluster with an integer spin ground state. However, overlap with the MCD spectrum of the $[Fe_4S_4]^{+}$ cluster has impeded reliable assessment of the temperature and field dependence of the MCD bands below 400 nm that are attributable to the $[Fe_3S_4]^{2-}$ center. Hence, the ground-state spin ($S = 0, 1, 2 \ldots$) remains to be determined. Although it seems unlikely that the $[Fe_3S_4]^{0,2-}$ couple is physiologically relevant in any of the 3Fe-containing enzymes or proteins investigated thus far, the discovery of $[Fe_3S_4]^{2-}$ clusters does illustrate the potential of $[Fe_3S_4]$ clusters to act as a multiple electron–proton transfer agents, and they are attractive candidates for intermediates in the assembly of cubane-type $[Fe_3S_4]$ and $[Fe_4S_4]$ clusters (*119*).

VI. Cluster Conversions

Although $[Fe_3S_4]$ clusters have been found to exhibit rich cluster conversion chemistry, there is as yet no evidence that these processes form the basis for regulatory roles to control enzyme activity or gene expression. The three major types of cluster conversions that have been observed or proposed for biological $[Fe_3S_4]$ clusters are summarized in Fig. 21. By far the most common type of cluster transformation involving biological $[Fe_3S_4]^{+,0}$ clusters is the reductive incorporation of Fe^{2+} ion to yield $[Fe_4S_4]^{2+,+}$ clusters, as first demonstrated in aconitase (*13*) and *D. gigas* FdII (*14*), and the reverse process, namely,

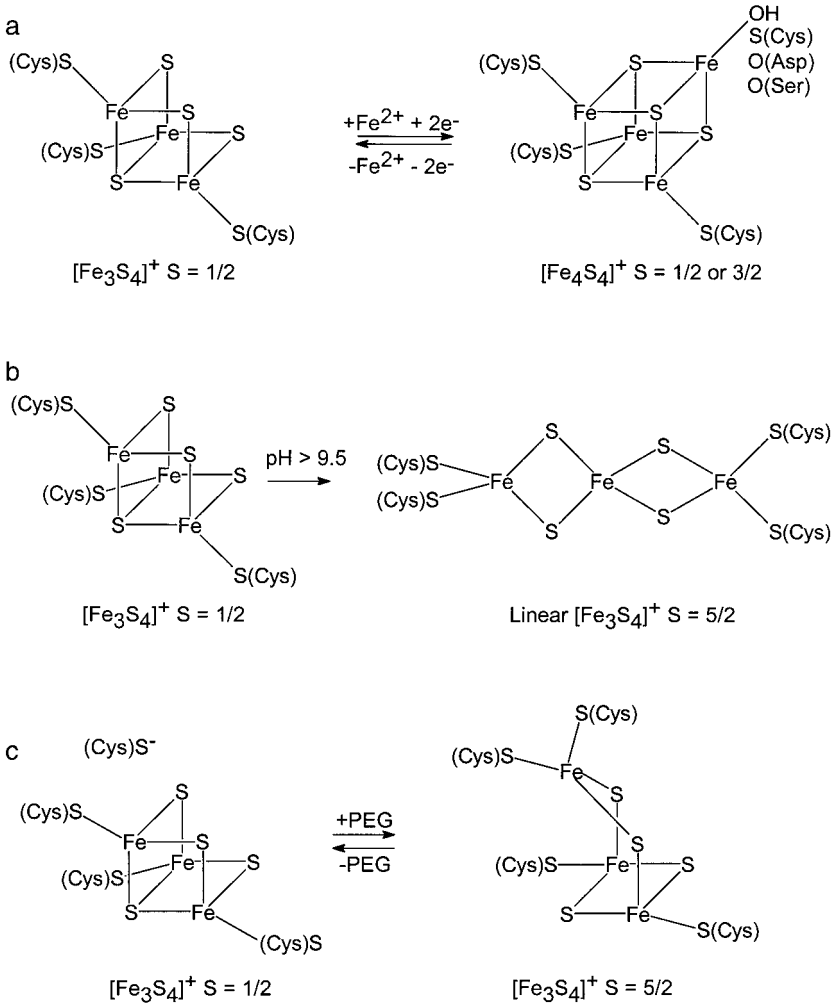

[Fe3S4]+ S = 1/2 [Fe3S4]+ S = 5/2

FIG. 21. Cluster conversions involving $[Fe_3S_4]^+$ clusters. The cluster conversion in (c) has been proposed on the basis of EPR, VTMCD, and resonance Raman studies, but has yet to be confirmed by Mössbauer or more direct structural techniques.

the oxidative loss of Fe from $[Fe_4S_4]^{2+,+}$ clusters to yield $[Fe_3S_4]^+$ clusters, as first demonstrated in *C. pasteurianum* 8Fe Fd (*10*); see Fig. 21a. With the exception of aconitase, which has hydroxyl coordination of the unique Fe site (*175*), the former process generally requires a coordinating residue such as cysteinate, aspartate, or serinate in close proximity to the tri–μ_2–S^{2-} face of the cluster in order to ligate and

stabilize the incorporated Fe. Ferricyanide has proven remarkably effective for inducing oxidative degradation of $[Fe_4S_4]^{2+,+}$ clusters and site-differentiated $[Fe_4S_4]^{2+,+}$ clusters with oxygenic coordination at a specific Fe site (e.g., hydroxyl in aconitase (*175*), and aspartyl in *P. furiosus* Fd (*42*) and *D. africanus* FdIII (*43*, *108*)) undergo particularly rapid and facile conversion to $[Fe_3S_4]^+$ clusters. In many enzymes and proteins, aerial oxidative degradation of $[Fe_4S_4]^{2+,+}$ clusters to yield $[Fe_3S_4]^+$ clusters can occur during aerobic or semianaerobic isolation procedures. Hence, there are numerous examples of enzymes and proteins that have stoichiometric or substoichiometric amounts of $[Fe_3S_4]^+$ clusters as purified, as judged by EPR spin quantitations, that turn out to be oxidative artifacts, such as 4Fe and 8Fe ferredoxins (*10*, *219*), aconitase (*13*) and other Fe–S dehydratases (*220*, *221*), endonuclease III (*222*), glutamine phosphoribosylpyrophosphate amidotransferase (*223*), lysine 2,3-aminomutase (*224*), anaerobic ribonucleotide reductase (*225*, *226*), pyruvate formate–lyase-activating enzyme (*227*), and fumarate and nitrate reductase regulation (FNR) protein (*228*, *229*).

The cuboidal $[Fe_3S_4]^+$ cluster in aconitase is unique in its ability to undergo conversion to a linear $[Fe_3S_4]^+$ cluster at pH > 9 (*44*). This cluster conversion was apparent from marked changes in the visible absorption spectrum (brown to purple), loss of the characteristic $g = 2.01$ EPR resonance, and the appearance of a rhombic $S = 5/2$ EPR signal with features at $g = 4.3$ and 9.6, similar to that observed for adventitiously bound Fe^{3+} ion. However, Mössbauer studies revealed that the $S = 5/2$ spin system resulted from three antiferromagnetically coupled Fe^{3+} ions, each in an approximately tetrahedral environment of S atoms (*44*). Analysis in terms of a spin coupling model revealed that the $S = 5/2$ ground state is a consequence of highly asymmetric coupling among the three Fe atoms, $J_{13} \approx J_{23} > 2J_{12}$. This is consistent with a linear as opposed to triangular arrangement of Fe atoms, and the close correspondence in absorption, EPR, Mössbauer, and VTMCD properties (*44*, *45*) compared to those of structurally characterized clusters with linear $[Fe_3S_4]^+$ cores (*48*), has provided unambiguous evidence for the structure shown in Fig. 21b. Protein-chemical methods have shown that only two of the cysteine residues ligating the cuboidal $[Fe_3S_4]^+$ cluster (Cys421 and Cys424) are retained for the linear $[Fe_3S_4]^+$ cluster, with the other two cysteine ligands (Cys250 and Cys257) being recruited from a nearby helix (*219*). On the basis of the crystal structure of aconitase (*167*), a considerable protein conformational change is required to bring these new ligands into position.

A new type of cluster conversion has been proposed in the A33C mutant of *P. furiosus* Fd as a result of EPR, VTMCD, and resonance Raman studies (*46*). On the basis of the 3D NMR structure of a $[Fe_4S_4]$-containing form, the A33C mutation is expected to position a fourth cysteine residue within 4 Å of one of the Fe atoms of the $[Fe_3S_4]$ cluster. As expressed in *E. coli,* the mutant Fd contains a normal cuboidal $[Fe_3S_4]^+$ cluster, but VTMCD and EPR data indicate that the cluster can be reversibly converted to a form with a rhombic $S = 5/2$ ground state by the addition of polyethylene glycol (PEG). Although the EPR resonance with features at $g = 9.7$ and 4.3 is very similar to those of adventitiously bound Fe^{3+} ion and a linear $[Fe_3S_4]^+$ cluster, the unique form of the VTMCD spectrum points to a new type of $S = 5/2$ $[Fe_3S_4]^+$ cluster. Since resonance Raman spectra in the presence of PEG comprise features expected for $[Fe_2S_2]^{2+}$ and $Fe^{III}S_4$ units, we have tentatively interpreted this medium-dependent spin state change in terms of ligation of the fourth cysteine and concomitant cleavage of one of the μ_3S–Fe bonds; see Fig. 21c. This type of structure was originally proposed as an alternative to the cuboidal $[Fe_3S_4]$ cluster, prior to definitive crystallographic characterization (*5*, *15*, *17*). Mössbauer and EXAFS studies are in progress to test the validity of this proposal.

VII. Synthetic Model Compounds

Shortly after the discovery of 3Fe centers, Henkel and co-workers synthesized the first example of a trinuclear Fe–S compound, $[Fe_3S(S_2\text{-}o\text{-xyl-}4,5\text{-}Me_2)_3]^{2-}$ (S_2-*o*-xyl = *o*-xylene-α,α'-dithiolate) (*230*). This compound and the closely related $[Fe_3S(S_2\text{-}o\text{-xyl})_3]^{2-}$ compounds synthesized by Holm and co-workers (*231*) contain an apical μ_3–S atom bonded to three Fe(II) ions in a nearly equilateral triangle. Each Fe is coordinated to one terminal and one bridging sulfur atom of the dithiolate ligand, giving $Fe^{II}S_4$ units and an overall structure that approximates to C_3 symmetry (**1**). The average metrical parameters (Fe–Fe = 2.82 Å; Fe–μ_3S = 2.32 Å; Fe–μ_2S = 2.36 Å; Fe–S^t = 2.29 Å (*231*)) are similar to those of the $[Fe_3S_4]^0$ cluster in the $[Fe_3S_4(LS_3)]^{3-}$ complex (Fe–Fe = 2.70 Å; Fe–μ_3S = 2.31 Å; Fe–μ_2S = 2.26 Å; Fe–S^t = 2.32 Å; see Table III), except for a 0.1-Å increase in the Fe–Fe and Fe–μ_2S distances, which is consistent with bridging thiolates as opposed to bridging sulfides.

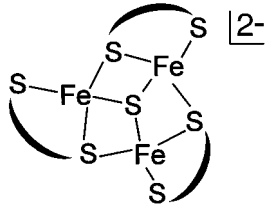

1

Since the complex $[Fe_3S(S_2\text{-}o\text{-}xyl)_3]^{2-}$ in acetonitile showed only one quasi-reversible oxidation and irreversible reduction at very negative potentials, characterization has been restricted to the overall −2 oxidation state. NMR studies demonstrated retention of the solid-state structure in acetonitrile solution, and the solution optical absorption and magnetic properties are indicative of magnetically interacting $Fe^{II}S_4$ units (*231*). Clearly, these compounds are excellent models for an all ferrous $[Fe_3S_4]^{2-}$ clusters with protonated μ_2–S atoms and merit more detailed investigation of their ground-state and excited-state properties using Mössbauer, saturation magnetization, and VTMCD studies. In the early 1980s, we carried out preliminary VTMCD studies of $[Fe_3S(S_2\text{-}o\text{-}xyl)_3]^{2-}$ in acetonitrile solutions (Kowal, A. T., Johnson, M. K., and Holm, R. H., unpublished results). The VTMCD spectrum is indeed similar to that deduced for the $[Fe_3S_4]^{2-}$ cluster in the four-electron reduced form of *S. acidocaldarius* 7Fe Fd (*119*), and magnetization studies indicate a paramagnetic, integer spin ground state.

The synthesis of a compound with a $[Fe_3S_4]$ core analogous to that found in proteins proved to be a challenging task that was finally accomplished by Zhou and Holm in 1995 (*49*). This was the result of an extensive research program initiated by the Holm group soon after the discovery of biological 3Fe centers in 1980. A brief overview of the different stages of this work is presented next.

In a systematic search for new species (*48*, *232*), the reactions of $FeCl_2$ or $[FeCl_4]^{2-}$ with 1–4 equivalents of thiolate were investigated. The intention was to use the resultant Fe(II)–thiolate complexes as reactants with elemental sulfur in the synthesis of Fe–S clusters. This approach led to the synthesis of trinuclear compounds such as $(Et_4N)_3[Fe_3(SPh)_3Cl_6]$ (*232*, *233*); an all-ferric cluster with a planar $Fe_3(\mu_2\text{–}SPh)_3$ ring ($\angle$Fe–S–Fe ~140°, Fe–Fe distances ~ 4.46 Å, and phenyl groups coplanar with the ring) and distorted tetrahedral $Fe(SPh)_2Cl_2$ units (*233*). Another of the products, $[Fe(SEt)_4]^{2-}$, proved to be very reactive and afforded direct entry to a variety of bi-, tri-,

and hexanuclear clusters (*48*). Of particular importance was the synthesis and characterization of $(Et_4N)_3[Fe_3S_4(SR)_4]$ (R = Et, Ph) (**2**), which contains the linear $[Fe(\mu_2\text{–}S)_2Fe(\mu_2\text{–}S)_2Fe]^+$ core (*48*, *234*). Each Fe atom occupies an approximately tetrahedral site with an Fe–Fe separation of 2.71 Å. Magnetic susceptibility and EPR measurements indicated an $S = 5/2$ ground state, and Mössbauer spectra revealed the presence of high-spin Fe(III) ions in two magnetic subsites in a 2 : 1 ratio. The more intense subsite corresponds to the two end Fe(III) sites, which have magnetic moments parallel to each other and to the total moment of the cluster. The less intense subsite is the central Fe(III) site, which has its magnetic moment antiparallel to the cluster total moment. Thus, individual iron spins, $S_i = 5/2$, combine to produce a total spin $|S| = |S_1 + S_2 + S_3| = 5/2$. As discussed in the preceding section, this complex was crucial to the discovery of linear $[Fe_4S_4]^+$ clusters in alkaline forms of mitochondrial aconitase. It also provided a synthetic route to several heterometallic cubanes, $[MFe_3S_4]$; see later discussion.

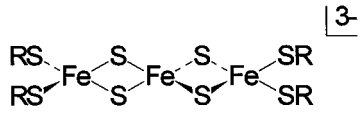

2

In the previous issue of this series devoted to "Iron–Sulfur Proteins," Holm summarized a body of work that showed how different terminal ligation at one Fe site of a protein-bound or synthetic $[Fe_4S_4]$ cluster leads to 3 : 1 site-differentiated clusters (*235*). This results not only in special properties for this unique Fe, but also in destabilization of this site upon oxidation and the formation of the cuboidal $[Fe_3S_4]$ clusters in proteins. This suggested a strategy for the synthesis of the cuboidal $[Fe_3S_4]$ core that was based on iron-site-differentiated $[Fe_4S_4]$ clusters. However, the synthetic analogs $[Fe_4S_4(SR)_4]^{2-,3-}$ possess effectively equivalent Fe subsites and undergo statistical ligand substitution reactions. This problem was solved by the synthesis of a semirigid trithiol ligand 1,3,5-tris((4,6-dimethyl-3-mercaptophenyl)thio)-2,4,6-tris(*p*-tolylthio)benzene (LS_3) ( ) (*236*). LS_3 is largely predisposed to capture a cubane cluster in a ligand substitution reaction. The ligand is sufficiently flexible that it binds the $[Fe_4Se_4]^{2+}$ core, which has a van der Waals volume ~25% larger than that of a $[Fe_4S_4]^{2+}$ core (*50*).

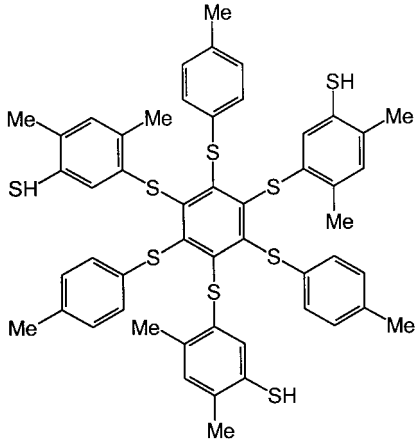

3

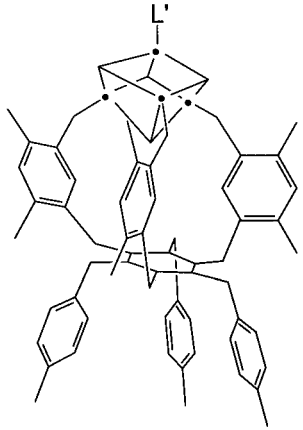

(• = Fe)

4

The single cubane cluster $[Fe_4S_4(LS_3)L']^{z-}$ (**4**) with L′ as Cl^- (z = 2), a good leaving group, formed the starting point for a systematic investigation of the site-specific reactivity of cubane clusters and the formation of a diverse set of products (*235–240*). The nature of the ligand(s) L′ at the unique iron subsite influenced the isotropically shifted ^1H NMR resonances of the 4Me, 5H, and 6Me substituents of the phenyl rings in the coordinating arms of the ligand and resulted

in shifts in the cluster redox potential. Both of these properties were also used for the characterization of mixed metal clusters coordinated by LS_3 (*51*).

The ^1H NMR isotropic shifts for nearly all $[Fe_4S_4(LS_3)L']^{z-}$ compounds were sufficiently similar to demonstrate a common $S = 0$ ground state, as expected for a $[Fe_4S_4]^{2+}$ core. However, this was not the case for clusters obtained from reactions with alkyl isonitriles, and the structure of the product revealed approximately octahedral coordination at the unique Fe site with three isonitriles bound in facial arrangement (*238*, *239*). Mössbauer spectroscopic and magnetic susceptibility studies of $[Fe_4S_4(LS_3)(t\text{-BuNC})_3]^-$ (*239*) demonstrated the existence of a valence-localized low-spin Fe(II) subsite ($S = 0$), assigned to the trigonal Fe(t-BuNC)$_3$ group, and a spin-isolated $[Fe_3S_4]^0$ cluster fragment. The latter was shown to have the same ground-state and valence-delocalization properties as a protein-bound $S = 2$ $[Fe_3S_4]^0$ cluster and hence provided the first evidence that these were intrinsic properties of the cluster core as opposed to being induced by the protein environment.

Based on the behavior in proteins, it might be expected that a simple oxidation step will transform an $[Fe_4S_4]$ cluster into an $[Fe_3S_4]$ cluster. Such behavior is indeed observed with synthetic $[Mo_4S_4]$ clusters (*235*). This procedure was attempted by Weterings *et al.* using $[Fe_4S_4(S\text{-}t\text{-Bu})_4]^{2-}$ (*241*). Oxidation by $[Fe(CN)_6]^{3-}$ in DMF/buffer at $-40°C$ yielded a cluster that was spectroscopically (EPR, Mössbauer) similar to the Fe_3S_4 cluster in proteins. Unfortunately, the cluster was not stable at room temperature, and no crystals could be obtained. A similar method was used by Roth and Jordanov (*242*). Oxidation of $[Fe_4S_4(S\text{-}2,4,6\text{-}(i\text{-Pr})_3C_6H_2)_4]^{2-}$ with $[Fe(CN)_6]^{3-}$ in aprotic media (CH_2Cl_2, CH_3CN) resulted in a species with a $[Fe_4S_4]^{3+}$ core. In aqueous media (DMF/H_2O or CH_3CN/H_2O) a $[Fe_3S_4]^+$ center was formed, but the cluster was unstable and underwent rapid decomposition.

Since no other attempts are described in the literature, it would appear that oxidative degradation of synthetic $[Fe_4S_4]$ clusters has thus far proven unsuccessful in furnishing $[Fe_3S_4]$ models suitable for crystallographic and detailed spectroscopic analysis. Holm and coworkers tried a different approach that led to the synthesis and detailed characterization of a synthetic compound containing a $[Fe_3S_4]^0$ core (*49*, *50*). The trinuclear cluster was formed by abstraction of a Fe^{2+} ion from a site-differentiated $[Fe_4S_4]^{2+}$ core ligated by the trithiolate cavitand ligand, LS_3. Reaction of $[Fe_4S_4(LS_3)(SEt)]^{2-}$ with $(Et_3NH)(OTf)$ (OTf = triflate) affords $[Fe_4S_4(LS_3)(OTf)]^{2-}$, in which the unique Fe site is activated toward terminal ligand substitution.

Treatment with 1 equivalent of the Fe^{2+}-ion chelator (Et_4N)(Meida) (Meida = *N*-methylimidodiacetate), affords $[Fe_4S_4(LS_3)(Meida)]$, which was readily converted to $[Fe_3S_4(LS_3)]^{3-}$ with 1–2 equivalents of additional reactant. The Fe^{2+} was abstracted as $[Fe(Meida)_2]^{2-}$. Subsequently an alternative synthesis was found involving removal of the $Mo(CO)_3$ fragment in $[(CO)_3MoFe_3S_4(LS_3)]^{3-}$ by treatment with CO in the presence of $NaPF_6$ (*243*). X-ray structure determination of $(Et_4N)_3[Fe_3S_4(LS_3)]$ showed that the cuboidal core is metrically very similar to the cubane core of $[Fe_4S_4(LS_3)Cl^-]^{2-}$ and to protein-bound $[Fe_3S_4]^{+,0}$ clusters (*50*). A detailed structural comparison was presented earlier; see Table III, Fig. 2, and Section IV. The similarity of the EPR and Mössbauer data compared to protein-bound $[Fe_3S_4]^0$ clusters (*50*), see Section V,B,1, showed unequivocally that the protein structure is not needed to sustain the arrangement of an $S = 9/2$ valence-delocalized $Fe^{2.5+}Fe^{2.5+}$ pair antiferromagnetically coupled to an $S = 5/2$ Fe^{3+} site that leads to the $S = 2$ ground state. Rather, it is an intrinsic property of the $[Fe_3S_4]^0$ core and was shown to be preserved in the $[Fe_3Se_4]^0$ core of the $[Fe_3Se_4(LS_3)]^{3-}$ complex. Both the $[Fe_3S_4(LS_3)]^{3-}$ and $[Fe_3Se_4(LS_3)]^{3-}$ were shown to undergo reversible one-electron oxidation ($E_m = -0.79$ and -0.80 V, respectively) and reduction ($E_m = -1.72$ and -1.67 V, respectively) in acetonitile solutions (*50*). Detailed spectroscopic and structural characterizations of these oxidized and reduced forms, containing $[Fe_3S_4]^+$ and $[Fe_3S_4]^-$ cores, respectively, would answer many of the unresolved questions concerning $[Fe_3S_4]$ clusters and is awaited with great interest.

VIII. Mixed Metal Clusters

A. Protein-Bound [MFe_3S_4] Clusters

The concept of an $[Fe_3S_4]$ cluster as a redox active, quasi-rigid ligand for heterometal ions to form heterometallic cubane clusters was first demonstrated in 1986 by the formation of a $[CoFe_3S_4]^{2+}$ cluster in *D. gigas* FdII (*31*). Since then, experiments with three distinct proteins, *D. gigas* FdII, *P. furiosus* Fd, and *D. africanus* FdIII, have reported the preparation and characterization of eight protein-bound heterometallic cubanes $[MFe_3S_4]$, M = Cr (*36*), Mn (*35*), Co (*35*, *64*), Ni (*34*, *64*, *198*), Cu (*36*, *40*), Zn (*32*, *35*, *38*, *198*), Cd (*33*, *38*, *64*), and Tl (*37*, *39*), using the generalized reaction ($n = 1, 2$):

$$[Fe_3S_4]^+ + M^{2+,+} + ne^- \rightleftharpoons [MFe_3S_4]^{2+,+}$$

Kinetics studies have provided evidence for binding of Co^{2+} and Mn^{2+} to the 3Fe cluster in aconitase (*244*), and electrochemical studies have shown that the 3Fe cluster in *D. africanus* FdIII has a high affinity for Pb^{2+} (*41*), but these clusters have yet to be characterized spectroscopically. No crystallographic data are available for proteins containing heterometallic cubanes, and evidence for their formation and properties comes from changes in EPR, Mössbauer, VTMCD, and redox properties in the presence of excess exogenous metal ion. The spectroscopic evidence is particularly persuasive for clusters with $S = 1/2$ ground states involving heterometals with naturally abundant magnetic nuclei, since they usually exhibit well-resolved nuclear hyperfine structure on one component of the EPR signal, for example, $[CoFe_3S_4]^{2+}$ (*31*, *35*), $[TlFe_3S_4]^{2+}$ (*37*, *39*) and $[CuFe_3S_4]^{2+}$ (*36*). The reliability of the spectroscopic approaches for assessing the formation of heterometallic cubanes in Fds has been attested to by the close similarity in the properties of protein-bound and crystallographically defined synthetic clusters with $[NiFe_3S_4]^{+}$ and $[CoFe_3S_4]^{2+}$ cores (*245*). Armstrong and co-workers have devised an elegant electrochemical method, in which the Fd is coadsorbed as a stable electroactive film, to assess the formation and redox properties of heterometallic cubanes in *D. africanus* FdIII (*38*). This has led to estimates of equilibrium dissociation constants as a function of the metal ion and established an affinity order $Pb^{2+} \gg Cu^{+} > Cd^{2+} > Tl^{+} \geq Zn^{2+} > Fe^{2+} \gg Co^{2+}$ with respect to metal ion binding to the $[Fe_3S_4]^0$ cluster (*41*).

A summary of the spin states identified for protein-bound $[MFe_3S_4]^{2,+}$ clusters is shown in Table VII. EPR and VTMCD studies have shown that the $[TlFe_3S_4]^{2+,+}$ and $[CuFe_3S_4]^{2+,+}$ clusters are best considered as Tl^{+} and Cu^{+} coordinated by $S = 1/2$ $[Fe_3S_4]^{+}$ or $S = 2$ $[Fe_3S_4]^0$ fragments (*36*, *37*, *39*, *40*). In general, $[Fe_3S_4]^{+}$ clusters have low affinity for binding metal ions and stable heterometallic clusters are only formed with large, polarizable, monovalent, thiophilic metal ions. For all other heterometallic cubanes, VTMCD and/or Mössbauer studies indicate that formulations in terms of a high-spin M^{2+} ion interacting with an $S = 2$ $[Fe_3S_4]^0$ or $S = 5/2$ $[Fe_3S_4]^{-}$ fragment are more appropriate (*31*, *33–40*, *198*). For example, all heterometallic clusters, except for $[TlFe_3S_4]^{2+}$ and $[CuFe_3S_4]^{2+}$, exhibit an intense positive MCD band centered between 700 and 800 nm, which is the hallmark of the $S = 9/2$ valence-delocalized $Fe^{2.5+}Fe^{2.5+}$ pair in the $[Fe_3S_4]^0$ and $[Fe_3S_4]^{-}$ cluster fragments. In 1991, this formulation led us to propose that the ground-state spin for clusters involving paramagnetic divalent transition metal ions could be rationalized on the basis of antiferromagnetic coupling between the high-spin M^{2+} ion and an $S = 2$

TABLE VII

SUMMARY OF PREDICTED AND OBSERVED GROUND-STATE PROPERTIES OF PROTEIN-BOUND $[MFe_3S_4]$ CLUSTERS

	Metal ion		Cluster fragment		Ground state		
Cluster	M^{n+}	Spin	Ox. state	Spin	Predicted	Observed	Ref.
$[Fe_4S_4]^+$	Fe^{2+}	2	$[Fe_3S_4]^-$	5/2	1/2	1/2, 3/2	*42*, *43*
$[Fe_4S_4]^{2+}$	Fe^{2+}	2	$[Fe_3S_4]^0$	2	0	0	*42*, *43*
$[CrFe_3S_4]^+$	Cr^{2+}	2	$[Fe_3S_4]^-$	5/2	1/2	3/2	*36*
$[CrFe_3S_4]^{2+}$	Cr^{2+}	2	$[Fe_3S_4]^0$	2	0	0	*36*
$[MnFe_3S_4]^+$	Mn^{2+}	5/2	$[Fe_3S_4]^-$	5/2	0	0	*35*
$[CoFe_3S_4]^+$	Co^{2+}	3/2	$[Fe_3S_4]^-$	5/2	1	1	*35*
	Co^+	1	$[Fe_3S_4]^0$	2	1	1	
$[CoFe_3S_4]^{2+}$	Co^{2+}	3/2	$[Fe_3S_4]^0$	2	1/2	1/2	*31*, *35*
$[NiFe_3S_4]^+$	Ni^{2+}	1	$[Fe_3S_4]^-$	5/2	3/2	3/2	*34*, *198*
	Ni^+	1/2	$[Fe_3S_4]^0$	2	3/2	3/2	
$[CuFe_3S_4]^+$	Cu^+	0	$[Fe_3S_4]^+$	1/2	1/2	1/2	*36*, *40*
$[CuFe_3S_4]^{2+}$	Cu^+	0	$[Fe_3S_4]^0$	2	2	2	*36*, *40*
$[ZnFe_3S_4]^+$	Zn^{2+}	0	$[Fe_3S_4]^-$	5/2	5/2	5/2	*32*, *35*, *38*, *198*
$[ZnFe_3S_4]^{2+}$	Zn^{2+}	0	$[Fe_3S_4]^0$	2	2	2	*35*, *38*
$[CdFe_3S_4]^+$	Cd^{2+}	0	$[Fe_3S_4]^-$	5/2	5/2	5/2	*36*, *38*
$[CdFe_3S_4]^{2+}$	Cd^{2+}	0	$[Fe_3S_4]^0$	2	2	2	*36*, *38*
$[TlFe_3S_4]^+$	Tl^+	0	$[Fe_3S_4]^0$	2	2	2	*37*, *39*
$[TlFe_3S_4]^{2+}$	Tl^+	0	$[Fe_3S_4]^+$	1/2	1/2	1/2	*37*, *39*

$[Fe_3S_4]^0$ or $S = 5/2$ $[Fe_3S_4]^-$ fragment (*35*, *246*); see Table VII. For example, the ground states of the $S = 1$ $[CoFe_3S_4]^+$ and $S = 1/2$ $[CoFe_3S_4]^{2+}$ clusters were rationalized by coupling a $S = 3/2$ Co^{2+} ion with an $S = 5/2$ $[Fe_3S_4]^-$ and $S = 2$ $[Fe_3S_4]^0$ fragment, respectively. Although the simplicity of this model is attractive, it lacks theoretical justification, and it does not explain the $S = 3/2$ $[Fe_3S_4]^+$ and $[CrFe_3S_4]^+$ clusters in *P. furiosus* Fd (see Table VII), the variability in redox potentials (see Table VIII), and the Mössbauer data for $[CoFe_3S_4]^+$ clusters (*14*) and $[NiFe_3S_4]^+$ clusters (*198*, *245*). The latter point is best illustrated by a comparison of Fe isomer shifts. The average Fe isomer shifts for the $[CoFe_3S_4]^+$ and $[NiFe_3S_4]^+$ clusters, $\delta = 0.53$ mm/s and 0.47–0.50 mm/s, respectively, are intermediate between the values established for an $[Fe_3S_4]^0$ cluster ($\delta \sim 0.42$ mm/s) or an $[Fe_3S_4]^-$ fragment ($\delta \sim 0.56$ mm/s), indicating heterometal ion oxidation states between +1 and +2. Hence, the underlying assumptions of this model, that is, well-defined oxidation states for the heterometal ion and the cluster fragment, with the redox chemistry confined exclusively to the cluster fragment, are not strictly valid.

TABLE VIII

REDOX POTENTIALS (mV VS NHE AT pH 7–8) FOR PROTEIN-BOUND CLUSTERS

Core couple	Protein			Refs.
	D. africanus Fd III	*D. gigas* Fd II	*P. furiosus* Fd	
$[Fe_3S_4]^{1+,0}$	−140[a]	−130[a]	−160[b]	*35*, *38*, *64*
$[MnFe_3S_4]^{2+,1+}$			>−100[b,c]	*35*
$[Fe_4S_4]^{2+,1+}$	−400[a]	−420[a]	−345[b]	*35*, *38*, *64*
$[CoFe_3S_4]^{2+,1+}$	−271[a]	−245[a]	−163[b]	*35*, *41*, *64*
$[NiFe_3S_4]^{2+,1+}$		−360[a]	>−100[b,c]	*35*, *64*
$[ZnFe_3S_4]^{2+,1+}$	−480[a]		−241[b]	*35*, *38*
$[CdFe_3S_4]^{2+,1+}$	−580[a]	−495[a]	−470[b]	*36*, *38*, *64*
$[PbFe_3S_4]^{2+,1+}$	−440[a]			*41*
$[CrFe_3S_4]^{2+,1+}$			−440[a]	*36*
$[CuFe_3S_4]^{2+,1+}$	+148[a]		+190[a]	*36*, *40*
$[TlFe_3S_4]^{2+,1+}$	+81[a]		+120[a,d]	*39*

[a] Determined by direct electrochemistry at a glassy carbon electrode (cyclic, differential pulse, or square-wave voltammetry).

[b] Determined by dye-mediated EPR redox titrations.

[c] At potentials above −100 mV, these clusters undergo loss of the heterometal ion with concomitant formation of $[Fe_3S_4]^+$ clusters.

[d] Fu, W., Adams, M. W. W., and Johnson, M. K., unpublished results.

Indeed, it seems likely that the success of the fragment formulation model in explaining the ground-state spins of the $S = 1$ $[CoFe_3S_4]^+$ and $S = 3/2$ $[NiFe_3S_4]^+$ clusters may be a consequence of both $M^+/[Fe_3S_4]^0$ and $M^{2+}/[Fe_3S_4]^-$ coupling schemes correctly predicting the observed ground states; see Table VII. More sophisticated spin coupling models for heterometallic cubanes based on density functional theory calculations are now starting to be developed (*247*).

In comparing the redox and detailed spectroscopic properties of the heterometallic cubanes assembled in *D. gigas* FdII, *P. furiosus* Fd, and *D. africanus* FdIII, differences in the ligation at the heterometal site must be borne in mind. Given the NMR evidence for aspartate binding to the unique Fe site of the $[Fe_4S_4]$ cluster in *P. furiosus* Fd (*63*), it is likely that the heterometal site is ligated by aspartate in both *P. furiosus* Fd and *D. africanus* FdIII. However, the ability of aspartate to act as a monodentate or bidentate ligand may be important in understanding heterogeneity and differences in the properties of the clusters in these two proteins; for example, see Section V,C. Convincing evidence that cysteinate ligates the heterometal site in *D. gigas* FdII comes from the observation that excess β-mercaptoethanol (at pH ≥ 10) converts the EPR of the $[Fe_4S_4]^+$, $[NiFe_3S_4]^+$, and

$[ZnFe_3S_4]^+$ clusters in *P. furiosus* into spectra indistinguishable from those observed for the equivalent clusters in *D. gigas* FdII (*35*, *248*). Moreover, mutation of the coordinating aspartate in *P. furiosus* Fd (*65*, *249*) and *D. africanus* FdIII (*250*) to cysteine converts the mixed spin ($S = 1/2$ and 3/2) $[Fe_3S_4]^+$ clusters into homogeneous $S = 1/2$ $[Fe_4S_4]^+$ clusters with EPR and MCD properties identical to those of the all-cysteine-ligated $[Fe_4S_4]^+$ cluster in *D. gigas* FdII. There is also persuasive spectroscopic evidence (EPR and/or VTMCD) for CN^- binding at the unique metal site of the $[ZnFe_3S_4]^+$, $[CoFe_3S_4]^+$, and $[NiFe_3S_4]^+$ clusters in *P. furiosus* Fd (*34*, *35*). Such behavior has been observed for the $[Fe_4S_4]^+$ cluster in *P. furiosus* Fd, with combinations of EPR, VTMCD, and ENDOR studies providing unambiguous evidence for the binding of a single CN^- at the unique Fe site (*251*, *252*).

The preceding discussion sets the stage for a qualitative rationalization of the trends in redox potentials of protein-bound $[MFe_3S_4]^{2+,+}$ clusters; see Table VIII. The clusters are divided into two groups, depending on whether or not they undergo formal redox cycling between $[Fe_3S_4]^{+,0}$ and $[Fe_3S_4]^{0,-}$ fragments within the biologically accessible range of potentials. In principle, both couples are accessible to each heterometallic cubane, but only one is observed, that is, thiophilic, monovalent ions such as Cu^+ and Tl^+ decrease the potential of both couples, bringing the $[Fe_3S_4]^{+,0}$ couple into the biologically accessible range and taking the $[Fe_3S_4]^{0,-}$ couple to < -700 mV, whereas divalent transition-metal ions increase the potential of both couples, taking the $[Fe_3S_4]^{+,0}$ couple above +400 mV and bringing the $[Fe_3S_4]^{0,-}$ couple into the biologically accessible range. (The negligible affinity of the $[Fe_3S_4]^+$ clusters for divalent heterometal ions would undoubtedly result in loss of the heterometal even if potentials $> +400$ mV were accessible.) Within each group, the range of potentials can be generally be rationalized on the basis of the ability of the heterometal site to donate or withdraw electron density from cluster fragments, resulting in a decrease or increase in the cluster potential, respectively. For clusters with $[Fe_3S_4]^{+,0}$ couples, the order of potentials Tl < Cu has been established in both *D. africanus* FdIII and *P. furiosus* Fd. This is consistent with Tl^+ being a better electron donor than Cu^+ as a result of its increased size and polarizability.

For heterometallic clusters with $[Fe_3S_4]^{0,-}$ couples, the order potentials can be summarized as follows:

Cd < Cr < Fe < Zn < Co < Mn,Ni in *P. furiosus* Fd
Cd < Zn < Fe < Co in *D. africanus* FdIII
Cd < Ni < Fe < Co in *D. gigas* FdII

The origin of the differences between these proteins, that is, the inversion of the order of Zn and Fe between *P. furiosus* Fd and *D. africanus* FdIII and the anomalously high potential of the Ni cluster in *D. gigas* FdII, is unknown at present, but may well reflect differences in the ligation of the heterometal (i.e., monodentate or bidentate aspartate in *D. africanus* FdIII and *P. furiosus* and cysteinate in *D. gigas* FdII). We have attempted to rationalize the sequence in *P. furiosus* on the basis of this model in light of the available spectroscopic data (*36*). Relative to Zn, the heterometal sites in the Fe, Cr, and Cd clusters are progressively better electron donors. For Cd, this is once again explained on the basis of increased size and polarizability, whereas for Cr and Fe this would require a formal oxidation state between +2 and +3 for the unique metal site in the $[FeFe_3S_4]^+$ and $[CrFe_3S_4]^+$ clusters. Such a conclusion is consistent with the propensity of these metal ions for +2 and +3 oxidation states and NMR and ^{57}Fe-ENDOR studies of *P. furiosus* that indicate that the aspartyl-ligated Fe atom of the $[Fe_4S_4]^+$ center is part of the valence-delocalized $Fe^{2.5+}Fe^{2.5+}$ pair (*170*, *253*). In contrast, the heterometal sites in the Co and Ni/Mn clusters are progressively better electron acceptors relative to Zn. Within the framework of this model, this would require a formal oxidation state between +1 and +2 for the Co, Ni, and Mn sites in $[CoFe_3S_4]^+$, $[NiFe_3S_4]^+$ and $[MnFe_3S_4]^+$ clusters. This is in accord with the Mössbauer data for the $[CoFe_3S_4]^+$ and $[NiFe_3S_4]^+$ clusters (see earlier discussion) which indicate an oxidation state slightly below +2 for Co and intermediate between +1 and +2 for Ni. Although additional Mössbauer studies for a wider range of clusters are required, it seems likely that the $[MFe_3S_4]^{2+,+}$ midpoint potential provides a reliable, albeit qualitative, indicator of the charge distribution between the heterometal and the cluster fragment.

These studies of protein-bound heterometallic cubanes have amply demonstrated that the heterometal site is redox active and able to bind small molecules. Although they have yet to be identified as intrinsic components of any protein or enzyme (except as part of the nitrogenase FeMo cofactor cluster (*254*)), they are clearly attractive candidates for the active sites of redox enzymes.

B. Synthetic $[MFe_3S_4]$ Clusters

The systematic development of the chemistry of synthetic $[MFe_3S_4]$ clusters is largely the work of Holm and co-workers and has occurred in parallel and synergistically with the development of the protein-bound analogs. A comprehensive review of this work up to 1992 can

be found in the previous issue in this series on iron–sulfur proteins (*235*). Here we present a brief overview of the early work and focus on the recent results, with particular emphasis on the metal ion incorporation reactions of the $[Fe_3S_4(LS_3)]^{3-}$ cluster.

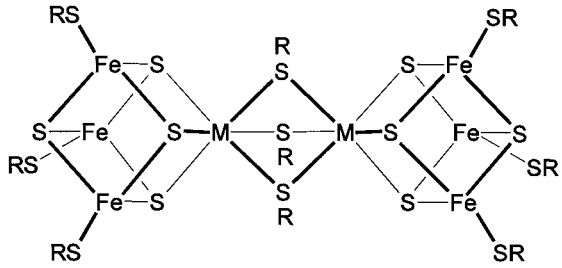

5

The initial motivation for the synthesis of heterometallic cubanes was provided by EXAFS data on nitrogenase, which indicated that the active site FeMo cofactor contained a cuboidal $MoFe_3S_3$ fragment (*255*, *256*). This led to the synthesis of a wide range of single and double (**5**) cubanes involving $[MoFe_3S_4]^{3+,2+}$, $[VFe_3S_4]^{3+,2+}$, $[WFe_3S_4]^{3+}$, $[NbFe_3S_4]^{3+,2+}$, and $[ReFe_3S_4]^{4+,3+}$ cores, via self-assembly reactions involving the appropriate tetrahedral $[MS_4]^{z-}$ precursor (*235*, *257*). An alternative route involving reductive rearrangement of a linear $[Fe_3S_4(SR)_4]^{3-}$ cluster in the presence of low-valent metals (Mo(0), W(0), Co(I), Ni(0)) was subsequently developed specifically for metals that do not have stable tetrathiometalates (*245*, *258*, *259*). This led to the synthesis of clusters with $[MoFe_3S_4]^0$, $[WFe_3S_4]^0$, $[CoFe_3S_4]^{2+}$, and $[NiFe_3S_4]^+$ cores. More recently, a range of new heterometallic cubanes have been synthesized with $[CuFe_3S_4]^+$, $[AgFe_3S_4]^+$, $[TlFe_3S_4]^+$, $[CoFe_3S_4]^+$ cores, and new routes to clusters with $[MoFe_3S_4]^0$, $[WFe_3S_4]^0$, and $[NiFe_3S_4]^+$ cores have been developed, by investigating the metal ion incorporation reactions of the $[Fe_3S_4(LS_3)]^{3-}$ cluster (*51*, *260*). These reactions and the compounds involved are summarized in Fig. 22. The conformational flexibility of the LS_3 ligand impedes crystallization, and the evidence for the heterometallic structures shown in Fig. 22 is based largely on ^1H NMR. Isotropic shifts of protons on the pendant arms of the LS_3 ligand have been found to be exquisitely sensitive to the identity of the heterometal (*51*).

It has not been possible to obtain homogeneous samples of synthetic

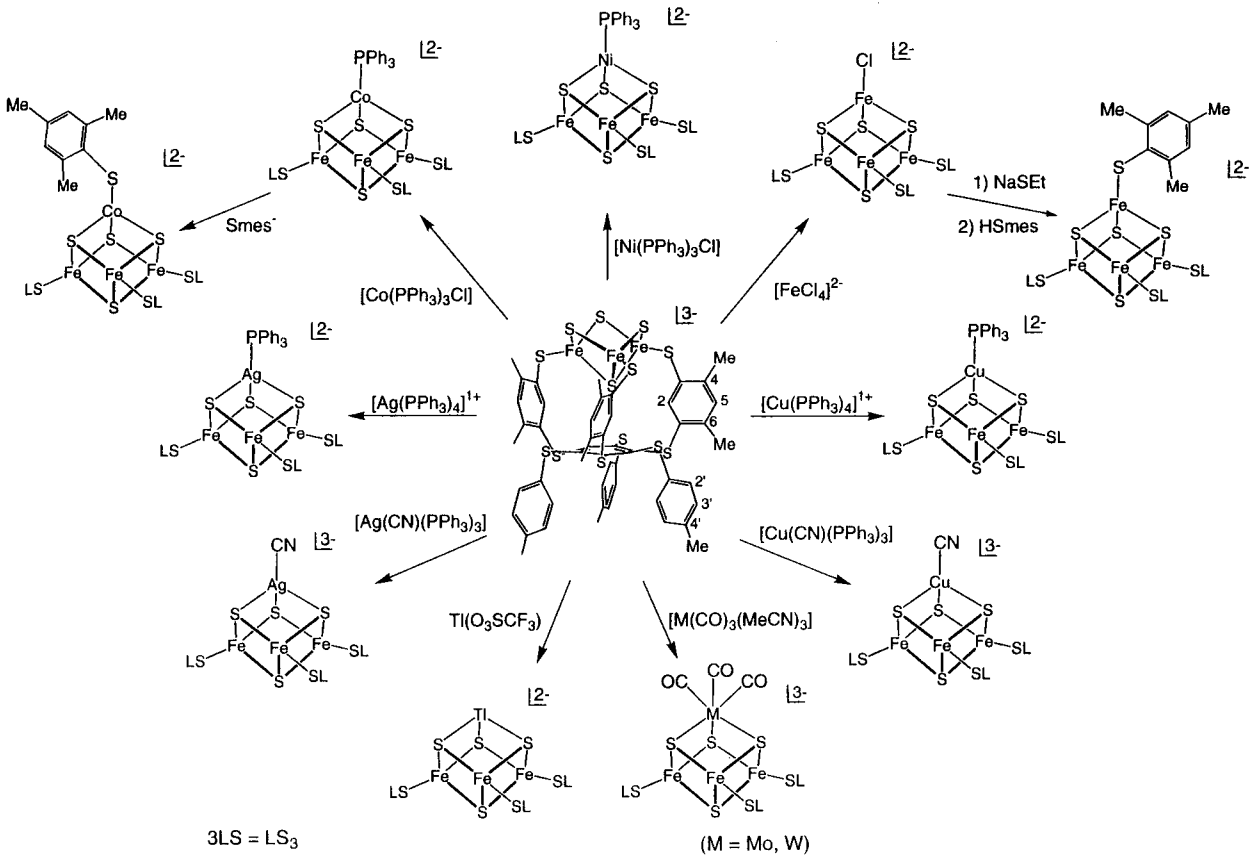

FIG. 22. Metal ion incorporation reactions of $[Fe_3S_4(LS_3)]^{3-}$ in acetonitrile solution. Taken with permission from Ref. (*51*).

TABLE IX

SUMMARY OF THE GROUND-STATE PROPERTIES OF REPRESENTATIVE EXAMPLES OF SYNTHETIC SINGLE AND DOUBLE CUBANES CONTAINING [MFe_3S_4] CLUSTERS AND RATIONALIZATION IN TERMS OF THE FRAGMENT FORMULATION MODEL

Complex[b]	Cluster core	Metal ion[a]		Cluster fragment		Ground state		Ref.
		M^{n+}	Spin	Ox. state	Spin	Predicted	Observed	
$[MoFe_3S_4(SR)_4(al_2cat)]^{2-}$	$[MoFe_3S_4]^{3+}$	Mo^{3+}	1/2	$[Fe_3S_4]^0$	2	3/2	3/2	*261*
$[MoFe_3S_4(SR)_3(al_2cat)(EtCN)]^{3-}$	$[MoFe_3S_4]^{2+}$	Mo^{3+}	1/2	$[Fe_3S_4]^-$	5/2	2	2	*261*
$[(CO)_3MoFe_3S_4(LS_3)]^{3-}$	$[MoFe_3S_4]^0$	Mo^0	0	$[Fe_3S_4]^0$	2	2	2	*243*
$[W_2Fe_6S_8(SEt)_9]^{3-}$	$[WFe_3S_4]^{3+}$	W^{3+}	1/2	$[Fe_3S_4]^0$	2	3/2	3/2	*257*
$[V_2Fe_6S_8(SEt)_9]^{3-}$	$[VFe_3S_4]^{3+}$	V^{3+}	1	$[Fe_3S_4]^0$	2	1	0	*257*
$[VFe_3S_4(SR)_3(DMF)_3]^-$	$[VFe_3S_4]^{2+}$	V^{2+}	1/2	$[Fe_3S_4]^0$	2	3/2	3/2	*262*
		V^{3+}	1	$[Fe_3S_4]^-$	5/2	3/2	3/2	
$[Nb_2Fe_6S_8(SEt)_9]^{3-}$	$[NbFe_3S_4]^{3+}$	Nb^{3+}	1	$[Fe_3S_4]^0$	2	1	0	*257*
$[Nb_2Fe_6S_8(SEt)_9]^{5-}$	$[NbFe_3S_4]^{2+}$	Nb^{2+}	1/2	$[Fe_3S_4]^0$	2	3/2	3/2	*257*
		Nb^{3+}	1	$[Fe_3S_4]^-$	5/2	3/2	3/2	
$[ReFe_3S_4(SEt)_4(dmpe)]^-$	$[ReFe_3S_4]^{3+}$	Re^{3+}	0	$[Fe_3S_4]^0$	2	2	2	*263*
		Re^{4+}	1/2	$[Fe_3S_4]^-$	5/2	2	2	
$[Re_2Fe_7S_8(SEt)_{12}]^{5-}$	$[ReFe_3S_4]^{4+}$	Re^{4+}	1/2	$[Fe_3S_4]^0$	2	3/2	3/2	*264*
$[(Ph_3P)CuFe_3S_4(LS_3)]^{2-}$	$[CuFe_3S_4]^+$	Cu^+	0	$[Fe_3S_4]^0$	2	2	2	*51*
$[(Ph_3P)AgFe_3S_4(LS_3)]^{2-}$	$[AgFe_3S_4]^+$	Ag^+	0	$[Fe_3S_4]^0$	2	2	2	*51*
$[TlFe_3S_4(LS_3)]^{2-}$	$[TlFe_3S_4]^+$	Tl^+	0	$[Fe_3S_4]^0$	2	2	2	*51*
$[(Ph_3P)CoFe_3S_4(LS_3)]^{2-}$	$[CoFe_3S_4]^+$	Co^{2+}	3/2	$[Fe_3S_4]^-$	5/2	1	1	*51*
		Co^+	1	$[Fe_3S_4]^0$	2	1	1	
$[CoFe_3S_4(Smes)_4]^{2-}$	$[CoFe_3S_4]^{2+}$	Co^{2+}	3/2	$[Fe_3S_4]^0$	2	1/2	1/2	*245*
$[(Ph_3P)NiFe_3S_4(SEt)_3]^{2-}$	$[NiFe_3S_4]^+$	Ni^{2+}	1	$[Fe_3S_4]^-$	5/2	3/2	3/2	*245*
		Ni^+	1/2	$[Fe_3S_4]^0$	2	3/2	3/2	

[a] d^3 and d^4 metal ions are assigned $S = 1/2$ and 0, respectively. This is reasonable for a second- or third-row transition-metal ion with a trigonally distorted octahedral environment, but is difficult to justify for V^{2+}.

[b] al_2cat = 3,6-diallylcatecholate(2−); dmpe = 1,2-dimethylphosphinoethane; Smes = mesitylthiolate(1−).

clusters with $[ZnFe_3S_4]^{2+,+}$, $[CdFe_3S_4]^{2+,+}$, $[MnFe_3S_4]^+$, or $[CrFe_3S_4]^{2+,+}$ cores. Only protein-bound forms of these clusters are known at present. Conversely, clusters with $[MoFe_3S_4]^{3+,2+,0}$, $[VFe_3S_4]^{3+,2+}$, $[WFe_3S_4]^{3+,0}$, $[NbFe_3S_4]^{3+,2+}$, $[ReFe_3S_4]^{4+,3+}$, and $[AgFe_3S_4]^+$ cores have yet to be formed in a protein matrix. The spin states of these cores in a representative example of each of these clusters, as determined by magnetic susceptibility, Mössbauer, proton isotropic shifts, or some combination thereof, are given in Table IX. The observed spin states are invariant to the nature of the ligation at the heterometal site and can generally be rationalized in terms of the fragment formulation model (see Table IX), with average isomer shifts providing an assessment of the oxidation state of the [Fe_3S_4] fragment and thereby the oxidation state of the heterometal ion (*51*, *235*, *245*, *257*). The most notable exceptions are the $[VFe_3S_4]^{3+}$ and $[NbFe_3S_4]^{3+}$ clusters, which

are predicted to be $S = 1$, but are diamagnetic with $S = 0$ ground states. For clusters containing $[CoFe_3S_4]^{2+,+}$, $[NiFe_3S_4]^{+}$, $[CuFe_3S_4]^{+}$, $[TlFe_3S_4]^{+}$ cores that have been characterized in both protein-bound and synthetic forms, the available evidence points to congruent ground-state properties and fragment formulations; cf. Tables VII and IX (*51*, *245*, *259*).

The ability to compare redox properties of synthetic clusters with identical ligation and parity of charge affords a meaningful comparison of the influence of the heterometal on redox potential. Reversible $[MFe_3S_4]^{2+,+}$ couples have been identified in cyclic voltammograms of $[(Smes)MFe_3S_4(LS_3)]^{2-}$ and the potential order of M = Fe < Co < Ni was established (*51*). In a related series of complexes, reversible $[MFe_3S_4]^{+,0}$ couples were characterized for $[(PPh_3)MFe_3S_4(LS_3)]^{2-}$ and the potential order of M = Co < Ni < Cu < Ag was determined (*51*). Hence, the intrinsic effect of the heterometal on the redox potentials of heterometallic cubanes has been established as Fe < Co < Ni < Cu < Ag, in excellent agreement with the order established for the protein-bound clusters in *P. furiosus* Fd.

IX. Future Directions

Although this review chronicles the remarkable progress that has been made over the past 15 years in understanding the function, properties, and reactivity of cuboidal $[Fe_3S_4]$ clusters, many questions remain unanswered. Given that the primary function appears to be electron transfer, understanding how the protein environment can tune the midpoint potential of the $[Fe_3S_4]^{+,0}$ couple over a range of >0.5 V is clearly of paramount importance. Determining the structural changes associated with cluster redox reactions via high-resolution crystal structures and the location of the valence-delocalized pair via protein NMR studies, will be crucial to this endeavor. Theoretical calculations based on protein crystal structures can then be used to assess the electrostatic gradient at the cluster and thereby assess how the protein determines the pair of irons that accepts the electron and the cluster redox potential. Elucidating the functions for biological $[Fe_3S_4]$ clusters presents another major challenge. The proven ability of $[Fe_3S_4]$ clusters to undergo several types of cluster conversions, incorporate heterometals, and exhibit redox-linked protonation makes them attractive candidates for sensors in regulatory processes, enzyme active sites, and coupling electron and proton transfer. The extent to which $[Fe_3S_4]$ clusters are involved in

these types of biological processes remains to be determined. Finally, there is clearly pressing need to develop rigorous spin coupling models that can rationalize the ground-state properties of heterometallic cubanes.

ACKNOWLEDGMENT

Research on Fe–S proteins in the Johnson laboratory is supported by grants from the National Institutes of Health (GM45597 and GM51962) and by a National Science Foundation Research Training Grant Award to the Center for Metalloenzyme Studies (BIR-9413236).

REFERENCES

1. Cammack, R. *Adv. Inorg. Chem.* **1992,** *38,* 281.
2. Johnson, M. K. In "Encyclopedia of Inorganic Chemistry"; King, R. B., Ed.; John Wiley & Sons: Chichester, 1994; pp. 1896–1915.
3. Beinert, H.; Holm, R. H.; Münck, E. *Science* **1997,** *277,* 653.
4. Johnson, M. K. *Curr. Opin. Chem. Biol.* **1998,** *2,* 173.
5. Beinert, H.; Thomson, A. J. *Arch. Biochem. Biophys.* **198 ,** *222,* 333.
6. Emptage, M. H.; Kent, T. A.; Huynh, B. H.; Rawlings, J.; Orme-Johnson, W. H.; Münck, E. *J. Biol. Chem.* **1980,** *255,* 1793.
7. Huynh, B. H.; Moura, J. J. G.; Moura, I.; Kent, T. A.; LeGall, J.; Xavier, A. V.; Münck, E. *J. Biol. Chem.* **1980,** *255,* 3242.
8. Stout, C. D.; Ghosh, D.; Pattabhi, V.; Robbins, A. H. *J. Biol. Chem.* **1980,** *255,* 1797.
9. Ghosh, D.; Furey, W., Jr.; O'Donnell, S.; Stout, C. D. *J. Biol. Chem.* **1981,** *256,* 4185.
10. Thomson, A. J.; Robinson, A. E.; Johnson, M. K.; Cammack, R.; Rao, K. K.; Hall, D. O. *Biochim. Biophys. Acta* **1981,** *637,* 423.
11. Johnson, M. K.; Spiro, T. G.; Mortenson, L. E. *J. Biol. Chem.* **1982,** *257,* 2447.
12. Bell, S. H.; Dickson, D. P. E.; Johnson, C. E.; Cammack, R.; Hall, D. O.; Rao, K. K. *FEBS Lett.* **1982,** *142,* 143.
13. Kent, T. A.; Dreyer, J.-C.; Kennedy, M. C.; Huynh, B. H.; Emptage, M. H.; Beinert, H.; Münck, E. *Proc. Natl. Acad. Sci. USA* **1982,** *79,* 1096.
14. Moura, J. J. G.; Moura, I.; Kent, T. A.; Lipscomb, J. D.; Huynh, B. H.; LeGall, J.; Xavier, A. V.; Münck, E. *J. Biol. Chem.* **1982,** *257,* 6259.
15. Beinert, H.; Emptage, M. H.; Dreyer, J.-C.; Scott, R. A.; Hahn, J. E.; Hodgson, K. O.; Thomson, A. J. *Proc. Natl. Acad. Sci. USA* **198 ,** *80,* 393.
16. Antonio, M. R.; Averill, B. A.; Moura, I.; Moura, J. J. G.; Orme-Johnson, W. H.; Teo, B.-K.; Xavier, A. V. *J. Biol. Chem.* **1982,** *257,* 6646.
17. Johnson, M. K.; Czernuszewicz, R. S.; Spiro, T. G.; Fee, J. A.; Sweeney, W. V. *J. Am. Chem. Soc.* **198 ,** *103,* 6671.
18. Stout, G. H.; Turley, S.; Sieker, L. C.; Jensen, L. H. *Proc. Natl. Acad. Sci. USA* **1988,** *85,* 1020.

19. Kissinger, C. R.; Adman, E. T.; Sieker, L. C.; Jensen, L. H. *J. Am. Chem. Soc.* **1988,** *110,* 8721.
20. Thomson, A. J.; Robinson, A. E.; Johnson, M. K.; Moura, J. J. G.; Moura, I.; Xavier, A. V.; LeGall, J. *Biochim. Biophys. Acta* **1981,** *670,* 93.
21. Johnson, M. K.; Thomson, A. J.; Richards, A. J. M.; Peterson, J.; Robinson, A. E.; Ramsay, R. R.; Singer, T. P. *J. Biol. Chem.* **1984,** *259,* 2274.
22. Johnson, M. K.; Morningstar, J. E.; Bennett, D. E.; Ackrell, B. A. C.; Kearney, E. B. *J. Biol. Chem.* **1985,** *260,* 7368.
23. Morningstar, J. E.; Johnson, M. K.; Cecchini, G.; Ackrell, B. A. C.; Kearney, E. B. *J. Biol. Chem.* **1985,** *260,* 13631.
24. Johnson, M. K.; Bennett, D. E.; Morningstar, J. E.; Adams, M. W. W.; Mortenson, L. E. *J. Biol. Chem.* **1985,** *260,* 5456.
25. Knaff, D. B.; Hirasawa, M.; Ameyibor, E.; Fu, W.; Johnson, M. K. *J. Biol. Chem.* **1991,** *266,* 15080.
26. Teixeira, M.; Moura, I.; Xavier, A. V.; DerVartanian, D. V.; LeGall, J.; Peck, H. D., Jr.; Huynh, B. H.; Moura, J. J. G. *Eur. J. Biochem.* **198 ,** *130,* 481.
27. Johnson, M. K.; Zambrano, I. C.; Czechowski, M. H.; Peck, H. D., Jr.; DerVartanian, D. V.; LeGall, J. In "Frontiers in Bioinorganic Chemistry"; Xavier, A. V., Ed.; VCH: Weinheim, 1985; pp. 36–44.
28. Johnson, M. K.; Morningstar, J. E.; Cecchini, G.; Ackrell, B. A. C. *Biochem. Biophys. Res. Commun.* **1985,** *131,* 653.
29. Papaefthymiou, V.; Girerd, J.-J.; Moura, I.; Moura, J. J. G.; Münck, E. *J. Am. Chem. Soc.* **1987,** *109,* 4703.
30. Kent, T. A.; Huynh, B. H.; Münck, E. *Proc. Natl. Acad. Sci. USA* **1980,** *77,* 6574.
31. Moura, I.; Moura, J. J. G.; Münck, E.; Papaefthymiou, V.; LeGall, J. *J. Am. Chem. Soc.* **1986,** *108,* 349.
32. Surerus, K. K.; Münck, E.; Moura, I.; Moura, J. J. G.; LeGall, J. *J. Am. Chem. Soc.* **1987,** *109,* 3805.
33. Münck, E.; Papaefthymiou, V.; Surerus, K. K.; Girerd, J.-J. In "Metal Clusters in Proteins"; Que, L., Jr., Ed.; American Chemical Society: Washington, D.C., 1988; pp. 302–325.
34. Conover, R. C.; Park, J.-B.; Adams, M. W. W.; Johnson, M. K. *J. Am. Chem. Soc.* **1990,** *112,* 4562.
35. Finnegan, M. G.; Conover, R. C.; Park, J.-B.; Zhou, Z.-H.; Adams, M. W. W.; Johnson, M. K. *Inorg. Chem.* **1995,** *34,* 5358.
36. Staples, C. R.; Dhawan, I. K.; Finnegan, M. G.; Dwinell, D. A.; Zhou, Z.-H.; Huang, H.; Verhagen, M. F. J. M.; Adams, M. W. W.; Johnson, M. K. *Inorg. Chem.* **1997,** *36,* 5740.
37. Fu, W.; Telser, J.; Hoffman, B. M.; Smith, E. T.; Adams, M. W. W.; Finnegan, M. G.; Conover, R. C.; Johnson, M. K. *J. Am. Chem. Soc.* **1994,** *116,* 5722.
38. Butt, J. N.; Armstrong, F. A.; Breton, J.; George, S. J.; Thomson, A. J.; Hatchikian, E. C. *J. Am. Chem. Soc.* **1991,** *113,* 6663.
39. Butt, J. N.; Sucheta, A.; Armstrong, F. A.; Breton, J.; Thomson, A. J.; Hatchikian, E. C. *J. Am. Chem. Soc.* **1991,** *113,* 8948.
40. Butt, J. N.; Niles, J.; Armstrong, F. A.; Breton, J.; Thomson, A. J. *Nature Struct. Biol.* **1994,** *1,* 427.
41. Butt, J. N.; Fawsett, S.; Breton, J.; Thomson, A. J.; Armstrong, F. A. *J. Am. Chem. Soc.* **1997,** *119,* 9729.
42. Conover, R. C.; Kowal, A. T.; Fu, W.; Park, J.-B.; Aono, S.; Adams, M. W. W.; Johnson, M. K. *J. Biol. Chem.* **1990,** *265,* 8533.

43. George, S. J.; Armstrong, F. A.; Hatchikian, E. C.; Thomson, A. J. *Biochem. J.* **1989,** *264,* 275.
44. Kennedy, M. C.; Kent, T. A.; Emptage, M. H.; Merkle, H.; Beinert, H.; Münck, E. *J. Biol. Chem.* **1984,** *259,* 14463.
45. Richards, A. J. M.; Thomson, A. J.; Holm, R. H.; Hagen, K. S. *Spectrochim. Acta* **1990,** *46A,* 987.
46. Duderstadt, R. E.; Brereton, P. S.; Adams, M. W. W.; Johnson, M. K. *J. Am. Chem. Soc.* **1998,** *120,* 8525.
47. Berg, J. M.; Holm, R. H. In "Iron–Sulfur Proteins"; Spiro, T. G., Ed.; Wiley-Interscience: New York, 1982; pp. 1–66.
48. Hagen, K. S.; Watson, A. D.; Holm, R. H. *J. Am. Chem. Soc.* **198 ,** *105,* 3913.
49. Zhou, J.; Holm, R. H. *J. Am. Chem. Soc.* **1995,** *117,* 11353.
50. Zhou, J.; Hu, Z.; Münck, E.; Holm, R. H. *J. Am. Chem. Soc.* **1996,** *118,* 1966.
51. Zhou, J.; Raebiger, J. W.; Crawford, C. A.; Holm, R. H. *J. Am. Chem. Soc.* **1997,** *119,* 6242.
52. Matsubara, H.; Saeki, K. *Adv. Inorg. Chem.* **1992,** *38,* 223.
53. Ackrell, B. A. C.; Johnson, M. K.; Gunsalus, R. P.; Cecchini, G. In "Chemistry and Biochemistry of Flavoenzymes"; Muller, F., Ed.; CRC Press: Boca Raton, FL, 1992; pp. 229–297.
54. Hägerhäll, C. *Biochim. Biophys. Acta* **1997,** *1320,* 107.
55. Guigliarelli, B.; Asso, M.; More, C.; Augier, V.; Blasco, F.; Pommier, J.; Giordano, G.; Bertrand, P. *Eur. J. Biochem.* **1992,** *207,* 61.
56. Vanoni, M. A.; Edmondson, D. E.; Zanetti, G.; Curti, B. *Biochemistry* **1992,** *31,* 4613.
57. Hirasawa, M.; Robertson, D. E.; Ameyibor, E.; Johnson, M. K.; Knaff, D. B. *Biochim. Biophys. Acta* **1992,** *1100,* 105.
58. Hirasawa, M.; Hurley, J. K.; Salamon, Z.; Tollin, G.; Knaff, D. B. *Arch. Biochem. Biophys.* **1996,** *330,* 209.
59. Teixeira, M.; Moura, I.; Xavier, A. V.; Moura, J. J. G.; LeGall, J.; DerVartanian, D. V.; Peck, H. D., Jr.; Huynh, B. H. *J. Biol. Chem.* **1989,** *264,* 16435.
60. Bruschi, M.; Guerlesquin, F. *FEMS Microbiol. Rev.* **1988,** *54,* 155.
61. Kissinger, C. R.; Sieker, L. C.; Adman, E. T.; Jensen, L. H. *J. Mol. Biol.* **1991,** *219,* 693.
62. Macedo, A. L.; Palma, P. N.; Moura, I.; LeGall, J.; Wray, V.; Moura, J. J. G. *Magn. Reson. Chem.* **199 ,** *31,* S59–S67.
63. Calzolai, L.; Gorst, C. M.; Zhou, Z.-H.; Teng, Q.; Adams, M. W. W.; La Mar, G. N. *Biochemistry* **1995,** *34,* 11373.
64. Moreno, C.; Macedo, A. L.; Moura, I.; LeGall, J.; Moura, J. J. G. *J. Inorg. Biochem.* **1994,** *53,* 219.
65. Brereton, P. S.; Verhagen, M. F. J. M.; Zhou, Z.-H.; Adams, M. W. W. *Biochemistry* **1998,** *37,* 7351.
66. Macedo, A. L.; Moura, I.; Surerus, K. K.; Papaefthymiou, V.; Liu, M.-Y.; LeGall, J.; Münck, E.; Moura, J. J. G. *J. Biol. Chem.* **1994,** *269,* 8052.
67. Gorst, C. M.; Zhou, Z.-H.; Ma, K.; Teng, Q.; Howard, J. B.; Adams, M. W. W.; La Mar, G. N. *Biochemistry* **1995,** *34,* 8788.
68. O'Keefe, D. P.; Gibson, K. J.; Emptage, M. H.; Lenstra, R.; Romesser, J. A.; Litle, P. J.; Omer, C. A. *Biochemistry* **1991,** *30,* 447.
69. Stout, C. D. *J. Mol. Biol.* **1989,** *205,* 545.
70. Johnson, M. K.; Bennett, D. E.; Fee, J. A.; Sweeney, W. V. *Biochim. Biophys. Acta* **1987,** *911,* 81.

71. Stephens, P. J.; Jensen, G. M.; Devlin, F. J.; Morgan, T. V.; Stout, C. D.; Martin, A. E.; Burgess, B. K. *Biochemistry* **1991,** *30,* 3200.
72. Hu, Z.; Jollie, D. R.; Burgess, B. K.; Stephens, P. J.; Münck, E. *Biochemistry* **1994,** *33,* 14475.
73. Iismaa, S. E.; Vázquez, A. E.; Jensen, G. M.; Stephens, P. J.; Butt, J. N.; Armstrong, F. A.; Burgess, B. K. *J. Biol. Chem.* **1991,** *266,* 21563.
74. Cheng, H.; Grohmann, K.; Sweeney, W. V. *J. Biol. Chem.* **1992,** *267,* 8073.
75. George, S. J.; Richards, A. J. M.; Thomson, A. J.; Yates, M. G. *Biochem. J.* **1984,** *224,* 247.
76. Armstrong, F. A.; George, S. J.; Thomson, A. J.; Yates, M. G. *FEBS Lett.* **1988,** *234,* 107.
77. Saeki, K.; Wakabayashi, S.; Zumft, W. G.; Matsubara, H. *J. Biochem.* **1988,** *104,* 242.
78. Hase, T.; Wakabayashi, S.; Matsubara, H. *FEBS Lett.* **1978,** *91,* 315.
79. Nagayama, K.; Imai, T.; Ohmori, D.; Oshima, T. *FEBS Lett.* **1984,** *169,* 79.
80. Nagayama, K.; Ohmori, D. *FEBS Lett.* **1984,** *173,* 15.
81. Nagayama, K.; Ohmori, D.; Imai, T.; Oshima, T. *FEBS Lett.* **198 ,** *158,* 208.
82. Macedo, A. L.; Besson, S.; Moreno, C.; Fauque, G.; Moura, J. J. G.; Moura, I. *Biochem. Biophys. Res. Com.* **1996,** *229,* 524.
83. Saeki, K.; Suetsugu, Y.; Tokuda, K.; Miyatake, Y.; Young, D. A.; Marrs, B. L.; Matsubara, H. *J. Biol. Chem.* **1991,** *266,* 12889.
84. Saeki, K.; Suetsugu, Y.; Yao, Y.; Horio, T.; Marrs, B. L.; Matsubara, H. *J. Biochem.* **1990,** *108,* 475.
85. Duport, C.; Jouanneau, Y.; Vignais, P. M. *Nucleic Acids Res.* **1990,** *18,* 4618.
86. Jouanneau, Y.; Duport, C.; Meyer, C.; Gaillard, J. *Biochem. J.* **1992,** *286,* 269.
87. Jouanneau, Y.; Meyer, C.; Gaillard, J.; Vignais, P. M. *Biochem. Biophys. Res. Commun.* **1990,** *171,* 273.
88. Ishikawa, Y.; Yoch, D. C. *Photosyn. Res.* **1995,** *46,* 371.
89. Battistuzzi, G.; Borsari, M.; Ferretti, S.; Luchinat, C.; Sola, M. *Arch. Biochem. Biophys.* **1995,** *320,* 149.
90. Bertini, I.; Dikiy, A.; Luchinat, C.; Macinai, R.; Viezzoli, M. S.; Vincenzini, M. *Biochemistry* **1997,** *36,* 3570.
91. Ohnishi, T.; Blum, H.; Sato, S.; Nakazawa, K.; Hon-Nami, K.; Oshima, T. *J. Biol. Chem.* **1980,** *255,* 345.
92. Sato, S.; Nakazawa, K.; Hon-Nami, K.; Oshima, T. *Biochim. Biophys. Acta* **1981,** *668,* 277.
93. Hille, R.; Yoshida, T.; Tarr, G. E.; Williams, C. H., Jr.; Ludwig, M. L.; Fee, J. A.; Kent, T. A.; Huynh, B. H.; Münck, E. *J. Biol. Chem.* **198 ,** *258,* 13008.
94. Hagen, W. R.; Dunham, W. R.; Johnson, M. K.; Fee, J. A. *Biochim. Biophys. Acta* **1985,** *828,* 369.
95. Hase, T.; Wakabayashi, S.; Matsubara, H.; Imai, T.; Matsumoto, T.; Tobari, J. *FEBS Lett.* **1979,** *103,* 224.
96. Ohmori, D.; Yamakura, K.; Suzuki, K.; Imai, T.; Nagayama, K. In "Iron–Sulfur Protein Research"; Matsubara, H., Katsube, Y., Wada, K., Eds.; Japan Sci. Soc. Press: Tokyo, 1987; pp. 116–124.
97. Imai, T.; Kamata, K.; Saito, H.; Urushiyama, A. *Bull. Chem. Soc. Japan* **1995,** *68,* 2923.
98. Imai, T.; Urushiyama, A.; Saito, H.; Sakamoto, Y.; Ota, K.; Ohmori, D. *FEBS Lett.* **1995,** *368,* 23.

99. Trower, M. K.; Emptage, M. H.; Sariaslani, F. S. *Biochim. Biophys. Acta* **1990,** *1037,* 281.
100. Trower, M. K.; Marshall, J. E.; Doleman, M. S.; Emptage, M. H.; Sariaslani, F. S. *Biochim. Biophys. Acta* **1990,** *1037,* 290.
101. Aono, S.; Bentrop, D.; Bertini, I.; Luchinat, C.; Macinai, R. *FEBS Lett.* **1997,** *412,* 501.
102. Aono, S.; Bertini, I.; Cowan, J. A.; Luchinat, C.; Rosato, A.; Viezzoli, M. S. *JBIC, J. Biol. Inorg. Chem.* **1996,** *1,* 523.
103. Aono, S.; Fukuda, N.; Okura, I. *J. Mol. Catal. A—Chemical* **1995,** *95,* 173.
104. Aono, S.; Kurita, H.; Uno, S.; Okura, I. *J. Biochem.* **1992,** *112,* 792.
105. Bertini, I.; Luchinat, C.; Mincione, G.; Soriano, A. *Inorg. Chem.* **1998,** *37,* 969.
106. Schlatter, D.; Waldvogel, S.; Zülli, F.; Suter, F.; Portmann, W.; Zuber, H. *Biol. Chem. Hoppe-Seyler* **1985,** *366,* 223.
107. Bovier-Lapierre, G.; Bruschi, M.; Bonicel, J.; Hatchikian, E. C. *Biochim. Biophys. Acta* **1987,** *913,* 20.
108. Armstrong, F. A.; George, S. J.; Cammack, R.; Hatchikian, E. C.; Thomson, A. J. *Biochem. J.* **1989,** *264,* 265.
109. Ogata, M.; Kondo, S.; Okawara, N.; Yagi, T. *J. Biochem.* **1988,** *103,* 121.
110. Okawara, N.; Ogata, M.; Yagi, T.; Wakabayashi, S.; Matsubara, H. *J. Biochem.* **1988,** *104,* 196.
111. Asso, M.; Mbarki, O.; Guigliarelli, B.; Bertrand, P. *Biochem. Biophys. Res. Commun.* **1995,** *211,* 198.
112. Iwasaki, T.; Wakagi, T.; Isogai, Y.; Tanaka, K.; Iizuka, T.; Oshima, T. *J. Biol. Chem.* **1994,** *269,* 29444.
113. Wakagi, T.; Fujii, T.; Oshima, T. *Biochem. Biophys. Res. Commun.* **1996,** *225,* 489.
114. Fujii, T.; Hata, Y.; Oozeki, M.; Moriyama, H.; Wakagi, T.; Tanaka, H.; Oshima, T. *Biochemistry* **1997,** *36,* 1505.
115. Iwasaki, T.; Oshima, T. *FEBS Lett.* **1997,** *417,* 223.
116. Iwasaki, T.; Suzuki, T.; Kon, T.; Imai, T.; Urushiyama, A.; Ohmori, D.; Oshima, T. *J. Biol. Chem.* **1997,** *272,* 3453.
117. Minami, Y.; Wakabayashi, S.; Wada, K.; Matsubara, H.; Kerscher, L.; Oesterhelt, D. *J. Biochem.* **1985,** *97,* 745.
118. Breton, J. L.; Duff, J. L. C.; Butt, J. N.; Armstrong, F. A.; George, S. J.; Petillot, Y.; Forest, E.; Schafer, G.; Thomson, A. J. *Eur. J. Biochem.* **1995,** *233,* 937.
119. Duff, J. L. C.; Breton, J. L.; Butt, J. N.; Armstrong, F. A.; Thomson, A. J. *J. Am. Chem. Soc.* **1996,** *118,* 8593.
120. Teixeira, M.; Batista, R.; Campos, A. P.; Gomes, C.; Mendes, J.; Pacheco, I.; Anemüller, S.; Hagen, W. R. *Eur. J. Biochem.* **1995,** *227,* 322.
121. Bentrop, D.; Bertini, I.; Luchinat, C.; Mendes, J.; Piccioli, M.; Teixeira, M. *Eur. J. Biochem.* **1996,** *236,* 92.
122. Nakajima, Y.; Fujiwara, T.; Fukumori, Y. *J. Biochem.* **1998,** *123,* 521.
123. Stout, C. D. *J. Biol. Chem.* **1988,** *263,* 9256.
124. Stout, C. D. *J. Biol. Chem.* **199 ,** *268,* 25920.
125. Stephens, P. J.; Morgan, T. V.; Stout, C. D.; Burgess, B. K. In "Frontiers in Bioinorganic Chemistry"; Xavier, A. V., Ed.; VCH: Weinheim, 1986; pp. 637–646.
126. Morgan, T. V.; Stephens, P. J.; Burgess, B. K.; Stout, C. D. *FEBS Lett.* **1984,** *167,* 137.
127. Morgan, T. V.; Lundell, D. J.; Burgess, B. K. *J. Biol. Chem.* **1988,** *263,* 1370.
128. Isas, J. M.; Yannone, S. M.; Burgess, B. K. *J. Biol. Chem.* **1995,** *270,* 21258.
129. Isas, J. M.; Burgess, B. K. *J. Biol. Chem.* **1994,** *269,* 19404.

130. Yannone, S. M.; Burgess, B. K. *JBIC, J. Biol. Inorg. Chem.* **1998,** *3,* 253.
131. Fujii, T.; Hata, Y.; Wakagi, T.; Tanaka, H.; Oshima, T. *Nature Struct. Biol.* **1996,** *3,* 834.
132. Kerscher, L.; Nowitzki, S.; Oesterhelt, D. *Eur. J. Biochem.* **1982,** *128,* 223.
133. Hederstedt, L.; Ohnishi, T. In "Molecular Mechanisms in Bioenergetics"; Ernster, L., Ed.; Elsevier: New York, 1992; pp. 163–198.
134. Ackrell, B. A. C.; Kearney, E. B.; Mims, W. B.; Peisach, J.; Beinert, H. *J. Biol. Chem.* **1984,** *259,* 4015.
135. Werth, M. T.: Cecchini, G.; Manodori, A.; Ackrell, B. A. C.; Schröder, I.; Gunsalus, R. P.; Johnson, M. K. *Proc. Natl. Acad. Sci. USA* **1990,** *87,* 8965.
136. Kowal, A. T.; Werth, M. T.; Manodori, A.; Cecchini, G.; Schröder, I.; Gunsalus, R. P.; Johnson, M. K. *Biochemistry* **1995,** *34,* 12284.
137. Manodori, A.; Cecchini, G.; Schröder, I.; Gunsalus, R. P.; Werth, M. T.; Johnson, M. K. *Biochemistry* **1992,** *31,* 2703.
138. Hägerhäll, C.; Sled, V.; Hederstedt, L.; Ohnishi, T. *Biochim. Biophys. Acta* **1995,** *1229,* 356.
139. Janssen, S.; Schäfer, G.; Anemüller, S.; Moll, R. *J. Bacteriol.* **1997,** *179,* 5560.
140. Blasco, F.; Iobbi, G.; Giordano, M.; Chippaux, M.; Bonnefoy, V. *Mol. Gen. Genet.* **1989,** *218,* 249.
141. Guigliarelli, B.; Magalon, A.; Asso, M.; Bertrand, P.; Frixon, C.; Giordano, G.; Blasco, F. *Biochemistry* **1996,** *35,* 4828.
142. Augier, V.; Guigliarelli, B.; Asso, M.; Bertrand, P.; Frixon, C.; Giordano, G.; Chippaux, M.; Blasco, F. *Biochemistry* **199 ,** *32,* 2013.
143. Augier, V.; Asso, M.; Guigliarelli, B.; More, C.; Bertrand, P.; Santini, C. L.; Blasco, F.; Chippaux, M.; Giordano, G. *Biochemistry* **199 ,** *32,* 5099.
144. Magalon, A.; Rothery, R. A.; Giordano, G.; Blasco, F.; Weiner, J. H. *J. Bacteriol.* **1997,** *179,* 5037.
145. Berg, B. L.; Li, J.; Heider, J.; Stewart, V. *J. Biol. Chem.* **1991,** *266,* 22380.
146. Krafft, T.; Bokranz, M.; Schröder, I.; Fahrenholz, F.; Kojro, E.; Kröger, A. *Eur. J. Biochem.* **1992,** *206, 5456.*
147. Weiner, J. H.; Rothery, R. A.; Sambasivarao, D.; Trieber, C. A. *Biochim. Biophys. Acta* **1992,** *1102,* 1.
148. Vanoni, M. A.; Fischer, F.; Ravasio, S.; Verzotti, E.; Edmondson, D. E.; Hagen, W. R.; Zanetti, G.; Curti, B. *Biochemistry* **1998,** *37,* 1828.
149. Vanoni, M. A.; Verzotti, E.; Zanetti, G.; Curti, B. *Eur. J. Biochem.* **1996,** *236,* 937.
150. Rendina, A., **1980,** Ph.D. Dissertation, University of Wisconsin.
151. Albracht, S. P. J. *Biochim. Biophys. Acta* **1994,** *1188,* 167.
152. Frey, M. *Struct. Bonding* **1998,** *90,* 97.
153. Huynh, B. H.; Patil, D. S.; Moura, I.; Teixeira, M.; Moura, J. J. G.; DerVartanian, D. V.; Czechowski, M. H.; Prickril, B. C.; Peck, H. D., Jr.; LeGall, J. *J. Biol. Chem.* **1987,** *262,* 795.
154. Albracht, S. P. J.; van der Zwaan, J. W.; Fontijn, R. D. *Biochim. Biophys. Acta* **1984,** *766,* 245.
155. Surerus, K. K.; Chen, M.; van der Zwaan, J. W.; Rusnak, F. M.; Kolk, M.; Duin, E. C.; Albracht, S. P. J.; Münck, E. *Biochemistry* **1994,** *33,* 4980.
156. Przybyla, A. E.; Robbins. A. H.; Menon, N.; Peck, H. D., Jr. *FEMS Microbiol. Rev.* **1992,** *88,* 109.
157. Volbeda, A.; Charon, M.-H.; Piras, C.; Hatchikian, E. C.; Frey, M.; Fontecilla-Camps, J. C. *Nature* **1995,** *373,* 580.

158. Volbeda, A.; Garcin, E.; Piras, C.; de Lacey, A. L.; Fernandez, V. M.; Hatchikian, E. C.; Frey, M.; Fontecilla-Camps, J. C. *J. Am. Chem. Soc.* **1996,** *118,* 12989.
159. Bagley, K. A.; Duin, E. C.; Roseboom, W.; Albracht, S. P. J.; Woodruff, W. H. *Biochemistry* **1995,** *34,* 5527.
160. Happe, R. P.; Roseboom, W.; Pierik, A. J.; Albracht, S. P. J.; Bagley, K. A. *Nature* **1997,** *385,* 126.
161. de Lacey, A. L.; Hatchikian, E. C.; Volbeda, A.; Frey, M.; Fontecilla-Camps, J. C.; Fernandez, V. M. *J. Am. Chem. Soc.* **1997,** *119,* 7181.
162. Higuchi, Y.; Yagi, T.; Yasuoka, N. *Structure* **1997,** *5,* 1671.
163. Teixeira, M.; Moura, I.; Fauque, G.; DerVartanian, D. V.; LeGall, J.; Peck, H. D., Jr.; Moura, J. J. G.; Huynh, B. H. *Eur. J. Biochem.* **1990,** *189,* 381.
164. Rousset, M.; Montet, Y.; Guigliarelli, B.; Forget, N.; Asso, M.; Bertrand, P.; Fontecilla-Camps, J. C.; Hatchikian, E. C. *Proc. Natl. Acad. Sci. USA* **1998,** *95,* 11625.
165. Stout, C. D.; Stura, E. A.; McRee, D. E. *J. Mol. Biol.* **1998,** *278,* 629.
166. Kissinger, C. R.; Adman, E. T.; Sieker, L. C.; LeGall, J. *FEBS Lett.* **1989,** *244,* 447.
167. Robbins, A. H.; Stout, C. D. *Proteins* **1989,** *5,* 289.
168. Freeman, H. In "Spectroscopic Methods in Bioinorganic Chemistry"; Solomon, E. I., Hodgson, K. O., Eds.; American Chemical Society: Washington, D. C., 1998; pp. 62–95.
169. Shen, B.; Martin, L. L.; Butt, J. N.; Armstrong, F. A.; Stout, C. D.; Jensen, G. M.; Stephens, P. J.; La Mar, G. N.; Gorst, C. M.; Burgess, B. K. *J. Biol. Chem.* **199 ,** *268,* 25928.
170. Telser, J.; Huang, H.; Lee, H.-I.; Adams, M. W. W.; Hoffman, B. M. *J. Am. Chem. Soc.* **1998,** *120,* 861.
171. Sweeney, W. V.; Rabinowitz, J. C.; Yoch, D. C. *J. Biol. Chem.* **1975,** *250,* 7842.
172. Fan, C.; Houseman, A. L. P.; Doan, P. E.; Hoffman, B. M. *J. Phys. Chem.* **199 ,** *97,* 3017.
173. Van Heerikhuizen, H.; Albracht, S. P. J.; Slater, E. C.; Van Rheenen, P. S. *Biochim. Biophys. Acta* **1980,** *657,* 26.
174. Surerus, K. K.; Kennedy, M. C.; Beinert, H.; Münck, E. *Proc. Natl. Acad. Sci. USA* **1989,** *86,* 9846.
175. Beinert, H.; Kennedy, M. C.; Stout, C. D. *Chem. Rev.* **1996,** *96,* 2335.
176. Gayda, J.-P.; Bertrand, P.; Theodule, F-X.; Moura, J. J. G. *J. Chem. Phys.* **1982,** *77, 3387.*
177. Day, E. P.; Peterson, J.; Bonvoisin, J. J.; Moura, I.; Moura, J. J. G. *J. Biol. Chem.* **1988,** *263,* 3684.
178. Macedo, A. L.; Moura, I.; Moura, J. J. G.; LeGall, J.; Huynh, B. H. *Inorg. Chem.* **199 ,** *32,* 1101.
179. Yoo, S. J.; Hu, Z.; Goh, C.; Bominaar, E. L.; Holm, R. H.; Münck, E. *J. Am. Chem. Soc.* **1997,** *119,* 8732.
180. Frauenfelder, H.; Sligar, S. G.; Wolynes, P. G. *Science* **1991,** *254,* 1598.
181. Guigliarelli, B.; Gayda, J.-P.; Bertrand, P.; More, C. *Biochim. Biophys. Acta* **1986,** *871,* 149.
182. Guigliarelli, B.; More, C.; Bertrand, P.; Gayda, J.-P. *J. Chem. Phys.* **1986,** *85,* 2774.
183. Hagen, W. R. *Adv. Inorg. Chem.* **1992,** *38,* 165.
184. Duderstadt, R. E.; Staples, C. R.; Brereton, P. S.; Adams, M. W. W.; Johnson, M. K. Submitted.
185. Gorst, C. M.; Yeh, Y.-H.; Teng, Q.; Calzolai, L.; Zhou, Z.-H.; Adams, M. W. W.; La Mar, G. N. *Biochemistry* **1995,** *34,* 600.

186. Teng, Q.; Zhou, Z.-H.; Smith, E. T.; Busse, S. C.; Howard, J. B.; Adams, M. W. W.; La Mar, G. N. *Biochemistry* **1994,** *33,* 6316.
187. Duin, E. C., **1996,** Ph.D. Dissertation, University of Amsterdam, The Netherlands.
188. Breton, J.; Farrar, J. A.; Kennedy, M. C.; Beinert, H.; Thomson, A. J. *Biochem. J.* **1995,** *311,* 197.
189. Johnson, M. K.; Robinson, A. E.; Thomson, A. J. In "Iron–Sulfur Proteins"; Spiro, T. G., Ed.; Wiley-Interscience: New York, 1982; pp. 367–406.
190. Anemüller, S.; Hettmann, T.; Moll, R.; Teixeira, M.; Schafer, G. *Eur. J. Biochem.* **1995,** *232,* 563.
191. Fu, W., **1990,** M.S. Dissertation, University of Georgia.
192. Busse, S. C.; La Mar, G. N.; Yu, L. P.; Howard, J. B.; Smith, E. T.; Zhou, Z.-H.; Adams, M. W. W. *Biochemistry* **1992,** *31,* 11952.
193. Butt, J. N.; Sucheta, A.; Martin, L. L.; Shen, B.; Burgess, B. K.; Armstrong, F. A. *J. Am. Chem. Soc.* **199 ,** *115,* 12587.
194. Zener, C. *Phys. Rev.* **1951,** *82,* 403.
195. Kilpatrick, L. K.; Kennedy, M. C.; Beinert, H.; Czernuszewicz, R. S.; Qui, D.; Spiro, T. G. *J. Am. Chem. Soc.* **1994,** *116,* 4053.
196. Armstrong, F. A.; Butt, J. N.; George, S. J.; Hatchikian, E. C.; Thomson, A. J. *FEBS Lett.* **1989,** *259,* 15.
197. Spiro, T. G.; Czernuszewicz, R. S.; Han, S. In "Resonance Raman Spectra of Heme and Metalloproteins"; Spiro, T. G., Ed.; John Wiley & Sons: New York, 1988; pp. 523–554.
198. Srivastava, K. K. P.; Surerus, K. K.; Conover, R. C.; Johnson, M. K.; Park, J.-B.; Adams, M. W. W.; Münck, E. *Inorg. Chem.* **199 ,** *32,* 927.
199. Donaire, A.; Gorst, C. M.; Zhou, Z.-H.; Adams, M. W. W.; La Mar, G. N. *J. Am. Chem. Soc.* **1994,** *116,* 6841.
200. Anderson, P. W.; Hasegawa, H. *Phys. Rev.* **1955,** *100,* 675.
201. Girerd, J.-J. *J. Chem. Phys.* **198 ,** *79,* 1766.
202. Bominaar, E. L.; Hu, Z.; Münck, E.; Girerd, J.-J.; Borshch, S. A. *J. Am. Chem. Soc.* **1995,** *117,* 6976.
203. Borshch, S. A.; Bominaar, E. L.; Blondin, G.; Girerd, J.-J. *J. Am. Chem. Soc.* **199 ,** *115,* 5155.
204. Kröckel, M.; Grodzicki, M.; Papaefthymiou, V.; Trautwein, A. X.; Kostikas, A. *JBIC, J. Biol. Inorg. Chem.* **1996,** *1,* 173.
205. Crouse, B. R.; Meyer, J.; Johnson, M. K. *J. Am. Chem. Soc.* **1995,** *117,* 9612.
206. Achim, C.; Golinelli, M.-P.; Bominaar, E. L.; Meyer, J.; Münck, E. *J. Am. Chem. Soc.* **1996,** *118,* 8168.
207. Johnson, M. K.; Duin, E. C.; Crouse, B. R.; Golinelli, M.-P.; Meyer, J. In "Spectroscopic Methods in Bioinorganic Chemistry"; Solomon, E. I., Hodgson, K. O., Eds.; American Chemical Society: Washington, D.C., 1998; pp. 286–301.
208. Noodleman, L.; Peng, C. Y.; Case, D. A.; Mazowiecki, J.-M. *Cohord. Chem. Rev.* **1995,** *144,* 199.
209. Hamelin, D. R.; Bominaar, E. L.; Kirk, M. L.; Wieghardt, K.; Solomon, E. I. *J. Am. Chem. Soc.* **1996,** *118,* 8085.
210. Blondin, G.; Girerd, J.-J. *JBIC, J. Biol. Inorg. Chem.* **1996,** *1,* 170.
211. Noodleman, L.; Case, D. A.; Mouesca, J.-M. *JBIC, J. Biol. Inorg. Chem.* **1996,** *1,* 177.
212. Bertini, I.; Luchinat, C. *JBIC, J. Biol. Inorg. Chem.* **1996,** *1,* 183.
213. Belinsky, M. I. *JBIC, J. Biol. Inorg. Chem.* **1996,** *1,* 186.
214. Bennett, D. E.; Johnson, M. K. *Biochim. Biophys. Acta* **1987,** *911,* 71.

215. Spiro, T. G.; Hare, J.; Yachandra, V.; Gewirth, A.; Johnson, M. K.; Remsen, E. In "Iron–Sulfur Proteins"; Spiro, T. G., Ed.; Wiley-Interscience: New York, 1982; pp. 407–423.
216. Smith, E. T.; Blamey, J. M.; Zhou, Z.-H.; Adams, M. W. W. *Biochemistry* **1995,** *34,* 7161.
217. Tong, J.; Feinberg, B. A. *J. Biol. Chem.* **1994,** *269,* 24920.
218. Sucheta, A.; Cammack, R.; Weiner, J. H.; Armstrong, F. A. *Biochemistry* **199 ,** *32,* 5455.
219. Guigliarelli, B.; Bertrand, P.; More, C.; Papavassiliou, P.; Hatchikian, E. C.; Gayda, J.-P. *Biochim. Biophys. Acta* **1985,** *810,* 319.
220. Flint, D. H.; Allen, R. M. *Chem. Rev.* **1996,** *96,* 2315.
221. Flint, D. H.; Emptage, M. H.; Finnegan, M. G.; Fu, W.; Johnson, M. K. *J. Biol. Chem.* **199 ,** *268,* 14732.
222. Cunningham, R. P.; Asahara, H.; Bank, J. F.; Scholes, C. P.; Salerno, J. C.; Surerus, K. K.; Münck, E.; McCracken, J.; Peisach, J.; Emptage, M. H. *Biochemistry* **1989,** *28,* 4450.
223. Onate, Y. A.; Switzer, R. L.; Vollmer, R. A.; Johnson, M. K. *J. Biol. Chem.* **1989,** *264,* 18386.
224. Petrovich, R. M.; Ruzicka, F. J.; Reed, G. H.; Frey, P. A. *Biochemistry* **1992,** *31,* 10774.
225. Mulliez, E.; Fontecave, M.; Gaillard, J.; Reichard, P. *J. Biol. Chem.* **199 ,** *268,* 2296.
226. Ollangnier, S.; Mulliez, E.; Gaillard, J.; Eliasson, R.; Fontecave, M.; Reichard, P. *J. Biol. Chem.* **1996,** *271,* 9410.
227. Külzer, R.; Pils, T.; Kappl, R.; Hüttermann, J.; Knappe, J. *J. Biol. Chem.* **1998,** *273,* 4897.
228. Khoroshilova, N.; Beinert, H.; Kiley, P. J. *Proc. Natl. Acad. Sci. USA* **1995,** *92,* 2499.
229. Khoroshilova, N.; Popescu, C.; Münck, E.; Beinert, H.; Kiley, P. J. *Proc. Natl. Acad. Sci. USA* **1997,** *94,* 6087.
230. Henkel, G.; Tremel, W.; Krebs, B. *Angew. Chem. Int. Ed. Engl.* **1981,** *20,* 1033.
231. Hagen, K. S.; Christou, G.; Holm, R. H. *Inorg. Chem.* **198 ,** *22,* 309.
232. Hagen, K. S.; Holm, R. H. *J. Am. Chem. Soc.* **1982,** *104,* 5496.
233. Whitener, M. A.; Bashkin, J. K.; Hagen, K. S.; Girerd, J.-J.; Gamp, E.; Edelstein, N.; Holm, R. H. *J. Am. Chem. Soc.* **1986,** *108,* 5607.
234. Girerd, J.-J.; Papaefthymiou, G. C.; Watson, A. D.; Gamp, E.; Hagen, K. S.; Edelstein, N.; Frankel, R. B.; Holm, R. H. *J. Am. Chem. Soc.* **1984,** *106,* 5941.
235. Holm, R. H. *Adv. Inorg. Chem.* **1992,** *38,* 1.
236. Stack, T. D. P.; Holm, R. H. *J. Am. Chem. Soc.* **1988,** *110,* 2484.
237. Stack, T. D. P.; Carney, M. J.; Holm, R. H. *J. Am. Chem. Soc.* **1998,** *111,* 1670.
238. Weigel, J. A.; Holm, R. H.; Surerus, K. K.; Münck, E. *J. Am. Chem. Soc.* **1989,** *111,* 9246.
239. Weigel, J. A.; Srivastava, K. K. P.; Day, E. P.; Münck, E.; Holm, R. H. *J. Am. Chem. Soc.* **1990,** *112,* 8015.
240. Weigel, J. A.; Holm, R. H. *J. Am. Chem. Soc.* **1991,** *113,* 4184.
241. Weterings, J. P.; Kent, T. A.; Prins, R. *Inorg. Chem.* **1987,** *26,* 324.
242. Roth, E. K. H.; Jordanov, J. *Inorg. Chem.* **1992,** *31,* 240.
243. Raebiger, J. W.; Crawford, C. A.; Zhou, J.; Holm, R. H. *Inorg. Chem.* **1997,** *36,* 994.
244. Faridoon, K. Y.; Zhuang, H.-Y.; Sykes, A. G. *Inorg. Chem.* **1994,** *33,* 2212.

245. Zhou, J.; Scott, M. J.; Hu, Z.; Peng, G.; Münck, E.; Holm, R. H. *J. Am. Chem. Soc.* **1992,** *114,* 10843.
246. Conover, R. C.; Finnegan, M. G.; Park, J.-B.; Adams, M. W. W.; Johnson, M. K. *J. Inorg. Biochem.* **1991,** *43,* 245.
247. Mouesca, J.-M.; Noodleman, L.; Case, D. A.; Lamotte, B. *Inorg. Chem.* **1995,** *34,* 4347.
248. Conover, R. C., **199 ,** Ph.D. Dissertation, University of Georgia.
249. Brereton, P. S.; Staples, C. R.; Duderstadt, R. E.; Johnson, M. K.; Adams, M. W. W. Submitted.
250. Busch, J. L. H.; Breton, J. L.; Bartlett, B. M.; Armstrong, F. A.; James, R.; Thomson, A. J. *Biochem. J.* **1997,** *323,* 95.
251. Conover, R. C.; Park, J.-B.; Adams, M. W. W.; Johnson, M. K. *J. Am. Chem. Soc.* **1991,** *113,* 2799.
252. Telser, J.; Smith, E. T.; Adams, M. W. W.; Conover, R. C.; Johnson, M. K.; Hoffman, B. M. *J. Am. Chem. Soc.* **1995,** *117,* 5133.
253. Calzolai, L.; Gorst, C. M.; Bren, K. L.; Zhou, Z.-H.; Adams, M. W. W.; La Mar, G. N. *J. Am. Chem. Soc.* **1997,** *119, 9341.*
254. Kim, J.; Rees, D. C. *Science* **1992,** *257,* 1677.
255. Cramer, S. P.; Gillum, W. O.; Hodgson, K. O.; Mortenson, L. E.; Stiefel, E. I.; Chisnell, J. R.; Brill, W. J.; Shah, V. K. *J. Am. Chem. Soc.* **1978,** *100,* 3814.
256. Cramer, S. P.; Hodgson, K. O.; Gillum, W. O.; Mortenson, L. E. *J. Am. Chem. Soc.* **1978,** *100,* 3398.
257. Cen, W.; Lee, S. C.; Li, J.; MacDonnell, F. M.; Holm, R. H. *J. Am. Chem. Soc.* **199 ,** *115,* 9515.
258. Coucouvanis, D.; Al-Ahmad, S.; Salifoglou, A.; Papaefthymiou, V.; Kostikas, A.; Simpoulos, A. *J. Am. Chem. Soc.* **1992,** *114,* 2472.
259. Ciurli, S.; Ross, P. K.; Scott, M. J.; Yu, S.-B.; Holm, R. H. *J. Am. Chem. Soc.* **1992,** *114,* 5415.
260. Zhou, C.; Holm, R. H. *Inorg. Chem.* **1997,** *36,* 4066.
261. Mascharak, P. K.; Papaefthymiou, G. C.; Armstrong, W. H.; Foner, S.; Frankel, R. B.; Holm, R. H. *Inorg. Chem.* **198 ,** *22,* 2851.
262. Carney, M. J.; Kovacs, J. A.; Zhang, Y.-P.; Papaefthymiou, G. C.; Spartalian, K.; Frankel, R. B.; Holm, R. H. *Inorg. Chem.* **1987,** *26,* 719.
263. Ciurli, S.; Holm, R. H. *Inorg. Chem.* **1991,** *30,* 743.
264. Ciurli, S.; Carney, M. J.; Holm, R. H.; Papaefthymiou, G. C. *Inorg. Chem.* **1989,** *28,* 2696.

ADVANCES IN INORGANIC CHEMISTRY, VOL. 47

THE STRUCTURES OF RIESKE AND RIESKE-TYPE PROTEINS

THOMAS A. LINK

Universitätsklinikum Frankfurt, ZBC, Institut für Biochemie I, Molekulare Bioenergetik, D-60590 Frankfurt/Main, Germany

I. Introduction
II. Historical Background
III. Structural Aspects
  A. Primary Structures: Amino Acid Sequences
  B. 3D Structures: X-Ray Crystallography
  C. Mutational Studies
IV. Spectroscopy
  A. Electronic Spectroscopy: Absorption, Circular Dichroism, and Magnetic Circular Dichroism (MCD) Spectroscopy
  B. Mössbauer Spectroscopy
  C. Resonance Raman Spectroscopy
  D. X-Ray Absorption Spectroscopy
  E. Magnetic Spectroscopy
V. Electrochemistry
  A. Rieske Clusters: Cytochrome *bc* Complexes
  B. Rieske-Type Clusters
VI. Biosynthesis
VII. Function
  A. Rieske Clusters: Cytochrome *bc* Complexes
  B. Rieske-Type Clusters: Dioxygenases
VIII. Outlook
Abbreviations
References

I. Introduction

In 1964, Rieske and co-workers reported the observation of an EPR signal around $g = 1.90$ in the cytochrome bc_1 complex (*1*). They succeeded in the isolation of the iron sulfur protein that gave rise to the EPR signal and showed that it contained a [2Fe–2S] cluster. Over the

Copyright 1999 by Academic Press.
All rights of reproduction in any form reserved.
0898-8838/99 $30.00

past 35 years, numerous studies of this so-called Rieske protein have tried to unravel the molecular basis of its unusual properties; the understanding of the properties of the Rieske protein should also provide insight into general properties of iron sulfur clusters. The essential feature of Rieske clusters is their novel (His_2–Cys_2) coordination environment, which was first established by magnetic spectroscopy and finally proven by the crystal structure determination. In this review, I will discuss how the distinct spectroscopic, electrochemical, and functional properties of the Rieske protein are determined by the ligand environment and by the protein structure. I will use the term Rieske protein or cluster for hydroquinone-oxidizing electron transport complexes and Rieske-type protein or cluster for dioxygenases or homologous systems where the Rieske-type cluster does not interact with quinone.

II. Historical Background

In 1960, Beinert and Sands (*2*) reported the observation of an EPR signal around $g = 1.94$ in fragments of the mitochondrial electron transfer chain; this signal could be attributed to a complex containing iron and inorganic sulfur (S^{2-}), which established the biological significance of iron sulfur clusters. In 1964, Rieske and H. Beinert working at the Institute for Enzyme Research of the Medical College of Wisconsin, reported the observation of an EPR signal around $g = 1.90$ in complex III (the cytochrome bc_1 complex) of the mitochondrial respiratory chain (*1*). They succeeded in the isolation of the iron sulfur protein that gave rise to the EPR signal and showed that it contained a [2Fe–2S] cluster. This protein, which is generally referred to as Rieske protein (after its discoverer), was shown to have unique spectroscopic properties. An EPR signal comparable to that of the Rieske protein of the mitochondrial bc_1 complex has been observed in the b_6f complex of photosynthetic electron transfer chains and in the membranes of archaebacteria containing hydroquinone-oxidizing electron transfer complexes but no bc_1 complex (*3*). Similar signals have also been observed in water-soluble bacterial dioxygenases; these [2Fe–2S] clusters are referred to as Rieske-type clusters.

From an analysis of the EPR spectra, Blumberg and Peisach (*4*) suggested that the coordination environment of Rieske clusters must include "one or more atoms which are less electron donating than sulfur." This was significantly substantiated by studies of the Rieske

protein from the archaebacterium *Thermus thermophilus* (*5*). First direct spectroscopic evidence for histidine coordination was obtained by ENDOR spectroscopy of the Rieske-type cluster of phthalate dioxygenase from *Burkholderia cepacia* (formerly known as *Pseudomonas cepacia*) (*6*) and then by ENDOR and ESEEM spectroscopy of the Rieske cluster in bc_1 and b_6f complexes (*7*, *8*). Finally, the X-ray structures of the water-soluble domains of the Rieske proteins from bovine heart mitochondrial bc_1 complex (*9*) and from spinach b_6f complex (*10*) could be determined that allow an in-depth analysis of the information obtained from spectroscopic analyses, and electrochemical and mutational studies. The first structure of a Rieske-type cluster has been reported in naphthalene dioxygenase (*11*).

III. Structural Aspects

A. Primary Structures: Amino Acid Sequences

The first sequence of a Rieske protein has been obtained by sequencing of the nuclear gene of the Rieske protein of the bc_1 complex from the fungus *Neurospora crassa* (*12*). The primary structure of the Rieske protein from bovine mitochondrial bc_1 complex has been determined by direct amino acid sequencing (*13*). Subsequently, the genes of Rieske proteins from many mitochondrial, bacterial, and plastidial complexes have been sequenced, as well as numerous gene clusters of bacterial dioxygenases. From the sequences of established Rieske and Rieske-type proteins as well as from three-dimensional structures, it is known that the four ligands of Rieske and Rieske-type clusters show the following sequence motif:

$$\text{Cys–X–His–X}_{15-47}\text{–Cys–X–X–His}$$

In order to get an insight into the diversity of proteins that may contain a Rieske or Rieske-type cluster, a database search was performed in the following way.

A similarity search was performed using the program BLAST through the service provided by the ExPASy Molecular Biology Server (http://www.expasy.ch) and using the sequences of established Rieske proteins: the water soluble fragment of the Rieske protein from bovine heart bc_1 complex and of spinach b_6f complex or the ferredoxin and the α subunit of benzene dioxygenase from *Pseudomonas putida.* After eliminating all sequences that did not contain the Rieske ligand mo-

tif, approximately 125 sequences were obtained that were regarded as proteins which may contain a Rieske or Rieske-type cluster. These sequences were aligned and clustered using the programs ClustalW and Multalin from the Antheprot suite (*14*). The sequences could be grouped in the following way:

IA1. Rieske proteins from mitochondrial bc_1 complexes [12]
IA2. Rieske proteins from bacterial bc_1 complexes [7]
IB. Rieske proteins from plastidial b_6f complexes [11]
IC. Bacterial Rieske proteins that are not from bc_1 or b_6f complexes or of unknown origin [9]
IIA. Bacterial Rieske-type ferredoxins [37]
IIB. Bacterial Rieske-type oxygenases [33]
IIC. Proteins from eukaryotes that show homology to bacterial Rieske-type oxygenases [9]
IID. Other putative Rieske-type proteins [6]

1. Rieske Proteins

Rieske proteins are constituents of the *bc* complexes that are hydroquinone-oxidizing multisubunit membrane proteins. All *bc* complexes, that is, bc_1 complexes in mitochondria and bacteria, b_6f complexes in chloroplasts, and corresponding complexes in menaquinone-oxidizing bacteria, contain three subunits: cytochrome *b* (cytochrome b_6 in b_6f complexes), cytochrome c_1 (cytochrome *f* in b_6f complexes), and the Rieske iron sulfur protein. Cytochrome *b* is a membrane protein, whereas the Rieske protein, cytochrome c_1, and cytochrome *f* consist of water-soluble catalytic domains that are bound to cytochrome *b* through a membrane anchor. In Rieske proteins, the membrane anchor can be identified as an N-terminal hydrophobic sequence (*13*).

In addition to the four ligands of the Rieske cluster, three residues are fully conserved in all Rieske proteins:

$$\textbf{Cy}\ \text{–X–}\textbf{Hi}\ \text{–X–Gly–}\underline{\text{Cys}}\text{–}X_{12\text{–}44}\text{–}\textbf{Cy}\ \text{–X–}\underline{\text{Cys}}\text{–}\textbf{Hi}$$

The residues printed in bold are the ligands of the cluster; the two underlined cysteine residues form a disulfide bidge stabilizing the cluster (*9*).

a. Group IA: Rieske Proteins from Cytochrome bc_1 Complexes. Mitochondrial Rieske proteins include those of plant mitochondria, *Chlamydomonas reinhardtii, C. elegans,* three species of fungi, and of higher vertebrates. Fifty residues (26%) are fully conserved between 11 Rieske proteins; two of the conserved residues are located in the

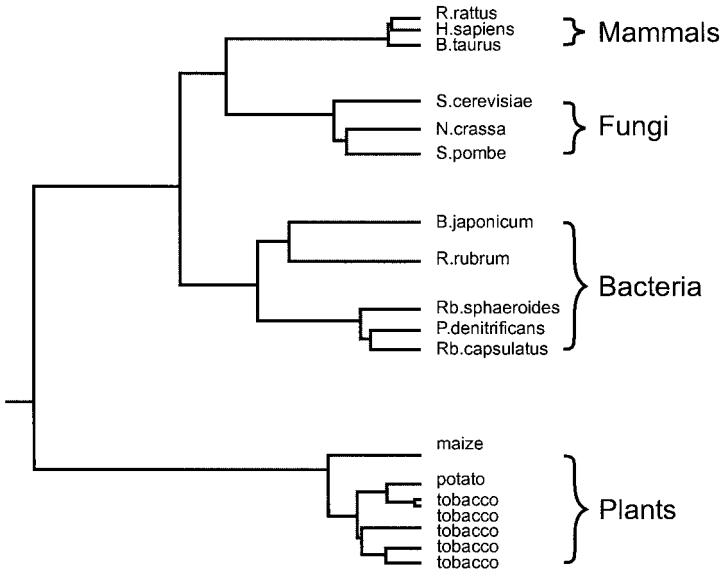

FIG. 1. Phylogenetic tree of Rieske proteins from mitochondrial and bacterial bc_1 complexes. The tree was generated from the ProtoMap web site, Release 2.0 (http://www.protomap.cs.huji.ac.il).

flexible linker (Asp 67 and Ala 70 in bovine heart numbering; cf. Section III,B,5), while all other conserved residues are in the C-terminal region comprising the catalytic domain. No insertions or deletions are observed within the catalytic domain except at the C-terminus. In a highly conserved sequence of 44 residues, 30 residues (68%) are fully conserved; these 44 residues form the cluster binding subdomain (see Section III,B,2).

The bacterial Rieske proteins contain 3–20 extra residues in the catalytic domain; these insertions occur in the helix–loop structure and in the loop $\beta 5$–$\beta 6$ (see Section III,B). The insertion of a single residue is observed in some bacterial sequences between the flexible linker and β strand 1 as well as in the "Pro loop." Twenty-eight residues are fully conserved between 11 mitochondrial and 6 bacterial sequences; 22 of these conserved residues are located in the cluster binding subdomain.

Figure 1 shows the phylogenetic relationship of the mitochondrial and bacterial Rieske proteins. Plant mitochondrial Rieske proteins form a separate cluster, whereas bacterial Rieske proteins are more closely related to Rieske proteins from fungi or mammals, although the subunit composition and organization of the bc_1 complex is compa-

rable in mitochondria from plants, fungi, and mammals: All mitochondrial bc_1 complexes contain up to eight subunits without redox centers (two "core" proteins that are related to the general mitochondrial protease (MPP) α and β subunits as well as several small subunits), whereas bacterial bc_1 complexes comprise only the three subunits that contain the redox centers and at most one small subunit with no known function.

b. Group IB: Rieske Proteins from Cytochrome b_6f Complexes Rieske proteins from b_6f complexes include those from higher plants (spinach, tobacco, pea), from algae (*Chlamydomonas*), and from cyanobacteria (*Anabaena, Nostoc, Synechocystis*). Fifty out of 177–180 residues (28%) are fully conserved between all 11 sequences; 24 of the conserved residues are located in the cluster binding subdomain (59% conservation over a 41-residue stretch).

The Rieske proteins of menaquinone-oxidizing *bc* complexes from *Bacilli* cluster with the Rieske proteins of b_6f complexes, although the complexes differ in their subunit composition: Both contain a short cytochrome $b(b_6)$ that comprises only the first four transmembrane helices of the full length cytochrome *b* as found in bc_1 complexes, but the menaquinone-oxidizing *bc* complexes from *Bacilli* contain, not cytochrome *f*, but rather a soluble cytochrome *c* that is fused to subunit IV of b_6f complexes (*15*). However, the Rieske protein of the menaquinone-oxidizing *bc* complex from *Chlorobium limicola,* which is coded in a *pet*CB transcription unit together with the full-length cytochrome *b* (*16*), is more closely related to Rieske proteins from bc_1 complexes than to Rieske proteins from b_6f complexes. Therefore, it appears that in *bc* complexes the character of the Rieske protein is related not to the type of substrate, but to the nature of the cytochrome *b:* b_6f-type Rieske proteins (group IB) are found in complexes together with a split cytochrome $b(b_6)$, whereas bc_1-type Rieske proteins (group IA) are found in complexes together with a full-length cytochrome *b*.

c. Group IC: Rieske Proteins That Are Not from Cytochrome bc Complexes This group includes sequences of Rieske proteins where the nature of the corresponding complex has not been established; several of the sequences show similarity to Rieske proteins of menaquinone-oxidizing *bc* complexes from *Bacilli* discussed in the previous section. In addition, there are three sequences of Rieske proteins from archaebacteria that do not contain a "classical" *bc* complex; the Rieske protein (TRP) from *Thermus aquaticus* and two Rieske proteins (SoxF and SoxL) from *Sulfolobus acidocaldarius (17*). *Sulfolobus* has no bc_1

complex and the two Rieske proteins are constituents of hydroquinone (caldariellaquinone) oxidizing terminal oxidases: Rieske protein II (SoxF) is part of the SoxM oxidase complex (*18*), whereas Rieske protein I (SoxL) is likely to be part of a yet unidentified terminal oxidase (*19*). SoxF and SoxL cluster together in sequence alignments (together with the Rieske protein from *Thermus aquaticus*), but they differ substantially from each other: 67 residues (27%) are identical in SoxF and SoxL; 23 of these are in the cluster binding subdomain (39% identity).

2. Rieske-Type Proteins

Sequences of proteins containing Rieske-type clusters have been deduced from the complete operons of several dioxygenases; these dioxygenases require electrons from NAD(P)H to convert aromatic compounds to *cis*-arene diols. The water-soluble dioxygenase systems consist of a reductase and a terminal dioxygenase; many dioxygenases also contain a [2Fe–2S] ferredoxin (*20*). The terminal oxygenases contain a Rieske-type cluster and the ferredoxins may contain either a Rieske-type or a 4-cysteine coordinated [2Fe–2S] cluster.

a. Group IIA: Bacterial Rieske-Type Ferredoxins These proteins are water-soluble electron transfer proteins of typically 95–111 residues that show no similarity to plant-type ferredoxins containing a 4-cysteine coordinated [2Fe–2S] cluster. Rieske-type ferredoxins show a high degree of variability; only the four residues coordinating the cluster are fully conserved between the 37 proteins that can be classified as Rieske-type ferredoxins based on their size and the conserved ligand pattern:

$$\mathbf{Cy}\ \text{–X–}\mathbf{Hi}\ \mathbf{–}\text{X}_{16\text{–}17}\mathbf{–Cy}\ \text{–X–X–}\mathbf{Hi}$$

Only a few residues show more than 75% sequence identity, including four glycine residues, a proline residue at the beginning of the "Pro loop," and a phenylalanine residue in a position corresponding to the conserved residue Tyr 165 of the bovine heart Rieske protein. However, structure prediction and sequence comparison with Rieske proteins from bc_1 complexes suggests that the fold will be very similar in all Rieske-type ferredoxins, as in the other Rieske or Rieske-type proteins (see Section III,B,1).

b. Group IIB: Bacterial Rieske-Type Oxygenases The catalytic subunit of bacterial oxygenases consists of 439–461 amino acid residues and contains a Rieske cluster as well as a catalytic mononuclear iron

site. Most of the sequences have been determined from various strains of *Pseudomonas,* but two ORFs coding for members of the group have been found in the genome of *E. coli.* The Rieske cluster is coordinated within a separate Rieske domain within the N-terminal third of the protein (*11*). Only the sequences of the Rieske domains will be discussed here.

Within the whole group of 33 sequences, 8 amino acid residues are fully conserved: in addition to the four ligands to the Rieske cluster, two glycine residues (Gly 112 and Gly 146 in naphthalene dioxygenase, NDO), one tryptophan (Trp 39 in NDO) and one arginine (Arg 68 in NDO). Gly 112 corresponds to Gly 169 in the Rieske protein from bovine heart bc_1 complex; this residue is conserved in all Rieske and Rieske-type proteins analyzed here with only three exceptions (the Rieske protein from *Chromatium vinosum* and the Rieske-type ferredoxins from *Pseudomonas putida* OUS82 and from α Proteobacterium M2), which makes it the most highly conserved residue in all Rieske and Rieske-type proteins after the ligands of the Rieske cluster. Surprisingly, the other fully conserved residues are at least 20 Å away from the Rieske cluster.

When the distantly related sequences are excluded from the alignment, a total of 22 residues are found to be conserved between 28 sequences; 14 of 42 residues around the cluster binding loops are conserved. Therefore, it can be concluded that Rieske domains of the α subunits of dioxygenases show a higher degree of conservation than Rieske-type ferredoxins.

In addition to the dioxygenase subunits just discussed, several bacterial sequences show a more distant homology to dioxygenases but contain the conserved cluster binding ligands. Most of these sequences are shorter than established dioxygenase subunits (347–397 residues). Whether these sequences represent a distant subgroup of dioxygenase subunits, truncated genes, or pseudogenes remains to be established.

c. Group IIC: Proteins from Eukaryotes that Show Homology to Bacterial Rieske-Type Oxygenases Several gene products from eukaryotic cells show homology to bacterial dioxygenases and contain the ligand pattern to accommodate a Rieske-type cluster as well as a mononuclear iron site (Table I). EPR spectra of choline monooxygenase from spinach (*21*) and of CMP-*N*-acetylneuraminic acid hydroxylase from pig (*22*) unequivocally demonstrated the presence of a Rieske-type cluster in these proteins. While CMP-*N*-acetylneuraminic acid hydroxylase from pig and from mouse contains the Rieske cluster

TABLE I

PROTEINS FROM EUKARYOTES THAT SHOW HOMOLOGY TO BACTERIAL RIESKE-TYPE OXYGENASES

ID	Protein	Organism	Related to	Reference
O22553	Choline monooxygenase	*B. vulgaris*	O04121	*122*
O04121	Choline monooxygenase	*S. oleracea*	O22553	*21*
O04127	LLS1 cell death suppressor	*Z. mays*	O04422	*25*
O04422	LLS1 cell death suppressor	*A. thaliana*	O04127	*123*
PSTIC55	TIC55, chloroplast inner envelope import complex	*P. sativum*	O04127, O04422, S74825	*24*
S74825	?	*Synechocystis* sp.	O04127, O04422	*124*
O14004	SPAC29A4.01C	*S. pombe*	O42346	*125*
O42346	Nrfl (neurula-specific ferredoxin reductase-like protein)	*Xenopus merula*	O14004	*126*
Q19655	F20D6.11	*C. elegans*	—	*127*
D21826	CMP-neuraminic acid hydroxylase	Mouse	—	*22*

within the N-terminal 100 residues, the human protein lacks these N-terminal residues and therefore the Rieske cluster (*23*). The N-terminal truncation of the human enzyme is caused by a deletion of an exon in human genomic DNA. Since the enzyme is inactive in the absence of the Rieske cluster, *N*-acetylneuraminic acid is synthesized in most mammals but not in humans.

The TIC55 protein contains a Rieske-type iron sulfur cluster and a mononuclear iron site; there is good evidence indicating that the protein is part of the chloroplast inner envelope translocation machinery (*24*). The function of TIC55 is yet unknown; the primary structure shows the highest homology to the LLS1 protein, which is highly conserved in plants. The LLS1 (lethal leaf spot 1) protein functions as a suppressor of cell death in mature leaves (*25*); it contains the ligands for both a Rieske-type cluster and a mononuclear iron site, and it has been suggested that the LLS1 protein may degrade phenolic compounds that would promote cell death.

d. Group IID: Proteins That May Contain a Rieske-Type Cluster The small subunit (NasE or NirD) of the assimilatory nitrite reductase from *Bacillus subtilis* (EC 1.6.6.4) is a protein of 106 amino acid residues that shows sequence homology to Rieske-type ferredoxins (see Section III,A,2,a). It contains the sequence

Cy –Pro–**Hi** –X_{16}–**Cy** –Pro–Met–**Hi**

which suggests that the protein might contain a Rieske-type cluster. However, the putative Rieske ligands are not conserved in the corresponding NasD protein of the assimilatory nitrite reductase from *E. coli*.

In order to check whether the occurrence of the Rieske-type sequence motif is unique for the assimilatory nitrite reductase from *Bacillus subtilis*, the sequences of other assimilatory nitrite reductases were searched for the presence of the four putative ligands of Rieske-type clusters. A well-conserved sequence pattern

$$\textbf{Cy}\ \text{–Pro–}\textbf{Hi}\ \text{–Lys–}X_{16\text{–}21}\text{–}\textbf{Cy}\ \text{–Pro–X–}\textbf{Hi}$$

was found in four fungal assimilatory nitrite reductases from *N. crassa* (Nit-6) (*26*), *Aspergillus nidulans* (niiA) (*27*), *Aspergillus fumigatus* (*28*), and *Hansenula polymorpha* (yni1) (*29*). The four proteins contain between 1044 and 1176 amino acid residues; they are homologous to sulfite reductases that contain flavin as well as siroheme in close vicinity to a [4Fe–4S] cluster. The likely flavin binding site is close to the N-terminus of the protein; the potential NAD(P) binding site is located between residues 150 and 210, whereas the ligands of the [4Fe–4S] cluster are located around residue 760. The putative binding site for the Rieske-type cluster is located in the sequence between the flavin binding site and the potential NAD(P) binding site within the N-terminal part of the protein. Little is known about the biochemistry of fungal assimilatory nitrite reductases; knowledge of siroheme-containing enzymes is largely based on studies of sulfite reductases. However, sulfite reductases are much smaller than nitrite reductases (570 compared to 1100 residues) and lack the part of the sequence containing the putative binding site for the Rieske-type cluster. Therefore, it is an open issue whether a Rieske-type cluster is present in fungal nitrite reductases.

B. 3D Structures: X-Ray Crystallography

The X-ray structures of three water-soluble proteins containing a Rieske or Rieske-type cluster have been reported so far (Fig. 2):

- The water-soluble fragment of the Rieske protein from bovine heart bc_1 complex (ISF) was crystallized by Link *et al.* (*30*) and the structure was solved at 1.5 Å resolution by Iwata *et al.* (*9*) (PDB file 1RIE).
- The water soluble fragment of the Rieske protein from spinach

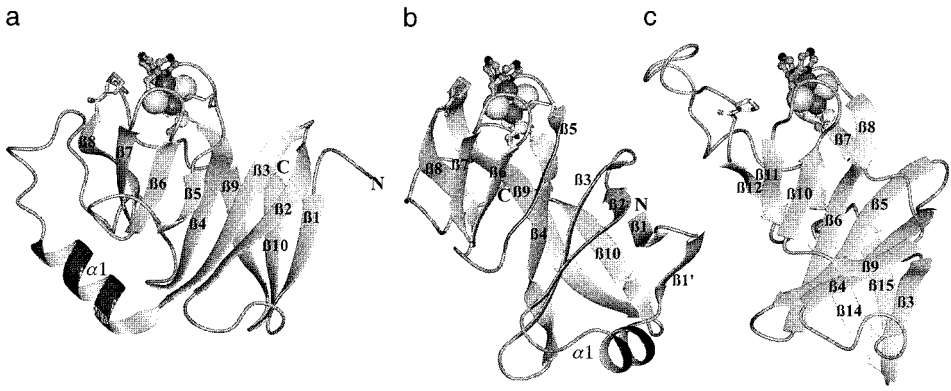

FIG. 2. Ribbon diagram of the structures of (a) the water-soluble Rieske fragment from bovine heart bc_1 complex (ISF, *left*; PDB file 1RIE), (b) the water-soluble Rieske fragment from spinach b_6f complex (RFS, *middle*; PDB file 1RFS), and (c) the Rieske domain of naphthalene dioxygenase (NDO, *right*; PDB file 1NDO). The [2Fe–2S] cluster is shown in a space-filling representation, the ligands as ball-and-stick models, and residues Pro 175 (ISF)/Pro 142 (RFS)/Pro 118 (NDO) as well as the disulfide bridge in the ISF and RFS as wireframes.

b_6f complex (RFS) was crystallized by Zhang *et al.* (*31*) and the structure was solved at 1.83 Å resolution by Carrell *et al.* (*10*) (PDB file 1RFS).

• Naphthalene-1,2-dioxygenase (NDO) from *Pseudomonas* sp. NCIB 9816-4 expressed in *E. coli* was crystallized by Lee *et al.* (*32*), and the structure was solved at 2.25 Å resolution by Kauppi *et al.* (*11*) (PDB file 1NDO).

The crystallography as well as the quality criteria of the crystallographic models are summarized in Table II. In NDO, the Rieske domain is formed by residues 38–155 of the α subunit; only this part of the structure will be discussed in this review.

The structure of the full-length Rieske protein has been determined by X-ray crystallography of the whole bc_1 complex, but at lower resolution (3.0 Å), by Zhang *et al.* (*41*) and by Iwata *et al.* (*42*).

1. The "Rieske Fold"

When we reported the first Rieske structure of the bovine heart fragment (ISF) (*9*), we could not detect any similar structure in the

TABLE II

CRYSTALLOGRAPHY OF RIESKE AND RIESKE-TYPE PROTEINS

	1RIE	1RFS	1NDO
Protein	cytochrome bc_1 complex	cytochrome b_6f complex	naphthalene dioxygenase
Organism	bovine heart	spinach	*Pseudomonas* sp. NCIB 9816-4 *E. coli* (expression)
Crystallized Form	water-soluble Rieske fragment	water-soluble Rieske fragment	holoprotein hexamer ($\alpha_3\beta_3$)
Size	129 aa, M_r = 14,593	139 aa, M_r = 14,797	3 × (449 + 194) aa, M_r = 218,322
Crystallization conditions	pH 6.2 PEG 6000 (23%) 22°C hanging drop	pH 4.6 PEG 4000 (30%) 20°C hanging drop	pH 6.0 $(NH_4)_2SO_4$(2.31 M), PEG (2%) 8°C hanging drop
State of the Rieske cluster	reduced	reduced	oxidized
Space group	$P2_1$	$P1$	$I222$
Cell dimensions	a = 32.1 Å, b = 53.0 Å, c = 38.0 Å β = 100.3°	a = 29.05 Å, b = 31.87 Å, c = 35.79 Å α = 95.6°, β = 106.1°, γ = 117.3°	a = 105.0 Å, b = 173.9 Å, c = 282.5 Å
Solvent content	41%	31%	53%
Data collection	1.000 Å, 100 K	1.500 Å, 110 K	0.95 Å, 100 K
d_{min}	1.5 Å	1.83 Å	2.25 Å
No. of unique reflections	18,058	8,785	117,067
Completeness (%)[a]	89.4 (68.0)	89.7 (57.3)	96 (97)
R_{sym} (%)[a]	5.1 (27.0)	4.8 (10.8)	9.1 (38.6)
Phasing[b]	MAD	MAD	MAD + MIR (Se-Met)
R-factor (no. of reflections)	19.2% (15,880)	17.0% (8,367)	19.4% (110,479)
R-free (no. of reflections)	21.4% (817)	22.0 (391)	23.8% (5,868)
Residues in model	127	127	640 + 640 + 638
Non-H atoms	1169	1110	15250
Water sites	167	143	1061
Average B values (Å^2)			
Main chain	6.9	10.3	31.7
Side chain	7.8	11.4	35.5
Rieske cluster	7.0	7.4	26.2
Water	20.4	26.9	39.0
Reference	Link *et al.,* 1996 (*30*) Iwata *et al.,* 1996 (*9*)	Zhang *et al.,* 1996 (*31*) Carrell *et al.,* 1997 (*10*)	Lee *et al.,* 1997 (*32*) Kauppi *et al.,* 1998 (*11*)

[a] Values in parantheses are for the last shell.

[b] MAD: multiwavelength anomalous dispersion; MAD + MIR (Se-Met): The phasing was done using MAD on a selenomethionine-substituted protein.

databases using the program DALI (*33*). (The similarities of the cluster binding loops are discussed in Section III,B,4). However, the topology observed in the bovine Rieske protein has been found to be well conserved in the other Rieske proteins investigated; it is also present in the Rieske-type ferredoxin of biphenyl oxygenase from *Burkholderia cepacia* (BphF; Colbert, C. L.; Couture, M. M.-J.; Eltis, L. D.; Bolin, J. T., manuscript in preparation). Therefore, the "Rieske fold" is present in all four major groups of Rieske proteins. It appears that

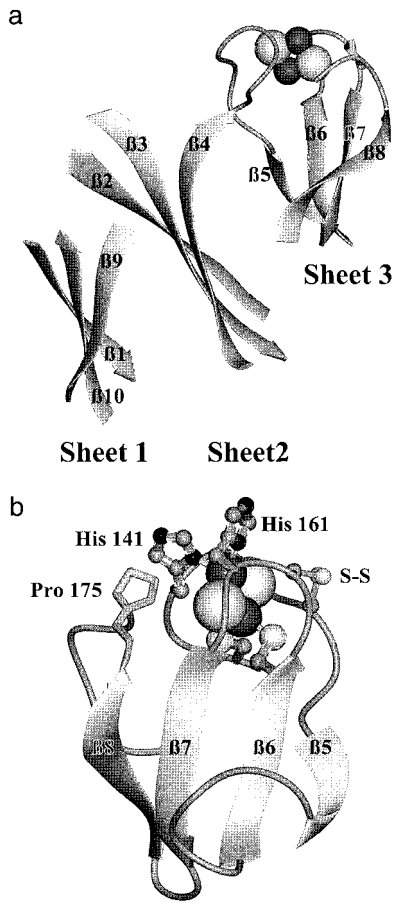

FIG. 3. (a) The "Rieske fold." Only the 10 β strands forming the three antiparallel β sheets and the loops surrounding the Rieske cluster in the cluster binding subdomain are shown. The numbering of the β strands corresponds to the ISF and RFS. (b) Structure of the Rieske cluster binding subdomain of the ISF. The [2Fe–2S] cluster is shown in a space-filling representation, the ligands as well as the disulfide bridge as ball-and-stick models and residue Pro 175 in the "Pro loop" as a wireframe model.

the "Rieske fold" is an archaetypical structural unit, comparable to, for example, the "cupredoxin fold" observed in copper proteins.

The Rieske fold consists of three antiparallel β sheets (Fig. 3a): Sheet 1 is formed by the conserved β strands 1, 10, and 9; sheet 2 is formed by the β strands 2, 3, and 4; and sheet 3 by the β strands 5–8. Sheet 3 and its loops form the "cluster binding subdomain," which is described in the next section. The three sheets can be considered as a

"double β sandwich." The central β sheet 2 contains longer strands and can be regarded as the "spine" of the structure; it interacts with both sheets 1 and 3. Sheets 1 and 2 interact through mostly hydrophobic residues at their interface. In the chloroplast protein (RFS), β sheet 1 is distorted so that it forms a barrel-like structure with β sheet 2 rather than the β sandwich observed in the other three proteins.

Highly conserved residues are found predominantly in the loops between the β strands, in particular in the loops $\beta1$–$\beta2$, $\beta2$–$\beta3$, $\beta8$–$\beta9$ (the "Pro loop"), and in the cluster binding loops.

2. The Rieske Cluster Binding Subdomain and the Rieske Cluster

The cluster binding subdomain comprises 43 or 44 residues in the Rieske proteins from bc_1 or b_6f complexes and in Rieske-type ferredoxins (Colbert, C. L.; Couture, M. M.-J.; Eltis, L. D.; Bolin, J. T., manuscript in preparation) and 32 residues in dioxygenases. The subdomain is formed by the β sheet 3 (β strands 5–8 in the ISF and RFS; β strands 8–12 in NDO) and the loops connected to it (Fig. 3b). Loops $\beta4$–$\beta5$ and $\beta6$–$\beta7$ contain the ligands coordinating the [2Fe–2S] cluster: Each loop contributes one cysteine and one histidine ligand. The inner iron (Fe-1) is coordinated by Cys 139 (ISF)/Cys 107 (RFS)/Cys 81 (NDO) from the loop $\beta4$–$\beta5$ and Cys 158 (ISF)/Cys 125 (RFS)/Cys 101 (NDO) from the loop $\beta6$–$\beta7$, whereas the outer iron (Fe-2) is coordinated by His 141 (ISF)/His 109 (RFS)/His 83 (NDO) from the loop $\beta4$–$\beta5$ and His 161 (ISF)/His 128 (RFS)/His 104 (NDO) from the loop $\beta6$–$\beta7$. Thus, the coordination pattern is 2 + 2 compared to the 3 + 1 pattern observed in 4-cysteine coordinated [2Fe–2S] clusters.

In the Rieske proteins from bc_1 or b_6f complexes, loops $\beta4$–$\beta5$ and $\beta6$–$\beta7$ both contain an additional cysteine residue (Cys 144 and Cys 160 in the ISF and Cys 112 and Cys 127 in RFS); these cysteines form a disulfide bridge connecting the two loops (Fig. 3b). These cysteines are not present in the sequences of Rieske-type proteins, that is, in neither NDO nor Rieske-type ferredoxins. In Rieske proteins, the disulfide bridge appears to be important for the stabilization of the fold around the cluster as the two loops are not shielded by other parts of the protein; in NDO, the Rieske cluster is stabilized without a disulfide bridge since it is completely buried by surrounding α and β subunits.

In the Rieske proteins from bc_1 or b_6f complexes, a third loop ("Pro loop," part of $\beta8$–$\beta9$ containing the highly conserved sequence Gly-Pro-Ala-Pro) covers the cluster from the other side. Mutations in the "Pro loop" have shown that this loop is critical for cluster stability

TABLE III

COMPARISON OF DISTANCES AND ANGLES IN THE [2Fe–2S] CLUSTER IN RIESKE PROTEINS AND IN PROTEINS CONTAINING 4-CYSTEINE COORDINATED [2Fe-2S] CLUSTERS

Cluster	Rieske		4-Cys-coordinated	
PDB file[a]	1RIE (*9*)	1RFS (*10*)	1AWD (*70*)	1FRR (*71*)
Fe1–Fe2	2.71 Å	2.72 Å	2.73 Å	2.76 Å
Fe–S^b (av.)	2.24 Å	2.32 Å	2.20 Å	2.23 Å
Fe–S^t (Fe^{III} site, av.)	2.26 Å	2.27 Å	2.28 Å	2.25 Å
Fe2–N (Fe^{II} site, av.)	2.14 Å	2.21 Å		
Fe–S^t (Fe^{II} site, av.)			2.32 Å	2.28 Å
Fe–S^b–Fe (av.)	74°	72°	77°	77°
S^b–Fe–S^b (av.)	106°	107°	103°	103°
S^t–Fe–S^t (Fe^{III} site)	106°	110°	105°	111°
N–Fe–N (Fe^{II} site)	91°	91°		
S^t–Fe–S^t (Fe^{II} site)			105°	106°

[a] 1AWD: ferredoxin from the alga *Chlorella fusca,* resolution 1.4 Å; 1FRR: ferredoxin from *Equisetum* (horsetail), resolution 1.8 Å.

S^b, bridging sulfurs; S^t, terminal sulfurs (cysteine Sγ); Nδ, coordinating imidazoles; av., average distances.

(*34*). In NDO, the corresponding loop is much longer and does not interact with the environment of the Rieske cluster, but is involved in subunit interactions with the catalytic domain in a neighboring subunit (*11*).

The cluster is coordinated at the tip of the cluster binding subdomain. Fe^{II} (Fe-2) is close to the surface of the protein with its histidine ligands fully exposed to the solvent, whereas Fe^{III} (Fe-1) is buried within the protein and surrounded by the three loops forming the cluster binding subdomain. However, in NDO the histidine ligands are not solvent accessible, but buried at the interface between the Rieske domain and the catalytic domain; both histidine ligands form hydrogen bonds with acidic side chains in the catalytic site close to the catalytic iron.

The geometry of the Rieske cluster is the same within the error of the X-ray experiment in all three structures. Table III compares distances and angles within the Rieske clusters to those observed in high-resolution structures of proteins containing 4-cysteine coordinated [2Fe–2S] clusters. In all these [2Fe–2S] clusters, the coordinating sulfurs form an almost perfect tetrahedron around the iron of the Fe^{III} site. In contrast, the geometry around the nitrogen-coordinated iron in Rieske clusters is distorted from tetrahedral geometry; the

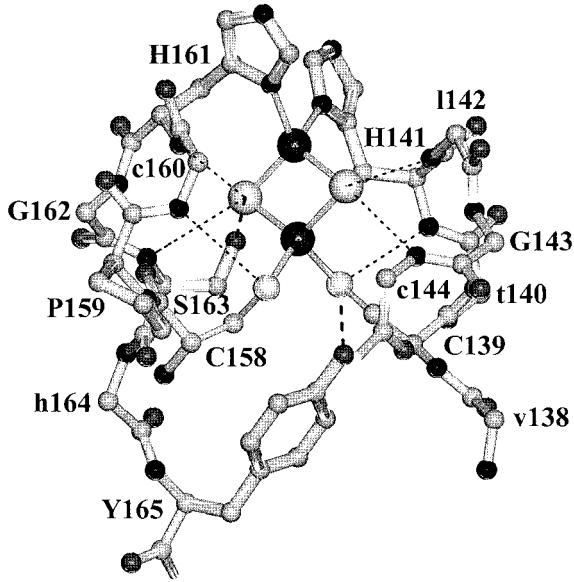

FIG. 4. Structure of the Rieske [2Fe–2S] cluster in the water-soluble Rieske fragment from bovine heart bc_1 complex (ISF). Residues where the side chains have been omitted are indicated by lowercase lettering. Dotted lines indicate hydrogen bonds to the sulfur atoms; the two OH–S hydrogen bonds formed by the side chains of Ser 163 and Tyr 165 are shown as dashed lines.

angle Nδ–Fe–Nδ is 91° in all Rieske proteins studied so far, a value expected for octahedral rather than for tetrahedral coordination.

All sulfur atoms of the cluster are highly constrained by the presence of multiple hydrogen bonds (Fig. 4); these hydrogen bonds are highly conserved between the Rieske proteins from bc_1 and b_6f complexes, whereas three of these hydrogen bonds are absent in NDO (Table IV). Sulfur S-1 participates in three hydrogen bonds; S-2 and the Sγ of the coordinating Cys in loop 1 participate in two hydrogen bonds each; only the Sγ of the Cys in loop 2 (Cys 158 in the ISF, Cys 125 in RFS, and Cys 101 in NDO) has only a single hydrogen bond to the nitrogen atom of Cys 160 (ISF)/Cys127 (RFS)/Cys 103 (NDO). Hydrogen bonds between a cysteine Sγ atom of a residue i and a main-chain N atom of residue $(i + 2)$ are frequently observed in iron sulfur proteins. In the three Rieske proteins, the hydrogen bonds between the coordinating cysteines (i, j) and the nitrogen atoms of residues $(i + 2, j + 2)$, respectively, stabilize type-I turns. In the Rieske proteins from bc_1 and b_6f complexes, two of the eight hydrogen bonds are OH–S hydrogen bonds from amino acid side chains: the Oγ of a

TABLE IV

HYDROGEN BONDS INTO THE [2Fe–2S] CLUSTER IN THE X-RAY STRUCTURES OF RIESKE AND RIESKE-TYPE PROTEINS

1RIE (*9*)	Distance	1RFS (*10*)	Distance	1NDO[a] (*11*)	Distance
S-1–His 161 N	3.2 Å	S-1–His 128 N	3.2 Å	S-2–His 104 N	3.4 Å
S-1–Ser 163 N	3.6 Å	S-1–Ser 130 N	3.4 Å	S-2–Trp 106 N	3.6 Å
S-1–Ser 163 Oγ	3.2 Å	S-1–Ser 130 Oγ	3.2 Å	—	
S-2–Leu 142 N	3.2 Å	S-2–Leu 110 N	3.4 Å	S-1–Arg 84 N	3.2 Å
S-2–Cys 144 N	3.6 Å	S-2–Cys 112 N	3.6 Å	[S-1–Lys 86 N	4.0 Å][b]
Cys 139 Sγ–Tyr 165 Oη	3.1 Å	Cys 107 Sγ–Tyr 132 Oη	3.2 Å	—	
Cys 139 Sγ–His 141 N	3.5 Å	Cys 107 Sγ–His 109 N	3.6 Å	Cys 81 Sγ–His 83 N	3.5 Å
Cys 158 Sγ–Cys 160 N	3.8 Å	Cys 125 Sγ–Cys 127 N	3.6 Å	Cys 101 Sγ–Cys 103 N	3.6 Å

[a] S-2 in 1NDO is equivalent to S-1 in 1RIE or 1RFS and S-1 in 1NDO is equivalent to S-2 in 1RIE or 1RFS.
[b] This distance is too long for a hydrogen bond.

highly conserved serine (Ser 163 in the ISF, Ser 130 in RFS) forms a hydrogen bond to the bridging sulfur S-1, and the Oη of a highly conserved tyrosine (Tyr 165 in the ISF, Tyr 132 in RFS) forms a hydrogen bond to the Sγ of the coordinating Cys in loop 1 (Cys 139 in the ISF, Cys 107 in RFS). The serine and the tyrosine are not conserved in Rieske-type proteins; the absence of these hydrogen bonds contributes to the difference of the redox potential between Rieske and Rieske-type proteins (see Section V). The importance of these hydrogen bonds for the redox potential of the cluster has been tested by site directed mutagenesis in yeast (*35*) and in *Paracoccus denitrificans* (*36*).

3. Comparative Aspects of Rieske Proteins: Similarity and Diversity

Overall, a very high degree of similarity is observed between the three Rieske proteins whose structures are known thus far. Of the 127 Cα atoms of the Rieske fragment from bovine heart bc_1 complex (*79*) (normal text site), can be superposed on the corresponding Cα atoms of the Rieske fragment from spinach b_6f complex with an rms deviation of 1.75 Å; the corresponding value for the superposition of 84 Cα atoms of the ISF and the Rieske domain of NDO is 1.8 Å. The structural similarity is even closer in the Rieske cluster binding subdomain and in particular in the loops coordinating the Rieske cluster; here, the rms deviation is less than 0.5 Å between 56 backbone atoms in loop 1 and loop 2 of 1RIE, 1RFS, and 1NDO. The structural similarity extends to the Rieske-type ferredoxin from biphenyl oxygenase (BphF): The rms deviation between 24 Cα atoms in loop 1, loop 2, and the "Pro loop" in 1RIE and BphF is 0.93 Å (Colbert, C. L.;

Couture, M. M.-J.; Eltis, L. D.; Bolin, J. T., manuscript in preparation); the corresponding value for 1RIE and 1RFS is 0.64 Å.

Despite this close structural similarity, specific differences are observed between different Rieske and Rieske-type proteins. Although the essential features of the "Rieske fold," that is, the three β sheets as well as the metal cluster binding loops in the Rieske cluster binding subdomain, are well conserved, great variability among different Rieske proteins is observed in sequence alignments (see Section III,A). Most Rieske or Rieske-type proteins contain insertions between the conserved structural elements comprising the "Rieske fold" compared to a "minimal" structure; these insertions occur in the loops between the 10 conserved β strands and at the C-terminus and vary in length between 1 and 34 residues. The structure that appears to be closest to the "minimal" structure is that of Rieske-type ferredoxins; these proteins are smaller (104–111 amino acid residues) than any of the structures reported so far (118–127 residues). Figure 5 gives a structure-based alignment of the sequences of the three proteins whose crystal structures are known and Fig. 6 compares their topologies. The Rieske protein from mitochondrial bc_1 complex has a helix and a long loop with a total length of 29 residues between the strands β3 and β4 of β sheet 2; this compares to a short loop of 3–4 residues between strands β3 and β4 in the Rieske proteins from b_6f complexes or in dioxygenases. The helix and the loop interact with the "bottom" of the Rieske cluster binding subdomain, that is, the loop between the strands β7–β8 and the β strand β8 (*9*). The β strand β8 extends into the "Pro loop" that covers one side of the exposed Rieske cluster; therefore, the helix–loop structure is critical for the stabilization of the environment of the Rieske cluster. In Rieske proteins from several bacterial bc_1 complexes, the helix–loop insertion is even longer, by 11 residues.

Rieske proteins from b_6f complexes contain an insertion of 11 residues between strands β1 and β2 compared to mitochondrial Rieske proteins as well as an extension of 16 residues at the C-terminus. In the N-terminal part, there is an additional short β strand (β1′), as well as a short helix that has no counterpart in the mitochondrial Rieske protein or in NDO. The N-terminus of β strand β1 is hydrogen-bonded to strand β10 in β sheet 1 as it is in the other Rieske proteins, but the end of strand β1 connects to strand β2 in β sheet 2; thus, the sandwich structure of the β sheets 1 and 2 is perturbed and a barrel-like structure is formed. The core of this barrel is less hydrophobic than the core of the sandwich formed by β sheets 1 and 2 in the ISF.

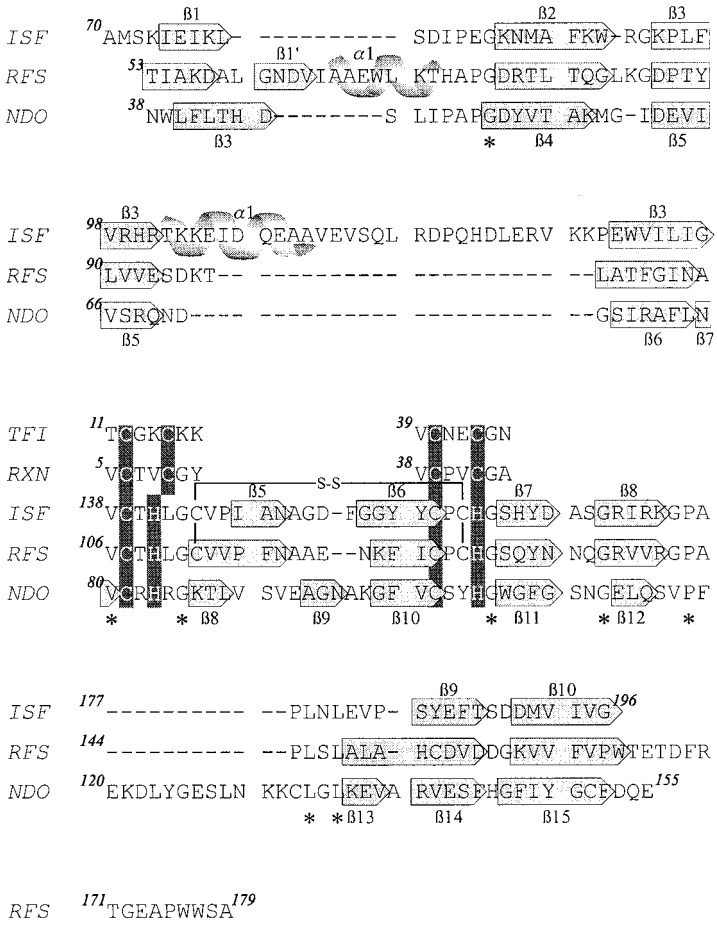

FIG. 5. Structure-based alignment of the sequences of the water-soluble Rieske fragment from bovine heart bc_1 complex (ISF), the water-soluble Rieske fragment from spinach b_6f complex (RFS), and of the Rieske domain of naphthalene dioxygenase (NDO) and of the metal binding loops of rubredoxin (RXN) and transcriptional factor TFIIS (TFI). The numbering of the β strands is the same for the ISF and RFS. The metal binding ligands are highlighted; the asterisks indicate those residues that are fully conserved between the three Rieske proteins.

The C-terminal extension (residues 163–179) of the Rieske proteins of the b_6f complex appears to have the same role in stabilizing the "open" side of the cluster binding subdomain as the helix–loop insertion in the mitochondrial Rieske protein. The C-terminal part of RFS contains a fully conserved arginine (Arg 170 in spinach); this arginine

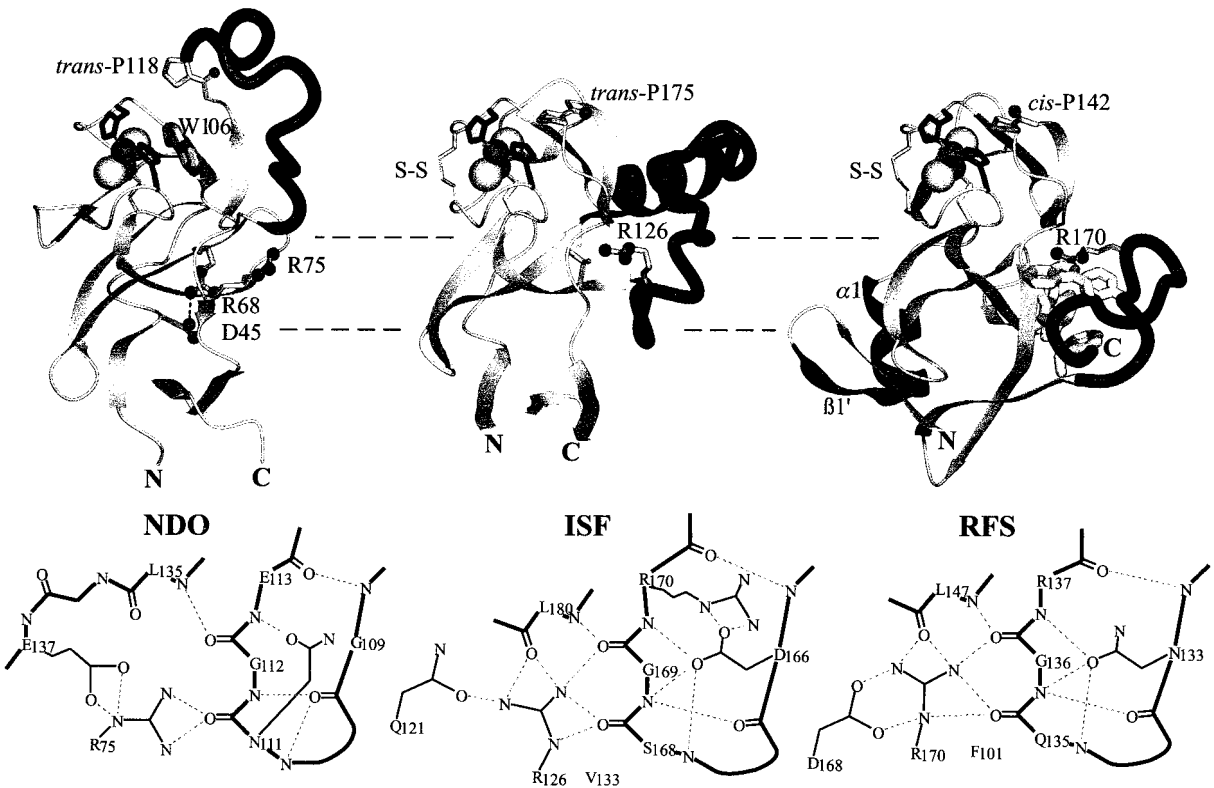
trans-P118
W106
R75
R68
D45
N
C
trans-P175
S-S
R126
N
C
cis-P142
S-S
R170
α1
C
ß1'
N
NDO
ISF
RFS

has the same position and the same function as Arg 126 of the ISF. Arg 170/126 form hydrogen bonds with two backbone oxygens in β strand β8 (the carbonyl oxygens of Gln 135 and Gly 136 in RFS corresponding to Ser 168 and Gly 169 in the ISF, respectively); in addition, both Nη groups of Arg 170 (RFS) and Arg 126 (ISF) form hydrogen bonds with the carbonyl oxygen of Leu 147 (RFS)/Leu 180 (ISF) in the "Pro loop." Arg 170/Arg 126 is backed up by two hydrogen bonds from the fully conserved Asp 168 in RFS or by a hydrogen bond from Gln 121 in the ISF. The part of the loop that is interacting with the cluster binding subdomain is stabilized by the adjacent helix in mitochondrial Rieske proteins, but is stabilized by a cluster of five aromatic residues in RFS (Phe 101, Trp 164, Phe 169, Trp 176, and Trp 177; Phe 169 is next to the critical residue Arg 170).

Therefore, although the function of the helix–loop insertion in mitochondrial Rieske proteins appears to be the same as that of the C-terminal extension in chloroplast Rieske proteins, both structures show no structural similarity or sequence homology.

Another difference between Rieske proteins from bc_1 and from b_6f complex occurs in the conserved "Pro loop." The peptide bond between Gly 141 and Pro 142 is in the *cis* conformation in 1RFS, whereas the peptide bond between Gly 174 and Pro 175 is in the *trans* conformation in the ISF. The *cis*-Pro conformation is 1RFS is stabilized by a hydrogen bond of the carbonyl oxygen of Gly 141 through a well-ordered water molecule to the Nε of Arg 140; the corresponding residue in the ISF is Lys 173, which cannot form a hydrogen bond with the adjacent glycine residue. The *trans*-Pro conformation in the ISF is stabilized through a bifurcated hydrogen bond of the carbonyl oxy-

FIG. 6. Comparison of the structures of the water-soluble Rieske fragment from bovine heart bc_1 complex (ISF, *middle*), the water-soluble Rieske fragment from spinach b_6f complex (RFS, *right*), and of the Rieske domain of naphthalene dioxygenase (NDO, *left*). (*Top*) Ribbon diagram indicating the location of the insertions in the three proteins. The conserved Rieske fold is shown as a thin ribbon; the inserted structural elements are shown as thick black ribbons. The dashed lines show the approximate borders of the three sheets of the "Rieske fold." The structurally equivalent residues Arg 126 (ISF)/Arg 170 (RFS)/Arg 75 (NDO) are shown as ball-and-stick models; residue Trp 106 in NDO as well as the cluster of aromatic residues stabilizing the C-terminal loop of RFS are shown as wireframe models. (*Bottom*) The hydrogen bond/salt bridge network around β strand β8 (β12 in NDO) involving residues Arg 126 (ISF)/Arg 170 (RFS)/Arg 75 (NDO). Backbone bonds are shown as heavy lines, hydrogen bond/salt bridges as dotted lines. In the sequence, Arg 75 of NDO is equivalent to Val 133 of the ISF (shown above as wireframe model adjacent to Arg 126) and Phe 101 of RFS, which is part of the cluster of aromatic residues shown above.

gen of Gly 174 with both Nη atoms of Arg 118 in the inserted loop between the α helix and strand β4.

In bovine heart mitochondrial bc_1 complex, the *trans* conformation is observed for Pro 175 of the Rieske protein in the $P6_522$ crystal form, whereas the *cis* conformation is observed in the $P6_5$ crystal form (*42*) (see Section III,B,5).

The structure of the Rieske domain of NDO is very similar to the structure of the ISF, but contains an insertion of three residues compared to mitochondrial Rieske proteins in the loop β3–β4 (corresponding to β1–β2 in other Rieske proteins) as well as an insertion of 12 residues in the region of the "Pro loop." The side chains of the three extra residues in the loop β3–β4 (His 44–Asp 45–Ser 46) are involved in stabilizing interactions both within the Rieske domain and with the catalytic domain: the side chain of Ser 46 interacts with the backbone atoms of Leu 182 in the catalytic domain; the carboxylate group of Asp 45 forms a salt bridge with the fully conserved Arg 68 at the end of strand β5 (corresponding to β3 in other Rieske proteins); and the imidazole ring of His 44 interacts with the phenyl ring of Phe 147 in strand β15 (corresponding to β10 in other Rieske proteins).

The long extra loop in NDO (residues 118–132) replaces the fully conserved residues Pro-Ala-Pro in the "Pro loop" of Rieske proteins from bc_1 and b_6f complexes (175–177 in the ISF, 142–144 in RFS), which are in a position similar to that of residue Trp 106 in NDO. The side chain of Trp 106 covers one side of the Rieske cluster and stacks against the iron ligand His 83; therefore, this side chain is the structural equivalent of the "Pro loop" in the ISF or RFS. The long extra loop does not interact with the environment of the Rieske cluster, but is involved in subunit interactions with the catalytic domain in a neighboring subunit (*11*). In the Rieske domain of NDO, there is a small salt bridge/hydrogen bond network stabilizing the "bottom" of the Rieske cluster binding subdomain, that is, the loop between the strands β11–β12 and the β strand β12 (corresponding to strands β7 and β8 in the ISF or RFS). This network involves residue Arg 75 from β strand β6 (corresponding to strand β4 in the ISF and RFS); this residue has a similar role as Arg 126 in the ISF or Arg 170 in RFS. Both Nη atoms of Arg 75 form a bifurcated hydrogen bond with the carboxyl oxygen of Asn 111 in the loop β11–β12. The Nε atom of Arg 75 forms a bifurcated salt bridge with the carboxylate group of Glu 137 in the short β strand 13 that is connected to sheet 2; therefore, Arg 75 mediates the interaction of residues that are located at the N- and the C-terminus of the extra loop.

From the detailed description given here, it is apparent that a simi-

lar salt bridge/hydrogen bond network exists in all three Rieske proteins; although the structural motives are similar in the three proteins, the residues involved are not homologous in amino acid sequence. The network has a quite different function in Rieske proteins from bc_1 and b_6f complexes and in NDO: In Rieske proteins from bc_1 and b_6f complexes, the exposed cluster has to be stabilized by the "Pro loop," which is supported by the salt bridge/hydrogen bond network. In NDO, the cluster is not exposed, but completely buried by surrounding α and β subunits; the parts of the structure corresponding to the "Pro loop" are used to stabilize subunit interactions. In the NDO $\alpha_3\beta_3$ hexamer, the histidine ligands of the Rieske cluster are also buried at the interface between the Rieske domain and the catalytic domain; both form hydrogen bonds with carboxylate residues in the catalytic domain (His 83–Glu 410 and His 104–Asp 205). This is in contrast to the situation in Rieske proteins of bc_1 and b_6f complexes, where the histidine ligands are completely exposed to solvent.

4. Comparison to Other Metalloproteins

The "Rieske fold" has been found only in Rieske and Rieske-type proteins. Although no similarity is observed to proteins (ferredoxins) containing a 4-cysteine coordinated [2Fe–2S] cluster, the topology of the cluster binding subdomain shows similarity to that of rubredoxins. Rubredoxins are small (45–54 amino acids) electron transport proteins containing a single iron atom coordinated by four cysteine residues. The X-ray structures of several rebredoxins have been reported, the first being that of rubredoxin from *Desulfovibrio vulgaris* (RdDv) (*37*). In rubredoxins, two metal binding loops are supported by a three-stranded β sheet (Fig. 7); two of the four cysteines coordinating the iron are in equivalent positions to the coordinating cysteines in Rieske clusters. The metal-binding loops of Rieske proteins and rubredoxin (PDB file 7RXN) (*38*) can be superposed with an rms deviation of 0.66 Å; the two coordinating cysteine residues and iron atom Fe-1 of the Rieske cluster superpose with two of the coordinating cysteine residues (Cys 6 and Cys 39) and the iron atom of RdDv, while the acid-labile sulfur atoms of the Rieske cluster superpose with the Sγ atoms of the two other cysteine residues (Cys 9 and Cys 42) of RdDv (*9*).

The general topology of rubredoxins is also observed in the general zinc-ribbon motif in RNA polymerases or in transcription factors (*39*). The first published zinc-ribbon structure was that of the nucleic-acid binding domain of human transcriptional elongation factor TFIIS (PDB file 1TFI) (*40*). These zinc binding domains and rubredoxins

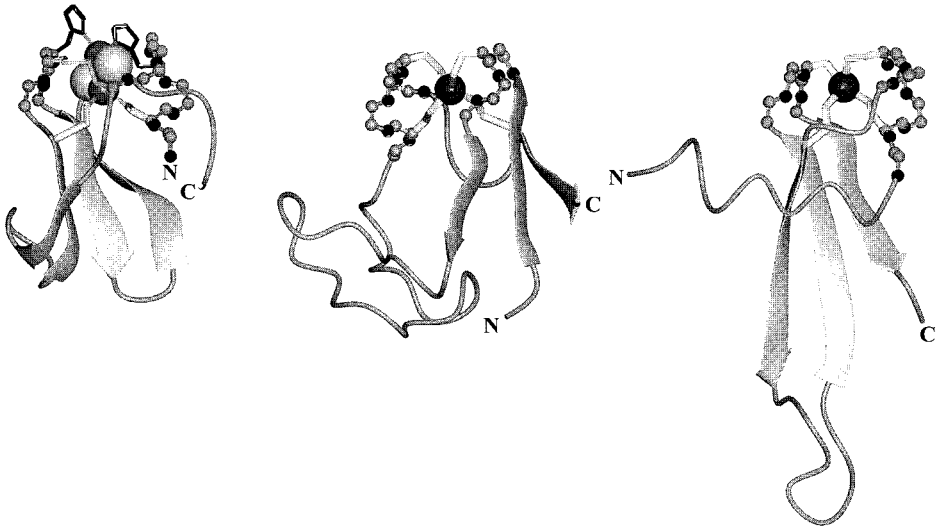

FIG. 7. Comparison of the cluster binding fold of the water-soluble Rieske fragment from bovine heart bc_1 complex (ISF, *left;* PDB file 1RIE) with the structure of rubredoxin (*middle;* PDB file 7RXN) and with the zinc-ribbon motif (*right;* PDB file 1TFI). The metal binding loops are shown as ball-and-stick models of the backbone atoms.

have the same spacing of the four cysteine residues coordinating the metal ion and a similar topology comprising a three-stranded β sheet supporting two metal binding loops. However, the only conserved amino acid residues in the metal binding loops of Rieske proteins, rubredoxins, and the zinc-ribbon domain are two coordinating cysteines (Fig. 5). Despite this sequence variation, the two loops of TFIIS can be superposed on the loops of the four other structures shown in Fig. 5 with an rms deviation of 0.9–1.1 Å for either 14 Cα atoms or 56 backbone atoms. This value compares to an rms deviation of 0.8 Å for the superposition of the loops of RdDv on the loops in the three Rieske structures and an rms deviation of 0.3–0.5 Å for the superposition of the loops of one Rieske structure on those of another. These values show that a similar metal binding motif is observed not only in different classes of electron transport proteins, but also in a metal binding domain of nucleic acid binding proteins. This relationship is particularly intriguing in view of concurrent hypotheses of the evolution of life from an "iron sulfur world."

In view of the structural homology, it is likely that the cluster binding subdomain of Rieske proteins accommodating two metal ions has evolved from an archaic mononuclear metal binding domain. A simi-

lar situation as in the Rieske protein is observed in subunit II of cytochrome oxidase. This subunit has a dinuclear copper center (Cu_A), but the protein fold is related to the mononuclear copper protein plastocyanin. In both the Rieske protein and subunit II, one of the metal ions of the cluster superposes on the metal ion of the respective mononuclear counterpart. Therefore, these subunits seem to have originated from water-soluble mononuclear redox proteins that were incorporated into the respective membrane protein complexes.

5. Structure of the Rieske Protein in Cytochrome bc Complexes

In *bc* complexes (bc_1 complexes of mitochondria and bacteria and b_6f complexes of chloroplasts), the catalytic domain of the Rieske protein corresponding to the isolated water-soluble fragments that have been crystallized is anchored to the rest of the complex (in particular, cytochrome *b*) by a long (37 residues in bovine heart bc_1 complex) transmembrane helix acting as a membrane anchor (*41*, *42*). The great length of the transmembrane helix is due to the fact that the helix stretches across the bc_1 complex dimer and that the catalytic domain of the Rieske protein is "swapped" between the monomers, that is, the transmembrane helix interacts with one monomer and the catalytic domain with the other monomer. The connection between the membrane anchor and the catalytic domain is formed by a 12-residue flexible linker that allows for movement of the catalytic domain during the turnover of the enzyme (Fig. 8a; see Section VII). Three different positional states of the catalytic domain of the Rieske protein have been observed in different crystal forms (Fig. 8b) (*41*, *42*):

- A "c_1 positional state" where the exposed NεH group of His 161 which is a ligand of the Rieske cluster forms a hydrogen bond with a propionate group of heme c_1 (*42*)
- An "intermediate state" where the environment of the Rieske cluster does not interact with any other subunit of the bc_1 complex
- A "*b* positional state" that is stabilized by the interaction of His 161 with a molecule of the inhibitor stigmatellin bound in the quinone binding pocket (*41*), which is supposed to mimic the hydrogen bonding pattern of the reaction intermediate, semiquinone (*43*)

In addition to this large movement of the Rieske protein, small but nevertheless significant conformational differences within the functional domain are observed. The structure of the functional domain of the Rieske subunit in the $P6_222$ crystal form showing the "c_1 positional state" is the same as that of the water soluble fragment

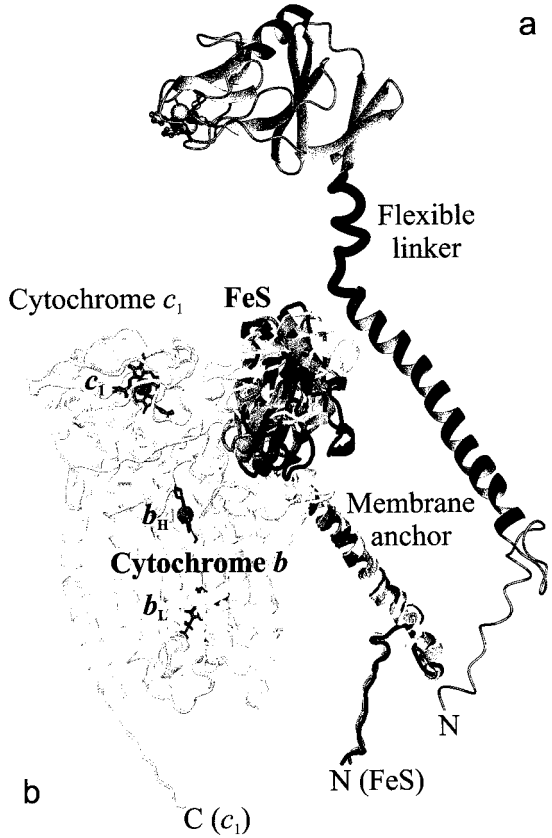

FIG. 8. (a) Structure of the full-length Rieske protein from bovine heart mitochondrial bc_1 complex. The catalytic domain is connected to the transmembrane helix by a flexible linker. (b) Superposition of the three positional states of the catalytic domain of the Rieske protein observed in different crystal forms. The "c_1 state" is shown in white, the "intermediate state" in gray, and the "b state" in black. Cytochrome b consists of eight transmembrane helices and contains two heme centers, heme b_L and b_H. Cytochrome c_1 has a water-soluble catalytic domain containing heme c_1 and is anchored by a C-terminal transmembrane helix. The heme groups are shown as wireframes, the iron atoms as well as the Rieske cluster in the three states as space-filling representations.

(ISF). However, in the $P6_5$ crystal form ("intermediate state"), the cluster binding subdomain appears to be detached from the base fold (β sheets 1 and 2) in an "open" conformation (*42*). If the functional domains of the two crystal forms are superposed using the base fold residues, the rms deviation of the Cα positions of the cluster binding

subdomain is 1.6 Å. The relative position between the cluster binding subdomain and the base fold in the $P6_5$ form shows greater similarity to the structure of the RFS than to the ISF in the $P6_522$ form. When the structure of the Rieske protein in the $P6_522$ form and that of the soluble b_6f fragment (1RFS) were superposed on the $P6_5$ structure using the common base fold residues (β2 and β3), the rms deviation of the Cα atoms in the cluster binding fold was 1.6 Å for the $P6_522$ form and 1.0 Å for the RFS (*42*).

The similarity of the Rieske protein in the $P6_5$ crystal form to the structure of the spinach RFS is also obvious from the conformation of residue Pro 175 in the "Pro loop": As in the structure of the soluble ISF, the *trans* conformation is observed for Pro 175 of the Rieske protein in the $P6_522$ crystal form, while the *cis* conformation, as in the RFS, is observed in the $P6_5$ crystal form (*42*). The conformational change occurring at Pro 175 as well as a bend occurring at Gly 137 lead to a rotation by approximately 6° of the cluster binding subdomain between the two crystal forms.

C. Mutational Studies

1. Rieske Proteins from Cytochrome bc_1 Complexes

Early mutational studies of the Rieske protein from bc_1 complexes have been performed with the intention of identifying the ligands of the Rieske cluster. These studies have shown that the four conserved cysteine residues as well as the two conserved histidine residues are essential for the insertion of the [2Fe–2S] cluster (*44*, *45*). Small amounts of a Rieske cluster with altered properties were obtained in *Rhodobacter capsulatus* when the second cysteine in the cluster binding loop II (Cys 155, corresponding to Cys 160 in the bovine ISF) was replaced by serine (*45*). The fact that all four cysteine residues are essential in Rieske clusters from *bc* complexes, but that only two cysteines are conserved in Rieske-type clusters, led to the suggestion that the Rieske protein may contain a disulfide bridge; the disulfide bridge was finally shown to exist in the X-ray structure (*9*).

Using a random mutagenesis approach, respiratory-deficient (*34*) and temperature-sensitive (*46*, *47*) mutants of the Rieske protein of the yeast bc_1 complex have been selected. A large fraction of the point mutants had changes of residues in the "bottom" of the cluster binding subdomain (the loop β7–β8) and in the "Pro loop" comprising residues 174–180 of the ISF (Fig. 9; see Section III,B,3); this indicates the importance of the "Pro loop" for the stability of the protein. Amino

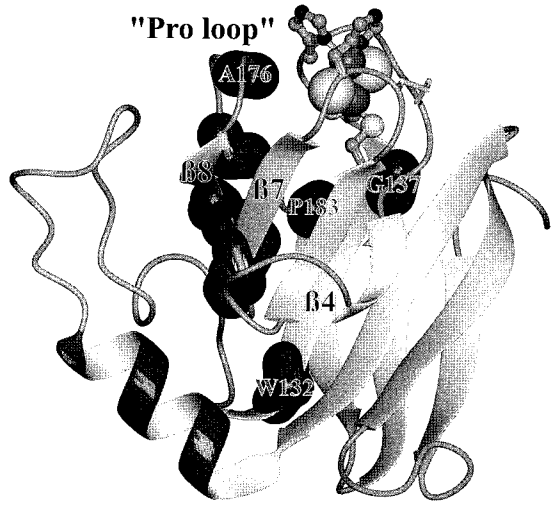

FIG. 9. The structure of the Rieske fragment from bovine heart bc_1 complex, indicating positions where deficient mutations have been selected in yeast (see text).

acid exchanges that led to the loss of the iron sulfur cluster or complete loss of activity (when the cluster content was not checked) include Asp 166 → Asn, Ser 168 → Pro, Gly 169 → Asp, Arg 170 → Gly, Ala 176 → Val, and Asn 179 → Lys (the bovine numbering system is used throughout this section; the corresponding numbers for the mature yeast Rieske protein are obtained by subtracting 10). In the mutant Pro 175 → Ser, the Rieske cluster content was 20% of wild type levels while the specific activity per Rieske cluster was not reduced (*34*). Additional amino acid exchanges that led to complete loss of the cluster or of the activity were found in Trp 132 → Arg, Gly 137 → Asp, and Pro 183 → Ser; these residues are fully conserved in all Rieske proteins from bc_1 complexes (except for the exchange of Trp for Tyr in the bc_1 complex of *Chlamydomonas reinhardtii*) (*48*), and they have important structural roles. Gatti *et al.* (*34*) have identified three mutants in which the midpoint potential of the Rieske cluster was shifted to more negative values by 50 to 100 mV: Gly 143 → Asp, Pro 146 → Leu, and Pro 159 → Leu. All these mutations will lead to a distortion of the protein environment of the [2Fe–2S] cluster and most probably of the hydrogen bond network surrounding the cluster [discussed by Iwata *et al.* (*9*)]; the cluster content of the three mutants is reduced by 32–70%.

The importance of hydrogen bonds for the redox potential of the Rieske cluster has been demonstrated by site-directed mutagenesis of

the conserved residues that form the following OH–S hydrogen bonds from side-chain hydroxyl groups to sulfur atoms of the cluster: Ser 163 Oγ–S-1 and Tyr 165 Oη–Cys 139 Sγ.

Both residues were replaced by other amino acids through point mutations introduced on plasmids either containing the gene for the Rieske protein in yeast (*35*) or containing the *fbc* operon in *Paracoccus denitrificans* (*36*), and the effect was comparable in both organisms. When Ser 163 was replaced by alanine (eliminating the hydrogen bond to the S-1 of the cluster), the midpoint potential was lowered by 95 or 130 mV, and when Tyr 165 was replaced by phenylalanine (eliminating the hydrogen bond to the Sγ of Cys 139), the midpoint potential was lowered by 45 or 65 mV. Eliminating both hydrogen bonds had an approximately additive effect. In all these variants, the stability of the cluster was not perturbed; this is in contrast to the effect of most other mutations, where rather small changes of the midpoint potential are accompanied by a marked decrease of the stability. The activity of the bc_1 complex decreases with the decrease in midpoint potential of the Rieske cluster; this clearly shows that the midpoint potential of the Rieske cluster is critical for hydroquinone oxidation. The interaction between the Rieske cluster and quinones was not perturbed by the mutations (*36*).

A different effect was observed when Tyr 165 was replaced by nonaromatic amino acids; in this case the Rieske protein was no longer found in the membranes. The aromatic side chain is essential for the stability of the environment of the cluster, so that protein is unstable and susceptible to proteolytic degradation when the tight packing around the cluster is perturbed. A different effect was observed in the mutant Ser 165 $\rightarrow$ Cys, where the protein was present in full amount but without any detectable Rieske cluster; this mutation affects, not the stability of the protein, but the insertion of the cluster (*35*). In the mutant Ser 165 $\rightarrow$ Thr where the hydrogen bond can be formed, a slight decrease of both the midpoint potential and the activity of the bc_1 complex was observed, indicating a slight perturbation of the cluster environment without loss of stability.

When the fully conserved residue Thr 140, which is packed against the "Pro loop," was substituted by Gly, His, or Arg in *Rhodobacter capsulatus*, the midpoint potential of the Rieske cluster was decreased by 50–100 mV, the cluster interacted with the quinone pool and the bc_1 complex had 10–24% residual activity but the Rieske cluster was rapidly destroyed upon exposure to oxygen (*49*). In contrast, the residual activity was $<5\%$, the cluster showed no interaction with the quinone pool, and the interaction with the inhibitor stigmatellin

was altered when Leu 142 was substituted by Gly, His, Arg, or Asp. Leu 142 is exposed at the hydrophobic tip of the protein, adjacent to the histidine ligands. In the mutants of Leu 142, the redox potential of the cluster was lowered by 20–115 mV; this result is in contrast to a preliminary report (*50*). Revertants of these photosynthetically incompetent mutants were found at the same position (Leu 142 → Ala, Leu 142 → Tyr) as well as in the flexible linker connecting the catalytic domain of the Rieske protein to the membrane anchor (Val 68 → Leu, Val 68 → Phe, Ala 70 → Thr, Ala 70 → Val (bovine heart numbering system) (*51*). The mutation Ala 70 → Thr has also been found as an intergenic second-site suppressor for a mutation in cytochrome *b* (Thr 163 → Phe in the *Rhodobacter capsulatus* sequence) (*52*). The cytochrome *b* reduction rate, which was essentially zero in the mutant Leu 142 → Gly, was five- to ten-fold slower in the second-site revertants compared with the wild-type strain, but the interaction with the quinone pool as observed in the EPR spectrum (cf. Fig. 15) was not restored; this indicates that the second-site revertants suppress the defect inferred by the mutation in position 142 without eliminating it.

When the second-site revertants were segregated from the original mutations, the bc_1 complexes carrying a single mutation in the linker region of the Rieske protein had steady-state activities of 70–100% of wild-type levels and cytochrome *b* reduction rates that were approximately half that of the wild type. In all these mutants, the redox potential of the Rieske cluster was increased by about 70 mV compared to the wild type (*51*). Since the mutations are in residues that are in the flexible linker, at least 27 Å away from the cluster, it is extremely unlikely that any of the mutations would have a direct effect on the redox potential of the cluster that would be observed in the water-soluble fragments. However, the mutations in the flexible linker will affect the mobility of the Rieske protein. Therefore, the effect of the mutations described is due to the interaction between the positional state of the Rieske protein and its electrochemical properties (i.e., the redox potential of the cluster).

2. Dioxygenase Systems

The coordination of the Rieske cluster in the α subunit of benzene dioxygenase has been studied by site-directed mutagenesis. The replacement of His 98 or His 119 (corresponding to His 83/104 in NDO) by Cys resulted in a protein that was unable to coordinate a normal Rieske-type cluster (*53*). In the mutant His 98 → Cys, a novel EPR spectrum with $g_{av} = 1.94$ was detected that is intermediate between

the g values observed for Rieske proteins (g_{av} = 1.96) and those observed for plant type ferredoxins (g_{av} = 1.91); however, the EPR spectrum represents only a minority species (<10%). A slightly perturbed Rieske-type cluster with a shifted g_x value was observed in the mutant Tyr 118 → Ser (corresponding to the conserved Y103 in NDO); this residue is located in the cluster coordinating loop II between the two ligands and its sidechain is packed against one inorganic sulfur (S-2). The EPR intensity of the Rieske cluster was approximately half of that from the wild type and the activity was 1% of the wild-type level.

The environment of the Rieske-type cluster was explored in site-directed mutants of the Rieske-type ferredoxin from benzene dioxygenase (*54*). Four mutants where highly conserved residues in the vicinity of the cluster were exchanged have been studied: Gly 46 → Ala, Gly 57 → Ala, Glu 61 → Thr (this acidic residue is adjacent to Cys 62, which is a ligand to the Rieske cluster), and Leu 64 → Phe (this residue corresponds to residue Tyr 118 in the α subunit). These exchanges led to small shifts of the redox potential (+45 and +25 mV in the mutants Gly 46 → Ala, and Leu 64 → Phe, respectively; −35 mV in the mutant Glu 61 → Thr). Only the mutant E61T showed an altered EPR spectrum (broadening of g_x). On first sight it is surprising that the exchange of an acidic, negatively charged residue in the vicinity of the cluster for a neutral residue led to a decrease of the redox potential.

IV. Spectroscopy

A. Electronic Spectroscopy: Absorption, Circular Dichroism, and Magnetic Circular Dichroism (MCD) Spectroscopy

The spectra of iron sulfur proteins in the visible and near-UV range show a broad absorption envelope resulting from a large number of overlapping absorption bands deriving from transitions with predominantly S → Fe^{III} charge transfer character. The complexity of these transitions is partially resolved in the natural circular dichroism (CD) and magnetic circular dichroism (MCD) spectra because of different selection rules and the appearance of both positive and negative bands (Fig. 10). Natural CD spectra also serve as a sensitive monitor of distortions of the iron sulfur cluster.

Both Rieske and Rieske-type proteins have absorption spectra which are significantly different from those of proteins with 4-cysteine

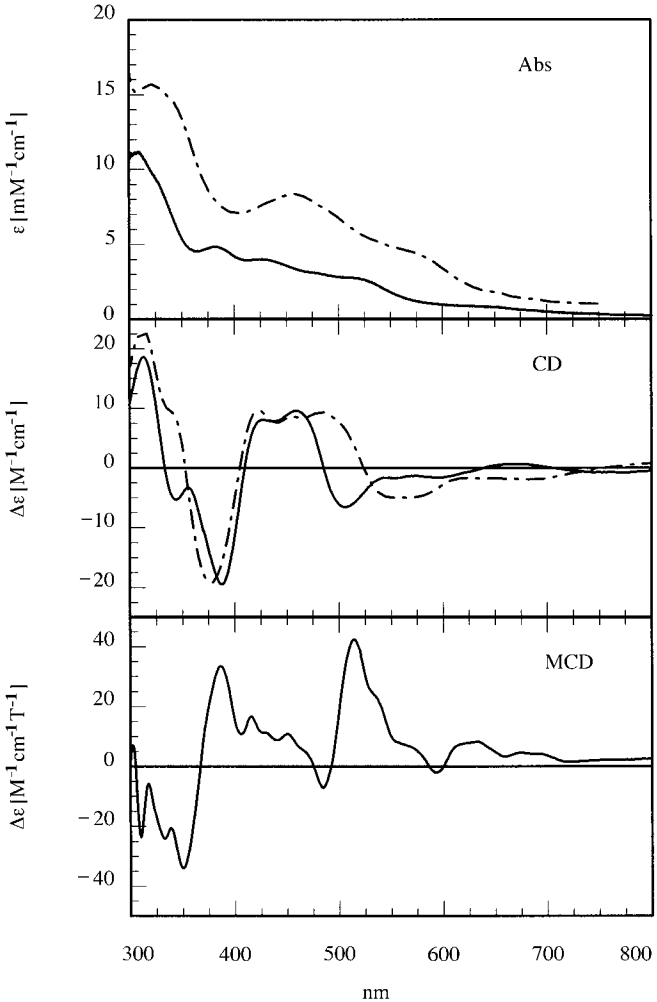

FIG. 10. Absorption, CD, and MCD spectra of the Rieske fragment from bovine heart bc_1 complex. (*Top panel*) absorption spectra (298 K); (*middle panel*) CD spectra (298 K); (*bottom panel*) MCD spectra (1.7 K). ——, reduced protein; - . -, oxidized protein.

coordinated [2Fe–2S] clusters. In the oxidized state, maxima at 325 nm and 458 nm as well as a shoulder between 560 and 580 nm are observed (Table V) (*5*, *30*, *55*). In the reduced state, maxima are observed around 380–383 nm, 425–432 nm, and between 505 and 550 nm.

TABLE V

EXTINCTION COEFFICIENTS AND ELLIPTICITIES OF THE RIESKE PROTEIN FROM BOVINE HEART bc_1 COMPLEX (ISF) AND OF THE RIESKE-TYPE FERREDOXIN FROM BENZENE DIOXYGENASE (Fd_{BED})

	ISF		Fd_{BED}	
Absorption	λ (nm)	ε ($mM^{-1}cm^{-1}$)	λ (nm)	ε ($mM^{-1}cm^{-1}$)
Oxidized	323	15.7	325	9.0
	458	8.4	457	4.8
	579	4.3	573	2.7
Reduced	305	11.1		
	383	4.8	382	4.1
	428	4.0	432	3.3
	520	2.7	505	2.1
	ISF		Fd_{BED}	
CD	λ (nm)	$\Delta\varepsilon$ ($M^{-1}cm^{-1}$)	λ (nm)	$\Delta\varepsilon$ ($M^{-1}cm^{-1}$)
Oxidized	314	+22.7	323.5	+21.2
	379	−18.8	376.5	−17.7
Reduced	314.5	+18.1	312	+16.1
	389.5	−19.4	386.5	−9.3
	506	−6.6	502	−8.9

The CD spectra reveal several distinct features that are highly significant for both Rieske and Rieske-type clusters. The CD spectra of the oxidized proteins show two positive bands between 310 and 350 nm, a negative band at 375–380 nm, and a set of positive bands between 400 and 500 nm. The CD spectra of the reduced proteins show positive bands at 314 nm, a negative band at 384–390 nm and a negative band around 500 nm.

These characteristic CD spectra differ significantly from those of other iron sulfur proteins (Fig. 11); for example, proteins containing 4-Cys-coordinated [2Fe–2S] clusters (plant type ferredoxins as well as adrenodoxin) show CD spectra that are dominated by strong positive CD bands between 420 and 460 nm in the oxidized state and negative CD bands between 440 and 510 nm in the reduced state (*56*). Therefore, CD spectra of Rieske proteins are highly significant and can be used to identify Rieske and Rieske-type clusters even in the absence of other evidence (*57*). The strong negative CD band of the reduced cluster around 500 nm can be used to monitor the redox state of the Rieske cluster even in the presence of hemes, such as in the cytochrome bc_1 complex.

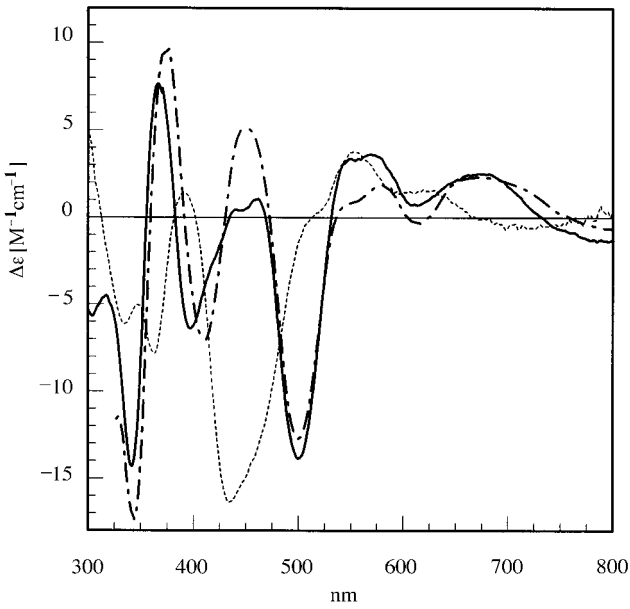

FIG. 11. Comparison of the difference CD spectra (reduced − oxidized) of the Rieske fragment from bovine heart mitochondria (ISF, ——), of the Rieske-type ferredoxin from benzene dioxygenase (Fd_{BED}, - . -) and of spinach ferredoxin containing a 4-cysteine coordinated [2Fe–2S] cluster (·····).

The CD spectra of the oxidized Rieske protein from bc_1 complexes are pH dependent. Although the general features of the spectra persist, small but significant shifts of all bands in the near UV and visible regions occur between pH 6.5 and 10, while the far UV (secondary structure) CD spectrum is not altered, indicating that the structure of the oxidized protein does not change (*58*). The analysis of the CD spectra indicated the presence of two deprotonation events with $pK_{a,ox}$ values of 7.7 and 9.1 for the bovine protein. No deprotonation was observed on the reduced protein over pH 6 to 11. The redox dependent deprotonation has been ascribed to the histidine ligands of the [2Fe–2S] cluster. In the Rieske-type ferredoxin of benzene dioxygenase from *Pseudomonas putida,* no redox-dependent deprotonation of the histidine ligands is observed below pH 9, but the deprotonation triggers the unfolding of the oxidized protein with a pK_a of 9.5 (Hatzfeld, O. M.; Unalkat, P.; Cammack, R.; Mason, J. R.; Link, T. A., manuscript in preparation).

$S \rightarrow Fe^{III}$ charge transfer bands are more intense in oxidized than

in reduced iron sulfur proteins; upon reduction, the absorption intensity of the Rieske cluster drops to approximately half the value observed in the oxidized protein. However, the CD bands at 500 and at 760 nm are observed only in the reduced Rieske proteins; their assignment should provide valuable information on the ligand field splitting of the iron ions, since strong CD bands are expected for magnetically allowed transitions, that is, d–d bands. High-spin Fe^{III} has no spin-allowed d–d transitions, whereas high-spin Fe^{II} has spin-allowed d–d transitions derived from the excitation of the lowest-lying d orbital into the orbitals of the t_{2g} set; these transitions are characterized by anisotropy factors (dissymmetry ratios, $\Delta\varepsilon/\varepsilon) > 0.05$. In reduced plant-type ferredoxins, CD bands belonging to the transitions $d_{z^2} \rightarrow d_{xz}$ and $d_{z^2} \rightarrow d_{yz}$ have been identified at energies ΔE_{xz} and ΔE_{yz} of 6000 and 3800 cm^{-1} (*59*). From a ligand field analysis of Rieske clusters, it has been suggested that the energy difference ΔE_{xz} should be increased in Rieske clusters compared to plant-type ferredoxins (*60*). The only strong CD bands of the reduced cluster between 7000 and 22,000 cm^{-1} are those at 13,000 cm^{-1} (760 nm) and 20,000 cm^{-1} (500 nm); the anisotropy factor of the band at 760 nm has been calculated to be around 0.01, which is not indicative of a d–d transition. Therefore, Link *et al.* (*55*) have assigned the band at 500 nm to the highest energy d–d transition ($d_{z^2} \rightarrow d_{xz}$), giving $\Delta E_{xz} = 20{,}000$ cm^{-1}. This assignment is consistent with the EPR analysis of Bertrand *et al.* (*60*), but it has been questioned based on the results of molecular orbital (MO) calculations: (i) Model calculations for distorted tetragonal 4-coordinate high-spin Fe^{II} show that the energy difference ΔE_{xz} is always significantly smaller than 20,000 cm^{-1} (Grodzicki, M., unpublished results). As there are no other putative d–d transitions observed above 7000 cm^{-1}, this would suggest that the ligand field splitting in Rieske proteins is not significantly larger than in plant-type ferredoxins. (ii) MO calculations applying density functional theory on the structure of the cluster of the water-soluble fragment of the bovine Rieske protein indicate that the ligand field of the Fe^{II} is more symmetric in Rieske proteins than in plant-type ferredoxins, and the spin-allowed d–d transition should be below 7000 cm^{-1} (Grodzicki, M.; Link, T. A., manuscript in preparation). This issue will be discussed in the context of the interpretation of the EPR spectra.

In its reduced state, the paramagnetic Rieske cluster shows a temperature-dependent MCD spectrum composed of numerous positive and negative C-terms that originate from the $S = \frac{1}{2}$ ground state. The MCD spectra lack the $Fe^{II} \rightarrow S$ charge transfer bands that are observed as intense negative bands between 300 and 350 nm and a posi-

tive band around 275 nm in rubredoxins, as well as in proteins containing 4-Cys-coordinated [2Fe–2S] clusters (*61*). These transitions should be shifted to higher energy (lower wavelength) in Rieske proteins where the Fe^{II} of the reduced cluster is coordinated by two histidine residues.

B. Mössbauer Spectroscopy

Fee *et al.* (*5*) have studied the ^{57}Fe-enriched Rieske protein from *T. thermophilus* (TRP) using Mössbauer spectroscopy. The oxidized (diamagnetic) TRP showed a temperature-independent four-line spectrum resulting from a superposition of two quadrupole doublets of equal intensity. The reduced (paramagnetic) protein displayed temperature- and field-dependent spectra that were "strikingly similar" to those reported for putidaredoxin from *Pseudomonas putida* containing a four-cysteine-coordinated [2Fe–2S] cluster (*72*). The major difference between TRP and putidaredoxin as well as other proteins containing a four-cysteine-coordinated [2Fe–2S] cluster is a more positive isomer shift δ of the Fe^{II} site of the reduced cluster (0.68 mm/s compared to 0.55–0.59 mm/s in four-cysteine-coordinated [2Fe–2S] clusters at 200 K), indicating coordination of a less electron donating ligand than cysteinate to the Fe^{II} site. An isomer shift similar to that in TRP was observed in putidamonoxin from *Pseudomonas putida* (*63*), which has a Rieske-type EPR spectrum (*64*), as well as in the Rieske-type ferredoxin from toluene 4-monooxygenase (T4MOC) (*64a*).

In TRP, the Fe^{III} site was shown to have a fairly isotropic A tensor, while the A tensor of the Fe^{II} site was quite anisotropic (*5*). The EFG tensor of the Fe^{II} site was axially symmetric around the x axis of the A tensor, and the largest component was positive both for the Rieske protein and for putidaredoxin. In contrast, in plant-type ferredoxins the A tensor is symmetric around the z axis and the largest component is negative. This field gradient is consistent with the Fe^{II} having an orbital ground state with d_{z^2} symmetry while the EFG tensor of both the Rieske protein and putidaredoxin suggests a $d_{x^2-y^2}$ ground state; however, an alternative explanation has been given by Bertrand and Gayda (*65*). This issue is discussed in Section IV,E,1 together with the interpretation of the EPR spectra.

In summary, the Mössbauer data presented by Fee *et al.* (*5*) gave the first conclusive evidence that Rieske clusters contain noncysteine ligands bound to the Fe^{II} site of a localized mixed valence cluster. In addition, strong similarities with [2Fe–2S] clusters in bacterial dioxy-

genases were noted that gave a strong indication for the existence of Rieske-type clusters in these systems.

C. Resonance Raman Spectroscopy

Resonance Raman (RR) spectroscopy provides information about the vibrational characteristics of a chromophore, for example, a metal center, within the complex environment of a protein. In RR spectra, those vibrational transitions are observed selectively that are coupled to electronic transitions. In iron sulfur proteins, this technique has been used to resolve the complex electronic absorption spectra and to identify both vibrational and electronic transitions.

RR spectra of the Rieske protein from *T. thermophilus* (TRP) and of phthalate dioxygenase from *Burkholderia cepacia* (PDO) have been reported by Kuila *et al.* (*66*, *67*), and those of the Rieske protein from *Sulfolobus* sp. strain 7 tentatively called "sulredoxin" by Iwasaki *et al.* (*68*). Although no complete analysis is yet available, several conclusions can be drawn from these spectra, in comparison to the spectra of proteins containing a 4-cysteine coordinated [2Fe–2S] cluster (Table VI).

In oxidized Rieske proteins, a larger number of peaks are observed that have been attributed to vibrations of the iron–sulfur core; this is indicative of the reduced symmetry of the iron–sulfur core in Rieske proteins since *ungerade* vibrations are Raman-inactive in the centrosymmetric (in first approximation) [2Fe–2S]-Cys_4 core (point group D_{2h} or C_{2h}) while the corresponding modes are Raman-active in C_{2v} symmetry. The characteristic peak of the B_{3u}^t mode of proteins con-

TABLE VI

Selected Resonance Raman Modes of Rieske Proteins and of Proteins Containing a [2Fe-2S]-Cys_4 Cluster[a]

Mode (D_{2h} symmetry)	Oxidized cluster		Reduced cluster		Mode (C_{2v} symmetry)
	[2Fe-2S]-Cys_4	Rieske	[2Fe-2S]-Cys_4	Rieske	
Symmetry	D_{2h}		C_{2v}		Symmetry
B_{3u}^t	283–291 cm^{-1}	—	263–273 cm^{-1}	—	A_1^t
A_g^t	329–338 cm^{-1}	?	307–314 cm^{-1}	299–300 cm^{-1}	A_1^t
B_{1u}^t	350–357 cm^{-1}	357–360 cm^{-1}	319–328 cm^{-1}	316–321 cm^{-1}	B_2^t
A_g^b	387–400 cm^{-1}	382–396 cm^{-1}	370–385 cm^{-1}	373–380 cm^{-1}	A_1^b

[a] Assignments for [2Fe–2S]-Cys_4 clusters were taken from Han *et al.* (*128*), those for oxidized Rieske clusters from Kuila *et al.* (*67*). Symmetry labels refer to idealized cluster cores.

taining a 4-cysteine coordinated [2Fe–2S] cluster around 291 cm^{-1} is absent in oxidized Rieske proteins; this normal mode is the asymmetric combination of the breathing motions of the terminal (^{t}) sulfurs that cannot occur in Rieske proteins where one iron atom is coordinated by histidine residues. Rieske proteins show a (weak) peak at 266–270 cm^{-1} that is not observed in proteins containing a 4-cysteine coordinated [2Fe–2S] cluster; this peak has a unique excitation profile when compared to the other Raman peaks and has been tentatively assigned to a Fe^{III}–N(His) stretching mode. This peak is upshifted 8 cm^{-1} at alkaline pH values, which is consistent with the suggested deprotonation of histidine at elevated pH values.

A peak at 357–360 cm^{-1} in oxidized Rieske proteins has been assigned to a B_2^t mode (*67*); this mode corresponds to the B_{1u}^t mode in proteins containing a 4-cysteine coordinated [2Fe–2S] cluster that is predominantly Fe^{III}–S^t stretching and that is observed at 350–357 cm^{-1}. The similarity is an indication that the Fe^{III} site is structurally very similar in Rieske proteins and in proteins containing a 4-cysteine coordinated [2Fe–2S] cluster; the upshift in the frequencies of the Fe^{III}–S^t stretching mode in Rieske proteins could be explained either by different hydrogen bonding interactions or by differences in the Fe–Sγ–Cβ–Cα dihedral angles. Higher frequencies of the $B_2^t(B_{1u}^t)$ mode correspond to increased coupling between the Fe^{III}–S^t stretching and the S^t–Cβ–Cα bending modes that occurs when the dihedral angle is close to 180°, whereas lower frequencies correspond to angles closer to 90°. In the X-ray structure of the bovine Rieske fragment, the dihedral angles are 172° and 151° for Cys 139 and Cys 158, respectively, whereas the dihedral angles in the high-resolution structure of the [2Fe–2S] ferredoxin from the alga *Chlorella fusca* (PDB file 1AWD) (*70*) and from *Equisetum* (horsetail, PDB file 1FRR) (*71*) are close to 120°. This suggests that the differences observed in the $B_2^t(B_{1u}^t)$ modes correlate with the variation of the dihedral angles of the coordinating cysteine residues.

In the reduced [2Fe–2S]–Cys_4 cluster, the B_2^t mode is observed at 319–328 cm^{-1}; this peak is the only strong peak upon excitation below 450 nm (*61*). In the reduced bovine Rieske fragment (ISFb), two intense peaks are observed at 321 and 341 cm^{-1} upon excitation below 450 nm (Link, T. A.; Crouse, B. R.; Johnson, M. K., unpublished results). The difference observed in the excitation profiles indicates that S–Fe^{III} ligand-to-metal charge transfer bands are blue-shifted to higher energies in Rieske clusters compared to [2Fe–2S]–Cys_4 clusters.

Upon excitation of the reduced Rieske cluster above 500 nm, in-

tense peaks are observed at 299–300 and 373–380 cm^{-1}. These spectra are remarkably similar to those reported for reduced proteins containing a 4-cysteine coordinated [2Fe–2S] cluster upon excitation above 500 nm (*61*) with the exception of the absence of the peak of the A_1^t mode (in C_{2v} symmetry) corresponding to the B_{3u}^t mode (in D_{2h} symmetry) of the [2Fe–2S]–Cys_4 cluster. The peaks observed at 299–300 and 373–380 cm^{-1} correspond to A_1^t and A_1^b modes (^{b}, involving the bridging sulfurs), respectively, which are observed at 307–314 and 370–385 cm^{-1} in reduced 4-cysteine coordinated [2Fe–2S] clusters (*61*).

In general, the resonance Raman spectra reveal strong structural similarity of the Fe^{III} site in Rieske proteins and in proteins containing a 4-cysteine coordinated [2Fe–2S] cluster, while additional modes are observed for vibrations involving the Fe^{II} site and the histidine ligands.

D. X-Ray Absorption Spectroscopy

X-ray absorption spectroscopy has been performed on the isolated Rieske protein from bovine heart mitochondrial bc_1 complex (*69*) as well as on the Rieske-type cluster in *Burkholderia cepacia* phthalate dioxygenase (PDO) (*72*). The analysis performed by Powers *et al.* (*69*) was significantly hampered by the fact that the presence of two histidine ligands was not fully recognized; therefore, only the results obtained with the dioxygenase where the mononuclear iron has been depleted will be considered here. Table VII gives a comparison of the distances obtained from the fit of the EXAFS spectra assuming an idealized Rieske model and of the distances in the crystal structures

TABLE VII

Comparison of the Distances within the Rieske Cluster Obtained from EXAFS Measurements (*72*) and from X-Ray Crystallography

Cluster	Oxidized	Reduced		
Distance[a]	EXAFS (*72*)	EXAFS (*72*)	1RIE (*9*)	1RFS (*10*)
Fe1–Fe2	2.68 ± 0.03 Å	2.68 ± 0.03 Å	2.71 Å	2.72 Å
Fe–S^b	2.20 Å	2.25 Å	2.24 Å	2.32 Å
Fe1–S^t	2.32 Å	2.31 Å	2.26 Å	2.28 Å
Fe2–Nδ	2.05 ± 0.04 Å	2.09 ± 0.04 Å	2.15 Å	2.21 Å

[a] S^b, bridging sulfurs (average distances); S^t, terminal sulfurs (cysteine Sγ, average distances); Nδ, coordinating imidazoles (average distances).

of the water-soluble Rieske fragments from bovine heart (PDB file 1RIE, 1.5 Å resolution) and spinach (1RFS, 1.8 Å resolution). Considering the error margins and the fact that the EXAFS data can only give convoluted distances, there is excellent agreement between these data; they show that the [2Fe–2S] core is structurally very similar to that found in proteins containing a 4-cysteine coordinated [2Fe–2S] cluster or in model compounds. The EXAFS data indicate a contraction of the [2Fe–2S] cluster upon oxidation; unfortunately, no high-resolution structure of an oxidized Rieske cluster is yet available.

From an analysis of the intensity of the 1*s*–3*d* pre-edge transition in the XANES spectra, Tsang *et al.* (*72*) have suggested that the histidine-coordinated Fe^{II} of the reduced cluster may be 5-coordinated; this is not supported by the X-ray structures.

E. Magnetic Spectroscopy

1. EPR Spectroscopy

The nonheme iron protein of the cytochrome bc_1 complex has been discovered through its unique EPR properties, that is, the "g = 1.90 EPR signal" (*1*). The average g value g_{av} of Rieske proteins (1.90–1.91) is well outside the range observed for other binuclear iron sulfur proteins (1.945–1.975) (*4*). Since substitution of sulfur by selenium (which is a more electron-donating ligand than sulfur) causes an increase in g_{av}, the decreased g_{av} of Rieske proteins compared to plant-type ferredoxins prompted Blumberg and Peisach (*4*) to suggest that "the chemical makeup . . . must include one or more atoms which are less electron donating than sulfur."

a. Theoretical Models. The g values in antiferromagnetically coupled [2Fe–2S] clusters with an effective spin $S = \frac{1}{2}$ are given by

$$g_i = \tfrac{7}{3} g_i(\mathrm{Fe^{III}}) - \tfrac{4}{3} g_i(\mathrm{Fe^{II}}) \, (i = x, y, z), \tag{1}$$

assuming parallel g tensors (*73*). The g tensor around the Fe^{III} site with almost ideal tetrahedral geometry is nearly isotropic ($g_{x,y,z} \approx 2.02$) so that the effective g values of the whole cluster are determined by the g tensor around the Fe^{II} site. The g tensor around the Fe^{II} site depends on the energy splitting and rotational relationship of the d orbitals and can be described by

$$g_i = g_e + \frac{n_i \lambda}{\Delta E_i}, \tag{2}$$

with g_e being the free electron g value (2.00232), λ the spin–orbit coupling constant (-105 cm^{-1} for the free Fe^{2+} ion), $n_i = 2 \times \langle$rotation matrix element$\rangle^2$, where the rotation matrix describes the rotations relating the ground-state orbital to higher energy d orbitals by rotations around the three axes $i = (x, y, z)$, and ΔE_i being the energy differences between these d orbitals. Bertrand *et al.* (*60*) have developed a model where they can explain both the differences between [2Fe–2S] clusters belonging to the "$g_{av} = 1.96$ class" and Rieske-type clusters and the variation within both groups. In this model, the ligand field at the Fe^{II} site is strongly compressed in Rieske-type clusters so that the ligand field splitting between the ground state and the highest energy state is increased compared to [2Fe–2S] clusters belonging to the "$g_{av} = 1.96$ class." The model is compatible both with a d_{z^2} ground state (highest energy orbital d_{xz}) and with a $d_{x^2-y^2}$ ground state (highest energy orbital d_{xy}). In both cases, the energy difference between the ground state and highest energy state (ΔE_{xz} or ΔE_{xy}, respectively), must be significantly greater than 10,000 cm^{-1} in order to explain the observed g values. Because of the compression, the energy differences between the ground state and the lower excited states (ΔE_{xy} and ΔE_{yz} in the case of the d_{z^2} ground state, ΔE_{xz} and ΔE_{yz} in the case of the $d_{x^2-y^2}$ ground state), are small, which then leads to low g values along two of the three axes in Rieske clusters.

The transition between the ground state and the highest energy state is magnetically allowed both for a d_{z^2} and a $d_{x^2-y^2}$ ground state and should be observable in CD spectroscopy. Therefore, Link *et al.* (*55*) have suggested that the strong negative CD band of the reduced protein at 20,000 cm^{-1} should correspond to this transition. However, this interpretation is not consistent with molecular orbital (MO) calculations (Grodzicki, M.; Link, T. A., manuscript in preparation) since an energy difference ΔE_{xz} or $\Delta E_{xy,}$ respectively, of 20,000 cm^{-1} is incompatible with a four-coordinate Fe^{II} site. The MO calculations indicate a smaller splitting of the t_{2g} set of d orbitals in Rieske proteins compared to plant-type ferredoxins and a $d_{x^2-y^2}$ ground state as well as a positive EFG tensor, which is consistent with the results of the Mössbauer experiments.

The existence of the $d_{x^2-y^2}$ ground state, which is well founded on both experiment and theory, suggests a different model to account for the observed EPR parameters. The general theoretical model for [2Fe–2S] ferredoxins developed by Bertrand and Gayda (*65*) involves mixing between the d_{z^2} and $d_{x^2-y^2}$ orbitals in the ground state φ_0, which is described by a mixing angle θ:

$$\varphi_0 = \cos\theta\,|z_2\rangle + \sin\theta\,|x^2 - y^2\rangle. \qquad (3)$$

A value of $\theta = 0°$ corresponds to a pure d_{z^2} ground state, and $\theta = 90°$ to a pure $d_{x^2-y^2}$ ground state. Since the d orbital rotation matrix elements are different for the d_{z^2} and $d_{x^2-y^2}$ orbitals, this will lead to a variation of the local g tensor of the Fe^{II} site with the mixing angle θ:

$$g_x(Fe^{II}) = g_e - \frac{8\lambda}{\Delta E_{yz}} \sin^2\left(\theta + \frac{\pi}{3}\right) \tag{4a}$$

$$g_y(Fe^{II}) = g_e - \frac{8\lambda}{\Delta E_{xz}} \sin^2\left(\theta + \frac{\pi}{3}\right) \tag{4b}$$

$$g_z(Fe^{II}) = g_e - \frac{8\lambda}{\Delta E_{xy}} \sin^2(\theta). \tag{4c}$$

By applying the values obtained in MO calculations using the core structures of the ISFb (Grodzicki, M.; Link, T. A., manuscript in preparation), $\Delta E_{yz} \approx 3200\ cm^{-1}$, $\Delta E_{xy} \approx 5400\ cm^{-1}$, $\Delta E_{xz} \approx 6800\ cm^{-1}$, to the model, we find that at $\theta = 90°$ ($d_{x^2-y^2}$ ground state), $g_z < g_x < g_y$ with $g_{av} \approx 1.94$. However, the g values depend critically upon the mixing between $d_{x^2-y^2}$ and d_{z^2}; when some d_{z^2} character is mixed into the ground state, the order is reversed so that $g_x < g_z < g_y$ with $g_{av} < 1.92$. In this situation, g_x and g_z show opposite behavior upon variation of θ: g_z will increase with decreasing g_x and vice versa. This model predicts that g_x should be oriented along the Fe–Fe axis; this is consistent with conclusions drawn from studies on oriented membranes (W. Nitschke, this volume). However, the details of the model have yet to be worked out.

b. EPR Spectra. Within the group of Rieske proteins, the EPR g values vary considerably; Table VIII gives a compilation of published g tensors. The values of g_z vary between 2.008 and 2.042, of g_y between 1.888 and 1.92, and of g_x between 1.72 and 1.834; the calculated average g value g_{av} varies between 1.883 and 1.921. The rhombicity of the spectra can be calculated as

$$300(g_y - g_x)/(2g_z - g_y - g_x)[\%] \tag{5a}$$

when g_z is the unique g value (R_z), or as

$$300(g_y - g_z)/(2g_x - g_y - g_z)[\%] \tag{5b}$$

TABLE VIII

g Values and Calculated Rhombicity of Rieske and Rieske-Type Clusters

Protein	Species	g_z	g_y	g_x	g_{av}	R_z (%)	R_x (%)	Reference
Isolated Rieske proteins								
ISF (ISP)	beef	2.029	1.896	1.761	1.897	101	99	*30*
ISF	yeast	2.030	1.903	1.760	1.900	108	92	Merbitz-Zahradnik, T.; Link, T. A., unpublished
ISF	*P. denitrificans*	2.033	1.901	1.770	1.903	99	101	Merbitz-Zahradnik, T.; Link, T. A., unpublished
ISF	*P. denitrificans*	2.021	1.890	1.758	1.892	101	99	*89*
ISP	*N. crassa*	2.031	1.900	1.752	1.894	108	92	cf. Ding *et al.* (*79*)
ISF	spinach	2.03	1.90	1.74	1.89	114	87	*31*
ISP	*T. thermophilus*	2.033	1.908	1.807	1.917	86	115	*129*
ISP	*T. thermophilus*	2.023	1.906	1.78	1.905	105	95	*82*
SoxL	*Sulfolobus acidocaldarius*	2.035	1.895	1.768	1.901	94	107	*130*
SoxF	*Sulfolobus acidocaldarius*	2.042	1.895	1.785	1.909	82	120	*111*
ISP	*Nostoc*	2.03	1.89	1.74	1.89	105	95	*110*
Isolated *bc* complexes								
bc_1 complex	beef (asc.)	2.019	1.891	1.805	1.906	75	128	*131*
bc_1 complex	beef (dith.)	2.024	1.895	1.775	1.900	95	105	*131*
bc_1 complex	beef (Q_2H_2)	2.023	1.90	1.76	1.90	109	92	*80*
bc_1 complex	beef + EFA	2.017	1.90	1.80	1.91	90	111	*80*
bc_1 complex	yeast (asc.)	2.025	1.89	1.81	1.91	69	137	*75*
bc_1 complex	yeast (dith.)	2.026	1.89	1.79	1.904	81	121	*75*
bc_1 complex	yeast (dith.)	2.028	1.902	1.760	1.899	108	93	Merbitz-Zahradnik, T.; Link, T. A., unpublished
bc_1 complex	*P. denitrificans* (asc.)	2.021	1.888	1.797	1.903	76	127	*89*
bc_1 complex	*P. denitrificans* (dith.)	2.03	1.898	1.76	1.898	103	97	*131a*
bc_1 complex	*R. capsulatus*	2.019	1.893	1.762	1.893	103	97	cf. Ding *et al.* (*79*)
bc_1 complex	*R. sphaeroides* (asc.)	2.03	1.90	1.81	1.915	77	126	*132*
bc_1 complex	*R. sphaeroides* (dith.)	2.029	1.90	1.76	1.898	106	95	*132*
bc complex	*H. chlorum* (asc.)	2.035	1.89	1.81	1.91	65	143	*133*
bc complex	*B. firmus* (asc.)	2.028	1.90	1.832	1.921	63	145	*100*
bc complex	*B. firmus* (dith.)	2.03	1.90	1.823	1.919	69	137	*100*
b_6f complex	spinach (dith.)	2.03	1.90	1.76	1.90	105	95	*134*
Rieske-type ferredoxins								
Fd_{BED}	*Ps. putida*	2.026	1.890	1.834	1.918	51	165	*135*
T4MOC	*Ps. mendocina*	2.009	1.897	1.76	1.897	138	68	*64a*
BphF	*B. cepacia*	2.02	1.92	1.82	1.92	100	100	*135a*
Oxygenases								
Pyrazon DO	?	2.02	1.91	1.79	1.91	106	94	*136*
Putidamonooxin	*Ps. putida*	2.008	1.913	1.72	1.883	151	59	*64*
Benzene DO	*Ps. putida*	2.018	1.917	1.754	1.898	134	71	*135*
Phthalate DO	*B. cepacia*[a]	2.016	1.914	1.763	1.900	128	76	*82*
Naphthalene DO	*B. cepacia*[a]	2.01	1.91	1.80	1.91	106	94	*137*
2-Halobenzoate-1,2-DO	*B. cepacia*[a]	2.025	1.91	1.79	1.91	103	97	*86*
2-Oxo-1,2-dihydroquinoline 8-MO	*Ps. putida*[a]	2.01	1.91	1.76	1.895	129	75	*104*
Trichlorophenoxyacetate-MO	*B. cepacia*[a]	2.01	1.91	1.76	1.895	129	75	*86a*
CMP-*N*-acetylneuraminic acid hydroxylase	pig	2.01	1.91	1.78	1.90	118	83	*22*
Alkene MO	*Xanthobacter*	2.016	1.918	1.776	1.905	126	77	*106*
Choline MO	spinach	2.008	1.915	1.736	1.889	147	62	*21*

ISF, water soluble fragment of the Rieske protein; ISP, isolated Rieske protein; DO, dioxygenase; MO, monooxygenase; EFA, ethoxyformic anhydride. For the isolated *bc* complexes, the reducing agent is given in parentheses: asc., ascorbate; dith. sodium dithionite; Q_2H_2, ubihydroquinone-2. The rhombicity along the z axis R_z was calculated as $300(g_y - g_x)/(2g_z - g_y - g_x)$ [%], the rhombicity R_x along the x axis as $300(g_y - g_z)/(2g_x - g_y - g_z)$ [%].

[a] *Burkholderia cepacia* has formerly been known as *Pseudomonas cepacia.*

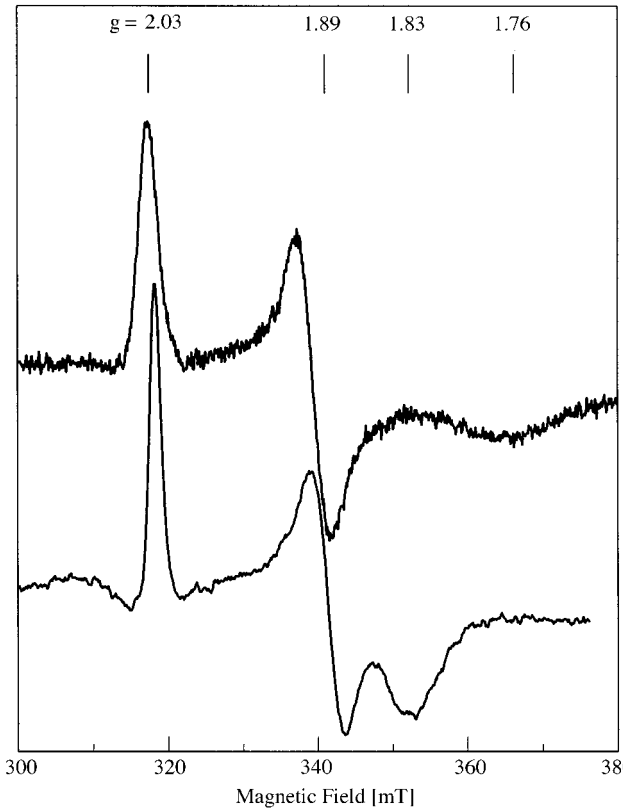

FIG. 12. EPR spectra of the Rieske fragment from the bc_1 complex of *Paracoccus denitrificans* (ISFpd, top) and of the Rieske-type ferredoxin from benzene dioxygenase (Fd_{BED}, bottom). EPR conditions were as follows (ISF/Fd_{BED}): microwave frequency, 9.021 GHz; modulation amplitude, 1 mT/0.9 mT; microwave power, 1 mW/9 mW; temperature, 15 K/30 K.

when g_x is the unique g value (R_x). For a completely rhombic g tensor, the value of both R_z and R_x will be 100%. Values of $R_z > 100\%$ correspond to R_x values $<100\%$ and vice versa; therefore, when R_z goes from $<100\%$ to $>100\%$, the unique axis changes from z to x. The rhombicity is sensitive to the ligand field splitting and therefore also to the geometry around the Fe^{II} site (*4*).

The rhombicity calculated for the Rieske proteins compiled in Table VIII varies from 51% along the z axis over 100% to 59% along the x axis; Fig. 12 shows the EPR spectra of the protein showing the lowest

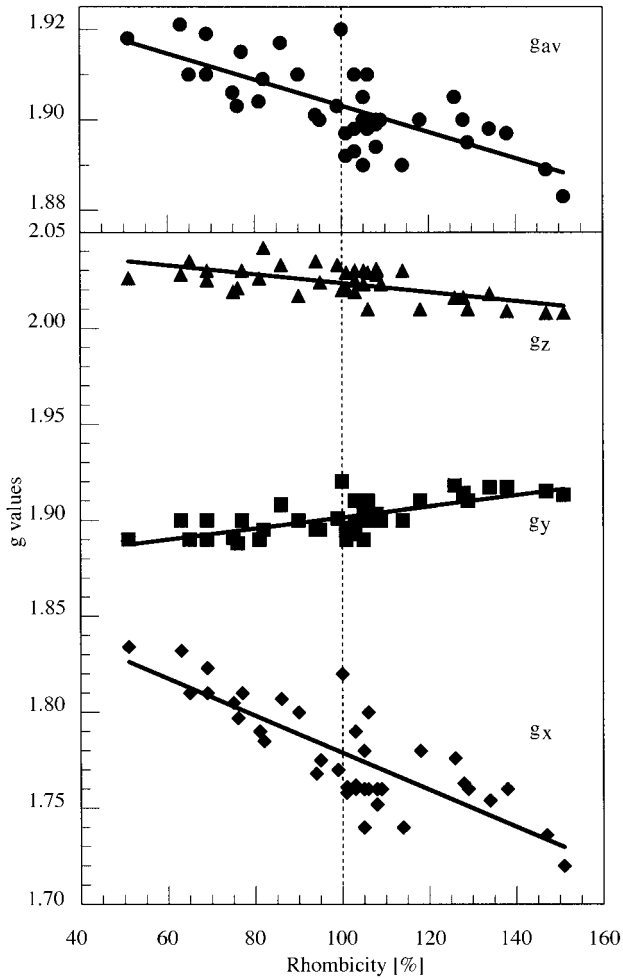

FIG. 13. Plot of the g values (g_x, g_y, g_z) and of the average g value g_{av} vs rhombicity (R_z) of the Rieske and Rieske-type proteins listed in Table VIII. The lines represent linear fits to the data points.

rhombicity, the Rieske-type ferredoxin from benzene dioxygenase (Fd_{BED}, R_z = 51%), and the rhombic EPR spectrum of the ISF ($R_z \approx R_x \approx 100\%$). In contrast to proteins having a 4-cysteine coordinated [2Fe–2S] cluster (*4*), Rieske and Rieske-type protein show a strong correlation between the three g values and the calculated rhombicity. In Fig. 13, the average g value g_{av} as well as the three g values g_z, g_y,

and g_x are plotted against the rhombicity (in order to avoid confusion about the axis change, the rhombicity along the z axis R_z is used over the whole range; values $> 100\%$ correspond to a rhombicity of approximately $200\% - R_z$ along the x axis). g_{av}, g_z, and g_x decrease with increasing R_z while g_y increases with increasing R_z. The scatter in the data points is at least in part due to the difficulty of determining the exact value of g_x that gives a broad feature in the EPR spectra of most Rieske and Rieske-type proteins.

The fact that all components of the g tensor correlate with the single parameter rhombicity identifies that as a good parameter for the description of the EPR spectra of Rieske and Rieske-type proteins and therefore of the ligand field around the Fe^{II} site having histidine coordination. This situation is clearly different from that observed in proteins having a 4-cysteine coordinated [2Fe–2S] cluster (*4*). The fact that the variation of the EPR properties is controlled only by the ligand environment of the Fe^{II} site is consistent with the resonance Raman spectra discussed previously, which show that the Fe^{II} site is very similar in all Rieske proteins. It also reflects the close similarity of the protein environment around the [2Fe–2S] cluster in all members of the protein family so that the ligand field of Fe^{II} site and the electron distribution are controlled by subtle changes, including hydrogen bonds into the [2Fe–2S] cluster.

The effect of hydrogen bonds has been studied in the Rieske protein of the bc_1 complex; this was possible because two of the eight hydrogen bonds formed with sulfur atoms of the cluster are derived from side chains (see Section III,B). The highly conserved Ser 163 forms a OH–S hydrogen bond to the bridging sulfur S-1, and Tyr 165 forms a hydrogen bond to the Sγ of Cys 139 that is a ligand of the 4-sulfur coordinated Fe-1 (*9*). We have replaced these residues both in yeast and in *Paracoccus denitrificans* by residues that are unable to form OH–S hydrogen bonds (*35*, *36*). These replacements had effects both on the redox potential (discussed in Section V) and on the EPR spectra of the Rieske cluster while the structural integrity of the protein and of the cluster was maintained. The EPR g values of the variants fall close to the line correlating the g values with rhombicity (Fig. 14a); the effect of the removal of a hydrogen bond can be described by a decrease of the rhombicity compared to the wild-type enzyme. This is consistent with the fact that very low values are calculated for the rhombicity of Rieske proteins in menaquinone-utilizing bacteria (e.g., *Heliobacter* or *Bacilli*) where the residue corresponding to Ser 163 is replaced by alanine, which cannot form the OH–S hydrogen bond (*16*).

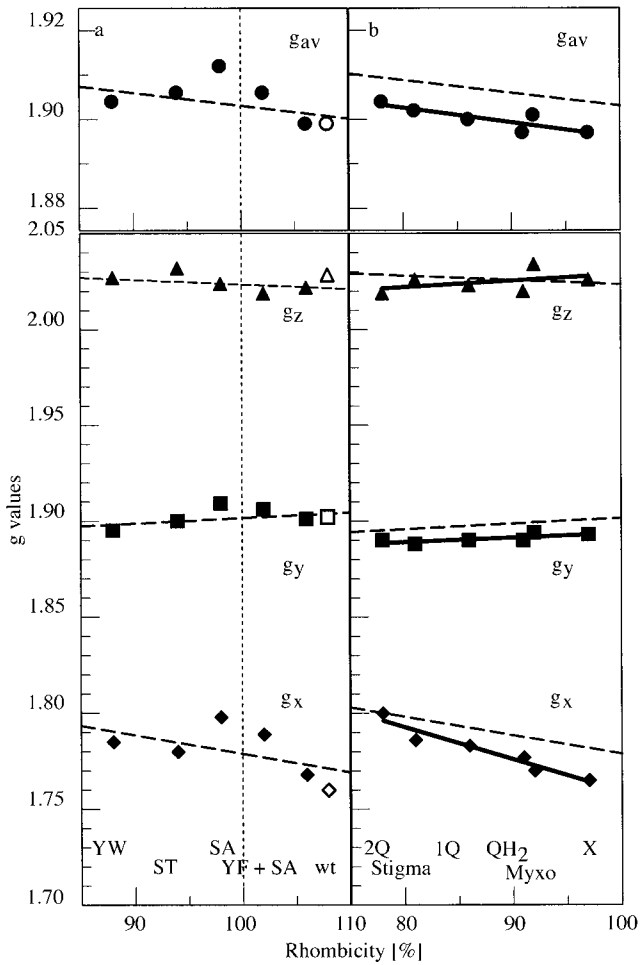

FIG. 14. Plot of the g values (g_x, g_y, g_z) and of the average g value g_{av} vs rhombicity (R_z) of (a) wild type (open symbol) and variant forms (closed symbols) of the Rieske protein in yeast bc_1 complex where the residues Ser 183 and Tyr 185 forming hydrogen bonds into the cluster have been replaced by site-directed mutagenesis [Denke *et al.* (*35*); Merbitz-Zahradnik, T.; Link, T. A., manuscript in preparation] and of (b) the Rieske cluster in membranes of *Rhodobacter capsulatus* in different redox states of the quinone pool and with inhibitors added [data from Ding *et al.* (*79*)]. The solid lines represent linear fits to the data points; the dashed lines reproduce the fits to the g values of all Rieske and Rieske-type proteins shown in Fig. 13.

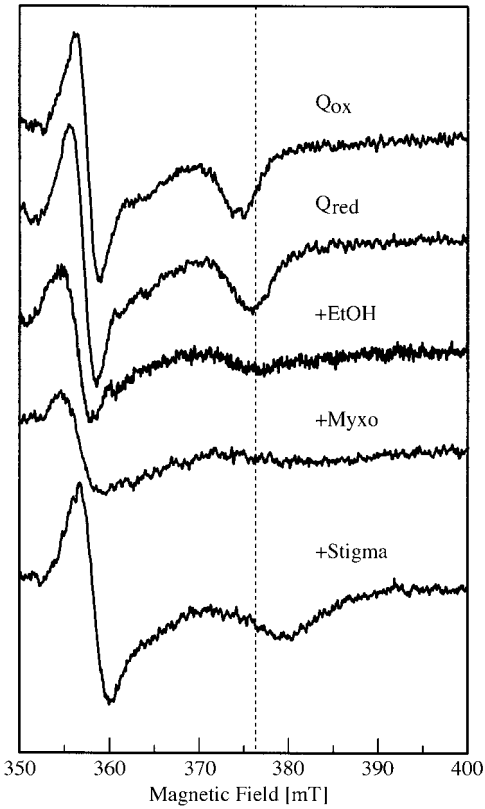

FIG. 15. EPR spectra of the Rieske cluster in membranes of *Paracoccus denitrificans* in different redox states of the quinone pool and with inhibitors added. Q_{ox}, ascorbate reduced; Q_{red}, reduced with trimethylhydroquinone dissolved in dimethyl sulfoxide; +EtOH, reduced with trimethylhydroquinone dissolved in 90% ethanol; +Myxo, ascorbate reduced with myxothiazol added; +Stigma, ascorbate reduced with stigmatellin added. Only the g_y and g_x signals are shown. The dotted line has been drawn at $g = 1.80$.

In *bc* complexes, the EPR signal of the Rieske cluster was found to be heterogenous (*74*); it varies with the redox state of the system, in particular of the quinone pool (cf. Table VIII) (*75*, *76*). Binding of quinonoid inhibitors such as stigmatellin leads to a significant shift and a sharpening of the signals (*77*). Figure 15 shows the effect of the oxidation or reduction of the quinone pool as well as the effect of addition of inhibitors on the Rieske cluster in membranes from *Paracoccus*

denitrificans (*36*). Addition to short-chain alcohols also has an effect on the shape of the EPR signal (*78*).

The effect of quinones on the EPR signal of the Rieske cluster has been systematically explored in membranes from *Rhodobacter capsulatus* (*79*). From the changes of the EPR lineshape, Ding *et al.* (*79*) have concluded that two molecules of quinone can bind simultaneously to the Rieske cluster, but this issue is still controversial. When the g values for the different states ("empty," 1/2 hydroquinone (QH_2) bound, 1 quinone (Q) bound, 2 Q bound, and in the presence of either stigmatellin or myxothiazol) are plotted against the calculated rhombicity, the points all fall close to the line describing the relationship of the g values vs rhombicity for the whole family (Fig. 14b). This shows that also the effect of the binding of quinones or inhibitors to the histidine ligands of the [2Fe–2S] cluster in membranes of *Rhodobacter capsulatus* can be adequately described as a change of the rhombicity of the cluster in the order of the states assigned as free (X bound) > myxothiazol bound ≈ QH_2 bound > 1 Q bound > stigmatellin bound > 2 Q bound.

Treatment of bovine heart bc_1 complex with ethoxyformic anhydride (EFA), which is known to modify amino acid residues covalently (preferentially histidine residues), inhibits electron transfer and has an effect on the EPR spectra of the Rieske cluster comparable to that observed upon addition of stigmatellin, that is, a decrease in rhombicity (*80*). This further supports the suggestion that quinones as well as quinonoid inhibitors interact directly with the histidine ligands of the Rieske cluster.

A completely different effect is observed when chloroplast b_6f complex is incubated with the inhibitor dibromothymoquinone (DBMIB), leading to a shift of the EPR signal to $g_{av} = 1.95$; this effect is reversed by inhibitors such as undecylhydroxybenzothiazol (UHDBT), which bind more strongly than DBMIB (*81*). The addition of DBMIB does not alter the magnetic couplings of the nitrogen ligands (*8*); this indicates that histidine ligation alone is not sufficient to explain the EPR spectra with $g_{av} = 1.91$ observed in Rieske proteins. A similar shift of the EPR signal to g values of 2.008, 1.95, and 1.91 has been observed in bovine heart bc_1 complex, although at higher DBMIB concentrations (Link, T. A., unpublished results).

2. ENDOR and ESEEM Spectroscopy

Nitrogen coordination of the Rieske cluster had been suggested by Blumberg and Peisach (*4*) as early as 1974. However, it was only after the pioneering Mössbauer studies of Fee *et al.* (*5*) that the coordina-

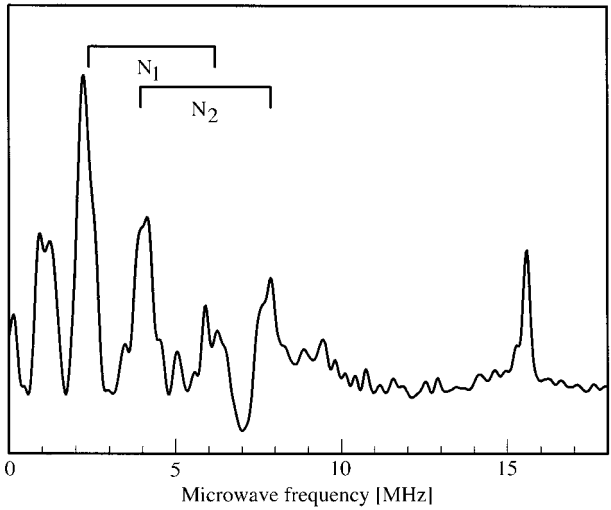

FIG. 16. Three-pulse ESEEM spectrum of the Rieske cluster in bovine heart submitochondrial particles at $g_y = 1.89$ and 3.7 K. The pairs of transitions belonging to the two nitrogen atoms are indicated. Conditions of measurement are as stated in (*87*).

tion environment was studied directly using ENDOR and ESEEM spectroscopy. Cline *et al.* (*82*) reported X-band ENDOR and ESEEM spectra of the Rieske protein from *Thermus thermophilus* (TRP) and of the Rieske-type cluster in phthalate dioxygenase from *Burkholderia cepacia* (PDO). The ENDOR signals were erroneously interpreted as arising from a strongly coupled ligand with a ^{14}N hyperfine coupling constant $A^N \approx 26–28$ MHz and a weakly coupled ligand with $A^N \approx 9$ MHz; the ESEEM spectra revealed several peaks between 0.8 and 6.7 MHz. Very similar spectra have been observed for the Rieske protein in yeast bc_1 complex (*83*); this supported the conclusion that the [2Fe–2S] cluster is very similar in Rieske and Rieske-type proteins. Using Q-band ENDOR spectroscopy, Gurbiel *et al.* (*6*) could show that the higher frequency resonances attributed to strongly coupled nitrogens are in fact due to protons.

ENDOR and ESEEM studies of phthalate dioxygenase (PDO) (*7*, *84*), benzene dioxygenase (*85*), 2-halobenzoate 1,2-dioxygenase (*86*), 2,4,5-trichlorophenoxyacetate monooxygenase (*86a*), spinach b_6f complex (*8*), and the bc_1 complexes from *Rhodobacter capsulatus* (*7*, *84*) and in bovine mitochondrial membranes (*87*) (Fig. 16) have identified two nitrogen nuclei coupled to the [2Fe–2S] cluster with isotropic ^{14}N

TABLE IX

HYPERFINE COUPLING VALUES OF THE NITROGEN LIGANDS OF RIESKE AND RIESKE-TYPE CLUSTERS DETERMINED BY ENDOR AND ESEEM SPECTROSCOPY

Cluster[a]	Method	A (MHz)		e^2qQ (MHz)		Ref.
		N_1	N_2	N_1	N_2	
Rieske						
bc_1 (*R. caps.*)	ENDOR	4.5	5.5	—	—	*7*
b_6f (spinach)	ESEEM	3.8	4.6	2.5–2.9	2.5–2.9	*8*
bc_1 (bovine)	ESEEM	3.6	5.2	2.1–2.4	2.7–3.15	*87*
bc_1 (bovine) + UHDBT	ESEEM	3.4	5.3	2.3–2.65	2.6–3.0	*87*
Rieske-type						
PDO	ENDOR	4.3	5.5	2.3	2.6	*6*
BDO	ESEEM	3.6	4.8	2.2–2.8	2.2–2.4	*85*
Halobenzoate-DO	ESEEM	3.7	4.7	2.0–2.3	3.6–4.1	*86*
2,4,5-T-MO	ESEEM	4.0	4.9	2.0–2.8	1.9–2.7	*86a*

[a] PDO, phthalate dioxygenase; BDO, benzene dioxygenase; 2,4,5-T-MO, 2,4,5-trichlorophenoxyacetate monooxygenase; UHDBT, undecylhydroxybenzothiazole.

hyperfine coupling constants in the range of 3.4–4.5 MHz and 4.6–5.5 MHz, respectively, and quadrupolar coupling constants e^2qQ of 2–3 MHz (Table IX). Approximately 1.5–4% of the unpaired electron spin density resides on each of the nitrogen ligands of the cluster (*6*, *7*, *85*).

The hyperfine coupling values are consistent with coordination of the Rieske cluster by imidazole nitrogens. This conclusion was further supported by labeling with ^{15}N (nuclear spin $I = \frac{1}{2}$), both for PDO (*6*) and the bc_1 complex from *Rhodobacter capsulatus* (*7*). From the ENDOR spectra, the hyperfine coupling tensors for both nitrogen ligands and their orientation with respect to the g tensor could be determined; when an improved algorithm was used to analyze the spectra, the geometry was found to be essentially identical in the Rieske-type cluster in PDO and in the Rieske cluster of the bc_1 complex (*84*). In both systems, the nitrogen ligands lie in the g_1–g_3 plane. The "bite angle" N–Fe–N was 80° (or 100°) in the simulations; this compares to an angle of 90° observed in the X-ray structures.

No alteration of the nitrogen couplings was observed when spinach b_6f complex was treated with dibromothymoquinone (DBMIB) (*8*) or bovine mitochondrial membranes with undecylhydroxybenzothiazol (UHDBT) (*87*), although these inhibitors cause shifts in the EPR spectra of the Rieske cluster; therefore, the changes of the EPR spectra

TABLE X

^{1}H NMR Resonances of Reduced Rieske and Rieske-Type Proteins

Fd (*Xanthobacter* Py2) (400 MHz, 300 K) (*88*) chemical shift (ppm)	Fd (T4MOC) (400 MHz, 293 K) (*88a*) chemical shift (ppm)	ISF (*P. denitrificans*) (300 MHz, 284 K) (*89*) chemical shift (ppm)	H/D exchange	*T* dependence[a]	Assignment
82	82.7	≈109	−	Curie	Cys H^{β}
73	76.7	≈77	−	Curie	Cys H^{β}
62	61.1	≈69	−	Curie	Cys H^{β}
54	52.6	≈54	−	Curie	Cys H^{β}
23.9	25.5	≈26	−	Curie	His $H^{\varepsilon 1}$
−1.4			−	pseudo-Curie	
−2.4			−	pseudo-Curie	
−3.2			−	pseudo-Curie	
−5.4[b]	−6.6[b]	≈−7[b]	−	pseudo-Curie	
−11.4			+	?	peptidyl H^N?
−15.5[b]	−12.3[b]	≈−9[b]	+	pseudo-Curie	peptidyl H^N?
		≈−15	−	pseudo-Curie	
		≈−23	−	pseudo-Curie	

[a] Curie: Δ ppm/$\Delta T < 0$; pseudo-Curie: Δ ppm/$\Delta T > 0$.

[b] Since the signals have not yet been assigned, it is not clear whether they correlate with each other in the three proteins listed here.

represent an altered electron distribution, but no change in the coordination environment of the cluster.

3. NMR Spectroscopy

^{1}H NMR spectra have been reported for the Rieske-type ferredoxins from *Xanthobacter* strain Py2 (*88*) and of toluene 4-monooxygenase from *Pseudomonas mendocina* (T4MOC) (*88a*) as well as for the water-soluble Rieske fragment from the bc_1 complex of *Paracoccus denitrificans* (ISFpd) (*89*). The spectra of these proteins are similar, which is consistent with the close structural relationship between the three proteins. In the reduced (paramagnetic) state, all three proteins show several hyperfine-shifted ^{1}H resonances between +83 and −16 ppm at 400 MHz or between −110 and +25 ppm at 300 MHz (Table X).

Four strongly downshifted signals in each spectrum, between 50 and 110 ppm, were assigned to the four Cß protons of the cysteines coordinating the Fe^{III}. The contact shifts of the protons reflect the coordination of cysteine to the Fe^{III} of the antiferromagnetically coupled Fe^{III}–Fe^{II} pair as the cysteine protons sense the spin down orientation of the Fe^{III} ($S = \frac{5}{2}$) site. This is supported by the observation that the temperature dependence of the cysteine $H^{ß}$ protons (measured between 276 and 308 K) follows Curie behavior (decreasing contact shift with increasing temperature).

A sharp resonance around 25 ppm in all three proteins that had

been tentatively assigned to one of the two cysteine H^{α} protons based solely on analogy with plant-type ferredoxins has been shown by selective isotope labeling in T4MOC to arise from the histidine $H^{\varepsilon 1}$ proton of one of the histidine ligands (*88a*). This histidine $H^{\varepsilon 1}$ proton exhibited a weak Curie temperature dependence, whereas a pseudo-Curie temperature dependence (increasing contact shift with increasing temperature) would have been expected for a ligand bound to the Fe^{II} of the antiferromagnetically coupled Fe^{III}–Fe^{II} pair if a simple spin coupling model was valid. This shows that the NMR spectra of Rieske and Rieske-type proteins show unique properties when compared to ferredoxins having a 4-cysteine coordinated [2Fe–2S] cluster and rules out any assignment by simple analogy. In particular, this is the case for several upshifted ^1H resonances between -0.1 and -23 ppm showing pseudo-Curie temperature dependence that had been tentatively assigned to the histidine ligands. One or two of these resonances between -9 and -15.5 ppm have been shown to be solvent exchangable in D_2O buffer and have been thought to arise from $H^{\varepsilon 2}$ proton(s) of the $N^{\varepsilon}H$ groups of the imidazole ligands. However, in T4MOC the solvent exchange was very slow in the oxidized state (2 days at room temperature) while no measurable exchange was observed in the reduced state even after four weeks (*88a*). These results indicate a group donating a strong hydrogen bond to the Rieske cluster and a redox dependence of the hydrogen bond strength. The fact that exchange is slow also on the oxidized protein and that the number of exchangable protons differs between different proteins (two in the ferredoxin from *Xanthobacter*, one in T4MOC and the ISFpd) suggests that these ^1H resonances may be due to (a) peptidyl NH group(s) rather than histidine $H^{\varepsilon 2}$ proton(s) of the ligand(s).

The two iron ions of the Rieske cluster are antiferromagnetically coupled; therefore, the ground state has a spin $S = \frac{1}{2}$, while excited states of the spin ladder $S = \frac{3}{2}, \frac{7}{2}, \frac{5}{2}$, and $\frac{9}{2}$, are at energies $-3J$, $-8J$, $-15J$, and $-24J$ (J, exchange coupling constant). The fact that the temperature dependence did not strictly follow Curie behavior could be explained by the population of excited states at room temperature, indicating that the value of $-3J$ must be in the order of kT (around 200 cm^{-1} at room temperature). By fitting the temperature dependence of the resolved protons, Holtz *et al.* (*88*) determined the exchange coupling constant $-2J$ as 124 ± 26 cm^{-1}; this value compares to values of 100 ± 10 cm^{-1} and 190 ± 20 cm^{-1} determined for the TRP and for benzene dioxygenase, respectively, by EPR spectroscopy from the temperature dependence of the spin–lattice relaxation rate (*89a*). For proteins having a 4-cysteine coordinated [2Fe–2S] cluster, the ex-

TABLE XI

REDOX POTENTIALS OF RIESKE AND RIESKE-TYPE PROTEINS

Protein	Organism	Preparation[a]	E_m (mV)	Method[b]	pH	T (°C)	I (M)	Reference
Rieske proteins								
bc_1 complex	pigeon heart	M	+285	EPR	7.0	*	0.06	*138*
bc_1 complex	beef heart	C	+290	EPR	7.2	*	0.12	*77*
bc_1 complex	beef heart	C	+304	CD/OTTLE	7.0	9	0.1	*102*
bc_1 complex	beef heart	F	+312	CV	7.0	25	0.075	*92*
bc_1 complex	beef heart	F	+306	EPR	7.0	*	0.075	*30*
bc_1 complex	beef heart	F	+315	CD/OTTLE	7.0	9	0.1	*55*
bc_1 complex	yeast	M	+262	EPR	7.0	*	0.05	*34*
bc_1 complex	yeast	C	+286	EPR	7.4	*	0.25	*139*
bc_1 complex	yeast	C	+285	CD/OTTLE	7.0	5	0.12	*35*
bc_1 complex	yeast	F	+285	CV	7.0	25	0.1	Merbitz-Zahradnik, T.; Link, T. A., unpublished
bc_1 complex	*P. denitrificans*	C	+298	CD/OTTLE	7.0	20	0.4–0.5	*36*
bc_1 complex	*P. denitrificans*	F	+280	CV	7.0	25	0.1	*140*
bc_1 complex	*R. capsulatus*	M	+310	EPR	7.2	*	0.12	*141*
bc_1 complex	*R. capsulatus*	M	+321	EPR	7.0	*	0.13	*78*
bc_1 complex	*R. capsulatus*	M (+EtOH)	+294	EPR	7.0	*	0.13	*78*
bc_1 complex	*R. capsulatus*	F	+285	EPR	7.0	*	0.13	*52*
bc_1 complex	*R. sphaeroides*	M	+285	EPR	7.2	*	0.12	*141*
bc_1 complex	*R. sphaeroides*	M	+300	CD	7.0	21	0.1	*141a*
bc_1 complex	*R. sphaeroides*	C	+300	CD	7.0	21	0.1	*141a*
bc_1 complex	*Chromatium vinosum*	M	+285	EPR	8.0	*	0.05	*142*
bc_1 complex	*R. rubrum*	M	+265	EPR	7.7	*		[c]
b_6f complex	spinach	C	+320	EPR	<8.0	*	[d]	*99*
b_6f complex	spinach	F	+375	EPR	7.0	*	0.07	*31*
b_6f complex	spinach	F	+320	Abs	7.0	25	0.07	*31*
b_6f complex	*Nostoc*	R	+321	CD	7.0	25	0.13	*110*
bc complex	*Chlorobium limicola*	M	+160	EPR	7.0	*	0.1	*96*
bc complex (?)	*B. alcalophilus*	M	+150	EPR	7.0	*	0.115	*143*
bc complex	*Heliobacterium chlorum*	M	+120	EPR	7.0	*	0.05	*133*
bc complex	*Bacillus* PS3	M	+165	EPR	7.0	*	0.05	*98*
bc complex	*B. firmus*	M	+105	EPR	7.0	*	0.02	*100*
Rieske protein	*T. thermophilus*	P	+140	Abs	7.0			*129*
Rieske protein II (SoxF)	*S. acidocaldarius*[e]	P	+375	CD/OTTLE	7.5	25	0.025	*111*
Rieske-type proteins[f,g]								
Fd_{BED}	*Ps. putida*	P	−155	EPR	7.0	*	0.05	*135*
Fd_{BED}	*Ps. putida*	P	−156	CD/OTTLE	7.0	9	0.025	*55*
Fd_{BED}	*Ps. putida*	P	−155	CV	7.0	25	0.15	*55*
Benzene dioxygenase	*Ps. putida*	P[h]	−112	EPR	7.0	*	0.05	*135*
2-Halobenzoate 1,2-dioxygenase	*B. cepacia*[k]	P[i]	−125	EPR	7.0	*	0.025	*86*
2-Oxo-1,2-dihydroquinoline 8-monooxygenase	*B. cepacia*[k]	P[j]	−100	EPR	7.2	*	0.025	*104*

* The temperature is not well defined during an EPR monitored redox titration since the protein will reequilibrate with the mediators during freezing [cf. discussion in Hagedoorn *et al.* (*143a*)].

[a] Preparation: M, membranes; C, isolated complexes; P, isolated Rieske or Rieske-type proteins; F, isolated Rieske fragments; R, reconstituted proteins.

TABLE XI (*Continued*)

[b] Method: Abs, chemical reduction, monitored by absorption spectroscopy; CD, chemical reduction, monitored by CD spectroscopy; CD/OTTLE, electrochemical reduction using an optically transparent thin layer (OTTLE) cell, monitored by CD spectroscopy; CV, cyclic voltammetry; EPR, chemical reduction, monitored by EPR.

[c] Quoted in Malkin, R.; Bearden, A. J. *Biochim. Biophys. Acta* **1978,** *505,* 147, but the E_m value is not given in the reference referred to.

[d] Ammonium sulfate precipitate.

[e] Heterologous expression in *E. coli.*

[f] Putidamonooxin: A value of +5 mV at pH 7.8 has been quoted (Bernhardt, F.-H.; Ruf, H.-H.; Ehrig, H. *FEBS Lett.* **1974,** *43,* 53), but experimental details have not been reported.

[g] Phthalate dioxygenase (PDO): Conflicting values have been quoted [−60 mV at pH 6.9 in an absorption monitored titration performed at 10°C: Kuila and Fee (*129*); −120 mV at pH 7.0: Correll *et al.* (*119*)] but experimental details have not been reported.

[h] Isolated dioxygenase with $\alpha_2\beta_2$ subunit composition.

[i] Isolated dioxygenase with $\alpha_3\beta_3$ subunit composition.

[j] Isolated dioxygenase with α_6 subunit composition.

[k] *Burkholderia cepacia* has formerly been known as *Pseudomonas cepacia.*

change coupling constant in adrenal ferredoxin has been determined as 170 ± 10 cm^{-1} (*89a*) while a value of $-2J \leq 100$ cm^{-1} was measured in reduced spinach ferredoxin (*90*). This indicates that the magnitude of the exchange coupling constant is determined by the bridge between the two iron atoms and not by the nature of the terminal ligands (*89a*).

V. Electrochemistry

A. Rieske Clusters: Cytochrome *bc* Complexes

The second distinguishing feature of the Rieske protein apart from its unique EPR spectrum that was recognized early is its high redox potential (*91*). The redox potentials of Rieske clusters from mitochondrial and bacterial bc_1 complexes are in the range of +265 to +310 mV (Table XI); the potentials in b_6f complexes are even slightly higher (around +320 mV). The redox potentials of Rieske clusters in menahydroquinone oxidizing systems (e.g., *Bacilli*) are approximately 150 mV lower than those in ubihydroquinone-oxidizing bc_1 complexes; the potential difference between the Rieske clusters is the same as that between the two types of quinones (ubiquinone: +90 mV; menaquinone: −60 mV).

The lower redox potential in menaquinone-oxidizing *bc* complexes can be attributed to the absence of the hydrogen bond from the Oγ of Ser 163 (ISF)/Ser 130 (RFS) to the bridging sulfur S-1 (see Section III,B,2). This serine is completely conserved in Rieske proteins of bc_1 and b_6f complexes, but in all sequences of Rieske proteins from menaquinone-oxidizing *bc* complexes, alanine or glycine is found in

this position. When the serine present in the Rieske protein of the bc_1 complex was converted to alanine by site-directed mutagenesis in yeast (*35*) or in *Paracoccus denitrificans* (*36*), the redox potential of the Rieske cluster was decreased by 100–130 mV. The magnitude of the redox potential shift observed upon mutation of the serine is comparable to the redox potential difference between Rieske proteins from menaquinone-oxidizing complexes and Rieske proteins from bc_1 and b_6f complexes; therefore, it can be stated that the exchange of the single serine residue can fully account for the observed redox potential difference.

Various methods have been used to determine the redox potentials (Table XI). Very commonly, EPR-monitored chemical redox titration is performed, which can be used to measure the redox potential not only in isolated complexes but also in membrane preparations. In general, there is good agreement between redox potentials determined in membranes, isolated complexes, or isolated Rieske proteins or fragments; the only exception is the water-soluble Rieske fragment from spinach b_6f complex where differences of more than 50 mV have been observed by the same group but using different methods (*31*).

The use of direct electrochemical methods (cyclic voltammetry; Fig. 17) has enabled us to measure the thermodynamic parameters of isolated water-soluble fragments of the Rieske proteins of various bc_1 complexes (Table XII)). (*55*, *92*). The values determined for the standard reaction entropy, $\Delta S°$, for both the mitochondrial and the bacterial Rieske fragments are similar to values obtained for water-soluble cytochromes; they are more negative than values measured for other electron transfer proteins (*93*). Large negative values of $\Delta S°$ have been correlated with a less exposed metal site (*93*). However, this is opposite to what is observed in Rieske proteins, since the cluster appears to be less exposed in Rieske-type ferredoxins that show less negative values of $\Delta S°$ (see Section V,B).

Cyclic voltammetry has also allowed us to observe for the first time the second reduction step ($[Fe^{II}Fe^{III}–2S]$ to $[Fe^{II}Fe^{II}–2S]$) in a biological [2Fe–2S] cluster (*94*). This transition was observed at −840 mV, that is, approximately 1.1 V more negative than the first transition $[Fe^{III}Fe^{III}–2S]$ to $[Fe^{II}Fe^{III}–2S]$); this compares to a difference of approximately 0.7 V for two subsequent transitions in [4Fe–4S] clusters (*95*).

The most striking electrochemical feature of Rieske proteins is the pH dependence of the redox potential. This pH dependence has first been demonstrated for the Rieske protein from *Chlorobium,* where the redox potential shifted from +165 mV at pH 6.8 to +60 mV at

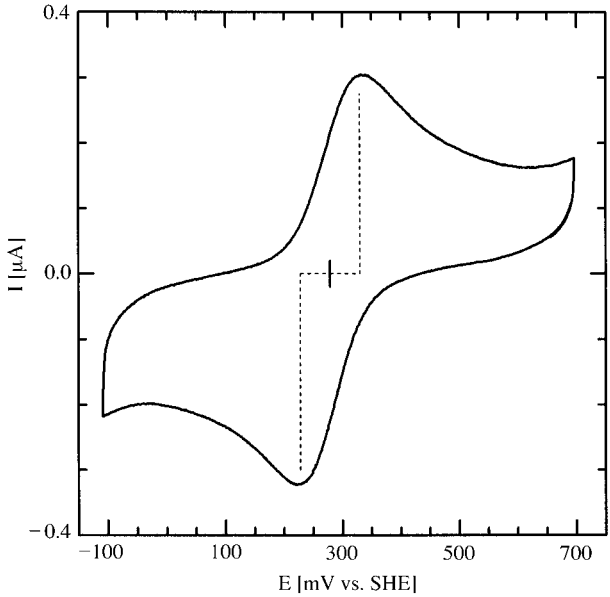

FIG. 17. Cyclic voltammogram of the water-soluble Rieske fragment from the bc_1 complex of *Paracoccus denitrificans* (ISFpd) at the nitric acid modified glassy carbon electrode. Protein concentration, 1 mg/ml in 50 mM NaCl, 10 mM MOPS, 5 mM EPPS, pH 7.3; T, 25°C; scan rate, 10 mV/s. The cathodic (reducing branch, $I < 0$) and anodic (oxidizing branch, $I > 0$) peak potentials and the resulting midpoint potential are indicated. SHE, standard hydrogen electrode.

TABLE XII

THERMODYNAMIC PARAMETERS OF THE RIESKE FRAGMENTS FROM THE bc_1 COMPLEXES OF BOVINE HEART (ISFb) (*92*) AND *Paracoccus dentrificans* (ISFpd) (*140*) AND OF THE RIESKE-TYPE FERREDOXIN FROM BENZENE DIOXYGENASE (Fd_{BED}) (*55*)

	ISFb	ISFpd	Fd_{BED}
$E^{\circ\prime}$ (mV)	+312 ± 5	+280 ± 5	−155 ± 5
$\Delta G^{\circ\prime}$ (kJ mol^{-1})	−30 ± 1	−28 ± 1	+15 ± 1
$\Delta H^{\circ\prime}$ (kJ mol^{-1})	−76 ± 4	−71 ± 4	−7 ± 4
$\Delta S^{\circ\prime}$ (J mol^{-1} K^{-1})	−153 ± 11	−144 ± 11	−75 ± 10
ΔS°_{rc} (J mol^{-1} K^{-1})	−88 ± 11	−79 ± 11	−10 ± 10
$dE^{\circ\prime}/d\sqrt{I}$ (mV M$^{-1/2}$)	−26 ± 1	−10 ± 1	0

pH 8.4 (*96*); this corresponds to a shift of −66 mV/pH. Subsequently, Prince and Dutton (*97*) showed that in pigeon heart mitochondria or in membranes from *Rhodobacter sphaeroides*, the redox potential was pH independent below pH 7.5 but showed a pH dependence with −60 mV/pH above pH 8, indicating a deprotonation of the oxidized protein only with a redox-dependent $pK_{a,ox}$ of approximately 8 on the oxidized form. Using cyclic voltammetry, Link *et al.* (*92*) could measure the pH dependence of the redox potential of the water-soluble Rieske fragment (ISF) up to pH 10, and they could show that the slope ($\Delta E_m/\Delta pH$) approached −120 mV/pH above pH 9.5, indicating two redox-dependent deprotonation reactions of the oxidized form; the data could be fitted with two $pK_{a,ox}$ values of 7.6 and 9.2 (Fig. 18a).

This result was confirmed by CD spectroscopy, where the visible CD spectra of the oxidized ISF were measured over pH 6.1 to 10.6; the CD spectra could be fitted with two $pK_{a,ox}$ values of 7.7 and 9.1 (Fig. 18b) (*58*). These values are identical within 0.1 pH unit to the values obtained by cyclic voltammetry. No structural change of the oxidized protein was observed in the far UV CD spectra between pH 6.0 and 10.7, and no deprotonation of the reduced cluster was observed over pH 6 and 11. Therefore, it can be concluded that the pK_a of a group that is in contact with the Rieske cluster shifts from 7.6 on the oxidized protein to above 11 on the reduced protein; the pK_a of a second group shifts from 9.2 to above 11. Two redox-dependent pK_a values or at least a slope $-\Delta E_m/\Delta pH > 60$ mV that cannot be explained with a single deprotonation step have been observed in all Rieske proteins (*98–101*); therefore, they can be considered as a characteristic feature of Rieske proteins. Although this has not yet been demonstrated directly, there is strong cumulative evidence that both residues undergoing redox-dependent protonation/deprotonation are the exposed histidine ligands of the Rieske cluster:

- Only the ligands of the Rieske cluster, the two cysteines forming the disulfide bridge, and one glycine are fully conserved in all Rieske proteins (see Section III,A,1)
- The CD spectra show that the groups with redox-dependent pK_a values must interact electronically with the [2Fe–2S] cluster
- Deprotonation of aspartate, glutamate, or tyrosine could be excluded by FTIR spectroscopy (Baymann, F.; Link, T. A.; Robertson, D. E.; Mäntele, W., manuscript in preparation)
- In the structure, we could not identify any residues in the vicinity of the cluster except the histidine ligands that are likely to undergo redox-dependent protonation/deprotonation (*9*)
- No major structural change occurs upon deprotonation

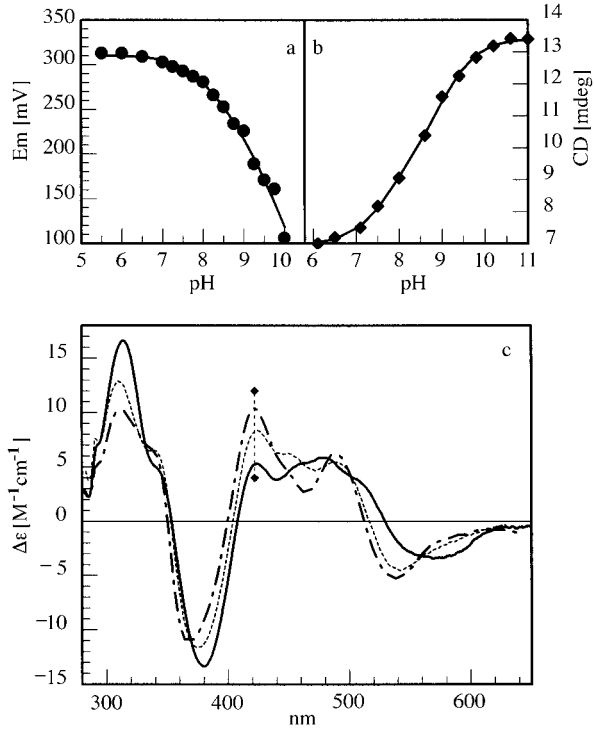

FIG. 18. pH dependence of the oxidized Rieske fragment from bovine heart mitochondria (ISF). (a) Redox potential determined by cyclic voltammetry. The line was fitted to the data points, giving p$K_{a,ox1}$ = 7.6 and p$K_{a,ox2}$ = 9.2. (b) CD intensity of the oxidized ISF at 422 nm. The line was fitted to the data points, giving p$K_{a,ox1}$ = 7.7 and p$K_{a,ox2}$ = 9.1. (c) CD spectra of the three forms of the ISF obtained from a CD monitored pH titration by singular value decomposition (SVD) analysis: ——, acidic form; ····, intermediate form; - - -, basic form. The wavelength of the fit shown in (b) is indicated by ◆--◆.

The same p$K_{a,ox}$ values as for the water-soluble Rieske protein have been determined for the Rieske protein in bovine heart mitochondrial bc_1 complex (*102*); this is consistent with the fact that the redox potential of the Rieske cluster is unperturbed within the bc_1 complex and indicates that the environment of the Rieske cluster must be accessible within the complex. However, in the bc_1 complex from *Paracoccus denitrificans*, the redox potential at pH 6.0 was found to be 45 mV lower than at pH 7, indicating the presence of a third group with a redox-dependent pK_a value below 7 (*36*). No redox potential difference between pH 6 and 7 was found for the water-soluble Rieske

fragment from *Paracoccus denitrificans*; therefore, the group with a redox-dependent pK_a value below 7 is not located on the Rieske protein but on other subunits, most likely cytochrome *b*.

Since the first pK_a value of mitochondrial Rieske proteins is at 7.6, the primary function cannot be redox-dependent proton uptake or release, since only a fraction of a proton would be taken up during oxidation/reduction. However, the shift of the pK_a values of the histidine ligands, which is a consequence of the electronic structure of the cluster, will influence the strength of hydrogen bonds formed by the histidine ligands: Upon reduction, the strength of hydrogen bonds will be greatly increased. As a consequence, the inhibitor stigmatellin, which binds directly to the His 161 of the bovine Rieske cluster (*41*), binds four orders of magnitude more tightly to the reduced than to the oxidized Rieske cluster as indicated by a 250-mV shift of the redox potential of the Rieske cluster to higher values upon binding of stigmatellin (*77*). Upon oxidation of the Rieske cluster, the tight binding of stigmatellin will be released. The hydrogen bonding pattern of stigmatellin resembles that of deprotonated hydroquinone or semiquinone (*43*); therefore, it is reasonable to assume that the binding of semiquinone will also depend on the redox state of the Rieske cluster ("affinity change mechanism") (*116*). Similar but weaker effects have been observed for hydroxyquinone inhibitors, such as UHDBT (*103*).

B. Rieske-Type Clusters

While the redox potentials of Rieske clusters are above +100 mV at pH 7, values between −100 and −150 mV have been determined for the redox potentials of Rieske-type clusters (Table XI). Several 4-cysteine coordinated [2Fe–2S] clusters have redox potentials similar to those of Rieske-type clusters, for example, the [2Fe–2S] clusters of the dioxygenase reductases [compilation in (*104*)]; therefore, the redox potential is not useful for distinguishing between Rieske-type and ferredoxin-type clusters.

Although the redox potential of Rieske-type clusters is approximately 400 mV lower than that of Rieske clusters, it is 300 mV more positive than the redox potential of plant-type ferredoxins (approximately −400 mV). Multiple factors have been considered to be essential for the redox potential of iron sulfur proteins:

- The overall charge of the cluster, 0/−1 for oxidized and reduced Rieske clusters, respectively, compared to −2/−3 for 4-cysteine coordinated [2Fe–2S] clusters

- The electronegativity of the ligands (here: histidine vs sulfur)
- The presence of hydrogen bonds to bridging or terminal sulfur atoms
- The solvent exposure of the cluster

The first two factors contribute to the difference between both Rieske and Rieske-type proteins compared to plant-type ferredoxins while the latter two factors are essential for the difference between Rieske and Rieske-type clusters. In the hydrogen bond network around the Rieske cluster, three of the eight hydrogen bonds formed by the sulfur atoms of the Rieske cluster are not observed in the structure of NDO (see Section III,B,2); two of these hydrogen bonds derive from side chain oxygen atoms (Ser 163 and Tyr 165 in the bovine heart ISF) and these residues are not present in Rieske-type proteins. The exchange of both serine and tyrosine for residues that cannot form hydrogen bonds from the side chains to the sulfur atoms of the cluster will lower the redox potential by approximately 200 mV (*35*); therefore, hydrogen bonds into the cluster account for approximately half of the observed redox potential difference between Rieske and Rieske-type clusters.

A comparative study of the water-soluble Rieske fragment of the bc_1 complex (ISF) and of the Rieske-type ferredoxin from benzene dioxygenase (Fd_{BED}) has provided additional insight into the factors that are responsible for the different electrochemical properties (*55*). The entropy of the redox reaction, ΔS°_{rc}, was comparable to values reported for cytochromes for the ISF, whereas it was close to zero for Fd_{BED}. Moreover, although a strong pH dependence and a weaker ionic strength dependence were observed for the ISF, the redox potential was independent of pH or ionic strength in Fd_{BED} (Table XII); the pH independence has also been shown for various dioxygenases (*86*). These data led us to the conclusion that "the [2Fe–2S] cluster is buried within the protein so that the solution dipoles do not 'see' the cluster" (*55*). In the structure of naphthalene dioxygenase, the Rieske cluster is buried at the interface with the catalytic domain of another α subunit of the $\alpha_3\beta_3$ hexamer; both histidines are hydrogen-bonded to carboxylate groups in the catalytic domain. However, in the structure of the ferredoxin of biphenyl oxygenase from *Burkholderia cepacia* (BphF), it is not true that the histidines and cluster are shielded by a loop; the histidine ligands are as exposed as in the ISF or RFS (Colbert, C. L.; Couture, M. M.-J.; Eltis, L. D.; Bolin, J. T., manuscript in preparation). This finding is surprising in view of the fact that the electrochemical properties of Rieske-type clusters in ferredoxins and

in dioxygenases are comparable. One possible explanation might be if Fd_{BED} forms a dimer in solution so that the Rieske cluster is shielded at the dimer interface. This is inconsistent with a molecular weight determination of the Fd_{BED} (*105*); however, the ferredoxin of alkene monooxygenase from *Xanthobacter* strain Py2 has recently been shown to form a dimer (*106*).

VI. Biosynthesis

Little is known about the biosynthesis of Rieske and Rieske-type clusters. There seems to be no requirement for a specialized assembly protein since the *fbc* operons coding for bacterial bc_1 complexes or the gene clusters coding for dioxygenases contain only the genes coding for the structural proteins, and since several Rieske-type ferredoxins and dioxygenases have been successfully overexpressed heterologously in *E. coli.*

The Rieske protein in mitochondrial bc_1 complexes is assembled when the protein is incorporated into the complex. The Rieske protein is encoded in the nucleus and synthesized in the cytosol with a mitochondrial targeting presequence, which is required to direct the apoprotein to the mitochondrial matrix. The C-terminus is then targeted back to the outside of the inner mitochondrial membrane where the Rieske cluster is assembled. In addition, the presequence is removed and the protein is processed to its mature size after the protein is inserted into the bc_1 complex. In mammals, the presequence is cleaved in a single step by the "core" proteins 1 and 2, which are related to the general mitochondrial matrix processing protease (MPP) α and β subunits; the bovine heart presequence is retained as a 8.0 kDa subunit of the complex (*42*, *107*). In *Saccharomyces cerevisiae,* processing occurs in two steps: Initially, the yeast MPP removes 22 amino acid residues to convert the precursor to the intermediate form, and then the mitochondrial intermediate protease (MIP) removes 8 residues after the intermediate form is in the bc_1 complex (*47*). Cleavage by MIP is independent of the assembly of the Rieske cluster: Conversion of the intermediate to the mature form was observed in a yeast mutant that did not assemble any Rieske cluster (*35*). However, in most mutants where the assembly of the Rieske cluster is prevented, the amount of Rieske protein is drastically reduced, most likely because of instability (*35*, *44*).

The assembly of the Rieske cluster requires the correct folding of the Rieske protein, which will be aided by other subunits of the com-

plex. The involvement of the 7.3-kDa subunit in the assembly of the Rieske cluster has been implied in *Saccharomyces cerevisiae* (*47*, *108*). Subunits 10 and 11 (which is homologous to the yeast 7.3 kDa subunit) of the bovine heart bc_1 complex form an invagination in the membrane, which has been suggested to accommodate the Rieske cluster binding subdomain during the assembly of the Rieske cluster (*42*).

As mentioned previously, Rieske-type proteins have been successfully expressed in *E. coli;* this has facilitated the production of large amounts of Rieske-type proteins for biophysical studies [e.g., (*55*)] and for crystallography (*32*). The situation is quite different for Rieske proteins of *bc* complexes. Homologous expression of the full-length Rieske protein of the bc_1 complex from *Rhodobacter sphaeroides* in a strain from which the genes coding for cytochrome *b* and c_1 had been deleted gave a very small amount (1–2% of wild type level) of Rieske protein containing the Rieske cluster (*109*). The low content has been ascribed to instability due to enhanced susceptibility to proteolysis. However, when the full-length Rieske protein from *Rhodobacter sphaeroides* was expressed in *E. coli,* no typical Rieske cluster was assembled, but weak signals were observed in the EPR spectrum at $g = 1.93$ or $g = 1.95$, indicating assembly of a distorted iron sulfur cluster (*109*). Expression in *E. coli* of the full-length Rieske protein behind the mature portion of the *E. coli* maltose binding protein or of a truncated form lacking the N-terminal membrane anchor did not result in any EPR-detectable iron sulfur cluster.

Expression in *E. coli* of a water-soluble form of the Rieske protein of the b_6f complex from the cyanobacterium *Nostoc* sp. PCC 7906 produced only a very low level of soluble Rieske fragment (*110*). Expression of the full-length Rieske protein from *Nostoc* in *E. coli* gave inclusion bodies containing the Rieske protein that did not show the characteristic EPR signal of the Rieske cluster. When the molecular chaperones GroEL and GroES were coexpressed, an iron sulfur cluster, but no Rieske cluster, was incorporated into the Rieske protein inclusion bodies. However, the Rieske cluster could be reconstituted into the full-length *Nostoc* Rieske protein isolated from the inclusion bodies (*110*): After unfolding in 5 M guanidine-HCl, the protein was allowed to refold in the presence of 0.5% β-mercaptoethanol and was made anaerobic before $FeCl_3$ and Na_2S were added in the presence of 1% β-mercaptoethanol or dithiothreitol. In an alternate procedure, $FeCl_3$ and Na_2S were added before the protein was allowed to refold by dilution from 8 M urea. Approximately one-third of the reconstituted Rieske protein contained the Rieske cluster with a characteris-

tic EPR spectrum with $g_z = 2.03$, $g_y = 1.89$, and $g_x = 1.74$ and a redox potential of $E^{\circ\prime} = +321$ mV (*110*). It is remarkable that apparently the disulfide bridge connecting the cluster binding loops has been reformed even in the presence of 1% β-mercaptoethanol; although the presence of the disulfide bridge has not been demonstrated, it is highly unlikely that the Rieske cluster could be unperturbed if it was stable at all in the absence of the disulfide bridge.

The Rieske protein II (SoxF) from *Sulfolobus acidocaldarius,* which is part, not of a bc_1 or b_6f complex, but of the SoxM oxidase complex (*18*), could be expressed in *E. coli,* both in a full-length form containing the membrane anchor and in truncated water-soluble forms (*111*). In contrast to the results reported for the Rieske protein from *Rhodobacter sphaeroides,* the Rieske cluster was more efficiently inserted into the truncated soluble forms of the protein. Incorporation of the cluster was increased threefold when the *E. coli* cells were subject to a heat shock (42°C for 30 min) before induction of the expression of the Rieske protein, indicating that chaperonins facilitate the correct folding of the soluble form of SoxF. The iron content of the purified soluble SoxF variant was calculated as 1.5 mol Fe/mol protein; the cluster showed g values very close to those observed in the SoxM complex and a redox potential of $E^{\circ\prime} = +375$ mV (*111*).

In summary, it appears that the protein has to adopt the correct fold before the Rieske cluster can be inserted. The correct folding will depend on the stability of the protein; the Rieske protein from the thermoacidophilic archaebacterium *Sulfolobus* seems to be more stable than Rieske proteins from other bacteria so that the Rieske cluster can be inserted into the soluble form of the protein during expression with the help of the chaperonins. If the protein cannot adopt the correct fold, the result will be either no cluster or a distorted iron sulfur cluster, perhaps using the two cysteines that form the disulfide bridge in correctly assembled Rieske proteins.

VII. Function

A. Rieske Clusters: Cytochrome *bc* Complexes

The group of the *bc* complexes comprises bc_1 complexes in mitochondria and bacteria and b_6f complexes in chloroplasts. These complexes are multisubunit membrane proteins containing four redox centers in three subunits: cytochrome *b* (cytochrome b_6 in b_6f complexes) comprising two heme *b* centers in a transmembrane arrangement, cyto-

chrome c_1 (cytochrome f in b_6f complexes), and the Rieske iron sulfur protein (Fig. 8b). All *bc* complexes oxidize hydroquinones (ubihydroquinone and plastohydroquinone, respectively) and transfer electrons to their respective acceptors, cytochrome *c* or plastocyanin. In addition, they translocate protons across the respective membranes by the "Q-cycle mechanism" first proposed by Mitchell (*112*). The essential reaction of the "Q-cycle mechanism" is the bifurcation of the pathway of electrons upon oxidation of hydroquinone: The hydroquinone oxidation reaction is strictly coupled in that always one electron is transferred to the Rieske cluster and from there via cytochrome c_1 to cytochrome *c*, while the second electron is transferred to heme b_L and from there across the membrane dielectric to heme b_H. From heme b_H, the electron is transferred to a molecule of quinone, which is reduced again to hydroquinone; thus, half of the electrons from the oxidation of hydroquinone are cycled back to quinone, which leads to a doubling of the protonmotive efficiency of *bc* complexes [reviews in (*113–117*)].

The Rieske protein is essential for hydroquinone oxidation and for the bifurcation of electron pathways: it catalyzes the oxidation of hydroquinone and it is the first electron acceptor. Not only is the Rieske cluster involved in electron transfer, but it also interacts directly with the substrate: Quinones and quinonoid inhibitors bind directly to the exposed histidine ligands. This is supported both by EPR spectroscopy (see Section IV,E,1,b) and by X-ray crystallography: In the X-ray structure of the bc_1 complex with the inhibitor stigmatellin bound, there is a hydrogen bond between the inhibitor and the NεH group of His 161 that is one of the ligands of the Rieske cluster (*41*). In the bc_1 complex, stigmatellin binds four orders of magnitude more tightly to the reduced than to the oxidized Rieske cluster (see Section V). Since stigmatellin appears to mimic the hydrogen bonding pattern of semiquinone (*43*), it appears that the stigmatellin inhibited state resembles the intermediate semiquinone state during hydroquinone oxidation. The tight binding of stigmatellin/semiquinone to the reduced Rieske cluster will lower the barrier for hydroquinone oxidation; thus, the Rieske protein catalyzes the oxidation of hydroquinone ("affinity change mechanism") (*116*).

The bifurcation of the electron pathways is aided by the mobility of the catalytic domain of the Rieske protein. Three positional states of the catalytic domain of the Rieske protein have been observed in different crystal forms of the bc_1 complex (Fig. 8b; see Section III,B,5) (*41*, *42*). In each single positional state, the Rieske protein is unable to perform all electron transfer reactions occuring during turnover:

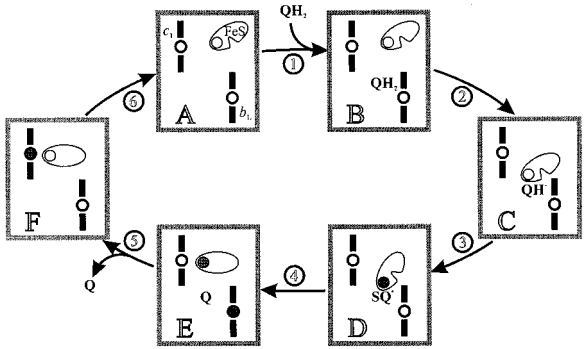

FIG. 19. Proposed mechanism of hydroquinone oxidation by the cytochrome bc_1 complex (see text). Open circles indicate oxidized metal centers; filled circles indicate reduced metal centers.

• In the "c_1 positional state," fast electron transfer from the Rieske protein to cytochrome c_1 will be facilitated by the close interaction and by the hydrogen bond between His 161 of the Rieske protein and a propionate group of heme c_1, but the Rieske cluster is far away from the quinone binding site.

• In the "*b* positional state," The Rieske cluster can interact with quinone bound in the reaction pocket, but the distance to heme c_1 is too large (>30 Å) to allow fast electron transfer.

• In the "intermediate state," the Rieske protein interacts neither with cytochrome *b* nor with cytochrome c_1; the existence of this state is consistent with the fact that the electrochemical properties of the Rieske protein are apparently unperturbed within the bc_1 complex.

Therefore, the Rieske protein has to switch between the positional states during turnover. The following reaction scheme combines the movement of the catalytic domain of the Rieske protein with the redox-dependent stabilization of the intermediate semiquinone (Fig. 19) (*42*):

• When the complex is fully oxidized and before substrate is bound, the catalytic domain of the Rieske protein is in the "intermediate state" (A).

• Hydroquinone will bind in a quinone binding site that is provided by cytochrome *b*. Before hydroquinone can be oxidized, it must first be deprotonated (step 2).

• The interaction with the deprotonated hydroquinone (QH^-) will move the Rieske protein toward the "*b* positional state" (C).

• After the electron transfer (step 3), the resulting semiquinone is tightly bound to the reduced Rieske cluster in the "*b* positional state" (D); in this state, the semiquinone intermediate will be stabilized (*116*).

• After the second electron transfer from semiquinone to heme b_L (step 4), the interaction between the Rieske cluster and the resulting quinone is weakened so that the reduced Rieske protein can now occupy the preferred "c_1 positional state" (E), which allows rapid electron transfer from the Rieske cluster to heme c_1 (step 5).

• When both electrons have been transferred to cytochrome *c* and to heme b_H, the Rieske protein can go back to the "intermediate state" (step 6) and the site is ready for the next reaction cycle.

The reaction mechanism presented here combines the evidence from X-ray structures (*41*, *42*) with elements of the "affinity change mechanism" (*116*) and of the "catalytic switch mechanism" (*118*). All electron transfer reactions occur between species when they are hydrogen bonded to each other; therefore, electron transfer will be extremely rapid and most likely not rate limiting.

Because of the exposed histidine ligands of the [2Fe–2S] cluster, the Rieske is capable of binding quinones in a redox-dependent manner. The variation of the hydrogen bond strength and of the electrostatic properties will control the movement of the catalytic domain of the Rieske protein. Therefore, the function depends on the unique structural and electrochemical properties of the Rieske cluster.

B. Rieske-Type Clusters: Dioxygenases

Rieske-type clusters are found in aromatic-ring hydroxylating dioxygenase systems (*20*). These enzymes catalyze the conversion of different aromatic compounds into *cis*-arene diols:

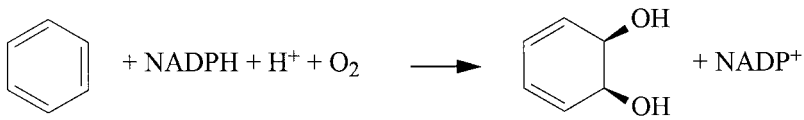

The dioxygenase systems consist of a reductase and a terminal oxygenase; many dioxygenases also contain a [2Fe–2S] ferredoxin. The reductase reacts with NAD(P)H; it can be any of the following (*20*):

- An iron sulfur–flavoprotein that transfers electrons directly to the dioxygenase, as in phthalate dioxygenase (class I)
- A flavoprotein that transfers electrons to the ferredoxin, as in benzene dioxygenase (class II)
- An iron sulfur–flavoprotein that transfers electrons to the ferredoxin, as in naphthalene dioxygenase (class III)

The structure of phthalate dioxygenase reductase that transfers electrons directly from NADPH to phthalate dioxygenase has been determined by X-ray crystallography (*119*). In class II or class III dioxygenases, the ferredoxin obligately transfers electrons from the reductase to the terminal dioxygenase (*64a*); it can be either a Rieske-type ferredoxin or a ferredoxin containing a 4-cysteine coordinated [2Fe–2S] cluster.

The terminal oxygenase contains a Rieske-type cluster as well as a catalytic mononuclear iron site; the two centers are bound in different domains but are in close proximity (12 Å) (*11*). In naphthalene dioxygenase (NDO), His 104 (which is a ligand of the Rieske-type cluster) and His 208 (which is a ligand of the catalytic iron) are bridged by one carboxylate oxygen of Asp 205 so that the electron can be easily transferred from the Rieske-type cluster to the catalytic iron site. The importance of Asp 205 has been demonstrated by site-directed mutagenesis; when the residue was converted to alanine, the enzyme lost all activity (*120*). It is conceivable that the linkage between Rieske cluster and the catalytic iron site does not only allow rapid electron transfer, but that the redox state of the Rieske center controls interactions within the catalytic site through the hydrogen bonds provided by Asp 205 and that in return the Rieske cluster senses the ligand state of the catalytic site. In putidamonooxin, an interaction between the substrate binding site and the Rieske-type cluster has been demonstrated by CD spectroscopy (*121*).

NDO can be classified as class III dioxygenase; the electron transfer chain involves a Rieske-type ferredoxin. Electrons enter NDO through the Rieske-type cluster of the dioxygenase. Kauppi *et al.* (*11*) have suggested that the binding site of NDO for the ferredoxin involves the β strands 10 and 12 of the Rieske domain as well as residues from the catalytic domain that form a depression in the protein surface close to Cys 101, which is a ligand of the Rieske cluster. In Rieske proteins from *bc* complexes, access to this side of the cluster is blocked by an acidic surface residue (Asp 152 in the ISF, Glu 120 in RFS).

Unlike Rieske clusters in *bc* complexes, Rieske-type clusters are involved only in electron transfer and not in substrate binding or cataly-

sis. This is consistent with the structure of Rieske-type proteins where the ligands of the cluster are not exposed but buried inside the protein, distant from the substrate binding site.

VIII. Outlook

Since their discovery, Rieske proteins have been the object of numerous studies aimed at gaining insight into the molecular basis of their unique properties. These studies not only have shed light on Rieske and Rieske-type clusters, but also have contributed to the understanding of iron sulfur proteins in general.

By the application of modern spectroscopic techniques and through the recent availability of high-resolution structural information, several issues could be resolved, in particular the nature of the ligands of the Rieske cluster. Now that structures are available, the research will focus on new questions in order to provide a better understanding of the electronic properties of Rieske and Rieske-type clusters as well as of their function:

- How are the spectroscopic and electrochemical properties of Rieske and Rieske-type clusters related to their structure?
- How is the affinity of Rieske clusters for the binding of ligands (e.g., semiquinone) controlled, and what is the role of the exposed histidine residues?
- How is the mobility of the Rieske cluster within the bc_1 complex and the switch between different positional states related to (and controlled by) the electrostatic properties of the Rieske cluster?
- What is the interaction between the Rieske-type cluster and the catalytic iron site of dioxygenases?

I hope that this review will be regarded as a starting point for future research rather than a historical recollection.

Abbreviations

ISF, water-soluble fragment of the Rieske protein from bc_1 complex; RFS, water-soluble fragment of the Rieske protein from b_6f complex; NDO, naphthalene dioxygenase; TRP, Rieske protein from *Thermus thermophilus;* PDO, phthalate dioxygenase; Fd_{BED}, ferredoxin from benzene dioxygenase; BphF, ferredoxin from biphenyl dioxygenase; rms, root mean square; CD, circular dichroism; MCD, magnetic circular dichroism; EPR, electron paramagnetic resonance; ENDOR, electron nuclear double resonance; ESEEM, electron spin echo envelope modulation; EFG, electric field gradient; RR, reso-

nance Raman; EXAFS, extended X-ray absorption fine structure; XANES, X-ray absorption near edge structure.

Acknowledgments

I thank E. A. Berry, W. A. Cramer, and S. Ramaswamy for making coordinates of their structures available in advance. I thank J. T. Bolin and L. D. Eltis for communicating information about the structure of the ferredoxin from biphenyl oxidase BphF, and J. L. Markley and co-workers for sending a preprint of their manuscript on the NMR spectroscopy of T4MOC. The ESEEM spectrum of the Rieske cluster in bovine heart submitochondrial particles was kindly provided by R. Cammack. Figures 1–4 and 6–9 were generated using the program Molmol (*144*). Finally, I thank all the coworkers and collaborators with whom I had the pleasure to collaborate over the past years for their support. The research leading to the determination of the structure of the water-soluble fragment of the Rieske protein from bovine heart bc_1 complex was supported by the Deutsche Forschungsgemeinschaft (DFG), Priority Programme "Transition Metals in Biology and their Coordination Chemistry" (grant Li 474/2); the spectroscopic studies in collaboration with M. K. Johnson were made possible by travel grant Li 474/4-1, and the present research on Rieske proteins is supported by the DFG through grant Li 474/7-1.

References

1. Rieske, J. S.; MacLennan, D. H.; Coleman, R. *Biochem. Biophys. Res. Commun.* **1964,** *15,* 338.
2. Beinert, H.; Sands, R. H. *Biochem. Biophys. Res. Commun.* **1960,** *3,* 41.
3. Anemüller, S.; Schmidt, C. L.; Schäfer, G.; Teixeira, M. *FEBS Lett.* **1993,** *318,* 61.
4. Blumberg, W. E.; Peisach, J. *Arch. Biochem. Biophys.* **1974,** *162,* 502.
5. Fee, J. A.; Findling, K. L.; Yoshida, T.; Hille, R.; Tarr, G. E.; Hearshen, D. O.; Dunham, W. R.; Day, E. D.; Kent, T. A.; Münck, E. *J. Biol. Chem.* **1984,** *259,* 124.
6. Gurbiel, R. J.; Batie, C. J.; Sivaraja, M.; True, A. E.; Fee, J. A.; Hoffman, B. M.; Ballou, D. P. *Biochemistry* **1989,** *28,* 4861.
7. Gurbiel, R. J.; Ohnishi, T.; Robertson, D. E.; Daldal, F.; Hoffman, B. M. *Biochemistry* **1991,** *30,* 11579.
8. Britt, R. D.; Sauer, K.; Klein, M. P.; Knaff, D. B.; Kriauciunas, A.; Yu, C.-A.; Yu, L.; Malkin, R. *Biochemistry* **1991,** *30,* 1892.
9. Iwata, S.; Saynovits, S.; Link, T. A.; Michel, H. *Structure* **1996,** *4,* 567.
10. Carrell, C. J.; Zhang, H.; Cramer, W. A.; Smith, J. L. *Structure* **1997,** *5,* 1613.
11. Kauppi, B.; Lee, K.; Carredano, E.; Parales, R. E.; Gibson, D. T.; Eklund, H.; Ramaswamy, S. *Structure* **1998,** *6,* 571.
12. Harnisch, U.; Weiss, H.; Sebald, W. *Eur. J. Biochem.* **1985,** *149,* 95.
13. Schägger, H.; Borchart, U.; Machleidt, W.; Link, T. A.; von Jagow, G. *FEBS Lett.* **1987,** *219,* 161.
14. Geourjon, C.; Deléage, G. *J. Mol. Graph.* **1995,** *13,* 209.
15. Yu, J.; Hederstedt, L.; Piggot, P. J. *J. Bacteriol.* **1995,** *177,* 6751.

16. Schütz, M.; Zirngibl, S.; le Coutre, J.; Büttner, M.; Xie, D.-L.; Nelson, N.; Deutzmann, R.; Hauska, G. *Photosynthesis Res.* **1994,** *39,* 163.
17. Schmidt, C. L.; Anemüller, S.; Schäfer, G. *FEBS Lett.* **1996,** *388,* 43.
18. Lübben, M.; Arnaud, S.; Castresana, J.; Warne, A.; Albracht, S. P. J.; Saraste, M. *Eur. J. Biochem.* **1994,** *224,* 151.
19. Schäfer, G.; Purschke, W.; Schmidt, C. L. *FEMS Microbiol. Rev.* **1996,** *18,* 173.
20. Mason, J. R.; Cammack, R. *Annu. Rev. Microbiol.* **1992,** *46,* 277.
21. Rathinasabapathi, B.; Burnet, M.; Russell, B. L.; Gage, D. A.; Liao, P.-C.; Nye, G. J.; Scott, P.; Golbeck, J. H.; Hanson, A. D. *Proc. Natl. Acad. Sci. USA* **1997,** *94,* 3454.
22. Schlenzka, W.; Shaw, L.; Kelm, S.; Schmidt, C. L.; Bill, E.; Trautwein, A. X.; Lottspeich, F.; Schauer, R. *FEBS Lett.* **1996,** *385,* 197.
23. Irie, A.; Koyama, S.; Kozutsumi, Y.; Kawasaki, T.; Suzuki, A. *J. Biol. Chem.* **1998,** *273,* 15866.
24. Caliebe, A.; Grimm, R.; Kaiser, G.; Lübeck, J.; Soll, J.; Heins, L. *EMBO J.* **1997,** *16,* 7342.
25. Gray, J.; Close, P. S.; Briggs, S. P.; Johal, G. S. *Cell* **1997,** *89,* 25.
26. Exley, G. E.; Colandene, J. D.; Garrett, R. H. *J. Bacteriol.* **1993,** *175,* 2379.
27. Johnstone, I. L.; McCabe, P. C.; Greaves, P.; Gurr, S. J.; Cole, G. E.; Brow, M. A. D.; Unkles, S. E.; Clutterbuck, A. J.; Kinghorn, J. R.; Innis M. A. *Gene* **1990,** *90,* 181.
28. Amaar, Y. G.; Moore, M. M. *Current Genetics* **1998,** *33,* 206.
29. Brito, N.; Avila, J.; Perez, M.; Gonzalez, C.; Siverio, J. M. *J. Biochem.* **1996,** *317,* 89.
30. Link, T. A.; Saynovits, M.; Assmann, C.; Iwata, S.; Ohnishi, T.; von Jagow, G. *Eur. J. Biochem.* **1996,** *237,* 71.
31. Zhang, H.; Carrell, C. J.; Huang, D.; Sled, V.; Ohnishi, T.; Smith, J. L.; Cramer, W. A. *J. Biol. Chem.* **1996,** *271,* 31360.
32. Lee, K.; Kauppi, B.; Parales, R. E.; Gibson, D. T.; Ramaswamy, S. *Biochem. Biophys. Res. Commun.* **1997,** *241,* 553.
33. Holm, L.; Sander, C. *J. Mol. Biol.* **1993,** *233,* 123.
34. Gatti, D. L.; Meinhardt, S. W.; Ohnishi, T.; Tzagoloff, A. *J. Mol. Biol.* **1989,** *205,* 421.
35. Denke, E.; Merbitz-Zahradnik, T.; Hatzfeld, O. M.; Snyder, C. H.; Link, T. A.; Trumpower, B. L. *J. Biol. Chem.* **1998,** *273,* 9085.
36. Schröter, T.; Hatzfeld, O. M.; Gemeinhardt, S.; Korn, M.; Friedrich, T.; Ludwig, B.; Link, T. A. *Eur. J. Biochem.* **1998,** *255,* 100.
37. Herriott, J. R.; Sieker, L. C.; Jensen, L. H.; Lovenberg, W. *J. Mol. Biol.* **1970,** *50,* 391.
38. Adman, E. T.; Sieker, L. C.; Jensen, L. H. *J. Mol. Biol.* **1991,** *217,* 337.
39. Wang, B.; Jones, D. N. M.; Kaine, B. P.; Weiss, M. A. *Structure* **1998,** *6,* 555.
40. Qian, X.; Gozani, S. N.; Yoon, H.; Jeon, C.; Agarwal, K.; Weiss, M. A. *Biochemistry* **1993,** *32,* 9944.
41. Zhang, Z.; Huang, L.; Shulmeister, V. M.; Chi, Y.-I.; Kim, K. K.; Hung, L.-W.; Crofts, A. R.; Berry, E. A.; Kim, S.-H. *Nature* **1998,** *392,* 677.
42. Iwata, S.; Lee, J. W.; Okada, K.; Lee, J. K.; Iwata, M.; Rasmussen, B.; Link, T. A.; Ramaswamy, S.; Jap, B. K. *Science* **1998,** *281,* 64.
43. Lancaster, C. R. D.; Michel, H. *Structure* **1997,** *5,* 1339.
44. Graham, L. A.; Trumpower, B. L. *J. Biol. Chem.* **1991,** *266,* 22485.

45. Davidson, E., Ohnishi, T.; Atta-Asafo-Adjei, E.; Daldal, F. *Biochemistry* **1992,** *31,* 3342.
46. Beckmann, J. D.; Ljungdahl, P. O.; Trumpower, B. L. *J. Biol. Chem.* **1989,** *264,* 3713.
47. Graham, L. A.; Brandt, U.; Sargent, J. S.; Trumpower, B. L. *J. Bioenerg. Biomembr.* **1992,** *25,* 245.
48. Atteia, A.; Franzen, L. G. *Eur. J. Biochem.* **1996,** *237,* 792.
49. Liebl, U., Sled, V.; Brasseur, G.; Ohnishi, T.; Daldal, F. *Biochemistry* **1997,** *36,* 11675.
50. Liebl, U., Sled, V.; Ohnishi, T.; Daldal, F. In "Photosynthesis: from Light to Biosphere"; Mathis, P., Ed.; Kluwer Academic Publishers, Dordrecht, 1995; Vol. II, 749–752.
51. Brasseur, G.; Sled, V.; Liebl, U., Ohnishi, T.; Daldal, F. *Biochemistry* **1997,** *36,* 11685.
52. Saribas, S.; Valkova-Valchanova, M.; Tokito, M. K.; Zhang, Z.; Berry, E. A.; Daldal, F. *Biochemistry* **1998,** *37,* 8105.
53. Mason, J. R.; Butler, C. S.; Cammack, R.; Shergill, J. K. *Biochem. Soc. Trans.* **1997,** *25,* 90.
54. Unalkat, P.; Hatzfeld, O. M.; Link, T. A.; Tan, H.-M.; Cammack, R.; Mason, J. R. *J. Inorg. Biochem.* **1995,** *59,* 528.
55. Link, T. A.; Hatzfeld, O. M.; Unalkat, P.; Shergill, J. K.; Cammack, R.; Mason, J. R. *Biochemistry* **1996,** *35,* 7546.
56. Palmer, G.; Brintzinger, H.; Estabrook, R. W. *Biochemistry* **1967,** *6,* 1658.
57. Degli Esposti, M.; Ballester, F.; Solain, G.; Lenaz, G. *Biochem. J.* **1987,** *241,* 285.
58. Link, T. A. *Biochim. Biophys. Acta* **1994,** *1185,* 81.
59. Eaton, W. A.; Palmer, G.; Fee, J.; Kimura, T.; Lovenberg, W. *Proc. Natl. Acad. Sci. USA* **1971,** *68,* 3015.
60. Bertrand, P.; Guigliarelli, B.; Gayda, J.-P.; Beardwood, P.; Gibson, J. F. *Biochim. Biophys. Acta* **1985,** *831,* 261.
61. Fu, W.; Drozdzewski, P. M.; Davies, M. D.; Sligar, S. G.; Johnson, M. K. *J. Biol. Chem.* **1992,** *267,* 15502.
62. Münck, E.; Debrunner, P. G.; Tsibris, J. C. M.; Gunsalus, I. C. *Biochemistry* **1972,** *11,* 855.
63. Bill, E.; Bernhardt, F.-H.; Trautwein, A. X. *Eur. J. Biochem.* **1981,** *121,* 39.
64. Twilfer, H.; Bernhardt, F.-H.; Gersonde, K. *Eur. J. Biochem.* **1981,** *119,* 595.
64a. Pikus, J. D.; Studts, J. M.; Achim, C.; Kaufmann, K. E.; Münck, E.; Steffan, R. J.; McClay, K.; Fox, B. G. *Biochemistry* **1996,** *35,* 9106.
65. Bertrand, P.; Gayda, J.-P., *Biochim. Biophys. Acta* **1979,** *579,* 107.
66. Kuila, D.; Fee, J. A.; Schoonover, J. R.; Woodruff, W. H.; Batie, C. J.; Ballou, D. P. *J. Am. Chem. Soc.* **1987,** *109,* 1559.
67. Kuila, D.; Schoonover, J. R.; Dyer, R. B.; Batie, C. J.; Ballou, D. P.; Fee, J. A.; Woodruff, W. H. *Biochim. Biophys. Acta* **1992,** *1140,* 175.
68. Iwasaki, T.; Imai, T.; Urushiyama, A.; Oshima, T. *J. Biol. Chem.* **1996,** *271,* 27659.
69. Powers, L.; Schägger, H.; von Jagow, G.; Smith, J.; Chance, B.; Ohnishi, T. *Biochim. Biophys. Acta* **1989,** *975,* 293.
70. Bes, M. T.; Parisini, E.; Inda, L. A.; Saraiva, L.; Peleato, M. L.; Sheldrick, G. M., to be published.
71. Ikemizu, S.; Bando, M.; Sato, T.; Morimoto, Y.; Tsukihara, T.; Fukuyama, K. to be published.

72. Tsang, H.-T.; Batie, C. J.; Ballou, D. P.; Penner-Hahn, J. E. *Biochemistry* **1989,** *28,* 7233.
73. Gibson, J. F.; Hall, D. O.; Thornley, J. H. M.; Whatley, F. R. *Proc. Natl. Acad. Sci. USA* **1966,** *56,* 987.
74. de Vries, S.; Albracht, S. P. J.; Leeuwerik, F. J. *Biochim. Biophys. Acta* **1979,** *546,* 316.
75. Siedow, J. N.; Power, S.; de la Rosa, F. F.; Palmer, G. *J. Biol. Chem.* **1978,** *253,* 2392.
76. de Vries, S.; Albracht, S. P. J.; Berden, J. A.; Slater, E. C. *Biochim. Biophys. Acta* **1982,** *681,* 41.
77. von Jagow, G.; Ohnishi, T. *FEBS Lett.* **1985,** *185,* 311.
78. Sharp, E. R.; Palmitessa, A.; Gibney, B. R.; Moser, C. C.; Daldal, F.; Dutton, P. L. *FEBS Lett.* **1998,** *431,* 423.
79. Ding, H.; Robertson, D. E.; Daldal, F.; Dutton, P. L. *Biochemistry* **1992,** *31,* 3144.
80. Ohnishi, T.; Meinhardt, S. W.; von Jagow, G.; Yagi, T.; Hatefi, Y. *FEBS Lett.* **1994,** *353,* 103.
81. Malkin, R. *Biochemistry* **1982,** *21,* 2945.
82. Cline, J. F.; Hoffman, B. M.; Mims, W. B.; LaHaie, E.; Ballou, D. P.; Fee, J. A. *J. Biol. Chem.* **1985,** *260,* 3251.
83. Telser, J.; Hoffman, B. M.; LoBrutto, R.; Ohnishi, T.; T'sai, A.-L.; Simpkin, D.; Palmer, G. *FEBS Lett.* **1987,** *214,* 117.
84. Gurbiel, R. J.; Doan, P. E.; Gassner, G. T.; Macke, T. J.; Case, D. A.; Ohnishi, T.; Fee, J. A.; Ballou, D. P.; Hoffman, B. M. *Biochemistry* **1996,** *35,* 7834.
85. Shergill, J. K.; Joannou, C. L.; Mason, J. R.; Cammack, R. *Biochemistry* **1995,** *34,* 16533.
86. Riedel, A.; Fetzner, S.; Rampp, M.; Lingens, F.; Liebl, U.; Zimmermann, J.-L.; Nitschke, W. *J. Biol. Chem.* **1995,** *270,* 30869.
86a. Dikanov, S. A.; Xun, L.; Karpiel, A. B.; Tyryshkin, A. M.; Bowman, M. K. *J. Am. Chem. Soc.* **1996,** *118,* 8408.
87. Shergill, J. K.; Cammack, R. *Biochim. Biophys. Acta* **1994,** *1185,* 35.
88. Holtz, R. C.; Small, F. J.; Ensign, S. A. *Biochemistry* **1997,** *36,* 14690.
88a. Xia, B.; Pikus, J. D.; Xia, W.; McClay, K.; Steffan, R. J.; Kee Chae, Y.; Westler, W. M.; Markley, J. L.; Fox, B. G. *Biochemistry* **1999,** *38,* 727.
89. de Vries, S.; Cherepanov, A.; Berg, A.; Canters, G. W. *Inorg. Chimica Acta* **1998,** *275–276,* 493.
89a. Bertrand, P.; Gayda, J.-P.; Fee, J. A.; Kuila, D.; Cammack, R. *Biochim. Biophys. Acta* **1987,** *916,* 24.
90. Palmer, G.; Dunham, W. R.; Fee, J. A.; Sands, R. H.; Iizuka, T.; Yonetani, T. *Biochim. Biophys. Acta* **1971,** *245,* 201.
91. Rieske, J. S. In "Nonheme Iron Proteins: Role in Energy Conservation"; San Pietro, E., Ed.; The Antioch Press: Yellow Springs, OH, 1965, 461–468.
92. Link, T. A.; Hagen, W. R.; Pierik, A. J.; Assmann, C.; von Jagow, G. *Eur. J. Biochem.* **1992,** *208,* 685.
93. Taniguchi, V. T.; Sailasuta-Scott, N.; Anson, F. C.; Gray, H. B. *Pure & Appl. Chem.* **1980,** *52,* 2275.
94. Verhagen, M. F. J. M.; Link, T. A.; Hagen, W. R. *FEBS Lett.* **1995,** *361,* 75.
95. Holm, R. H.; Ibers, J. A. In "Iron–Sulfur Proteins"; Lovenberg, W., Ed.; Academic Press: New York, 1977; Vol. III, 205–281.
96. Knaff, D. B.; Malkin, R. *Biochim. Biophys. Acta* **1976,** *430,* 244.
97. Prince, R. C.; Dutton, P. L. *FEBS Lett.* **1976,** *65,* 117.

98. Liebl, U.; Pezennec, S.; Riedel, A.; Kellner, E.; Nitschke, W. *J. Biol. Chem.* **1992,** *267,* 14068.
99. Nitschke, W.; Joliot, P.; Liebl, U.; Rutherford, A. W.; Hauska, G.; Müller, A.; Riedel, A. *Biochim. Biophys. Acta* **1992,** *1102,* 266.
100. Riedel, A.; Kellner, E.; Groditzki, D.; Liebl, U.; Hauska, G.; Müller, A.; Rutherford, A. W.; Nitschke, W. *Biochim. Biophys. Acta* **1993,** *1183,* 263.
101. Anemüller, S.; Schmidt, C. L.; Schäfer, G.; Bill, E.; Trautwein, A. X.; Teixeira, M. *Biochem. Biophys. Res. Commun.* **1994,** *202,* 252.
102. Link, T. A.; Hatzfeld, O. M.; Saynovits, M. In "Bioinorganic Chemistry—Transition Metals in Biology and their Coordination Chemistry"; Trautwein, A. X., Ed.; Wiley-VCH: Weinheim, 1997, 312–325.
103. Bowyer, J. R.; Edwards, C. A.; Ohnishi, T.; Trumpower, B. L. *J. Biol. Chem.* **1982,** *257,* 8321.
104. Rosche, B.; Fetzner, S.; Lingens, F.; Nitschke, W.; Riedel, A. *Biochim. Biophys. Acta* **1995,** *1252,* 177.
105. Crutcher, S. E.; Geary, P. J. *Biochem. J.* **1979,** *177,* 393.
106. Small, F. J.; Ensign, S. A. *J. Biol. Chem.* **1997,** *272,* 24913.
107. Brandt, U.; Yu, L.; Yu, C.-A.; Trumpower, B. L. *J. Biol. Chem.* **1993,** *268,* 8387.
108. Phillips, J. D.; Graham, L. A.; Trumpower, B. L. *J. Biol. Chem.* **1993,** *268,* 11727.
109. Van Doren, S. R.; Yun, C.-H.; Crofts, A. R.; Gennis, R. B. *Biochemistry* **1993,** *32,* 628.
110. Holton, B.; Wu, X.; Tsapin, A.; Kramer, D. M.; Malkin, R.; Kallas, T. *Biochemistry* **1996,** *35,* 15485.
111. Schmidt, C. L.; Hatzfeld, O. M.; Petersen, A.; Link, T. A.; Schäfer, G. *Biochem. Biophys. Res. Commun.* **1997,** *234,* 283.
112. Mitchell, P. *J. Theor. Biol.* **1976,** *62,* 327.
113. Trumpower, B. L. *J. Biol. Chem.* **1990,** *265,* 11409.
114. Brandt, U.; Trumpower, B. L. *CRC Crit. Rev. Biochem. Mol. Biol.* **1994,** *29,* 165.
115. Brandt, U. *FEBS Lett.* **1996,** *387,* 1.
116. Link, T. A. *FEBS Lett.* **1997,** *412,* 257.
117. Brandt, U. *Biochim. Biophys. Acta* **1998,** *1365,* 261.
118. Brandt, U.; Haase, U.; Schägger, H.; von Jagow, G. *J. Biol. Chem.* **1991,** *266,* 19958.
119. Correll, C. C.; Batie, C. J.; Ballou, D. P.; Ludwig, M. L. *Science* **1992,** *258,* 1604.
120. Jiang, H.; Parales, R. E.; Lynch, N. E.; Gibson, D. T. *J. Bacteriol.* **1996,** *178,* 3133.
121. Bernhardt, F.-H.; Ruf, H.-H.; Ehrig, H. *FEBS Lett.* **1974,** *43,* 53.
122. Russell, B. L.; Rathinasabapathi, B.; Hanson, A. D. *Plant Physiology* **1998,** *116,* 859.
123. Gray, J.; Johal, G. S. Submitted to EMBL/Genbank/DDBJ databases, 1996.
124. Kaneko, T.; Sato, S.; Kotani, H.; Tanaka, A.; Asamizu, E.; Nakamura, Y.; Miyajima, N.; Hirosawa, M.; Sugiura, M.; Sasamoto, S.; Kimura, T.; Hosouchi, T.; Matsuno, A.; Muraki, A.; Nakazaki, N. Naruo, K.; Okumura, S.; Shimpo, S.; Takeuchi, C.; Wada, T.; Watanabe, A.; Yamada, M.; Yasuda, M.; Tabata, S. *DNA Research* **1996,** *3,* 109.
125. Brown, D.; Churcher, C. M.; Wood, V.; Barrell, B. G.; Rajandream, M. A.; Walsh, S. V. Submitted to EMBL/Genbank/DDBJ databases, 1996–1997.
126. Hatada, S.; Kinoshita, M.; Sakumoto, H.; Nishihara, R.; Noda, M.; Asashima, M. *Gene* **1997,** *194,* 297.
127. Wilson, R.; Ainscough, R.; Anderson, K.; Baynes, C.; Berks, M.; Bonfield, J.; Burton, J.; Connell, M.; Copsey, T.; Cooper, J.; Coulson, A.; Craxton, M.; Dear, S.; Du,

Z.; Durbin, R.; Favello, A.; Fulton, L.; Gardner, A.; Green, P.; Hawkins, T.; Hillier, L.; Jier, M.; Johnston, L.; Jones, M.; Kershaw, J.; Kirsten, J.; Laister, N.; Latreille, P.; Lightning, J.; Lloyd, C.; McMurray, A.; Mortimore, B.; O'Callaghan, M.; Parsons, J.; Percy, C.; Rifken, L.; Roopra, A.; Saunders, D.; Shownkeen, R.; Smaldon, N.; Smith, A.; Sonnhammer, E., Staden, R., Sulston, J.; Thierry-Mieg, J., Thomas, K.; Vaudin, M.; Vaughan, K.; Waterston, R.; Watson, A.; Weinstock, L., Wilkinson-Sproat, J.; Wohldman, P. *Nature* **1994,** *368,* 32.

128. Han, S.; Czernuszewicz, R. S.; Kimura, T.; Adams, M. W. W.; Spiro, T. G. *J. Am. Chem. Soc.* **1989,** *111,* 3505.

129. Kuila, D.; Fee, J. A. *J. Biol. Chem.* **1986,** *261,* 2768.

130. Schmidt, C. L.; Anemüller, S.; Teixeira, M.; Schäfer, G. *FEBS Lett.* **1995,** *359,* 239.

131. de Vries, S.; Albracht, S. P. J.; Berden, J. A.; Marres, C. A. M.; Slater, E. C. *Biochim. Biophys. Acta* **1983,** *723,* 91.

131a. Yang, X.; Trumpower, B. L. *J. Biol. Chem.* **1986,** *261,* 12282.

132. Andrews, K. M.; Crofts, A. R.; Gennis, R. B. *Biochemistry* **1990,** *29,* 2645.

133. Liebl, U.; Rutherford, A. W.; Nitschke, W. *FEBS Lett.* **1990,** *261,* 427.

134. Riedel, A.; Rutherford, A. W.; Hauska, G.; Müller, A.; Nitschke, W. *J. Biol. Chem.* **1991,** *266,* 17838.

135. Geary, P. J.; Saboowalla, F.; Patil, D. S.; Cammack, R. *Biochem. J.* **1984,** *217,* 667.

135a. Haddock, J. D.; Pelletier, D. A.; Gibson, D. T. *J. Ind. Microbiol. Biotechnol.* **1997,** *19,* 355.

136. Sauber, K.; Fröhner, C.; Rosenberg, G.; Eberspächer, J.; Lingens, F. *Eur. J. Biochem.* **1977,** *74,* 89.

137. Suen, W.-Ch; Gibson, D. T. *J. Bacteriol.* **1993,** *175,* 5877.

138. Wilson, D. F.; Leigh, J. S., Jr. *Arch. Biochem. Biophys.* **1972,** *150,* 154.

139. T'sai, A.-L.; Palmer, G. *Biochim. Biophys. Acta* **1983,** *722,* 349.

140. Hatzfeld, O. M. Ph.D. Thesis. Frankfurt, 1998.

141. Prince, R. C.; Lindsay, J. G.; Dutton, P. L. *FEBS Lett.* **1975,** *51,* 108.

141a. Ugulava, N. B.; Crofts, A. R. *FEBS Lett.* **1998,** *440,* 409.

142. Evans, M. C. W.; Lord, A. V.; Reeves, S. G. *Biochem. J.* **1974,** *138,* 177.

143. Lewis, R. J.; Prince, R. C.; Dutton, P. L.; Knaff, D. B.; Krulwich, T. A. *J. Biol. Chem.* **1981,** *256,* 10543.

143a. Hagedoorn, P. L.; Driessen, M. C. P. F.; van den Bosch, M.; Landa, I.; Hagen, W. R. *FEBS Lett.* **1998,** *440,* 311.

144. Koradi, R.; Billeter, M.; Wüthrich, K. *J. Mol. Graphics* **1996,** *14,* 51.

This Page Intentionally Left Blank

ADVANCES IN INORGANIC CHEMISTRY, VOL. 47

STRUCTURE, FUNCTION, AND BIOSYNTHESIS OF THE METALLOSULFUR CLUSTERS IN NITROGENASES

BARRY E. SMITH

John Innes Centre, Nitrogen Fixation Laboratory, Norwich Research Park, Colney, Norwich NR4 7UH, United Kingdom

I. Introduction
  A. The Nitrogenases
  B. This Review
II. The Fe Proteins of Molybdenum Nitrogenase
  A. Structure
  B. Redox and Spectroscopic Properties of the Fe Proteins
  C. Interactions between the Fe Protein and Nucleotides
III. The MoFe Proteins
  A. Structure
  B. Redox and Spectroscopic Properties of the MoFe Proteins
  C. Substrate Interactions with the MoFe Protein
IV. Biosynthesis of Molybdenum Nitrogenase
  A. The *nif* Genes
  B. Biosynthesis of the Fe Protein
  C. Biosynthesis of the MoFe Protein
V. The Mechanism of Molybdenum Nitrogenase
  A. The Lowe–Thorneley Mechanism
  B. The Nitrogenase Complex
  C. The Role of MgATP Hydrolysis
  D. Electron Transfer within the MoFe Protein
  E. Substrates and Inhibitors
VI. The Alternative Nitrogenases
  A. Biosynthesis of the Vanadium and Iron-Only Nitrogenases
  B. Vanadium Nitrogenase
  C. Iron-Only Nitrogenase
  D. Nitrogenase from *Streptomyces Thermoautotrophicus*
VII. Conclusions and Outlook
References

Copyright 1999 by Academic Press.
All rights of reproduction in any form reserved.
0898-8838/99 $30.00

I. Introduction

If a plant is healthy and is supplied with enough water, then in most agricultural soils, its growth is limited by the supply of nitrogen. In intensive agriculture nitrogen is usually supplied as ammonium or nitrate fertilizer and worldwide about 60M tonnes of N is applied to agricultural soil annually. However, another 90M tonnes per year is supplied to agriculture through biological nitrogen fixation. Thus biological nitrogen fixation is still the major contributor of new N to agriculture and the food supply. Biological nitrogen fixation is mediated solely by bacteria, although in agriculture their contribution is mainly through symbioses with legume plants.

A. The Nitrogenases

The enzyme systems responsible for fixing atmospheric N_2 to form ammonia are known as the nitrogenases. These enzymes function at field temperatures and 0.8 atm N_2 pressure, whereas the industrial Haber–Bosch process requires high temperatures (300–400°C) and high pressures (200–300 atm) in a capital-intensive process that relies on burning fossil fuel. Small wonder, then, that the chemistry of the nitrogenases has attracted considerable attention for many years.

Three major types of nitrogenase have been identified: one containing molybdenum with iron, a second containing vanadium with iron, and a third apparently containing iron only. There have been reports of a fourth type of nitrogenase, also based on molybdenum but having many unique features, which will be discussed in Section VI,C. Apart from that section, this chapter will mainly describe the other three nitrogenases and most reference will be made to the molybdenum nitrogenase, which has been isolated from a wide range of organisms and studied intensively. Each of these nitrogenases consists of two essential metallosulfur proteins: an iron protein (Fe protein) and a molybdenum iron (MoFe) or vanadium iron (VFe) or an iron iron (FeFe) protein. The Fe proteins are all α_2 dimers of molecular weights of around 60–70 kDa. The larger MoFe, VFe, and FeFe proteins are either $\alpha_2\beta_2$ (MoFe) tetramers or $\alpha_2\beta_2\gamma_2$ (VFe and FeFe) hexamers of M_r 220–250 kDa. Figure 1 shows an overall electron transfer pathway for the nitrogenases where the Fe proteins act as very specific, essential electron donors to the larger proteins. This is not the only role for the Fe proteins (see Section IV,C) and their role in the mechanism is almost certainly more complex than that of a simple electron transfer agent (see below, Section V). Electron transfer from the Fe protein to

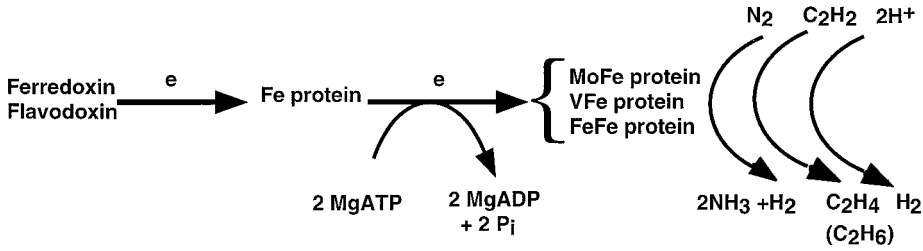

FIG. 1. The electron transfer path through the nitrogenases.

the larger proteins is accompanied by hydrolysis of MgATP. When the enzyme is at its most efficient 2MgATP molecules are hydrolyzed to MgADP for every electron transferred to substrate. The details of this energy transduction process are still unclear (see Section V,C). Of the three nitrogenases the Mo enzyme is probably the most efficient (at least at 30°) at reducing N_2 to ammonia with a limiting stoichiometry of the reaction as described by

$$N_2 + 8H^+ + 16MgATP + 8e^- \rightarrow 2NH_3 + H_2 + 16MgADP + 16P_i. \quad (1)$$

Equation (1) demonstrates that, even at its most efficient, one H_2 molecule is evolved for every N_2 molecule reduced to ammonia by nitrogenase. Perturbation of the enzymic reaction conditions by temperature or protein ratio can lead to this reaction becoming far less efficient, with a large quantity of H_2 being produced per molecule of N_2 reduced and/or the ratio of MgATP hydrolysed to electrons transferred exceeding two.

As indicated in Fig. 1, nitrogenase can reduce substrates other than N_2. In the absence of other reducible substrates it will reduce protons to dihydrogen, but it can also reduce a number of other small triple-bonded substrates, as indicated in Section V,E,1. Large substrates are not reduced efficiently, indicating physical limitations on access to the enzyme's active site. CO is a potent inhibitor of all nitrogenase substrate reductions except that of the proton to H_2. In the presence of CO the rate of electron transfer is generally not inhibited, but all electrons go toward the production of H_2.

B. THIS REVIEW

In late 1992 the first crystal structures of the Fe and MoFe proteins of Mo nitrogenase from *Azotobacter vinelandii* were published (*1–3*).

These were relatively low-resolution structures, and with refinement some errors in the initial structural assignments have been detected (*4–7*). Since the structures were first reported the subject has been extensively reviewed in this series (*8*) and elsewhere (*9–15*). This review will focus on the structure, biosynthesis, and function of the metallosulfur clusters found in nitrogenases. This will require a broader overview of some functional aspects, particularly the involvement of MgATP in the enzymic reaction, and also some reference will be made to the extensive literature (*9*, *15*) on biomimetic chemistry that has helped to illuminate possible modes of nitrogenase function, although a detailed review of this chemistry will not be attempted here. This review cannot be fully comprehensive in the space available, but concentrates on recent advances and attempts to describe the current level of our understanding.

Molybdenum nitrogenase has been the subject of intensive study for more than 30 years, but much less work has been done on the vanadium and iron-only nitrogenases. Consequently, we first review the properties of Mo nitrogenase, and then in later sections outline what is known of the other two enzymes.

II. The Fe Proteins of Molybdenum Nitrogenase

A. Structure

Although separable from the MoFe proteins, the Fe proteins are essential to the enzymic process, where they act as very specific electron donors to the MoFe protein in a MgATP-activated reaction. No other reductant has been shown to substitute for the Fe protein in this reaction, and it seems probable that its interaction with the MoFe protein is more complex than simply that of electron donation. The DNA sequences of the *nifH* genes encoding the Fe protein polypeptides from well over 20 N_2-fixing bacteria, including Archaebacteria, Eubacteria and Cyanobacteria, yield derived amino acid sequences that are not less than 45% and usually greater than 85% identical. There are five invariant cysteine residues in highly conserved regions of the encoded polypeptides.

The Fe proteins are homodimers containing a single Fe_4S_4 cluster. Site-directed mutagenesis experiments showed that the cluster was probably held between the two subunits by ligation to two of the invariant cysteine residues from each subunit (*16*). This observation was confirmed later by X-ray crystallography (*1*) of the Fe protein

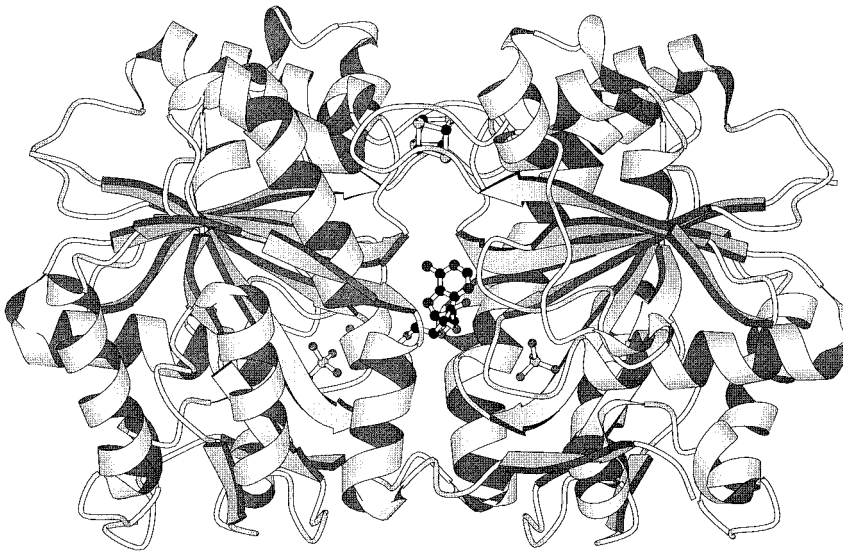

FIG. 2. The structure of the Fe protein (Av2) from *Azotobacter vinelandii*, after Georgiadis *et al.* (*1*). The dimeric polypeptide is depicted by a ribbon diagram and the Fe_4S_4 cluster and ADP by space-filling models (MOLSCRIPT (*196*)). The Fe_4S_4 cluster is at the top of the molecule, bound equally to the two identical subunits, and the ADP molecule spans the interface between the subunits with MoO_4^{2-} apparently binding in place of the terminal phosphate of ATP.

(Av2)[1] from *Azotobacter vinelandii.* The crystal structure of Av2 reveals that each subunit consists of a single large domain of an eight-stranded β sheet flanked by nine α helices (Fig. 2). The Fe_4S_4 cluster is situated at one end of the dimer interface and is exposed to solvent. Analysis of the 2.9-Å structure revealed, about 20 Å from the Fe_4S_4 cluster, an ADP molecule (at about half occupancy) that was bound across the subunit interface with the adenosine bound to one subunit and the phosphate to the other. No ADP had been added to the crystallization medium, so it is assumed that it copurified with the Av2. Although in the same region of the protein, this binding mode differs from that found in the Fe protein:MoFe protein putative transition-state complex described in Section V,B and may not indicate a normal binding mode of nucleotides to the Fe proteins.

[1] The nitrogenase proteins are generally characterized by two letters indicating the species and strains of bacteria and the numerals 1 for the MoFe protein and 2 for the Fe protein. Thus, the Fe protein from *Azotobacter vinelandii* is Av2 and the MoFe protein from *Klebsiella pneumoniae* is Kp1.

As well as donating electrons to the MoFe protein, the Fe protein has at least two and possibly three other functions (see Section IV,C): It is involved in the biosynthesis of the iron molybdenum cofactor, FeMoco; it is required for insertion of the FeMoco into the MoFe protein polypeptides; and it has been implicated in the regulation of the biosynthesis of the alternative nitrogenases.

Since the nitrogenase proteins are damaged by exposure to oxygen, the reductant sodium dithionite is generally added to all buffers during their isolation. The EPR spectra of dithionite-reduced Fe proteins show a mixture of $S = \frac{1}{2}$ and $S = \frac{3}{2}$ spin systems (*17–19*). This observation indicates that the protein can exist in at least two conformations of similar energy, which may have implications for nitrogenase turnover. However, ^{1}H NMR studies (*20*) have been interpreted as indicating that only the $S = \frac{1}{2}$ spin state is populated at room temperature, implying that the $S = \frac{3}{2}$ system is an artifact of freezing the protein for EPR studies.

B. Redox and Spectroscopic Properties of the Fe Proteins

Until the mid-1990s, the Fe proteins were regarded as one-electron donors to the MoFe proteins cycling between $[Fe_4S_4]^{1+}$ and $[Fe_4S_4]^{2+}$ oxidation states during turnover. However, it is now known that in the absence of sodium dithionite the protein can be reduced further to the $[Fe_4S_4]^0$ form (*21*). The potential for this reduction, at −460 mV, is within the physiological range and the reduction can be carried out by flavodoxin in the hydroquinone state as well as the artificial electron donors, methyl viologen and titanium citrate. These data may therefore imply that *in vivo* the Fe protein can act as a two-electron donor to the MoFe protein. This would have important consequences for current ideas on the mechanism of enzyme turnover (see Section V). There are conflicting reports on changes in the optical spectrum of the Fe_4S_4 cluster following reduction from the $[Fe_4S_4]^{1+}$ to the $[Fe_4S_4]^0$ state. One group (*21*) observed no significant change in the spectrum, whereas the other observed a general bleaching but the appearance of a band at 520 nm (*22*). The latter authors implied that excess citrate, added with the titanium citrate reductant, might be in some way affect the optical spectrum. EXAFS spectroscopy (*23*) had earlier shown that iron–iron and iron–sulfur distances in the cluster are changed by less than 0.02 Å when the Fe_4S_4 cluster is reduced from the 2+ to the 1+ state but has not yet been reported for the all-ferrous cluster and will be required to ascertain any changes in the cluster dimensions. An interesting phenomenon observed with the ni-

trogenase Fe proteins is their ability to "self-oxidize" in the presence of sodium dithionite (*24*). This process involves the initial degradation of residual sodium dithionite followed by eventual oxidation of the cluster from the 1+ to the 2+ state. Since it takes a considerable period to prepare crystals of the Fe protein, it is probable that the published crystal structure (*1*) is of the protein cluster in the $[Fe_4S_4]^{2+}$ state. It may be possible to reduce the cluster prior to freezing and collection of low-temperature crystallographic data and in this way to obtain the structure of the protein in the 1+ and 0 oxidation states. However, it is unlikely with the current resolution of 2.9 Å that this approach would yield statistically significant information on changes in the dimensions of the Fe_4S_4 cluster, although it may give information on protein conformational changes concomitant with electron transfer.

C. Interactions between the Fe Protein and Nucleotides

It has long been known that the Fe proteins bind 2 mol MgATP or MgADP per mol dimeric protein. Binding of these nucleotides induces conformational changes that alter the EPR, circular dichroism, ^{1}H NMR, and Mössbauer spectroscopies of the protein. The midpoint potential of the Fe_4S_4 cluster is lowered by approximately 100 mV on binding either of the nucleotides. In addition, the iron in the Fe_4S_4 cluster becomes much more susceptible to extraction by reaction with bathophenanthroline (*12*, *14*).

Robson (*25*) was the first to recognize the Walker A nucleotide binding motifs in the derived amino acid sequences of the iron proteins. The Walker A and B motifs are common to a large family of nucleotide binding proteins (e.g., ras p21 and rec A). In the three-dimensional structure of the Fe protein these motifs are close to the intersubunit interface, implying the existence of two nucleotide binding sites (one per subunit) at the interface. As noted previously this nucleotide binding site is 15–20 Å from the Fe_4S_4 cluster, and yet apparently hydrolysis of MgATP is associated with electron transfer from the cluster to the MoFe protein. Therefore, the hydrolysis must be accompanied by conformational changes in the protein that are transmitted through the polypeptide chain to the cluster. This could be via the breaking of salt bridges or hydrogen bonds concomitant with hydrolysis and has been investigated by site-directed mutagenesis of residues in potentially critical positions in the transmission pathway (*26–28*). Such experiments have gone some way towards confirming the hypothesis. One very important observation (*29*) was that by de-

leting a residue, Leu 127, in the putative transmission pathway the protein becomes locked into a conformation that is strikingly similar to the MgATP-bound state even in the absence of nucleotide.

A range of techniques has indicated that the conformational changes induced by the binding of MgATP to the reduced Fe protein differ from those induced by the binding of MgADP (*12*, *14*). Very recent ^{31}P NMR studies have now indicated that there are different interactions between MgATP and MgADP with the oxidized Fe protein (*30*). These differences have been interpreted in terms of the mechanism of nitrogenase turnover.

III. The MoFe Proteins

A. Structure

The MoFe proteins are all $\alpha_2\beta_2$ tetramers of M_r 220–240 kDa, the α and β subunits being encoded by the *nifD* and *K* genes, respectively. The proteins can be described as dimers of $\alpha\beta$ dimers. They contain two unique metallosulfur clusters: the $MoFe_7S_9 \cdot$ homocitrate, FeMo-cofactors (FeMoco), and the Fe_8S_7, P clusters. Neither of these two types of cluster has been observed elsewhere in biology, nor have they been synthesized chemically. Each molecule of fully active MoFe protein contains two of each type of cluster (*2*–*7*).

The X-ray crystallographic structure of the MoFe protein from *Azotobacter vinelandii* (Av1) was reported by Kim and Rees in 1992 (*2*). This 2.7-Å structure of Av1 was at too low a resolution to produce definitive structures for the clusters in the MoFe protein. Data are now available on Av1(2–4,6), Cp1(5,31) and Kp1(7).

Figure 3 shows the three-dimensional structure of the MoFe protein from *Klebsiella pneumoniae,* Kp1, obtained at 1.65-Å resolution (*7*). The overall structure of the polypeptides is fully consistent with that reported earlier for Av1 (*3*). The α and β subunits exhibit similar polypeptide folds with three domains of parallel β sheet/α helical type. At the interface between the three domains in the α subunit is a wide shallow cleft with the FeMoco at the bottom of the cleft about 10 Å from the solvent. FeMoco is enclosed within the α subunit. The P cluster, however, is buried within the protein at the interface between the α and β subunits, being bound by cysteine residues from each subunit. A pseudo-twofold rotation axis passes between the two halves of the P cluster and relates the α and β subunits. Each $\alpha\beta$ pair of subunits contains one FeMoco and one P cluster and thus appears

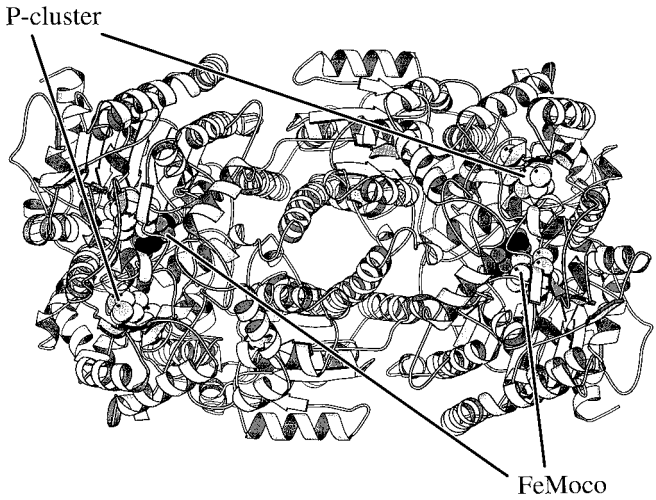

FIG. 3. The tetrameric structure of the MoFe protein (Kp1) from *Klebsiella pneumoniae* (*7*). The two FeMoco clusters and the P clusters are depicted by space-filling models and the $\alpha_2\beta_2$ polypeptides by ribbons diagrams (MOLSCRIPT (*196*)). The FeMoco clusters are bound only to the α subunits, whereas the P clusters span the interface of the α and β subunits.

to be a functional unit, although they have never been isolated as such. Between the two $\alpha\beta$ dimers is an open channel of about 8 Å diameter with the tetramer twofold axis passing through it. The tetramer interface is dominated by interactions between helices from the two β subunits and exhibits a cation binding site (probably occupied by calcium) that is coordinated by residues from both β subunits.

1. Structure of the FeMo cofactors

FeMoco can be extracted from the MoFe protein into *N*-methylformamide (NMF) solution (*32*) and has been analyzed extensively using a wide range of spectroscopic techniques both bound to the protein and in solution after extraction from it (*33*). The extracted FeMoco can be combined with the MoFe protein polypeptides, isolated from strains unable to synthesize the cofactor, to generate active protein. The structure of the FeMoco is now agreed (*4*, *5*, *7*) as $MoFe_7S_9 \cdot$ homocitrate as in Fig. 4. FeMoco is bound to the α subunit through residues Cys 275, to the terminal tetrahedral iron atom, and His 442 to the molybdenum atom (residue numbers refer to *A. vinelandii*). A number of other residues in its environment are hydrogen bonded to FeMoco and are essential to its activity (see Section V,E,2). The metal

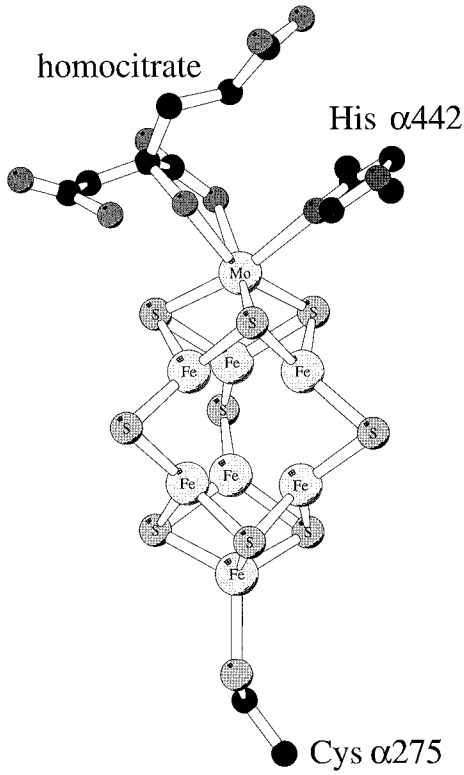

FIG. 4. Structure of the iron molybdenum cofactor, FeMoco (after Chan, Kim, and Rees, (*4*); Bolin *et al.* (*5*); and Mayer *et al.* (*7*)). The FeMoco is ligated, within the α subunits of the $\alpha_2\beta_2$ tetrameric structure, by residues Hisα442 and Cysα275 (Av1 residue numbers).

sulfur cluster can be regarded as being derived from $MoFe_3S_4$ and Fe_4S_4 clusters, each of which has lost a sulfur atom and which are then joined by three additional sulfur atoms bridging iron atoms. The data from Av1 were earlier (*2*) interpreted in terms of one of these bridging sulfur atoms having a lower atomic number, such as N or O, since the electron density was less defined. This possibility has now been discounted with the advent of higher resolution data (*4*, *5*, *7*). Furthermore, there was an early suggestion (*2*) that there might be a hexavalent sulfur atom at the center of the cluster and bonded to each iron atom, but this also has now been ruled out. This suggestion arose partially at least because six of the iron atoms have trigonal geometry, that is, they have only three sulfur atoms bonded to them rather

than the four or six ligands normally found in iron complexes. However, if each of these iron atoms is considered in relation to the plane formed by the three bonded sulfur atoms, then there is clear displacement of the iron atom from that plane toward the center of the molecule. Therefore, there may be some iron–iron bonding between the apparently trigonal iron atoms in the FeMoco center. The metal–metal and metal–sulfur distances in the model shown in Fig. 4 fit well with those derived from EXAFS spectroscopy (*34–36*), which, as well as characterizing nearest-neighbor interactions, identified long-range structural order with iron–iron bond distances of 3.6 Å (*36*) and molybdenum–iron distances of about 5.1 Å (*37*). These observations could be made both with FeMoco bound to the protein and when it was extracted into NMF solution and provide confirmation of the structural integrity of extracted FeMoco. A further suggestion to attempt to explain the apparently trigonal iron atoms in FeMoco was that they were ligated by hydride ions, which could be important during nitrogenase turnover as a source of protons for reduction of N_2. However, ENDOR spectroscopy (*38*) of the enzyme before and after turnover in the presence of ^2H_2O revealed the presence of no exchangeable protons in addition to those found with the isolated MoFe protein. This observation implies that the trigonal iron atoms are unlikely to be ligated by hydrides.

Homocitrate is bound to the molybdenum atom by its 2-carboxy and 2-hydroxy groups and projects down from the molybdenum atom of the cofactor toward the P clusters. This end of FeMoco is surrounded by several water molecules (*5*, *7*), which has led to the suggestion that homocitrate might be involved in proton donation to the active site for substrate reduction. In contrast, the cysteine-ligated end of FeMoco is virtually anhydrous.

2. *Structure of the P Clusters*

As noted previously, the P clusters are bonded at the interface of the α and β subunits by cysteine ligands. Each subunit provides three cysteine ligands; two of these bind single iron atoms, and the other bridges two iron atoms, that is, binding the eight iron atoms of the P cluster there are in total four single cysteine–iron bonds with two bridging cysteine residues. The precise structure of the P clusters has proved controversial, but has now been rationalized. Initially it was suggested that the P clusters consisted of two Fe_4S_4 clusters linked only through the bridging cysteine residues (*2*). This was then modified (*4*) to a proposal that the two Fe_4S_4 clusters were also joined through a sulfur–sulfur bond at one corner. This interpretation of the

data was challenged by Bolin and co-workers (*5*), who proposed the structure in Fig. 5a, where the two Fe_4S_4 clusters, as well as being bridged by two cysteine ligands, are joined through a common sulfur atom, that is, with an overall stoichiometry of Fe_8S_7. The data have now been fully rationalized (*6*, *7*) and it is known that their interpretation was complicated by the ready oxidation of the P clusters to the form shown in Fig. 5b, where two of the iron–sulfur bonds in Fig. 5a have been broken to generate a more open structure in one half of the P cluster. During the relatively long time required to produce crystals of the MoFe proteins, the P clusters become oxidized. However, sodium dithionite is normally added prior to data collection. In more recent data collections, the protein has been frozen at this juncture so that data can be collected at 100 K with minimal radiation damage. With prolonged reduction the structure in Fig. 5a is observed, but if crystals are frozen quickly before reduction can occur, the structure in Fig. 5b is present. Thus, Fig. 5b represents oxidized and Fig. 5a reduced P clusters. These observations have now been confirmed with Av1 (*6*) with data collected at 2-Å resolution and with Kp1 (*7*) with data collected at 1.65-Å resolution. Since essentially identical data have been obtained by two different groups of workers in two different laboratories with proteins from two bacterial sources, it can be reasonably assumed that the controversy concerning the P cluster structure is now at an end.

B. Redox and Spectroscopic Properties of the MoFe Proteins

The MoFe proteins exhibit complex redox properties. Each tetrameric $\alpha_2\beta_2$ molecule of MoFe protein contains two P clusters and two FeMoco centers and, as normally isolated in the presence of sodium dithionite, the FeMoco centers are EPR-active, exhibiting an $S = \frac{3}{2}$ spin state with g values near 4.3 and 3.7 and 2.01 (Fig. 6). The P clusters are EPR silent and there is a wealth of evidence (*39*) using a variety of techniques that indicates that the iron atoms in these clusters are all reduced to the Fe^{2+} state.

During oxidation of the MoFe protein the P clusters are the first to be oxidized at about −340 mV. This redox potential was first measured (*40*) using Mössbauer spectroscopy and exhibited a Nernst curve consistent with a two-electron oxidation process. It is possibly low enough for this redox process to be involved in enzyme turnover (see Section V). No additional EPR signal was observed from this oxidized form at this time. However, later a weak signal near $g = 12$ was detected and was finally confirmed, using parallel mode EPR

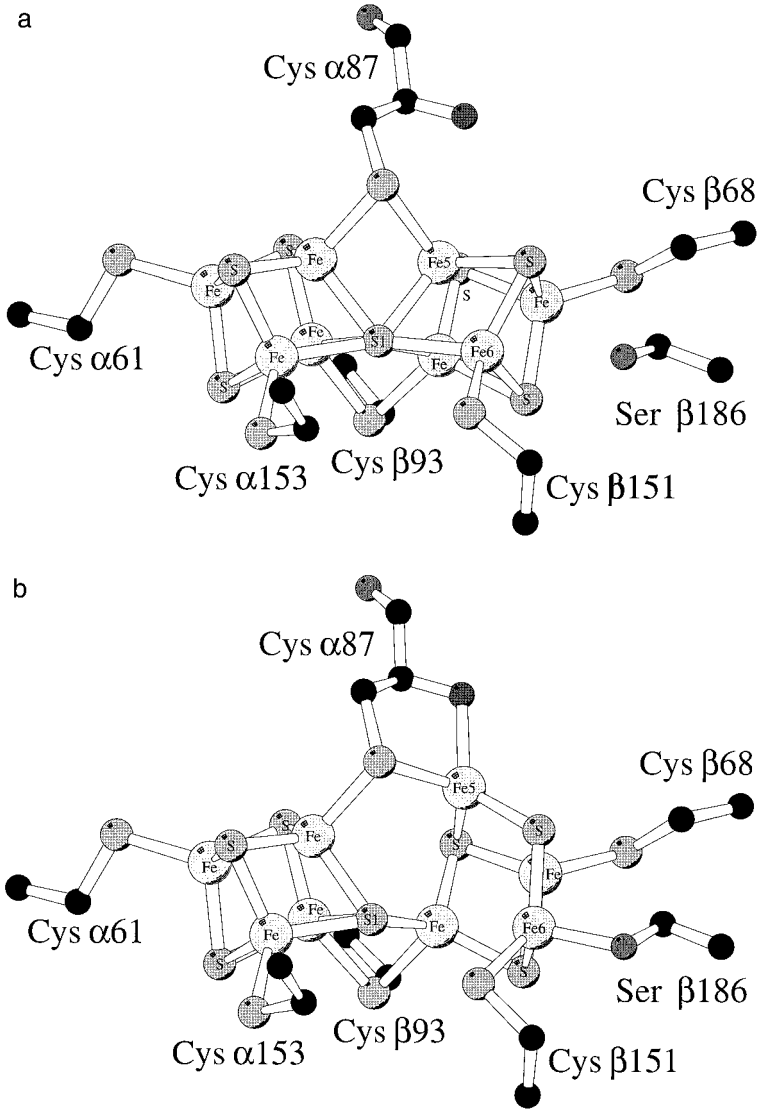

FIG. 5. Structure of the P clusters. (a) Reduced Fe_8S_7 as proposed by Bolin *et al.* (*5*) and confirmed by Peters *et al.* (*6*) and Mayer *et al.* (*7*). (b) Oxidized Fe_8S_7 as described by Peters *et al.* (*6*) and Mayer *et al.* (*7*).

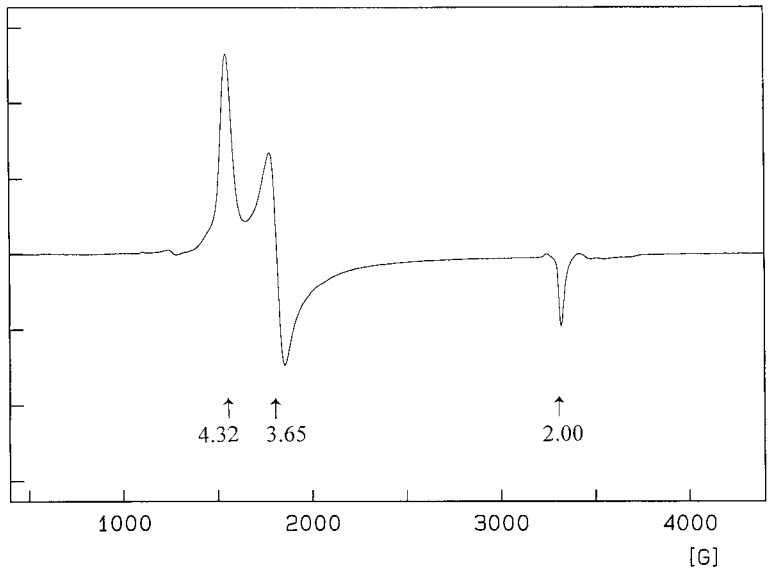

FIG. 6. The electron-paramagnetic resonance spectrum of Kp1 in frozen solution at 10 K.

spectroscopy (*41*), as arising from an integer spin system ($S = 3$ or 4). Careful redox titration allows the observation of two half-integer spin signals (*41*, *42*) before the development of the $g = 12$ signal. The two signals arise from $S = \frac{1}{2}$ and $S = \frac{5}{2}$ spin systems with redox potentials very close to each other. We now know, from the crystallographic studies just discussed, that oxidation of the P clusters to the $g = 12$ spin state results in the breaking of two iron–sulfur bonds. It is possible that breaking one of these bonds would give rise to the $S = \frac{1}{2}$ state and breaking the other would give rise to the $S = \frac{5}{2}$ state, the different spin states arising because of the slightly different environments of the cluster in the one-electron oxidized forms. If this is the case, then it seems that the bonds are broken randomly to give a mixture of spin states on oxidation. The two-electron oxidized P clusters in the $g = 12$ state have been characterized by Mössbauer (*40*, *41*), EPR (*42*, *43*), and magnetic circular dichroism (*44*, *45*) spectroscopies.

Removing two electrons from each P cluster renders each MoFe protein molecule oxidized by four electrons. Further oxidation leads to removal of electrons from the FeMoco centers. The potential of this oxidation is both species and pH dependent. At pH 7.9 the E_m for Kp1 is −180 mV, whereas for Cp1 it is 0 mV and for Av1 −95 mV (*46*).

These potentials are almost certainly too high for this oxidation state to be involved in enzymic turnover. One electron is removed from each FeMoco center, rendering it EPR inactive and diamagnetic.

Yet further oxidation removes at least one more electron from each P cluster with an $E_m \simeq +90$ mV to yield a protein oxidized by a total of at least eight electrons and with EPR signals from mixed spin states of $S = \frac{1}{2}$ and $S = \frac{7}{2}$ (*42*, *47*). The combined integrations of these signals demonstrated that their intensity was equivalent to that of the FeMoco EPR signals in the same preparations. This provided the first evidence (*47*) that MoFe proteins contained equivalent numbers of FeMoco centers and P clusters and that P clusters contained 8 Fe atoms. Previously it had been considered that the P clusters were fully reduced Fe_4S_4 clusters and thus that there were two P clusters for every FeMoco center per molecule.

There are differing accounts of the stability of MoFe proteins to further oxidation. Oxidation of Kp1 above +200 mV results in oxidative damage (*48*) and further oxidation of Av1 (*47*) above +100 mV leads to the appearance of EPR signals from an $S = \frac{9}{2}$ system which is very unstable. However, there are reports that Av1 can be oxidized by up to 12 electrons without damage. Furthermore, there are a number of reports that instead of the previously discussed oxidation processes removing first four electrons from the P clusters and then two from the FeMoco centers it is possible to observe two redox waves of three electrons each (*49*). These observations are to some extent dependent on the nature of the oxidizing agent, but similar reductive waves have been observed using microcoulometry. One clue as to the possible provenance of this unusual behavior is that the oxidative and reductive waves differ by over 200 mV. These data imply that protein structural changes, or changes in coordination number or ligand type, may be occurring and causing heterogeneity in the P clusters.

C. Substrate Interactions with the MoFe Protein

1. Interactions with Reducible Substrates

In general there are few reproducible data on binding of reducible substrates to the isolated MoFe proteins. However, the $S = \frac{3}{2}$ EPR signal from the FeMoco centers of Kp1 is pH dependent, the g values changing with a pK_a of 8.7 (*50*). Of course, the proton is a substrate of nitrogenase; however, there is no direct evidence for the proton associated with the pK_a being bound directly to FeMoco. Nevertheless, this pK_a can be perturbed by addition of the analog substrate acety-

lene, in the presence of which the pK_a is shifted down to ≃8, implying competition between the acetylene and the proton for the site.

2. Interactions with Nucleotides

Both MgATP and MgADP have been reported to bind to MoFe proteins, although the data in the literature are somewhat confused and conflicting. Careful experiments with Kp1 revealed that MgADP did not bind to the reduced protein, but did bind to protein with oxidized P clusters and FeMoco centers reduced (*51*). This species bound approximately 4 mol MgADP per mol Kp1. Both rapid reversible and slower nonreversible reactions were observed. Over a period of 2 h Kp1 reacted with MgADP to form a stable conjugate that was identified as covalently bound AMP by ^{31}P NMR spectroscopy and thin layer chromatography (*52*). This modified MoFe protein was catalytically functional and hydrolyzed slowly over a period of 6 h to yield AMP and normal Kp1.

The significance of the observed interactions between MoFe proteins and nucleotides is not easy to determine. However, as noted in Section IV, ATP is involved in the maturation of the MoFe protein and the biosynthesis of FeMoco. It is therefore possible that the nucleotide interactions noted here are associated with the maturation of the MoFe protein and not with its catalytic activity.

IV. Biosynthesis of Molybdenum Nitrogenase

A. The *nif* Genes

Nitrogenases are complex enzymes and their biosynthesis is tightly regulated by microorganisms. If there is sufficient fixed nitrogen available for growth, then nitrogenase is not required and its biosynthesis is repressed. All nitrogenase enzymes are damaged by exposure to oxygen, and so if the level of oxygen within the cell is too high, then nitrogenase synthesis is again suppressed. The intracellular pathways sensing the levels of fixed N and O_2 within a bacterium have been elucidated to some extent, but major questions remain (*53*). Figure 7 shows the organization of the genes associated with nitrogen

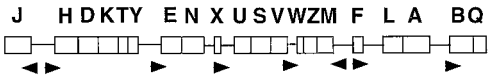

FIG. 7. The nitrogen fixation (*nif*) genes of *Klebsiella pneumoniae* are contiguous on ca. 23 kb of chromosomal DNA. The arrowheads indicate transcription starts.

TABLE I

FUNCTIONS OF NITROGEN FIXATION (*nif*) GENE PRODUCTS IN *Klebsiella pneumoniae*

Regulatory gene products	
NifA	Activator of *nif* gene expression
NifL	Repressor of NifA activity
Structural gene products	
NifH	Fe protein polypeptide; NifH is also involved in FeMoco and MoFe protein biosynthesis
NifK, NifD	MoFe protein polypeptides
Electron transfer	
NifJ	Pyruvate: flavodoxin oxidoreductase
NifF	Flavodoxin; electron donor to nitrogenase
Processing gene products	
NifM	Modifies and activates NifH to form active Fe protein
NifQ	Involved in molybdenum processing
NifB	Product is NifB-co, an iron–sulfur species incorporated into FeMoco
NifN, NifE	Subunits of $NifN_2E_2$ possibly a scaffold for FeMoco biosynthesis
NifV	Homocitrate synthase
NifY	Attaches to apo$NifK_2D_2$ to assist FeMoco insertion in *Klebsiella pneumoniae*; an equivalent protein in *Azotobacter vinelandii* is γ
NifS	Cysteine desulfurase
NifU	Probably involved with NifS in iron–sulfur cluster synthesis
NifW and NifZ	Possibly accelerate MoFe protein maturation
NifT, NifX	Unknown function

fixation in the facultative anaerobe *Klebsiella pneumoniae.* In *K. pneumoniae* there are 20 contiguous genes, arranged in seven operons, involved in the process of nitrogen fixation by a molybdenum nitrogenase. The products of two of these genes, *nifA* and *nifL,* control the last step in the regulation of the expression of the other *nif* genes in response to fixed N and O_2 levels. NifA is the activator for expression of the other seven operons of *nif* genes and NifL is a repressor of NifA activity. NifL is a flavoprotein that is inactive when reduced, but when oxidized, binds to NifA and inactivates it, thus preventing activation of the other *nif* operons (*54*). In addition, NifL is sensitive to energy charge (i.e., the ratio of ADP to ATP) and possibly directly sensitive to the presence of ammonium. The roles of some of the other *nif* genes are still unclear, but what is known is listed in Table I. Regulation of the biosynthesis of nitrogenase by fixed N and O_2 and the availability of metals is an extremely complex subject. For reviews the reader is referred to Refs. (*53*) and (*55*).

B. Biosynthesis of the Fe Protein

The Fe protein polypeptide is encoded by the *nifH* gene. The synthesis of functional Fe protein also requires the *nifM* product, although the role of the latter is undefined. Functional Fe protein can be biosynthesized in *Escherichia coli* that has been transformed with just *nifH* and *nifM,* implying that other *nif* gene products are not required (*56*). However, it is likely that the *nifS* product, now identified as a pyridoxal phosphate-activated cysteine desulfurase (*57*, *58*) that is capable of providing the sulfide necessary for the *in vitro* synthesis of the iron–sulfur cluster of the Fe protein (*59*), and also the cotranscribed *nifU* product are involved in the biosynthesis of the iron–sulfur cluster in the Fe protein. Homologs of *nifS* and *nifU* are found in many organisms and therefore are likely to be available for iron–sulfur cluster biosynthesis in *E. coli.*

The *nifU* gene product (NifU) from *A. vinelandii* has been overexpressed in *E. coli* and the recombinant protein purified and characterized (*60*). NifU is a homodimer of 33-kDa subunits with ~2 Fe atoms per subunit. Spectroscopic studies showed the presence of $[Fe_2S_2]^{2+,+}$ clusters with $E_m = -254$ mV and only cysteinyl coordination, but with properties unlike other $[Fe_2S_2]$ containing ferredoxins. The exact role of NifU in the full activation of nitrogenase is still unclear.

C. Biosynthesis of the MoFe Protein

The biosynthesis of the MoFe protein is extremely complex. Here we will first describe the biosynthesis of FeMoco, then that of the "apo-MoFe protein," encoded by the *nifD* and *nifK* genes and containing the P clusters, and finally we will summarize what is known about the combination of FeMoco with the "apo-MoFe protein" to form active MoFe protein.

1. Biosynthesis of FeMoco

At least six gene products are involved in the biosynthesis of FeMoco: the products of *nifQ, nifB, nifV, nifN, nifE,* and *nifH.* A system for the *in vitro* synthesis of FeMoco has been developed (see Ref. *61* for a review). This system involves combining extracts from an *A. vinelandii nifB* mutant strain with one from a strain containing a mutation in *nifN* or *nifE* and adding molybdate, homocitrate, and MgATP. The system has been used to provide an enzymatic assay during the purification of some of the components required for the

biosynthesis of FeMoco. The roles of these *nif* gene products will be described in turn.

a. NifQ In levels of molybdate above micromolar, *nifQ* mutants exhibit a Nif^+ phenotype, but when molybdate concentrations are much lower, that is, in the nanomolar range, then *nifQ* mutants of *K. pneumoniae* are Nif^- (*62*). Similar observations have been made with strains of *A. vinelandii* (*63*) and *Rhodobacter capsulatus* (*64*). Although *nifQ* mutant strains do accumulate lower levels of Mo than the wild type, they are defective only in FeMo cofactor biosynthesis, not molybdenum cofactor biosynthesis (the molybdenum cofactor is a molybdenum pterin found in all other molybdenum-containing enzymes). Increasing the levels of cystine available can overcome the *nifQ* mutant phenotype (*65*) and *nifQ* gene sequences predict a cysteine region near the C-terminus of the protein (*66*). These data are consistent with NifQ being involved in the formation of a complex between molybdenum and sulfur at an early step in FeMoco biosynthesis. However, the structure of such a complex has not been elucidated.

b. NifB Mutations in *nifB* result in the formation of MoFe protein that lacks FeMoco but can be activated *in vitro* by adding isolated FeMoco (*67*). The product of *nifB* can be solubilized in detergents and isolated as an iron sulfur cluster: NifB cofactor or NifBco (*68*). NifBco is stable in *N*-methylformamide, as is FeMoco, and has a similar greenish-brown color. It is extremely oxygen labile and contains no molybdenum, just iron and sulfur. Radiolabeling experiments demonstrated that both the iron and the sulfur from NifBco are incorporated into FeMoco and activity measurements indicate that NifBco may be the only source of iron for FeMoco (*69*). Current ideas on the biosynthesis of FeMoco suggest that NifBco binds to the NifN and E products during the process. In *Clostridium pasteurianum* the *nifN* and *nifB* genes are fused (*70*). This suggests that perhaps NifB and not just NifBco interacts directly with $NifN_2E_2$ during FeMoco biosynthesis.

c. $NifN_2E_2$ DNA sequence analysis revealed that the products of the *nifE* and *nifN* genes exhibit considerable homology when compared respectively with those of the *nifD* and *nifK* genes (which encode the MoFe protein α and β subunits). This structural homology indicated that the *nifEN* gene products probably form an $\alpha_2\beta_2$ complex, as do the *nifD* and *nifK* products. Furthermore, the homologies indicated that there might be a functional relationship with the MoFe

protein. Since mutations in *nifE* or *nifN* prevent FeMoco biosynthesis, it has been suggested that the $NifN_2E_2$ complex might act as a scaffold on which FeMoco is biosynthesized before transfer to the MoFe protein (*71*).

The $NifN_2E_2$ complex has been isolated from both a *nifB* mutant (*72*) and a *nifH* mutant (*73*), that is, mutants blocked at different stages in FeMoco biosynthesis, with the aim of determining whether FeMoco precursors might accumulate on $NifN_2E_2$.

The initial characterization of $NifN_2E_2$ from a *nifB* mutant of *A. vinelandii* (*72*) confirmed that it was an $\alpha_2\beta_2$ tetramer and found that it was oxygen sensitive and contained 4.6 g-atoms of Fe, 1.2 g-atoms of Zn, and 0.6 g-atoms of Cu per molecule. The UV visible spectrum indicated that the iron might be present as iron sulfur clusters. An additional factor was identified during the purification that proved necessary for the full activation of $NifN_2E_2$ in the *in vitro* FeMoco biosynthesis assay. This factor partially separated from $NifN_2E_2$ during the purification, was oxygen-stable, was inactivated when boiled, and could not pass through a 30-kDa ultrafiltration membrane. The factor was only made by *A. vinelandii* under ammonia limiting conditions, that is, when nitrogenase synthesis was activated.

A later investigation compared the properties of $NifN_2E_2$ from *nifB* and *nifH* deletion strains. In both of these strains the polypeptides encoding in the MoFe protein, *nifD* and *nifK,* were also deleted. It was observed that the mobility on anaerobic native gels of $NifN_2E_2$ was different when isolated from the two strains. The results were consistent with the product of NifB, NifBco, binding to $NifN_2E_2$ in the ΔNifHDK strain and modifying its mobility on the gel. These data support a model where NifBco binds to $NifN_2E_2$ during FeMoco biosynthesis (*73*). However, 1 mol purified $NifN_2E_2$ is required for every 2 mol FeMoco synthesized in the *in vitro* system (*72*). Thus, $NifN_2E_2$ does not act as a catalyst in this system, but perhaps donates a precursor (which is not regenerated in the *in vitro* assay) to FeMoco. This precursor could be NifBco, but nevertheless it is still puzzling that $NifN_2E_2$ does not function catalytically. It is possible that the preparations of $NifN_2E_2$ used contained an additional substance required for FeMoco synthesis that was only present in stoichiometric amounts and therefore became exhausted during the assay.

d. NifV Mutations in the *nifV* gene result in the formation of a nitrogenase with close to wild-type acetylene reduction activity but severely impaired N_2 fixation activity. Furthermore, unlike the wild-

type, the H_2 evolution activity is inhibited by carbon monoxide (*74*, 75). It has been known for many years that this change in activity is associated with the FeMoco. When FeMoco from the MoFe protein from a *nifV* mutant strain was extracted and combined with the MoFe protein polypeptides from a strain unable to synthesize FeMoco, the resultant active protein had the $NifV^-$ phenotype (*76*). This experiment provides the most convincing evidence available that FeMoco is the site of substrate binding and reduction in nitrogenase. Homocitrate has been isolated from MoFe protein and characterized by NMR and mass spectrometry (*77*). Similar experiments with a *nifV* mutant of *Klebsiella pneumoniae* showed that citrate rather than homocitrate was bound to the nitrogenase (*78*). These observations implied that the *nifV* gene encoded a homocitrate synthase. NifV from *Azotobacter vinelandii* has been recombinantly expressed at high levels in *E. coli.* Purification and characterization of NifV showed that it is a homodimer that catalyzes the condensation of acetyl coenzyme A and α-ketoglutarate to form homocitrate (*79*).

The *in vitro* synthesis of FeMoco requires homocitrate which, as shown in Fig. 4, is bound to the molybdenum atom in the holoprotein. Substitution of homocitrate in the *in vitro* synthesis of FeMoco by a range of organic acids revealed that aberrant forms of FeMoco could be synthesized but exhibited altered substrate specificities and inhibition susceptibilities (*80*). Specifically, the stereochemistry, chain length, and position of the hydroxyl group of the organic acid can have dramatic effects on the catalytic properties of the resulting enzyme. The stereochemistry at the C1 position of homocitrate is crucial to the functioning of FeMoco, and the *in vitro* FeMoco synthesis system exhibits a strong preference for the R isomer of the organic acid when racemic mixtures are provided. Synthesis of a catalytically competent FeMoco requires (a) the 1- and 2-carboxyl group, (b) the hydroxyl group, (c) the *R* configuration of the chiral center, and (d) the 4–6 carbon chain link with two terminal carboxyl groups (*61*, *81*).

It is clear from these data that homocitrate is intimately involved in the mechanism of substrate reduction and that close homologs such as citrate cannot entirely fill this role. Rationalization of this phenomenon is difficult, but comparisons of the reactivity of extracted FeMoco from the MoFe protein from wild type and $NifV^-$ strains have led to an intellectually satisfying explanation (see Section V,E,2).

e. NifH Filler *et al.* (*82*) first demonstrated the involvement of the Fe protein in the biosynthesis of FeMoco. At that time this was a

radical suggestion since the Fe protein was only thought of as the specific electron donor to the MoFe protein. Active Fe protein was not essential, since its carboxy terminal end could be shortened slightly without loss of FeMoco synthesis activity despite loss of all Fe protein catalytic activity. It was also shown that NifH was not involved in the control of the transcription of the other *nif* gene products in FeMoco synthesis or in stabilizing preformed FeMoco. Other workers (*83*) demonstrated that NifH that was ADP-ribosylated and therefore unable to reduce the MoFe protein during turnover was active in the FeMoco biosynthesis. ADP ribosylation occurs at Ala 100, which is on the surface of the Fe protein, close to the Fe_4S_4 cluster that interacts with the MoFe protein (see Section V,B). This observation indicated that the iron sulfur cluster and redox properties of the Fe protein may not be required in its participation in FeMoco biosynthesis. This hypothesis was later confirmed when it was shown that Fe protein from which the Fe_4S_4 cluster had been removed was still active in the *in vitro* FeMoco biosynthesis reaction (*84*).

Furthermore, a mutant, Ala157Ser, that cannot function in nitrogenase turnover and does not undergo the MgATP-induced conformational change is nevertheless active in FeMoco biosynthesis (*86*). It is clear from the foregoing that the form of the Fe protein and the nature of its role in FeMoco biosynthesis differs markedly from its role in nitrogenase turnover. The *in vitro* synthesis of FeMoco apparently requires specific redox levels of the proteins involved, but it seems that reductant is not utilized in the process. Reductant is routinely added to the assay to protect against contamination by oxygen; however, when *A. vinelandii* crude extracts are prepared in buffer that lacks reductant, *in vitro* FeMoco synthesis can still function. Nevertheless, reductant is required if the *A. vinelandii* crude extract is chemically oxidized prior to addition to the assay (*85*). It seems likely, therefore, that the proteins must be in the appropriate redox state to function.

2. *Biosynthesis and Properties of the "apo-MoFe Protein"*

There is now some understanding of the processes involved in insertion of FeMoco into the $\alpha_2\beta_2$ polypeptides (see Section IV,C,3). However, it is clear that there are other processes involved in generating "apo-MoFe protein"[2] capable of being activated. These processes in-

[2] The term "apo-MoFe protein" will be used here to denote the MoFe protein lacking FeMoco, although this protein is not devoid of prosthetic groups since it has bound P clusters.

volve other gene products in ways which are not yet understood, for example, there is no understanding of how the P clusters are synthesized or inserted. They may be synthesized *in situ* in the MoFe protein, but this seems unlikely since they span the interface of the α and β subunits and are buried at least 10 Å below the surface of the MoFe protein. Mutating to alanine some of the cysteine ligands to the P clusters prevents assembly of the tetramer, which implies that P cluster insertion and tetramer assembly may be concerted processes (*87*, *88*). Interestingly, it is possible to mutate both of the P cluster bridging cysteine ligands to alanine without losing all activity. However, if just one cysteine is mutated the tetramer does not assemble.

No mutants capable of binding FeMoco but lacking P clusters have been identified. A number of *nif* gene products have been implicated in the maturation of the MoFe protein polypeptides or P cluster. Specifically NifW, NifZ, and NifT appear to be involved in optimizing MoFe protein activity in both *K. pneumoniae* (*56*) and *A. vinelandii* (*89*), although they do not appear to be absolutely required for nitrogen fixation (*90*, *91*). It is possible that they supplement activities already available in the microorganisms.

The "apo-MoFe protein" has been isolated from both *K. pneumoniae* (*92*) and *A. vinelandii* (*93*) strains lacking the ability to synthesize FeMoco. The protein contains P clusters and has been useful in identifying the spectroscopic characteristics of P clusters in the absence of FeMoco. A particularly useful protocol is to generate the holo-protein with FeMoco and P clusters differentially labeled with ^{57}Fe; for example, if the "apo-protein" is grown on medium containing normal ^{56}Fe and is combined with FeMoco isolated from the MoFe protein from a strain grown on medium enriched with ^{57}Fe, then the resultant protein can be used to monitor reactions specific to FeMoco using ^{57}Fe Mössbauer spectroscopy or the broadening of EPR signals and the associated changes to ENDOR spectra due to the spin-$\frac{1}{2}$ nucleus of the ^{57}Fe.

The purified preparations of the "apo-MoFe proteins" from both organisms included a small additional polypeptide of around 20 kDa. This was shown to be the *nifY* product in *K. pneumoniae* (*94*) and a non-*nif* protein denoted γ in *A. vinelandii* (*95*). These proteins are apparently essential for effective reaction with FeMoco and are associated with the MoFe protein polypeptide through its interaction with the Fe protein and MgATP (*96*, *97*) (see Section IV,C,3). These observations demonstrate a third role for the Fe protein in generating a form of "apo-MoFe protein" that is capable of accepting FeMoco.

3. Formation of the Holo-protein

Given the information in the previous two sections, it is now possible to summarize what we know of the biosynthetic processes that lead to the formation of active MoFe protein.

1. Molybdate enters the cell and is processed by NifQ, or possibly just cystine, to form a putative Mo-S containing species.
2. Iron (possibly from NifU) and sulfur (from NifS activity) are combined by NifB to form NifBco.
3. NifBco binds to $NifN_2E_2$.
4. The next events are still obscure, but it is widely assumed that $NifN_2E_2$ acts as a scaffold for the combination of NifBco with the putative MoS species to form FeMoco. NifH and MgATP (*98*) are apparently involved in this process, but NifH does not need to contain the Fe_4S_4 cluster, nor does it have to undergo the conformational change normally observed on binding MgATP. A study (*99*) has demonstrated that VnfH, the Fe protein from the vanadium nitrogenase, can function in place of NifH both in the *in vitro* biosynthesis of FeMoco and in the maturation of the "apo-MoFe protein." These data suggest that NifH is not involved specifically in the reaction of NifBco with the hetero-metal.
5. In the final stage of activation, FeMoco is bound to the "apo-MoFe protein." As noted previously, for this to happen the "apo-MoFe proteins" must be bound to NifY or γ. NifY or γ dissociate after the activation of the MoFe protein by FeMoco. The crystallographic structure demonstrates that FeMoco is eventually bound to Cys 275 and His 442 of the α subunit of the MoFe protein. Cys 275 in "apo-MoFe protein" reacts rapidly with alkylating agents, indicating that it is exposed to solvent, although in the holo-protein it is buried some 10 Å below the surface of the protein (*100*). These data imply that the role of γ (NifY) may be to hold the "apo-MoFe protein" in an open conformation that will allow access of FeMoco to its binding site. It has been suggested (*100*) that this might come about through a relative shifting at the domains in the α subunit, induced by interaction with the Fe protein and MgATP, and maintained in this conformation by interaction with γ (NifY).

Before leaving this section we should note that GroEL, a chaperonin, has been implicated in the biosynthesis of nitrogenase (*101*). Using ^{35}S pulse-chased experiments on the kinetics of nitrogenase synthesis, high molecular weight intermediates in MoFe protein assembly were identified, as was transient binding of newly synthesized

NifH and NifDK to GroEL. It is not clear from these data at which stage in the biosynthetic pathway just described GroEL might be involved in MoFe protein maturation, but it could be during P cluster insertion.

V. The Mechanism of Molybdenum Nitrogenase

A. The Lowe–Thorneley Mechanism

A comprehensive description of the mechanism of molybdenum nitrogenase has been provided by the Lowe–Thorneley scheme (*102*) (Figs. 8 and 9). In this scheme the Fe protein (with MgATP) functions as a single electron donor to the MoFe protein in the Fe protein cycle (Fig. 8), which is broken down into four discrete steps, each of which may be a composite of several reactions:

1. The reduced Fe protein · MgATP complex forms a complex with the MoFe protein
2. An electron is transferred from the Fe protein to the MoFe protein with concomitant hydrolysis of MgATP to MgADP and P_i
3. The oxidized Fe protein · MgADP complex dissociates from the reduced MoFe protein
4. The Fe protein is reduced by $Na_2S_2O_4$ and the MgADP is replaced by MgATP

In this cycle, step 3, the dissociation of the two proteins, is rate determining and is rate determining in the overall enzyme turnover.

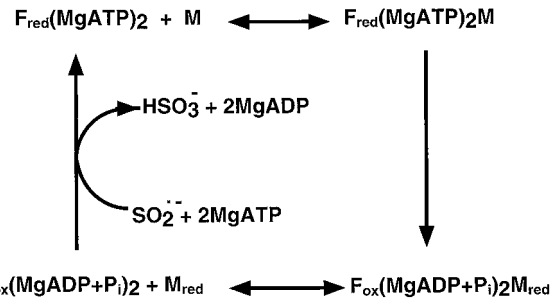

FIG. 8. The Fe protein cycle of molybdenum nitrogenase. This cycle describes the transfer of one electron from the Fe protein (F) to one $\alpha\beta$ half of the MoFe protein (M) with the accompanying hydrolysis of 2MgATP to 2MgADP + $2P_i$. The rate-determining step is the dissociation of F_{ox} $(MgADP)_2$ from M_{red}. Subscript red = reduced and ox = oxidized.

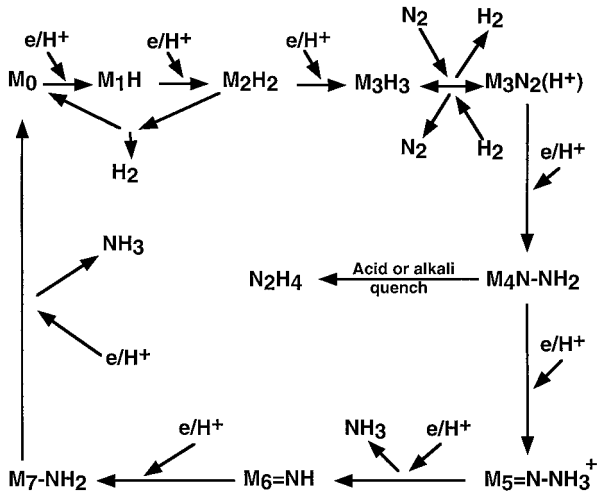

FIG. 9. The MoFe protein cycle of molybdenum nitrogenase. This cycle depicts a plausible sequence of events in the reduction of N_2 to $2NH_3 + H_2$. The scheme is based on well-characterized model chemistry (*15, 105*) and on the pre-steady-state kinetics of product formation by nitrogenase (*102*). The enzymic process has not been characterized beyond M_5 because the chemicals used to quench the reactions hydrolyze metal nitrides. As in Fig. 8, M represents an $\alpha\beta$ half of the MoFe protein. Subscripts 0–7 indicate the number of electrons transferred to M from the Fe protein via the cycle of Fig. 8.

Eight Fe protein cycles are required for the transfer of eight electrons from the Fe protein to the MoFe protein to reduce one N_2 molecule to $2NH_3$ with concomitant release of one H_2 molecule. These eight steps are shown in Fig. 9, which assumes that the kinetic constants of the Fe protein cycle are the same no matter what the redox state of the MoFe protein. This assumption has been shown to hold true for the first two steps of the MoFe protein cycle (*103*). Figure 9 was developed by analyzing the time dependence of the pre-steady-state release of H_2, N_2H_4, and NH_3 from acid-quenched reaction mixtures. There were substantial lags in the formation of all of these products, for example, a lag of 100 msec before H_2 evolution became linear; a lag of 250 msec in the development of the intermediate that gives rise to N_2H_4 on quenching the reaction with acid or alkali; and a lag of about 400 msec before linear production of NH_3 was observed. The levels of the intermediate giving rise to N_2H_4 rose to a maximum and then decreased slightly, in the steady state, to a level corresponding to about 12% of the total MoFe protein concentration.

These lags in product formation were interpreted in terms of repetitive slow steps in enzyme turnover, each slow step being equated to

one Fe protein cycle (Fig. 8), that is, each slow step was equated to the dissociation of the two proteins after the electron transfer. On this model the 100 msec lag was associated with two Fe protein cycles being needed before H_2 evolution could occur under an argon atmosphere. When this atmosphere was replaced with N_2, the time course of H_2 evolution was identical to that under argon until three Fe protein cycles had occurred. This indicated that N_2 could not bind to the MoFe protein until three electrons had been transferred from the Fe protein.

It is probable that the negative charge induced by these three electrons on FeMoco is compensated by protonation to form metal hydrides. In model hydride complexes two hydride ions can readily form an η-bonded H_2 molecule that becomes labilized on addition of the third proton and can then dissociate, leaving a site at which N_2 can bind (*104*). This biomimetic chemistry satisfyingly rationalizes the observed obligatory evolution of one H_2 molecule for every N_2 molecule reduced by the enzyme, and also the observation that H_2 is a competitive inhibitor of N_2 reduction by the enzyme. The bound N_2 molecule could then be further reduced by a further series of electron and proton additions as shown in Fig. 9. The chemistry of such transformations has been extensively studied with model complexes (*15*, *105*).

If N_2 is bound end-on, protonation occurs at the terminal nitrogen atom. Reduction by two electrons and protonation yields an M–N–NH_2 species (M = metal), which, when treated with acid or base, yields N_2H_4. Since N_2H_4, although not normally a product, is released from a bound intermediate in N_2 reduction by the enzyme, this chemistry seems to provide a reasonable model for that occurring on the enzyme. Further reduction and protonation of such chemical model species can yield NH_3 and a metal nitride (M≡N), which can in turn be reduced and protonated to yield a second NH_3 molecule. These later stages of the reaction have not been followed in the enzymic process as yet, since the quenching procedures used in the pre-steady-state reaction result in degradation of metal nitrides to NH_3. Nevertheless, the reaction sequence shown in Fig. 9 is chemically logical and has been demonstrated experimentally with model complexes and so is a feasible model for the overall enzymic reaction.

Thus, the Lowe–Thorneley scheme has proved extremely useful over the past 15 years. At the time it explained all available data on N_2 fixation by the enzyme, it has been predictive and allowed investigation of the reduction of other substrates, and it has been developed so that some of the steps shown in Figs. 8 and 9 have been broken down into more detailed reaction schemes that can still be encompassed within the overall mechanism. For example, the coupling of

MgATP hydrolysis and electron transfer between the two proteins seems not to be direct and the order of reactions may depend on the precise conditions of the experiment; at low temperature, electron transfer seems to be reversible (see Ref. (*12*) for a discussion). One innovation is incorporation of data in which the release of inorganic phosphate was monitored. With other MgATP hydrolyzing enzymes, this step is often the "work" step in which the energy released by MgATP hydrolysis is utilized. With nitrogenase this step takes place before the dissociation of the two proteins (*106*).

However, some data have been more difficult to incorporate into the mechanism shown in Figs. 8 and 9. As reported (*21*) in Section II,B the Fe protein can be reduced by two electrons to the $[Fe_4S_4]^0$ redox state. In this state the protein is apparently capable of passing two electrons to the MoFe protein during turnover, although it is not clear whether dissociation was required between electron transfers. More critically, it has been shown that the natural reductant flavodoxin hydroquinone (*107*) and the artificial reductant photoexcited eosin with NADH (*108*) are both capable of passing electrons to the complex between the oxidized Fe protein and the reduced MoFe protein, that is, with these reductants there appears to be no necessity for the complex to dissociate. Since complex dissociation is the rate-limiting step in the Lowe–Thorneley scheme, these observations could indicate a major flaw in the scheme.

The Lowe–Thorneley scheme was devised using sodium dithionite as reductant, but the foregoing data imply that when other reductants are used, including the natural reductants, the same path is not necessarily followed. It seems clear that some reinvestigation of the Lowe–Thorneley scheme using alternative reductants is necessary. However, the detailed simulation of product formation provided by the scheme implies that much of it is likely to remain intact, although the exact nature of the rate-determining step may not be the same with all reductants.

B. The Nitrogenase Complex

As noted in Section II,C parts of the primary sequences of Fe proteins have strong similarities to those of various GTPases and ATPases. With these enzymes, aluminum fluoride (AlF_4^-)[3] has been

[3] The author is aware that in aqueous solution Al^{3+} and F^- form several complexes, but these are represented here as AlF_4^- for simplicity.

used as an analog of phosphate together with GDP or ADP to trap putative intermediates. Two groups (*109*, *110*) discovered that AlF_4^- acts as a potent inhibitor of nitrogenase and were able to isolate a 2 : 1 Fe protein : MoFe protein complex from Av1 + Av2 with MgADP/MgATP and AlF_4^-. This putative "transition state" complex is proving extremely useful in the analysis of the interactions between the two proteins and nucleotides.

Model-independent analysis (*111*) of small-angle X-ray scattering data collected using synchrotron radiation with such a complex formed from *K. pneumoniae* nitrogenase demonstrated that the complex had a 2 : 1 Fe protein : MoFe protein structure in solution and that the interaction of Kp2 with Kp1 was consistent with that predicted through modeling studies (*8*) on the three-dimensional structures of the individual proteins. These modeling studies utilized data from a range of site-directed mutagenesis and chemical cross-linking experiments and predicted docking of the "top" surface of the Fe protein, which includes the Fe_4S_4 cluster, with the $\alpha\beta$ subunit interface of the MoFe protein. This conformation placed the Fe_4S_4 cluster of the Fe protein about 18 Å from the P cluster of the MoFe protein, which in turn is about 14 Å (edge to edge) from FeMoco, and thus firmly placed the P clusters on the electron transfer route to FeMoco from the Fe protein.

Subsequently, the three-dimensional crystallographic structure, at 3 Å resolution (*112*), of this putative transition state complex was reported. This confirmed the predicted overall structure but demonstrated that the Fe protein had undergone substantial conformational changes. Interestingly, the crystal structure provided a better fit to the profile deduced from the low angle scattering data than did the predicted docking model. This observation demonstrates the power of analysis of the scattering data (*111*). The result (*112*) of these conformational changes in the Fe protein structure was that the Fe_4S_4 moved closer to the P cluster with about 14 Å separating the closest atom-to-atom distances, i.e., the P cluster in the complex is approximately equidistant between the Fe protein Fe_4S_4 cluster and FeMoco (Fig. 10). This change was brought about by an apparent 13° rotation of each Fe protein monomer towards the subunit interface, resulting in a more compact quaternary structure in the complex and shifting the Fe_4S_4 cluster approximately 4 Å toward the Fe protein surface in the complex. This rotation also resulted in a new dimer interface involving interactions between a number of highly conserved residues. Within the complex, two $ADP \cdot AlF_4^-$ molecules were bound per Av2 dimer, with each nucleotide associated largely with one monomer and

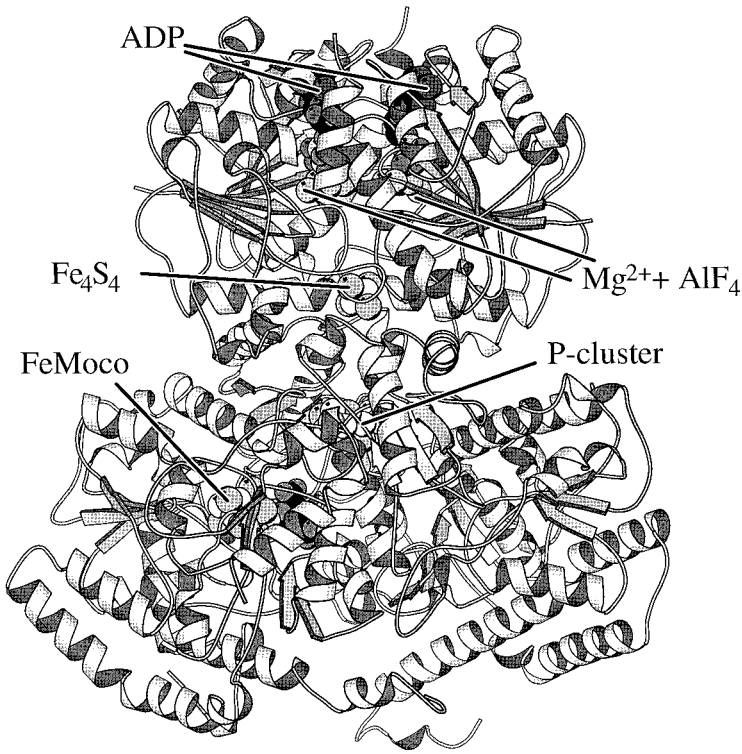

FIG. 10. The putative "transition-state" complex formed between the Fe protein: MgADP · AlF_4^- and the MoFe protein. For simplicity only one $\alpha\beta$ pair of subunits of the MoFe protein is shown. The polypeptides are indicated by ribbon diagrams and the metal–sulfur clusters and MgADP · AlF_4^- by space-filling models (MOLSCRIPT (*196*)). The figure indicates the spatial relationship between the metal–sulfur clusters of the two proteins in the complex.

bound roughly parallel to the dimer interface. This nucleotide conformation differs from that observed in the isolated Fe protein (*1*) with partial occupancy by ADP where the ADP straddled the subunit interface (Section II,A).

Studies (*113*) on Fe protein with an Asp39Asn mutation in the nucleotide binding site indicate that the conformational change observed in the crystal structure of the complex is dependent on electron transfer from the Fe protein to the MoFe protein.

A further important discovery has resulted from studies on complex formation (*114*). With *K. pneumoniae* nitrogenase it has been shown that the MoFe protein containing a full complement of metal is com-

plexed more slowly than that containing only half its full complement, that is, one FeMoco and one P cluster per tetramer. These data demonstrate that MoFe protein that has only one FeMoco binding site occupied has an altered conformation compared with the protein with both FeMoco sites filled. The Fe protein reacts with these different conformations at different rates to form the stable putative transition-state complexes. These data confirm an earlier hypothesis based on Mössbauer spectroscopy, where it was observed that all MoFe protein preparations had the same ratio of iron species present no matter what their total iron content. These data were interpreted (*40*) in terms of an all-or-none hypothesis in which it was suggested that MoFe proteins contain all, or exactly half, or none of their total metal content.

Only limited studies on the nature of the nitrogenase proteins within the complex have yet been carried out. Formation of the complex is reversible with a very long half-life of approximately 20 h (*109*, *110*) and thus the complex can be isolated and studied. There has been a study (*115*) of redox potentials of the metal clusters within the complex, but instead of the $ADP \cdot ALF_4^-$ complex described previously, this study used one that is formed between a mutant of the Fe protein with Leu 127 deleted (*29*). This Fe protein has properties much like the wild-type Fe protein complex with MgATP and forms a nondissociating nitrogenase complex with the MoFe protein. Redox studies on this complex showed that the midpoint potential of the Fe_4S_4 cluster was decreased by 200 mV to −620 mV in the complex. It is clear from these studies that in addition to the observed decrease in potential, it is possible to reduce the oxidized Fe_4S_4 cluster within the complex. In addition, the redox potential of the P cluster was lowered by about 80 mV to −380 mV within the complex, but no significant change in the redox potential of the FeMoco centers was observed.

From the crystal structure of the complex (Fig. 10) it appears that only minimal conformational changes occur within the MoFe protein on complexation, although it is hard to be dogmatic about these when at 3 Å resolution. Nevertheless, ENDOR (*116*) studies on the FeMoco center demonstrated that at least one class of protons in the vicinity of the FeMoco center is altered in the complex relative to the free protein.

C. The Role of MgATP Hydrolysis

Despite intensive efforts by many groups the roles of MgATP hydrolysis in nitrogenase turnover is still enigmatic. MgATP binds to both

proteins, although as noted earlier (Section III,C,2), the interaction with the MoFe protein may not be associated with catalysis, but rather with biosynthesis. Binding MgATP to the Fe protein induces a conformational change and a change in the redox potential of the Fe_4S_4 cluster (Section II,C). However, the binding of the inhibitor MgADP results in similar effects. Two MgATP molecules are hydrolyzed to MgADP and inorganic phosphate for every electron transferred to substrate when the enzyme is working at its greatest efficiency. This apparent coupling of MgATP hydrolysis to electron transfer can be readily uncoupled by changing the component ratio or the temperature of the reaction. There is evidence from the ΔLeu127 mutant of the Fe protein, which has a conformation similar to that induced by binding MgATP (*29*), that MgATP is unnecessary for electron transfer from the Fe protein to the MoFe protein, although the complex formed is inactive in catalysis. Pre-steady-state stopped-flow spectrophotometric studies (*117*) have indicated that electron transfer may precede MgATP hydrolysis in the functioning complex. All of these data imply that the energy released by MgATP hydrolysis is not required for protein–protein electron transfer. However, the MgATP-induced conformation of the Fe protein is apparently required for its effective binding to the MoFe protein.

Nevertheless, MgATP is required for nitrogen fixation by nitrogenase and its hydrolysis, at normal rates, requires both the Fe and the MoFe protein (much slower hydrolysis reactions with the isolated proteins and both MgATP and MgADP have been observed) (*30*, *51*, *52*). The exact point during the catalytic cycle when MgATP is hydrolyzed has not been determined. Proton release, which is probably associated with MgATP hydrolysis, has been observed to have a rate constant of $14 \pm 4\ s^{-1}$ at 20°, far slower than protein–protein electron transfer, which occurred at the rate of $100\ s^{-1}$. Phosphate release from the enzyme, which must come after MgATP hydrolysis, occurs at a rate of $22\ s^{-1}$ at 23°C and a change in absorbance at 430 nm with a rate constant of $6.6 \pm 0.8\ s^{-1}$, but preceding protein–protein dissociation has also been observed.

Thus, current evidence implies that MgATP hydrolysis occurs later than electron transfer during nitrogenase turnover. What, then, is its purpose? Two possibilities have been suggested. One is that the hydrolysis is necessary to induce a further conformational change in the Fe protein that will allow the complex to dissociate to allow the Fe protein to be rereduced. The second suggestion is that the conformational change induced by hydrolysis is transmitted to the MoFe protein and in some way "gates" an electron transfer within the MoFe

protein from the P clusters to FeMoco and possibly thence to substrates. The first of these possibilities seems unlikely, since it would be biologically inefficient to utilize so much energy simply to allow dissociation of electron transfer partners. Therefore, it seems much more probable that protein–protein interaction is critically important and that the energy expended in hydrolyzing two molecules of MgATP for every electron transferred is required for some critical process within the MoFe protein.

D. Electron Transfer within the MoFe Protein

Electrons transferred from the Fe protein to the MoFe protein appear very rapidly on the FeMoco center, causing the loss of intensity of the $S = \frac{3}{2}$ EPR signal (*118*). In ^{57}Fe Mössbauer studies, no changes in the components in the spectra associated with the P clusters were observed, and thus the role of P clusters in electron transfer within the MoFe protein was obscure. The three-dimensional X-ray crystallographic structure of the putative transition state complex (*112*) clearly places the P clusters on the electron transfer pathway between the Fe_4S_4 cluster of the Fe protein and the FeMoco center. However, there is currently only one spectroscopic observation that supports this view (*119*). Optical changes occurring during the first 600 ms of turnover have been correlated with EPR spectra with g values near 5.4 and 5.7. These spectroscopic changes were only observed under an argon or N_2 atmosphere and not under C_2H_2 or CO. The EPR signals were attributed to Fe clusters in an $S = \frac{7}{2}$ state. An $S = \frac{7}{2}$ spin state can be observed in P clusters that have been oxidized to above +90 mV (*42*). However, it is unlikely that this is the state being observed in these experiments. It is much more likely that the signals arise from the one-electron oxidized P clusters that in the isolated protein give rise to $S = \frac{1}{2}$ or $\frac{5}{2}$ spin states (*42*, *43*). Thus, under argon or N_2, the P clusters seem to become transiently oxidized during turnover. This observation was rationalized (*119*) in terms of the P clusters transferring electrons to FeMoco when bound N_2 is irreversibly committed to being reduced and is protonated to the hydrazide (2-) level, that is, M–N–NH_2, as in Fig. 9.

Additional evidence that there is an intermediate step in the electron transfer from the Fe protein to the FeMoco center was obtained by perturbing the reaction by increasing the salt level (*120*). In the presence of salt, a lag period was observed before the FeMoco was reduced but after the Fe protein was oxidized, and it was proposed

that the electron transfer to FeMoco consisted of two steps: (1) electron transfer from the Fe protein to an unidentified site on the MoFe protein, followed by (2) transfer from that site to the FeMoco.

There has been an attempt (*121*) to perturb electron transfer from P clusters to FeMoco by modifying Tyrβ98, which is on a helix that spans the distance between the P cluster and FeMoco, but does not directly contact either the P cluster or FeMoco. Mutating this residue to His resulted in a significant increase in diazotrophic growth doubling time and a significantly reduced maximal specific activity for N_2 fixation, H_2 evolution, and C_2H_2 reduction by the isolated enzyme. These data are consistent with electrons being transferred through the protein between the P clusters and FeMoco.

E. Substrates and Inhibitors

1. Substrate Reduction

Nitrogenase is a relatively promiscuous enzyme, and a wide range of neutral and anionic substrates containing NN, NO, NC or CC (*122–124*) and more recently (*125*, *126*) CO and CS triple or double bonds have been identified (Table II). Hydrazine is the only single-bonded substrate known. All products require the enzyme to supply multiples of two electrons with two protons. Reactions requiring between 2 and 14 electrons have been described. Some substrates give multiple products, and at high electron flux (which can be generated by increasing the ratio of Fe protein to MoFe protein) products requiring larger numbers of electrons are favored. For example, high electron flux favors N_2 reduction over H_2 evolution with up to a maximum of 75% of the electrons going to form ammonia. Mainly the six-electron products, methane and ammonia, are produced from HCN, but some two- and four-electron products can be observed. This variation in the product distribution with electron flux implies that any site-directed mutagenesis of either protein that changes the rate of electron transfer is likely to change the product specificity of the mutant. It is important to note this and not to interpret such results as directly affecting the enzyme's active site.

Early data on the substrate and inhibitor reactions of nitrogenase were interpreted in terms of five binding sites, with competitive, noncompetitive, unclassified, and negative inhibition being observed (*127*). This apparent complexity can be readily rationalized in terms of the Lowe–Thorneley scheme (Fig. 9) by assuming that different substrates bind at different oxidation states of the same site.

TABLE II

REACTIONS CATALYZED BY NITROGENASES[a]

$N_2 + 8H^+ + 8e \longrightarrow 2NH_3 + H_2$
$(N_2 + 12H^+ + 12e \longrightarrow 2NH_3 + 3H_2)$

$C_2H_2 + 2H^+ + 2e \longrightarrow C_2H_4$
$(C_2H_2 + 4H^+ + 4e \longrightarrow C_2H_6)$

$2H^+ + 2e \longrightarrow H_2$

$HCN + 6H^+ + 6e \longrightarrow CH_4 + NH_3$
$HCN + 4H^+ + 4e \longrightarrow CH_3 + NH_2$

$HN_3 + 6H^+ + 6e \longrightarrow N_2H_4 + NH_3$
$N_3^- + 3H^+ + 2e \longrightarrow N_2 + NH_3$

$N_2O + 2H^+ + 2e \longrightarrow N_2O + H_2O$

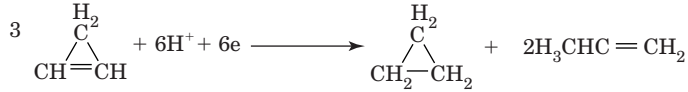

$NO_2^- + 7H^+ + 6e \longrightarrow NH_3 + 2H_2O$
$COS + 2H^+ + 2e \longrightarrow CO\ H_2S$
$CO_2 + 2H^+ + 2e \longrightarrow CO + H_2O$

[a] Parentheses indicate reactions catalyzed by the alternative nitrogenases. Data taken from reviews (*13, 123, 124*) and Ref. (*125*).

The pH dependence of nitrogenase activity has been interpreted in terms of a group with a $pK_a = 6.3$ that must be deprotonated for activity and another group with a $pK_a = 9$ that must be protonated for activity (*128*). The pK_a of the latter group was moved about 0.5 pH units more acid in the presence of acetylene and carbon monoxide and the group with the pK_α of 6.3 was moved about 0.4 pH units more acid by acetylene. The behavior of the group with the pK_a of 9 is fully consistent with earlier observations (*50*) on the effect of acetylene on

the pH dependence of the form of the EPR signal from the isolated MoFe protein (see Section III,C,1). The authors (*128*) proposed that these p*K* values are associated with amino acid residues close to the active site.

In the presence of the product ethylene during turnover the MoFe protein exhibits an EPR signal, with *g* values at 2.12, 1.998, and 1.987 (*129*), which has been demonstrated to arise from FeMoco in an $S = \frac{1}{2}$ spin state (*130*). However, direct interaction of the ethylene with the metal–sulfur cluster was not demonstrated.

CO is a potent, noncompetitive inhibitor of N_2 reduction but is not reduced itself. Under turnover conditions, two distinct EPR signals can be observed from the enzyme under CO. At low partial pressures of CO a signal with *g* values of 2.09, 1.97, and 1.93 is seen and is replaced under higher CO partial pressure by a signal with *g* values of 2.17, 2.06, and 2.06 (*129*, *131*, *132*). Neither of these signals shows broadening in the presence of ^{13}CO, but ENDOR spectroscopy detected signals in the presence of ^{13}CO and not ^{12}CO (*133*). ^{57}Fe ENDOR spectroscopy showed that these EPR signals arose from the FeMoco center (*134*). The ^{13}C ENDOR data were interpreted (*133*, *135*) in terms of the low CO signal arising from FeMoco with a single CO bound and the high CO signal from FeMoco with a second CO molecule bound. It was suggested that under high CO the two CO molecules were terminally ligated to FeMoco, but that the single CO, bound under low CO, might possibly bridge two iron atoms of FeMoco.

A new technique of stopped-flow Fourier transform infrared spectroscopy (SF FTIR) has been applied to nitrogenase (*136*). This technique has the potential to monitor vibrations associated with bound small molecules directly. During turnover under high CO conditions, three time-dependent infrared bands were observed: a relatively intense band at 1935.6 cm^{-1} and two smaller bands at 1958 and 1906 cm^{-1}. These bands were all confirmed as arising from CO by isotopic substitution with ^{13}CO. The time-dependent behavior of the bands was very different. The intensity of the 1906 cm^{-1} band rose rapidly, peaked at about 7 or 8 s, and then decayed rapidly, whereas the peak at 1935.6 cm^{-1} peaked at 55 s, and that at 1958 cm^{-1} at 100 s. These latter two both decreased slowly with time. Under low CO conditions a single band at 1904 cm^{-1} was observed that exhibited the same time-dependent behavior as the high CO 1906 cm^{-1} band. An analysis of carbonyl complexes (*137*) reported that complexes with bridging CO have carbonyl stretching frequencies between 1785 and 1898 cm^{-1} and those with terminally bound carbonyl residues have stretching frequencies between 1718 and 2128 cm^{-1}. On this basis, the peak at

1904 cm^{-1} is probably from a terminally bound CO, but it is also at the margin of the bridging CO range.

Certainly, all three of the bands observed with SF-FTIR must arise from different species, since they appear and disappear with different time courses. The peak at 1904 cm^{-1} probably corresponds with that observed by ENDOR under low CO conditions, but the relationship of the other two bands to those observed under high CO is not clear, since the ENDOR technique will only detect CO molecules bound to paramagnetic species, whereas FTIR should detect all species. The SF-FTIR technique has the potential to observe the binding and reduction of a wide range of nitrogenase substrates, provided that the appropriate spectroscopic range can be accessed. This will be technically difficult, but well worth the effort.

2. Where Do Substrates Bind on FeMoco?

a. Evidence from Site-Directed Mutants FeMoco is bound to the protein only by Cys 275 to the terminal tetrahedral iron and by His 442 to the molybdenum atom (Fig. 4). However, it is clear that the polypeptide environment of FeMoco is important for its activity. For example, extraction of FeMoco from the protein yields an intact metal–sulfur cluster with bound homocitrate, but which is inactive in substrate reduction. Furthermore, mutating a number of amino acids in the environment of FeMoco has radical effects on substrate reduction activity. Figure 11 shows FeMoco and its immediate amino acid neighbors. Mutation of Arg 96 to Gln generates a strain that grows slowly diazotrophically, but mutation of Arg 359 to Gln or Phe 381 to Arg results in strains that cannot grow on N_2 (*138*). Phe 381 is close to the bridging sulfurs in FeMoco. Arg 277 is close to Cys 275, a ligand to FeMoco, and plays an important part in FeMoco activity (*139*). Mutating it to His yields a mutant that does not reduce N_2 but does reduce acetylene, cyanide, azide, and protons. The activity of this Arg227His mutant MoFe protein under nonsaturating CO was interpreted in terms of there being two acetylene reduction sites. Furthermore, CO inhibition was different from cyanide inhibition of acetylene reduction. These results imply that there are multiple binding and reducing sites on FeMoco. Mutation of Gln 191 to Lys yields a mutant that is unable to reduce N_2 but can reduce aetylene to ethylene and also to ethane (*140, 141*). In addition, CO inhibits H_2 evolution with this mutant.

Probably the most interesting mutant discovered thus far is His195Gln (*140*). Mutating His 195 to other amino acids yields a phenotype much like the Gln191Lys mutation; however, mutation to Gln

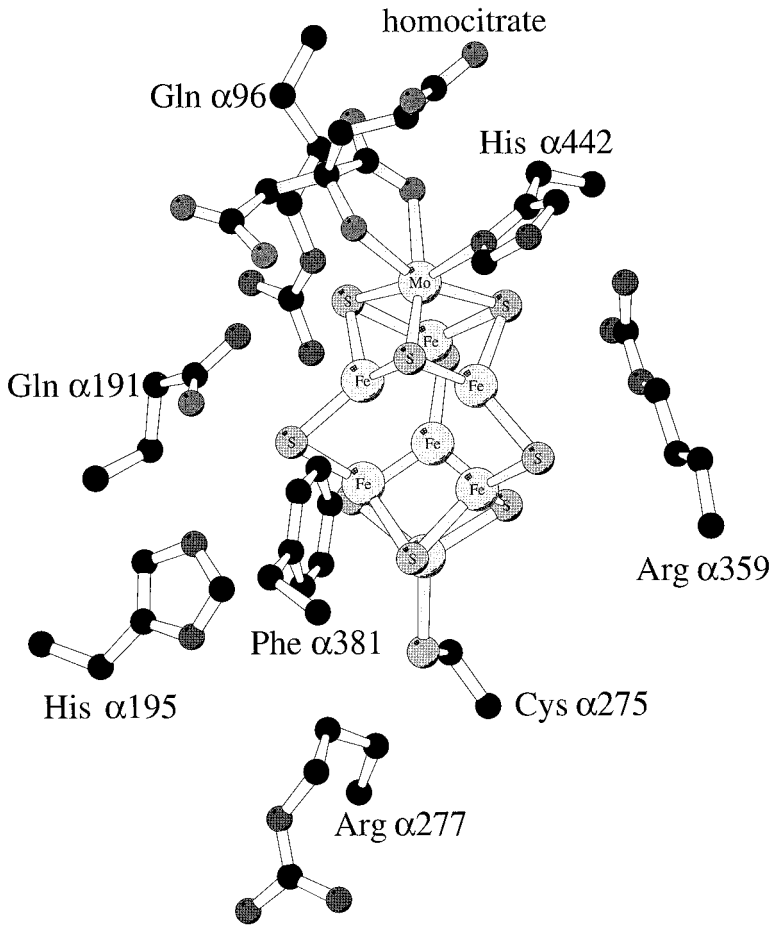

FIG. 11. FeMoco, its ligands, and some surrounding amino acids, mutagenesis of which causes changes in substrate specificity.

yields a fascinating phenotype where N_2 is not reduced but can inhibit acetylene and proton reduction (*142*). This must mean that the N_2 can bind but is not reduced. The three-dimensional structure of the MoFe protein indicates that there is likely to be a hydrogen bond from the nitrogen of His 195 to a bridging sulfur. Substitution by Gln could probably retain this hydrogen bond, but other substitutions would not. These data indicate that this hydrogen bond is important for N_2 binding and probably for the positioning of FeMoco to make it accessi-

ble to substrates and particularly N_2. The authors postulate that the hydrogen bond stabilizes an early intermediate in N_2 reduction.

b. Theoretical Predictions Since publication of the structure of FeMoco, there has been a wide range of theoretical calculations attempting to predict the mode of N_2 binding and the mechanism of its reduction. These calculations have focused solely on the central iron sites in FeMoco. There are reasonable arguments to support this bias: First, the common factor between all three nitrogenase cofactors is that they contain iron; second, the molybdenum atom in FeMoco is apparently coordinatively saturated; and third, the central iron atoms within FeMoco are apparently coordinatively unsaturated. However, this reasoning ignores two important factors. First, there is now a huge literature on the feasibility of binding N_2 and reducing it at the molybdenum site, and it is well known that the molybdenum can become seven or eight coordinate so that the apparent coordinate saturation of molybdenum in FeMoco need not rule out molybdenum as the site of N_2 binding (*15, 105*). A second, more telling argument arises from model studies, which have revealed that reduction and protonation of molybdenum sites with carboxyl ligands can lead to dissociation of the carboxyl groups to yield a site where N_2 can combine followed by H_2 evolution (*143*). This would accord precisely with the stoichiometry observed for N_2 reduction and H_2 evolution by nitrogenase and would rationalize the need for the puzzling homocitrate ligand on the molybdenum atom. Under this model the carboxyl group of the homocitrate would dissociate from the molybdenum atom, leaving it still tethered by its hydroxyl group. N_2 reduction chemistry could then take place at the molybdenum site in a manner similar to that established with model complexes.

However, theoretical studies have thus far mainly ignored this possibility and focused on the apparently unsaturated iron atoms at the center of the cofactor. A range of theoretical methods has been used. Extended Hückel calculations (*144*) favor binding of N_2 in an end-on fashion with one N atom bound to four Fe atoms on one of the central faces of FeMoco. These calculations also indicate that there is extensive metal–metal bonding within the cluster and that the highest occupied molecular orbital (HOMO) is a singly occupied orbital in the approximate center of a block of iron 3*d* orbitals. Three-electron reduction of the cluster to generate a state that will bind N_2 did not dramatically affect the electron density at N_2, since the three electrons go into the block of 3*d* orbitals, which has little effect on N_2 binding.

Ab initio density functional calculations (*145, 146*) also predict extensive metal–metal bonding within the cluster, but favor side-on binding of N_2 to four Fe atoms on the face of the trigonal cavity. In this model flexing of the cofactor cluster is brought into play to assist in twisting and breaking the N–N bond. These calculations indicate that the bridging sulfur atoms absorb redox changes.

Intermediate neglect of differential overlap (INDO) calculations suggest that N_2 binds within the cofactor between the trigonal iron atoms (*147, 148*). Unfortunately, N_2 is 0.5 Å too large to fit into the cavity with FeMoco in its semireduced state, and so some expansion of the cavity would be necessary before binding could occur. Protonation of N_2 would make this situation worse. EXAFS data (*149*) have been interpreted in terms of one-electron reduction causing a decrease in the volume of the cluster; however, more recent results from the author and colleagues (*150*) detected no change in FeMoco dimensions on reduction. In either case there is certainly no indication of expansion of the cavity on reduction as would be required for N_2 to bind and be reduced.

Semiempirical complete neglect of differential overlap (CNDO) calculations indicate that N_2 can bind within the cavity, but with one nitrogen atom at the center and one on the outside, that is, the N_2 would bind end-on to the cluster (*151*). CNDO and INDO calculations suggest that the bridging sulfur atoms would act as proton carriers. Later INDO calculations (*148*) suggest a model with one N atom bound by the iron atoms while the other is close to the three bridging sulfur atoms, which could each denote a proton. This would then result in cleavage of the N–N bond and the release of NH_3, followed by similar protonation of the remaining nitrido species. This mechanism is very similar to that which has been developed on molybdenum phosphine complexes (*15, 105*), the only difference being the nature of the site that binds the terminal N. A further indication from these studies was that electron addition could lead to changes in molybdenum coordination, yielding a site at which N_2 could bind. This suggestion is fully in concert with the experimental observations on molybdenum carboxyl complexes (*143*) discussed previously.

c. Reactions of Isolated FeMoco The Lowe–Thorneley scheme predicts that FeMoco must be reduced by at least two electrons from its dithionite-reduced state before it can reduce any of its substrates. When extracted from the MoFe protein into NMF, FeMoco exhibits the $S = \frac{3}{2}$ signal, although broadened relative to the signal in the protein, consistent with it being in the normal dithionite-reduced

state (*33*). FeMoco can be oxidized and also possibly reduced electrochemically by one electron from this state (*152*), but substrate reduction by this one-electron reduced state has not been established.

There are reports (reviewed in Ref. (*33*)) of acetylene reduction by FeMoco using very powerful reductants such as sodium borohydride or sodium amalgam. Unfortunately, in most of these experiments the integrity of FeMoco after reaction was not established, and thus the reaction could have been carried out by fragments of FeMoco. Reduction of acetylene bound to a metal site by powerful reductants is well established.

There have been numerous investigations of the binding of ligands to FeMoco. As isolated, FeMoco lacks the amino-acid ligands tethering it to the protein; therefore, there are vacant coordination sites on these two atoms that can be taken up by other ligands. FTIR spectroscopy indicated that the NMF anion is bonded to extracted FeMoco through the nitrogen atom (*153*). Reaction with thiols can be monitored through a sharpening of the EPR signal to more closely resemble that of the cofactor in the protein. Careful titration reveals that one molecule of thiol binds to each molecule of FeMoco (*154*). If the thiol is replaced by selenol, then once again one selenol binds per FeMoco and iron and selenium EXAFS spectroscopy of the resultant complex reveals that the selenium binds to iron (*155, 156*). By inference, the thiols must also bind to iron, almost certainly to the terminal tetrahedral iron atom. The histidine analog imidazolate also binds to FeMoco and sharpens the EPR spectrum (*157*). Presumably, in this case it binds to the molybdenum atom, although this has not been confirmed.

Of the reducible substrates of nitrogenase, the binding of cyanide has the most dramatic effect on FeMoco, resulting in a considerable sharpening of the EPR spectrum (*158*). Titrations reveal that more than one cyanide ion seems to bind per FeMoco molecule. These data are puzzling because Job plots of the titrations indicate that 1.5 cyanide ions bind per molybdenum atom, and thus may imply that FeMoco in solution is a dimer that binds three cyanide ions. Alternatively, the fault could lie in the Job plot analysis, which assumes equivalent binding constants for multiple ligands. If one cyanide ion binds tightly and the other much more weakly, then the data may be explicable. It seems clear that one of the cyanide ions binds at the terminal tetrahedral iron atom in competition with thiol. This competition can be monitored using EPR spectroscopy, and at approximately equal concentrations thiol binding is favored. EXAFS studies on FeMoco have identified cyanide binding to molybdenum (*37*),

which therefore presumably provides the second cyanide binding site.

EPR investigations are necessarily carried out in frozen solution at low temperature. Room temperature binding of thiols to FeMoco has been monitored by ^{19}F NMR spectroscopy using p-$CF_3C_6H_4S^-$ as the reporter ligand. These experiments revealed that the binding of thiolate is characterized by a dynamic equilibrium between the FeMoco and thiolate (*159*) and that cyanide and methyl isocyanide can bind to isolated FeMoco complexed with thiol (*160*).

A novel kinetic method has been developed to identify substrate binding sites on isolated FeMoco (*161*). The principal reaction used in this approach is the substitution, at the tetrahedral iron atom, of bound NMF by thiol, causing an optical change that can be studied by stopped-flow spectrophotometry. The rate of this reaction is independent of the concentration of thiol, implying a mechanism involving rate-limiting dissociation of NMF. If other molecules are bound to the cluster, they will perturb the overall electron distribution, and this will in turn affect the lability of the iron–NMF bond. The extent of this labilization indicates where the ligand binds relative to the site of thiol substitution. A ligand binding close to or at the tetrahedral iron atom would cause a large perturbation, whereas a smaller perturbation would be expected from a ligand binding close to or at the molybdenum atom.

Perturbations to the rate were observed with azide, *t*-butyl isocyanide, cyanide, imidazole, and protons, but not with acetylene or CO. It was concluded that these last two molecules did not bind tightly to isolated cofactor in the $S = \frac{3}{2}$ state. Consistent with the EPR and EXAFS studies, cyanide was found to bind both at the tetrahedral iron and at a site remote from it, probably the molybdenum atom. Cyanide was the only ligand to bind at more than one site. Data obtained with azide, *t*-butyl isocyanide, and imidazole were consistent with these ligands binding at the molybdenum end of FeMoco. Interestingly, when imidazole was the ligand, the acceleration was dependent on the concentration of thiolate ligand. These data were interpreted as the thiolate acting not only as a nucleophile to FeMoco, but also as a base that could deprotonate imidazole, with the rate of the substitution reaction with thiolate being sensitive to the state of protonation of the coordinated imidazole.

Earlier studies (*162*) on synthetic iron–sulfur-based clusters showed that protons bind to the bridging sulfur atoms and increase the rate of substitution at the metal atoms. FeMoco exhibits similar behavior, with protonation causing considerable acceleration in the

rate of thiol substitution. This large acceleration suggested that the protonation is at a bridging sulfur atom close to the tetrahedral iron atom.

In an extension of this work, the reactivities of wild-type and NifV$^-$ FeMoco have been compared (*163*). NifV$^-$ FeMoco from *K. pneumoniae* nitrogenase has citrate rather than homocitrate bound to the molybdenum atom (*78*). No differences were observed between the reactivities of wild-type and NifV$^-$ FeMocos with thiol when they were complexed with cyanide, azide, or protons. However, when imidazole was bound, the kinetics of the reactions of thiol with the two cofactors were very different. These data were interpreted in terms of (*R*)-homocitrate, but not citrate, hydrogen bonding to the imidazole ligand on molybdenum, thus perturbing the electron distribution within the cluster and hence its reactivity with thiol, that is, hydrogen bonding of homocitrate to imidazole gives it imidazolate character.

However, when the X-ray crystal structure of the MoFe protein was examined, it was clear that homocitrate could not directly hydrogen bond to the histidine, since the carboxylate group and imidazole are stacked parallel to each other in the crystal. Nevertheless, as noted in the previous section, studies on model complexes have suggested that homocitrate can become monodentate during nitrogenase turnover, with the molybdenum carboxylate bond breaking to open up a vacant site at molybdenum suitable for binding N_2.

Using a molecular modeling approach it was established that monodendate homocitrate was able to establish a hydrogen bond between the carboxylate group of the $CH_2CH_2COO^-$ and the NH group of His α442 without the imidazole group changing its orientation. In the crystal structure the $CH_2CH_2CO_2^-$ arm of homocitrate hydrogen bonds to Ile α425. This bond would be broken by the rotation of homocitrate necessary to hydrogen bond to the histidine. However, a new hydrogen bond can be formed to a side-chain nitrogen of the next protein residue, Lys α426, which is conserved in all known nitrogenases. The proposed rotation in homocitrate does not substantially perturb the other hydrogen bond between the short CH_2CO_2 arm of the homocitrate and the side-chain nitrogen of Gln α191. Site-directed mutagenesis experiments (*140*) have established that Gln α191 is essential to nitrogen fixation (Section V,E,2,a).

Forming a hydrogen bond between (*R*)-homocitrate and His 442 could effectively release electron density into the cluster. Studies on structurally defined N_2 complexes have shown that the binding of N_2 to a metal site and its ability to be protonated are favored by electron-rich sites. Thus, it is postulated that the electron-richness of the

FeMoco could be affected by switching the hydrogen bonding of homocitrate, thus favoring N_2 binding and reduction. This model explains in a very attractive way the absolute requirement for (*R*)-homocitrate for N_2 reduction by the enzyme. When (*R*)-homocitrate is replaced with citrate, the hydrogen bonding to the histidine cannot be achieved, and thus the enzyme is a very poor nitrogen fixer.

d. Conclusions It is clear from the foregoing that there is as yet no consensus on where N_2 might bind to FeMoco during turnover. It is of course possible that N_2 can bind in one mode and during its reduction rotate to form other interactions, and so there is the possibility that everybody is right. There are many documented examples of N_2 binding to molybdenum and being activated for reduction, and there are others where it binds to single iron atoms and can be reduced. Furthermore, there are examples of N_2 bound between two metals being reduced to ammonia, although the complexity of the multicenter interactions suggested by some theoretical calculations has not yet been observed with model complexes. It is clear that perturbations in the vicinity of one part of FeMoco are transmitted throughout the cluster, and therefore site-directed mutagenesis experiments must be interpreted with great care.

Spectroscopic developments such as stopped-flow FTIR may allow direct observation of the binding and reduction of substrates during turnover, and this may help to narrow down the possible pathways of substrate reduction. However, the complexity of the interactions of substrates with nitrogenase is such that it would probably be unwise to extrapolate from the behavior of any other substrate to that of N_2. Only direct observations of N_2 binding and reduction will solve this problem.

VI. The Alternative Nitrogenases

In 1980 Bishop and co-workers suggested that molybdenum may not be essential for nitrogen fixation by the bacterium *Azotobacter vinelandii* (*164*). This idea was not widely accepted at first, but was established beyond question when the structural genes *nifK*, *D* and *H* for molybdenum nitrogenase in *Azotobacter* were deleted and the resulting deletion strains shown capable of fixing N_2 in the absence of molybdenum (*165, 166*). Subsequently, vanadium was shown to stimulate diazotrophic growth of such strains, and later the existence of a third nitrogenase system in *A. vinelandii* was demonstrated when it

was grown under both molybdenum and vanadium limitations (*167*). Molecular genetics studies have shown that molybdenum-independent nitrogenases are quite widely distributed among diazotrophs, but biochemical studies have been restricted to the vanadium nitrogenases from *A. chroococum* and *A. vinelandii* and the Fe nitrogenases for *A. vinelandii* and *Rhodobacter capsulatus.*

A. Biosynthesis of the Vanadium and Iron-Only Nitrogenases

Figure 12 shows the nitrogen fixation genes detected in *Azotobacter vinelandii* (*168*). This organism has genes responsible for three nitrogenases: the molybdenum, vanadium, and Fe-only nitrogenases. The proteins involved in these systems are encoded by respectively the *nif*, *vnf*, and *anf* genes. As indicated in Fig. 12, some of the *nif* genes, *nifB*, *nifM*, *nifS*, *nifV*, and *nifU*, are required for the biosynthesis of all three nitrogenases (see Ref. (*13*) for a review). Nevertheless, each enzyme has a separate activator gene, *nifA*, *vnfA*, and *anfA*, and separate genes encoding the structural polypeptides. Expression of the *vnf* and *anf* systems is inhibited by molybdenum, that is, in its presence only the molybdenum nitrogenase is synthesized. In the absence of

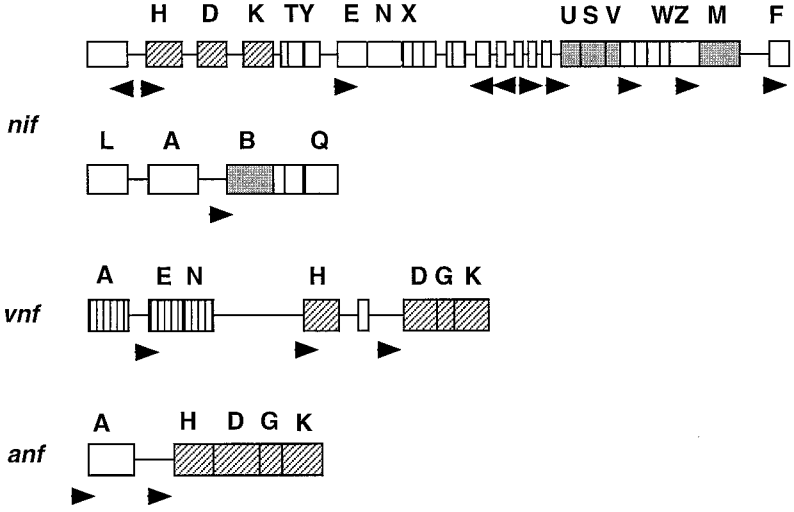

Fig. 12. The nitrogen fixation genes of *Azotobacter vinelandii*. This organism has three nitrogenase systems, *viz nif*, *vnf*, and *anf*, which it uses for fixing N_2 under different environmental conditions. The boxes with slanted hatching indicate the structural genes of the three systems, those colored dark gray are required for all three systems, and those with vertical hatching are required for both the *vnf* and *anf* systems.

molybdenum but the presence of vanadium, expression of the *vnf* system is activated, and in the absence of both molybdenum and vanadium, the *anf* system is activated. In addition to the specific structural genes *vnfH*, *D*, *G*, and *K* and the activator gene *vnfA*, the *vnf* system also contains specific homologs of the *EN* genes, *vnfEN*. As noted in Section IV,C,1,c, *nifE* and *N* are thought to encode a scaffold protein on which FeMoco is biosynthesized. It therefore seems probable that *vnfEN* encode a similar scaffold protein for FeVaco. Since *nifB* is also required for the vanadium system, it seems probable that NifBco binds to $VnfN_2E_2$ in the biosynthesis of FeVaco and that at some juncture homocitrate biosynthesized by NifV is also incorporated.

NifM is required for maturation of VnfH, and NifS and U seem to be important for provision of sulfide and probably iron for the biosynthesis of the vanadium nitrogenase. The "apo VFe protein" has been isolated from an *A. vinelandii* strain deleted for *nifKD* and *nifB* (*169*). It was an $\alpha_2\beta_2\delta_2$ hexamer that could be activated *in vitro* by the addition of FeVaco to form a fully active protein. Under some conditions the δ subunit could be dissociated from the "apo VFe protein," and the protein resulting from the combination of the latter with FeVaco was inactive but could be reactivated by addition of the δ subunit. When the "apo VFe protein" was activated with FeMoco, a hybrid enzyme was produced that was unable to reduce N_2 but could reduce acetylene. Unusually, this latter activity was insensitive to CO inhibition. In later *in vitro* experiments it was demonstrated that FeVaco associates with the dimer of the δ subunit to form a complex that is necessary for the activation of "apo VFe protein" (*170*).

As indicated in Fig. 12, the *nifB*, *nifV*, *nifS*, *nifU*, and *nifM* genes are all required for maturation of the iron-only nitrogenase. The Fe protein of iron nitrogenase is very similar in sequence and properties to the Fe protein of the molybdenum and vanadium nitrogenases. In addition to the *nif* genes, the *vnf E* and *N* genes are required for biosynthesis of the iron nitrogenase, implying that $VnfN_2E_2$ can act as a scaffold for the biosynthesis of FeFeco as well as FeVaco.

B. Vanadium Nitrogenase

1. Structure

The *vnfH* genes of *A. vinelandii*, *A. chroococum*, and *Anabaena variabilis* have been sequenced and show approximately 90% identity with *nifH*. In particular, the five conserved cysteine residues of NifH,

two of which bind to the iron sulfur cluster are retained. Not surprisingly, the Fe proteins of vanadium-nitrogenase of *A. vinelandii* and *A. chroococum*, when purified, have the physical and chemical properties characteristic of molybdenum nitrogenase Fe proteins. The proteins are dimeric with $M_r \simeq 63$ kDa and one Fe_4S_4 cluster per dimer. The dithionite-reduced proteins exhibit EPR spectra with g values characteristic of an $[Fe_4S_4]^{1+}$ cluster in a spin mixture of $S = \frac{1}{2}$ and $\frac{3}{2}$ states. MgATP binding induces a conformational change in the protein, making the $[Fe_4S_4]$ cluster more accessible to reaction with bipyridyl and changing the rhombicity of the EPR signal. The redox potentials of the $[Fe_4S_4]$ clusters are very similar to those of the Fe proteins from molybdenum nitrogenases. The *vnfD* and *K* genes that encode the α and β subunits of the VFe protein show clear homology with the *nifD* and *K* genes encoding the α and β subunits of the MoFe protein. The encoded proteins of the vanadium nitrogenase have the amino acid residues necessary for binding the cofactor and the P clusters. However, the amino acid sequence around His α442 is different and characterizes the type of nitrogenase (see Ref. (*13*) for discussion). The VFe proteins have an additional small polypeptide encoded by *vnfG*. This third (δ) subunit is essential for function (*171*) and in the VFe protein (Acl^v), isolated from *A. chroococcum*, is present in a 1:1:1 stoichiometry with the other subunits (*172*). However, the stoichiometry of the α and β subunits of the VFe protein from *A. vinelandii* (Avl^v) has been shown to be variable, species with subunit compositions of $\alpha\beta_2$ and $\alpha_2\beta_2$ being isolated (*173*). The δ subunit was present, but its stoichiometry with the α and β subunits was not established.

The metal and acid labile sulfur contents of these proteins was somewhat lower than expected by comparison with the MoFe proteins. $Ac1^v$ contained 2 ± 0.3 vanadium atoms, 21 ± 1 iron atoms, and 19 ± 0.2 acid-labile sulfur atoms per $\alpha_2\beta_2\delta_2$ hexamer (*172*). The $\alpha_2\beta_2(\delta)$ form of $Av1^v$ was reported to contain 1.4 ± 0.2 vanadium atoms, 21.4 iron atoms, and 24 acid-labile sulfur ions per molecule, and the $\alpha\beta_2$ form had lower levels of metal and sulfur (*173*).

Mössbauer spectroscopy of $Av1^v$ clearly demonstrated the presence of P clusters (*174*). The EPR spectra of dithionite-reduced VFe proteins are complex, indicating the presence of several paramagnetic species. $Av1^v$ exhibits broad EPR signals, with g values of 5.8 and 5.4 integrating to 0.9 spins per V atom, which have been assigned to transitions from the ground and first excited state of a spin $S = \frac{3}{2}$ system (*175*). EPR data for $Ac1^v$ are more complex, with g values at 5.6, 4.3, and 3.77 that appear to arise from a mixture of $S = \frac{3}{2}$ species (*176*). The signals were associated with a midpoint potential of

−125 mV and have been assigned to a FeVaco center analogous to FeMoco, but with EPR signals some tenfold lower in intensity (*176*). The presence of a FeVaco center was demonstrated by its extraction and combination with the polypeptides of the MoFe protein from a *nifB* mutant, that is, lacking FeMoco (*177*) to form an active hybrid protein.

Both the EPR and Mossbäuer spectra of $Av1^{v}$ are consistent with the dithionite-reduced P clusters being oxidized by one electron relative to these in the MoFe proteins. EPR signals with g values near 6.67 and 5.3 were assigned to these clusters. These signals do not disappear with normal reductants, but are reduced by enzymic reduction with the iron protein and MgATP (*174*). Oxidative titration of enzymically reduced $Av1^{v}$ leads first to the increase of the intensity of the signals at 6.67 and 4.3 as the signals from FeVaco (g values 5.71 and 5.42) lose 50% of their intensity (*178*). Further oxidation results in the decrease in intensity of all of these signals and the concomitant appearance of a signal at $g = 11.9$ in the parallel mode, which was assigned to two-electron oxidized P clusters. The MCD spectroscopy of $Av1^{v}$ is very similar to that of Av1 and is consistent with both FeVaco and P clusters being present (*179*).

The X-ray absorption spectra of $Ac1^{v}$ (*180*) and $Av1^{v}$ (*181*) at the vanadium K-edge indicate an oxidation level of V^{II} or V^{IV} in a distorted octahedral coordination. The EXAFS region was simulated with a three-component fit with Fe, S, and O or N as nearest-neighbor atoms to the vanadium atom. This is very similar to the analysis of the EXAFS data on Mo in the FeMoco center, except for a longer (2.75 Å) V–Fe distance compared with the Mo–Fe distance. We now know the structure of FeMoco, and since homocitrate is a probable component of FeVaco (see Section VI,A) and His 442 is conserved in the sequences of the VFe proteins, we can assign the light atoms in the environment of the vanadium atom to the carboxyl and hydroxyl groups of homocitrate and an N atom of the imidazole ring of His 442.

The iron K-edge EXAFS measurements on $Av1^{v}$ (*182*) and the extracted FeVaco from $Ac1^{v}$ (*183*) show Fe–S and Fe–Fe interactions at 2.32 and 2.64 Å, with a longer Fe–Fe distance of 3.7 Å very similar again to the EXAFS data on FeMoco. These data emphasize the structural similarities between the cofactor centers of the MoFe and VFe proteins.

As noted previously, FeVaco can be extracted from $Ac1^{v}$ by the methods used to extract FeMoco from MoFe proteins (*177*). When FeVaco was combined with the polypeptides of the MoFe proteins from a *nifB* mutant, an active hybrid protein was created. However, although this protein had the H_2 evolution and acetylene reduction

properties of the VFe protein, even including the production of some ethane from acetylene, N_2 was not reduced by the hybrid protein either to NH_3 or to N_2H_4. This observation was the first to demonstrate that specific interactions with amino acids in the vicinity of the cofactor are required for the reduction of N_2.

2. Vanadium Nitrogenase Activity

The requirements for vanadium nitrogenase activity are very similar to those of the molybdenum nitrogenase, that is, both the Fe protein and the VFe protein are essential and MgATP is required, as is a low-potential reductant, normally dithionite, and the absence of oxygen. Pre-steady-state reaction kinetic studies of vanadium nitrogenase are few, and only the first two steps of the Fe protein cycle (Fig. 8) have been examined (*184*) that is, the binding of MgATP to the Fe protein and the subsequent electron transfer from $Ac2^{v}$ to $Ac1^{v}$. The MgATP concentration dependence ($K_d = 230 \pm 10\ \mu M$) and competitive inhibition by MgADP ($K_i^{MgADP} = 30 \pm 5\ \mu M$) were very similar to those of molybdenum nitrogenase. However, the rate of electron transfer within the $Ac2^{v}$–$Ac1^{v}$ complex, with $k = 46\ s^{-1}$, was significantly slower than the equivalent rate for the molybdenum enzyme of $k = 220\ s^{-1}$.

Substrate reduction by vanadium nitrogenase has not been investigated as extensively as has molybdenum nitrogenase, but there are clear differences. Acetylene is a poor substrate and N_2 does not compete as effectively with protons for the electrons available during turnover. Therefore, high rates of H_2 evolution are observed in the presence of these substrates. Furthermore, acetylene is reduced to both ethylene and a minor product, ethane (*172*). Equation (2) summarizes the most efficient N_2 reduction data yet observed for vanadium nitrogenase.

$$N_2 + 12e + 12H^+ \rightarrow 2NH_3 + 3H_2 \qquad (2)$$

This apparent low efficiency for reducing N_2 was observed under conditions of saturating N_2 and is not due to restrictions in electron transfer rate. Furthermore, the low efficiency is mirrored in bacterial cultures at 30°C (*185*).

In contrast with the molybdenum enzyme, hydrazine (N_2H_4) is a minor product from the reduction of N_2 by vanadium nitrogenase (*186*). The production of N_2H_4 increases with increasing temperature up to 50°C, at which temperature the ability of vanadium nitrogenase to produce to NH_3 ceases, although the production of N_2H_4 increases

threefold between 40 and 50°C. This observation has been interpreted as arising from a conformational change at the higher temperature rendering $Ac1^{v}$ incapable of reducing N_2 to NH_3. It was suggested (*186*) that this conformation decreased interactions between FeVaco and amino acid residues in its environment that were essential for the final protonation step. If the temperature of the assay is dropped below 30°C toward 5°, then the specific activity for N_2 reduction of molybdenum nitrogenase decreases tenfold more than that of vanadium nitrogenase (*187*). This behavior is associated with $Ac2^{v}$ and can be observed in cultures of the organism. Furthermore, at lower temperatures, molybdenum no longer represses the expression of the genes encoding vanadium nitrogenase (*188*). This observation has led to the suggestion that the vanadium nitrogenase may be essential for the growth of the organism at lower temperatures.

As noted earlier, acetylene is reduced by vanadium nitrogenase to both ethylene and ethane. The mechanism by which ethane is formed is not clear, but is apparently not dependent on release and then rereduction of ethylene. The reduction of acetylene to form ethane by cultures of microorganisms grown under conditions of molybdenum deficiency is presumptive evidence for the existence of a functioning molybdenum-independent nitrogenase and has been used to identify a vanadium nitrogenase in *Anabaena variabilis* (*189*). However, as noted in Section V,E,2,a, site-directed mutagenesis of amino acids of the MoFe protein close to FeMoco can result in significant levels of ethane being formed from acetylene. Furthermore, very small amounts are formed by the wild-type molybdenum enzyme when assayed at 50°C (*186*). Inhibition of vanadium nitrogenase substrate reduction by CO is complex (*190*). Under conditions of high electron flux CO inhibits acetylene reduction by vanadium nitrogenase less strongly than it does molybdenum nitrogenase. However, at low partial pressures of CO and lower electron flux, the rate of ethylene formation from acetylene reduction was doubled. Furthermore, ethane formation from acetylene was enhanced at low CO levels under both high and low electron flux. There is as yet no explanation of these phenomena.

C. Iron-Only Nitrogenase

Although, as indicated in Fig. 12, there is clear genetic evidence for a third nitrogenase in *Azotobacter vinelandii*, the initial preparations of this enzyme had low activity and contained small quantities of molybdenum as well as iron, and thus the activity might have been

associated with the molybdenum content (reviewed in (*13*)). More recently, an improved rapid purification of the FeFe protein has been reported that has activities approaching those of the VFe proteins (*191*). This protein was isolated from Δ*nifHDK*, *mod B* double mutant, defective in molybdenum uptake and unable to synthesize the MoFe protein of *Rhodobacter capsulatus*. This FeFe protein had an $\alpha_2\beta_2\gamma_2$ subunit structure of 268 kDa and was reported to contain about 20 iron atoms and only about 0.2 molybdenum atoms per mol. The reduced FeFe protein exhibited an EPR spectrum with g values of 4.3, 2.05, and 1.93. The weak 4.3 signal was assigned to adventitious ferric iron contamination and the other signals to an $S = \frac{1}{2}$ spin system similar to that observed in some preparations of VFe proteins. The most recent preparations of FeFe protein from *R. capsulatus* are reported to contain 26 ± 4 Fe atoms per mol of 95% pure protein (*192*).

Substrate reduction by the iron nitrogenase is very similar to that observed with vanadium nitrogenases. Acetylene is a relatively poor substrate, and N_2 reduction is accompanied by considerable H_2 evolution. Acetylene reduction leads to the production of some ethane as well as ethylene. Beyond this, little has been investigated. Under optimal conditions for N_2 reduction, the ratio of N_2 reduced to H_2 produced was 1:7.5 compared with 1:1 for molybdenum nitrogenase (*192*).

An Fe-only nitrogenase has also been isolated from a *nifH* mutant of *Rhodospirillum rubrum* and was characterized as an $\alpha_2\beta_2\delta_2$ hexamer containing only iron, no molybdenum or vanadium, with an $\alpha_2Fe_4S_4$-containing Fe protein. A factor could be extracted from the FeFe protein into NMF that combined with "apo-MoFe protein" to form an active enzyme (*193*).

A preparation of the third nitrogenase from *A. vinelandii*, isolated from a molybdenum-tolerant strain but lacking the structural genes for the molybdenum and vanadium nitrogenases, was discovered to contain FeMoco (*194*). The δ subunit encoded by *anfG* was identified in this preparation, which contained 24 Fe atoms and 1 Mo atom per mol. EPR spectroscopy and extraction of the cofactor identified it as FeMoco. The hybrid enzyme could reduce N_2 to ammonia and reduced acetylene to ethylene and ethane. The rate of formation of ethane was nonlinear and the ethane:ethylene ratio was strongly dependent on the ratio of nitrogenase components.

These data confirm the sequence similarity of the three nitrogenases and indicate that cofactor exchange experiments are relatively straightforward. However, the environment of the cofactor clearly affects the substrate reduction activity, as observed with mutations in

the environment of FeMoco in the molybdenum enzyme (Section V,E,2,a).

D. Nitrogenase from *Streptomyces Thermoautotrophicus*

Streptomyces thermoautotrophicus UbT1 occurs naturally in the covering soil of burning charcoal piles. The bacterium is characterized by the utilization of gases as sources of energy. It is a free-living nitrogen-fixing organism and is able to fix N_2 under aerobic chemolithoautotrophic and thermophilic conditions with CO or $H_2 + CO_2$ as growth substrates. The N_2 fixation reaction is reported (*195*) to be defined by the equation

$$N_2 + 8H^+ + 8e + 4\text{–}12\,MgATP \rightarrow 2NH_3 + H_2 + 4\text{–}12\,MgADP + 4\text{–}12\,P_i.$$

The reaction is coupled to the oxidation of CO by a molybdenum-containing CO dehydrogenase that transfers the electrons derived from CO oxidation to O_2, thereby producing superoxide anion radicals. A manganese-containing superoxide oxidoreductase reoxidizes the superoxide anions to O_2 and transfers the electrons to a molybdenum-, iron-, and sulfur-containing nitrogenase for the reduction of N_2 to ammonia. Thus, this nitrogenase is reported to be dependent on O_2 and superoxide. All of its components are apparently insensitive to O_2 and hydrogen peroxide. It is unable to reduce acetylene or ethylene and has a relatively low MgATP requirement.

The enzyme is described as consisting of two proteins ST1 and ST2. ST1 is a trimer of 93, 33, and 18 kDa subunits with a total molecular mass of 144 kDa containing one molybdenum, 13.8–21.7 iron, and 8.5–15 acid-labile sulfide atoms per mol. The authors reported a moderate sequence similarity between the N-terminal sequences of the ST1 large subunit (93 kDa) and the Kpl β-subunit and between the ST1 medium subunit (33 kDa) and the Kp1 α-subunit. The visible spectra of oxidized and reduced ST1 protein are reported to be similar to those of Kp1. The ST2 protein was a dimeric protein of 24 kDa subunits, pale yellowish green in color and containing substoichiometric amounts of manganese and zinc. ST1, ST2, MgATP, N_2, and dithionite were required for activity, but MgADP was apparently not an inhibitor. Formation of ammonium from N_2 was linear with time for at least 2.5 h at the assay temperature of 65°C. The activities of the proteins were very low, purified ST1 being reported as having a specific activity of 139 nmol of NH_4^+ produced/mg protein/h and ST2 a specific activity of 233 nmol NH_4^+ produced/mg protein/h. The authors

concluded that ST2 was a superoxide oxidoreductase. Clearly this astonishing enzyme requires further investigation.

VII. Conclusions and Outlook

The solutions of the structures of the Fe protein, the MoFe proteins, and the putative transition-state complex of these two proteins with ADP and AlF^{4-} represent major advances in our understanding of nitrogenase, but still many questions remain.

It is becoming clear that the MgATP hydrolysis is not required to induce protein–protein electron transfer, but its role in nitrogenase function is still undefined. The most likely hypothesis at the moment is that its hydrolysis, on the Fe protein, induces important changes in the MoFe protein, presumably by altering the conformation of the enzyme complex. Nevertheless, the nature of the changes in the MoFe protein remain obscure.

Some aspects of the Lowe–Thorneley mechanism for nitrogenase action, which has served us well over the past 15 years, are being called into question. In particular, the necessity for protein–protein dissociation after each electron transfer, the rate-determining step with dithionite as reductant, is being questioned when the natural electron donor flavodoxin or other artificial systems are used. Some aspects of the mechanism should be reinvestigated.

There is no consensus on where substrates bind on FeMoco or how they are reduced. A great deal of data with the enzyme and model complexes is available, and theoretical approaches are generating fresh insights but are unlikely to be definitive. New spectroscopic approaches and work with isolated FeMoco may provide additional insights, but perhaps more could be done by more detailed comparisons with the alternative nitrogenases. The new nitrogenase from *Streptomyces* is a great surprise and could, if confirmed, revolutionize our ideas about biological nitrogen fixation.

A great deal has been learned about the biosynthesis of nitrogenases, but at the moment the process is understood only in broad outline. The detailed roles of the individual gene products require much further investigation, which may once more indicate fresh approaches to some of the problems identified herein. In particular, if the biosynthetic steps can be emulated chemically, then it may be possible to synthesize FeMoco in large quantities in order to allow its detailed analysis at the atomic level.

The first active preparations of nitrogenase were isolated in 1966.

We have learned a great deal in the 30 years since then, but it seems clear that many more years of research will be required before we fully understand this fascinating and important enzyme.

Acknowledgments

I thank Sue Riches and June Dye for translating my draft dictation and scribbles into a manuscript; David Lawson for the structural figures; Bob Eady for helping me to draw the other figures; and BBSRC for support.

References

1. Georgiadis, M. M.; Komiya, H.; Chakrabarti, P.; Woo, D.; Kornue, J. J.; Rees, D. C. *Science* **1992,** *257,* 1653.
2. Kim, J.; Rees, D. C. *Science* **1992,** *257,* 1677.
3. Kim, J.; Rees, D. C. *Nature* **1992,** *360,* 553.
4. Chan, M. K.; Kim, J.; Rees, D. C. *Science* **199 ,** *260,* 792.
5. Bolin, J. T.; Campobasso, N.; Muchmore, S. W.; Morgan, T. V.; Mortenson, L. E. In "Molybdenum Enzymes, Cofactors and Model Systems"; Stiefel, E. I., Coucouvanis, D., Newton, W. E., Eds., ACS Symposium Series 535; American Chemical Society: Washington, DC, 1993; pp. 186–195.
6. Peters, J. W.; Stowell, M. H. B.; Soltis, S. M.; Finnegan, M. G.; Johnson, M. K.; Rees, D. C. *Biochemistry* **1997,** *36,* 1181.
7. Mayer, S. M.; Lawson, D. M.; Gormal, C. A.; Roe, S. M.; Smith, B. E. submitted.
8. Rees, D. C.; Chan, M. K.; Kim, J. *Adv. Inorg. Chem.* **199 ,** *40,* 89.
9. Leigh, G. J. *New J. Chem.* **1994,** *18,* 157.
10. Peters, J. W.; Fisher, K.; Dean, D. R. *Annu. Rev. Microbiol.* **1995,** *49,* 335.
11. Howard, J. B.; Rees, D. C. *Annu. Rev. Biochem.* **1994,** *63,* 235; *Chem. Rev.* **1996,** *96,* 2965.
12. Burgess, B. K.; Lowe, D. J. *Chem Rev.* **1996,** *96,* 2983.
13. Eady, R. R. *Chem. Rev.* **1996,** *96,* 3013.
14. Seefeldt, L. C.; Dean, D. R. *Acc. Chem. Res.* **1997,** *30,* 260.
15. Evans, D. J.; Henderson, R. A.; Smith, B. E. In "Bioinorganic Catalysis," 2nd ed.; Reedijk, J.; Bouwman, E., Eds; Marcel Dekker Inc.: New York, 1999; pp. 153–208.
16. Hausinger, R. P.; Howard, J. B. *J. Biol. Chem.* **198 ,** *258,* 13486.
17. Hagen, W. R.; Eady, R. R.; Dunham, W. R.; Haaker, H. *FEBS Lett.* **1985,** *189,* 250.
18. Watt, G. D.; McDonald, J. W. *Biochemistry* **1985,** *24,* 7226.
19. Lindahl, P. A.; Day, E. P.; Kent, T. A.; Orme-Johnson, W. H.; Münck, E. *J. Biol. Chem.* **1985,** *260,* 11160.
20. Meyer, J.; Gaillard, J.; Moulis, J.-M. *Biochemistry* **1988,** *27,* 6150.
21. Watt, G. D.; Reddy, K. R. N. *J. Inorg. Biochem.* **1994,** *53,* 281.
22. Angove, H. C.; Yoo, S. J.; Burgess, B. K.; Münck, E. *J. Am. Chem. Soc.* **1997,** *119,* 8730.
23. Lindahl, P. A.; Teo, B.-K.; Orme-Johnson, W. H. *Inorg. Chem.* **1987,** *26,* 3912.
24. Stephens, P. J.; McKenna, C. E.; McKenna, M. C.; Nguyen, H. T.; Morgan, T. V.;

Devlin, F. In "Current Perspectives in Nitrogen Fixation"; Gibson, A. H.; Newton, W. E., Eds.; Elsevier/North Holland Biomedical Press: New York, 1981; p. 357.
25. Robson, R. L. *FEBS Lett.* **1984,** *173,* 394.
26. Seefeldt, L. C.; Morgan, T. V.; Dean, D. R.; Mortenson, L. E. *J. Biol. Chem.* **1992,** *267,* 6680.
27. Wolle, D.; Dean, D. R.; Howard, J. B. *Science* **1992,** *258,* 992.
28. Ryle, M. J.; Lanzilotta, W. N.; Mortenson, L. E.; Watt, G. D.; Seefeldt, L. C. *J. Biol. Chem.* **1995,** *270,* 13112.
29. Ryle, M. J.; Seefeldt, L. C. *Biochemistry* **1996,** *35,* 4766.
30. Miller, R. W.; Eady, R. R.; Gormal, C.; Fairhurst, S. A.; Smith, B. E. *Biochem. J.* **1998,** *334,* 601.
31. Kim, J.; Woo, D.; Rees, D. C. *Biochemistry* **199 ,** *32,* 7104.
32. Shah, V. K.; Brill, W. *W. Proc. Natl. Acad. Sci. USA* **1977,** *74,* 3249.
33. Burgess, B. K. *Chem. Rev.* **1990,** *90,* 1377, and references therein.
34. Eidsness, M. K.; Flank, A. M.; Smith, B. E.; Flood, A. C.; Garner, C. D.; Cramer, S. P. *J. Am. Chem. Soc.* **1986,** *108,* 2746.
35. Conradson, S. D.; Burgess, B. K.; Newton, W. E.; Mortenson, L. E.; Hodgson, K. O. *J. Am. Chem. Soc.* **1987,** *109,* 7507.
36. Arber, J. M.; Flood, A. C.; Garner, C. D.; Gormal, C. A.; Hasnain, S.; Smith, B. E. *Biochem. J.* **1988,** *252,* 421.
37. Liu, H. I.; Filippani, A.; Gavini, N.; Burgess, B. K.; Hedman, B.; Cicco, A. D.; Natoli, C. R.; Hodgson, K. O. *J. Am. Chem. Soc.* **1994,** *116,* 2418.
38. Howes, B. D.; Fisher, K.; Lowe, D. J. *Biochem. J.* **1994,** *297,* 261.
39. Smith, B. E.; Eady, R. R. *Eur. J. Biochem.* **1992,** *205,* 1, and references therein.
40. Smith, B. E.; O'Donnell, M. J.; Lang, G.; Spartalian, K. *Biochem. J.* **1980,** *191,* 449.
41. Surerus, K. K.; Hendrich, M. P.; Christie, P. D.; Rottgardt, D.; Orme-Johnson, W. H.; Münck, E. J. *J. Am. Chem. Soc.* **1992,** *114,* 8579.
42. Pierik, A. J.; Wassink, H.; Haaker, H.; Hagen, W. R. *Eur. J. Biochem.* **199 ,** *212,* 51.
43. Tittsworth, R. C.; Hales, B. J. *J. Am. Chem. Soc.* **199 ,** *115,* 9763.
44. Johnson, M. K.; Thomson, A. J.; Robinson, A. E.; Smith, B. E. *Biochem. Biophys. Acta* **1981,** *671,* 61.
45. Morningstar, J. E.; Johnson, M. K.; Case, E. E.; Hales, B. J. *Biochemistry* **1987,** *26,* 1795.
46. O'Donnell, M. J.; Smith, B. E. *Biochem. J.* **1978,** *173,* 881.
47. Hagen, W. R.; Wassink, H.; Eady, R. R.; Smith, B. E.; Haaker, H. *Eur. J. Biochem.* **1987,** *169,* 457.
48. O'Donnell, M. J.; Smith, B. E. *FEBS Lett.* **1980,** *120,* 251.
49. Watt, G. D.; Huang, H.; Reddy, K. R. N. In "Molybdenum Enzymes, Cofactors and Model Systems"; Stiefel, E. I.; Coucouvanis, D.; Newton, W. E., Eds., ACS Symposium Series 535; American Chemical Society: Washington, DC, 1993; pp. 243–256 and references therein.
50. Smith, B. E.; Lowe, D. J.; Bray, R. C. *Biochem. J.* **197 ,** *135,* 331.
51. Miller, R. W.; Smith, B. E.; Eady, R. R. *Biochem. J.* **199 ,** *291,* 709.
52. Miller, R. W.; Eady, R. R.; Gormal, C.; Fairhurst, S. A.; Smith, B. E. *Biochem. J.* **1997,** *322,* 737.
53. Dixon, R. *Arch. Microbiol.* **1998,** *169,* 371, and references therein.
54. Hill, S.; Austin, S.; Eydmann, T.; Jones, T.; Dixon, R. *Proc. Natl. Acad. Sci. USA* **1996,** *93,* 2143.
55. Pau, R. N.; Klipp, W.; Leimkühler, S. In "Transition Metals in Microbial Metabo-

lism"; Winkelmann, G.; Carrano, C. J., Eds.; Harwood Academic Publishers: Amsterdam, 1997; pp. 217–234.
56. Paul, W.; Merrick, M. *Eur. J. Biochem.* **1989,** *178,* 675.
57. Zheng, L.; White, R. H.; Cash, V. L.; Jack, R. F.; Dean, D. R. *Proc. Natl. Acad. Sci. USA* **199 ,** *90,* 2754.
58. Zheng, L.; White, R. H.; Cash, V. L.; Dean, D. R. *Biochemistry* **1994,** *33,* 4714.
59. Zheng, L.; Dean, D. R. *J. Biol. Chem.* **1994,** *269,* 18723.
60. Fu, W.; Jack, R. F.; Morgan, T. V.; Dean, D. R.; Johnson, M. K. *Biochemistry* **1994,** *33,* 13455.
61. Allen, R. M.; Chatterjee, R.; Madden, M. S.; Ludden, P. W.; Shah, V. K. *Crit. Rev. Biotech.* **1994,** *14,* 225.
62. Imperial, J.; Ugalde, R. A.; Shah, V. K.; Brill, W. J. *J. Bacteriol.* **1984,** *158,* 187.
63. Joerger, R. D.; Bishop, P. E. *J. Bacteriol.* **1998,** *170,* 1475.
64. Moreno-Vivian, C.; Hennecke, S.; Pühler, A.; Klipp, W. *J. Bacteriol.* **1989,** *171,* 2591.
65. Imperial, J.; Ugalde, R. A.; Shah, V. K.; Brill, W. J. *J. Bacteriol.* **1985,** *163,* 1285.
66. Dean, D. R.; Jacobson, M. R. In "Biological Nitrogen Fixation"; Stacey, G.; Burns, R. H.; Evans, H. J., Eds.; Chapman and Hall: New York, 1992; pp. 763–834.
67. Roberts, G. P.; MacNeil, T.; MacNeil, D.; Brill, W. J. *J. Bacteriol.* **1978,** *136,* 267.
68. Shah, V. K.; Allen, J. R.; Spangler, N. J.; Ludden, P. W. *J. Biol. Chem.* **1994,** *269,* 1154.
69. Allen, R. M.; Chatterjee, R.; Ludden, P. W.; Shah, V. K. *J. Biol. Chem.* **1995,** *270,* 26890.
70. Chen, J.-S.; Wang, S.-Z.; Johnson, J. L. In "Nitrogen Fixation: Achievements and Objectives"; Gresshoff, P. M.; Roth, L. E.; Stacey, G.; Newton, W. E., Eds.; Chapman and Hall: New York, 1990; pp. 483–490.
71. Brigle, K. E.; Weiss, M. C.; Newton, W. E.; Dean, D. R. *J. Bacteriol.* **1987,** *169,* 1547.
72. Paustian, J. D.; Shah, V. K.; Roberts, G. P. *Proc. Natl. Acad. Sci. USA* **1989,** *86,* 6082.
73. Roll, J. T.; Shah, V. K.; Dean, D. R.; Roberts, G. P. *J. Biol. Chem.* **1995,** *270,* 4432.
74. McLean, P. A.; Dixon, R. A. *Nature* **1981,** *292,* 655.
75. McLean, P. A.; Smith, B. E.; Dixon, R. A. *Biochem. J.* **198 ,** *211,* 589.
76. Hawkes, T. R.; McLean, P. A.; Smith, B. E. *Biochem. J.* **1984,** *217,* 317.
77. Hoover, T. R.; Robertson, A. D.; Cerny, R. L.; Hayes, R. N.; Imperial, J.; Shah, V. K.; Ludden, P. W. *Nature* **1987,** *329,,* 855.
78. Liang, J.; Maden, M.; Shah, V. K.; Burns, R. H. *Biochemistry* **1990,** *29,* 8577.
79. Zheng, L.; White, R. H.; Dean, D. R. *J. Bacteriol.* **1997,** *179,* 5963.
80. Hoover, T. R.; Imperial, J.; Liang, J.; Ludden, P. W.; Shah, V. K. *Biochemistry* **1988,** *27,* 3647.
81. Imperial, J.; Hoover, T. R.; Madden, M. S.; Ludden, P. W.; Shah, V. K. *Biochemistry* **1989,** *28,* 7796.
82. Filler, W. A.; Kemp, R. M.; Ng, J. C.; Hawkes, T. R.; Dixon, R. A.; Smith, B. E. *Eur. J. Biochem.* **1986,** *160,* 371.
83. Shah, V. K.; Hoover, T. R.; Imperial, J.; Paustian, T. D.; Roberts, G. P.; Ludden, P. W. In "Nitrogen Fixation: Hundred Years After"; Bothe, E.; de Bruijn, F. J.; Newton, W. E., Eds.; Gustav Fischer: Stuttgart, 1988; pp. 115–120.
84. Rangaraj, P.; Shah, V. K.; Ludden, P. W. *Proc. Natl. Acad. Sci. USA* **1997,** *94,* 11250.

85. Allen, R. M.; Chatterjee, R.; Ludden, P. W.; Shah, V. K. *J. Biol. Chem.* **1996,** *271,* 4256.
86. Gavini, N.; Burgess, B. K. *J. Biol. Chem.* **1992,** *267,* 21179.
87. Kent, H. M.; Ioannidis, I.; Gormal, C.; Smith, B. E.; Buck, M. *Biochem. J.* **1989,** *264,* 257.
88. Kent, H. M.; Baines, H.; Gormal, C.; Smith, B. E.; Buck, M. *Mol. Microbiol.* **1990,** *4,* 1497.
89. Jacobson, M. R.; Cash, V. L.; Wein, M. C.; Laird, N. F.; Newton, W. E.; Dean, D. R. *Mol. Gen. Genet.* **1989,** *219,* 49.
90. Harris, G. S.; White, T. C.; Flory, J. E.; Orme-Johnson, W. H. *J. Biol. Chem.* **1990,** *265,* 15909.
91. Kim, S.; Burgess, B. K. *J. Biol. Chem.* **1994,** *269,* 4215.
92. Hawkes, T. R.; Smith, B. E. *Biochem. J.* **1984,** *223,* 783.
93. Paustian, T. D.; Shah, V. K.; Roberts, G. P. *Biochemistry,* **1990,** *29,* 3515.
94. Homer, M. J.; Paustian, T. D.; Shah, V. K.; Roberts, G. P. *J. Bacteriol.* **199 ,** *175,* 4907.
95. Homer, M. J.; Dean, D. R.; Roberts, G. P. *J. Biol. Chem.* **1995,** *270,* 24745, and references therein.
96. Tal, S.; Chun, T. W.; Gavini, N.; Burgess, B. K. *J. Biol. Chem.* **1991,** *266,* 10654.
97. Allen, R. M.; Homer, M. J.; Chatterjee, R.; Ludden, P. W.; Roberts, G. P.; Shah, V. K. *J. Biol. Chem.* **199 ,** *268,* 23670.
98. Robinson, A. C.; Chun, T. W.; Li, J.-G.; Burgess, B. K. *J. Biol. Chem.* **1989,** *264,* 10088.
99. Chatterjee, R.; Allen, R. M.; Ludden, P. W.; Shah, V. K. *J. Biol. Chem.* **1997,** *272,* 21604.
100. Magnusson, J. K.; Paustian, T. D.; Shah, V. K.; Dean, D. R.; Roberts, G. P.; Rees, D. C.; Howard, J. B. *Tetrahedron* **1997,** *53,* 11971.
101. Govezensky, D.; Greener, T.; Segal, G.; Zamir, A. *J. Bacteriol.* **1991,** *173,* 6339.
102. Thorneley, R. N. F.; Lowe, D. J. In "Molybdenum Enzymes"; Spiro, T. G., Ed.; Wiley-Interscience: New York, 1985; pp. 117–159, and references therein.
103. Fisher, K.; Lowe, D. J.; Thorneley, R. N. F. *Biochem. J.* **1991,** *279,* 81.
104. Dawson, D.; Henderson, R. A.; Hills, A.; Hughes, D. L. *Polyhedron* **1989,** *8,* 1870.
105. Pickett, C. J. *J. Bioinorg. Chem.* **1996,** *1,* 601, and references therein.
106. Lowe, D. J.; Ashby, G. A.; Brune, M.; Knights, H.; Webb, M. R.; Thorneley, R. N. F. In "Nitrogen Fixation: Fundamentals and Applications"; Tikhonovich, I. A.; Provorov, N. A.; Romanov, V. I.; Newton, W. E., Eds.; Kluwer Academic Publishers: The Netherlands, 1995; pp. 103–108.
107. Duyvis, M. G., Ph.D. Thesis, Agricultural University, Wageningen, The Netherlands, 1997.
108. Druzhinin, S. Y.; Syrtsova, L. A., Uzenskaja, A. M.; Likhtenstein, G. I. *Biochem. J.* **199 ,** *290,* 627.
109. Duyvis, M. G.; Wassink, H., Haaker, H. *FEBS. Lett.* **1996,** *380,* 233.
110. Renner, K. A.; Howard, J. B. *Biochemistry* **1996,** *35,* 5353.
111. Grossman, J. G.; Hasnain, S. S.; Yousafzai, F. K.; Smith, B. E.; Eady, R. R. *J. Mol. Biol.* **1997,** *266,* 642.
112. Schindelin, H.; Kisker, C.; Schlessman, J. L.; Howard, J. B.; Rees, D. C. *Nature* **1997,** *387,* 370.
113. Lanzilotta, W. N.; Fisher, K.; Seefeldt, L. C. *J. Biol. Chem.* **1997,** *272,* 4157.
114. Yousafzai, F. K.; Eady, R. R. *Biochem. J.* **1997,** *326,* 637.
115. Lanzilotta, W. N.; Seefeldt, L. C. *Biochemistry* **1997,** *36,* 12976.

116. Lowe, D. J.; Mitchell, C. In "Nitrogen Assimilation: Molecular and Genetic Aspects"; Abstracts, University of South Florida, 1997.
117. Duyvis, M. G.; Wassink, H.; Haaker, H. *Eur. J. Biochem.* **1994,** *225,* 881.
118. Smith, B. E.; Lowe, D. J.; Bray, R. C. *Biochem. J.* **197 ,** *135,* 331.
119. Lowe, D. J.; Fisher, K.; Thorneley, R. N. F. *Biochem. J.* **199 ,** *292,* 93.
120. Duyvis, M. G.; Mensink, R. E.; Wassink, H.; Haaker, H. *Biochem. Biophys. Acta. Bioenergetics* **1997,** *1320,* 34.
121. Peters, J. W.; Fisher, K.; Newton, W. E.; Dean, D. R. *J. Biol. Chem.* **1995,** *270,* 27007.
122. Burgess, B. H. In "Molybdenum Enzymes"; Spiro, T. G., Ed.; Wiley Interscience, New York, 1985; pp. 161–220.
123. Yates, M. G. In "Biological Nitrogen Fixation"; Stacey, G.; Burris, R. H.; Evans, H. J., Eds.; Chapman and Hall: New York, 1992; pp. 685–735.
124. Burgess, B. K. In "Molybdenum Enzymes, Cofactors and Model Systems"; Stiefel, E. I.; Coucouvanis, D.; Newton, W. E., Eds., ACS Symposium Series 535; American Chemical Society: Washington DC, 1993; pp. 144–169.
125. Seefeldt, L. C.; Rasche, M. E.; Ensign, S. A. *Biochemistry* **1995,** *34,* 5382.
126. Rasche, M. E.; Seefeldt, L. C. *Biochemistry* **1997,** *36,* 8574.
127. Rivera-Ortiz, J. M.; Burris, R. H. *J. Bacteriol.* **1975,** *123,* 537.
128. Pham, D. N.; Burgess, B. K. *Biochemistry* **199 ,** *32,* 13725.
129. Lowe, D. J.; Eady, R. R.; Thorneley, R. N. F. *Biochem. J.* **1978,** *173,* 277.
130. Hawkes, T. R.; Lowe, D. J.; Smith, B. E. *Biochem. J.* **198 ,** *211,* 495.
131. Yates, M. G.; Lowe, D. J. *FEBS Lett.* **1976,** *72,* 121.
132. Davis, L. C.; Henzl, M. T.; Burris, R. H.; Orme-Johnson, W. H. *Biochemistry* **1979,** *18,* 4860.
133. Pollock, R. C.; Lee, H.-I.; Cameron, L. M.; De Rose, V. J.; Hales, B. J.; Orme-Johnson, W. H.; Hoffman, B. M. *J. Am. Chem. Soc.* **1995,** *117,* 8686.
134. Christie, P. D.; Lee, H.-I.; Cameron, L. M.; Hales, B. J.; Orme-Johnson, W. H.; Hoffman, B. M. *J. Am. Chem. Soc.* **1996,** *118,* 8707.
135. Lee, H.-I.; Cameron, L. M.; Hales, B. J.; Hoffman, B. M. *J. Am. Chem. Soc.* **1997,** *119,* 10121.
136. George, S. J.; Ashby, G. A.; Wharton, C. W.; Thorneley, R. N. F. *J. Am. Chem. Soc.* **1997,** *119,* 6450.
137. Braterman, P. S. In "Metal Carbonyl Spectra"; Academic Press: London, 1975, pp. 177–227.
138. Newton, W. E.; Dean, D. R. In "Molybdenum Enzymes, Cofactors and Model Systems"; Stiefel, E. I.; Coucouvanis, D.; Newton, W. E., Eds., ACS Symposium Series 535; American Chemical Society: Washington, DC, 1993; pp. 216–230.
139. Shen, J.; Dean, D. R.; Newton, W. E. *Biochemistry* **1997,** *36,* 4884.
140. Scott, D. J.; May, H. D.; Newton, W. E.; Brigle, K. E.; Dean, D. R. *Nature* **1990,** *343,* 188.
141. Scott, D. J.; Dean, D. R.; Newton, W. E. *J. Biol. Chem.* **1997,** *267,* 20002.
142. Kim, C.-H.; Newton, W. E.; Dean, D. R. *Biochemistry* **1995,** *34,* 2798.
143. Hughes, D. L.; Ibrahim, S. K.; Pickett, C. J.; Querne, G.; Laouenan, A.; Talarmin, J.; Queiros, A.; Fonseca, A. *Polyhedron* **1994,** *13,* 3341.
144. Deng, H.; Hoffman, R. *Angew. Chem. Int. Ed. Engl.* **199 ,** *32,* 1061.
145. Dance, I. G. *Aust. J. Chem.* **1994,** *47,* 979.
146. Dance, I. *J. Chem. Soc. Chem. Commun.* **1997,** 165.
147. Stavrev, K. K.; Zerner, M. C. *Chem. Eur. J.* **1996,** *2,* 83.
148. Stavrev, K. K.; Zerner, M. C. *Theor. Chem. Acc.* **1997,** *96,* 141.

149. Christiansen, J.; Tittsworth, R. C.; Hales, B. J.; Cramer, S. P. *J. Am. Chem. Soc.* **1995,** *117,* 10017.
150. Strange, R. W.; Murphy, L. M.; Hasnain, S. S.; Gormal, C.; Eady, R. R.; Smith, B. E. In preparation.
151. Zhong, S.-J.; Liu, C.-W. *Polyhedron* **1997,** *16,* 653.
152. Schultz, F. A.; Gheller, S. F.; Burgess, B. K.; Lough, S.; Newton, W. E. *J. Am. Chem. Soc.* **1985,** *107,* 5364.
153. Walters, M. A., Chapman, S. K.; Orme-Johnson, W. H. *Polyhedron* **1986,** *5,* 561.
154. Rawlings, J.; Shah, V. K.; Chisnell, J. R.; Brill, W. J.; Zimmermann, R.; Münck, E.; Orme-Johnson, W. H. *J. Biol. Chem.* **1978,** *253,* 1001.
155. Conradson, S. D.; Burgess, B. K.; Newton, W. E.; Di Cicco, A.; Filipponi, A.; Wu, Z. Y.; Natoli, C. R.; Hedman, B.; Hodgson, K. O. *Proc. Natl. Acad. Sci. USA* **1994,** *91,* 1290.
156. Harvey, I.; Strange, R. W.; Schneider, R.; Gormal, C. A.; Garner, C. D.; Hasnain, S. S.; Richards, R. L.; Smith, B. E. *Inorganica Chim. Acta* **1998,** *275,* 150.
157. Richards, A. J. M. Ph.D. Thesis, University of East Anglia, U.K., 1986.
158. Richards, A. J. M.; Lowe, D. J.; Richards, R. L.; Thomson, A. J.; Smith, B. E. *Biochem. J.* **1994,** *297,* 373.
159. Conradson, S. D.; Burgess, B. K.; Holm, R. H. *J. Biol. Chem.* **1988,** *263,* 13743.
160. Conradson, S. D.; Burgess, B. K.; Vaughn, S. A.; Roe, A. L.; Hedman, B.; Hodgson, K. O.; Holm, R. H. *J. Biol. Chem.* **1989,** *264,* 15967.
161. Grönberg, K. L. C.; Gormal, C. A.; Smith, B. E.; Henderson, R. A. *J. Chem. Soc. Chem. Commun.* **1997,** 713.
162. Grönberg, K. L. C.; Henderson, R. A. *J. Chem. Soc. Dalton Trans.* **1996,** 3667, and references therein.
163. Grönberg, K. L. C.; Gormal, C. A.; Durrant, M. C.; Smith, B. E.; Henderson, R. A., *J. Am. Chem. Soc.* **1998,** *120,* 10613.
164. Bishop, P. E.; Jarlenski, D. M. L.; Heatherington, D. R. *Proc. Natl. Acad. Sci. USA* **1980,** *77,* 7342.
165. Bishop, P. E.; Premakumar, R.; Dean, D.; Jacobson, M. R.; Chisnell, J. R.; Rizzo, T. M.; Kopczynaki, J. *Science* **1986,** *232,* 92.
166. Bishop, P. E.; Hawkins, M. E.; Eady, R. R. *Biochem. J.* **1986,** *238,* 437.
167. Chisnell, J. R.; Premakumar, R.; Bishop, P. E. *J. Bacteriol.* **1988,** *170,* 27.
168. Jacobson, M. R.; Brigle, K. E.; Bennet, L. T.; Setterquist, R. A.; Wilson, M. S.; Cash, V. L.; Beynon, J.; Newton, W. E.; Dean, D. R. *J. Bacteriol.* **1989,** *171,* 1017.
169. Chatterjee, R.; Allen, R. M.; Ludden, P. W.; Shah, V. K. *J. Biol. Chem.* **1996,** *271,* 6819.
170. Chatterjee, R.; Ludden, P. W.; Shah, V. K. *J. Biol. Chem.* **1997,** *272,* 3758.
171. Waugh, S. I.; Paulson, D. M.; Mylona, P. V.; Maynard, R. H.; Premakumar, R.; Bishop, P. E. *J. Bacteriol.* **1995,** *177,* 1505.
172. Eady, R. R.; Robson, R. L.; Richardson, T. H.; Miller, R. W.; Hawkins, M. *Biochem. J.* **1987,** *244,* 197.
173. Blanchard, C. Z.; Hales, B. J. *Biochemistry* **1996,** *35,* 472.
174. Ravi, N.; Moore, V.; Lloyd, S. G.; Hales, B. J.; Huynh, B. H. *J. Biol. Chem.* **1994,** *269,* 20920.
175. Hales, B. J.; Case, E. E.; Morningstar, J. E.; Dzeda, M. F.; Mauterer, L. A. *Biochemistry* **1986,** *25,* 7251.
176. Pierik, A. J.; Lowe, D. J.; Eldridge, M. E.; Marritt, S.; Farrar, J. A.; Thomson, A. J.; Eady, R. R. In "New Horizons in Nitrogen Fixation"; Palacios, R.; Mora, J.; Newton, W. E., Eds.; Kluwer Academic Publishers: Dordrecht, 1993, p. 147.

177. Smith, B. E.; Eady, R. R.; Lowe, D. J.; Gormal, C. *Biochem. J.* **1988,** *250,* 299.
178. Tittsworth, R. C.; Hales, B. J. *Biochemistry* **1996,** *35,* 479.
179. Morningstar, J. E.; Johnson, M. K.; Case, E. E.; Hales, B. J. *Biochemistry* **1987,** *26,* 1795.
180. Arber, J. M.; Dobson, B. R.; Eady, R. R.; Stevens, P.; Hasnain, S. S.; Garner, C. D.; Smith, B. E. *Nature* **1987,** *325,* 327.
181. George, G. N.; Coyle, C. L.; Hales, B. J.; Cramer, S. P. *J. Am. Chem. Soc.* **1988,** *110,* 4057.
182. Chen, J.; Christiansen, J.; Tittsworth, R. C.; Hales, B. J.; George, S. J.; Coucouvanis, D.; Cramer, S. P. *J. Am. Chem. Soc.* **199 ,** *115,* 5509.
183. Harvey, I.; Arber, J. M.; Eady, R. R.; Hasnain, S. S.; Garner, C. D.; Matsushita, T.; Nomura, M.; Smith, B. E. *Biochem. J.* **1989,** *258,* 733.
184. Thorneley, R. N. F.; Bergström, J.; Eady, R. R.; Lowe, D. J. *Biochem. J.* **1989,** *271,* 789 and references therein.
185. Dilworth, M. J.; Eldridge, M. E.; Eady, R. R. *Biochem. J.* **199 ,** *289,* 395.
186. Dilworth, M. J.; Eady, R. R. *Biochem. J.* **1991,** *277,* 465.
187. Miller, R. W.; Eady, R. R. *Biochem. J.* **1988,** *256,* 429.
188. Walmsley, J.; Kennedy, C. *Appl. Environ. Microbiol.* **1991,** *57,* 522.
189. Keutemitch, T.; Danneberg, G.; Hundshagen, B.; Bothe, H. *FEMS Microbiol. Lett.* **1988,** *51,* 19.
190. Cameron, L. A.; Hales, B. J. *J. Am. Chem. Soc.* **1996,** *118,* 279.
191. Schneider, K.; Gollan, U.; Selsemeier-Voigt, S.; Plass, W.; Müller, A. *Naturwissenschaften* **1994,** *81,* 405.
192. Schneider, K.; Gollan, U.; Drottboom, M.; Selsemeier-Voigt, S.; Müller, A. *Eur. J. Biochem.* **1997,** *244,* 789.
193. Davis, R.; Lehman, L.; Petsovich, R.; Shah, V. K.; Roberts, G. P.; Ludden, P. W. *J. Bacteriol.* **1996,** *178,* 1445.
194. Pau, R. N.; Eldridge, M. E.; Lowe, D. J.; Mitchenall, L. A.; Eady, R. R. *Biochem. J.* **199 ,** *293,* 101.
195. Ribbe, M.; Gadkari, D.; Meyer, O. *J. Biol. Chem.* **1997,** *272,* 26627.
196. Kraulis, P. J. *J. Appl. Crystallogr.* **1991,** *24,* 946.

THE SEARCH FOR A ''PRISMANE'' Fe–S PROTEIN

ALEXANDER F. ARENDSEN[1] and PETER F. LINDLEY[2]

CCLRC Daresbury Laboratory, Warrington, Cheshire WA44AD, United Kingdom

I. Introduction
II. Historical Discovery of "Prismane" Protein (Now Termed Fepr)
  A. Initial Studies
  B. Subsequent Studies
III. Crystallographic Studies
  A. Preliminary Studies
  B. Structure Elucidation
  C. Description of the Molecular Structure of the Fepr Protein
IV. Conclusion and Future Studies

I. Introduction

Iron–sulfur (Fe–S) clusters are found throughout nature. They usually function in electron transfer reactions and are found in small molecules such as the ferredoxins and in redox enzymes where they shuttle electrons to or from the active site. They contain iron and inorganic sulfur atoms and are bound to the protein, through the Fe atoms, primarily by the sulfur atoms of cysteine residues, but occasionally by histidine nitrogen or by aspartate oxygen atoms. Four basic Fe–S clusters can be distinguished. The simplest Fe–S cluster contains one Fe atom ligated by four cysteine sulfurs, although this is not a true Fe–S cluster because it lacks inorganic sulfur. The remaining three types of clusters contain two ([2Fe–2S]), three ([3Fe–4S]), and four ([4Fe–4S]) iron atoms, respectively. The valency of the iron atoms in a cluster is either 2+ or 3+ and because of the tetrahedral coordination, Fe is always high-spin ($S = \frac{5}{2}$ or $S = 2$). However, the J-coupling within a cluster is such that the observed overall spin

[1] Current address: Department of Biochemistry, University of Nebraska, Lincoln, NE, USA.

[2] Current address: ESRF, BP-220, F-38043, Grenoble Cedex, France.

Copyright 1999 by Academic Press.
All rights of reproduction in any form reserved.
0898-8838/99 $30.00

TABLE I

HIGH-SPIN Fe–S EPR ENZYMES

Enzyme	Reaction	Ref.
Nitrogenase MoFe protein	$N_2 + 8H^+ + 8e^- \rightarrow 2NH_3 + H_2$	*46*
[Fe-only] hydrogenase	$2H^+ + 2e^- \rightarrow H_2$	*9*
Dissimilatory sulfite reductase	$SO_3^{2-} + 6H^+ + 6e^- \rightarrow S^{2-} + 3H_2O$	*47*
		48
		49
CO dehydrogenase	$CO_2 + 2H^+ + 2e^- \rightarrow CO + H_2O$	*18*
		24
Fepr protein	Not known	*11*

of the cluster is the lowest possible combination of the magnetic states of the individual Fe atoms (i.e., $S = 0$ or $S = \frac{1}{2}$).

Biological Fe–S clusters usually act as single-electron transferring units, despite the fact that all true Fe–S clusters contain more than one Fe, each of which can formally exist in two redox states. Thus, a cluster containing n Fe atoms would be expected to possess $n + 1$ valency states. However, only two of these states are actually observed *in vitro*. Nevertheless, [4Fe–4S] clusters have been shown to occur in three valency states: 1+, 2+, and 3+ (biological chemists normally ignore the valency of the ligands when designating the overall valency of the cluster), but within one particular protein only two of the three possible redox states for a [4Fe–4S] are observed. However, there has been growing evidence that this general picture no longer holds. First, it has become clear that the biological role of Fe–S clusters is not limited to electron transfer. Functions such as acid base catalysis (*1*) and gene regulation (*2*, *3*) have been widely acknowledged. Secondly, an increasing number of proteins, including the Fepr protein, have been shown to exhibit very high-spin EPR signals (Table I). All but one of the enzymes listed in Table I catalyze an oxidation/reduction reaction involving the transfer of a pair of electrons, or a multiple thereof; the sole exception is the Fepr protein for which, to date, no physiological function is known. The anomalous magnetic properties, resulting in high-spin EPR signals, could not be explained by invoking the presence of one of the "basic" Fe–S clusters, and it was proposed that they arose from novel Fe–S clusters, possibly containing more than four Fe atoms. The rationale behind this hypothesis was that larger clusters (i.e., those with more than four Fe atoms) may be better equipped for multielectron redox reactions,

viz. the transfer of two or more electrons (the reader is reminded of the fact that all "common" Fe–S clusters, that is, those containing two, three, or four Fe atoms, can occur in two redox states only *in vitro*).

The elucidation of the crystal structures of two high-spin EPR proteins has shown that the proposals for novel Fe–S clusters are not without substance. Two, rather than one novel Fe–S cluster, were shown to be present in nitrogenase, the key enzyme in the biotic fixation of molecular nitrogen (*4*, *5*). Thus the FeMoco-cofactor comprises two metal clusters of composition [4Fe–3S] and [1Mo–3Fe–3S] bridged by three inorganic sulfur atoms, and this is some 14 Å distant from the P-cluster, which is essentially two [4Fe–4S] cubane moieties sharing a corner. The elucidation of the crystal structure of the Fepr protein (*6*) provides the second example of a high-spin EPR protein that contains yet another unprecedented Fe–S cluster.

This review presents an overview of the discovery of the Fepr protein, the spectroscopy that led to the suggestion that it contained a [6Fe–6S] cluster, and the subsequent crystal structure analysis that disproved this hypothesis, yet uncovered what is at a present a unique Fe–S cluster in biology.

II. Historical Discovery of "Prismane" Protein (Now Termed Fepr)

A. Initial Studies

In 1989 in Wageningen, the Netherlands, W. R. Hagen and colleagues (*7*) occasionally noticed a contamination during the purification of a hydrogenase from the sulfate-reducing bacterium *Desulfovibrio vulgaris* (strain Hildenborough). The unknown protein appeared to be a monomer with an approximate molecular mass of 50 kDa on SDS-PAGE, and, when purified to homogeneity, was found to have a brownish color. Chemical analysis revealed the presence of about six Fe atoms. Much to the surprise of these workers, the dithionite-reduced protein exhibited a most unusual EPR spectrum, a highly rhombic, fast relaxing spectrum with g-values of 2.004, 1.819, and 1.32 that appeared to arise from an isolated Fe–S cluster with $S = \frac{1}{2}$ ground state (Fig. 1).

Although this spectrum had never been observed for any Fe–S protein, it was reminiscent of, and indeed nearly identical to the EPR spectrum of the synthetic model compound $[Fe_6S_6(L)_6]^{3-}$ where L = Cl^-, Br^-, I^-, RS, or RO^- (*8*). The spectrum of this synthetic cluster,

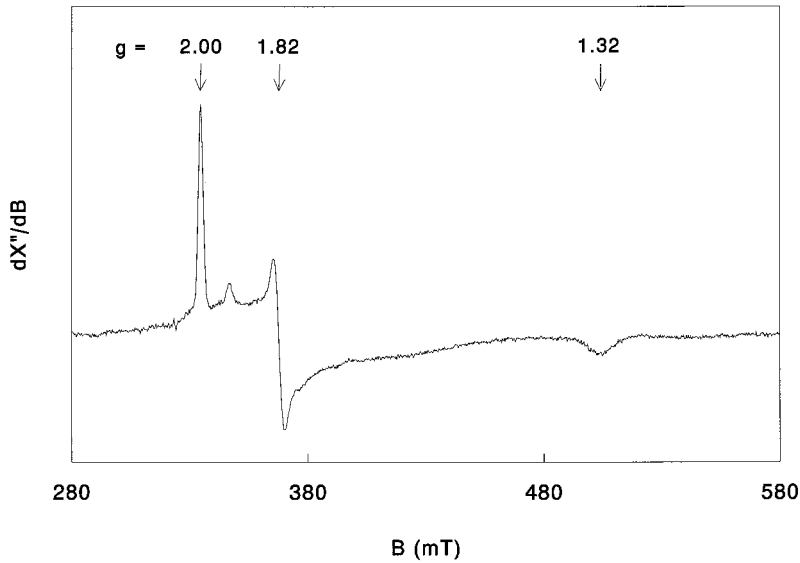

FIG. 1. EPR spectrum of the dithionite-reduced Fepr protein from *D. vulgaris* [from (*7*)]. The protein was 272 μmol dm^{-3} in 25 mmol dm^{-3} Hepes buffer, pH 7.5, and was reduced under argon with 10 mmol dm^{-3} sodium dithionite for 3 min at ambient temperature. EPR conditions: microwave frequency, 9331 $\pm$ 3 MHz; modulation frequency, 100 kHz; modulation amplitude, 0.63 mT; microwave power, 200 mW; temperature (relative gain) 16 K (6.3$\times$).

with the shape of a prismane basket (Fig. 2), was recorded by Hagen, who was the first person to record an EPR spectrum of a synthetic, prismane-type $[Fe_6S_6(L)_6]^{3-}$ cluster. When, 5 years later, he discovered a similar EPR spectrum of a protein of unknown function, he immediately realized that they might have discovered the first example of a biological [6Fe–6S] cluster.

A second unusual EPR spectrum was observed in the oxidized (as-isolated) protein (Fig. 3). This spectrum, which was assigned to an $S = \frac{1}{2}$ system, was not reminiscent of any Fe–S cluster. Indeed, with *g*-values of 1.968, 1.953, and 1.903, it looked more like a molybdenum or tungsten spectrum. However, chemical analysis ruled out the possibility that this EPR spectrum arose from Mo or W, and the spectrum was assigned to an Fe–S center instead. The spin concentration, however, was substoichiometric and sample-dependent. Furthermore, when the as-isolated protein was oxidized with ferricyanide, it became EPR silent. This, together with the iron determination and the fingerprint of the reduced protein, led Hagen and colleagues to the

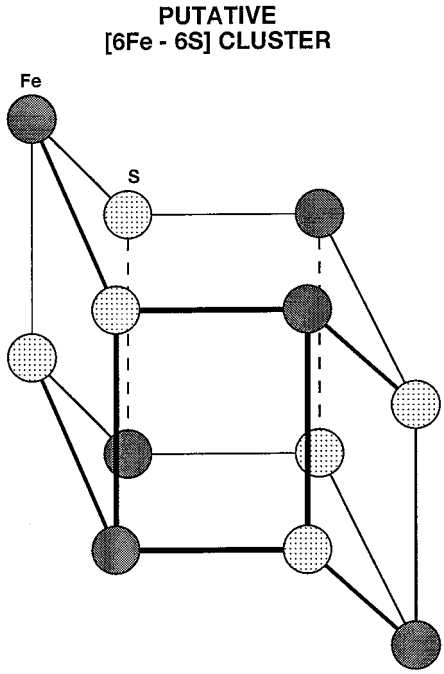

FIG. 2. Schematic drawing of the synthetic $[Fe_6S_6(L)_6]^{3-}$ cluster [from (*8*)]. Such a cluster will contain not only the usual Fe–Fe and Fe–S distances of 2.7 and 2.3 Å, respectively, but also a long Fe–Fe distance of 3.7 Å. This long distance is not observed in EXAFS measurements (*6*).

reasonable working hypothesis that they had isolated a protein that:

> . . . contains a single [6Fe–6S] cluster. The cluster can exist in four different redox states, namely, the fully oxidized state of $6Fe^{3+}$, i.e. $[6Fe–6S]^{6+}$, $S = 0$; the one-electron-reduced state $[6Fe–6S]^{5+}$, $S = \frac{1}{2}$; the two-electron reduced state $[6Fe–6S]^{4+}$, S = integer or 0; and the three-electron-reduced state $[6Fe–6S]^{3+}$, $S = \frac{1}{2}$.

This working model would be the framework for the interpretation of all subsequent biochemical, spectroscopic, and molecular biological studies on this unknown protein. The discovery of a putative [6Fe–6S] protein may have been a surprise to some, but its existence in

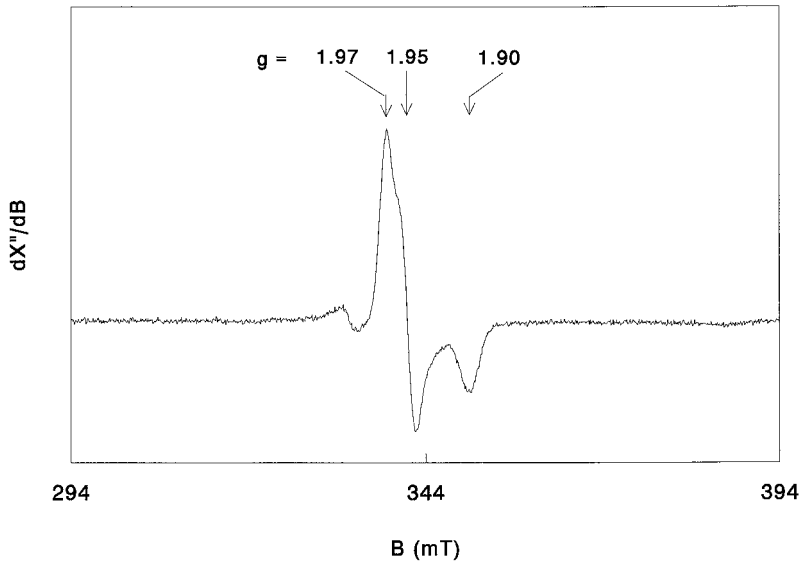

FIG. 3. EPR of as-isolated *D. vulgaris* Fepr protein [from (*7*)]. EPR conditions were the same as for Fig. 1, except for microwave power (0.32 mW), temperature (9 K), and relative gain (3.6×).

biology had already been anticipated some years earlier by Hagen, who proposed a six-iron cluster to constitute the active site of a hydrogenase (*9*). This hypothesis was based on the Fe content of the enzyme, as well as its primary sequence, but no EPR spectrum had been observed that could be assigned to a 6Fe cluster. With the discovery of a protein exhibiting an EPR spectrum that was considered to be a fingerprint of a prismane [6Fe–6S] cluster, the hypothesis of a biological [6Fe–6S] cluster suddenly seemed to have gained support.

B. SUBSEQUENT STUDIES

1. Molecular Weight Determination and EPR

Subsequent studies provided a wealth of information that appeared to support the hypothesis that the Fepr protein was a genuine [6Fe–6S]-containing protein. In a biochemical study (*10*) the elemental analysis was meticulously repeated, and, based on an assumed molecular mass of 52 kDa, the prismane protein was found to contain 6.3 Fe atoms, averaged over as many as nine different preparations. Again, no other metals than Fe were detected, suggesting that all

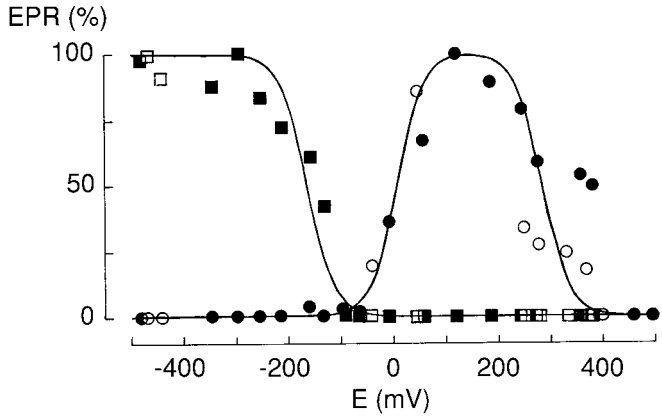

FIG. 4. EPR redox titration of *D. vulgaris* Fepr protein at pH 7.5 of $S = \frac{1}{2}$ components with dithionite and ferricyanide in the presence of mediators, [from (*11*)]. (□, ■) The Fepr protein-fingerprint signal (the 3+ state) monitored at $g = 1.825$; (○, ●) signal with all $g < 2$ (the 5+ state) monitored at $g = 1.898$ (■, ●) Titration in two directions starting from the isolated protein, which corresponds approximately to the top of the bell-shaped curve. (□, ○) A titration starting from the fully preoxidized state. EPR conditions: microwave frequency, 9.33 GHz; microwave power, 13 mW; modulation amplitude, 0.63 mT; temperature, 15 K.

EPR signals must come from Fe–S clusters. The previous assumption that the Fepr protein can occur in four different redox states appeared to be confirmed when, in an EPR-monitored redox titration (*11*), three subsequent redox transitions were observed (Fig. 4). The bell-shaped titration curve of the $S = \frac{1}{2}$ EPR spectrum of the as-isolated protein indicated an intermediate redox state. Moreover, the $S = \frac{1}{2}$ spectrum of the as-isolated protein and the "fingerprint" EPR spectrum of the fully reduced protein appeared to be well separated. Furthermore, in the two-electron oxidized protein (i.e., the putative 4+ state) an EPR signal was observed at $g = 16$. This signal was present in parallel-mode EPR, but absent in regular (i.e., perpendicular-mode) EPR, which pointed to an integer spin state, presumably S = 4. This was of course consistent with the proposed redox scheme, which predicted that the cluster in the two-electron reduced cluster must be either diamagnetic or integer-spin.

Another major discovery was the observation of unusually high-spin EPR signals in concentrated samples of the as-isolated Fepr protein. Low-field EPR resonances were observed with *g*-values up to 15 (Fig. 5). This further added to the concept of a [6Fe–6S] cluster. The high-spin EPR signals could be explained only by assuming an $S = \frac{9}{2}$

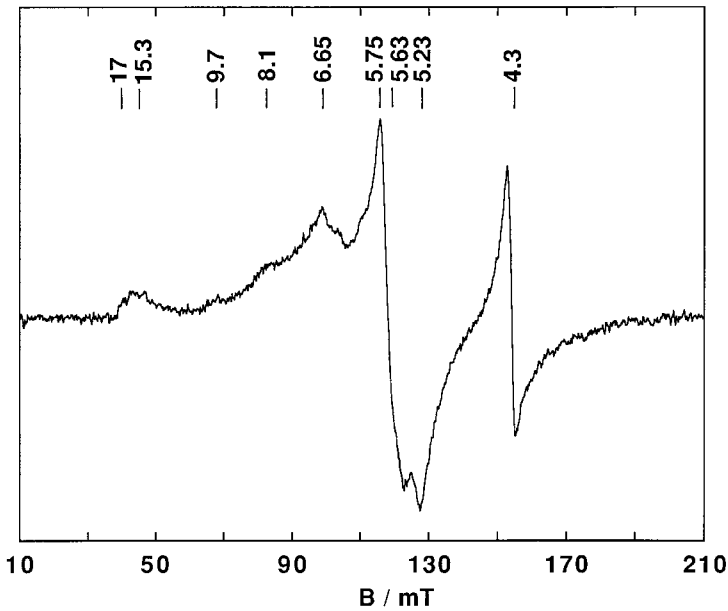

FIG. 5. Effective g assignment of the low-field $S = \frac{9}{2}$ EPR signals in *D. vulgaris* Fepr protein [from (*11*)]. The spectrum was recorded at the optimal temperature of 12 K, that is, at which the amplitude is maximal and lifetime broadening is not significant. EPR conditions: microwave frequency, 9.33 GHz; microwave power, 80 mW; modulation amplitude, 0.8 mT.

spin state. They did, however, not appear to represent another (i.e., fifth) redox state. Instead, the as-isolated protein seemed to behave as a spin mixture of $S = \frac{1}{2}$ and $S = \frac{9}{2}$, with 10% $S = \frac{1}{2}$ and 90% $S = \frac{9}{2}$. High-spin EPR signals similar to these had also been observed in a number of other multielectron redox proteins (see also Table I). Because of their complexity (all are multisubunit enzymes with more than a single Fe–S cluster, and therefore a relatively high Fe content) it is notoriously difficult to study their magnetic and structural properties. The Fepr protein, in contrast, being a monomer, oxygen stable, and believed to contain only a single Fe–S cluster, seemed to provide an ideal case to pursue the search for the nature of high-spin Fe–S clusters.

2. *Mössbauer and Multifrequency EPR Experiments*

Mössbauer data also seemed to agree with the proposal of a [6Fe–6S] cluster (*11*). About two-thirds of the Fe intensity of the reduced protein (i.e., four out of the proposed total of six) had isomer shift

and quadrupole splitting values similar to those found for $[4Fe–4S]^{2+}$ clusters, whereas the remaining third of the Fe sites (i.e., two out of six) was high-spin ferrous in character with considerably higher isomer shift and quadrupole splitting. The possibility of a $[4Fe–4S]^{2+}$ cluster was nonetheless rejected, mainly on analytical grounds. Assuming that the Fepr protein contains six Fe atoms (which was generally acknowledged), and assuming further that a [4Fe–4S] cluster were present, then the prismane "fingerprint" EPR spectrum must be accounted for by the two remaining (i.e., non-[4Fe–4S]) iron atoms. This was thought to be highly unlikely. The [4Fe–4S] concept was not altogether abandoned; a working model was proposed in which a [4Fe–4S] formed the center of a six-Fe cluster, with two Fe atoms flanking the central core.

The two outer Fe atoms were proposed to be nitrogen ligated. Evidence for the involvement of nitrogen (through the side chains of histidine residues) was obtained by multifrequency EPR. Unresolved hyperfine broadening of the EPR spectrum of the protein in the 3+ state, as well as in the 5+ state, indicated the presence of magnetic nuclei in the direct vicinity of at least some of the Fe atoms (*11*). Nitrogen ligation was also suggested by an observed dependence of the reduction potentials of the 3+ to 4+ transition and, to a lesser extent, of the 4+ to 5+ transition (*12*), suggesting a protonatable group (probably histidine) coordinating one or more Fe atoms.

3. A Second Fepr Protein from Desulfovibrio desulfuricans

In the same year, 1992, a second Fepr protein was isolated by Moura and colleagues from a bacterium closely related to *Desulfovibrio vulgaris*, *D. desulfuricans* (*13*). The features of the *D. desulfuricans* protein were almost identical to those of the *D. vulgaris* protein. Both proteins showed the prismane "fingerprint" EPR spectrum in the reduced state, as well as $S = \frac{9}{2}$ EPR signals in the as-isolated protein. However, despite the apparent similarity of the two proteins, the *D. desulfuricans* protein was argued to contain two, rather than one, Fe–S clusters. This conclusion was based on Mössbauer studies conducted on the as-isolated protein, in which two subspectra were distinguished: a paramagnetic spectrum and a diamagnetic spectrum. The paramagnetic component could be fitted only by assuming six Fe sites. This species was associated with the observed $S = \frac{9}{2}$ EPR signals, and it was thought to arise from a [6Fe–6S] cluster. The diamagnetic species was associated with a second cluster, which gave rise to the prismane "fingerprint" EPR spectrum. The latter cluster was possibly also a [6Fe–6S] cluster. This conclusion seemed to dis-

agree with Fe analysis that showed only 6.5 Fe atoms. How, then, could a protein with only 6.5 Fe atoms carry two [6Fe–6S] clusters? The authors attempted to reconcile this discrepancy by hypothesizing that the protein sample existed as a mixture of holo- and apoprotein.

4. Sequence Determination

A major breakthrough was heralded when Stokkermans *et al.* managed to sequence the putative prismane proteins from both organisms, *D. vulgaris* and *D. desulfuricans* (*14*, *15*). Not surprisingly, the two proteins showed extensive (66%) homology. Special attention was drawn to cysteines and histidines, as these amino acids are usually involved in cluster ligation. Nine cysteines and six histidines were found to be conserved. Four of these nine cysteines are located at the N-terminus where they form a Cys-X_2-Cys-X_7-Cys-X_5-Cys pattern. This motif is reminiscent of, but nevertheless significantly different from, typical [2Fe–2S] and [4Fe–4S] motifs (Cys-X_2-Cys-X_2-Cys-X_n-Cys). When the primary structures of the Fepr proteins were compared with known sequences of other proteins, no homology was found. However, when a homology search was carried out with an advanced screening program, the N-terminal part of the Fepr gene matched with part of the sequence of the carbon monoxide dehydrogenase from *Methanothrix soehngenii* (*16*) and *Clostridium thermoaceticum* (*17*). Table II shows the sequence alignment, in which homologous cysteine residues are marked in bold type. Similar homologous cysteine patterns were later found in the genes of carbon mon-

TABLE II

SEQUENCE COMPARISON BETWEEN THE N-TERMINAL PART OF THE Fepr GENES FROM *Desulfovibrio desulfuricans* (Dd) AND *Desulfovibrio vulgaris* (Dv), CARBON MONOXIDE DEHYDROGENASE FROM *Methanothrix soehngenii* (Ms), *Methanosarcina frisia* Göl (Mf), *Clostridium thermoaceticum* (Ct), *Rhodospirillum rubrum* (Rr), AND ANAEROBIC RIBONUCLEOTIDE REDUCTASE FROM *Escherichia coli* (Ec)[a]

				*		*																*			*	*
Dd	7	**C**	Y	Q	**C**	Q	E	T	V	G	N	K	—	—	—	—	G	C	T	Q	V	G	V	—	**C**	G
Dv	3	**C**	F	Q	**C**	Q	E	T	A	K	N	T	—	—	—	—	G	C	T	V	K	G	M	—	**C**	G
Ms	67	**C**	T	L	**C**	T	Y	G	P	C	D	L	—	—	—	—	T	G	N	K	K	G	A	—	**C**	G
Mf I	76	**C**	C	Y	**C**	T	Y	G	P	C	D	L	—	—	—	—	S	N	N	K	R	G	A	—	**C**	G
Mf II	76	**C**	C	Y	**C**	T	Y	P	G	C	D	L	—	—	—	—	S	G	N	K	R	G	A	—	**C**	G
Ct	63	**C**	R	F	**C**	M	A	G	P	C	R	I	K	A	T	D	G	P	G	S	R	G	I	—	**C**	G
Rr	50	**C**	R	I	**C**	L	K	G	P	C	R	I	D	P	F	G	E	G	P	K	Y	G	V	—	**C**	G
Ec	644	**C**	Y	E	**C**	G	F	T	G	E	F	E	—	—	—	—	—	C	T	S	K	G	F	T	**C**	P

[a] Homologous cysteine residues are in **bold** type.

oxide dehydrogenase from *Methanosarcina frisia* Gö1 (*18*) and *Rhodospirillum rubrum* (*19*), as well as in the anaerobic ribonucleotide reductase from *Escherichia coli* (*20*). Yet the homology, though significant, was very small and was confined to the N-terminal part of the sequence of the Fepr proteins. However, extensive homology to the Fepr protein has been found with genes from several other organisms: *Thiobacillus ferrooxidans* (*21*), *Escherichia coli* (*22*), and *Morganella morganii* (*23*) were all shown to possess a Fepr-type protein sequence.

Interestingly, in a similar manner to the Fepr protein, carbon monoxide dehydrogenase had been shown to exhibit $S = \frac{9}{2}$ EPR signals (see also Table I), and these high-spin EPR properties had been proposed to arise from a novel Fe–S cluster (*24*). The finding of $S = \frac{9}{2}$ EPR signals in the Fepr protein as well as in carbon monoxide dehydrogenase, together with their shared cysteine pattern, suggested that the unknown cluster in carbon monoxide dehydrogenase may also be a [6Fe–6S] cluster. The sequencing of the Fepr proteins was important for a number of other reasons. Among these was the opportunity to determine the exact molecular mass, which was found to be close to 60 kDa. This was rather unexpected, as a considerably smaller size had been inferred from analytical methods for the *D. vulgaris* protein, namely 52 kDa. This meant that the previously determined Fe number of 6.3 had to be adjusted to 7.3.

5. Mutation Studies

Subsequently, mutation studies became possible when an overexpression system was created for the Fepr proteins of *D. vulgaris*, as well as *D. desulfuricans*, by Stokkermans *et al.* and van den Berg *et al.*, respectively (*25*, *26*). Assuming the involvement of one or more of the four N-terminal cysteines in the ligation of the cluster, van den Berg and van Dongen started to mutate some of these cysteines into serines in the *D. desulfuricans* Fepr protein (*6*). To their dismay, the mutations resulted in insoluble protein. However, one of the mutant proteins, C428S, was expressed as a soluble protein (Cys 428 corresponds to Cys 434 in the *D. vulgaris* protein). Remarkably, the absorbance at 400 nm was only one-third that of the wild type protein. Furthermore, the protein was EPR silent except for a broad signal at $g = 4–5$. This signal, which is faint in the *D. vulgaris* protein but more pronounced in that of *D. desulfuricans*, had previously been detected by Moura *et al.*, who attributed it to a minor species of the 3+ state (*13*). Van Dongen and van den Berg had created a protein that exhibited this $S = \frac{3}{2}$ signal only. They were not able to grasp the sig-

nificance of this observation at that time, but when the crystal structure of the *D. vulgaris* Fepr protein became available, this information proved be invaluable for the reinterpretation of most of the previous EPR data.

Until then, the purification of the Fepr protein had been a laborous job as a 240-L batch yielded only as little as 5 mg of protein. With the overexpression clones of the Fepr proteins, the range of protein-consuming studies such as Mössbauer spectroscopy, EXAFS, and, last but not least, crystallization experiments was greatly extended. Thus, several groups set off to systematically investigate the spectroscopic properties of both Fepr proteins, poised at all four (proposed) redox states.

6. MCD Studies

MCD results more or less confirmed the conclusions drawn from previous EPR data (*27*). The shapes of the MCD spectra of the putative prismane protein in the 3+, 4+, and 5+ states had not been observed for any Fe–S protein. This was not surprising, since every single type of Fe–S cluster is considered to exhibit a unique MCD spectrum. Magnetization data confirmed the $S = \frac{9}{2}$ ground state of the 5+ state, as well as the $S = 4$ ground state of the 4+ state. Unexpectedly, in addition to the $S = 4$ contribution, a considerable diamagnetic contribution was observed for the 4+ state. The nature of the diamagnetic contribution was not understood; a physical spin mixture was considered to be a possible explanation.

7. Resonance Raman Studies

Resonance Raman studies on the putative prismane protein would provide other important information. In the frequency region of 200–430 cm^{-1}, the putative prismane protein showed bands that at first sight seemed to be typical for Fe–S clusters, but at a closer look appeared to be broader than those observed in basic Fe–S proteins. Also, the resonance frequencies were slightly different from known Fe–S clusters, and it was contended that "A prismane-type [6Fe–6S] core is clearly an excellent candidate in light of the available analytical and biophysical data" [28].

Even more exciting was the discovery of bands at higher frequency (430–1600 cm^{-1}). Exchanging the sample in $H_2{}^{18}O$ resulted in a shift to lower frequency. A shift to lower frequency was also observed when the protein was enriched in ^{54}Fe or ^{57}Fe (Fig. 6). These data indicated the presence of an iron-oxo species. It was argued that this functionality may be related to the physiological function.

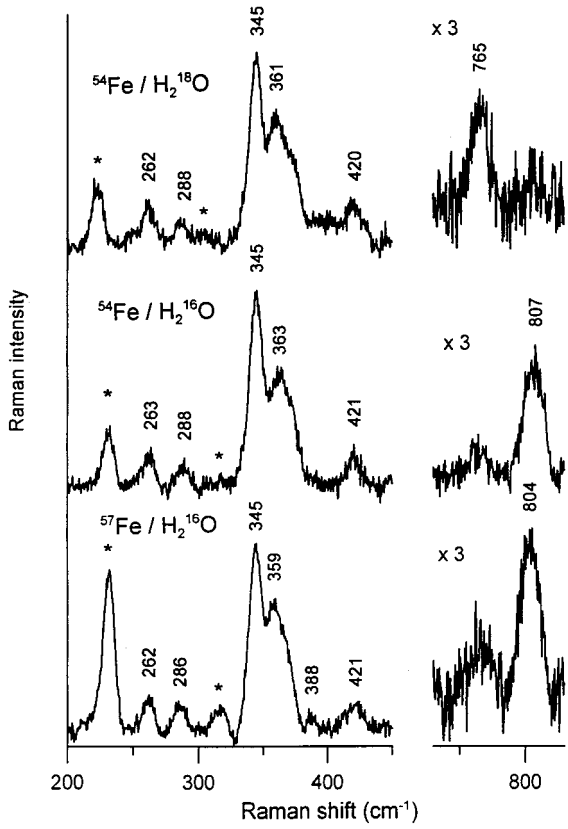

FIG. 6. Resonance Raman spectra of Fepr protein from *D. vulgaris* [from (*28*)]. Upper spectrum, ^{54}Fe-enriched protein in $H_2{}^{18}O$; middle spectrum, ^{54}Fe-enriched protein in $H^{16}O$; lower spectrum, ^{57}Fe-enriched protein in $H_2{}^{16}O$.

8. EXAFS

Fe–S and Fe–Fe distances in [2Fe–2S], [3Fe–4S], and [4Fe–4S] clusters are all very similar: 2.3 and 2.7 Å, respectively. In the [6Fe–6S] prismane model cluster, however, there is an additional Fe–Fe distance at 3.7 Å (Fig. 2). If a [6Fe–6S] cluster were present in the Fepr protein, then this longer Fe–Fe distance should be visible with extended X-ray absorption fine structure (EXAFS). As a consequence, EXAFS studies were carried out at the CCLRC Synchrotron Radiation facility in Daresbury, UK. The two Fepr proteins (those of *D. vulgaris* and *D. desulfuricans*), as well as a synthetic [6Fe–6S] cluster, were subjected to an EXAFS study. Low-temperature EXAFS

data on the synthetic cluster revealed an Fe–Fe distance of around 3.7 Å. However, whereas the typical Fe–S and Fe–Fe distances were readily observed in both Fepr proteins, no longer Fe–Fe distance (i.e., >3.5 Å) could be detected (*6*). Although this could be due to internal disorder or flexibility, it nevertheless shed some doubt on the hypothesis of the presence of a [6Fe–6S] cluster.

Whereas previous Mössbauer data on the prismane proteins of *D. vulgaris* (*11*) and *D. desulfuricans* (*13*) were interpreted to be in agreement with the presence of a [6Fe–6S] cluster, later studies gave indications that the Fepr protein may not contain a single [6Fe–6S] cluster (*6*, *50*). Fitting of the Mössbauer spectra required at least seven Fe sites. The invention of a seventh Fe was not farfetched, as the Fe content had already been adjusted from six to seven when the primary sequence was solved. At this stage crystallographic studies were initiated at CCLRC Daresbury Laboratory, UK.

III. Crystallographic Studies

A. Preliminary Studies

1. Bacterial Growth and Protein Purification

Desulfovibrio vulgaris (strain Hildenborough) NCIB 8303 holding an overproducing plasmid [pJSP104, (*14*)] for the Fepr protein was grown anaerobically as previously described (*26*). The Fepr protein was purified initially according to the procedure of Pierik *et al.* (*10*) and then further purified by fast protein-liquid chromatography (Pharmacia) on a Q-Sepharose HiLoad column. The protein was finally dialyzed against 5 mM Tris at pH 8.0, 50 mM NaCl, and concentrated to 24 mg ml^{-1}. Protein samples were then stored at 203 K prior to use.

2. Crystallization

It proved possible to crystallize the Fepr protein over a wide range of pH, 5.9–8.0, and PEG 8000 concentrations, using both sitting and hanging-drop techniques. The crystals used for the X-ray analysis were produced using the following procedure (*29*):

1. Protein solution (1.3–1.5 μl) prepared as indicated in the previous section was diluted to 4 μl with 0.1 M MES at pH 5.9, 66 mM magnesium acetate.

2. Samples (4 μl) were placed in crischem plates and equilibrated against 600 μl of well solution (0.1 M MES at pH 5.9, 66 mM magnesium acetate).
3. Plates were incubated at 277 K.

Crystals usually appeared within 4 days and grew to a maximum length of 0.7 mm within 10 days. The crystals were dark red in color with a prismatic habit.

3. X-Ray Data Collection

X-ray diffraction data were collected from one crystal mounted in a thin-walled glass capillary containing a small volume of mother liquor to keep the crystal wet. Data were collected on station 9.6 at the CCLRC Daresbury Laboratory using the SRS, a 2-GeV storage ring with an average circulating ring current of 200 mA. Station 9.6 derives its radiation from a supercooled three-pole wiggler magnet operating at 5 T and is equipped with a platinum-coated cylindrically curved fused quartz mirror as the first optical element, followed by a bent triangular Si(111) monochromator producing a wavelength of 0.87 Å. The diffraction images were recorded on a 30 cm diameter MAR-Research image plate detector system set at a distance of 265 mm from the crystal; this gave a maximum resolution of 1.7 Å, but enabled the collection of an almost complete data set without significant deterioration of the crystal due to radiation damage. A typical 1° diffraction pattern is shown in Fig. 7, which also indicates that the X-ray data extend to at least 1.5 Å resolution and that high-resolution data should be obtainable in the future. The sample was cooled to 277 K and a total of 87 1° oscillation images were collected with an exposure time of 60 s per image. All the images were processed using the *MOSFLM* program suite (*30*) and final scaling and data reduction were achieved using *ROTAVATA* and *AGROVATA* from the CCP4 suite of programs (*31*). The quality of the native data is high and the principal statistics are summarized in Table III.

B. Structure Elucidation

1. Structure Analysis

The structure was solved by the multiple isomorphous replacement technique using four heavy atom derivatives: uranyl acetate, platinous chloride, tetramethyllead acetate, and *p*-chloromercury benzoate. All four derivatives gave interpretable heavy atom Patterson syntheses. The heavy atom sites could be correlated between the de-

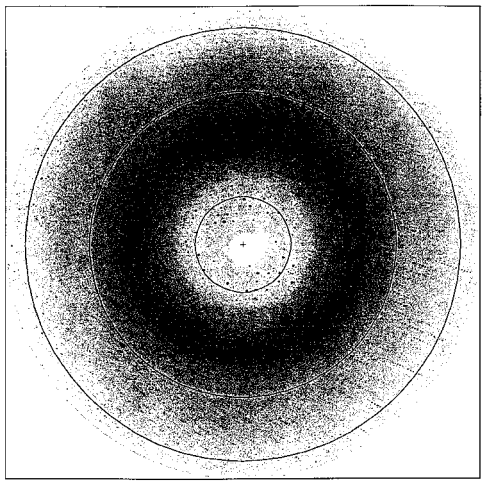

FIG. 7. A typical X-ray diffraction pattern of the Fepr protein from *D. vulgaris* (Hildenborough). The pattern was recorded on station 9.6 at the Synchrotron Radiation Source at the CCLRC Daresbury Laboratory using a wavelength 0.87 Å and a MAR-Research image-plate detector system with a crystal-to-detector distance of 220 mm. X-ray data clearly extend to a resolution of 1.5 Å, or even higher. The crystal system is orthorhombic, spacegroup $P2_12_12_1$ with unit cell dimensions, $a = 63.87$, $b = 65.01$, $c = 153.49$ Å. The unit cell contains four molecules of 60 kDa molecular weight with a corresponding solvent content of approximately 48%.

rivatives, and their presence was confirmed by phase calculation and conventional difference Fourier synthesis methods. Protein phases were generated using the program MLPHARE (*32*), leading to an electron density map at 2.5 Å that clearly showed the molecular boundary and various elements of secondary structure, including some pronounced helices. Improvement of the map with the program DM (*33*), incorporating solvent flattening, histogram matching, and phase extension to 2.0 Å, gave an electron density synthesis revealing some 90% of the molecule. The remainder was located by iterative Fourier syntheses. Map interpretation was undertaken using the computer graphics O program package (*34*).

2. *Structure Refinement*

The structure was refined with the program RESTRAIN (*35*) using all data between 12.0 and 1.72 Å. In the final cycles of refinement all the protein and solvent atoms were allowed to refine isotropically, but

TABLE III

X-RAY DATA FOR THE NATIVE Fepr PROTEIN SHOWING THE DATA QUALITY AND COMPLETENESS TO 1.71 Å RESOLUTION, λ = 0.87 Å

Resolution (Å)	N_{symm}	N_{unique}	R_{symm}	$I/\sigma(I)$	% Possible collected	N_{total}
22.38–6.61	3,190	921	0.031	9.0	82.6	1111
6.61–4.68	7,356	1,929	0.025	22.9	95.0	2203
4.68–3.82	9,432	2,480	0.024	18.7	96.7	2848
3.82–3.31	11,609	3,023	0.026	18.9	98.9	3413
3.31–2.96	13,011	3,424	0.026	20.2	98.4	3826
2.96–2.70	14,435	3,841	0.034	15.7	98.9	4234
2.70–2.50	15,869	4,277	0.041	8.0	100.0	4646
2.50–2.34	16,999	4,587	0.045	8.7	99.4	4937
2.34–2.21	18,130	4,943	0.050	9.3	99.9	5264
2.21–2.09	19,087	5,257	0.057	11.2	99.7	5567
2.09–2.00	20,046	5,481	0.067	9.4	99.7	5822
2.00–1.91	20,893	5,725	0.081	8.7	99.8	6089
1.91–1.84	21,805	5,969	0.104	6.9	100.0	6350
1.84–1.77	22,683	6,206	0.126	5.7	99.7	6573
1.77–1.71	16,550	4,873	0.190	3.3	85.1	5791
	231,095	65,936	0.036		97.2	68674
	(Average multiplicity = 3.4)					

the hetero atoms constituting the two Fe–S clusters were allowed to refine anisotropically. The reflection data were weighted according to a modified form of the scheme proposed by Rees (*36*) so that values of $\Sigma w \cdot \Delta^2$ (where $\Delta = \|F_{obs}| - |F_{calc}\|$) were constant when analyzed in batches of increasing $|F_{obs}|$ and sin θ/λ. All 553 residues were located in addition to the two Fe–S clusters and some 400 solvent molecules. Solvent molecules were retained in the model if they gave peaks at the 1 rms level in a weighted $[2|F_{obs}| - |F_{calc}|]$ Fourier synthesis, at or above the 3 rms level in a weighted difference $[F_{obs}| - |F_{calc}|]$ Fourier synthesis, if the peaks were in chemically sensible positions, and if the isotropic thermal coefficients refined to values below U_{iso} (= $B_{iso}/8\pi^2$) = 0.63 Å^2. The average thermal coefficients for the protein and solvent atoms are 0.27 and 0.40 Å^2, respectively. The principal details of the refinement are given in Table IV.

Full details of the structure analysis and refinement are not appropriate to this review and will be published elsewhere, but it is hoped that sufficient information has been given to validate the unusual structure of the Fepr protein from *Desulfovibrio vulgaris* (Hildenborough).

TABLE IV

PRINCIPAL DETAILS OF REFINEMENT OF Fepr PROTEIN [RESTRAIN (*30*)]

Resolution range	12.0–1.71 Å
No. of protein atoms	4,218
No. of cluster atoms	17
No. of solvent molecules	417
Total no. of (hkl)	68,674
No. of restraints	10,822
No. of positional parameters refined	13,956
No. of thermal parameters refined (cluster hetero atoms treated anisotropically)	4,737
Total no. of parameters refined (includes overall scale and temperature factor)	18,695
Ratio of observations [(hkl) + restraints] to parameters	3.75
Initial and final values of R (final value based on all data)	51.4% 17.1%
Initial and final values of R_{free} based on 4.9% of the data	52.1% 20.8%
R value for highest resolution shell (1.83–1.71 Å)	21.0%
Deviations (Å) of the geometry from ideal values, and in parentheses target σ	
Bond lengths	0.011 (0.020)
Bond angles (2.12 Å $< D <$ 2.65 Å)	0.011 (0.040)
Nonbonded distances ($D >$ 2.65 Å)	0.031 (0.050)
Peptide planarity	0.007 (0.010)
Other planes	0.007 (0.010)
Chirality	0.010 (0.020)

3. *Results of the Refinement*

a. Ramachandran Plot A Ramachandran plot (*37*) indicates that the quality of the model is high, with 94.1% of the residues (except glycine and proline) lying within the permitted regions, 5.7% lying in the additionally allowed regions, and only asparagine N303 lying on the border of the generously allowed and disallowed regions (Fig. 8). The electron density for N303 is well-defined and the residue is located on a turn between a β-strand and an α-helix.

b. Fe–S Cluster 2 It is necessary to make a cautionary comment regarding the interpretation of cluster 2 at this point. Although as indicated above the diffraction data are of high quality and the refinement carefully undertaken, the precise details of this cluster cannot be resolved from the X-ray data alone. Thus, the assignment of electron density peaks to the O and S atoms has been made on the basis of the peak heights in the electron density syntheses and the behavior of the thermal coefficients of the atoms, with respect to the local average, on refinement. Chemical considerations have

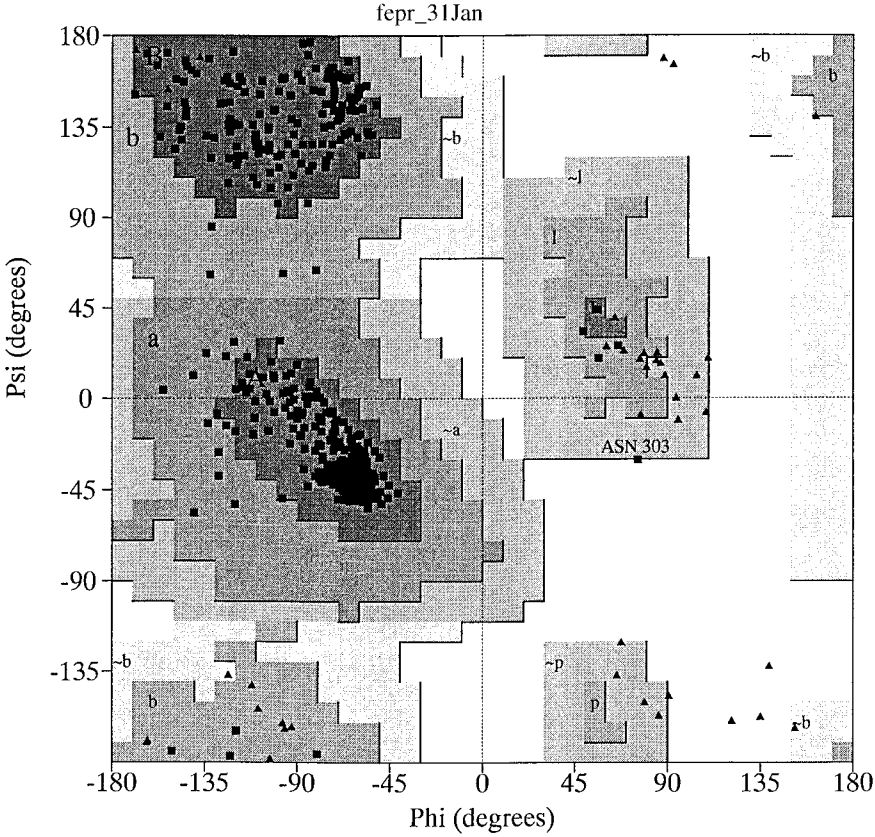

Plot statistics

Residues in most favoured regions [A,B,L]	450	94.3%
Residues in additional allowed regions [a,b,l,p]	26	5.5%
Residues in generously allowed regions [~a,~b,~l,~p]	0	0.0%
Residues in disallowed regions	1	0.2%
Number of non-glycine and non-proline residues	477	100.0%
Number of end-residues (excl. Gly and Pro)	3	
Number of glycine residues (shown as triangles)	50	
Number of proline residues	22	
Total number of residues	552	

Based on an analysis of 118 structures of resolution of at least 2.0 Angstroms and R-factor no greater than 20%, a good quality model would be expected to have over 90% in the most favoured regions.

FIG. 8. A Ramachandran plot (*37*) indicating the overall geometrical quality of the structure of the Fepr protein from *D. vulgaris* at 1.7 Å resolution. Some 94% of the residues lie within the most favored regions, 5.5% in the additional allowed regions, and only one residue, N303 on the border of a disallowed region. The electron density of this residue is very well defined (see text).

also been taken into account. However, it would be difficult from the X-ray data alone to determine unequivocally a situation whereby, for example, the various sites were partially occupied with O and S. What is described therefore represents the most likely interpretation. In addition, difference Fourier syntheses indicate that there may be a substrate bound between two of the Fe atoms, but with a low partial occupancy (and/or disorder) that may be dependent on the oxidation state of the cluster at the crystallization stage. However, it has proved very difficult with the present data to define the precise nature of this moiety, and mononuclear species such as oxygen (hydroxyl group or solvent molecule), dinuclear species such as CO and CN, and even larger substrates cannot be excluded. Clearly, further biochemical and spectroscopic studies are required, in conjunction with crystallographic studies at the highest possible resolution.

C. Description of the Molecular Structure of the Fepr Protein

1. The Domain Organization of the Fepr Molecule

The structure of the Fepr molecule has a number of unusual features, notwithstanding the absence of a prismane [6Fe–6S] cluster. Figure 9 is a ribbon diagram, drawn with the SETOR program (*38*), showing the organization of the molecule of the Fepr protein. The molecule comprises three domains and has two distinct Fe–S clusters some 12–13 Å apart. One of these lies close to the interfaces of the three domains, but the other, a [4Fe–4S] cubane cluster, is close to the outside of the molecule as shown in Fig. 10. The first domain, consisting of residues 1–221, is predominantly α-helical in nature, and six of the helices form two antiparallel three-helix bundles. Three-helix bundles have been reported in a number of proteins, for example, the fifth domain in the phosphotransferase pyruvate phosphate dikinase [PDB Brookhaven code (*39*):1dik], but it is believed that the Fepr protein is the first to contain two bundles arranged almost perpendicular to one another, as shown in Fig. 11. The two bundles are structurally very similar and a sequence identity of some 20% suggests evidence for gene duplication. The second and third domains of the Fepr structure (residues 222–375 and 376–553, respectively) have central β-sheets surrounded by helices and would be classified as three-layer β–α–β, doubly wound folds (*40*). Figures 12a and 12b show the tertiary folds of domains 2 and 3, respectively.

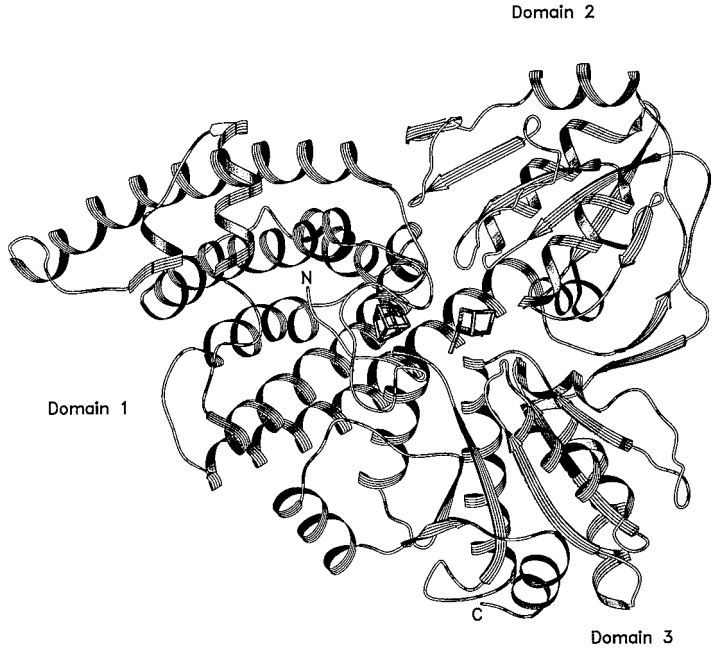

FIG. 9. An overall view of the Fepr molecule from *D. vulgaris* showing the three domains. Domain 1 is predominantly α-helical and contains an unusual configuration of two three-helix bundles approximately perpendicular to one another (see Fig. 11). Domains 2 and 3 have central β-sheets surrounded by helices. The two Fe–S clusters are at the center of the figure; the hybrid cluster is on the left, and located near the interfaces of the three domains.

2. Cluster 1: The Cubane Cluster

Cluster 1 is a conventional [4Fe–4S] cubane cluster bound near the N-terminus of the molecule as shown in Fig. 13. Within the cluster the Fe–S bonds range from 2.26 to 2.39 Å. The cluster is linked to the protein by four cysteine residues with Fe–S distances ranging from 2.21 to 2.35 Å, but the distribution of the cysteine residues along the polypeptide chain contrasts markedly with that found, for example, in the ferredoxins as indicated in Section II,B,4 [also see, for example, (*41*) and references therein]. In the Fepr protein all four cysteine residues (Cys 3, 6, 15, and 21) originate from the N-terminus of the molecule, and the fold of the polypeptide chain in this region is such that it wraps itself tightly around the cluster, yet keeps it near the surface of the molecule. In such a position the cluster is ideally placed to participate in one-electron transfer reactions with other molecules.

FIG. 10. An alternative view of the Fepr molecule showing that cluster 1, a [4Fe–4S] cubane cluster, is located toward the outside of the molecule and therefore in a position to participate in one-electron transfer interactions with other appropriate molecules.

3. Cluster 2: The "Hybrid" Cluster

Cluster 2 appears to be unique among Fe–S-containing proteins whose structures have so far been determined, and it has been termed the "hybrid" cluster (*6*) because of its diverse chemical nature. Figure 14 is a schematic drawing of the cluster as interpreted from the final electron density synthesis and the structure refinement. The cluster contains both oxygen and sulfur bridges, and X represents a site whose precise nature has not been determined, but which may contain a partially occupied and/or disordered substrate molecule (see Section III,B,3,b). The environments of the four iron atoms can be described as follows.

a. Fe5 Fe5 is coordinated to only one protein ligand, Cys 434, with an Fe–Sγ distance of 2.34 Å, but can be considered to be part of a [2Fe–2S] moiety involving Fe6 through the two bridging sulfur atoms, S5 and S6 (average Fe5–S distance is 2.20 Å). In the absence

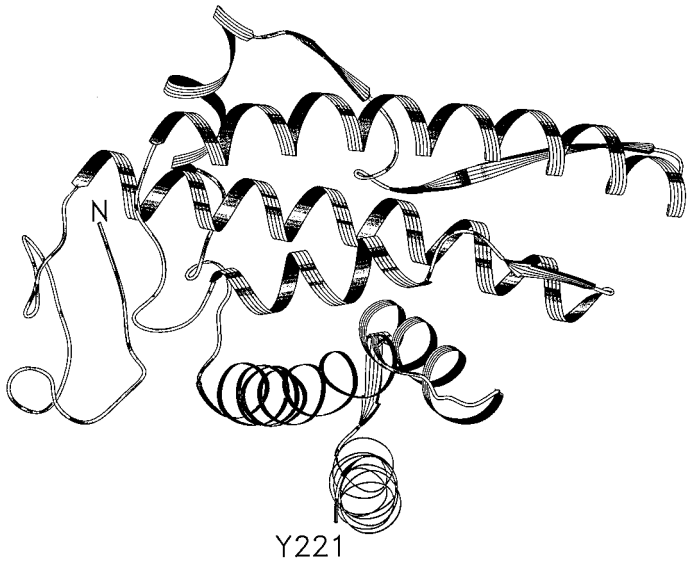

FIG. 11. Domain 1 of the Fepr protein. The two bundles, each containing three helices (two long and one short), are arranged almost perpendicular to one another.

of X the geometry is trigonal, but the addition of X would change this to tetrahedral.

b. Fe6 Fe6 is also bound to the protein by only one residue, Cys 312 (Fe6–Sγ distance = 2.37 Å) and this cysteine adopts a *cis*-peptide configuration. Fe6 is bound to the bridging sulfur atoms, S5 and S6, at an average distance of 2.23 Å. However, this iron atom is also coordinated to an oxygen atom O8, Fe–O8 distance = 1.98 Å, which bridges Fe6 and Fe8. The geometry of Fe6 can therefore be described as tetrahedral.

c. Fe7 Fe7 is bound to the protein by three residues, His 244 (Fe7–Nε2 = 2.16 Å), Glu 268 (Fe7–Oε2 = 2.18 Å), and Cys 459 (Fe7–Sγ = 2.42 Å). It is also bound to an oxygen atom, O9 (Fe7–O9 = 2.10 Å), which forms a bridge to Fe8. In the absence of X the geometry can be described as square pyramidal, but in the presence of X this would change to trigonal bipyramidal.

d. Fe8 Fe8 is only directly linked to one protein ligand, Glu 494 (Fe7–Oε1 = 2.10 Å), but also binds to two bridging oxygen atoms (Fe8–O8 = 2.17 Å and Fe8–O9 = 2.04 Å) and to a sulfur atom, S7, which appears to be part of a persulfide group (Fe8–S7 = 2.48 Å). It

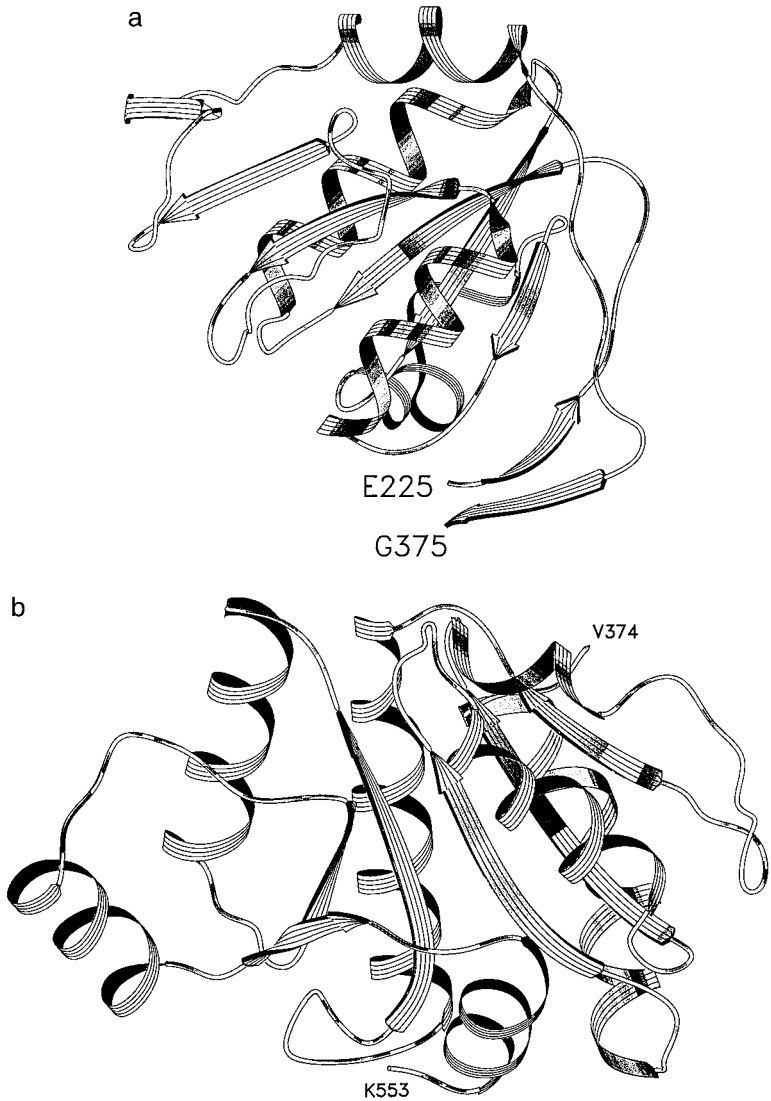

FIG. 12. The organization of domains 2(a) and 3(b). Both domains have central β-sheets surrounded by helices.

is also only 2.58 Å away from S6, which bridges Fe5 and Fe6, and with the fifth ligand the geometry can be considered as distorted trigonal bipyramidal. This geometry could, however, become octahedral, depending on how X binds to the hybrid cluster.

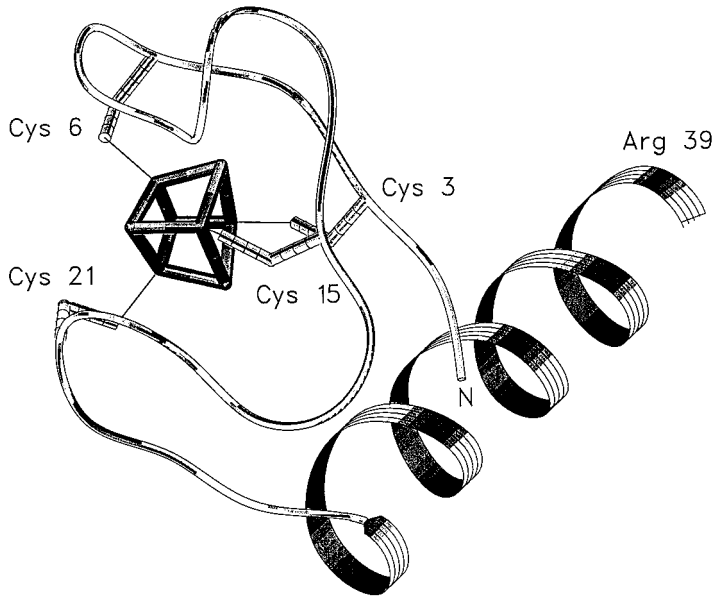

FIG. 13. Cluster 1 is a [4Fe–4S] cubane cluster located at the N-terminus of the Fepr molecule and close to the first long helix (residues 24–50 inclusive). The cluster is bound to the protein by four cysteine residues: Cys 3, Cys 6, Cys 15, and Cys 21. The distribution of these cysteine residues contrasts markedly with that found in the ferredoxins.

The presence of a persulfide group appears at first sight to be rather surprising. To our knowledge the structure of only one other protein, rhodanese (*42*), has been found to possess such a group. Rhodanese is an enzyme that catalyzes the transfer of sulfur from thiosulfate to cyanide to yield thiocyanate. There has also been a debate regarding the putative role of rhodanese in Fe–S formation [see, for example, (*43*, *44*)]. It is also interesting to note that the structure determination of formate dehydrogenase H (*45*) indicates that catalysis (two-electron oxidation of formate to carbon dioxide) appears to involve Mo, two molybdopterin guanine dinucleotide cofactors, a selenocysteine, and a [4Fe–4S] cluster. The biological function of the Fepr protein is, as yet, unknown, but it may well involve the persulfide moiety.

In the Fepr protein the two clusters are some 12–13 Å apart and probably within electron transfer range. However, as shown in Fig. 15, there are no obvious electron pathways involving the polypeptide chain. A tyrosine residue, Tyr 493, lies approximately midway be-

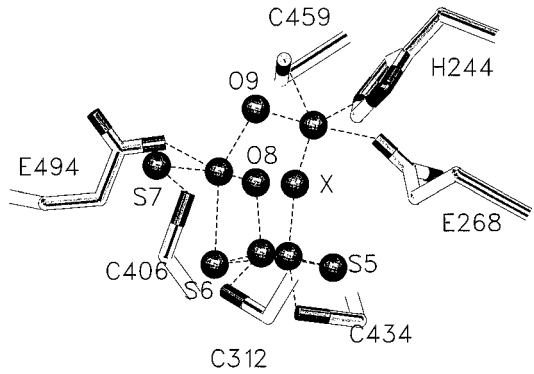

FIG. 14. Cluster 2. The "hybrid" cluster has a number of unusual features, including the existence of O and S bridges within the same cluster. At the base of the cluster, Fe5, Fe6, S5, and S6 form a [2Fe–2S] unit, bound to the protein by C434 (to Fe5) and C312 (to Fe6). O8 and O9 form oxygen bridges between Fe6 and Fe8, and Fe7 and Fe8, respectively. The nature of X, which bridges Fe5 and Fe7, is not known; it appears to be only partially occupied in the present crystal structure and could be a single atom such as O or a solvent molecule, a dinuclear species such as CO or CN, or an even larger moiety. Cys 406 and S7 constitute a persulphide group ligated to Fe8. The geometries of the individual Fe atoms are described in the text.

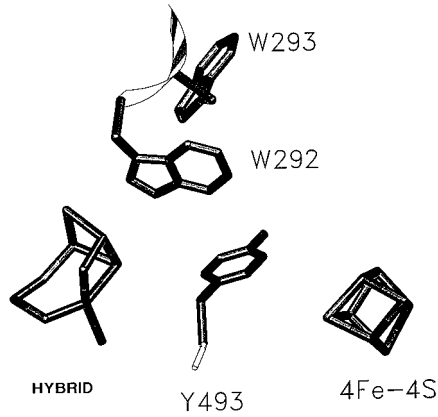

FIG. 15. The two Fe–S clusters are some 12–13 Å apart and within possible electron transfer range. A tyrosine residue, Y493, is situated roughly halfway between the two clusters, but whether it plays a role in any electron transfer is unclear. Two adjacent tryptophan residues are also located close to cluster 2; again, their possible roles in any enzymatic reaction remain to be defined.

tween the two clusters, but whether it plays any role in mediating electron transfer remains to be seen.

IV. Conclusion and Future Studies

Clearly, a number of outstanding questions remain regarding the Fepr protein. The first concerns the discrepancies between the structure as originally proposed and the crystallographic model. These discrepancies can now be better understood in terms of a number of remarkable coincidences of circumstances. Thus, the unusual shape of the molecule appears to give an incorrect apparent molecular mass in the analytical ultracentrifuge, leading to an underestimation of the Fe stoichiometry. The EPR spectrum of the cubane cluster 1 is very unusual and difficult to detect. Cluster 2 has a structure that has not been seen before, occurs in four stable oxidation states, and in the reduced form has an EPR spectrum that is almost identical to those of model compounds containing a $[6Fe–6S]^{3+}$ core. A reevaluation of the various types of spectroscopy has been initiated in several laboratories, and current interpretations have proved to be in excellent agreement with the X-ray structure (*6*, *50*). One important question that required to be addressed was the definition of the redox states. In the old (prismane) model, the redox properties of the Fepr protein were described under the assumption that it contained a single [6Fe–6S] cluster that can occur in four different redox states. With the crystal structure now available, the redox properties of the Fepr protein now have to be described considering the presence of two novel [4Fe–4S] clusters. Previous studies by van Dongen and van den Berg (*6*) on a mutant Fepr protein proved to be the key to the solution of this problem. As mentioned earlier, the C428S mutant Fepr protein from *D. desulfuricans* was found to be EPR silent except for a broad resonance at $g \approx 4.5$. Cys 428 corresponds to Cys 434 in the *D. vulgaris* protein, and the crystal structure shows that this residue ligates to Fe5, which is part of the hybrid cluster. The decreased absorbance at 400 nm, together with the absence of most of the EPR signals in the mutant protein, can now be confidently explained by assuming that in the C428S mutant Fepr protein, the hybrid cluster is also absent. This in turn implies that the $g \approx 4.5$ signal must arise from the cubane cluster and that, as a consequence, all *other* EPR signals must originate from the hybrid cluster. That this is the case is supported by newly obtained Mössbauer data strongly suggesting that all four irons atoms in the hybrid cluster in the three most positive oxidation

TABLE V

OXIDATION STATES OF THE HYBRID CLUSTER (*7*)[a]

"Prismane" valency	Hybrid cluster				Spin state
	Fe5	Fe6	Fe7	Fe8	
"6+"	III	III	III	III	0
"5+"	III	III	(III and II)		$\frac{9}{2}$; $\frac{1}{2}$
"4+"	III	III	II	II	0; 4
"3+"	(III and II)		II	II	$\frac{1}{2}$

[a] "Prismane" valency refers to the old model assuming the presence of a [6Fe–6S] cluster (*7*). Hybrid cluster refers to the 4Fe cluster found to be present in the crystal structure.

states (4^+, 5^+, and 6^+), are exchange coupled. A coupling scheme has been proposed in which the spin of one high-spin Fe^{3+} is oriented antiparallel to the spins of the other three (high-spin) iron sites, resulting in a total spin of $\frac{9}{2}$ for the hybrid cluster in the as-isolated Fepr protein (*6*, *50*). Reevaluation of Mössbauer, MCD, and EPR data has resulted in the oxidation scheme shown in Table V. According to this table, the hybrid cluster can exist in four different redox states. This clearly distinguishes the hybrid cluster in Fepr from all other known 4Fe clusters, which can assume not more than three, and usually only two, redox states. Resonance Raman (RR) studies on the Fepr protein showed a band around 800 cm^{-1}, which was probably due to an iron-oxo moiety (*28*). The RR data further predicted that the observed band is most likely due to the asymmetric stretch of an Fe–O–Fe species with an angle of 150–180°. The crystal structure shows the presence of not one, but two such species, namely, Fe6–O–Fe8 and Fe7–O–Fe8, but both species have angles close to 90° (94.6° and 106.4°, respectively). This implies that probably neither of these two moieties account for the RR band around 800 cm^{-1}. However, if "X" were a single oxygen, there would be a third iron-oxo group formed by Fe5–O–Fe7 with an angle of 163.2°, which could readily explain the observed RR spectra. Thus, RR data strongly suggest that "X" is a single oxygen, probably arising from a solvent molecule.

A second important question yet to be solved concerns the function of the Fepr protein in the organisms in which it has been found, and the mechanism by which it achieves this function. Clearly, X represents a potential substrate binding site within cluster 2, and the presence of a substrate in this position will complete the coordination of Fe5 and Fe7. The nature of X, however, remains an enigma, although

a solvent molecule with partial occupancy provides a working model for the current structure. Very careful X-ray studies at the highest resolution possible, in conjunction with biochemical and spectroscopic studies, will be required to determine what X can be and how the cubane cluster plays a role in any redox reaction.

The third concerns whether cluster 2 in the Fepr structure is unique, or whether it is representative of clusters of a similar type that are going to be discovered in, for example, the proteins listed in Table I. The elucidation of the structure of nitrogenase clearly showed that the Fe–S clusters more complex than the FeS_4, [2Fe–2S] and [4Fe–4S], occur in nature. The Fepr structure provides yet another example, and it would not be unreasonable to suppose that more will be found. Fepr genes have been found in several other organisms, including *Escherichia coli*. It is likely that more Fepr proteins will be discovered. Indeed, these proteins may not be a curiosity among sulfate-reducing bacteria, but instead may be widely distributed among the bacterial kingdom. Whether the elusive [6Fe–6S] cluster occurs in biology remains an open question.

ACKNOWLEDGMENTS

The authors gratefully acknowledge the support of Professor W. R. Hagen and his colleagues at Wageningen University, The Netherlands. They would also like to thank the members of the protein crystallographic facility group at CCLRC Daresbury Laboratory and, in particular, Drs. J. Hadden, V. Zaitsev, S. Bailey, A. McAlpine, E. Duke, and G. Card. All the structural diagrams were drawn with the program SETOR (*38*), and coordinates for pyruvate phosphate dikinase were extracted from the Protein Data Bank, Brookhaven National Laboratory, USA (*39*). Dr. C. Orengo also gave very helpful advice regarding the classification of the domains in the Fepr protein. Sequence data from Genbank (*51*) were used to construct Table II.

REFERENCES

1. Beinert, H.; Kennedy, M. C. *FASEB J.* **1993,** *7,* 1442–1449.
2. Klausner, R. D.; Harford, J. B. *Science* **1989,** *246,* 870–872.
3. Rouault, T. A.; Stout, C. D.; Kaptain, S.; Harford, J. B.; Klausner, R. D. *Cell* **1991,** *64,* 881–883.
4. Kim, J.; Rees, D. C. *Nature* **1992,** *360,* 553–560
5. Kim, J.; Rees, D. C. *Science* **1992,** *257,* 1677–1682.
6. Arendsen, A. F.; Hadden, J.; Card, G.; McAlpine, A. S.; Duke, E. H. M.; Bailey, S.; Zaitsev, V.; Lindley, P.; Kröckel, M.; Trautwein, A. X.; Feiters, M. C.; Charnock, J. M.; Garner, C. D.; Marritt, S. J.; Thomson, A. J.; Kooter, I. M.; Johnson, M. K.;

van den Berg, W. A. M.; van Dongen, W. M. A. M.; Hagen, W. R. *J. Biol. Inorg. Chem.* **1998,** *3,* 81–95.
7. Hagen, W. R.; Pierik, A. J.; Veeger, C. *J. Chem. Soc. Faraday Trans.* **1989,** *I85,* 4083–4090.
8. Kanatzidis, M. G.; Hagen, W. R.; Dunham, W. R.; Lester, R. K.; Coucouvanis, D. J. *J. Amer. Chem. Soc.* **1985,** *107,* 953–961.
9. Hagen, W. R.; van Berkel-Arts, A.; Krüse-Wolters, K. M.; Voordouw, G.; Veeger, C. *FEBS Lett.* **1985,** *203,* 59–63.
10. Pierik, A. J.; Wolbert, R. B. G.; Mutsaers, P. H. A.; Hagen, W. R.; Veeger, C. *Eur. J. Biochem.* **1992,** *206,* 697–704.
11. Pierik, A. J.; Hagen, W. R.; Dunham, W. R.; Sands, R. H. *Eur. J. Biochem.* **1992,** *206,* 705–719.
12. Hagen, W. R.; Marritt, S. J.; Keijser, B. J. F.; Arendsen, A. F.; Bulsink, Y. B. M.; van den Berg, W. A. M.; van Dongen, W. M. A. M.; Krockel, M.; Trautwein, A. X.; Feiters, M. C.; van Strijdonck, G. P. F.; Charnock, J.; Garner, C. D.; Farrar, J. A.; Thomson, A. J.; van Dam, P.; Reijerse, E. J. *J. Inorg. Biochem.* **1995,** *59,* 521.
13. Moura, I.; Tavares, P.; Moura, J. J. G.; Ravi, N.; Huynh, B. H.; Lui, M. Y.; LeGall, J. *J. Biol. Chem.* **1992,** *267,* 4489–4496.
14. Stokkermans, J. P. W. G.; Pierik, A. J.; Wolbert, R. B. G.; Hagen, W. R.; Van Dongen, W. M. A. M.; Veeger, C. *Eur. J. Biochem.* **1992,** *208,* 435–442.
15. Stokkermans, J. P. W. G.; Houba, P. H. J.; Pierik, A. J.; Hagen, W. R.; van Dongen, W. M. A. M.; Veeger, C. *Eur. J. Biochem.* **1992,** *210,* 983–988.
16. Eggen, H. I. L.; Geerling, A. C. M.; Jetten, M. S. M.; de Vos, W. M. *J. Biol. Chem.* **1991,** *266,* 6883–6887.
17. Morton, T. A.; Runquist, J. A.; Ragsdale, S. W.; Shanmugasundaram, T.; Wood, H. G.; Ljungdahl, L. G. J. *J. Biol. Chem.* **1991,** *266,* 23824–23828.
18. Eggen, R. I. L.; van Kranenburg, R.; Vrieseman, A. J. M.; Geerling, A. C. M.; Verhagen, M. F. J. M.; Hagen, W. R.; de Vos, W. M. *J. Biol. Chem.* **1996,** *271,* 14256–14263.
19. Kerby, R. L.; Hong, S. S.; Ensign, S. A.; Coppoc, L. J.; Ludden, P. W.; Roberts, G. P. *J. Bacteriol.* **1992,** *174,* 5284–5294.
20. Sun, X.; Harder, J.; Krook, M.; Jörnvall, H.; Sjöberg, B.-M.; Reichard, P. *Proc. Natl. Acad. Sci. USA* **1993,** *90,* 577–581.
21. Dominy, C. N.; Deane, S. M.; Rawlings, D. E. *Microbiology* **1997,** *143,* 3129–3136.
22. Bult, C. J.; White, O.; Olsen, G. J.; Zhou, L. X.; Fleischmann, R. D.; Sutton, G. G.; Blake, J. A.; Fitzgerald, L. M.; Clayton, R. A.; Gocayne, J. D.; Kerlavage, A. R.; Dougherty, B. A.; Tomb, J. F.; Adams, M. D.; Reich, C. I.; Overheek, R.; Kirkness, E. F.; Weinstock, K. G.; Merrick, J. M.; Glodek, A.; Scott, J. L.; Geoghagen, N. S. M.; Weidman, J. F.; Fuhrmann, J. L.; Nguyen, D.; Utterback, T. R.; Kelley, J. M.; Peterson, J. D.; Sadow, P. W.; Hanna, M. C.; Cotton, M. D.; Roberts, K. M.; Hurst, M. A.; Kaine, B. P.; Borodousky, M.; Klenk, H. P.; Fraser, C. M.; Smith, H. O.; Woese, C. R.; Venter, J. C. *Science* **1996,** *273,* 1058–1073.
23. Kühn, S.; Braun, V.; Köster, W. *J. Bacteriol.* **1996,** *178,* 496–504.
24. Jetten, M. S. M.; Pierik, A. J.; Hagen, W. R. *Eur. J. Biochem.* **1991,** *202,* 1291–1297.
25. Stokkermans, J. P. W. G.; van den Berg, W. A. M.; van Dongen, W. M. A. M.; Veeger, C. *Biochim. Biophys. Acta* **1992,** *1132,* 83–87.
26. Van den Berg, W. A. M.; Stevens, A. A. M.; Verhagen, M. F. J. M.; van Dongen, W. M. A. M.; Hagen, W. R. *Biochim. Biophys. Acta* **1994,** *1206,* 240–246.
27. Marritt, S. J.; Farrar, J. A.; Breton, J. L. J.; Hagen, W. R.; Thomson, A. J. *Eur. J. Biochem.* **1995,** *232,* 501–505.

28. De Vocht, M. L.; Kooter, I. M.; Bulsink, Y. B. M.; Hagen, W. R.; Johnson, M. K. *J. Am. Chem. Soc.* **1996,** *118,* 2766–2767.
29. Arendsen, A.; Bulsink, Y.; Hagen, W.; Hadden, J.; Card, G.; McAlpine, A. S.; Bailey, S.; Zaitsev, V.; Lindley, P. *Acta Cryst.* **1996,** *D52,* 1211–1213.
30. Leslie, A. G. W. In *Jnt. CCP4-EACMB Newslett. Prot. Crystallogr.* **1992,** *26,* CCLRC Daresbury Laboratory, Warrington WA44AD, UK.
31. Collaborative Computing Project, Number 4, *Acta Cryst.* **1994,** *D50,* 760–763.
32. Otwinowski, Z. In "Proceedings of the CCP4 Study Weekend;" Wolf, W.; Evans, P. R.; Leslie, A. W. G., Eds; **DL/SCI/ 32,** 80–86, CCLRC Daresbury Laboratory, Warrington WA44AD, UK, 1991.
33. Cowtan, K. D.; Main, P. *Acta Cryst.* **1993,** *D49,* 148–157.
34. Jones, T. A.; Zou, J.-Y.; Cowan, S. W.; Kjeldgaard, M. *Acta Cryst.* **1991,** *A47,* 110–119.
35. Driessen, H.; Haneef, M. I. J.; Harris, G. W.; Howlin, B.; Khan, G.; Moss, D. S. *J. Appl. Cryst.* **1989,** *22,* 510–516.
36. Rees, B. *Acta Cryst.* **1976,** *A32,* 483–488.
37. Ramakrishnan, C.; Ramachandran, G. N. *Biophys. J.* **1965,** *5,* 909–933.
38. Evans, S. V. *J. Mol. Graphics* **1993,** *11,* 134–138.
39. Bernstein, F. C.; Koetzle, T. F.; Williams, G. J. B.; Meyer, E. F. Jr.; Brice, M. D.; Rogers, J. R.; Kennard, O.; Shimanouchi, T.; Tasumi, M. *J. Mol. Biol.* **1997,** *112,* 535–542.
40. Orengo, C. A.; Flores, T. P.; Taylor, W. R.; Thornton, J. M. *Prot. Engineer.* **1993,** *6,* 485–500.
41. Lindley, P. F. *Reps. Progr. Phys.* **1996,** *59,* 867–933.
42. Ploegman, J. H.; Drenth, G.; Kalk, K. H.; Hol, W. G. J. *J. Mol. Biol.* **1978,** *123,* 557–594.
43. Sandberg, W.; Graves, M. C.; Rabinowitz, J. C. *Trends Biol. Sci.* **1987,** *12,* 56.
44. Cerletti, P. *Trends Biol. Sci.* **1987,** *12,* 57.
45. Boyington, J. C.; Gladyshev, V. N.; Khangulov, S. V.; Stadtman, T. C.; Sun, P. D. *Science* **1997,** *275,* 1305–1308.
46. Hagen, W. R.; Wassink, H.; Eady, R. R.; Smith, B. E.; Haaker, H. *Eur. J. Biochem.* **1987,** *169,* 457–465.
47. Pierik, A. J.; Hagen, W. R. *Eur. J. Biochem.* **1991,** *195,* 505–516.
48. Arendsen, A. F.; Verhagen, M. F. J. M.; Wolbert, R. B. G.; Stams, A. J. M.; Jetten, M. S. M.; Hagen, W. R. *Biochemistry* **1993,** *32,* 10323–10330.
49. Steuber, J.; Arendsen, A. F.; Hagen, W. R.; Kroneck, P. M. H. *Eur. J. Biochem.* **1995,** *233,* 873–879.
50. Kröckel, M.; Trautwein, A. X.; Arendsen, A. F.; Hagen, W. R. *Eur. J. Biochem.* **1998,** *251,* 454–461.
51. Burks, C.; Cassidy, M.; Cinkosky, M. J.; Cumella, K. E.; Gilna, P.; Hayden, J. E.-D.; Keen, G. M.; Kelley, T. A.; Kelly, M.; Kristofferson, D.; Ryals, J. *Genbank, Nucl. Acids Res.* **1991,** *19(suppl.),* 2221–2225.

This Page Intentionally Left Blank

NMR SPECTRA OF IRON–SULFUR PROTEINS

IVANO BERTINI,* CLAUDIO LUCHINAT,† and ANTONIO ROSATO*

*Department of Chemistry, University of Florence, 50121 Florence, Italy; and †Department of Soil Science and Plant Nutrition, University of Florence, 50144 Florence, Italy

I. Introduction
II. Electron Relaxation Times
  A. The Case of the Monomer
  B. Polymetallic Systems
III. Valence Delocalization
IV. Considerations on the Reduction Potential
V. Solution Structure
  A. Assignment and Standard Constraints
  B. Nonstandard Constraints: Nuclear Relaxation Rates
  C. Nonstandard Constraints: Hyperfine Shifts
  D. Examples
VI. Folding
VII. Perspectives
References

I. Introduction

From very early proton NMR studies on paramagnetic compounds, hyperfine shifted signals were observed for solutions of iron–sulfur proteins (*1–7*). A large variety of chemical shifts (upfield and downfield) were found, and a large variation of slopes were obtained as a function of temperature (*8*, *9*). Rationalization of these observations will be given in this review. The first reports tried to relate similar patterns with similar iron–sulfur content. Early in the literature of the NMR of these systems (relevant to this review) substitution of protons with deuterons in the amino acids coordinating to the metal ions was exploited to assign their resonances (*4*). ^{13}C labeling was also exploited at early stages (*7*, *10*, *11*). 1D NOEs, which had already been pioneered by La Mar for less severely broadened signals in heme-containing proteins (*12*), were first observed between hyperfine

Copyright 1999 by Academic Press.
All rights of reproduction in any form reserved.
0898-8838/99 $30.00

shifted signals in a 2[Fe_4S_4] ferredoxin (*13*) (Fd hereafter). With these tools it was possible to assign the βCH_2 pairwise (*13*, *14*) and, looking at a structural model, to obtain the first sequence and stereospecific assignments (*15–17*). In 1991, 2D NOESY cross peaks between fast-relaxing hyperfine shifted protons were reported for a HiPIP (*18*). The first COSY experiment on an iron–sulfur protein involving hyperfine shifted protons was reported in the same year (*19*), whereas the first TOCSY experiment was reported later (*20*). Since then, iron–sulfur proteins entered the field of high-resolution NMR, where proton assignments are no longer tentative but, if obtained with appropriate protocols, safe.

With these assignments at hand the analysis of the hyperfine shifts became possible. An Fe(III) in tetrahedral structures of iron–sulfur proteins has a high-spin electronic structure, with negligible magnetic anisotropy. The hyperfine shifts of the protons influenced by the Fe(III) are essentially Fermi contact in origin (*21*, *22*). An Fe(II), on the other hand, has four unpaired electrons and there may be some magnetic anisotropy, giving rise to pseudo-contact shifts. In addition, there is a quintet state at a few hundred cm^{-1}, which may complicate the analysis of hyperfine shifts, but the main contribution to hyperfine shifts is still from the contact shifts (*21*, *22*).

Contact shifts give information on the electronic structure of the iron atoms, particularly on the valence distribution and on the magnetic coupling within polymetallic systems. The magnetic coupling scheme, which is considered later, fully accounts for the variety of observed hyperfine shifts and the temperature dependence. Thus, through the analysis of the hyperfine shifts, ^1H NMR provides detailed information on the metal site(s) of iron–sulfur proteins, and, thanks to the progress in NMR spectroscopy, also the solution structure (*23*, *24*).

In this review we will deal with iron–sulfur proteins where the iron atoms are coordinated only by cysteine ligands and bridging sulfurs, as well as rubredoxin (Rd hereafter), which is the initial building block in all subsequent discussions.

II. Electron Relaxation Times

A. The Case of the Monomer

Electron relaxation times are important parameters that allow us to predict whether high-resolution NMR is feasible. The two most im-

portant parameters in NMR are the nuclear longitudinal and transverse relaxation rates R_1 and R_2. R_2 is related to the signal linewidth (measured in hertz) by $\pi\,\Delta\nu = R_2$, $\Delta\nu$ being the half-height linewidth. The paramagnetic contributions to the nuclear relaxation rates, R_{1M} and R_{2M}, are given by (*25*)

$$R_{1M} = \frac{2}{15}\left(\frac{\mu_0}{4\pi}\right)^2 \frac{\gamma_I^2 g_e^2 \mu_B^2 S(S+1)}{r^6}\left[\frac{7\tau_S}{1+\omega_S^2\tau_S^2} + \frac{3\tau_S}{1+\omega_I^2\tau_S^2}\right] \tag{1a}$$

$$R_{2M} = \frac{1}{15}\left(\frac{\mu_0}{4\pi}\right)^2 \frac{\gamma_I^2 g_e^2 \mu_B^2 S(S+1)}{r^6}\left[4\tau_S + \frac{13\tau_S}{1+\omega_S^2\tau_S^2} + \frac{3\tau_S}{1+\omega_I^2\tau_S^2}\right], \tag{1b}$$

where S is the spin moment of the electron, γ_I is the magnetogyric ratio of the nucleus, r is the metal-to-nucleus distance, τ_S is the correlation time for the nucleus–electron interaction (often equal to the electron relaxation time), ω_I and ω_S are the Larmor frequencies of the nucleus and of the electron, respectively, and all other symbols have their usual meaning. There is also a contribution to the linewidth, known as Curie relaxation, which is relevant for high S values and larger molecular weights. The contribution due to Curie relaxation to the nuclear transverse relaxation is (*26*, *27*)

$$R_{2M} = \frac{1}{5}\left(\frac{\mu_0}{4\pi}\right)^2 \frac{\omega_I^2 g_e^4 \mu_B^4 S^2(S+1)^2}{(3kT)^2 r^6}\left[4\tau_r + \frac{3\tau_r}{1+\omega_I^2\tau_r^2}\right], \tag{2}$$

where τ_r is the correlation time for the reorientation of the molecule, k is Boltzmann's constant, T is the absolute temperature, and all other symbols have already been defined. The contribution to transverse nuclear relaxation described by Eq. (2) increases with increasing magnetic field, because of the increase of ω_I. This implies that when $S > \frac{1}{2}$ and the magnetic field is higher than 500 MHz (11.7 T), the signals of protons close to the metal ion may be broadened beyond detection (depending on the value of τ_r). Indeed, it may happen, although this has never been reported for iron–sulfur proteins, that the signal of a given proton is detected at 90 MHz more easily than at 600 MHz because its transverse relaxation is much slower at the lower field (*28*).

Let us now refer to Rd, which in the oxidized state contains an Fe(III) with $S = \frac{5}{2}$, and in the reduced state an Fe(II) with $S = 2$. In both states the iron ion is tetrahedrically coordinated. From the nu-

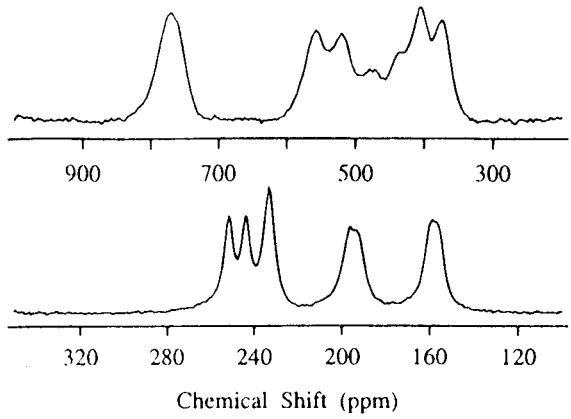

FIG. 1. *Top*: ^{2}H spectrum of oxidized [$^2H^{\beta 2,\beta 3}$]Cys labeled Rd (*29*). *Bottom*: ^{2}H spectrum of reduced [$^2H^{\beta 2,\beta 3}$]Cys labeled Rd. (*29*).

clear relaxation rates of protons at fixed distance from the metal, it is possible to calculate the electronic relaxation times of the foregoing equations and estimate the Curie contribution. Only the Hα protons are observed in the ^{1}H NMR spectrum (*29*). The signals of the Hβ nuclei were observed on a Bruker DMX400 spectrometer in the deuterium-labeled protein (*29*) (Fig. 1, top). The substitution of ^{1}H with ^{2}H eases the detection of the signals, because the magnetogyric ratio of the latter is 6.5 times smaller than the former, and thus the linewidth of its signals is, according to Eqs. (1) and (2), $\frac{1}{42}$ of the corresponding proton signals. The iron atom in oxidized Rd has an estimated electron relaxation time close to 0.1 ns (Table I). This value of the electron relaxation time sets a limit for high-resolution NMR, as it barely allows to observe the signals of the Hα protons but not those of the Hβ. The ^{2}H NMR spectrum of reduced Rd is reported in Fig. 1 (bottom) (*29*). Hβ protons are barely observable also in the ^{1}H NMR spectrum, and their linewidths allow us to calculate τ_S, which is of the order of 10^{-11} s (Table I).

By assuming that the hyperfine shifts are contact shifts in origin, it is possible to evaluate the hyperfine coupling constant from the following equation (*30*):

$$\delta^{con} = \frac{A}{\hbar}\frac{g_e \mu_B S(S+1)}{3\gamma_I kT}, \qquad (3)$$

where A is the hyperfine coupling constant, and all other symbols have their usual meaning. The value of A/h for the Hβ protons of Rd

TABLE I

EXPERIMENTAL LINEWIDTHS OF THE NMR SIGNALS ARISING FROM CYSTEINE Hβ PROTONS IN IRON–SULFUR PROTEINS[a]

System	Metal site[b]	Cysteine Hβ NMR linewidth (Hz)	τ_S (ps)[c]	Mechanism
Oxidized rubredoxin	Fe^{3+}	50,000–150,000	100	Dipolar
Reduced rubredoxin	Fe^{2+}	3,000–15,000	10	Dipolar ≈ Curie
Oxidized ferredoxin	$[Fe_2S_2]^{2+}$	1,500–20,000	100	Dipolar
Reduced ferredoxin[d]	$[Fe_2S_2]^{+}$–Fe^{3+}	1,000–3,000	5	Dipolar ≥ Curie
Reduced ferredoxin[e]	$[Fe_2S_2]^{+}$–Fe^{2+}	300–600	5	Dipolar ≥ Curie
Oxidized ferredoxin[f]	$[Fe_3S_4]^{+}$–Fe^{3+}_{aC}	50–100	1	Dipolar ≈ Curie
Oxidized ferredoxin[g]	$[Fe_3S_4]^{+}$–Fe^{3+}_{C}	200–500	1	Dipolar ≈ Curie
Oxidized HiPIP[h]	$[Fe_4S_4]^{3+}$–Fe^{3+}	200–500	1	Dipolar
Oxidized HiPIP[i]	$[Fe_4S_4]^{3+}$–$Fe^{2.5+}$	100–200	1	Dipolar
Reduced HiPIP/ oxidized ferredoxin	$[Fe_4S_4]^{2+}$–$Fe^{2.5+}$	200–600	5	Dipolar

[a] τ_s values and the dominant mechanism for line broadening have been evaluated from the reported linewidths through Eqs. (1) and (2) as described in text.

[b] When a system contains nonequivalent iron ions, the values relative to each site are reported in different lines.

[c] These values are estimated within a factor of 3.

[d] Values relative to the cysteines coordinated to the Fe^{3+} ion.

[e] Values relative to the cysteines coordinated to the Fe^{2+} ion.

[f] Values relative to the cysteines whose signals have an anti-Curie-type temperature dependence.

[g] Values relative to the cysteines whose signals have a Curie-type temperature dependence.

[h] Values relative to the cysteines coordinated to the Fe^{3+} ion.

[i] Values relative to the cysteines coordinated to the $Fe^{2.5+}$ ion.

is of the order of 1–2 MHz (*31*), in agreement with that estimated from NMR spectra of model compounds (*32*) (see also (*33*)). Its magnitude is related to the amount of unpaired spin density present on the *s* orbitals of observed nuclei. The value obtained is in agreement with ENDOR measurements in magnetically coupled polymetallic systems (*34*). From ^{57}Fe ENDOR (*35*) and Mössbauer (*36*, *37*) measurements, it is feasible to obtain the value of A/h for the metal ion itself.

B. POLYMETALLIC SYSTEMS

Polymetallic systems are magnetically coupled. The magnetic coupling in the simple Heisenberg model can be described by the following Hamiltonian (*38–40*):

$$H = \sum J_{ab} S_a S_b . \tag{4}$$

For all known cases of iron–sulfur proteins, $J > 0$, meaning that the system is antiferromagnetically coupled through the Fe–S–Fe moiety. Equation (4) produces a series of levels, each characterized by a total spin S', with an associated energy, which are populated according to the Boltzmann distribution. Note that for each S' level there is in principle an electron relaxation time. For most purposes it is convenient to refer to an effective relaxation time for the whole cluster.

Table I reports the observed NMR linewidths for the Hβ protons of the coordinating cysteines in a series of iron–sulfur proteins with increasing nuclearity of the cluster, and in different oxidation states. We have attempted to rationalize the linewidths on the basis of the equations describing the Solomon and Curie contributions to the nuclear transverse relaxation rate [Eqs. (1) and (2)]. When dealing with polymetallic systems, the S' value of the ground state has been used in the equations. When the ground state had $S' = 0$, reference was made to the S' of the first excited state and the results were scaled for the partial population of the state. In addition, in polymetallic systems it is also important to account for the fact that the orbitals of each iron atom contribute differently to the populated levels. For each level, the enhancement of nuclear relaxation induced by each iron is proportional to the square of the contribution of its orbitals (*34*). In practice, one has to calculate the following coefficient for each iron atom:

$$C_{ij} = \frac{\langle S_{jz} \rangle_i}{\langle S'_z \rangle_i} , \tag{5}$$

where $\langle S_{jz} \rangle_i$ is the contribution of metal j to the expectation value of $\langle S'_z \rangle$ of the ith level. In the present case we deal only with the ground state (see earlier discussion). The relaxation rate induced by metal j is proportional to C_{ij}^2. The analytical derivation of this coefficient has been reported for dimers (*41*), trimers (*42*), and tetramers (*43–45*). With these tools, it has been possible to evaluate from the experimental linewidths the effective electron relaxation times reported in Table I. It should be noted that the electron relaxation rate in polymetallic systems is always equal to or less than that obtained for the monomer (i.e., the iron in Rd) (*46*, *47*). It is also interesting to observe that nonequivalent irons belonging to the same cluster have the same electron relaxation times.

This was already known in the case of dimers (*48*), but has never been extended to cases of the trimers and tetramers.

For the Fe(III)–Fe(III) case in oxidized Fe_2S_2, with a diamagnetic $S = 0$ ground state, by assuming the two irons equivalent, the theory predicts that the linewidths of the Hβ protons are reduced by a factor of 2 with respect to the monomer if all levels are equally populated (*49*); otherwise, the linewidth is further decreased in proportion to the total magnetism. The electron relaxation rate is essentially equal to that of a single Fe(III) (Table I). Indeed, Hβ protons are in general hardly observed. In addition, the eight Hβ signals are often broad and with similar shifts so that a single very broad signal is observed (*4*, *33*, *50*) (Fig. 2A).

In reduced Fe_2S_2 there is a localization of valences between Fe(III) and Fe(II). The τ_s for both ions is shorter than that of the Fe(II) monomer (Table I), whereas the linewidths of the signals of the Fe(III) and Fe(II) domains depend on coefficients obtainable from the solution of Eq. (4). As a result, the signals of the Hβ protons of the cysteines bound to the Fe(III) are shifted beyond 100 ppm downfield with relatively large linewidths, while those of the cysteines bound to the Fe(II) domain are closer to the diamagnetic region and 5–10 times narrower (*50–53*) (Fig. 2B). There are cases in which there is delocalization of the valences (*54*, *55*) but no NMR investigation is available.

For the $[Fe_3S_4]^{1+}$ core, containing three Fe(III) ions, the signals of the Hβ protons of the coordinating cysteines are relatively narrow (*56–60*) (signals a–d in Fig. 2C), because of the existence of accessible magnetically coupled levels with the same total spin value, which leads to short electron relaxation times (Table I). For systems containing $[Fe_3S_4]^0$ there is a chemical exchange phenomenon that broadens all linewidths beyond detection, and nothing can be learned (*61*) (see next paragraph).

The $[Fe_4S_4]^{2+}$ clusters contain four equivalent irons and give relatively narrow signals (*3*, *7*, *62*, *63*) (Fig. 2E). The electron relaxation time is evaluated around 5×10^{-12} s (Table I), which is somewhat smaller than that of the Fe(II) monomer. Also, the signals of $[Fe_4S_4]^{3+}$ (*15*, *64–68*) (Fig. 2D) and $[Fe_4S_4]^{1+}$ (8, 13, 69–71) (Fig. 2F) systems are sharp.

III. Valence Delocalization

The application of the Hamiltonian in Eq. (4) allows the calculation of energies of the eigenfunctions describing the levels arising from the

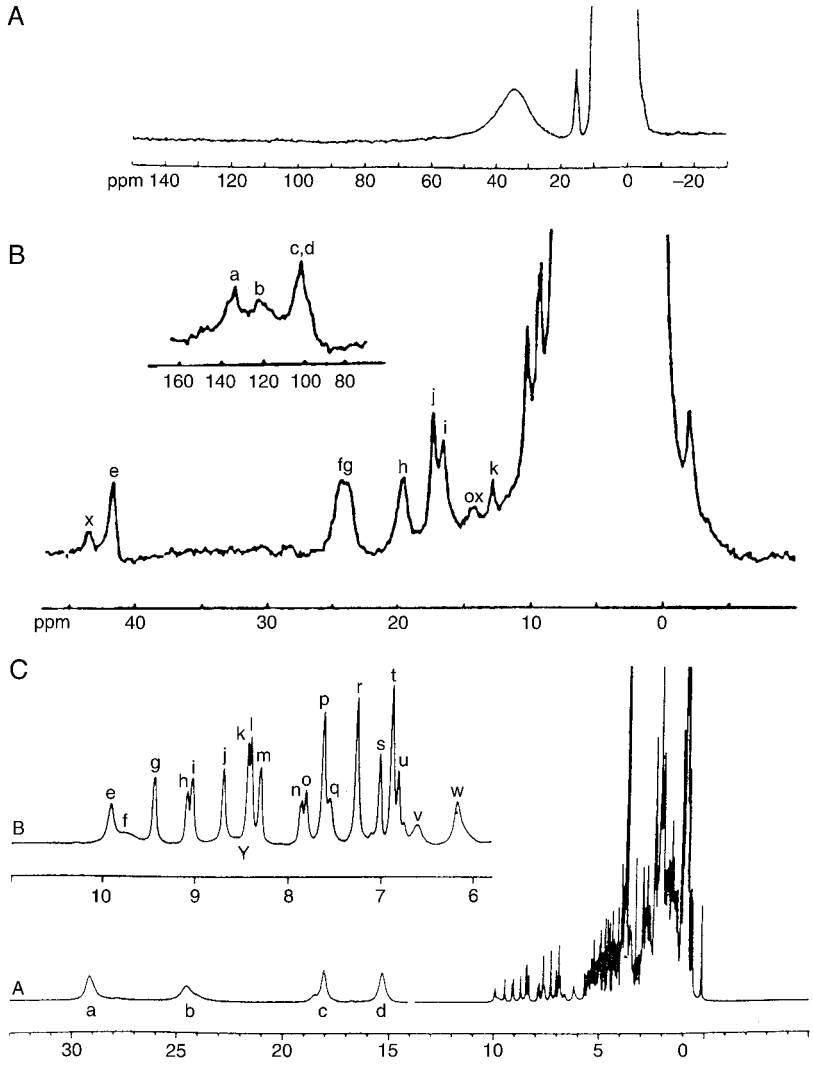

FIG. 2. ^{1}H NMR spectra of (A) oxidized spinach Fe_2S_2 ferredoxin (*33*); (B) reduced spinach Fe_2S_2 ferredoxin (*51*); (C) oxidized *Desulfovibrio gigas* Fe_3S_4 ferredoxin (*138*); (D) oxidized *ectothiorhodospira halophila* HiPIP iso-II (*18*); (E) reduced *Chromatium vinosum* HiPIP (*14*); (F) fully reduced *Clostridium pasteurianum* $2(Fe_4S_4)$ ferredoxin (*139*). Chemical shift values are in ppm.

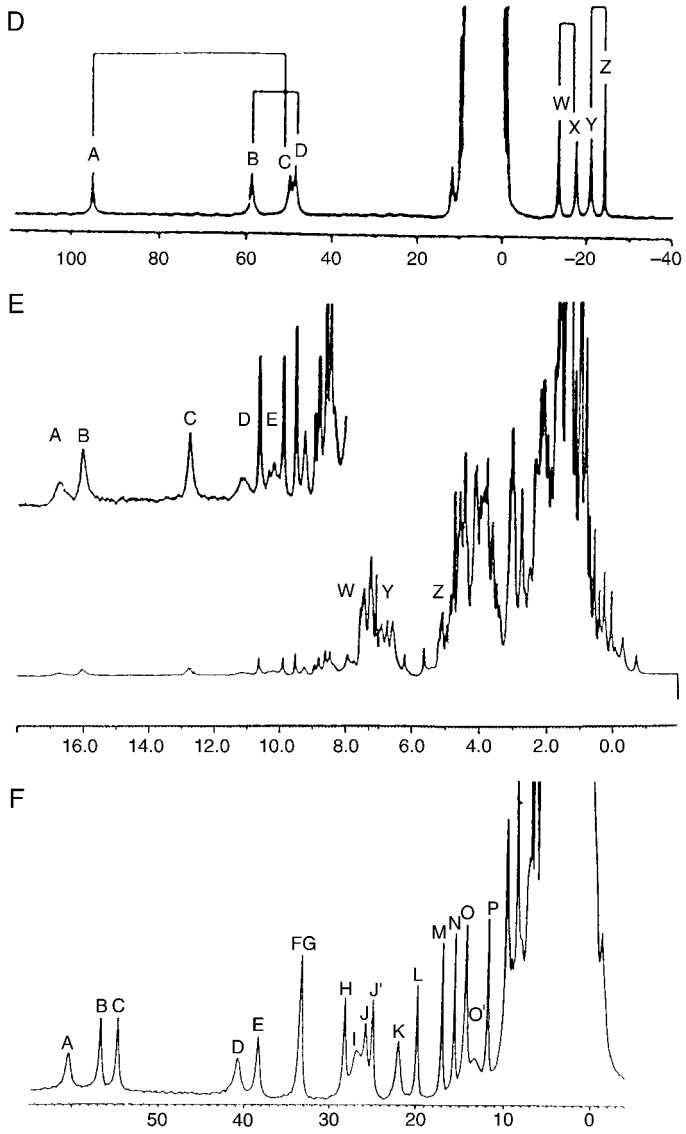

FIG. 2.—*Continued*

magnetic coupling. From these it is possible to obtain the hyperfine coupling between the unpaired electron(s) and the various nuclei. We avoid here a listing of equations that are available elsewhere (*47*). Instead, we report graphically the results obtained in Fig. 3. How-

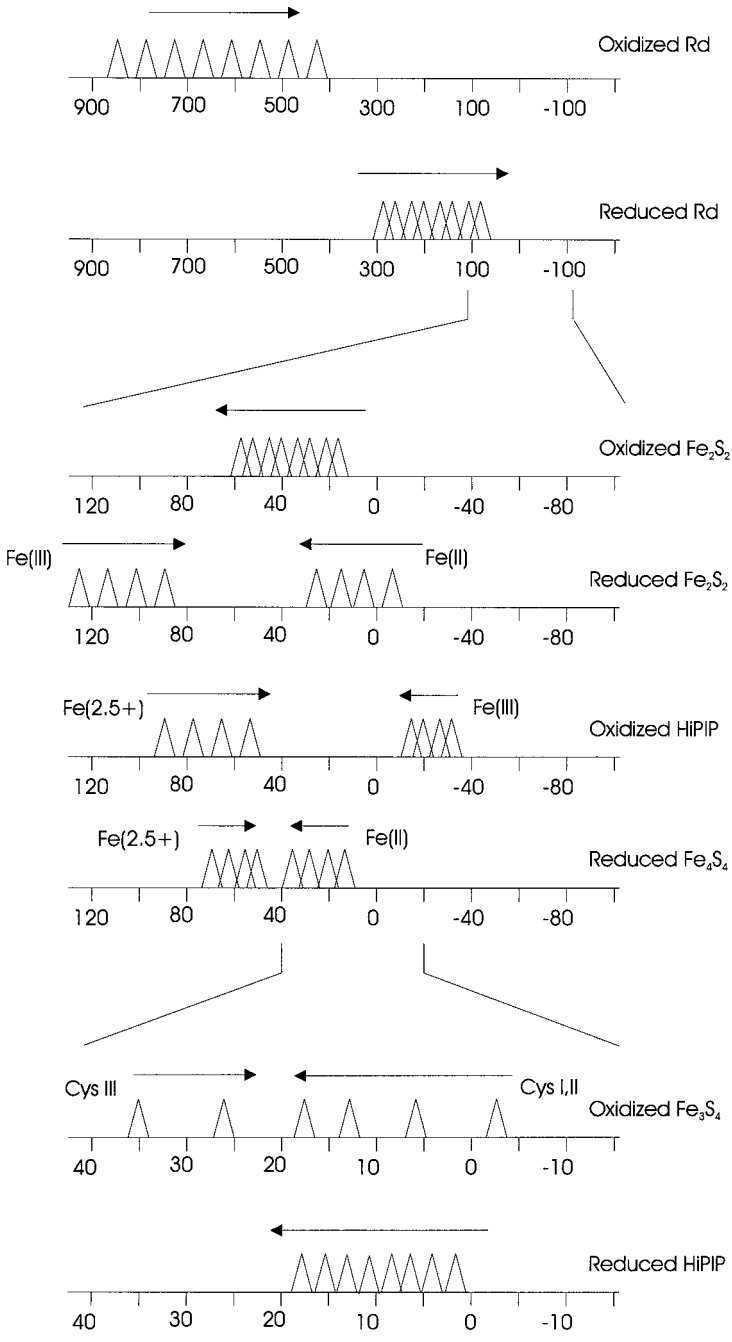
Oxidized Rd
900
700
500
300
100
-100
Reduced Rd
900
700
500
300
100
-100
Oxidized Fe_2S_2
120
80
40
0
-40
-80
Fe(III)
Fe(II)
Reduced Fe_2S_2
120
80
40
0
-40
-80
Fe(2.5+)
Fe(III)
Oxidized HiPIP
120
80
40
0
-40
-80
Fe(2.5+)
Fe(II)
Reduced Fe_4S_4
120
80
40
0
-40
-80
Cys III
Cys I,II
Oxidized Fe_3S_4
40
30
20
10
0
-10
Reduced HiPIP
40
30
20
10
0
-10

ever, some consideration of the ground state is appropriate and enlightening. Such reasoning allows us to localize the valences within the different clusters and within the protein frame. For example, in the reduced $[Fe_2S_2]^{1+}$ ferredoxins there is an Fe(III) ion with $S = \frac{5}{2}$ antiferromagnetically coupled to an $S = 2$ Fe(II). In the ground state the spins have opposite orientation, and in the external magnetic field the larger $S = \frac{5}{2}$ will be oriented along the magnetic field, whereas the smaller $S = 2$ will be oriented against it. Consequently, the hyperfine shift of the nuclei in the $S = 2$ domain will experience a shift of opposite sign with respect to an isolated $S = 2$ system. As the Hβ protons of the cysteines in Rd are shifted downfield, those of the cysteines coordinating to the Fe(II) in $[Fe_2S_2]^{1+}$ Fd are expected to be shifted upfield (Figs. 2B, and 3). An increase in the temperature will increase the population of excited states, thus decreasing the effect of the sign reversal (Fig. 3). At infinite temperature the effect of the magnetic coupling on the shifts will be zero. Figure 4 shows a comparison of the expected and experimental temperature dependence of the hyperfine coupling (as measured by hyperfine contact shift) in an $[Fe_2S_2]^{1+}$ system. The fact that $[Fe_2S_2]^{1+}$ systems conform to this behavior indicates that the valences are largely trapped and allows one to distinguish the cysteines bound to the Fe(II) from those bound to the Fe(III). A similar case is provided by $[Fe_4S_4]^{3+}$ systems in oxidized high-potential iron–sulfur proteins (HiPIP), where Mössbauer (*72*, *73*) and NMR (*74–76*) spectroscopy results are consistent with a picture of an Fe(III) and Fe(II) coupled to give a subspin $S = \frac{9}{2}$, with the two remaining Fe(III) centers giving a subspin $S = 4$. The two subspins are antiferromagnetically coupled to give a ground state total spin $S' = \frac{1}{2}$. The $S = \frac{9}{2}$ subspin is indeed attributed to two Fe ions ferromagnetically coupled with an average valence of 2.5+. The Hβ protons of the cysteines coordinating to the $Fe^{2.5+}$ ions are downfield shifted as usual, as they are bound to the larger subspin, whereas the other two are upfield shifted, as they are bound to the smaller subspin (Figs. 2D and 3). The temperature dependence is reported in Fig. 5. The actual spin wavefunctions are still a matter of debate (*43*, *77–80*), as the ground-state subspin values of $\frac{7}{2}$ and 3 provide a similar analy-

FIG. 3. Theoretically expected cysteine Hβ chemical shifts (ppm) for iron–sulfur proteins, together with associated temperature dependences (arrows). The arrows indicate the direction where the signals move when the temperature is raised. The signals arising from systems containing nonequivalent iron ions are labeled according to the ion to which the cysteine is bound. The case of reduced HiPIP is analogous to that of oxidized Fd.

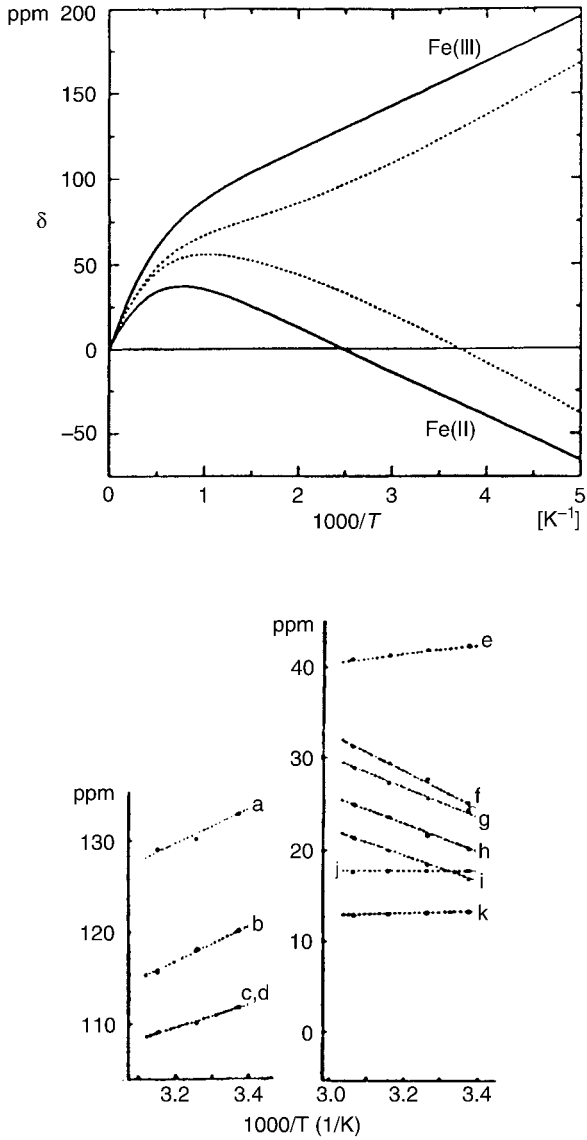

FIG. 4. *Top*: Theoretical temperature dependence of the hyperfine shift of the Hβ protons of reduced spinach $[Fe_2S_2]^{1+}$ ferredoxin (*151*). The solid line corresponds to the situation where only one species exists in solution, whereas the dashed line corresponds to a situation where there is fast equilibrium between two species (in a 20/80 ratio) differing for the location of the extra electron (*151*). *Bottom*: Experimental temperature dependence of the ^{1}H NMR shifts. The signals are labeled as in Fig. 2B.

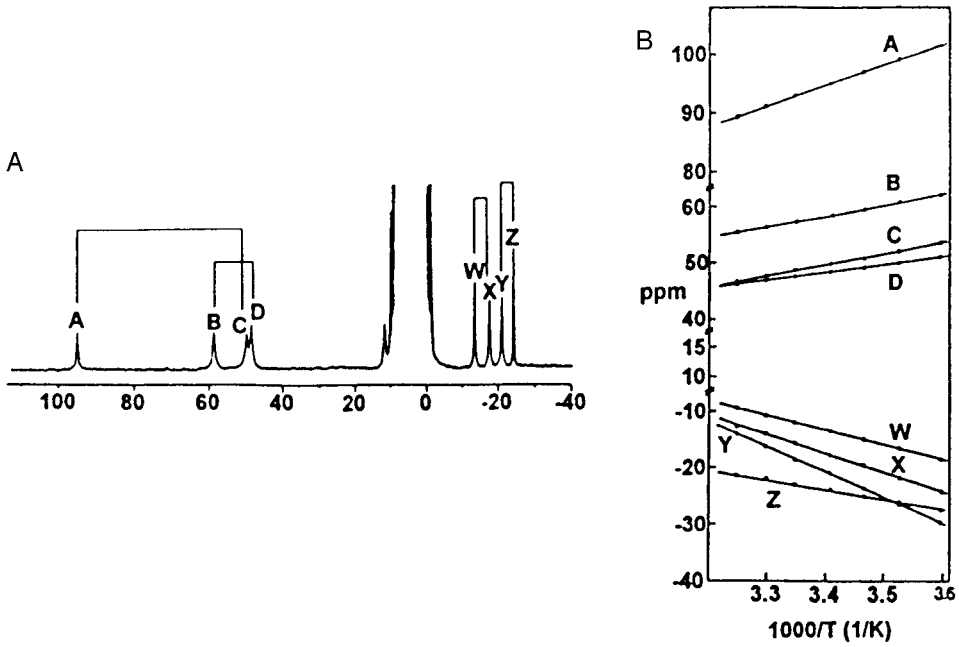

FIG. 5. ^{1}H NMR spectrum of oxidized *Ectothiorhodospira halophila* HiPIP iso-II (A) and experimental temperature dependence of the shifts of the signals (B) (*18*).

sis. The description is also more complicated if low-symmetry components are taken into account (*76*). In most cases, however, two pairs of Hβ protons have values intermediate between those upfield and downfield. This has been explained as due to an equilibrium between two species, as shown in Fig. 6 (*68*). If the equilibrium is faster than the difference in upfield and downfield shifts, one pair will belong to

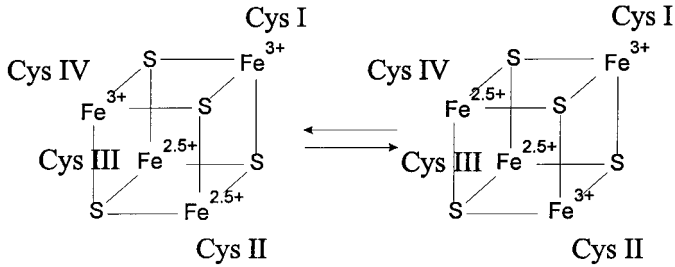

FIG. 6. Equilibrium between two electron distributions in oxidized $[Fe_4S_4]^{3+}$ clusters (*68*).

a metal that will always be Fe(III), and another to a metal that will always be Fe(2.5+), whereas the last two will belong to metals with intermediate values. The existence of two Fe(II) and two $Fe^{2.5+}$ ions has been postulated on the basis of analogous reasonings for proteins containing $[Fe_4S_4]^{1+}$ clusters, although here the smaller value of the antiferromagnetic coupling leads to a weaker differentiation between the two pairs of iron atoms. The equilibrium model of $[Fe_4S_4]^{3+}$ is confirmed by the fact that when a cysteine is substituted with a serine through site-directed mutagenesis, the iron bound to the serine acquires a percentage of Fe(III) character higher than in the wild-type protein because of the higher electronegativity of the bound oxygen. Indeed, the Fe bound to cysteine-77 in *C. vinosum* HiPIP is 40% ± 5% Fe(III), and becomes 65% ± 5% when cysteine-77 is replaced by a serine (coordinated to the iron as serinate) (*81*).

In the case of $[Fe_3S_4]^0$, Mössbauer studies suggested the existence of two Fe(2.5+) ions ferromagnetically coupled to give a subspin with $S = \frac{9}{2}$, in turn antiferromagnetically coupled to the $S = \frac{5}{2}$ Fe(III), the total spin value being 2 (*36*, *82*). The Fe(III) can be localized at the vertex of the triangle of metal atoms. It was proposed that a chemical equilibrium between the species with the Fe(III) at each of the three vertices occurs on a time scale of the same order of magnitude as the chemical shift differences between the two domains of the Fe. If this is of the order of 10^6 s^{-1}, the resulting line broadening would explain the fact that NMR signals of the cysteine Hβ can not be detected even in the ^{2}H NMR spectra of a deuterium labeled sample (*61*).

In the case of oxidized Fe_2S_2 the two ions are equal, so there is no valence trapping. The same holds, in principle, for $[Fe_3S_4]^{1+}$. However, here the three ions are always nonequivalent, i.e., two are more strongly coupled together than the third, or all three have different coupling values (*42*, *83*, *84*). The spectrum is reported in Fig. 2C. The nonequivalence of the three Fe atoms may lead to their identification within the protein frame. In the case of $[Fe_4S_4]^{2+}$ all the irons are equivalent with oxidation state 2.5+ (*85*, *86*).

The hyperfine shift patterns for all cases discussed above are summarized schematically in Fig. 3. It is worth pointing out again that the variety of different behaviors observed experimentally can be predicted in a semiquantitative way just on the grounds of simple spin-coupling considerations, based on the Hamiltonian in Eq. (4). At first glance the analysis of the ^{1}H NMR spectra provides precious information on the existence of trapped valence or of partial delocalization on pairs of irons formally at different oxidation states. Analysis of the magnetic coupling properties can be carried out by using Eq. (4), and

with the aid of variable-temperature spectra. NMR spectroscopy is thus a powerful tool for investigating the electronic structure of iron–sulfur clusters. The cases of valence trapping and valence delocalization can be readily distinguished. Furthermore, in the case of trapped valences, NMR provides the possibility of achieving a complete description of the localization of valences within the protein frame.

IV. Considerations on the Reduction Potential

The tendency of one iron to be reduced with respect to the other in a cluster has been extensively studied by NMR. In the case of Fe_2S_2 the more reducible iron is that which is most solvent exposed, because reduction gives an increase in the total negative charge on the active site (i.e., the charge of the $Fe_2S_2Cys_4$ moiety), which is stabilized by the higher dielectric constant of the solvent (*87*, *88*). Hydrogen bonding to the sulfur atoms of the cluster (i.e., the so-called inorganic sulfurs, and the Sγ atoms of the cysteines) is probably of secondary importance (*88*), although the difference in reduction potentials between animal and plant ferredoxins has been accounted for on the basis of a difference of one such hydrogen bond (*89*, *90*).

The Fe_4S_4 centers of HiPIPs and ferredoxins have a different number of hydrogen bonds to the sulfur donor atoms, where this difference is consistent with the observed lower potential of the $[Fe_4S_4]^{3+/2+}$ couple in the former (a higher number of hydrogen bonds gives higher reduction potential) (*91*). The structure and hydrophobicity of the active site surroundings in HiPIPs is responsible for the stabilization of the lower overall charge of the oxidized $[Fe_4S_4Cys_4]^{1-}$ moiety, and thus can help account for the observed high reduction potential (*87*, *92*, *93*). Solvent accessibility (*92*) and the net charges present on the polypeptide chain (*87*, *93*) have been proposed to account for the tuning of the reduction potential within a series of related iron–sulfur proteins. However, other authors have suggested that solvent accessibility plays only a minor role (*94*).

As mentioned previously, in $[Fe_3S_4]^{1+}$ clusters, the three Fe(III) ions are not completely equivalent. NMR spectroscopy may allow one to locate the iron with the lowest reduction potential, as being the one characterized by the weakest magnetic couplings with the other two irons. However, this is true only if the energetic contributions due to other factors, such as electrostatic effects or solvent accessibility (*93*), are less important than those due to the magnetic coupling of the

metal ions within the cluster. On the other hand, in $[Fe_4S_4]^{2+}$ clusters the four iron ions are all equivalent and indistinguishable.

The magnetic coupling among the irons in iron–sulfur clusters may also play a role in tuning their reduction potential. Indeed, the energy spacing of the S' levels is dependent on the values of the iron–iron coupling constants [see Hamiltonian in Eq. (4)], which thus affect the distribution of populated levels at room temperature. This may constitute a further reason for the wide range of reduction potentials observed in ferredoxins, and help rationalize the high occurrence of iron–sulfur clusters as redox centers in electron transfer proteins.

V. Solution Structure

The solution structure determination of iron–sulfur proteins is feasible in most cases. To achieve this result, it is necessary to have enough structural constraints to make it possible to obtain a family of conformers with similar folding from many randomly generated structures (*95*).

A. Assignment and Standard Constraints

The first step for the solution structure determination of a protein is to obtain an extensive assignment of the NMR signals arising from the protons of the various amino acids of the protein. Standard techniques have been developed to undergo this task (*95*), which are also applicable to iron–sulfur proteins. However, to obtain a reasonable number of assignments in the surroundings of the paramagnetic metal center(s), it is very important to optimally tune the experimental parameters in order to detect paramagnetically broadened proton signals (*96*). The criteria and practical methods for the optimization of the most widely employed NMR experiments have been discussed at length (*47*, *97*, *98*).

The second step is the detection of a high number of structural constraints. The constraints routinely used for solution structure determination of proteins (both diamagnetic and paramagnetic) are interproton upper distance limits obtained from NOESY cross peak intensities and ^3J coupling constants (which may be converted into dihedral angle constraints). The first class of constraints is the most important. Indeed, solution structures of proteins may be obtained by using only NOEs, but not by using only ^3J coupling constants. Detection of enough ^1H–^1H NOEs for the amino acids close to the metal

center(s) in iron–sulfur proteins is not a trivial task. In addition to performing optimized 2D NOESY experiments, the use of 1D NOE experiments is extremely useful in providing distance constraints for the protons of the coordinating cysteines that are hyperfine shifted outside the diamagnetic envelope (*23*). In the case of ^3J coupling constants, there are few examples available of their use for solution structure determination of iron–sulfur proteins (*99–101*). It is known that fast relaxation rates (e.g., as induced by a paramagnetic center) lead to an underestimation of the ^3J coupling values, and, ultimately, to a deviation from the Karplus relationships normally used to relate the measured couplings to structural parameters (*102*). In the two earliest works (*99*, *100*) no corrections were introduced for this effect, without any major problem, probably because no ^3J coupling values could be measured for the residues closer to the paramagnetic metal ions. More recently, a correction for $^3J_{\mathrm{HNH}\alpha}$ coupling values depending on the longitudinal relaxation rates of the Hα proton was introduced prior to the use of the couplings as structural constraints (*101*).

B. Nonstandard Constraints: Nuclear Relaxation Rates

In addition to the standard constraints introduced previously, structural constraints obtainable from the effects of the paramagnetic center(s) on the NMR properties of the nuclei of the protein can be used (*24*, *103*). In iron–sulfur proteins, both nuclear relaxation rates and hyperfine shifts can be employed for this purpose. The paramagnetic enhancement of nuclear relaxation rates [Eqs. (1) and (2)] depends on the sixth power of the nucleus–metal distance (note that this is analogous to the case of NOEs, where there is a dependence on the sixth power of the nucleus–nucleus distance). It is thus possible to estimate such distances from nuclear relaxation rate measurements, which can be converted into upper (and lower) distance limits. When there is more than one metal ion, the individual contributions of all metal ions must be summed up (*101*, *104–108*). If all the metal ions are equivalent (as in reduced HiPIPs), the global paramagnetic contribution to the Ith nuclear relaxation rate is given by

$$R_I = K \sum_{n=1}^{M} \frac{1}{r_{In}^6}, \tag{6}$$

where the sum spans all M metal ions. The term K serves to collect all the constants and all the electronic parameters present in Eqs. (1)

and (2). The actual constraints will thus be upper (and lower) limits for the sum in Eq. (6) (*101*, *105*). In the general case where the metal ions are not equivalent (e.g., in oxidized HiPIPs, where there are two pairs of equivalent irons), the following equation will apply:

$$R_I = \sum_{n=1}^{M} \frac{K_n}{r_{In}^6}, \tag{7}$$

where K_n contains the electronic parameters of the nth metal ion. In this case the different K_n values should be obtained by, for example, a fitting of the measured paramagnetic enhancements of nuclear relaxation rates to a preliminary structure obtained only with NOEs. Structure calculations will be run in which the system is constrained to fold in a way such that the calculated relaxation rates match the experimental values (within a certain tolerance, which is related to the error in the measurements and in the fitting) (*108*). Several examples of the application of this technique to solution structure determination of iron–sulfur proteins are already available (*101*, *105*, *108–111*).

C. Nonstandard Constraints: Hyperfine Shifts

As mentioned in the Introduction, in iron–sulfur proteins, the hyperfine shifts of the nuclei of the coordinating cysteines are essentially contact in origin (*21*, *22*). In the case of $[Fe_4S_4]^{2+}$ (*17*) and $[Fe_3S_4]^{+}$ (*112*) cluster, it has been shown that the hyperfine shift of the cysteinyl Hβ and Cα nuclei can be related to the value of the Fe–Sγ–Cβ–Hβ/Cα dihedral angle (θ) through a Karplus-type relationship of the form

$$\delta^{\text{hyp}} = a \sin^2 \theta + b \cos \theta + c, \tag{8}$$

where a, b, and c depend on the electronic structure. Equation (8) represents the sum of two contributions arising from two mechanisms for unpaired electron spin density delocalization. One is due to the overlap of the 1s orbital of the observed nucleus (Hβ or Cα) with the Fe–Sγ σ bond, and its contribution to the hyperfine shifts follows the Karplus relationship (*113*, *114*), as in

$$\delta^{\text{hyp}} = a' \cos^2 \theta + b' \cos \theta + c'. \tag{9}$$

TABLE II

BEST FITTING VALUES OF THE PARAMETERS a, b, AND c OF EQ. (7) (SEE TEXT FOR DETAILS)

	a	b	c
$[Fe_4S_4]^{2+}$ Hβ	10.3 ± 0.9	−2.2 ± 0.4	3.9 ± 0.5
$[Fe_4S_4]^{2+}$ Cα	16.2 ± 4.5	−5.3 ± 2.7	15.2 ± 3.7
$[Fe_3S_4]^{+}$ Hβ cysteines I and II	23.0 ± 4.0	1.0 ± 1.3	2.8 ± 1.6
$[Fe_3S_4]^{+}$ Hβ cysteine III	−12.9 ± 6.7	−2.3 ± 1.0	27.8 ± 1.9

The second mechanism for delocalization is the direct overlap between the 1s orbital of the observed nucleus (Hβ or Cα) with the nonbonding p_z orbital of the sulfur, and is described by (*115–117*)

$$\delta^{hyp} = a'' \sin^2 \theta + c''. \tag{10}$$

From the fitting of a number of data for proteins of known structure it has been possible to obtain the values of the three parameters a, b, and c in Eq. (8). For $[Fe_4S_4]^{2+}$ clusters, the four coordinating cysteines are equivalent, because of the equivalence of the irons. Instead, in the case of $[Fe_3S_4]^{+}$ containing systems, the first two cluster-bound cysteines in the sequence have the same angular dependence (with some approximation), whereas the third one has a different dependence. This is due to the magnetic coupling between the irons in the cluster (see the paragraph on valence delocalization). The two groups of cysteines have thus been fitted independently and have different parameter values. The values obtained for a, b, and c are listed in Table II, where the quality of the fits is shown in Fig. 7. As is evident from Fig. 7, a wealth of data is available for the Hβ protons of the coordinating cysteines in $[Fe_4S_4]^{2+}$ containing systems. A good, though smaller, number of data are available also for the Cα carbons in the same systems. Many fewer data are available for the Hβ protons of the coordinating cysteines in $[Fe_3S_4]^{+}$ containing systems, because, to date, only three systems have been satisfactorily characterized both from the NMR and the structural point of view. In spite of this the parametrizations obtained for $[Fe_3S_4]^{+}$-containing systems have proved useful and reliable in structural studies (*112*). It can be observed from Table II that for the cysteines bound to $[Fe_4S_4]^{2+}$ clusters and for the first two cysteines bound to $[Fe_3S_4]^{+}$ clusters, the a values are positive, and somewhat larger than the b and c values, whereas for the third cysteine of $[Fe_3S_4]^{+}$ clusters the a value is negative, and smaller than the constant term c. This indicates that in the former two cases the unpaired spin density delocalization mecha-

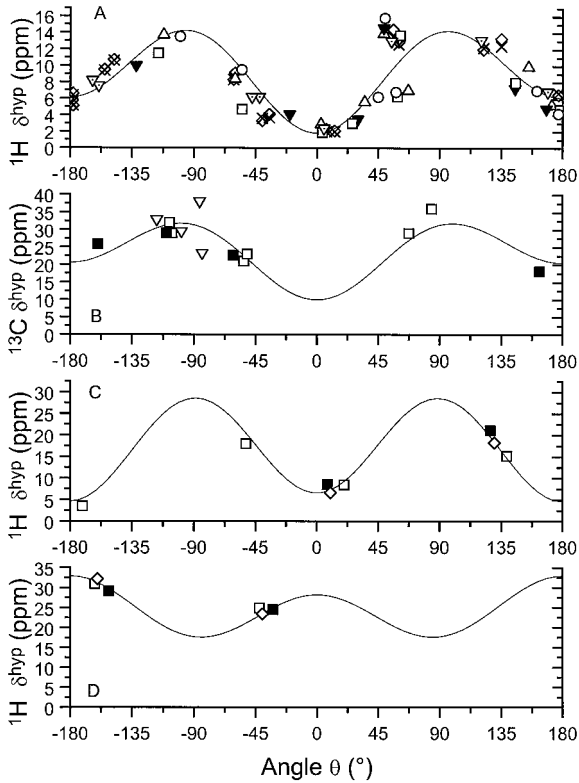

FIG. 7. Fittings to Eq. (7) of the hyperfine shifts of (A) Hβ protons of cysteines bound to $[Fe_4S_4]^{2+}$ clusters [open diamonds: oxidized *C. pasteurianum* Fd (*17*); crosses: oxidized *C. acidi urici* Fd (*17*); open up triangles: reduced *C. vinosum* HiPIP (*15*); open squares: reduced *E. halophila* HiPIP I (*95*); filled down triangles: reduced *E. halophila* HiPIP (*74*); open circles: reduced *E. vacuolata* HiPIP I (*66*); dotted down triangles: oxidized *B. schlegelii* Fd (*140*)]; (B) Cα carbons of cysteines bound to $[Fe_4S_4]^{2+}$ clusters [open squares: oxidized *C. acidi urici* Fd (*17*); filled squares: reduced *E. halophila* HiPIP I (*100*); open down triangles, oxidized *C. pasteurianum* Fd (*141*)]; (C) Hβ protons of the first two cysteines (in sequence) bound to the $[Fe_3S_4]^{1+}$ cluster in Fe_3S_4 or Fe_7S_8 ferredoxins [open squares: oxidized *D. gigas* Fd (*138*); filled squares: *A. vinelandii* Fd I (*142*); open diamonds: oxidized *B. schlegelii* Fd (*140*)]; (D) Hβ protons of the third cysteine (in sequence) bound to the $[Fe_3S_4]^{+}$ cluster in Fe_3S_4 or Fe_7S_8 ferredoxins [open squares: ozidized *D. gigas* Fd (*138*); filled squares: *A. vinelandii* Fd I (*142*); open diamonds: oxidized *B. schlegelii* Fd (*140*)].

nism is essentially the direct overlap of the hydrogen (or Cα) 1*s* orbital with a nonbonding *p* orbital of the sulfur. In the latter case instead the dominant mechanism is the overlap of the 1*s* orbital with the Fe–Sσ bond, leading to the negative sign of a. The large value of the constant term c indicates that both mechanisms are operative (as one is contrib-

uting to the hyperfine shift through a $\cos^2$ angle dependence, whereas the other is contributing through a $\sin^2$ angle dependence; when both are operative there is no angular dependence).

D. Examples

Table III reports structural statistics relative to the solution structures of iron–sulfur proteins available from the Protein Data Bank (*118*). The lowest percentage of residue assignment occurs for oxidized *Synechococcus elongatus* Fd (*119*). The highest percentage of proton assignment is instead obtained for oxidized *E. halophila* HiPIP, with a value as high as 95% (*120*). A close figure was also obtained for the reduced protein (94%). In the latter case, such high values are obtained also thanks to the availability of ^{15}N, ^{13}C labeled samples (*101*). The number of NOEs (including 1D NOEs) per assigned residue varies from around 10 up to 35, with the exception of *T. litoralis* Fd (*121*), values that are quite comparable with those obtained for diamagnetic proteins. Also, the backbone RMSD values are those typical of very well defined structures, although it must be said that the mean values reported in Table III do not allow one to tell whether there are poorly defined regions, such as in the surroundings of the metal center(s). The values of the target function show that in all cases there is very good agreement between the experimental constraints and the obtained structures. The relatively high target function value of oxidized *C. pasteurianum* Fd is due to the fact that in this case relaxation-rate-based constraints were introduced without readjusting the upper distance limits, which had been calibrated independently (105). This procedure leads to slight inconsistencies between the two groups of restraints, reflected in a higher value of the target function. However, in the present case the target function is still that typical of a good structure. As examples, the solution structures of reduced *E. halophila* HiPIP (*101*), oxidized *C. pasteurianum* Fe_8S_8 Fd (*105*), and oxidized *B. schlegelii* Fe_7S_8 Fd (*112*) are shown in Figs. 8–10. These three structures have been obtained by employing nonconventional paramagnetic constraints together with NOE constraints (Table III).

VI. Folding

Investigation of the polypeptide folding properties of iron–sulfur via NMR spectroscopy began in 1997 (*122*). All studies performed to date have focused on the effect of the addition of guanidinium chloride (GdmCl hereafter) to protein solutions. Under these conditions, re-

TABLE III

NMR Assignments, Structural Constraints, and Structural Parameters for the Available NMR Solution Structures of Iron–Sulfur Proteins[a,b]

Protein (cofactor)	Number of amino acids (assigned amino acids)	% ^{1}H assignment	Number of constraints			RMSD (BB) from mean (Å)	Number of conformers	Average target function (Å)	PDB entry
			NOE	R_1	Fe–Sγ–Cβ–Cα dihedral angle				
Reduced *C. p.* rubredoxin (Fe^{2+}) (*110*)	54 (46)	76	1267	36	—	0.58	20	0.54	1BFY
Oxidized parsley ferredoxin I ($[Fe_2S_2]^{2+}$) (*111*)	96 (87)	84	3066	33	—	0.52	20	0.84	1PFD
Oxidized *S.* sp. PCC 6803 ferredoxin ($[Fe_2S_2]^{2+}$) (*132*)	96 (76)	n.a.	605[c]	—	—	n.a.	3 + 3[d]	n.a.	1DOX, 1DOY
Oxidized *S. e.* ferredoxin ($[Fe_2S_2]^{2+}$) (*119*, *133*)	97 (76)	n.a.	946[e]	—	—	0.61	10	1.38	2CJO, 2CJN
Reduced *E. h.* HiPIP I ($[Fe_4S_4]^{2+}$) (*101*)	73 (72)	94	1285	58	4	0.31	15	0.59	1PIH, 1PIJ
Oxidized *E. h.* HiPIP I ($[Fe_4S_4]^{3+}$) (*108*)	73 (73)	95	1437	27	—	0.63	15	0.53	n.a.
Reduced *C. v.* HiPIP ($[Fe_4S_4]^{2+}$) (*134*)	85 (83)	85	1489	—	—	0.42	15	0.56	1HRQ, 1HRR
Oxidized *C. v.* HiPIP ($[Fe_4S_4]^{3+}$) (*135*)	85 (84)	85	1537	—	—	0.39	15	0.51	1NEH
Reduced C77S *C. v.* HiPIP ($[Fe_4S_4]^{2+}$) (*100*)	85 (85)	87	1591	—	—	0.42	15	<0.50	1NOE
Oxidized *T. m.* ferredoxin ($[Fe_4S_4]^{2+}$) (*136*)	60 (51)	n.a.	683	—	—	0.55	10	n.a.	1ROF
Oxidized *T. l* ferredoxin ($[Fe_4S_4]^{2+}$) (*121*)	59 (58)	n.a	331	32[f]	4	n.a.	5 + 5[g]	n.a.	n.a.
Oxidized *B. s.* ferredoxin ($[Fe_3S_4]^{+}$, $[Fe_4S_4]^{2+}$) (*112*)	77 (72)	79	1305	—	6	0.68	20	0.73	1BC6, 1BD6
Oxidized *C. p.* ferredoxin ($2[Fe_4S_4]^{2+}$) (*105*)	55 (53)	79	536	69	8	0.40	16	2.12	1CLF
Oxidized *D. a.* ferredoxin I($[Fe_4S_4]^{2+}$) (*137*)	64 (62)	n.a.	549[h]	—	4	0.49	19	n.a.	1DFD, 1DAX

[a] n.a.: not available.

[b] *a* – sign indicates that no constraints of that kind were used in structure calculations.

[c] Plus 52 upper distance limits from the cluster for protons that could not be detected, 126 lower distance limits from the cluster for protons without any appreciable paramagnetic line broadening, and 42 distance constraints derived from hydrogen bonds (*132*).

[d] Three structures were calculated with an imposed disulfide bridge, and three without it (*132*).

[e] Plus 241 distance constraints for the unassigned residues close to the iron–sulfur cluster derived from the X-ray structure (*119*).

[f] The constraints of 18 protons comprised both upper and lower limits, whereas other 14 had only upper distance limits (*121*).

[g] Five structures were calculated with Fe–Sγ–Cβ–Cα dihedral angle constraints, and five without (*121*).

[h] Plus 38 distance constraints derived from hydrogen bonds (*131*).

duced HiPIPs are characterized by the presence of a stable intermediate between the native and the denatured state, where the $Fe_4S_4^{2+}$ cluster is still intact (Fig. 11) (*122*). A comparison between 1D NOE experiments performed on the intermediate of *C. vinosum* HiPIP and 1D NOE performed on the native protein has shown that all four cys-

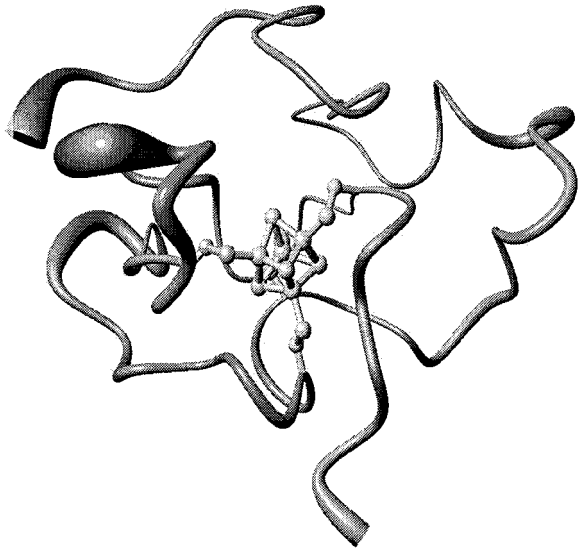

FIG. 8. Display of the backbone of the NMR structure of reduced *E. halophila* HiPIP (*100*) as a tube with variable radius, proportional to the backbone RMSD of each residue. The figure was generated with the program MOLMOL (*143*).

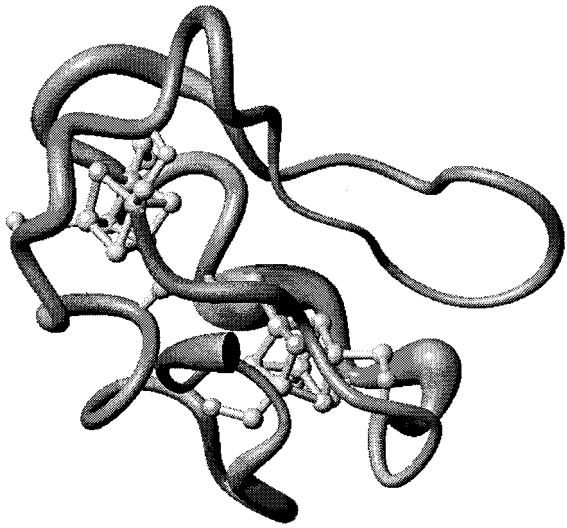

FIG. 9. Display of the backbone of the NMR structure of oxidized *C. pasteurianum* Fe_8S_8 Fd (104) as a tube with variable radius, proportional to the backbone RMSD of each residue. The figure was generated with the program MOLMOL (*143*).

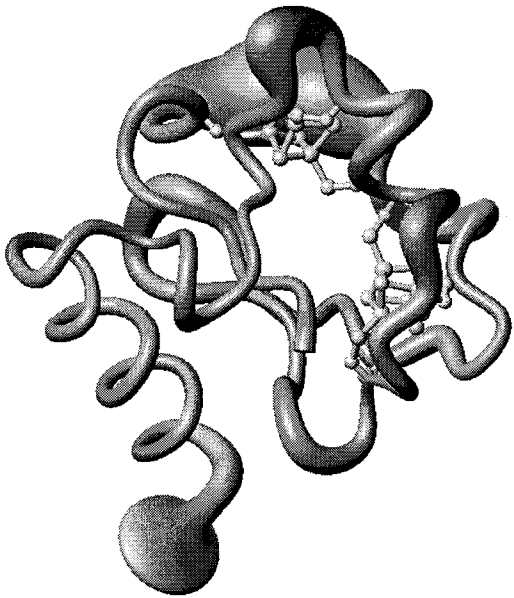

FIG. 10. Display of the backbone of the NMR structure of oxidized *B. schlegelii* Fe_7S_8 Fd (*111*) as a tube with variable radius, proportional to the backbone RMSD of each residue. The figure was generated with the program MOLMOL (*143*).

teines are coordinated to the cluster with the same spatial arrangement as in the native protein. On the other hand, the protein tertiary structure is essentially maintained only in the region close to cysteine I (i.e., the first ligand cysteine in the protein sequence, Cys 43), whereas it is deeply changed in proximity of cysteines III and IV (Cys 63 and 77, respectively). The free energy difference between the intermediate and the native state at [GdmCl] = 0 M has been estimated for both *C. vinosum* and *E. halophila* HiPIPs. Its value is the same, within experimental error, for both proteins: around 20 kJ mol^{-1} (*122*, *123*). The oxidized $Fe_4S_4^{3+}$ cluster is extremely unstable at any significant GdmCl concentration. Addition of GdmCl to a solution of oxidized *C. vinosum* HiPIP to a final concentration such as to generate less than 2% of the reduced intermediate species yielded a complete immediate bleaching of the solution, because of the irreversible loss of the cluster. From this observation, it has been proposed that the concentration of intermediate present in the absence of GdmCl (of the order of 0.01% with respect to the native protein) may mediate the experimentally observed slow hydrolytic decomposition of oxidized HiPIP (*122*). It is interesting to recall that it is possible to assemble

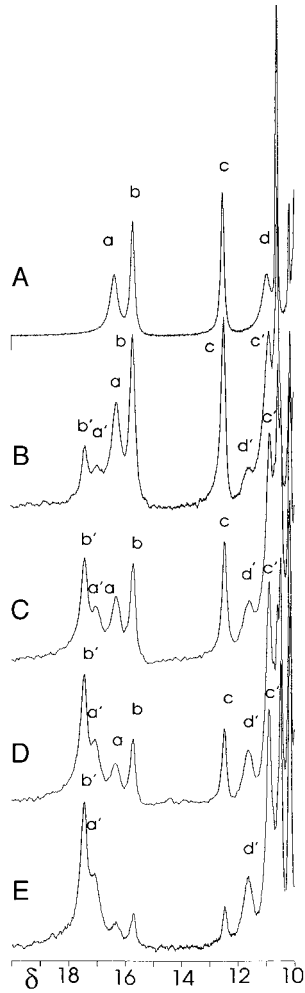

FIG. 11. 600 MHz ^{1}H NMR spectra of reduced *Chromatium vinosum* HiPIP with increasing GdmCl concentrations: (A) [GdmCl] = 0 M; (B) [GdmCl] = 3.3 M; (C) [GdmCl] = 3.7 M; (D) [GdmCl] = 4.0 M; (E) [GdmCl] = 4.4 M. (pH = 6.8, T = 290 K) (*122*).

model compounds containing the reduced $[Fe_4S_4]^{2+}$ cluster in protic solvents, whereas this is not possible for the oxidized $[Fe_4S_4]^{3+}$ cluster. This, together with the previously summarized findings, supports the hypothesis that the polypeptide chain plays a fundamental role in stabilizing the $[Fe_4S_4]^{3+}$ cluster in oxidized HiPIPs by shielding it from the solvent. When this protection is removed, for example, because of

the addition of denaturants, the cluster is immediately hydrolyzed. On the other hand, the reduced $[Fe_4S_4]^{2+}$ cluster is more stable toward hydrolysis, and an intermediate partially unfolded species is observable (*122*). However, the polypeptide chain still plays a role in the stabilization of this intermediate. Indeed, it has been observed that the intermediate reduced species formed by *E. halophila* HiPIP is less stable than that formed by *C. vinosum* HiPIP. As their free energy differences with respect to the native state are equal, it must be concluded that the differences in stability arise from the different kinetic control of the protein part of the hydrolysis reaction.

The information available for other iron–sulfur proteins is much less detailed. The titration of the Cys77Ser mutant of *C. vinosum* HiPIP, where cysteine IV has been replaced by a serine, showed the existence of an intermediate state, which, however, is much less stable than that of the wild-type protein (*123*). From the analysis of the variations in chemical shift at low [GdmCl], it was deduced that the structural rearrangement of the Fe–O–C–H dihedral angle upon addition of GdmCl was much larger than that of the corresponding Fe–S–C–H angle in the wild-type protein (*123*). Unfortunately, the low stability of the protein in the intermediate state prevented further structural investigations. For the Fe_8S_8 Fd from *C. pasteurianum*, containing two $[Fe_4S_4]^{2+}$ clusters, a marked difference in the behavior of the two clusters upon addition of GdmCl was reported (*123*). In the presence of the denaturant, the environment of cluster I gradually undergoes a major structural rearrangement, whereas cluster II remains essentially unaltered. This is revealed by the disappearance of the hyperfine shifted signals of the Hβ protons of the cysteines bound to cluster I, together with the simultaneous appearance of new hyperfine shifted signals, in contrast with the absence of significant changes in the signals of the cysteines coordinating to cluster II (*123*). However, the intermediate species is unstable, and a more detailed investigation was not possible. Cluster I in clostridial ferredoxins is also more reactive in the presence of ferricyanide, which leads to the formation of a Fe_3S_4 cluster (*124*).

VII. Perspectives

Perspectives on the field of NMR of iron–sulfur proteins are those common to the broader field of NMR of diamagnetic proteins, with a particular need for high technical skills. For some applications, new experiments/protocols tailored for the study of paramagnetic systems such as those described here will probably have to be designed and

developed. One such case may be that of the investigation via ^{15}N relaxation measurements of protein mobility in the 10^{-9}–10^{-12} s time scale. Here the effects of nuclear relaxation induced by the paramagnetic center(s) must be taken into account in order to obtain sensible information. This implies that the currently available programs and computational procedures must be integrated with the appropriate equations describing the paramagnetic contribution to the nuclear relaxation rates. Alternatively, different experimental procedures aimed at obtaining information on the motions of interest in a way such that the effects of paramagnetic relaxation become negligible may be introduced (*125*). Instead, the NMR experiments currently used to detect protein mobility in the 10^{-3}–10^{-6} s time scale are probably insensitive to paramagnetic relaxation (*126*).

Two fascinating problems (which are deeply interdependent) still open in the field of iron–sulfur proteins are those of the mechanisms of the folding and of the metal(s) uptake. Here NMR studies are already providing the first insights (see the paragraph on folding). However, complete structural and dynamic characterization of intermediate states on the folding pathway is still lacking. In addition, the effects of different denaturing conditions (e.g., low pH, high temperature) have never been investigated. Some studies providing insights on the mechanisms for degradation of the Fe_4S_4 cluster in HiPIPs are already available (*127–129*). Furthermore, it is known that under reducing conditions it is possible to reconstitute the iron–sulfur centers in ferredoxins (*130*). If an appropriate experimental setup can be devised, the application of NMR spectroscopy to such systems could provide intriguing results (*131*).

References

1. McDonald, C. C.; Phillips, W. D. *Biochem. Biophys. Res. Commun.* **1 6 ,** *35,* 43.
2. Phillips, W. D.; Poe, M.; Weiher, J. F.; McDonald, C. C.; Lovenberg, W. *Nature* **1 70,** *227,* 574.
3. Poe, M.; Phillips, W. D.; McDonald, C. C.; Lovenberg, W. *Proc. Natl. Acad. Sci. USA* **1 70,** *65,* 797.
4. Salmeen, I.; Palmer, G. *Arch. Biochem. Biophys.* **1 72,** *150,* 767.
5. "NMR of Paramagnetic Molecules"; La Mar, G. N.; Horrock, W. de W. Jr.; Holm, R. H. Eds.; Academic Press: New York, 1973.
6. Anderson, R. E.; Dunham, W. R.; Sands, R. H.; Bearden, A. J.; Crespi, H. L. *Biochim. Biophys. Acta* **1 75,** *408,* 306.
7. Packer, E. L.; Sweeney, W. V.; Rabinowitz, J. C.; Sternlicht, H.; Shaw, E. N. *J. Biol. Chem.* **1 77,** *252, 2245.*
8. Nagayama, K.; Ozaki, Y.; Kyogoku, Y.; Hase, T.; Matsubara, H. *J. Biochem.* **1 83,** *94,* 893.

9. Nagayama, K.; Ohmori, D.; Imai, Y.; Oshima, T. In "Iron–Sulfur Protein Research"; Matsubara, H. Ed.; Springer-Verlag: Berlin, 1986, 125.
10. Packer, E. L.; Rabinowitz, J. C.; Sternlicht, H. *J. Biol. Chem.* **1 78,** *253,* 7722.
11. Packer, E. L.; Sternlicht, H.; Lode, E. T.; Rabinowitz, J. C. *J. Biol. Chem.* **1 75,** *250,* 2062.
12. Johnson, R. D.; Ramaprasad, S.; La Mar, G. N. *J. Am. Chem. Soc.* **1 83,** *105,* 7205.
13. Bertini, I.; Briganti, F.; Luchinat, C.; Scozzafava, A. *Inorg. Chem.* **1 0,** *29,* 1874.
14. Bertini, I.; Briganti, F.; Luchinat, C.; Scozzafava, A.; Sola, M. *J. Am. Chem. Soc.* **1 1,** *113,* 1237.
15. Bertini, I.; Capozzi, F.; Ciurli, S.; Luchinat, C.; Messori, L.; Piccioli, M. *J. Am. Chem. Soc.* **1 2,** *114,* 3332.
16. Nettesheim, D. G.; Harder, S. R.; Feinberg, B. A.; Otvos, J. D. *Biochemistry* **1 2,** *31,* 1234.
17. Bertini, I.; Capozzi, F.; Luchinat, C.; Piccioli, M.; Vila, A. J. *J. Am. Chem. Soc.* **1 4,** *116,* 651.
18. Banci, L.; Bertini, I.; Briganti, F.; Luchinat, C.; Scozzafava, A.; Vicens Oliver, M. *Inorg. Chem.* **1 1,** *30,* 4517.
19. Bertini, I.; Briganti, F.; Luchinat, C.; Messori, L.; Monnanni, R.; Scozzafava, A.; Vallini, G. *FEBS Lett.* **1 1,** *289,* 253.
20. Sadek, M.; Brownlee, R. T. C.; Scrofani, S. D. B.; Weed, A. G. *J. Magn. Reson.* **1 3,** *101,* 309.
21. Holm, R. H.; Phillips, W. D.; Averill, B. A.; Mayerle, J. J.; Herskovitz, T. *J. Am. Chem. Soc.* **1 74,** *96,* 2109.
22. Reynolds, J. G.; Laskowski, E. J.; Holm, R. H. *J. Am. Chem. Soc.* **1 78,** *100,* 5315.
23. Banci, L.; Bertini, I.; Eltis, L. D.; Felli, I. C.; Kastrau, D. H. W.; Luchinat, C.; Piccioli, M.; Pierattelli, R.; Smith, M. *Eur. J. Biochem.* **1 4,** *225,* 715.
24. Bertini, I.; Luchinat, C.; Rosato, A. *Progr. Biophys. Mol. Biol.* **1 6,** *66,* 43.
25. Solomon, I. *Phys. Rev.* **1 5,** *99,* 559.
26. Guéron, M. *J. Magn. Reson.* **1 75,** *19,* 58.
27. Vega, A. J.; Fiat, D. *Mol. Phys.* **1 76,** *31,* 347.
28. Bertini, I.; Jonsson, B.-H.; Luchinat, C.; Pierattelli, R.; Vila, A. J. *J. Magn. Reson. Ser. B* ***1994,*** *104,* 230.
29. Xia, B.; Westler, W. M.; Cheng, H.; Meyer, J.; Moulis, J.-M.; Markley, J. L. *J. Am. Chem. Soc.* **1 5,** *117,* 5347.
30. McConnell, H. M.; Robertson, R. E. *J. Chem. Phys.* **1 58,** *29,* 1361.
31. Werth, M. T.; Kurtz, D. M., Jr.; Moura, I.; LeGall, J. *J. Am. Chem. Soc.* **1 7,** *109,* 273.
32. Hagen, K. S.; Watson, A. D.; Holm, R. H. *J. Am. Chem. Soc.* **1 83,** *105,* 3905.
33. Banci, L.; Bertini, I.; Luchinat, C. *Struct. Bonding* **1 0,** *72,* 113.
34. Mouesca, J.-M.; Rius, G. J.; Lamotte, B. *J. Am. Chem. Soc.* **1 3,** *115,* 4714.
35. Rius, G. J.; Lamotte, B. *J. Am. Chem. Soc.* **1 8 ,** *111,* 2464.
36. Moura, I.; Huynh, B. H.; Hausinger, R. P.; LeGall, J.; Xavier, A. V.; Münck, E. *J. Biol. Chem.* **1 80,** *255,* 2493.
37. Papaefthymiou, V.; Girerd, J.-J.; Moura, I.; Moura, J. J. G.; Münck, E. *J. Am. Chem. Soc.* **1 87,** *109,* 4703.
38. Palmer, G.; Dunham, W. R.; Fee, J. A.; Sands, R. H.; Izuka, T.; Yonetani, T. *Biochim. Biophys. Acta* **1 71,** *245,* 201.
39. Papaefthymiou, G. C.; Laskowski, E. J.; Frota-Pessoa, S.; Frankel, R. B.; Holm, R. H. *Inorg. Chem.* **1 82,** *21,* 1723.

40. Stevens, K. W. H. In "Magneto-Structural Correlations in Exchange Coupled Systems;" Willett, R. D., Gatteschi, D.; Kahn, O. Eds.; Reidel, Dordrecht, 1985, 105.
41. Luchinat, C.; Ciurli, S. *Biol. Magn. Reson.* **1 3,** *12,* 357.
42. Kent, T. A.; Huynh, B. H.; Munk, E. *Proc. Natl. Acad. Sci. USA* **1 80,** *77,* 6574.
43. Noodleman, L. *Inorg. Chem.* **1 88,** *27,* 3677.
44. Noodleman, L. *Inorg. Chem.* **1 1,** *30,* 246.
45. Noodleman, L. *Inorg. Chem.* **1 1,** *30,* 256.
46. Bertini, I.; Luchinat, C. "NMR of Paramagnetic Molecules in Biological Systems"; Benjamin/Cummings: Menlo Park, CA, 1986.
47. Bertini, I.; Luchinat, C. "NMR of Paramagnetic Substances"; Coord. Chem. Rev., Vol. 150, Elsevier: Amsterdam, 1996, 1–300.
48. Bertini, I.; Galas, O.; Luchinat, C.; Parigi, G.; Spina, G. *J. Magn. Reson.* **1 8,** *130,* 33.
49. Bertini, I.; Lanini, G.; Luchinat, C.; Mancini, M.; Spina, G. *J. Magn. Reson.* **1 85,** *63,* 56.
50. Skjeldal, L.; Westler, W. M.; Markley, J. L. *Arch. Biochem. Biophys.* **1 0,** *278,* 482.
51. Bertini, I.; Lanini, G.; Luchinat, C. *Inorg. Chem.* **1 84,** *23,* 2729.
52. Lindhal, P. A.; Gorelick, N. J.; Münck, E.; Orme-Johnson, W. H. *J. Biol. Chem.* **1 87,** *262,* 14945.
53. Dugad, L. B.; La Mar, G. N.; Banci, L.; Bertini, I. *Biochemistry* **1 0,** *29,* 2263.
54. Ding, X.-Q.; Bill, E.; Trautwein, A. X.; Winkler, H.; Kostikas, A.; Papaefthymiou, V.; Simopoulos, A.; Beardwood, P.; Gibson, J. F. *J. Chem. Phys.* **1 3,** *99,* 6421.
55. Crouse, B. R.; Meyer, J.; Johnson, M. K. *J. Am. Chem. Soc.* **1 5,** *117,* 9612.
56. Moura, J. J. G.; Xavier, A. V.; Bruschi, M.; LeGall, J. *Biochim. Biophys. Acta* **1 77,** *459,* 306.
57. Sweeney, W. V. *J. Biol. Chem.* **1 81,** *256,* 12222.
58. Nagayama, K.; Ohmori, D.; Imai, Y.; Oshima, T. *FEBS Lett.* **1 83,** *158,* 208.
59. Nagayama, K.; Ohmori, D. *FEBS Lett.* **1 84,** *173,* 15.
60. Nagayama, K.; Imai, Y.; Ohmori, D.; Oshima, T. *FEBS Lett.* **1 84,** *169,* 79.
61. Bertini, I.; Luchinat, C.; Mincione, G.; Soriano, A. *Inorg. Chem.* **1 8,** *137,* 969.
62. Nettesheim, D. G.; Meyer, T. E.; Feinberg, B. A.; Otvos, J. D. *J. Biol. Chem.* **1 83,** *258,* 8235.
63. Krishnamoorthi, R.; Markley, J. L.; Cusanovich, M. A.; Przysiecki, C. T.; Meyer, T. E. *Biochemistry* **1 86,** *25,* 60.
64. Bertini, I.; Capozzi, F.; Luchinat, C.; Piccioli, M.; Vicens Oliver, M. *Inorg. Chim. Acta* **1 2,** *198–200,* 483.
65. Banci, L.; Bertini, I.; Capozzi, F.; Carloni, P.; Ciurli, S.; Luchinat, C.; Piccioli, M. *J. Am. Chem. Soc.* **1 3,** *115,* 3431.
66. Banci, L.; Bertini, I.; Ciurli, S.; Ferretti, S.; Luchinat, C.; Piccioli, M. *Biochemistry* **1 3,** *32,* 9387.
67. Bertini, I.; Capozzi, F.; Luchinat, C.; Piccioli, M. *Eur. J. Biochem.* **1 3,** *212,* 69.
68. Bertini, I.; Capozzi, F.; Eltis, L. D.; Felli, I. C.; Luchinat, C.; Piccioli, M. *Inorg. Chem.* **1 5,** *34,* 2516.
69. Phillips, W. D., McDonald, C. C.; Stombaugh, N. A.; Orme-Johnson, W. H. *Proc. Natl. Acad. Sci. USA* **1 74,** *71,* 140.
70. Meyer, J.; Gaillard, J.; Moulis, J.-M. *Biochemistry* **1 88,** *27,* 6150.
71. Anzilotta, W. N.; Holz, R. C.; Seefeldt, L. C. *Biochemistry* **1 5,** *34,* 15646.
72. Middleton, P.; Dickson, D. P. E.; Johnson, C. E.; Rush, J. D. *Eur. J. Biochem.* **1 80,** *104,* 289.

73. Bertini, I.; Campos, A. P.; Luchinat, C.; Teixeira, M. *J. Inorg. Biochem.* **1 3,** *52,* 227.
74. Banci, L.; Bertini, I.; Briganti, F.; Luchinat, C.; Scozzafava, A.; Vicens Oliver, M. *Inorg. Chim. Acta* **1 1,** *180,* 171.
75. Noodleman, L.; Chen, J. L.; Case, D. A.; Giori, C.; Rius, G. J.; Mouesca, J.-M.; Lamotte, B. In "Nuclear Magnetic Resonance of Paramagnetic Macromolecules," NATO ASI Series; La Mar, G. N. Ed.; Kluwer Academic Publishers: Dordrecht, The Netherlands, 1995, 339.
76. Belinskii, M. I.; Bertini, I.; Galas, O.; Luchinat, C. *Inorg. Chim. Acta* **1 6,** *243,* 91.
77. Bertini, I.; Luchinat, C. *JBIC* **1 6,** *1,* 183.
78. Kröckel, M.; Grodzicki, M.; Papaefthymiou, V.; Trautwein, A. X.; Kostikas, A. *JBIC* **1 6,** *1,* 173.
79. Noodleman, L.; Case, D. A.; Mouesca, J.-M.; Lamotte, B. *JBIC* **1 6,** *1,* 177.
80. Belinskii, M. I. *JBIC* **1 6,** *1,* 186.
81. Babini, E.; Bertini, I.; Borsari, M.; Capozzi, F.; Dikiy, A.; Eltis, L. D.; Luchinat, C. *J. Am. Chem. Soc.* **1 6,** *118,* 75.
82. Emptage, M. H.; Kent, T. A.; Huynh, B. H.; Rawlings, J.; Orme-Johnson, W. H.; Münck, E. *J. Biol. Chem.* **1 80,** *255,* 1793.
83. Busse, S. C.; La Mar, G. N.; Yu, L. P.; Howard, J. B.; Smith, E. T.; Zhou, Z. H.; Adams, M. W. W. *Biochemistry* **1 2,** *31,* 11952.
84. Macedo, A. L.; Moura, I.; Moura, J. J. G.; LeGall, J.; Huynh, B. H. *Inorg. Chem.* **1 3,** *32,* 1101.
85. Carter, C. W. J.; Kraut, J.; Freer, S. T.; Alden, R. A.; Sieker, L. C.; Adman, E. T.; Jensen, L. H. *Proc. Natl. Acad. Sci. USA* **1 72,** *69,* 3526.
86. Thompson, C. L.; Johnson, C. E.; Dickson, D. P. E.; Cammack, R.; Hall, D. O.; Weser, U.; Rao, K. K. *Biochem. J.* **1 74,** *139,* 97.
87. Banci, L.; Bertini, I.; Gori Savellini, G.; Luchinat, C. *Inorg. Chem.* **1 6,** *35,* 4248.
88. Bertini, I.; Gori Savellini, G.; Luchinat, C. *JBIC* **1 7,** *2,* 114.
89. Rypniewski, W. R.; Breiter, D. R.; Benning, M. M.; Wesenberg, G.; Oh, B.-H.; Markley, J. L.; Rayment, I.; Holden, H. M. *Biochemistry* **1 1,** *30,* 4126.
90. Skjeldal, L.; Westler, W. M.; Oh, B.-H.; Krezel, A. M.; Holden, H. M.; Jacobson, B. L.; Rayment, I.; Markley, J. L. *Biochemistry* **1 1,** *30,* 7363.
91. Backes, G.; Mino, Y.; Loehr, T. M.; Meyer, T. E.; Cusanovich, M. A.; Sweeney, W. V.; Adman, E. T.; Sanders-Loehr, J. *J. Am. Chem. Soc.* **1 1,** *113,* 2055.
92. Jensen, G. M.; Warshel, A.; Stephen, P. J. *Biochemistry* **1 4,** *33,* 10911.
93. Capozzi, F.; Ciurli, S.; Luchinat, C. *Struct. Bonding* **1 8,** *90,* 127.
94. Soriano, A.; Li, D.; Bian, S.; Agarwal, A.; Cowan, J. A. *Biochemistry* **1 6,** *35,* 12479.
95. Wüthrich, K. "NMR of Proteins and Nucleic Acids"; Wiley: New York, 1986.
96. Bertini, I.; Felli, I. C.; Kastrau, D. H. W.; Luchinat, C.; Piccioli, M.; Viezzoli, M. S. *Eur. J. Biochem.* **1 4,** *225,* 703.
97. Banci, L.; Bertini, I.; Luchinat, C. In "Methods in Enzymology"; James, T. L., Oppenheimer, N. J. Eds.; Academic Press: London, 1994; Vol. 239, p. 485.
98. Bertini, I.; Luchinat, C.; Piccioli, M.; Tarchi, D. *Concepts Magn. Reson.* **1 4,** *6,* 307.
99. Bertini, I.; Donaire, A.; Feinberg, B. A.; Luchinat, C.; Piccioli, M.; Yuan, H. *Eur. J. Biochem.* **1 5,** *232,* 192.
100. Bentrop, D.; Bertini, I.; Capozzi, F.; Dikiy, A.; Eltis, L. D.; Luchinat, C. *Biochemistry* **1 6,** *35,* 5928.

101. Bertini, I.; Couture, M. M. J.; Donaire, A.; Eltis, L. D.; Felli, I. C.; Luchinat, C.; Piccioli, M.; Rosato, A. *Eur. J. Biochem.* **1 6,** *241,* 440.
102. Vuister, G. W.; Bax, A. *J. Am. Chem. Soc.* **1 3,** *115,* 7772.
103. Bertini, I.; Rosato, A. In "Molecular Modeling and Dynamics of Bioinorganic Systems"; Banci, L., Comba, P. Eds.; Kluwer Academic Publishers: Dordrecht, 1997, 1.
104. Bertini, I.; Felli, I. C.; Luchinat, C.; Rosato, A. *Proteins Struct. Funct. Genet.* **1 6,** *24,* 158.
105. Bertini, I.; Donaire, A.; Luchinat, C.; Rosato, A. *Proteins Struct. Funct. Genet.* **1 7,** *29,* 348.
106. Huber, J. G.; Moulis, J.-M.; Gaillard, J. *Biochemistry* **1 6,** *35,* 12705.
107. Donaire, A.; Zhou, Z.-H.; Adams, M. W. W.; La Mar, G. N. *J. Biomol. NMR* **1 6,** *7,* 35.
108. Bertini, I.; Donaire, A.; Felli, I. C.; Luchinat, C.; Rosato, A. *Inorg. Chem.* **1 7,** *36,* 4798.
109. Bentrop, D.; Bertini, I.; Iacoviello, R.; Luchinat, C.; Niikura, Y.; Piccioli, M.; Presenti, C.; Rosato, A. *Biochemistry* **1** , in press.
110. Bertini, I.; Kurtz, D. M., Jr.; Eidsness, M. K.; Liu, G.; Luchinat, C.; Rosato, A.; Scott, R. A. *JBIC* **1 8,** *3,* 401.
111. Sang-Choul, I.; Liu, G.; Luchinat, C.; Sykes, A. G.; Bertini, I. *Eur. J. Biochem.* **1 8,** *258,* 465.
112. Aono, S.; Bentrop, D.; Bertini, I.; Donaire, A.; Luchinat, C.; Niikura, Y.; Rosato, A. *Biochemistry* **1 8,** *37,* 9812.
113. Karplus, M. *J. Chem. Phys.* **1 5 ,** *30,* 11.
114. Karplus, M. *J. Am. Chem. Soc.* **1 63,** *85,* 2870.
115. Heller, C.; McConnell, H. M. *J. Chem. Phys.* **1 60,** *32,* 1535.
116. Karplus, M.; Fraenkel, G. K. *J. Chem. Phys.* **1 61,** *35,* 1312.
117. Stone, E. W.; Maki, A. H. *J. Chem. Phys.* **1 62,** *37,* 1326.
118. Bernstein, F. C.; Koetzle, T. F.; Williams, G. J. B.; Meyer, E. F., Jr.; Rodgers, J. R.; Kennard, O.; Shimanouchi, T.; Tasumi, M. *J. Mol. Biol.* **1 77,** *112,* 535.
119. Hatanaka, H.; Tanimura, R.; Katoh, S.; Inagaki, F. *J. Mol. Biol.* **1 7,** *268,* 922.
120. Bertini, I.; Eltis, L. D.; Felli, I. C.; Kastrau, D. H. W.; Luchinat, C.; Piccioli, M. *Chemistry—A European Journal* **1 5,** *1,* 598.
121. Wang, P. L.; Donaire, A.; Zhou, Z. H.; Adams, M. W. W.; La Mar, G. N. *Biochemistry* **1 6,** *35,* 11319.
122. Bertini, I.; Cowan, J. A.; Luchinat, C.; Natarajan, K.; Piccioli, M. *Biochemistry* **1 7,** *36,* 9332.
123. Bertini, I.; Luchinat, C.; Piccioli, M.; Soriano, A. *Inorg. Chim. Acta* **1 8,** *283,* 12.
124. Bertini, I.; Briganti, F.; Calzolai, L.; Messori, L.; Scozzafava, A. *FEBS Lett.* **1 3,** *332,* 268.
125. Felli, I. C.; Desvaux, H.; Bodenhausen, G. *J. Biomol. NMR* **1 8,** *12,* 509.
126. Banci, L.; Felli, I. C.; Koulougliotis, D. *J. Biomol. NMR* **1 8,** *12,* 307.
127. Agarwal, A.; Li, D.; Cowan, J. A. *Proc. Natl. Acad. Sci. USA* ***1995,*** *92,* 9440.
128. Bian, S.; Hille, C. R.; Hemman, C.; Cowan, J. A. *Biochemistry* **1 6,** *35,* 14544.
129. Cowan, J. A.; Lui, S. M. *Adv. Inorg. Chem.* **1 8,** *45,* 313.
130. (a) Rabinowitz, J. C. In "Methods in Enzymology"; Academic Press; London, 1972, Vol. 24, p. 431. (b) Smith, E. T.; Feinberg, B. A.; Richards, J. H.; Tomich, J. R. *J. Am. Chem. Soc.* **1 1,** *113,* 689.
131. Natorajan, K.; Cowan, J. A. *J. Am. Chem. Soc.* **1 7,** *119,* 4082.

132. LeLong, C.; Sétif, P.; Bottin, H.; André, F.; Neumann, J.-M. *Biochemistry* **1 5,** *34,* 14462.
133. Baumann, B.; Sticht, H.; Scharpf, M.; Sutter, M.; Haehnel, W.; Rosch, P. *Biochemistry* **1 6,** *35,* 12831.
134. Banci, L.; Bertini, I.; Dikiy, A.; Kastrau, D. H. W.; Luchinat, C.; Sompornpisut, P. *Biochemistry* **1 5,** *34,* 206.
135. Bertini, I.; Dikiy, A.; Kastrau, D. H. W.; Luchinat, C.; Sompornpisut, P. *Biochemistry* **1 5,** *34,* 9851.
136. Sticht, H.; Wildegger, G.; Bentrop, D.; Darimont, B.; Sterner, R.; Roesch, P. *Eur. J. Biochem.* **1 6,** *237,* 726.
137. Davy, S. L.; Osborne, M. J.; Moore, G. R. *J. Mol. Biol.* **1 8,** *277,* 683.
138. Macedo, A. L.; Palma, P. N.; Moura, I.; LeGall, J.; Wray, V.; Moura, J. J. G. *Magn. Reson. Chem.* **1 3,** *31,* S59.
139. Bertini, I.; Briganti, F.; Luchinat, C.; Messori, L.; Monnanni, R.; Scozzafava, A.; Vallini, G. *Eur. J. Biochem.* **1 2,** *204,* 831.
140. Aono, S.; Bertini, I.; Cowan, J. A.; Luchinat, C.; Rosato, A.; Viezzoli, M. S. *JBIC* **1 6,** *1,* 523.
141. Scrofani, S. D. B.; Brownlee, R. T. C.; Sadek, M.; Wedd, A. G. *Inorg. Chem.* **1 5,** *34,* 3942.
142. Cheng, H.; Grohmann, K.; Sweeney, W. V. *J. Biol. Chem.* **1 2,** *267,* 8073.
143. Koradi, R.; Billeter, M.; Wüthrich, K. *J. Mol. Graphics* **1 6,** *14,* 51.

NICKEL–IRON–SULFUR ACTIVE SITES: HYDROGENASE AND CO DEHYDROGENASE

JUAN C. FONTECILLA-CAMPS* and STEPHEN W. RAGSDALE†

*Laboratoire de Cristallographie et de Cristallogenèse des Protéines, Institut de Biologie Structurale 'Jean-Pierre Ebel' CEA-CNRS, 38027 Grenoble Cedex 1, France, and †Department of Biochemistry, University of Nebraska–Lincoln, The Beadle Center, Lincoln, Nebraska 68588

I. Introduction
  A. General Properties of Nickel and Iron
  B. Occurrence of Nickel and Iron in Proteins
II. General Concepts Regarding Nickel and Iron–Sulfur
  A. Uptake of Nickel and Iron
III. Hydrogenase
  A. Introductory Remarks
  B. Hydrogenase Synthesis and Maturation
  C. The Active Site
  D. Catalytic Mechanism Models
  E. Interaction of the Active Site with Other FeS Centers
IV. CODH/ACS
  A. Introduction to CODH/ACS
V. Conclusions
References

I. Introduction

This review concerns proteins that contain both nickel and iron. Below are listed the three known proteins of this class and the reactions that they catalyze. The active sites of all of these consist of heterometallic nickel–iron–sulfur (NiFeS) clusters. The terms used will be explained later in the text.

Hydrogenase: $2H^+ + 2e^-\cdot \longleftrightarrow H^+ + H^-\cdot \longleftrightarrow H_2$ (1)

CO dehydrogenase: $CO + H_2O \longleftrightarrow 2H^+ + CO_2 + 2e^-$ (2)

Acetyl-CoA synthase: $CH_3–CFeSP + CoA–SH + CO \longleftrightarrow CH_3–CO–SCoA + CFeSP$ (3)

Copyright 1999 by Academic Press.
All rights of reproduction in any form reserved.
0898-8838/99 $30.00

A. General Properties of Nickel and Iron

Derived from the German word meaning "devil's copper," nickel is found predominantly in two isotopic forms, ^{58}Ni (68% natural abundance) and ^{60}Ni (26%). Ni exists in four oxidation states, 0, I, II, III, and IV. Ni(II), which is the most common oxidation state, has an ionic radius of ~65 pm in the four-coordinate state and ~80 pm in the octahedral low-spin state. The Ni(II) aqua cation exhibits a pK_a of 9.9. It forms tight complexes with histidine (log K_f = 15.9) and, among the first-row transition metals, is second only to Cu(II) in its ability to complex with acidic amino acids (log K_f = 6–7 (*1*). Although Ni(II) is most common, the paramagnetic Ni(I) and Ni(III) states are also attainable. Ni(I), a d^9 metal, can exist only in the $S = \frac{1}{2}$ state, whereas Ni(III), a d^7 ion, can be either $S = \frac{1}{2}$ or $S = \frac{3}{2}$.

Iron is the most abundant, useful, and important of all metals. For example, in the 70-kg human, there is approximately 4.2 g of iron. It can exist in the 0, I, II, III, and IV oxidation states, although the II and III ions are most common. Numerous complexes of the ferrous and ferric states are available. The Fe(II) and Fe(III) aquo complexes have vastly different pK_a values of 9.5 and 2.2, respectively. Iron is found predominantly as ^{56}Fe (92%) with smaller abundances of ^{54}Fe (6%), ^{57}Fe (2.2%), and ^{58}Fe (0.3%). ^{57}Fe is highly useful for spectroscopic studies because it has a nuclear spin of $\frac{1}{2}$. There has been speculation that life originated at the surface of iron-sulfide precipitants such as pyrite or greigite that could have caused autocatalytic reactions leading to the first metabolic pathways (*2*, *3*).

B. Occurrence of Nickel and Iron in Proteins

There are *hundreds* of iron-containing enzymes. In general, the iron can exist as (a) a mononuclear site, in which it is coordinated by a tetrapyrrole structure (hemes) or strictly by amino acid residues that donate oxo, nitrogen, or sulfur ligands; (b) a dinuclear site in which the irons are bridged by oxo, nitrogen, or sulfur coordination; (c) a trinuclear site as in the 3Fe–4S clusters; or (d) a tetranuclear site as in the [4Fe–4S] clusters.

In contrast to the abundance of Fe-proteins, there are only six known nickel-containing enzymes: hydrogenase, CO dehydrogenase (CODA), acetyl-CoA synthase (ACS), superoxide dismutase, urease, and *S*-methyl-CoM methylreductase. Among these enzymes, it exists in very diverse environments, including a dinickel site (urease), a Ni–Fe heterobinuclear site (hydrogenase), a Ni–Fe_4S_4 heterometallic

cluster (CODH, ACS), and as the central ion in a tetrapyrrole (F430 in methyl-CoM reductase). Several recent reviews on aspects of Ni biochemistry are available. These include general reviews on nickel biochemistry (*4–7*) and the biomimetic chemistry of Ni (*8*). In addition, there are reviews dealing specifically with hydrogenases (*9–11*), CODHs (*12–14*), and methyl-CoM reductase (*15*).

II. General Concepts Regarding Nickel and Iron–Sulfur

A. Uptake of Nickel and Iron

The first problem that an organism faces in generating an active hydrogenase or CO dehydrogenase is to import the transition metal from the extracellular milieu. A review on transition metal uptake and storage is available (*16*). Here we will discuss the latest results concerning this process. For nickel, the problem is formidable—how to specifically extract nickel in the presence of other cations that are of similar charge and size and are present at higher concentrations. The total Ni concentration in most natural environments is in the low nanomolar range. For example, in freshwater or seawater, the total concentration is ~20 nM (*17*). Survival requires efficient and highly specific Ni uptake systems. The concentration of iron varies greatly in different systems. For example, in seawater, the iron concentration can be in the range of 0.05 to 5 nM. In the human bloodstream the total concentrations of nickel and iron are ~0.5 and 200 nM, respectively.

Delivery of nickel (*10*, *18*) and iron (*16*) and their assembly into the active sites of metalloenzymes are the subjects of recent reviews. The quantity of bioavailable metal ion poses an additional restriction, since this can be significantly less than the total amount of ion and is influenced by many factors, including the inherent complexation properties of the metal, the pH, and the concentration of potential chelators and precipitation agents (e.g., phosphate buffer) (1). For example, the solubility of hydrated ferric iron is 10^{-18} M (*16*) and tight complexing agents called siderophores are secreted by organisms to capture iron from the extracellular milieu and maintain its solubility (*19*). Of course, this solution raises another problem—how to release the metal from the strongly coordinating chelate complex. Release of iron apparently involves redox (conversion to Fe(II) and acid–base (lowering the pH) chemistry.

As will be discussed later, two types of high-affinity Ni transporters

have been identified. One is a multicomponent system that uses ATP to concentrate Ni (NikABCDE) (*20*, *21*). The other is a one-component Ni transporter (NixA, UreH, HupN, or HoxN, depending on the organism) (*10*, *22–25*).

III. Hydrogenase

A. Introductory Remarks

The uptake and/or production of molecular hydrogen by chemotrophic and phototrophic microorganisms according to the reaction shown in (1) is mediated by enzymes called hydrogenases (*26*, *27*). Reaction (**1**) is heterolytic (*28*), producing H^- and H^+ in the first step. Two major types of hydrogenases exist: Fe-only and Ni–Fe-containing enzymes (*29*, *30*). The Ni–Fe hydrogenases are by far the most extensively studied ones. They are heterodimeric enzymes with fairly conserved 60-kDa subunits and relatively diverse 30-kDa subunits (*31*). Crystal structures for the *Desulfovibrio gigas* and *D. desulfuricans* Miyazaki F enzymes have been published (*32*, *33*). In addition, the structures of *D. fructosovorans* Ni–Fe and *Desulfomicrobium baculatum* Ni–Fe–Se hydrogenases have also been recently determined (*34*, *35*). These studies have shown that the active site is deeply buried in the structure, thus requiring the presence of both proton and electron transfer pathways. Also, the issue of substrate accessibility to the active center has been addressed (*36*) and will be briefly discussed later. The structure of the *D. gigas* hydrogenase is depicted in Fig. 1.

B. Hydrogenase Synthesis and Maturation

Hydrogenase operons are complex in that they possess, in addition to the structural genes coding for the two subunits, many other open reading frames whose corresponding transcribed proteins have been described as either regulatory or accessory. Although the roles of the latter have not been elucidated in every case, in general they seem to be Ni-binding proteins involved in active center assembly and/or enzyme activation (*37*).

1. Nickel Transport

Functional proteins are also involved in high-affinity Ni transport for hydrogenase synthesis. One example is the *nikABCDE* gene cluster of *Escherichia coli* (*20*). NikA is a periplasmic Ni-binding protein,

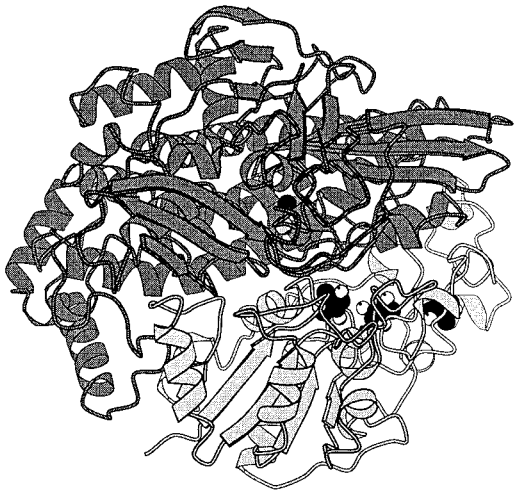

FIG. 1. Ribbon representation of the three-dimensional structure of *D. gigas* hydrogenase (*32*). The large subunit is represented in dark gray. Fe is represented by black spheres, Ni by gray spheres, and inorganic sulfur by white spheres. The C-terminal end of the large subunit is close to the Ni and completely buried in the structure.

NikB and NikC are integral membrane proteins, and NikD and NikE contain ATP binding motifs (*38*). Another example is the Ni permease HoxN of *Alcaligenes eutrophus,* whose expression is under the control of the hydrogenase *hox* operon (*25*). The HoxN protein seems to be generally involved in providing Ni to the cell because inactivation of *hoxN* not only led to an increase in Ni requirement for the synthesis of active NiFe-hydrogenases, but was also required for urease holoenzyme synthesis (*39*). HoxN has extremely high specificity and affinity for Ni ions and, as a consequence, only traces of this ion are required for the expression of *A. eutrophus* active Ni-dependent hydrogenases and ureases (*39*). Using a combination of hydropathic profile amino acid sequence analyses and genetically engineered insertion of specific markers for periplasmic and cytoplasmic activities, Wolfram, Friedich, and Eitinger (*25*) have generated a topological model of HoxN. According to these studies, HoxN appeared to be a membrane protein containing seven transmembrane helices. However, the correction of an error in the originally published *hoxN* nucleotide sequence has prompted these authors to add an eighth helix to their model (*38*). Mutations of a His–Asp–His motif conserved in this Ni permease, resulted in dramatically impaired Ni^{2+} uptake indicating that these residues are involved in substrate recognition (*38*).

2. Proteins Involved in Enzyme Maturation

In addition to transport proteins that fulfill the requirement of bringing Ni^{2+} ions to the cytoplasm, the correct assembly of hydrogenase active site requires several other types of proteins. As opposed to apoureases (*40*) and Ni-deficient CODH A-clusters (*41*), *in vitro* Ni incorporation is not possible in apohydrogenases. This is most likely due to the fact that hydrogenase maturation generally requires the proteolysis of a C-terminal peptide from the 60-kDa large subunit (*11*), a process that buries the Ni-containing active site in the structure (*32*) and, consequently, is likely to be an irreversible one (Fig. 1). If Ni is not present, the unprocessed form of the large subunit accumulates (*42, 43*). However, subsequent addition of Ni to cell-free extracts results in the processing of the subunit, indicating the existence of a Ni-dependent protease specific for hydrogenase maturation (*43*). Maier and Böck have confirmed and extended these observations by measuring the effect of the various accessory proteins on *E. coli* hydrogenase 3 maturation (*44*). Using Ni-free cell extracts of a *nik*$^-$ (Ni transport deficient) mutant, these authors have determined the need for accessory proteins HypB, HypC, HypD, HypE, HypF, and protease NycI for the development of hydrogenase activity starting from a HycE (large subunit) precursor. The requirement for each of these proteins was assessed by using *nik*$^-$/*accessory protein gene*$^-$ double mutants. Ni^{2+} specifically elicited hydrogenase large-subunit maturation, as none of Fe^{2+}, Co^{2+}, Cu^{2+}, or Zn^{2+} was able to replace it. The following conclusions were reached by Maier and Böck (*44*): (1) The HycE precursor that accumulates in mutants affected in *hypA*, *hypC*, *hypD*, *hypE*, or *hypF* functions is incompetent for processing; (2) addition of Ni to a *hypB* deletion mutant indicates that the accumulated HycE precursor can be partially processed *in vivo*, but not *in vitro*; (3) addition of Ni to a *nik*$^-$ mutant shows processing of HycE precursor both *in vivo* and *in vitro*; (4) the HycE precursor accumulated in a *hycI* deletion mutant already contains Ni *in vivo* and can be maturated by purified HycI protease *in vitro.* HoxW, a protease similar to HycI, has been described in *Alcaligenes eutrophus* (*45*). Massanz *et al.* (*46*) have shown that in *A. eutrophus* an Ala → Pro mutation at the first residue of the 24-amino acid normally cleaved peptide blocks proteolysis of the C-terminal region of the large subunit of the NAD-reducing hydrogenase. The resulting mutant could bind Ni but was not able to form the stable tetrameric (hydrogenase : diaphorase) holoenzyme. A second mutation introduced a stop codon at the Ala position. This time, the mutated enzyme could not bind

Ni, but it had the native enzyme oligomeric organization (*46*). Thus, the C-terminal extension is needed for Ni incorporation, which, in turn, is not needed for subunit assembly.

Very significant progress has been made in further characterizing the role of several of the previously identified gene products: HypB is a Ni-binding protein with GTPase activity found in *Bradyrhizobium japonicum* (*47*) and *Rhizobium leguminosum* (the equivalent *E. Coli* HydB GTPase does not seem to bind Ni). In contradiction with results reported for *A. vinelandii* (*43*), addition of GTP to cell extracts did not stimulate the *in vitro E. coli* HypB-mediated large subunit processing (*11*). HypC of hydrogenase 3 from *E. coli* has been found to bind the precursor of HycE, probably keeping it in a conformation that is accessible for metal incorporation (*48*). HypF of *R. capsulatus* participates in the maturation of the HupSL structural hydrogenase genes, probably mediating Ni insertion.

3. *Hydrogen Sensor Proteins and the Control of Hydrogenase Expression*

HypF also seems to be involved in the maturation of the sensor proteins HupU/V (*49*). These constitute an additional group of proteins homologous to hydrogenases that lack the C-terminal maturation peptide of the large subunit (*50–52*). These proteins are postulated to be part of two-component regulatory systems involved in the control of hydrogenase expression. In *B. japonicum*, *R. capsulatus*, and *A. eutrophus*, the respective hydrogenase-like gene sequences *hupU*, *hupV*, and *hoxB/C* are associated with genes coding for soluble protein histidine kinases (HupT in *B. japonicum* and *R. capsulatus* (*53*), HydH in *E. coli* and HoxJ in *A. eutrophus*) which are autophosphorylatable sensor proteins (*50*, *54*). HupU shares amino acid similarities with both the large and small subunits of hydrogenase and can be regarded as an in-frame fusion of the *hupL* and *hupS R. capsulatus* structural genes. Upon induction by H_2, the hydrogenase-like protein provokes the phosphorylation of a NtrC-like transcription regulator by the kinase. NtrC-like transcription regulators have been found in *E. coli* (HydG) (*54*), *R. capsulatus* (HupR) (*55*, *56*), and *B. japonicum* (*57*) and *A. alcaligenes* (HoxA) (*54*). Phosphorylated HupR has been shown to bind to DNA and act as a transducer of the H_2 signal, activating *in vivo* transcription of the hupS (hydrogenase small subunit) structural gene (*56*).

The hydrogenase-like proteins are known to catalyze the H/D exchange reaction, typical of hydrogenase (*58*). It remains to be determined to what extent the hydrogen binding site of these proteins re-

sembles the active site of Ni–Fe hydrogenases (*49*). As opposed to hydrogenases that are periplasmic enzymes, the *R. capsulatus* HupUV proteins seem to be cytoplasmic, as indicated by their insensitivity to external pH changes (*58*). That hydrogenase-like proteins are in general cytoplasmic is suggested by the fact that there is no signal peptide in HoxB. The signal peptide of the equivalent subunit in *A. hydrogenophilus* hydrogenase is normally responsible for translocation of the holoenzyme (*54*).

4. Occurrence of the Hydrogenase Maturation Process

The maturation process described earlier seems to be absent from a CO-dependent, CO-tolerant hydrogenase (CooH) whose gene lacks the sequence coding for the normally proteolyzed C-terminal peptide (*59*). The *cooH* gene is found upstream from *cooF*, a gene closely related to the *cooS* CODH structural gene (*60*). Although it is not clear whether CooH contains Ni, the four Ni cysteinyl active site ligands found in the *D. gigas* hydrogenase (see later discussion) are present in the CooH amino acid sequence. If this novel enzyme is indeed a Ni-protein, then the process of active site assembly must differ significantly from its counterpart in CO-independent [NiFe] hydrogenases. Since, as indicated previously, the *hupU* and *hupV* gene sequences also lack the C-terminal "maturation" region and may contain Ni, the assembly process could be similar in the two cases.

5. Effect of Posttranslational Processes on the Assembly of the Fe Ion at the Active Site

HypX from *Rhizobium leguminosarum* (*61*) and HoxX from *Bradyrhizobium japonicum* (*62*) are proteins associated with the posttranslational processing of Ni–Fe hydrogenases. Interestingly, these proteins present amino acid sequence homologies with N_{10}-formyl tetrahydrofolate-dependent enzymes, which are involved in the transfer of one-carbon units, and with the enoyl-coenzyme A hydratase/isomerase family of proteins. HypX has been proposed to play a role in the assembly of the Fe–Ni active center of hydrogenases. The one-carbon unit transfer putative activity of this protein implies that it might be involved in the synthesis of CO and/or CN^-, which are ligands to the Fe center (see Section C,2,c and Fig. 2).

C. The Active Site

1. X-ray Structure

a. A Binuclear Ni–Fe Center Prior to the solution of the crystal structure of *D. gigas* hydrogenase, its active site was thought to con-

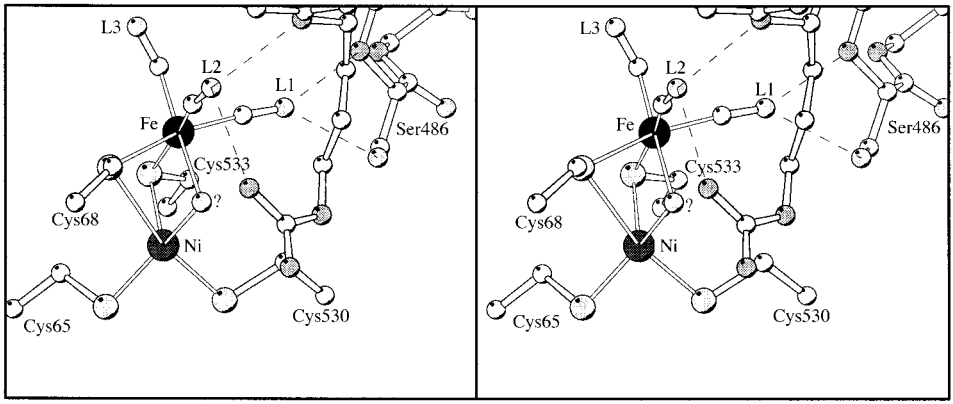

FIG. 2. Stereo view of the active site of *D. gigas* hydrogenase (reprinted with permission from (*65*); copyright 1997, American Chemical Society). L1 and L2 are diatomic ligands that form hydrogen bonds with the protein-; they are supposed to be the two CN's molecules. The third ligand L3 sits in a hydrophobic pocket and is assumed to be the CO. The ? designates the putative oxo bridging ligand.

sist of a mononuclear Ni center (*9*) with mixed N(O)/S(Cl) ligation (*63*, *64*). The crystallographic study indicated, however, that the metal center at the active site is actually binuclear containing an initially unidentified metal ion and Ni (*32*, *65*, *66*) with four cysteine thiolates coordinating the two metal ions (Fig. 2). This is in agreement with amino acid sequence comparison studies, since only four cysteine thiolates were found to be highly conserved in the large subunit (from motifs L2 and L5 in ref. (*9*), and with earlier XAS experiments (*67*). We have argued that the second metal site corresponds to Fe, based on metal content analysis of the enzyme and on anomalous dispersion effects detected on electron density maps (*65*).

b. Active Site Metal–Protein Ligation In *D. gigas* hydrogenase, two of the cysteine ligands (Cys65 and Cys530) are terminal, whereas the remaining ones (Cys68 and Cys533) bridge the Ni and Fe ions (Fig. 2). Electron paramagnetic resonance (EPR) and extended X-ray spectroscopy fine structure (EXAFS) data (*68–70*) from the *D. baculatum* NiFeSe enzyme, which had assigned the SeCys equivalent to Cys530 in *D. gigas* as a Ni ligand, were instrumental in initially distinguishing between the Ni and Fe ions in the electron density maps. In the initial medium-resolution study (*32*), the Ni ion coordination sphere seemed to be square pyramidal with an in-plane vacant site; that of the Fe ion was octahedral, also containing an empty site and including three nonprotein ligands. These ligands are deeply buried in the active site cavity and, consequently, are very likely nonexchangeable.

The atomic temperature factors obtained after crystallographic refinement are significantly higher for cys530 than for the other site cysteine residues. This is also true when the Ni ion is compared to the Fe center. This may reflect conformational disorder due to the fact that the crystals are made of a mixture of different Ni states (40% Ni–A, 10% Ni–B, and 50% of an EPR-silent species) (*32*).

c. A Putative Ni Oxo Ligand A subsequent study using higher resolution data of better overall quality showed that the apparently empty coordination sites of the two metal ions were, in fact, occupied in the oxidized enzyme by a bridging ligand (Fig. 2), possibly an oxo species (*65*). It also indicated that the three nonproteinaceous Fe ligands were diatomic molecules. From the stereochemistry of the crystallographically refined active site, the putative oxo ligand appears to be more tightly bound to the Ni ion than to the Fe ion (d = 1.7 Å and 2.1 Å, respectively, with an angle of 97°) (*65*). A very similar arrangement has been observed in a W–Os binuclear center with an unusual oxo bridge (*71*):

(4)

The distances and angles of the model compound are W=O = 1.76 Å, Os–O = 2.2 Å, and W=O → Os = 93°. The similarity in the stereochemistry of the two heterobinuclear centers raises the possibility that, in the unready Ni–A form, the Ni center is double-bonded to an oxo ligand. This would explain why the activation is very slow unless the temperature of the reaction is raised (*72*). This notion (or idea) could be tested by quantitating the number of electrons involved in the Ni–A ↔ Ni–SI transition.

2. Spectroscopic Studies

Spectroscopic studies have been instrumental in elucidating the catalytic mechanism of Ni–Fe hydrogenases. A great deal of controversy concerning this mechanism arises from the fact that, as the as the X-ray crystallographic analysis has shown, there are at least three potential redox-active species at the enzyme's active site: the thiolate ligands (*73*) and the Fe (*65*) and Ni (*9*) ions.

a. X-ray Absorption Spectroscopy The initial models of Ni coordination based on X-ray absorption spectroscopy (XAS) have been mentioned. Gu *et al.* have rationalized the inability of XAS to detect the

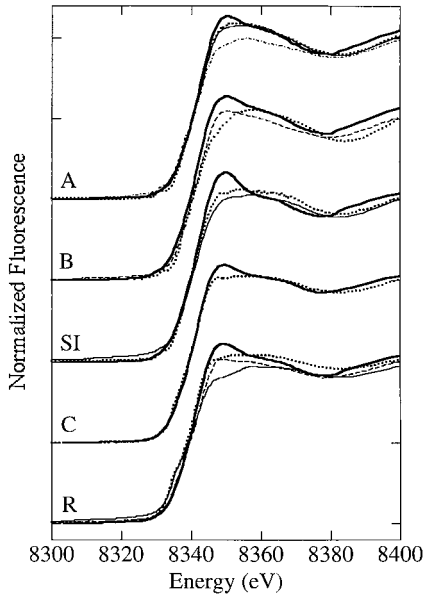

FIG. 3. A comparison of the Ni K-edge XAS spectra for redox poised samples of several hydrogenases (reprinted with permission from (*74*); copyright 1997, American Chemical Society). Bold lines, *T. roseopersicina*; light line, *D. gigas*; dotted line, *C. vinosum*; dashed line, *D. desulfuricans* ATCC 27774; dashed–dotted line, *E. coli.*

presence of the active center Fe ion (*74*). According to these authors, the problem is that the Ni–S distances corresponding to the bridging cysteines 65 and 533 in *D. gigas* are similar to the one between Ni and Fe (around 2.5–2.9 Å). This has the unfortunate consequence that the distance determined by fitting the long scattering atoms with either S or Fe represents neither distance in hydrogenase, since the net EXAFS is the sum of the two components (*74*). As reported earlier for *Thiocapsa roseopersicina* hydrogenase (*64*), reduction of the active site of several hydrogenases did not significantly affect the Ni K-edge energy. The observed energy shifts, with values between 0.9 and 1.5 eV, are compatible with no more than one-electron, metal-based redox change (Fig. 3). With the exception of the enzyme from *A. eutrophus*, most of the energy shift takes place when going from oxidized forms to a partially reduced state (Ni–A/Ni–B to Ni–SI; see later discussion).

X-ray absorption near-edge spectroscopy (XANES) suggests that, in most of the enzymes, the reduction to Ni–SI also implies a change in the coordination number of the Ni ion from 5 to 6 (*74*).

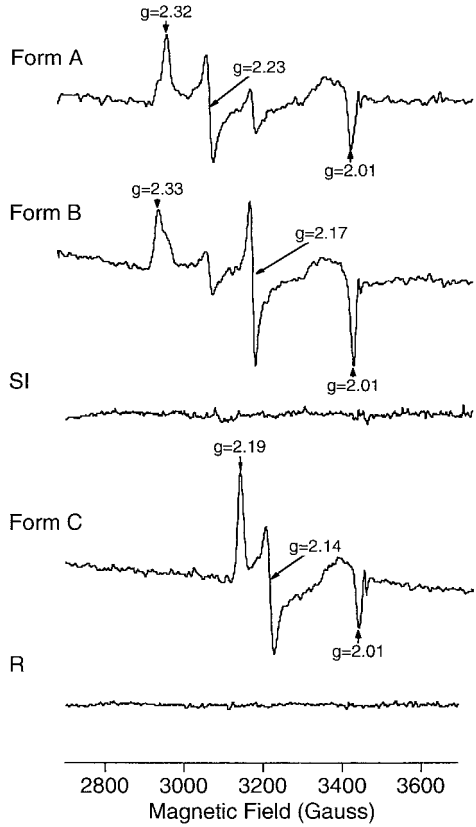

FIG. 4. EPR spectra of redox poised hydrogenase from *T. roseopercisina*. The *g* values are indicated. (Reprinted with permission from (*64*); copyright 1997, American Chemical Society).

b. Electron Paramagnetic Resonance In general, oxidized, as-prepared Ni–Fe hydrogenases are known to display two electron paramagnetic resonance (EPR) signals called Ni–A and Ni–B (Fig. 4). They are both supposed to arise from Ni(III) d^7 species, although there are fundamental chemical and spectroscopic differences between the two states (*9*, *72*). Activation of the enzyme displaying the Ni–A state is slow and temperature-dependent, whereas hydrogenase displaying the Ni–B signal can be readily activated (*72*). From EPR experiments using $^{17}O_2$, it has been postulated that both Ni–A and Ni–B states have bound oxygen at, or near, the active-site Ni ion (*75*). This is in agreement with the crystal structure of the as-prepared *D. gigas* hydrogenase that shows the presence of the putative oxo ligand

tightly bound to the active site Ni ion (Fig. 2). The crystalline *D. gigas* enzyme displays, for the most part, the Ni–A signal.

Upon reduction under hydrogen, a new paramagnetic species called Ni–C is generated. EPR studies have indicated that when hydrogenase is in the Ni–C state, it is possible to photolyze an active-site bond, giving rise to at least two additional paramagnetic species. The resulting EPR spectra are modified when ^2H is used instead of ^1H, indicating that the dissociation involves a hydrogen species bound, or close to, Ni (*9*, *76*). This hydrogen species has been postulated to be H^-, H^+, or H_2 (*9*, *77*). The Ni–C signal could arise from either Ni(III) d^7 or Ni(I) d^9 (*9*, *77*).

A Ni-bound $H-H^-$ species in the Ni–C form has been considered to be unlikely based on the very small hyperfine splitting observed due to exchangeable ^1H (*78*). It has been argued, however, that the observed small values could arise from an equatorially bound Ni hydride (*79*). It has also been postulated that the photolyzed hydrogen species contained in the Ni–C state is the proton of a thiol group bound to the Ni ion (*80*).

EPR spectra and *g* values for the various states of the hydrogenase from *Thiocapsa roseopersicina* (*64*) are depicted in Fig. 4. These spectra are representative of those of the other NiFe hydrogenases.

c. Fourier Transform Infrared The discovery of triple-bonded species in Ni–Fe hydrogenases (*81–83*), their crystallographic assignment as active-site Fe ligands (*65*, *66*), and their isotope-based identification (*81*) as being two CN^-s and one CO have provided a very powerful tool to probe active-site redox changes in these enzymes by Fourier transform infrared (FTIR) spectroscopy (*81–83*). Typically, each redox species is represented by a triplet of high-frequency bands. The two higher frequency CN^- bands are separated by about 6 cm^{-1}, whereas the stronger CO band is generally found at significantly lower frequencies (Fig. 5). It has been possible to tentatively assign the three ligands to the diatomic species detected in the crystal structure of the *D. gigas* enzyme, based on the protein environment (Fig. 2). The two putative CN^- ligands establish hydrogen bonds with both side-chain and main-chain protein atoms, whereas the CO ligand sits in a hydrophobic pocket.

By comparing EPR and FTIR data, it is possible to identify band triplets corresponding to the three paramagnetic species Ni–A, Ni–B, and Ni–C (*65, 83*). Also, the EPR-silent Ni–SI and Ni–R states (Fig. 4) have been correlated with additional FTIR triplets. In the case of the former, two species, Ni–SI1 and Ni–SI2, differing by one proton,

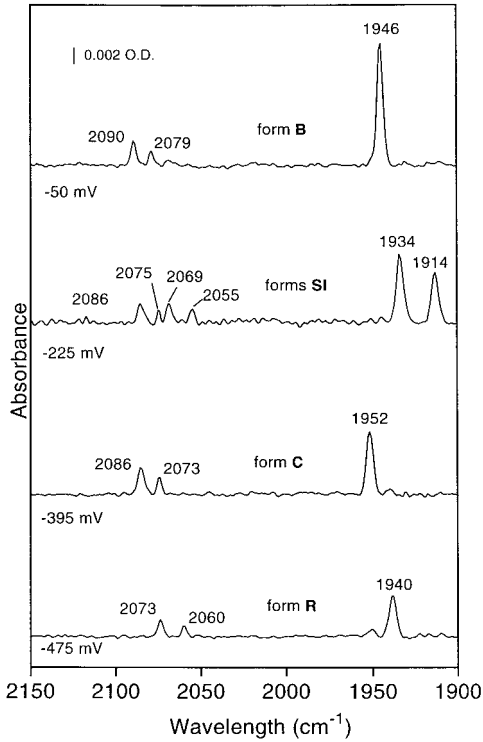

FIG. 5. FTIR spectra of redox-poised *D. gigas* hydrogenase. (Reprinted with permission from (*65*); copyright 1997, American Chemical Society). See also Table I.

have been identified (*84*). Furthermore, an EPR-silent, "unready," state called NI–SU, one electron more reduced than the Ni–A state, has also been found (*84*). A scheme depicting the protonations and reductions relating the various states is depicted in Fig. 6 and frequency data corresponding to these states are shown in Table I.

The enzyme poised at well-defined redox potentials appears to be in rather homogenous IR states (*65*, *84*). Curiously, in corresponding EPR-monitored experiments, the Ni signal generally corresponds to significantly less than one spin/mole, indicating that the sample is heterogeneous with respect to it (*77*).

Higushi and co-workers have published the 1.8-Å resolution structure of the hydrogenase from *D. desulfuricans* Miyazaki F (*33*). For the most part the structure is very similar to that of *D. gigas* hydrogenase. However, Higushi *et al.* have provided a radically different interpretation of the active-site structure. Instead of one CO and two

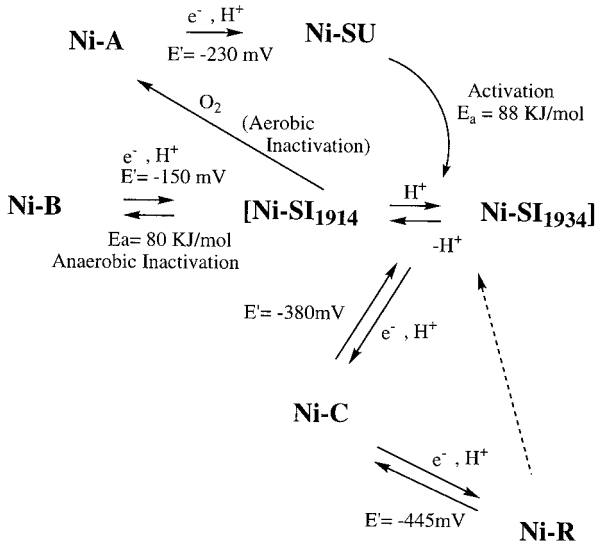

FIG. 6. Schematic representation of the midpoint redox potentials and electron and protron balances relating the various active site states as detected by FTIR (*65*).

CNs, the Fe ion is postulated to be coordinated by one SO and a mixture of CO and CNs. The interpretation is based on the temperature factor refinement and pyrolytic analysis of oxidized sulfur species (*33*). In addition, the bridging ligand is postulated to be an inorganic sulfur ion (instead of an oxo ligand, as proposed for the *D. gigas*). This

TABLE I

IR FREQUENCIES (cm^{-1}) OF THE VARIOUS ACTIVE-SITE REDOX STATES IN *D. Gigas* HYDROGENASE[a]

Redox state	Band 1	Band 2	Band 3	Angle (°)
Ni–A	1947	2083	2093	89
Ni–B	1946	2079	2090	69
Ni–SU	1950	2089	2099	83
Ni–SII	1914	2055	2099	71
Ni–SiII	1934	2075	2086	60
Ni–C	1952	2073	2086	73
Ni–R	1940	2060	2073	75

[a] The Ni–A, Ni–B, N–Si, Ni–C, and Ni–R were prepared as described in (*83*). Ni–SU was prepared using 1 mM sodium dithionite. (°) is the angle between two coupled oscillators (*84*), here assumed to be the two CNs.

model for the active site is an exceptional one. Unpublished results from the laboratory of one of the authors (J.C.F.-C.) indicated that neither SO nor a bridging S is likely to be present in *D. gigas* (2.3 Å resolution), *D. baculatum* (2.1 Å resolution), or *D. fructosovorans* (1.8 Å resolution) hydrogenases.

D. Catalytic Mechanism Models

1. Redox Titrations

EPR-monitored redox titrations of the *D. gigas* hydrogenase (*80*, *85*) have suggested that the observed alternating paramagnetic and diamagnetic Ni signals (Fig. 4) are most likely generated by successive one-electron reductions: the two-electron difference (TED) (in going from Ni–B to Ni–C) model.

The putative one-electron reduction of the Ni–B species (a similar titration of the Ni–A form has not been reported) gives rise to the EPR-silent Ni–SI state (*77*). A further one-electron reduction generates that Ni-C species discussed earlier. Ni–C has been often referred to as corresponding to the "active" form of the enzyme. According to Barondeau *et al.* (*77*), however, the Ni–C form is stable in the absence of molecular hydrogen and cannot spontaneously reduce protons to H_2. These authors conclude that Ni–C is not the "active" species but corresponds to one of three relevant Ni states during the catalytic cycle. Accordingly, the most likely state of the enzyme capable of binding molecular hydrogen is Ni–SI (the "active oxidant") and the most likely H_2 producer is the Ni–R form (the "active reductant"). An alternative view has been advanced by Coremans *et al.* (*86*), who argue that Ni–C can be reduced by molecular hydrogen to generate a transient species one electron more reduced than the Ni–R form. According to these authors, the discrepancies between their results and those of the Lindahl group arise from the fact that the latter used dyes in their experiments (*86*).

The one-electron reduction of the Ni–C form results in the diamagnetic species Ni–R. From the redox titration studies of Lindahl's group, a plausible catalytic cycle can be postulated where the enzyme in the Ni–SI state binds H_2 (*77*) and becomes the two-electron more reduced Ni–R state. Sequential one-electron oxidations from Ni–R to Ni–C and then to Ni–SI will close the cycle (Fig. 6). The various redox states differ not only in the extent of their reduction, but also in their protonation, as shown by the pH dependence of their redox potentials (*87*). It is remarkable that both EPR (which monitors the magnetic

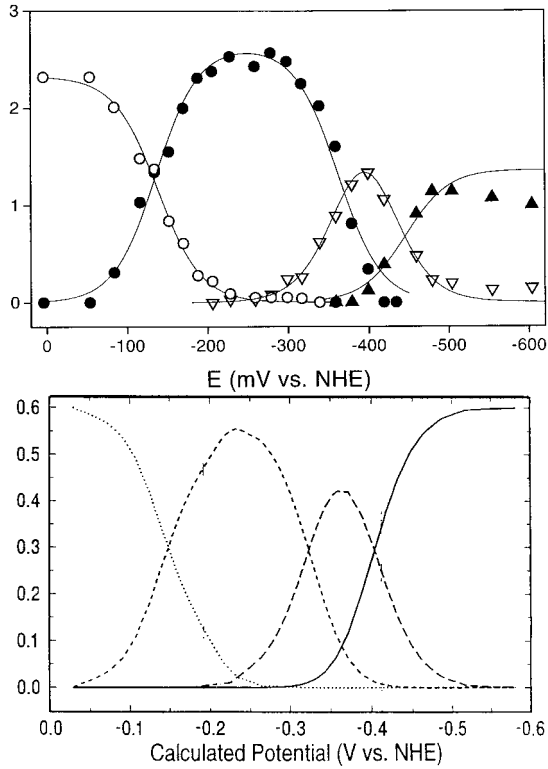

FIG. 7. A comparison of the FTIR and EPR redox titrations of the *D. gigas* hydrogenase. *Top panel:* FTIR titration based on the height of the low-frequency band. For experimental conditions, see (*65*). *Bottom panel:* Calculated potentials obtained from EPR-monitor titration and the TED model (*80*). The vertical axis represents the proportion of a redox species.

changes of, or near to, the Ni ion) and IR (which reports on electron density or coordination changes at the Fe center) redox titrations follow almost identical patterns (*80*, *84*, *85*) (Fig. 7). This indicates that the changes detected in the Fe environment through the diatomic ligands affect the Ni center in a similar manner.

2. The Nature of the Active-Site Fe Ion

The active-site Fe ion also eluded detection by either EPR (*9*) (and references therein) or Mössbauer (*88*, *89*) spectroscopy, suggesting that it is low spin and diamagnetic at least in those states that have been studied. This is consistent with the presence of one CO and two CN^-'s, which are strong ligands, in the active-site Fe coordination

sphere. The spectroscopic analyses are likely to have been further complicated by the three additional [FeS] clusters present in the enzyme (Fig. 1). The exact role of the active site Fe center remains to be established. Dole *et al.* (*90*) have advanced the proposition that neither Fe nor Ni would play a redox role during catalysis. Their conclusions are based on the fact that the temperature dependence of the paramagnetic states Ni–A, Ni–B, and Ni–C does not deviate from Curie's law. This imposes constrains on the magnitude of the possible magnetic interactions between the two metal centers (*90*). Furthermore, according to these authors, experiments performed in parallel-mode EPR indicated no paramagnetic excited level. Since large ferromagnetic interactions are not supposed to be consistent with the highly distorted structure of the catalytic center of hydrogenases, the Ni and Fe ions are considered to be independently diamagnetic in the Ni–SI and Ni–R states. Accordingly, Dole *et al.* conclude that the Fe center is a diamagnetic Fe(II) in all the catalytically relevant states.

Huyett *et al.* (*91*) have compared the Ni–A, Ni–B, and Ni–C states using ^{57}Fe Q-band pulsed electron nuclear double resonance (ENDOR) spectroscopy. They observe that the Ni–A form shows a clear hyperfine interaction with the Fe ion, whereas the Ni–B and Ni–C states lack an ENDOR signal. A possible explanation is that the bridging putative oxo ligand found in the active site by X-ray crystallography is present in the Ni–A state, but absent in the other paramagnetic Ni forms. Huyett *et al.* conclude that the Fe ion is low-spin ferrous in the three EPR-active studied states. Furthermore, using these results along with previously obtained data, the authors conclude that the Ni–A form is a trapped [Ni(III)–Fe(II)] species.

3. A Model for Ligand-Based Redox Chemistry

If the Fe–Ni center is not redox active, at least during catalysis, then the process must be ligand-based (*92*). Maroney and co-workers have argued that the paramagnetic Ni–C state could be generated by the interaction of a thyil radical with a Ni(II) ion. This species is isoelectronic with a thiolate-bound Ni(III) according to the reaction

$$\text{S–Ni(III)} \longleftrightarrow \text{S}^{\cdot}\text{–Ni(II)}. \qquad (5)$$

A relevant model compound with sulfur ligation to Ni(III) has been published by Choudhury *et al.* (*93*).

A model combining the ideas put forward by Maroney *et al.* with the EPR data mentioned previously has been proposed by Dole *et al.*

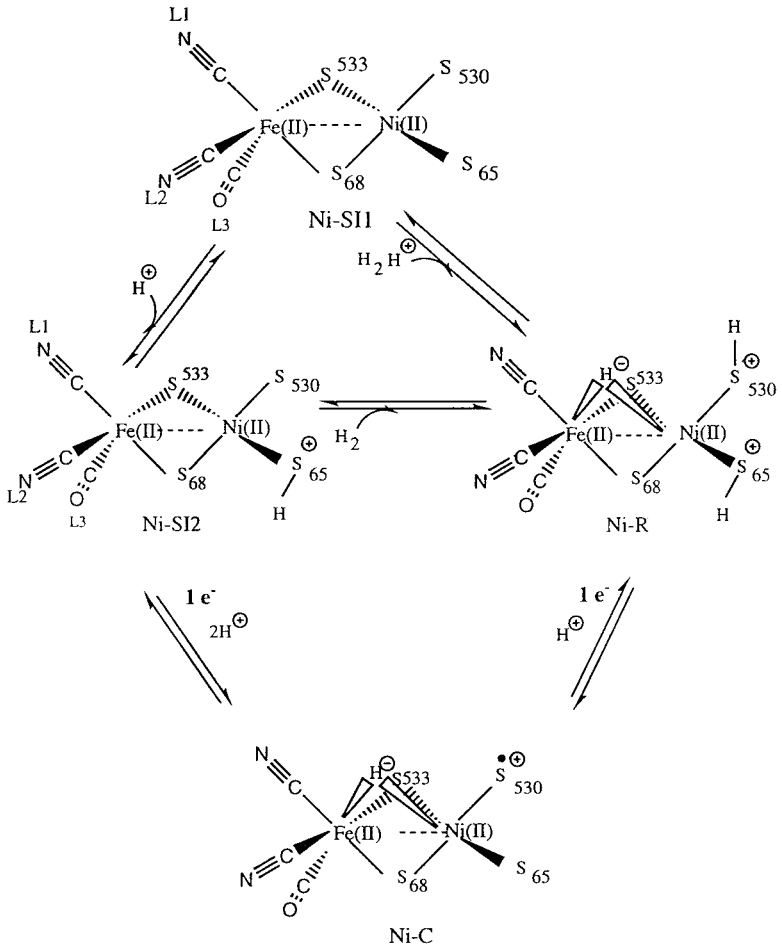

FIG. 8. A model for the catalytic cycle of hydrodenase based on several lines of evidence (see text).

(*90*). A somewhat more complete version of it is presented in Fig. 8. The model is attractive because it is consistent with many of the observations concerning the active site of Ni–Fe hydrogenases:

1. The Ni ion stays in the common Ni(II) state throughout the catalytic cycle. Redox processes that are purely Ni-based would imply three different Ni redox states: Ni–SI [Ni(II)] → Ni–C [Ni(I)] → Ni–R [Ni(O)]. Such changes, comprising potentials confined to those observed in hydrogenase (−100 to −400 mV), would be totally unprecedented (*66*, *94*, *95*). Also, successive one-electron changes at the Ni

center during catalysis are unlikely according to the XAS experiments mentioned earlier (*74*).

2. The heterolytic splitting of molecular hydrogen results in the protonation of cys530 (*D. gigas* numbering) and the formation of a bridging hydride. The idea of a bridging hydride is very appealing because it satisfies the coordination spheres of both Ni (square pyramidal) and Fe (octahedral) centers. Such a hydride species was suggested, either as an intermediate or as part of the active site, in the initial paper reporting the three-dimensional structure of *D. gigas* hydrogenase (*32*).

The postulated protonation of cys530 implies that this residue may be the base thought to be required for heterolytic cleavage of hydrogen (*96*, *97*). In the closely related Ni–Fe–Se hydrogenase from *D. baculatum*, as in several other hydrogenases (*98*), the equivalent of cys530 is a selenocysteine (*99*). The substitution of Cys by the unusual SeCys residue, which requires a special synthetic mechanism, results in H_2/HD ratios in the hydrogen–deuterium exchange reactions that are greater than 1.0, in contrast with Fe–Ni enzymes, which typically have ratios <0.5 (*98*). Thus, the nature of the chalcogenide species at position 530 has an influence on the catalytic characteristics of hydrogenases. Incidentally, the as-prepared Ni–Fe–Se hydrogenase from *D. baculatum* is normally EPR silent, suggesting that the putative oxo ligand found in the Ni–A/B forms is absent from its active site.

4. Alternatives to a Redox Inactive Ni–Fe Center

Not all the available data favors an inert Ni(II) as the species present in all the catalytically relevant states of hydrogenase. Instead, some of the aspects of the most relevant model chemistry favor a Ni(I) formal state as the molecular hydrogen binding species at the hydrogenase active site (*66*): (1) Thioethers and μ^2-metalated thiolates (such as the ones found in hydrogenase active site) are good Ni(I) stabilizing ligands (*100*); (2) a series of model compounds that bind molecular hydrogen and form Ni–H-adducts, and are also capable of binding CO, require Ni in the +1 oxidation state (79).

Concerning the role of the active site Fe ion, it has been argued that the observed FTIR band shifts (typically 20 cm^{-1}) resulting from one-electron redox changes are too small to correspond to metal-based redox processes, whose band shifts should amount to about 100 cm^{-1} per electron (*90*, *101*). There is, however, one example where the shift in $\nu(CN^-)$ upon one-electron reduction of a Fe(III) center is only of

about 24 cm^{-1} (M. Darensbourgh, personal communication). This study has been performed in a model compound that very closely reproduces the $Fe(CO)CN^{-})_2$ unit of the active site of hydrogenases (*102*). The relatively low frequency shift could be attributed to the fact that the excess in electron density at the metal center is distributed among the three diatomic ligands.

5. A Most Unusual Catalytic Center

Prior to the spectroscopic analyses that suggests that the active-site Fe center is not redox active (*90*, *91*), one of the authors (J.F.-C.) and co-workers had proposed mechanisms where the Ni ion was the catalytic site proper, heterolytically splitting the H_2 molecule into H^- and H^+ with the thiolate of Cys530 being the base, and the Fe ion intervening in the one-electron oxidation processes (*66*). One condition for the existence of redox-active metal centers at the active site is that they should be coupled, at least in the diamagnetic Ni–SI and Ni–R states (*66*). Since it appears now that the Fe and Ni ions are magnetically isolated (90), the unusual binuclear center (Fig. 2) can logically be expected to be designed as an optimal catalytic unit instead. The strong CO and CN^- ligands should help in stabilizing low Fe oxidation states. A soft Lewis acid Fe center should readily bind the soft hydride.

The role of the Ni ion can still be postulated to be the catalyst in the hydrogen cleavage reaction, assisted by (Se)Cys530. Such possibility is also indicated by the fact that an internal cavity connecting the molecular surface to the active site points at the empty Ni coordination site (not shown). Such cavities are thought to serve as gas pathways facilitating substrate access to the active center (*36*). The Fe ion could serve as a hydride binding center as indicated by the unusual FTIR shifts of the trans CO ligand relative to the equatorial CN^-s (J.C.F.-C, unpublished).

E. Interaction of the Active Site with Other FeS Centers

Many *Desulfovibrio* sp. hydrogenases contain what we now know to be an arrangement of three FeS clusters disposed in a quasi-linear fashion (Figs. 1 and 9). They are likely to constitute an electron transfer pathway going from the active site to the molecular surface. In the *D. gigas* enzyme, the [3Fe4S] cluster is intercalated between the two [4Fe4S] clusters (*32*) (Fig. 9). The cluster nearest to the active site is called proximal and the one close to the molecular surface is designated at distal. At first sight, such an arrangement may appear

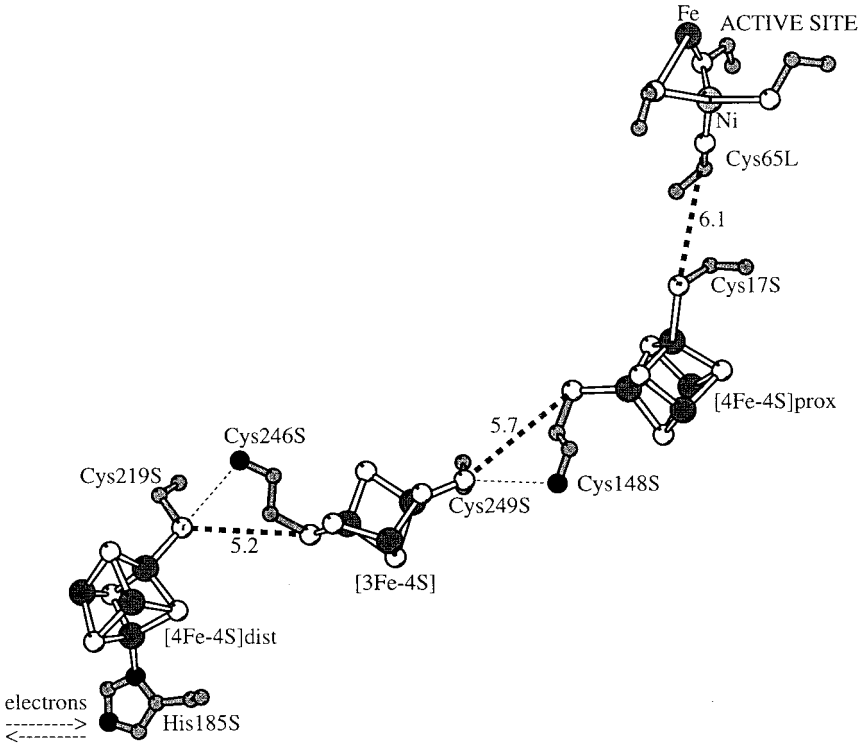

FIG. 9. Arrangement of redox centers in *D. gigas* hydrogenase. Edge-to-edge distances are indicated.

unusual since it is known that the [3Fe4S] cluster has a significantly higher redox potential than the other two FeS centers. The values summarized by Roberts and Lindahl (*80*, and references therein) for the *D. gigas* enzyme, based on the TED model, are $[3Fe4S]^{+1/0} = -80$ mV; $[4Fe4S]p^{+2/+1} = -445$ mV; and $[4Fe4S]d^{+2/+1} = -315$ mV. This difference could imply that the electrons have to overcome an energy barrier in going from the active site to the molecule's surface or vice versa. However, if electron transfer is not the rate-limiting step, then the presence of the [3Fe4S] cluster has little or no effect on the catalytic cycle.

The interaction of the partially reduced Ni–C form with the [4Fe4S] proximal cluster has been studied in *D. gigas* hydrogenase (*103*). From these studies it has been possible to predict the distance between the two redox centers. The value agrees well with that observed in the crystal structure (Fig. 9). In the readily available as-

prepared, inactive hydrogenase, both the Ni center and the [3Fe4S] cluster are in paramagnetic states (presumably Ni(III) and $[3Fe4S]^{1+}$]. Coupling of the oxidized Ni center with what it is supposed to be a close paramagnet has been indicated by Mössbauer spectroscopy in the case of the *C. vinosum* hydrogenase (*104*). Such a neighboring center, however, seems to be absent from the *D. gias* hydrogenase, as indicated from its three-dimensional structure.

IV. CODH/ACS

A. Introduction to CODH/ACS

CODH/ACS is an extremely oxygen-sensitive protein that has been found in anaerobic microbes. It also is one of the three known nickel iron–sulfur proteins. Some authors would consider that there are only two, since the CODH and ACS activities are tightly linked in many organisms. However, there is strong evidence that the ACS and CODH activities are associated with different protein subunits and the reactions that the two enzymes catalyze are quite different. CODH catalyzes a redox reaction and ACS catalyzes the nonredox condensation of a methyl group, a carbonyl group, and an organic thiol (coenzyme A).

1. Bioorganometallic Enzymology

CODH and ACS are remarkable in several respects. The reactions involve novel bioinorganic chemistry that includes the formation and breakage of organometallic bonds. The reactions also include novel enzymology in which the reaction intermediates are bound to the protein. In addition, CODH and ACS are important in environment chemistry. When these reactions are coupled, they allow organisms to metabolize carbon monoxide, which is a colorless, odorless, toxic gas that inhibits essential metalloproteins, notably cytochrome oxidase. Thus, an important role of CODH/ACS is to remove CO from the environment, helping to maintain this toxic gas at subhazardous levels. Annual CO removal from lower atmosphere and earth by bacteria is estimated to be $\sim 1 \times 10^8$ tons (*105*). Atmospheric concentrations range from about 0.1 ppm in rural to 200 ppm in urban settings (*106*). CO_2 is then further metabolized by one of several CO_2 fixation pathways— the Calvin cycle, the reductive tricarboxylic acid cycle, or the reductive acetyl-CoA pathway. The net result is to convert CO into cell carbon.

2. Evolutionary Implications

CODH and ACS are important from an evolutionary point of view. It has been considered that CODH/ACS are the extant survivors of a 3- to 4-billion-year-old process that could have given rise to the first metabolic reactions that eventually led to life on this planet. Possibly, it was involved in the first metabolic pathway (*2*, *107*).

3. Biomedical Importance of CODH / ACS

CODH and ACS play important biomedical roles in the gastrointestinal tracts of animals, such as humans and ruminants. The biodegradation of compounds in the natural environments, like that of the rumen and the human colon, generates H_2, which, at high levels, inhibits colon metabolism. Hydrogenotrophic bacteria, such as the methanogenic archaea, acetogenic bacteria, and sulfate-reducing bacteria, dispose of the excess reducing equivalents by synthesizing methane, acetate, and hydrogen sulfide, respectively. These three classes of hydrogen-metabolizing organisms compete for the available hydrogen. From a human biomedical standpoint, the acetogens are our allies, since acetogenesis removes H_2 gas and converts it to acetic acid, which is a major carbon source for the colon epithelia. Methanogens convert 5 mol of gas to 1 mol of methane, which also is a favorable gas balance. Sulfate reducers are our adversaries in this scenario because high levels of dietary sulfate lead to the formation of H_2S, which is a toxic compound and has been implicated as a contributor to the development of colitis and colon cancer (*108*, *109*).

4. History of the Study of CODH and ACS

Without the enzyme CODH/ACS, organisms are unable to fix carbon monoxide or carbon dioxide by the acetyl-CoA or Wood–Ljungdahl pathway. One of us has reviewed how this pathway was discovered (*110*). Figure 10 is a list of important results that have led to our current level of understanding of the structure and function of CODH/ACS. Studies of the enzymology of ACS and CODH are historically linked to the ancient discovery by an unnamed person that apple or grape juice can be fermented, first to alcohol and then to acetic acid, producing cider vinegar, which contains 3–6% acetic acid. The 1922 report of CO metabolizing bacteria was another landmark (*111*). It is now known that CO can serve as a carbon and electron source for many bacteria (*112–115*), including acetogenic bacteria such as *C. thermoaceticum* (*116*, *117*).

Yagi laid the foundation for the enzymology of CODH when he discovered an enzymatic activity in sulfate-reducing bacteria that oxidizes CO to CO_2 (*118*). Twenty-five years later, the first CODH was purified to homogeneity (*119*, *120*). The homogeneous *C. thermoaceticum* CODH was shown to contain 2 mol of nickel, ~12 iron, ~1 zinc, and ~14 acid-labile inorganic sulfide per $\alpha\beta$ dimeric unit (*120*).

The most important physiological role of CODH in the metabolism of acetogenic bacteria was unknown until 1985, when it was shown that the enzyme is bifunctional and has acetyl-CoA synthase activity (*121*). It was previously thought that acetyl-CoA was synthesized at the cobalt center of a vitamin-B_{12}-containing protein. In the same paper, it was proposed that nickel is the active site of CO oxidation and acetyl-CoA synthesis.

Over the past 10 years, two novel features of the acetyl-CoA pathway have gained acceptance. The first is that the intermediates in the acetyl-CoA pathway are enzyme-bound. This contrasts with most biochemical pathways, which proceed by the stepwise conversion of one discrete organic chemical to another where each of the compounds can be isolated and characterized by standard analytical methods such as thin-layer chromatography or NMR spectroscopy. This is probably the major reason that the acetyl-CoA pathway, which came under investigation in the mid-1940s (*122*), took 50 years to elucidate. The second unique feature is that key intermediates appear to be bound to metals. The Wood–Ljungdahl pathway has been called a bioorganometallic pathway. The involvement of CODH/ACS in this bioorganometallic pathway is the major focus of this section of the review. It has become clear that analogous chemistry/enzymology is responsible for acetate conversion to methane by methanogenic archaea.

5. Characteristics of CODH/Acetyl-CoA Synthase

The properties of CODH/acetyl-CoA synthase are summarized in Table II.[1] The enzyme has been isolated from eight species. There exist three types of CODH. One, which lacks nickel and acetyl-CoA synthase activity, contains a molybdopterin active site and will not be

[1] The reader should note that the Greek letter designations, α, β, etc., refer to the sizes of the protein subunits and the Arabic letter designations refer to the position of the gene in a particular gene cluster. Therefore, the *alpha* subunit of CODH/ACS from *C. thermoaceticum* is the largest of the two subunits; however, it is designated AcsB because it is the second of at least five genes in the gene cluster.

MILESTONES IN THE STUD OF CODH/ACS

1951	A new pathway of CO_2 fixation proposed (to become the Wood–Ljungdahl pathway).[1]
1959	Enzymatic CO oxidation identified.[2]
1977	CODH activity found in methanogens.[3]
1978	CODH activity found in acetogenic bacteria.[4]
1981	Fractionation of a five-component system from *C. thermoaceticum* that catalyzes acetyl-CoA synthesis.[5] CODH activity was in fraction F3.
1980	CODH shown to contain nickel.[6,7]
1982	Fraction F3 catalyzes an isotope exchange reaction between CO and the carbonyl group of acetyl-CoA.[8]
1982	The adduct between CO and a nickel center in CODH identified by EPR spectroscopy.[9]
1983	CODH purified to homogeneity.[10,11]
1984	B_{12} protein that accepts the methyl group of CH_3-H_4 folate partially purified from fraction F3.[12]
1985	CODH from acetogens found to catalyze acetyl-CoA synthesis and nickel proposed to be the active site of CO oxidation and acetyl-CoA synthesis.[13]
1985	CODH found to contain a heterometallic cluster consisting of nickel and iron that binds CO and proposed to be the active site of acetyl-CoA synthesis.[14]
1986	Growth of acetogens on nitrate disables the acetyl-CoA pathway.[15]
1987	Corrinoid iron–sulfur protein (CFeSP) purified and characterized; acetyl-CoA synthesis reconstituted from CH_3–H_4 folate, CO, and CoA using purified proteins.[16]
1988	Hydrogenotrophic acetogenesis found in human colon.[17]
1989	Gene cluster encoding CODH/ACS, the CFeSP, and methyltransferase isolated and characterized.[18]
1990–1	CODH/ACS shown to contain a [Ni–X–Fe_4S_4] cluster.[19,20] Strong evidence that the methanotrophic bacteria use the Wood–Ljungdahl pathway in reverse for the conversion of acetate to methane.[21,22]
1993	CODH and ACS shown to occur at discrete [Ni–X–Fe_4S_4] clusters, called Cluster C and Cluster A, respectively.[23,24]
1995	Methyl transfer reaction from methyl-Co to Ni modeled and demonstrated to occur through a radical mechanism.[25] CO shown to be an obligatory intermediate in the acetyl-CoA pathway.[26] CO sensing transcriptional activator characterized.[27]
1996	A model describing the interactions between Ni and Fe in Cluster C proposed.[28]
1998	Demonstration that the enzymatic methyl transfer from methyl-Co to Ni uses an S_N2, not a radical, mechanism.[29]

(1) Utter, M. F.; Wood, H. G. *Adv. Enzymol. Relat. Areas Mol. Biol.* **1951,** *12,* 41–151.
(2) Yagi, T. *Biochim. Biophys. Acta* **1959,** *30,* 194–195.
(3) Daniels, L.; Fuchs, G.; Thauer, R. K.; Zeikus, J. G. *J. Bacteriol* **1977,** *132,* 118–26.
(4) Diekert, G. B.; Thauer, R. K. *J. Bacteriol.* **1978,** *136,* 597–606.
(5) Drake, H. L.; Hu, S.-I.; Wood, H. G. *J. Biol. Chem.* **1981,** *256,* 11137–11144.
(6) Drake, H. L.; Hu, S.-I.; Wood, H. G. *J. Biol. Chem.* **1980,** *255,* 7174–7180.
(7) Hu, S.-I.; Drake, H. L.; Wood, H. G. *J. Bacteriol.* **1982,** *149,* 440–448.
(8) Ragsdale, S. W.; Ljungdahl, L. G.; DerVartanian, D. V. *Biochem. Biophys. Res. Commun.* **1982,** *108,* 658–663.

FIG. 10. Milestones in the study of CODH/ACS. Important discoveries beginning with the postulate of a new CO_2 fixation pathway.

(9) Diekert, G.; Ritter, M. *FEBS Lett.* **1983,** *151,* 41–44.
(10) Ragsdale, S. W.; Clark, J. E.; Ljungdahl, L. G.; Lundie, L. L.; Drake, H. L. *J. Biol. Chem.* **1983,** *258,* 2364–2369.
(11) Ragsdale, S. W.; Clark, J. E.; Ljungdahl, L. G.; Lundie, L. L.; Drake, H. L. *J. Biol. Chem.* **1983,** *258,* 2364–2369.
(12) Hu, S.-I.; Pezacka, E.; Wood, H. G. *J. Biol. Chem.* **1984,** *259,* 8892–8897.
(13) Ragsdale, S. W.; Wood, H. G. *J. Biol. Chem.* **1985,** *260,* 3970–3977.
(14) Ragsdale, S. W.; Wood, H. G.; Antholine, W. E. *Proc. Natl. Acad. Sci. USA* **1985,** *82,* 6811–6814.
(15) Fröstl, J. M.; Seifritz, C.; Drake, H. L. *J. Bacteriol.* **1986,** in press.
(16) Ragsdale, S. W.; Lindahl, P. A.; Münck, E. *J. Biol. Chem.* **1987,** *262,* 14289–14297.
(17) Lajoie, S. F.; Bank, S.; Miller, T. L.; Wolin, M. J. *Appl. Environ. Microbiol.* **1988,** *54,* 2723–2727.
(18) Roberts, D. L.; James-Hagstrom, J. E.; Smith, D. K.; Gorst, C. M.; Runquist, J. A.; Baur, J. R.; Haase, F. C.; Ragsdale, S. W. *Proc. Natl. Acad. Sci. U.S.A.* **1989,** *86,* 32–36.
(19) Lindahl, P. A.; Ragsdale, S. W.; Münck, E. *J. Biol. Chem.* **1990,** *265,* 3880–3888.
(20) Fan, C.; Gorst, C. M.; Ragsdale, S. W.; Hoffman, B. M. *Biochemistry* **1991,** *30,* 431–435.
(21) Abbanat, D. R.; Ferry, J. G. *J. Bacteriol.* **1990,** *172,* 7145–7150.
(22) Grahame, D. A. *J. Biol. Chem.* **1991,** *266,* 22227–22233.
(23) Kumar, M.; Lu, W.-P.; Liu, L.; Ragsdale, S. W. *J. Am. Chem. Soc.* **1993,** *115,* 11646–11647.
(24) Anderson, M. E.; DeRose, V. J.; Hoffman, B. M.; Lindahl, P. A. *J. Am. Chem. Soc.* **1993,** *115,* 12204–12205.
(25) Ram, M. S.; Riordan, C. G. *J. Am. Chem. Soc.* **1995,** *117,* 2365–2366.
(26) Menon, S.; Ragsdale, S. W. *Biochemistry* **1996,** *35,* 12119–12125.
(27) He, Y. P.; Shelver, D.; Kerby, R. L.; Roberts, G. P. *J. Biol. Chem.* **1996,** *271,* 120–123.
(28) Hu, Z. G.; Spangler, N. J.; Anderson, M. E.; Xia, J. Q.; Ludden, P. W.; Lindahl, P. A.; Münck, E. *J. Am. Chem. Soc.* **1996,** *118,* 830–845.
(29) Menon, S.; Ragsdale, S. W. *Biochemistry* **1998,** *37,* 5689–5698.

FIG. 10.—*Continued*

further discussed here (*123*). The photosynthetic bacterial enzyme is a second class that contains nickel and iron–sulfur yet lacks acetyl-CoA synthase activity. The third class of CODH, called CODH/ACS, is a bifunctional enzyme that contains an associated acetyl-CoA synthase activity (Fig. 11, the yin–yang bifunctional figure). Here, we will cover the CODH activity first and then focus on the ACS active site.

Alignments of the eight homologs of the large subunit of CODH/ACS that were identified by a BLAST search are shown in Figure 12. The most homologous protein to the *C. thermoaceticum* large subunit was an ORF in the *M. thermoautotrophicum* genome sequence. The *M. thermophila* beta subunit and an ORF in the *A. fulgidus* genome

TABLE II

PROPERTIES OF Ni–CODHs AND Ni–ACSs

Organism (class)[a]	Subunit (gene) size	Metal content	Cluster content	Catalytic activities	Ref.[b]
C. thermoaceticum (A)	α (*acsB*) 78 kDa; β (*acsA*) 71 kDa	2 Ni, 11–14 Fe, 14 S^{2-}, 1 Zn/ 149 kDa	ABC	COSH, ACS	*1*, *2*
A. woodii (A)	α, 80 kDa; β, 68 kDa	1.4 Ni, 9 Fe, 14 S^{2-}, ~1 Zn, or Mg/148 kDa	ABC	CODH, ACS	*3*
Ms. barkerii (M)	α, 84–92 kDa; β, 63 kDa; γ, 53 kDa; δ, 51 kDa; ε, 20 kDa	0.7 Ni, 8–15 Fe, 0.9 Co, 0.5 Zn/266 kDa	ABC	CODH, ACS	*4–6*
Ms. barkerii (M)	α, 84–92 kDa; ε, 20 kDa	0.7 Ni, 8–15 Fe, 0.5 Zn/ 100 kDa	ABC	CODH	*7*
Ms. thermophila (M)	α (*cdhA*) 89 kDa; β (*cdhC*) 71 kDa; γ (*cdhD*), 60 kDa; δ (*cdhE*), 58 kDa; ε (*cdhB*), 19 kDa	3.6 Ni, 25 Fe/ 297 kDa	ABC	CODH, ACS	*8–10*
Ms. thermophila	α, 79 kDa; ε, 19 kDa	0.2 Ni, 7.7 Fe; 2.7 Zn/98 kDa	ABC	CODH, ACS	*8–10*
Mt. soehngenii (M)	α (*cdhA*) 79 kDa; ε (*cdhB*), 19 kDa	2 Ni, 12.5 Fe–98 kDa	ABC	CODH, ACS	*11–13*
Mc. vannielii (M)	α (*cdhA*) 89 kDa; ε (*cdhB*), 21 kDa	1.0 Ni, 8 Fe, 0.2 Zn/110 kDa	ND	CODH	*14*
R. rubrum (purple bacterium)	62 kDa (*cooS*)	1 Ni, 8 Fe	BC	CODH	*15*

[a] A, acetogen; M, methanogen.

[b] References:

(1) Ragsdale, S. W.; Clark, J. E.; Ljungdahl, L. G.; Lundie, L. L.; Drake, H. L. *J. Biol. Chem.* **1983,** *258,* 2364–2369.

(2) Ragsdale, S. W.; Wood, H. G. *J. Biol. Chem.* **1985,** *260,* 3970–3977.

(3) Ragsdale, S. W.; Ljungdahl, L. G.; DerVartanian, D. V. *J. Bacteriol.* **1983,** *155,* 1224–1237.

(4) Krzycki, J. A.; Zeikus, J. G. *J. Bacteriol.* **1984,** *158,* 231–237.

TABLE II—*Continued*

(5) Krzycki, J. A.; Mortenson, L. E.; Prince, R. C. *J. Biol. Chem.* **1989,** *264,* 7217–7221.
(6) Grahame, D. A.; Stadtman, T. C. *J. Biol. Chem.* **1987,** *262,* 3706–3712.
(7) Grahame, D. A. *J. Biol. Chem.* **1991,** *266,* 22227–22233.
(8) Terlesky, K. C.; Nelson, M. J. K.; Ferry, J. G. *J. Bacteriol.* **1986,** *168,* 1053–1058.
(9) Abbanat, D. R.; Ferry, J. G. *Proc. Natl. Acad. Sci. USA* ***1991,*** *88,* 3272–3276.
(10) Lu, W.-P.; Jablonski, P. E.; Rasche, M.; Ferry, J. G.; Ragsdale, S. W. *J. Biol. Chem.* **1994,** *269,* 9736–9742.
(11) Jetten, M. S. M.; Stams, A. J. M.; Zehnder, A. J. B. *FEBS Lett.* **1989,** *181,* 437–441.
(12) Jetten, M. S. M.; Hagen, W. R.; Pierik, A. J.; Stams, A. J. M.; Zehnder, A. J. B. *Eur. J. Biochem.* **1991,** *195,* 385–391.
(13) Eggen, R. I. L.; Geerling, A. C. M.; Jetten, M. S. M.; de Vos, W. M. *J. Biol. Chem.* **1991,** *266,* 6883–6887.
(14) DeMoll, E.; Grahame, D. A.; Harnly, J. M.; Tsai, L.; Stadtman, T. C. *J. Bacteriol.* **1987,** *169,* 3916–3920.
(15) Ensign, S. A.; Ludden, P. W. *J. Biol. Chem.* **1991,** *266,* 18395–18403.

sequence also were closely related. A 51-amino-acid block near a tryptophan residue that was implicated in CoA binding (*124*) and a 40-amino-acid region that is rich in acidic amino acids and cysteine residues were also highly conserved among all eight homologs.

Alignments of the eight homologs of the small subunit of CODH/ACS are also shown in Fig. 12. The most striking homologies are a cysteine-rich region that is likely to represent the ligands to Cluster B and a histidine-rich region in the second block. The most closely related sequence to the *C. thermoaceticum* small subunit is that of *R. rubrum* CooS.

Functional homology is readily apparent in the EPR spectra of all the CODHs so far studied. These proteins share Clusters B and C, which have nearly identical spectral morphologies and redox properties. Both of these clusters are required for CO_2 reduction or CO oxidation (see later discussion). Although CODH has been highly purified from *Defulfovibrio desulfuricans* (*125*), ironically, it was purified to homogeneity from a sulfate reducer, *Archaeoglobus fulgidus,* only recently. This organism is an archaeon and the protein is most similar to the methanogenic enzyme.

6. Genes Encoding CODH and Regulation of Expression

The most extensive studies on the genetics and molecular biology of CODH have been performed with the *coo* system of *R. rubrum.* A *coo* gene cluster contains CODH (CooS), an Fe–S electron-transfer protein (CooF), metal cluster assembly proteins (CooCTJ) (*126*), and

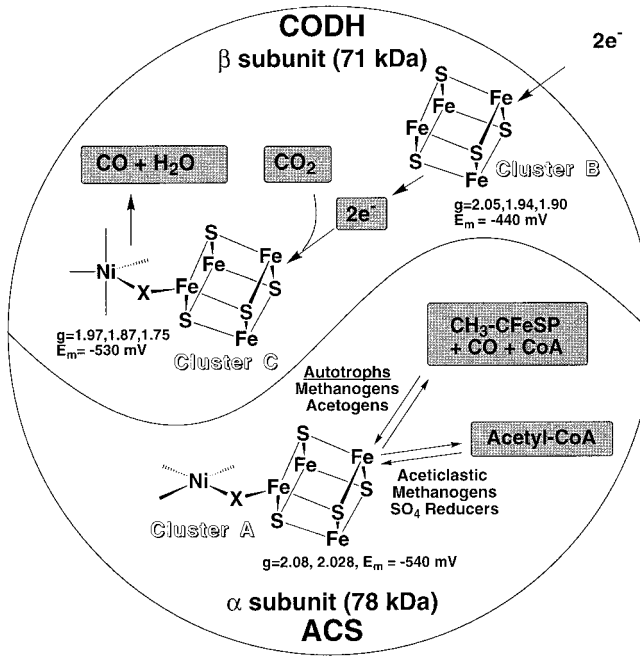

FIG. 11. Active sites and reactions of the bifunctional CODH/ACS. For synthesis of acetyl-CoA, two electrons are transferred from external electron donors to Cluster B of the CODH subunit. Electrons are relayed to Cluster C which reduces CO_2 to CO. The CO is proposed to be channeled to Cluster A of the ACS subunit to form a metal-CO adduct that combines with the methyl group of the CFeSP and CoA to form acetyl-CoA. For utilization of acetyl-CoA, these reactions are reversed. The abbreviations are: CODH, CO dehydrogenase; ACS, acetyl-CoA synthase; CFeSP, the corrinoid iron–sulfur protein; CoA, Coenzyme A.

a CO-induced hydrogenase, discussed earlier, (CooH) (59). The *coo* genes undergo approximately 100-fold increased expression when CO is sensed. This CO-dependent expression is modulated by a CO-sensing transcriptional regulator (CooA) (*127–129*) that binds to the *coo* promoter region when its heme group binds O (*128*).

C. thermoaceticum contains a gene cluster encoding at least five genes in the Wood–Ljungdahl pathway (*130*). These genes are apparently not regulated by CO. The CODH activity does increase about fourfold when methanogenic cells are exposed to CO (*131*). There is

```
HIGHLY CONSERVED REGIONS IN THE LARGE ACS SUBUNIT

CODHLarB, width = 51
 gi_144786  (  35)   390 IYGRKMQADFEGVLERRIHDFINYGEGLWHTGQRNINWLRVSKDAVAKGFR
gi_1575540  (  35)    74 IGGELVEPDLESVVERRVHDFINYCQGIMHLNQRYDVWMRVSKDTAGKMDS
gi_1590910  (  32)   365 VSGSNLEEDLEGVLERRIHEFLNYIEGVMHLNQRDQVWIRINKNSFNKGLR
gi_1590913  (  32)    72 VSGSNLEEDLEGVLERRIHEFLNYIEGVMHLNQRDQVWIRINKDSFNKGLR
gi_2127796  (  32)   365 VSGSNLEEDLEGVLERRIHEFLNYIEGVMHLNQRDQVWIRINKNSFNKGLR
gi_2127798  (  32)    72 VSGSNLEEDLEGVLERRIHEFLNYIEGVMHLNQRDQVWIRINKDSFNKGLR
gi_2622842  (  33)    73 VAGSELEEELESVIERRLHELCNYVKGFMHLNQRDQIWCRVSTEAKDAGFR
gi_2650254  (  35)    95 IAGEMVETDLEPVIERRNHDFQNYIEGYMHLNQRYDIWIRIGKNAIKKGLK

          CODHLarC, width = 40
 gi_144786  (  40)   481 AREKYKERDDRMRGLTDETVDTFYSCVLCQSFAPNHVCIV
gi_1575540  (  39)   164 AKEIFKARDARTKDLHDEDVDVFYGCTLCQSFAPTNVCVV
gi_1590910  (  39)   455 AKEIYKKRDEKTKSIREEDVDVFYGCVMCQSFAPTHVCII
gi_1590913  (  39)   162 AREIYNKRDEKTKALHEEDVDVFYGCVMCQSFAPTHVCVI
gi_2127796  (  39)   455 AKEIYKKRDEKTKSIREEDVDVFYGCVMCQSFAPTHVCII
gi_2127798  (  39)   162 AREIYNKRDEKTKALHEEDVDVFYGCVMCQSFAPTHVCVI
gi_2622842  (  39)   163 AREKYETRDSRARELSDEDVDVFYGCLMCQSFAPTHVCIV
gi_2650254  (  41)   187 AMPIFEERDARVEALSDEDVDEFYSCTLCQSFAPTNVCIV

HIGHLY CONSERVED REGIONS IN THE SMALL CODH SUBUNIT
    150036 (  55) CTLCTYGPCDLT  48
Af_2648697 (  49) CQLCSMGPCRIS 100
Af_2649482 (  68) CNLCTMGPCDLS  60
Af_2650695 (  68) CCLCTMGKCDLT  52
C.thermoCO (  68) CRFCMAGPCRIK 100
Dcma_24944 (  77) CCLCTFGKCDLS  50
Dcma_P2669 (  55) CTLCTYGPCDLT  48
Mbt_262284 (  76) CCLCTYGKCELL  87
 Mf_Q49161 (  76) CCYCTYGPCDLS  48
 Mf_Q49163 (  76) CCYCTYGPCDLS  48
Mj_2826254 (  76) CCLCTFGKCDLS  50
 Mj_B64319 (  77) CCLCTFGKCDLS  50
Mst_157553 (  76) CCYCTYGPCDLS  48
Mts_A39764 (  67) CTLCTYGPCDLT  48


BL   XXX motif=[12,0,0] motomat=[1,1,-15] width=42 seqs=15
    150036 (  68) NKKGACGIDMAAACGKIVLVAVLMGTCAHTAHGRHLYHWCLD  32
Af_2648697 (  63) KPTGACGIDAAGMVVRNFTHKNMLGTEAYTYHAIEAAKTLKA 100
Af_2649482 (  81) NKRGACGIDLKTAKARLVTIACCIGASAHTAHARHLVDHLIE  34
Af_2650695 (  81) NKRGACGIDLAAQTGRIVTIACSIGVSAHTGHARHMLHDIEH  52
C.thermoCO (  85) GSRGICGASAWTIVARNVGLMILTGAAAHCEHGNHIAHALVE  49
Dcma_24944 (  90) GKKGACGLNIKAQQARIVLIACCIGAACHAGHSRHLVHHLIE  29
Dcma_P2669 (  68) NKKGACGIDMAAACGKIVLVAVLMGTCAHTAHGRHLYHWCLD  32
Mbt_262284 (  88) GKKGACGIDAATQQARTVLLACLIGTAAHAGHARHLVDHLIE  29
 Mf_Q49161 (  89) NKRGACGIDMLGHNGREFFLRVITGTACHAAHGRHLLDHLIE  31
 Mf_Q49163 (  89) NKRGACGIDMMGHNGREFFLRVITGTACHAAHGRHLLDHLIE  32
Mj_2826254 (  89) GKKGACGLNIKAQQARIVLIACCIGAACHAGHSRHLVHHLIE  29
 Mj_B64319 (  90) GKKGACGLNIKAQQARIVLIACCIGAACHAGHSRHLVHHLIE  29
Mst_157553 (  89) NKRGACGIDMLGHNGREFFLRVITGTACHAAHGRHLLDHLIE  31
Mts_A39764 (  80) NKKGACGIDMAAACGKIVLVAVLMGTCAHTAHGRHLYHWCLD  32
```

FIG. 12

an unknown mechanism by which the acetyl-CoA pathway is downregulated when cells are exposed to nitrate (*132*). These studies indicate that the concentrations of electron transport proteins (cytochrome *b*) are lowered, but that the activity of the major pathway enzymes, such as CODH/ACS, do not change.

7. CO Oxidation

a. Occurrence of CO Oxidation and Acetyl-CoA Synthesis at Separate Active Sites: Studies on the Clostridial Enzyme Although it has been known since 1985 that the enzyme previously called CODH also catalyzes acetyl-CoA synthesis (*121*), these two reactions could occur either at the same or at separate active sites. To complicate matters worse, both of these reactions were thought to occur at a heterometallic cluster(s) containing nickel and at least three irons (see later discussion). It seemed almost unbelievable that a single protein could contain two distinct Ni/Fe/S clusters, which have yet to be demonstrated in any other class of protein. However, it was known that CO oxidation is inhibited by low-micromolar levels of cyanide, whereas inhibition of acetyl synthesis requires millimolar concentrations (*121*), which provided support for this apparently implausible hypothesis. There was a long-standing bet between one of the authors (SWR), who wagered that both reactions occurred a common active site, and one of his postdoctoral associates (Wei-Ping Lu), who took the opposite view.

Wei-Ping won the bet. A series of rapid kinetic experiments provided strong support for the concept of two independent active sites. CODH/ACS was reacted with CO and the rate of development of each of the enzyme's characteristic EPR signals was compared with the rates of CO oxidation and acetyl-CoA synthesis. On the basis of these

---

FIG. 12.—*Continued.* Sequence homologies among CODH and ACS active sites. Two regions of homology are found in the ACS subunit. Two highly conserved regions are found in the CODH subunit. Abbreviations in the top two sequences: gi_144786, CODH alpha subunit, *C. thermoaceticum*; gi_1575540 CODH beta subunit, *M. thermophila*; gi_1590910 CODH, alpha subunit, *M. jannaschii*; gi_1590913 CODH, beta subunit (cdhC), *M. jannaschii*; gi_2127796, CODH alpha chain, *M. jannaschii*; gi_2127798, CODH alpha subunit, *M. jannaschii*; gi_2622842 CODH, alpha subunit, *M. thermoautotrophicum*; gi_2650254 CODH, beta subunit, *Archaeoglobus fulgidus.* Abbreviations in the bottom two sequences are: 150036, CODH alpha chain (pir‖A39764), *M. soehngenii*; Af, *A. fulgidus*; C.thermoCO, *C. thermoaceticum* beta subunit (sp|P27989| or gi|98639); Dcma_24944, CODH alpha subunit—*M. jannaschii* (pir‖B64319); Dcma_P2669, *A. fulgidus* section 169 of 172 of the complete genome (gi|2689433); Mbt, *M. thermoautotrophicum*; Mf, *Methanosarcina frisia*; Mj, *M. jannaschii*; Mst *Methanosarcina thermophila*; Mts, *Methanothrix soehngenii.*

experiments, Kumar *et al.* (*133*) proposed the two-separate-site hypothesis, that CO oxidation is catalyzed by a NiFe–S center called Cluster C, and that acetyl-CoA synthesis occurs at Cluster A. The EPR signal of Cluster C changes very rapidly with a first-order dependence on the CO concentration. The second-order rate constant for this spectral change is much faster than the value of k_{cat}/K_m for the CO oxidation reaction. The spectral changes in Cluster C are followed by Cluster B reduction with a rate constant that is similar to the steady-state k_{cat} value. On the other hand, the rate of formation of the characteristic EPR signal for the CO adduct at Cluster A is much slower. Its rate constant matches that for acetyl-CoA synthesis, but is several orders of magnitude slower than CO oxidation. Therefore, it was proposed that the following steps are involved in CO oxidation: (1) CO binds to Cluster C, (2) EPR spectral changes in Cluster C are accompanied by oxidation of CO to CO_2 by Cluster C, (3) Cluster C reduces Cluster B, and (4) Cluster B couples to external electron acceptors (*133*).

Almost simultaneously, Lindahl and co-workers proposed that Cluster C is the CO oxidation site based on EPR and ENDOR studies of the cyanide adduct of the enzyme (*134*). That proposal was based on the premise that CO and cyanide compete for the same binding site. Additionally, Xia and Lindahl have shown that, by mild SDS treatment, they can partially dissociate CODH/ACS, which is a tetrameric enzyme with an $\alpha_2\beta_2$ subunit composition, into an isolated α subunit and an $\alpha\beta_2$ form (135). The $\alpha\beta_2$ form has the same level of CO oxidation activity as the native protein indicating that the α subunit is not involved in CO oxidation and that the β subunit must contain the clusters required for CO oxidation (*135*). In addition, CO_2 alters the g values of the C_{red1} form of the enzyme (*136*).

b. A Homologous Cluster in the R. rubrum and Methanogenic Enzyme The β subunit (AcsA) of the *C. thermoaceticum* (CODH (*124*) and *Rhodospirillim rubrum* CooS (*60*) are homologous, which provided further evidence that Cluster C is the CO oxidation site. CooS is a 67-kDa enzyme that contains CODH activity and Clusters B and C, but lacks the acetyl-CoA synthase activity and Cluster A (*137*).

In 1984, the first methanogenic CODH was isolated from *Methanosarcina barkeri* (*138*) and was shown to consist of a complex of the α and ε subunits, with an apparent molecular mass of 232 kDa. Similar results have been found for other methanogenic CODH preparations (*139–143*). CODH activity must reside in the α subunit of the methanogenic enzyme, since the ε subunit lacks cysteine residues and could

TABLE III

COMPARISON OF THE METAL CENTERS IN CODHs/ACSs[a]

Source of CODH/ACS	Center A–CO Adduct		Center B		Center C		
	g values	E'_0 (mV)	g values	E'_0 (mV)	g values	E'_0 (mV)	Ref.[b]
C. thermoaceticum	2.08, 2.07, 2.03 2.06, 2.05, 2.03	−530	2.04, 1.94, 1.90	−440	2.01, 1.81, 1.65 1.97, 1.87, 1.75	−220 −530[c] −360[d]	*1*
Ms. thermophila	2.06, 2.05, 2.03	ND	2.04, 1.93, 1.89	−444	2.02, 1.87, 1.72	−154	*2*
Ms. barkeri	NO		2.05, 1.94, 1.90	−390	2.005, 1.91, 1.76	−35	*3*
Mt. soehngenii	NO		2.05, 1.93, 1.86	−410	2.005, 1.89, 1.73	−230	*4*
R. rubrum	NO		2.04, 1.94, 1.89	−418	2.03, 1.88, 1.71 1.97, 1.87, 1.75	−110	*5–8*

[a] ND = not determined; NO = not observed.

[b] References:

(1) Lindahl, P. A.; Münck, E.; Ragsdale, S. W. *J. Biol. Chem.* **1990,** *265,* 3873–3879.

(2) Lu, W.-P.; Jablonski, P. E.; Rasche, M.; Ferry, J. G.; Ragsdale, S. W. *J. Biol. Chem.* **1994,** *269,* 9736–9742.

(3) Krzycki, J. A.; Mortenson, L. E.; Prince, R. C. *J. Biol. Chem.* **1989,** *264,* 7217–7221.

(4) Jetten, M. S. M.; Hagen, W. R.; Pierik, A. J. Stams, A. J. M.; Zehnder, A. J. B. *Eur. J. Biochem.* **1991,** 385.

(5) Bonam, D.; Ludden, P. W. *J. Biol. Chem.* **1987,** *262,* 2980–2987.

(6) Stephens, P. J.; McKenna, M.-C.; Ensign, S. A.; Bonam, D.; Ludden, P. W. *J. Biol. Chem.* **1989,** *264,* 16347–16350.

(7) Spangler, N. J.; Lindahl, P. A.; Bandarian, V.; Ludden, P. W. *J. Biol. Chem.* **1996,** *271,* 7973–7977.

(8) Hu, Z. G.; Spangler, N. J.; Anderson, M. E.; Xia, J. Q.; Ludden, P. W.; Lindahl, P. A.; Münck, E. *J. Am. Chem. Soc.* **1996,** *118,* 830–845.

[c] Determined in the presence of argon.

[d] Determined in the presence of CO_2.

not ligate Fe–S (*144*). Thus, the large 89-kDa subunit of the methanogenic CODH/ACS complex must contain Clusters B and C.

8. Structure of Cluster C

It appears that Cluster C catalyzes the chemistry of CO oxidation and transfers electrons to Cluster B, which donates electrons to external acceptors such as ferredoxin. Since a crystal structure of this protein does not exist, the proposed structure of Cluster C is based on spectroscopic measurements. In some cases, the EPR spectrum of a metal center is diagnostic of the type of center. However, the EPR spectra of Cluster C are unusual. The paramagnetic states of Cluster C (C_{red1} and C_{red2}) have g-values that are atypical of standard [4Fe-4S] clusters (Table III) and are similar to those in a variety of structurally unrelated systems including a μ-oxo bridged ion dimer), a $[Fe_4S_4]^{2+/1+}$

cluster in which one of the ions is six-coordinate, a $[Fe_4S_4]^{2+/1+}$ cluster in which the cluster bridges two subunits, and the Rieske $[Fe_2S_2]$ cluster. The oxidized protein is diamagnetic. Mild reduction leads to the formation of C_{red1}. A further one-electron reduction leads to the diamagnetic C_{dia} state, which can be further reduced to paramagnetic C_{red2} state (*145*, *146*). Other states of Cluster C that have been studied include an anion adduct, which is formed by reaction with thiocyanate, azide, or isocyanide and has all three *g*-values *above* 2, and a CN adduct with all *g* values *below* 2.

A number of studies indicate that Cluster C is composed of a [4Fe-4S] cluster that is ligated through an unknown bridging ligand to a Ni ion (Fig. 11).

a. Discovery of Fe–S in Cluster C When ^{57}Fe is substituted in the growth medium, the spectrum of Cluster C is much broader than that of protein obtained from cells grown in natural-abundance iron (*147*). Mössbauer spectroscopic results indicate that the irons in Cluster C are associated with an Fe–S cluster (*147*). Later Mössbauer spectra have more definitively characterized Cluster C (*148*). There is apparently an $S = \frac{1}{2}$ $[4Fe4S]^{1+}$ cluster with a distinct subsite called ferrous component II (FCII) that is pentacoordinate and resembles the subsite Fe–a component in the cluster of aconitase. FCII changes significantly when cyanide binds, suggesting that this is the cyanide binding site.

b. Discovery of Ni in the Active Site The first evidence that Ni is part of Cluster C was provided by EPR spectra of the *R. rubrum* enzyme isolated from cells grown in Ni-deficient medium. The resulting protein lacks nickel, has no CODH activity, and cannot bind cyanide (*149*, *150*); however, when Ni is added, the CO oxidation activity is reconstituted and cyanide can bind. The EPR spectrum of Cluster C_{red1} in the ^{61}Ni-substituted enzyme exhibits an 8-G broadening. In addition, the EPR spectrum of Cluster C_{red1} is absent in the Ni-depleted enzyme and reappears when Ni is replaced (*151*). On the bases of these results is was concluded that CO and CN bind to the Ni component of this cluster.

c. Evidence for a Heterometallic Cluster Containing Ni and Fe EPR studies of the thiocyanate adduct of Cluster C indicate that Ni is bonded to the iron–sulfur cluster. The *g*-values of this adduct (g_{av} of 2.17) more closely resemble the spectra of paramagnetic Ni(I) than those of a $[Fe_4S_4]^{2+/1+}$ cluster (*152*, *153*).

The unusual *g*-values and the small ^{61}Ni coupling constant for the

different states of Cluster C have been explained by assuming that a high spin Ni(II) site is weakly coupled ($J \sim 2$ cm^{-1}) to the $S = \frac{1}{2}$ state of the $[Fe_4S_4]^{2+/1+}$ cluster (*148*). The change in the EPR spectra when anions such as azide and thiocyanate bind apparently results from a change in the sign of the coupling constant J which increases the value of g_{av} above 2 by approximately the same amount that it was below 2.0 in the C_{red1} state.

9. Mechanism of CO Oxidation

CO oxidation occurs in two half-reactions: (1) oxidation of CO to CO_2 generating the two-electron reduced enzyme and (2) reoxidation of the enzyme by the electron acceptor. The ping-pong nature of this reaction was first proposed based on studies with cell extracts from *C. thermoaceticum* (*54*) and *C. pasteurianum* (*155*).

$$E_{ox} + CO + H_2O \longleftrightarrow CO_2 + 2H^+ + E_{red} \text{ (first half-reaction)}$$

$$E_{red} + Fd_{ox} \longleftrightarrow E_{ox} + Fd_{red} \text{ (second half-reaction)}$$

a. First Half-Reaction Earlier experiments using cell extracts indicated that water, not hydroxide, is the substrate and CO_2, not bicarbonate, is the product of this reaction (*156*). Studies of the pH dependence of the reverse reaction of the purified protein also indicate that CO_2 is the product. There was no observable reaction above pH 6.6, where the ratio of $NaHCO_3/CO_2$ is high (*157*). Water was shown to be the donor of the second oxygen in CO_2 for the *Pseudomonas* enzyme (*158*).

The mechanism of the first half-reaction has been studied by a combination of reductive titrations with CO and sodium dithionite and pre-steady-state kinetic studies by rapid freeze quench EPR spectroscopy (FQ-EPR) and stopped-flow kinetics (*159*). These combined studies have led to the following mechanism. The resting enzyme is assumed to have a metal-bound hydroxide nucleophile. Evidence for this species is based on the similarities between the pH dependence of the EPR spectrum of Cluster C and the pK_a for the k_{cat}/K_m for CO, determined by steady-state kinetics (*153*).

Next, (1) CO binds to Cluster C to yield a C_{red1}–CO complex; (2) CO undergoes attack by the metal-bound hydroxide and is oxidized to CO_2 as Cluster C is reduced by two electrons to the C_{red2} state; (3) CO_2 is released and a second CO molecule binds to Cluster C to form a C_{red2}–CO complex; (4) electrons are transferred from C_{red2}–CO to reduce Cluster B as the second molecule of CO_2 is released. This mecha-

nism predicts that two molecules of CO are required for one cycle of turnover. Our results indicate that this is true at high CO concentrations; however, when CO is present at low concentrations, only one CO molecule per turnover binds and undergoes oxidation.

Results from Lindahl's and SWR's laboratories indicate the existence of a UV-visible and EPR silent electron acceptor denoted Center S that does not appear to be associated with any of the other metal centers in the protein.

b. Second Half-Reaction The second half-reaction closes the catalytic cycle by transferring electrons from reduced enzyme to an electron acceptor protein, such as ferredoxin. Ferredoxin or flavodoxin (when iron is limiting) are likely to be the natural electron acceptors for the *C. thermoaceticum* enzyme (*120*, *160*). Ferredoxin also significantly stimulates the rate of the CO/acetyl-CoA exchange reaction (*121*) and the synthesis of acetyl-CoA from methyl-H_4 folate, CO, and CoA (*161*). An electrostatically stabilized complex between ferredoxin and residues 229–239 of the large subunit was isolated by cross-linking the two proteins with a carbodiimide (*162*). In *R. rubrum*, a 22-kDa iron–sulfur protein was isolated that coupled CO oxidation to H_2 evolution via a CO-induced membrane-bound hydrogenase (*163*). The gene encoding this Fe–S protein, *cooF*, has been sequenced and is part of the gene cluster containing CODH and the hydrogenase (*60*).

c. The Reverse Reaction: CO_2 Reduction to CO Probably the most important reaction catalyzed by Cluster C is the reverse reaction in which CO is produced from CO_2. Studies have demonstrated that, even when acetogenic bacteria grow on glucose, they generate CO as an intermediate in the formation of the carbonyl group of acetyl-CoA (*164*). This involves a coupled reaction between pyruvate ferredoxin oxidoreductase and CODH. The carboxyl group of pyruvate is converted to CO_2. Next, CO_2 and electrons derived from the decarboxylation are transferred to CODH, which reduces the CO_2 to CO. CO then is used by the ACS active site (see later discussion), which incorporates CO into acetyl-CoA.

d. Analogous Reaction of CODH CODH is a highly promiscuous electron transfer protein. It can reduce nitrous oxide to N_2 approximately as fast as the copper containing nitrous oxide reductases from denitrifying bacteria (*165*). The $E^{O'}$ of the N_2O/N_2 redox couple is +1175 mV (*166*). It can reduce carbonyl sulfide (COS), a CO_2 analog, to CO and H_2S (*167*, *168*). The binding constant for COS is about 2 mM (*167*, *169*). Another CO_2 analog, CS_2, inhibits CO_2 reduction

competitively with respect to CO_2 (*167*) and reverses cyanide inhibition (*169*, *170*). When CODH is in the reduced state and electron acceptors are not present, it can reduce protons to H_2 (*171*). The rate of hydrogen formation is fast enough to account for the rate of H_2 production by growing cultures of *C. thermoaceticum* and could solve the paradox that the highly CO-sensitive hydrogenases from acetogenic bacteria evolve H_2 when grown on CO.

10. Anions and Their Reactivity with Cluster C

A variety of anions bind to Cluster C, including cyanide, azide, thiocyanate, cyanate, and isocyanides. Among the anions, cyanide binds most tightly to the enzyme. It is a specific and potent inhibitor ($K_i <$ 10 mM) (*172*) of CO oxidation with little effect on acetyl-CoA synthesis (*120*, *121*, *173*). Cyanide is a potent slow binding inhibitor (*149*, *172*). CO can protect against and can relieve cyanide inhibition (*149*, *170*, *172*). CO_2, COS, and CS_2 also can reverse cyanide inhibition (*169*, *170*). Extensive kinetic studies by Ludden's group on the *R. rubrum* CODH indicate that CO and cyanide bind at the same site, specifically at the nickel site in Cluster C (*149*). Results with the *C. thermoaceticum* enzyme also indicate that CO and CN are mutually competitive (*172*). Another possibility is espoused by Anderson and Lindahl (*170*): that CO and cyanide bind at separate sites. Cyanide binding to the *R. rubrum* CODH perturbs the Mössbauer signal of a Fe(II) site (apparently a five-coordinate site called ferrous component II or Fe_A) of Cluster C (*148*).

Azide, thiocyanate, and cyanate also have been shown to bind to Cluster C (*152*). Although they are weak inhibitors of the enzyme, they cause marked changes in the EPR spectrum of Cluster C (*153*), converting the C_{red1} state (with all *g*-values below 2) to a state in which all *g*-values are above 2.

Isocyanides [RNC] (*174*, *175*) are isoelectronic with CO and have been extensively used as CO analogs in studies of heme proteins (*176–180*). *N*-Butyl isocyanide (N-BIC) behaves as a CO analog at both the CODH and ACS active sites (*181*). N-BIC competes with CO in the CO oxidation reaction, is a sluggish reductant, and causes EPR spectral changes at Clusters A, B, and C similar to those elicited by CO.

11. Acetyl-CoA Synthesis

a. The ACS Active Site: a Ni / FeS Cluster at Center A; Demonstration of a Heterometallic Cluster Containing Ni, Fe, and Bound CO (*see Fig. 11.*) Nickel was first shown to be a component of CODH/ACS in

1982. When the enzyme is exposed to CO, a slow relaxing EPR signal is observed with *g*-values at 2.08, 2.07, and 2.03 that is called the NiFeC signal (*145*). This EPR signal exhibits significant broadening when the enzyme is isolated from cells grown in the presence of a stable isotope of Ni (^{61}Ni, $I = \frac{3}{2}$) (*182*). That CO is present in this species was clearly demonstrated by EPR studies. Incubation with ^{13}CO causes the EPR signal to split into a doublet because of the spin–spin interactions with the ^{13}C nucleus ($I = \frac{1}{2}$) (*182*). Similar isotope substitution studies with ^{57}Fe showed that at least three iron atoms are part of this center (*183*). Therefore, it was clear that the CO binding site was a complicated heterometallic metal cluster with unusual magnetic properties. On the basis of ENDOR (*184*) and Mössbauer (*147*) spectroscopic studies, it was proposed that Cluster A consists of a nickel ion that is bridged to a $[Fe_4S_4]^{2+/1+}$ cluster, for example, [Ni-X-Fe_4S_4], where X is an unknown bridge between the Ni ion and one of the irons in the cubane cluster.

CO is the precursor of the carbonyl group of acetyl-CoA (discussed earlier). An identical EPR signal is observed when other precursors of the carbonyl group of acetyl-CoA are reacted with CODH/ACS: for example, CO_2 in the presence of reductant (*145*) and pyruvate (*164*). Incubation with acetyl-CoA itself also gives rise to this EPR signal (*185*).

The two subunits of CODH/ACS have been dissociated to offer a clearer picture of the ACS active site (*135*). The holoenzyme contains 2 Ni, 12 Fe, and 14 S^{2-} (*120*) that are organized into 3 discrete clusters, whereas the isolated α subunit contains only 1 Ni and 4 Fe and has spectroscopic properties similar to those of Cluster A in the native enzyme (*186*). Based on EXAFS spectroscopy of the α subunit, the Ni site in Cluster A has been proposed to be coordinated to 2 sulfur ligands at 2.19 Å and 2 nitrogen or oxygen ligands at 1.89 Å in a distorted square plane (*186*).

Is the paramagnetic adduct between CO and Cluster A a kinetically intermediate in acetyl-CoA synthesis? Questions have been raised about whether this adduct is a catalytic intermediate in the pathway of acetyl-CoA synthesis (*187*, *188*) (as shown in Fig. 13), or is formed in a side reaction that is not on the main catalytic pathway for acetyl-CoA synthesis (*189*). A variety of biochemical studies have provided strong support for the intermediacy of the [Ni–X–Fe_4S_4]–CO species as the precursor of the carbonyl group of acetyl-CoA during acetyl-CoA synthesis (*133*, *183*, *185*, *190*). These studies have included rapid freeze-quench EPR, stopped flow, rapid chemical quench, and isotope exchange.

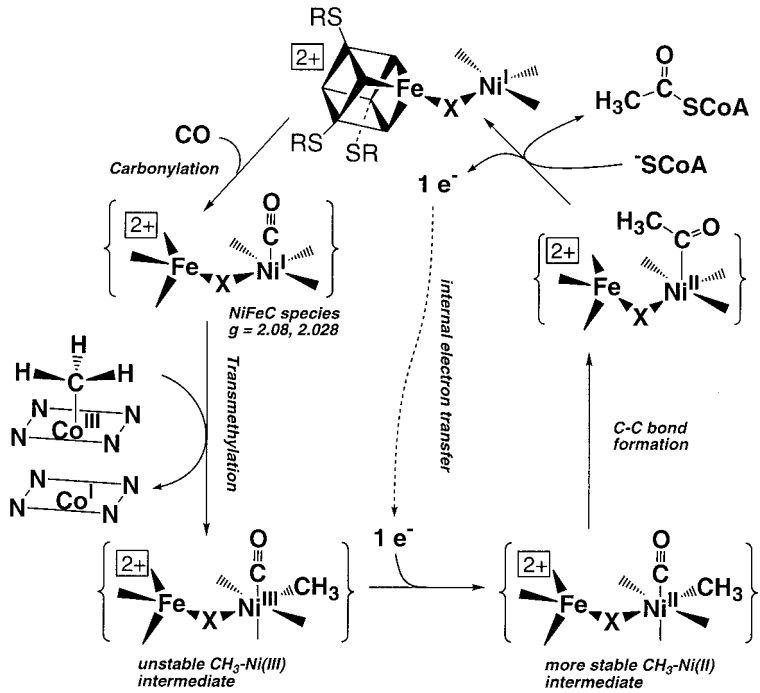

FIG. 13. Proposed reaction mechanism for ACS. The reaction involves the sequential assembly of acetyl-CoA from a carbonyl, methyl, and CoA. We favor a Ni(I) nucleophile to form a catalytically competent paramagnetic M–CO complex, but see text for discussion of an alternative mechanism.

12. Methyl Group Transfer from Methyl-Co to Cluster A

a. Possible Mechanisms After Cluster A binds CO, the methyl group is transferred from the methylated CFeSP. This reaction can occur by a heterolytic or a homolytic mechanism. The heterolytic mechanism (mechanism 1) involves nucleophilic attack on the methyl group by an incoming nucleophile, presumably Ni(I). The methyl group in this mechanism is transferred as a cationic species and the immediate product would be methylnickel(III). This mechanism is similar to the manner in which the methyl–CFeSP is formed from CH_3–H_4 folate (*191*).

Mechanism 1: CH_3–Co(III) + Ni(I) $\rightleftharpoons$ or $\leftrightarrow$ CH_3–Ni(III) + Co(I)

A homolytic mechanism can also be considered. This could occur in two possible ways. In mechanism 2, Ni(I) would capture the product

of fragmentation of methyl–Co(III) species to yield Co(II) and methyl–Ni(II). In this case the methyl group is transferred as a radical. This mechanism has been ruled out by stopped-flow studies that demonstrated Co(I) to be the product of the transmethylation reaction and is formed at a rate that mirrors the rate of methyl–Co^{3+} decay (*192*).

$$\text{Mechanism 2: } CH_3\text{–Co(III)} + \text{Ni(I)} \longleftrightarrow CH_3\text{–Ni(II)} + \text{Co(II)}$$

Another possible mechanism also involves a methyl radical (mechanism 3). In this case, electron transfer from one of the reduced clusters on CODH/ACS to methyl-Co(III) would form a methyl–Co(II) species that can disproportionate to form Co(I) and methyl–Ni(II).

$$\text{Mechanism 3: } CH_3\text{–Co(III)} + \text{CODH/ACS}_{red} \longleftrightarrow CH_3\text{–Co(II)} + \text{CODH/ACS}_{ox}$$

$$CH_3\text{–Co(II)} + \text{Ni(I)} \longleftrightarrow CH_3\text{–Ni(II)} + \text{Co(I)}$$

b. Biochemical Evidence Supporting heterolytic Methyl Transfer Mechanism A radical mechanism would be attractive, since if there were a strong enough reductant to convert methyl–Co(III) to methyl–Co(II), then the organometallic bond would cleave extremely rapidly. The relevant model chemistry supports mechanism 3. However, based on several lines of evidence, we favor mechanism 1 for the biochemical reaction.

The first evidence that appears inconsistent with a homolytic methyl group transfer is based on stereochemical studies of acetyl-CoA synthesis from chiral CHTD-H_4 folate. CHTD-H_4 folate is converted to acetyl-CoA with retention of configuration (*193*). Net retention is explained by one inversion of configuration occurring when the methyl group is donated by CH_3-H_4 folate to the CFeSP and another when the methyl group is transferred to CODH. In addition, the stereochemical configuration of [CHTD]-acetyl-CoA is during the isotope exchange reaction between CO and acetyl-CoA (*194*). Most radical reactions occur with racemization unless, in this case, the sp^2 carbon radical is captured before it has a chance to rotate during its path from the Co center of the CFeSP to the Ni center of CODH.

A second theoretical inconsistency with a radical mechanism for the biochemical reaction was described by Finke. Although cleavage of the methyl–Co(II) bond is very efficient and rapid process, he argued that homolysis of methyl–Co does not occur in enzymes because reduction of CH_3–Co^{3+} requires too low a potential for biochemically relevant electron donors (< -1.0 V vs NHE) (*195*). For example, the mid-

point potential for Cluster A is ~−540 mV (*185*). A solution of methylated CFeSP is stable even after extensive (over 4 hours) incubation at low redox potentials (−620 mV), indicating that a heterolytic cleavage mechanism is unlikely (*196*).

The third reason for favoring a non-radical pathway is based on studies of a mutant version of the CFeSP. This mutant was generated by changing a cysteine residue to an alanine, which converts the 4Fe–4S cluster of the CFeSP into a 3Fe–4S cluster (*14*). This mutation causes the redox potential of the 3Fe–4S cluster to increase by about 500 mV. The mutant is incapable of coupling the reduction of the cobalt center to the oxidation of CO by CODH. Correspondingly, it is unable to participate in acetate synthesis from CH_3–H_4 folate, CO, and CoA unless chemical reductants are present. If mechanism 3 (discussed earlier) is correct, then the methyl transfer from the methylated corrinoid protein to CODH should be crippled. However, this reaction occurred at equal rates with the wild-type protein and the CFeSP variant. We feel that this result rules out the possibility of a radical methyl transfer mechanics and offers strong support for mechanism 1.

c. Biomimetic Chemistry Supporting a Radical Mechanism Riordan has used monomeric synthetic Ni and Co complexes to provide a chemical rationale for the biochemical transmethylation reaction. The reaction involved a methyl transfer from a CH_3–Co(III) complex to a macrocyclic Ni(I) center (*197*). The results of this study strongly support a mechanism involving free radical intermediates (mechanism 3). Further studies using a radical clock probe 5-hexenyl-Co(III) also strongly implicate a radical pathway (*198*). Studies of alkylnickel formation from alkyl halides and a macrocyclic Ni(I) complex also indicate the predominance of a radical akyl transfer mechanism (*199*).

It is puzzling that the model chemistry and the biochemistry do not coincide. The interaction between the CFeSP and CODH/ACS must form a transition state in which the radical pathway is disfavored. Different possibilities to explain this distinction include control of coordination chemistry of the CFeSP and/or the Ni site at Cluster A of CODH/ACS. The cobalt cobamide center in the CFeSP from acetogens and methanogens has a base-off coordination (*200*, *201*). This particular conformation, i.e., base-off five-coordinate methyl–Co(III), is thought to help prevent radical chemistry and to promote S_N2-type mechanisms. For example, five-coordinate organocobalamins are about 1000-fold more stable to homolytic fission than the six-coordinate form (*202*). Correspondingly, thiolate nucleophiles demethylated

base-off methylcobinamide about 1000-fold faster than base-on methylcobalamin (*203*).

13. The Final Steps in Acetyl-CoA Synthesis

a. Carbon–Carbon Bond Formation The final steps in acetyl-CoA synthesis involve formation of the C–C and C–S bonds of acetyl-CoA. The acetyl-metal intermediate could be formed by a methyl migration to the bound carbonyl group or a carbonyl insertion between a methyl-metal species. Either mechanism would be consistent with the stereochemical constraints described earlier, since both methyl migration and carbonyl insertion would be expected to proceed with retention of configuration at carbon (*204*, *205*). There is another possible intermediate in the mechanism in which CO is positioned adjacent to the methyl group and on the same metal before insertion (*206–209*).

b. Carbon–Sulfur Bond Formation ACS could catalyze formation of the thioester bond of acetyl-CoA by two types of mechanisms. One possibility is that CoA binds through noncovalent interactions with the protein and then displaces the bound acyl group in an S_N2 type reaction. Another possibility (*208*) is that CoA could first ligate to Cluster A and then reductively eliminate the acetyl-metal species. There is spectroscopic evidence for binding of CoA to Cluster A (*121*, *190*, *210*). Such a mechanism would provide a way to reduce Cluster A for the next catalytic cycle. Significant binding energies are available in Coenzyme A that could be used to enhance catalysis or to aid in control of the specificity of the type of mechanism (*211*). This area is unexplored for CODH/ACS.

14. Studies of the Isolated Subunits of CODH/ACS

The subunits of CODH/ACS have been isolated (see earlier discussion). The isolated "α" subunit contains one Ni and four Fe and has spectroscopic properties (*186*) similar to those of Cluster A, the active site of acetyl-CoA synthesis (*212*). Unfortunately, it has no ACS activity. Therefore, ACS activity may reside in the α subunit or it may require both the α and the β subunits. If Clusters B and/or C of the β subunit are involved in acetyl-CoA synthesis, one possible role could be in electron transfer. Although acetyl-CoA synthesis and the CO/ exchange reactions do not involve net electron transfer, both of these reactions are stimulated by ferredoxin, indicating that internal electron transfer within CODH/ACS may be required during the reaction (*121*). Further studies with the isolated subunits and the reconstitu-

ted enzyme are required to resolve the roles of the two subunits in acetyl-CoA synthesis.

The active site structure of the acetogenic and methanogenic CODH/ACS appears to be highly similar. The most active preparations of the methanogenic enzyme contain CODH and ACS activities as part of a five-subunit complex. Grahame has shown that this complex from *Ms. barkeri* can catalyze the cleavage of acetyl-CoA and transfer the methyl group to tetrahydrosarcinapterin (*213*). The analogous complex from *Mechanosarcina thermophila* can synthesize acetyl-CoA from methyl iodide, CoA, and CO (*214*), a typical assay for ACS activity used in study of the *C. thermoaceticum* enzyme. Currently it seems most likely that the ACS activity resides in the β subunit of this complex or requires a complex association of components ($\alpha\varepsilon$ or $\alpha\varepsilon\beta$). There is 68% functional similarity between the N-terminal 397 amino acids of *CdhC* (the β *subunit* of the methanogenic five-enzyme complex) and residues 317–729 of the α subunit of the *C. thermoaceticum* enzyme (which harbors ACS activity) (*215*). This homology includes two cysteine-rich motifs and several tryptophan and arginine residues thought to be important in CoA binding. Grahame has shown that an isolated truncated form of the β subunit of the methanogenic complex retains full ability to cleave and resynthesize the C–S bond of acetyl-CoA (*216*). This preparation of the subunit, however, is unable to catalyze the exchange reaction between CO and acetyl-CoA, a diagnostic of the ability to synthesize acetyl-CoA. Possibly an interaction between the CODH active site on the α subunit and the C–S bond cleavage activity on the β subunit is required for acetyl-CoA synthesis.

V. Conclusions

The biologically uncommon Ni center associated with FeS clusters is a powerful and unique catalytic unity. In this chapter we have reviewed the structural and mechanistic aspects of three NiFeS centers: the active site of hydrogenase and Clusters A and C of CODH/ACS. In the former, the association of a Ni center with the most unusual $FeCOCN_2^-$ unit is a fascinating one. Model chemists, spectroscopists, and crystallographers have joined efforts to try and elucidate the reaction mechanism. Although a consensus is being slowly reached, the exact roles of the different active site components have not yet been fully established. Ni appears to be the catalytic center proper, whereas the unusual Fe center may be specially suited to bind a hy-

dride and help electron transfer from it to the FeS clusters and the redox partners.

Although the crystal structure of CODH or CODH/ACS has not yet been solved, a great deal of work has been done on these enzymes and plausible catalytic mechanisms have been proposed. Concerted action between the Ni ion and one of the Fe centers of a 4Fe–4S cluster are thought to elicit the formation of CO_2 from CO. But perhaps the most extraordinary reaction is the one catalyzed by Cluster A: the insertion of CO to a Ni–CH_3 complex. Through the two reactions catalyzed by CODH/ACS, the highly toxic, CO is not only removed, but is used as a source of carbon and electrons.

Under the prebiotic conditions of primordial Earth, most of the energy had to be obtained from inorganic sources. It is easy to imagine that near volcanic vents, metabolic reactions involving hydrogen and carbon monoxide occurred, eventually leading to the emergence of microorganisms. Consequently, it is very likely that the three reactions catalyzed by NiFeS centers are at the very origin of life on Earth.

References

1. Hughes, M. N.; Poole, R. K. *Journal of General Microbiology.* **1991,** *137,* 72.
2. Russell, M. J.; Hall, A. J. *Journal of the Geological Society, London.* **1997,** *154,* 337.
3. Wächtershäuser, *G. Prog. Biophys. Molec. Biol.* **1992,** *58,* 85.
4. Fontecilla-Camps, J.-C. *Structure and Bonding.* **1998,** *91,* 160.
5. Cammack, R. "Catalysis by Nickel in Biological Systems"; Marcel Dekker: New York, 1993.
6. Hausinger, R. P. "Biochemistry of Nickel"; Plenum Press: New York, 1993.
7. Koloweicz, A. F. *Prog. Inorg. Chem.* **1994,** *41,* 493.
8. Halcrow, M. A.; Christou, G. *Chemical Reviews* ***1994,*** *94,* 2421.
9. Albracht, S. P. J. *Biochim. Biophys. Acta* **1994,** *1188, 167.*
10. Eitinger, T.; Friedrich, B. "Microbial Nickel Transport and Incorporation into Hydrogenases"; Harwood Academic Publishers: London, 1997.
11. Maier, T.; Bock, A. "Nickel Incorporation into Hydrogenases"; VCH Publishers: New York, 1996.
12. Ragsdale, S. W.; Wood, H. G.; Ljungdahl, L. G.; Morton, T.; DerVartanian, D. V. "Nickel in CO dehydrogenase"; VCH Publishers: New York, 1988.
13. Ragsdale, S. W.; Riordan, C. G. *J. Bioinorganic Chemistry* **1996,** *1,* 489.
14. Ragsdale, S. W.; Kumar, M.; Zhao, S.; Menon, S.; Seravalli, J.; Doukov, T. "Discovery of a Bio-organometallic Reaction Sequence Involving Vitamin B_{12} and Nickel/Iron–Sulfur Clusters"; Wiley-VCH: Weinheim, Germany, 1998.
15. Telser, J. *Structure and Bonding* **1998,** *91,* 32.
16. Theil, E. C.; Raymond, K. M. "Transition-Metal Storage, Transport, and Biomineralization; University Science Books: Mill Valley, CA, 1994.
17. Nriagu, J. O. "The Global Cycle of Nickel"; John Wiley and Sons: New York, 1980.
18. Hausinger, R. P. *J. Biol. Inorg. Chem.* **1997,** *2,* 279.

19. Matzanke, B. F.; Muller, G.; Raymond, K. N. In "Iron Carriers and Iron Proteins" T. M. Loehr, Ed. pp. 1–121. VCH, 1989.
20. Navarro, C.; Wu, L.-F.; Mandrand-Berthelot, M.-A. *Molecular Microbiology* **1993,** *9,* 1181.
21. Hendricks, J. K.; Mobley, H. L. T. *J. Bacteriol.* **1997,** *179,* 5892.
22. Mobley, H. L. T.; Garner, R. M.; Bauerfeind, P. G. *Mol. Microbiol.* **1995,** *16,* 97.
23. Maeda, M.; Hidaka, M.; Nakamura, A.; Masaki, S.; Vozumi, T. *J. Bacteriol.* **1994,** *176,* 432.
24. Fu, C.; Javedan, S.; Moshiri, F.; Maier, R. *Proc. Natl. Acad. Sci USA.* **1994,** *91,* 5099.
25. Wolfram, L.; Friedrich, B.; Eitinger, T. *J. Bacteriol.* **1995,** *177,* 1840.
26. Bartha, R.; Ordal, E. J. *J. Bacteriol.* **1965,** *89,* 1015.
27. Lancaster, J. R. *FEBS Lett.* **1980,** *115,* 285.
28. Krasna, A. I. *Enzyme Microb. Technol.* **1979,** *1,* 165.
29. Graf, E. G.; Thauer, R. K. *FEBS Lett.* **1981,** *136,* 165.
30. Hatchikian, C. E.; Forget, N.; Fernandez, V. M.; Williams, R.; Cammack, R. *Eur. J. Biochem.* **1992,** *209,* 357.
31. Przybyla, A. E.; Robbins, J.; Menon, N.; JR., H. D. P. *FEMS Microbiol. Rev.* **1992,** *88,* 109.
32. Volbeda, A.; Charon, M. H.; Piras, C.; Hatchikian, E. C.; Frey, M.; Fontecilla-Camps, J. C. *Nature* **1995,** *373,* 580.
33. Higuchi, Y.; Yagi, T.; Yasuoka, N. *Structure* **1997,** *5,* 1671.
34. Garcin, E.; Volbeda, A.; Vernede, X.; Hatchikian, E. C.; Frey, M.; Fontecilla-Camps, J. C. *Vth Inter. Conference on Mol. Biol. of Hydrogenases,* Albertville, **1997,** 37.
35. Montet, Y.; Volbeda, A.; Vernede, X.; Rousset, M.; Hatchikian, E. C.; Amara, P.; Field, M. J.; Frey, M.; Fontecilla-Camps, J. C. *Vth Inter. Conference on the Mol. Biol. of Hydrogenases,* Albertville, **1997,** 38.
36. Montet, Y.; Amara, P.; Vernede, X.; Hatchikian, E. C.; Field, M.; Frey, M.; Fontecilla-Camps, J. C. *Nat. Struct. Biol.* **1997,** *4,* 523.
37. Friedich, B.; Schwartz, E. *Annu. Rev. Microbiol.* **1993,** *47,* 351.
38. Eitinger, T.; Wolfram, L.; Degen, O.; Anthon, C. *J. Biol. Chem.* **1997,** *272,* 17139.
39. Eitinger, T.; Friedrich, B. *J. Biol. Chem.* **1991,** *266,* 3222.
40. Park, I. S.; Hausinger, R. P. *Science* **1995,** *267,* 1156.
41. Shin, W.; Lindahl, P. A. *J. Am. Chem. Soc.* **1992,** *114,* 9718.
42. Rodrigue, A.; Boxer, D. H.; Mandranberthelot, M. A.; Wu, L. F. *FEBS Lett.* **1996,** *392,* 81.
43. Menon, A. L.; Robson, R. L. *J. Bacteriol.* **1994,** *176,* 219.
44. Maier, T.; Böck, A. *Biochemistry* **1996,** *35,* 10089.
45. Thiemermann, S.; Dernedde, J.; Bernhard, M.; Schroeder, W.; Massanz, C.; Friedrich, B. *J. Bacteriol.* **1996,** *178,* 2368.
46. Massanz, C.; Fernandez, V. M.; Friedrich, B. *Eur. J. Biochem.* **1997,** *245,* 441.
47. Olson, J. W.; Fu, C. L.; Maier, R. J. *Mol. Microbiol.* **1997,** *24,* 119.
48. Drapal, N.; Boeck, A. *Biochemistry* **1998,** *37,* 2941.
49. Colbeau, A.; Elsen, S.; Tomiyama, M.; Zorin, N. A.; Dimon, B.; Vignais, P. M. *J. Bacteriol.* **1998,** *251,* 65.
50. Elsen, S.; Richaud, P.; Colbeau, A.; Vignais, P. M. *J. Bacteriol.* **1993,** *175,* 7404.
51. Lenz, O.; Strack, A.; TranBetcke, A.; Friedrich, B. *J. Bacteriol.* **1997,** *179,* 1655.
52. Black, L. K.; Fu, C.; Maier, R. J. *J. Bacteriol.* **1994,** *176,* 7102.
53. Elsen, S.; Colbeau, A.; Vignais, P. M. *J. Bacteriol.* **1997,** *179,* 968.

54. Stoker, K.; Reijnders, W. M.; Oltmann, L. F.; Stouthamer, A. H. *J. Bacteriol.* **1989,** *171,* 4448.
55. Richaud, P.; Colbeau, A.; Toussaint, B.; Vignais, P. M. *J. Bacteriol.* **1991,** *173,* 5928.
56. Toussaint, B.; d'Aspremont, R. d. S.; Delic-Attree, I.; Berchet, V.; Elsen, S.; Colbeau, A.; Dischert, W.; Lazzaroni, Y.; Vignais, P. M. *Mol. Microbiol.* **1997,** *26,* 927.
57. Van Soom, C.; De Wilde, P.; Vanderleyden, J. *Mol. Microbiol.* **1997,** *23, 967.*
58. Vignais, P. M.; Dimon, B.; Zorin, N. A.; Colbeau, A.; Elsen, S. *J. Bacteriol.* **1997,** *179,* 290.
59. Fox, J. D.; Kerby, R. L.; Roberts, G. P.; Ludden, P. W. *J. Bacteriol.* **1996,** *178,* 1515.
60. Kerby, R. L.; Hong, S. S.; Ensign, S. A.; Coppoc, L. J.; Ludden, P. W.; Roberts, G. P. *J. Bacteriol.* **1992,** *174,* 5284.
61. Rey, L.; Fernandez, D.; Brito, B.; Hernando, Y.; Palacios, J.-M.; Imperial, J.; Ruiz-Argüeso, T. *Mol. Gen. Genetics* **1990,** *252,* 237.
62. Durmowicz, M. C.; Maier, R. J. *J. Bacteriol.* **1997,** *179,* 3676.
63. Maroney, M. J.; Colpas, G. J.; Bagynka, C.; Baidya, N.; Mascharak, P. K. *J. Am. Chem. Soc.* **1991,** *113,* 3962.
64. Bagyinka, C.; Whitehead, J. P.; Maroney, M. J. *J. Am. Chem. Soc.* **1993,** *115,* 3576.
65. Volbeda, A.; Garcia, E.; Piras, C.; deLacey, A. L.; Fernandez, V. M.; Hatchikian, E. C.; Frey, M.; Fontecilla-Camps, J. C. *J. Am. Chem. Soc.* **1996,** *118,* 12989.
66. Fontecilla-Camps, J. C. *J. Biol. Inorg. Chem.* **1996,** *1,* 91.
67. Scott, R. A.; Wallin, S. A.; Csechowski, M.; DerVartanian, D. V.; Legall, J.; Peck Jr, H. D.; Huynh, B. H. *J. Am. Chem. Soc.* **1984,** *106,* 6864.
68. He, S. H.; Teixeira, M.; Legall, J.; Patil, D. S.; Moura, I.; Moura, J. J. G.; Dervartanian, D. V.; Huyhn, B.-H.; JR, H. D. P. *J. Biol. Chem.* **1989,** *264,* 2678.
69. Eidsness, M. K.; Scott, R. A.; Prickril, B. C.; DerVartanian, D. V.; Legall, J.; Moura, I.; Moura, J. J. G.; Peck, Jr., H. D. *Biophysics* **1989,** *86,* 147.
70. Sorgenfrei, O.; Klein, A.; Albracht, S. P. J. *FEBS Lett.* **1993,** *332,* 291.
71. Churchill, M. R.; Bueno, C.; Park, J. T.; Shapley, J. R. *Inorg. Chem.* **1984,** *23,* 1017.
72. Fernandez, V. M.; Hatchikian, E. C.; Cammack, R. *Biochim. Biophys. Acta* **1985,** *832,* 69.
73. Kumar, M.; Day, R. O.; Colpas, G. J.; Maroney, M. J. *J. Am. Chem. Soc.* **1989,** *111,* 5974.
74. Gu, Z. J.; Dong, J.; Allan, C. B.; Choudhury, S. B.; Franco, R.; Moura, J. J. G.; Legall, J.; Przybyla, A. E.; Roseboom, W.; Albracht, S. P. J.; Axley, M. J.; Scott, R. A.; Maroney, M. J. *J. Am. Chem. Soc.* **1996,** *118,* 1115.
75. Van der Zwaan, J. W.; Coremans, J. M. C. C.; Bouwens, E. C. M.; Albracht, S. P. J. *Biochim. Biophys. Acta* **1990,** *1041,* 101.
76. Medina, M.; Hatchikian, E. C.; Cammack, R. *Biochim. Biophys. Acta* **1996,** *1275,* 227.
77. Barondeau, D. P.; Roberts, L. M.; Lindahl, P. A. *J. Am. Chem. Soc.* **1994,** *116,* 3442.
78. Van der Zwaan, J. W.; Albracht, S. P. J.; Fontijn, R. D.; Slater, E. C. *FEBS Lett.* **1985,** *179,* 271.
79. Marganian, C. A.; Vazir, H.; Baidya, N.: Olmstead, M. M.; Mascharak, P. K. *J. Am. Chem. Soc.* **1995,** *117,* 1584.
80. Roberts, L. M.; Lindahl, P. A. *Biochemistry* **1994,** *33,* 14339.
81. Happe, R. P.; Roseboom, W.; Pierik, A. J.; Albracht, S. P. J.; Bagley, K. A. *Nature* **1997,** *385,* 126.
82. Bagley, K. A.; Garderen, C. J. V.; Chen, M.; Duin, E. C.; Albracht, S. P. J.; Woodruff, W. H. *Biochemistry* **1994,** *33,* 9229.

83. Bagley, K. A.; Duin, E. C.; Rosenboom, W.; Albracht, S. P. J.; Woodruff, W. H. *Biochemistry* **1995,** *34,* 5527.
84. deLacey, A. L.; Hatchikian, E. C.; Volbeda, A.; Frey, M.; Fontecilla-Camps, J. C.; Fernandez, V. M. *J. Am. Chem. Soc.* **1997,** *119,* 7181.
85. Roberts, L. M.; Lindahl, P. A. *J. Am. Chem. Soc.* **1995,** *117,* 2565.
86. Coremans, J. M. C. C.; van Garderen, C. J.; Albracht, S. P. J. *Biochim. Biophys. Acta* **1992,** *1119,* 148.
87. Cammack, R.; Patil, D. S.; Hatchikian, E. C.; Fernandez, V. M. *Biochim. Biophys. Acta* **1987,** *912,* 98.
88. Huynh, B. H.; Patil, D. S.; Moura, I.; Teixeira, M.; Moura, J. J. G.; DerVartanian, D. V.; Czechovski, M. H.; Prickrill, B. C.; JR., H. D. P.; Gall, J. L. *J. Biol. Chem.* **1987,** *262,* 795.
89. Teixeira, M.; Moura, I.; Fauque, G.; DerVartanian, D. V.; Legall, J.; Peck Jr., H. D.; Moura, J. J. G.; Huynh, B.-H. *Eur. J. Biochem.* **1990,** *189,* 381.
90. Dole, F.; Fournel, A.; Magro, V.; Hatchikian, E. C.; Bertrand, P.; Guigliarelli, B. *Biochemistry* **1997,** *36,* 7847.
91. Huyett, J. E.; Carepo, M.; Pamplona, A.; Franco, R.; Moura, I.; Moura, J. J. G.; Hoffman, B. M. *J. Am. Chem. Soc.* **1997,** *119,* 9291.
92. Kumar, M.; Day, R. O.; Colpas, G. J.; Maroney, M. J. *J. Am. Chem. Soc.* **1989,** *111,* 5974.
93. Choudhury, S. B.; Ray, D.; Chakravorty, A. *Inorg. Chem.* **1990,** *29,* 4603.
94. Kruger, H. J.; Peng, G.; Holm, R. H. *Inorg. Chem.* **1991,** *30,* 734.
95. Kruger, H.-J.; Holm, R. H. *J. Am. Chem. Soc.* **1990,** *112,* 2955.
96. Sellmann, D.; Rackelmann, G.H.; Heinemann, F. W. *Chem. Eur. J.* **1997,** *3,* 2071.
97. Shoner, S. C.; Olmstead, M. M.; Kovacs, J. A. *Inorg. Chem.* **1994,** *33,* 7.
98. Fauque, G.; Peck Jr., H. D.; Moura, J. J. G.; Huynh, B. H.; Berlier, Y.; DerVartanian, D. V.; Teixeira, M.; Przybyla, A. E.; L'espinat, P. A.; Moura, I.; Legall, J. *FEMS Microbiol. Rev.* **1998,** *54,* 299.
99. Teixeira, M.; Fauque, G.; Moura, I.; L'espinat, P. A.; Berlier, Y.; Prickrill, B.; JR., H. D. P.; Xavier, A. V.; Legall, J.; Moura, J. J. G. *Eur. J. Biochem.* **1987,** *167,* 47.
100. Farmer, P. J.; Reibenspies, J. H.; Lindahl, P. A.; Darensbourg, M. Y. *J. Am. Chem. Soc.* **1993,** *115,* 4665.
101. Hsu, H. F.; Koch, S. A.; Popescu, C. V.; Munck, E. *J. Am. Chem. Soc.* **1997,** *119,* 8371.
102. Darensbourg, D. J.; Reibenspies, J. H.; Lai, C. H.; Lee, W. Z.; Darensbourgh, M. Y. *J. Am. Chem. Soc.* **1997,** *119,* 7903.
103. Guigliarelli, B.; More, C.; Fournel, A.; Asso, M.; Hatchikian, E. C.; Williams, R.; Cammack, R.; Bertrand, P. *Biochemistry* **1995,** *34,* 4781.
104. Surerus, K. K.; Chen, M.; Zwaan, J. W. V. D.; Rusnak, F. M.; Kolk, M.; Duin, E. C.; Albracht, S. P. J.; Münck, E. *Biochemistry* **1994,** *33,* 4980.
105. Bartholomew, G. W.; Alexander, M. *Appl. Environ. Microbiol.* **1979,** *37,* 932.
106. Meyer, O. In "Microbial Gas Metabolism, Mechanistic, Metabolic, and Biotechnological Aspects"; R. K. Poole and C. S. Dow, Eds., pp. 131–151. Academic Press: London, 1985.
107. Russell, M. J.; Daniel, R. M.; Hall, A. J.; Serringham, J. A. *J. Mol. Evolution* **1994,** *39,* 231.
108. Gibson, G. R.; Cummings, J. H.; Macfarlane, G. T. *FEMS Microbiol. Ecol.* **1991,** *86,* 103.
109. Pitcher, M. C. L.; Cummings, J. H. *Gut* **1996,** *39,* 1.
110. Ragsdale, S. W. *BioFactors* **1997,** *9,* 1.

111. Lantzsch, K. *Zentralblatt für Bakteriologie, II Abteilung* **1922,** *57,* 309.
112. Zavarzin, G. A.; Nozhevnikova, A. N. *Microbiol. Ecol.* **1977,** *3,* 305.
113. Uffen, R. L. *J. Bacteriol.* **1983,** *155,* 956.
114. Meyer, O.; Schlegel, H. G. *Ann. Rev. Microbiol.* **1983,** *37,* 277.
115. Colby, J.; Dalton, H.; Whittenbury, R. *Ann. Rev. Microbiol.* **1979,** *33,* 481.
116. Daniel, S. L.; Hsu, T.; Dean, S. I.; Drake, H. L. *J. Bacteriol.* **1990,** *172,* 4464.
117. Kerby, R.; Zeikus, J. G. *Curr. Microbiol.* **1983,** *8,* 27.
118. Yagi, T. *Biochim. Biophys. Acta* **1959,** *30,* 194.
119. Diekert, G.; Ritter, M. *FEBS Lett.* **1983,** *151,* 41.
120. Ragsdale, S. W.; Clark, J. E.; Ljungdahl, L. G.; Lundie, L. L.; Drake, H. L. *J. Biol. Chem.* **1983,** *258,* 2364.
121. Ragsdale, S. W.; Wood, H. G. *J. Biol. Chem.* **1985,** *260,* 3970.
122. Barker, H. A.; Kamen, M. D. *Proc. Natl. Acad. Sci. USA* **1945,** *31,* 219.
123. Meyer, O.; Frunzke, K.; Mörsdorf, G. "Biochemistry of the Aerobic Utilization of Carbon Monoxide"; Intercept Ltd.: Andover, U.K., 1993.
124. Morton, T. A.; Runquist, J. A.; Ragsdale, S. W.; Shanmugasundaram, T.; Wood, H. G.; Ljungdahl, L. G. *J. Biol. Chem.* **1991,** *266,* 23824.
125. Meyer, O.; Fiebig, K. "Enzymes Oxidizing Carbon Monoxide"; D. Reidel: Dordrecht, The Netherlands, 1985.
126. Kerby, R. L.; Ludden, P. W.; Roberts, G. P. *J. Bacteriol.* **1997,** *179,* 2259.
127. Shelver, D.; Kerby, R. L.; He, Y. P.; Roberts, G. P. *J. Bacteriol.* **1995,** *177,* 2157.
128. Shelver, D.; Kerby, R. L.; He, Y. P.; Roberts, G. P. *Proc. Natl. Acad. Sci. USA* **1997,** *94,* 11216.
129. Aono, S.; Nakajima, H.; Saito, K.; Okada, M. *Biochem. Biophys. Res. Commun.* **1996,** *228,* 752.
130. Roberts, D. L.; James-Hagstrom, J. E.; Smith, D. K.; Gorst, C. M.; Runquist, J. A.; Baur, J. R.; Haase, F. C.; Ragsdale, S. W. *Proc. Natl. Acad. Sci. USA* **1989,** *86,* 32.
131. Krzycki, J. A.; Lehman, L. J.; Zeikus, J. G. *J. Bacteriol.* **1985,** *163,* 1000.
132. Frostl, J. M.; Seifritz, C.; Drake, H. L. *J. Bacteriol.* **1996,** *178,* 4597.
133. Kumar, M.; Lu, W.-P.; Liu, L.; Ragsdale, S. W. *J. Am. Chem. Soc.* **1993,** *115,* 11646.
134. Anderson, M. E.; DeRose, V. J.; Hoffman, B. M.; Lindahl, P. A. *J. Inorg. Biochem.* **1993,** *51,* Abstract B149.
135. Xia, J. Q.; Lindahl, P. A. *Biochemistry* **1995,** *34,* 6037.
136. Anderson, M. E.; Lindahl, P. A. *Biochemistry* **1995,** *35,* 8371.
137. Bonam, D.; Ludden, P. W. *J. Biol. Chem.* **1987,** *262,* 2980.
138. Krzycki, J. A.; Zeikus, J. G. *J. Bacteriol.* **1984,** *158,* 231.
139. Krzycki, J. A.; Mortenson, L. E.; Prince, R. C. *J. Biol. Chem.* **1989,** *264,* 7217.
140. DeMoll, E.; Grahame, D. A.; Harnly, J. M.; Tsai, L.; Stadtman, T. C. *J. Bacteriol.* **1987,** *169,* 3916.
141. Jetten, M. S. M.; Hagen, W. R.; Pierik, A. J.; Stams, A. J. M.; Zehnder, A. J. B. *Eur. J. Biochem.* **1991,** *195,* 385.
142. Jetten, M. S. M.; Stams, A. J. M.; Zehnder, A. J. B. *FEBS Lett.* **1989,** *181,* 437.
143. Jetten, M. S. M.; Hagen, W. R.; Pierik, A. J.; Stams, A. J. M.; Zehnder, A. J. B. *Eur. J. Biochem.* **1991,** *195,* 385.
144. Eggen, R. I. L.; Geerling, A. C. M.; Jetten, M. S. M.; de Vos, W. M. *J. Biol. Chem.* **1991,** *266,* 6883.
145. Ragsdale, S. W.; Ljungdahl, L. G.; DerVartanian, D. V. *Biochem. Biophys. Res. Commun.* **1992,** *108,* 658.
146. Lindahl, P. A.; Münck, E.; Ragsdale, S. W. *J. Biol. Chem.* **1990,** *265,* 3873.
147. Lindahl, P. A.; Ragsdale, S. W.; Münck, E. *J. Biol. Chem.* **1990,** *265,* 3880.

148. Hu, Z.; Spangler, N. J.; Anderson, M. E.; Xia, J.; Ludden, P. W.; Lindahl, P. A.; Münck, E. *J. Am. Chem. Soc.* **1996,** *118,* 830.
149. Ensign, S. A.; Hyman, M. R.; Ludden, P. W. *Biochemistry* **1989,** *28,* 4973.
150. Ensign, S. A.; Bonam, D.; Ludden, P. W. *Biochemistry* **1989,** *28,* 4968.
151. Stephens, P. J.; McKenna, M.-C.; Ensign, S. A.; Bonam, D.; Ludden, P. W. *J. Biol. Chem.* **1989,** *264,* 16347.
152. Kumar, M.; Lu, W.-P.; Smith, A.; Ragsdale, S. W.; McCracken, J. *J. Am. Chem. Soc.* **1995,** *117,* 2939.
153. Seravalli, J.; Kumar, M.; Lu, W. P.; Ragsdale, S. W. *Biochemistry* **1995,** *34,* 7879.
154. Diekert, G. B.; Thauer, R. K. *J. Bacteriol.* **1978,** *136,* 597.
155. Thauer, R. K.; Fuchs, G.; Käufer, B.; Schnitker, U. *Eur. J. Biochem.* **1974,** *45,* 343.
156. Bott, M.; Thauer, R. K. *Zeitschrift für Naturforschung* **1989,** *44,* 392.
157. Kumar, M.; Lu, W.-P.; Ragsdale, S. W. *Biochemistry* **1994,** *33,* 9769.
158. Kim, Y. M.; Hegeman, G. D. *Int. Rev. Cytol.* **1983,** *81,* 1.
159. Seravalli, J.; Kumar, M.; Lu, W.-P.; Ragsdale, S. W. *Biochemistry* **1997,** *36,* 11241.
160. Ragsdale, S. W.; Ljungdahl, L. G.; DerVartanian, D. V. *J. Bacteriol.* **1983,** *155,* 1224.
161. Roberts, J. R.; Lu, W.-P.; Ragsdale, S. W. *J. Bacteriol.* **1992,** *174,* 4667.
162. Shanmugasundaram, T.; Wood, H. G. *J. Biol. Chem.* **1992,** *267,* 897.
163. Ensign, S. A.; Ludden, P. W. *J. Biol. Chem.* **1991,** *266,* 18395.
164. Menon, S.; Ragsdale, S. W. *Biochemistry* **1996,** *35,* 12119.
165. Lu, W. P.; Ragsdale, S. W. *J. Biol. Chem.* **1991,** *266,* 3554.
166. Jones, C. W. In "Aspects of Microbiology"; J. A. Cole and C. J. Knowles, Eds., Thomas Nelson and Sons, Ltd. 1982, *5,* 41.
167. Ensign, S. A. *Biochemistry* **1995,** *34,* 5372.
168. Gorst, C. M. Ph.d. Thesis. University of Wisconsin–Milwaukee, **1991**.
169. Hyman, M. R.; Ensign, S. A.; Arp, D. J.; Ludden, P. W. *Biochemistry* **1989,** *28,* 6821.
170. Anderson, M. E.; Lindahl, P. A. *Biochemistry* **1994,** *33,* 8702.
171. Menon, S.; Ragsdale, S. W. *Biochemistry* **1996,** *35,* 15814.
172. Morton, T. A. Ph.d. Thesis. University of Georgia, **1991**.
173. Raybuck, S. A.; Bastian, N. R.; Orne-Johnson, W. H.; Walsh, C. T. *Biochemistry* **1988,** *27,* 7698.
174. Singelton, E.; Oosthuizen, H. E. *Adv. Organometal. Chem.* **1983,** *22,* 209.
175. Ugi, I. "Isonitrile Chemistry: Organic Chemistry"; Academic Press: New York, 1971.
176. Ruckpaul, K. J.; Scheler, W.; Jung, F. *Acta Biol. Med. Ger.* **1972,** *28,* 751.
177. Reichmann, L. M.; Annaev, B.; Belova, V. S.; Rogentev, E. G. *Nature* **1972,** *237,* 31.
178. Olson, J. G.; Gibson, Q. H. *J. Biol. Chem.* **1971,** *246,* 5241.
179. Olson, J. G.; Gibson, Q. H. *J. Biol. Chem.* **1972,** *247,* 1713.
180. Pauling, L. *Nature* **1964,** *203,* 182.
181. Kumar, M.; Ragsdale, S. W. *J. Am. Chem. Soc.* **1995,** *117,* 11604.
182. Ragsdale, S. W.; Ljungdahl, L. G.; DerVartanian, D. V. *Biochem. Biophys. Res. Commun.* **1983,** *115,* 658.
183. Ragsdale, S. W.; Wood, H. G.; Antholine, W. E. *Proc. Natl. Acad. Sci. USA* **1985,** *82,* 6811.
184. Fan, C.; Gorst, C. M.; Ragsdale, S. W.; Hoffman, B. M. *Biochemistry* **1991,** *30,* 431.
185. Gorst, C. M.; Ragsdale, S. W. *J. Biol. Chem.* **1991,** *266,* 20687.
186. Xia, J. Q.; Dong, J.; Wang, S. K.; Scott, R. A.; Lindahl, P. A. *J. Am. Chem. Soc.* **1995,** *117,* 7065.

187. Grahame, D. A.; Khangulov, S.; Demoll, E. *Biochemistry* **1996,** *35,* 593.
188. Barondeau, D. P.; Lindahl, P. A. *J. Am. Chem. Soc.* **1997,** *119,* 3959.
189. Grahame, D. A.; Demoll, E. *Biochemistry* **1995,** *34,* 4617.
190. Shanmugasundaram, T.; Ragsdale, S. W.; Wood, H. G. *BioFactors* **1988,** *1,* 147.
191. Zhao, S.; Roberts, D. L.; Ragsdale, S. W. *Biochemistry* **1995,** *34,* 15075.
192. Kumar, M.; Qiu, D.; Spiro, T. G.; Ragsdale, S. W. *Science* **1995,** *270,* 628.
193. Lebertz, H.; Simon, H.; Courtney, L. F.; Benkovic, S. J.; Zydowsky, L. D.; Lee, K.; Floss, H. G. *J. Am. Chem. Soc.* **1987,** *109,* 3173.
194. Raybuck, S. A.; Bastian, N. R.; Zydowsky, L. D.; Kobayashi, K.; Floss, H. G.; Orme-Johnson, W. H.; Walsh, C. T. *J. Am. Chem. Soc.* **1987,** *109,* 3171.
195. Martin, B. D.; Finke, R. G. *J. Am. Chem. Soc.* **1990,** *112,* 2419.
196. Harder, S. A.; Lu, W.-P.; Feinberg, B. F.; Ragsdale, S. W. *Biochemistry* **1989,** *28,* 9080.
197. Ram, M. S.; Riordan, C. G. *J. Am. Chem. Soc.* **1995,** *117,* 2365.
198. Riordan, C. G.; Ram, M. S. Unpublished results.
199. Bakac, A.; Espenson, J. H. *J. Am. Chem. Soc.* **1986,** *108,* 713.
200. Jablonski, P. E.; Lu, W.-P.; Ragsdale, S. W.; Ferry, J. G. *J. Biol. Chem.* **1993,** *268,* 325.
201. Ragsdale, S. W.; Lindahl, P. A.; Münck, E. *J. Biol. Chem.* **1987,** *262,* 14289.
202. Pratt, J. M. "Coordination Chemistry of the B_{12} Dependent Isomerase Reactions"; Wiley: New York, 1982.
203. Hogenkamp, H. P.; Bratt, G. T.; Sun, S. Z. *Biochemistry* **1985,** *24,* 6428.
204. Whitesides, G.; Boschetto, D. *J. Am. Chem. Soc.* **1969,** *91,* 4313.
205. Whitesides, G.; Boschetto, D. *J. Am. Chem. Soc.* **1971,** *93,* 1529.
206. Stavropoulos, P.; Carrié, M.; Muetterties, M. C.; Holm, R. H. *J. Am. Chem. Soc.* **1990,** *112,* 5385.
207. Stavropoulos, P.; Muetterties, M. C.; Carrié, M.; Holm, R. H. *J. Am. Chem. Soc.* **1991,** *113,* 8485.
208. Tucci, G. C.; Holm, R. H. *J. Am. Chem. Soc.* **1995,** *117,* 6489.
209. Stoppioni, P.; Dapporto, P.; Sacconi, L. *Inorg. Chem.* **1978,** *17,* 718.
210. Shanmugasundaram, T.; Kumar, G. K.; Wood, H. G. *Biochemistry* **1988,** *27,* 6499.
211. Whitty, A.; Fierke, C. A.; Jencks, W. P. *Biochemistry* **1995,** *34,* 11678.
212. Xia, J. Q.; Lindahl, P. A. *J. Am. Chem. Soc.* **1996,** *118,* 483.
213. Grahame, D. A. *J. Biol. Chem.* **1991,** *266,* 22227.
214. Abbanat, D. R.; Ferry, J. G. *J. Bacteriol.* **1990,** *172,* 7145.
215. Maupin-Furlow, J. A.; Ferry, J. G. *J. Bacteriol.* **1996,** *178,* 6849.
216. Grahame, D. A.; Demoll, E. *J. Biol. Chem.* **1996,** *271,* 8352.

This Page Intentionally Left Blank

ADVANCES IN INORGANIC CHEMISTRY, VOL. 47

IRON–SULFUR CENTERS INVOLVED IN PHOTOSYNTHETIC LIGHT REACTIONS

BARBARA SCHOEPP, MYRIAM BRUGNA, EVELYNE LEBRUN, and WOLFGANG NITSCHKE

Laboratoire de Bioénergétique et Ingénierie des Protéines (UPR 9036), Institut de Biologie Structurale et Microbiologie, 13402 Marseille Cedex 20, France

I. Introduction
II. 2[4Fe–4S] Proteins
  A. 2[4Fe–4S] Ferredoxins as Water-Soluble Electron Carriers
  B. The F_A/F_B-Binding Subunit of RCI-Type Photosystems
III. The Bridging Cluster F_X
IV. [2Fe–2S] Ferredoxins
V. High-Potential Iron–Sulfur Proteins
VI. The Rieske Protein
  A. Rieske Proteins from Photosynthetic and Respiratory Chains: The Wrong Dichotomy
  B. The Rieske Center, an Unusual [2Fe–2S] Cluster
  C. Structure and Sequence Comparisons
  D. A Unique Functional Mechanism Involving the Rieske Protein
  E. Reduction Potentials and Their pH Dependence
VII. Evolutionary Remarks
References

I. Introduction

During the 1960s, research on proteins containing iron–sulfur clusters was closely related to the field of photosynthesis. Whereas the first ferredoxin, a 2[4Fe–4S] protein, was obtained in 1962 from the nonphotosynthetic bacterium *Clostridium pasteurianum* (*1*), in the same year, a plant-type [2Fe–2S] ferredoxin was isolated from spinach chloroplasts (*2*). Despite the fact that members of this latter class of protein have been reported for eubacteria and even archaebacteria (for a review, see Ref. (*3*)), the name "plant-type" ferredoxin is often used to denote this family of iron–sulfur proteins. The two decades

Copyright 1999 by Academic Press.
All rights of reproduction in any form reserved.
0898-8838/99 $30.00

that followed the discovery of the chloroplast ferredoxin were marked by extensive involvement of iron–sulfur proteins in photosynthesis research (e.g., 4–6). The 1980s, however, witnessed some uncoupling of the two fields. This loss of contact is at least partially due to important methodological (both experimental and theoretical) advances in bioinorganic chemistry leading to emancipation of the discipline from being merely instrumental to other fields of research. A few standard (i.e., abundant and relatively easy to purify) proteins rose to the rank of model systems in bioinorganic teaching, and their physiological importance to the parent organisms often became secondary. A striking example of this phenomenon is provided by the high-potential iron–sulfur proteins (HiPIPs), which have been studied by virtually all the modern spectroscopic and computational techniques, but for which no physiological functional role was known until a few years ago.

Since the beginning of the 1990s, the trend appears to have reverted to strong interactions between the fields of photosynthetic studies and bioinorganic chemistry largely due to the impact of molecular biology, in particular site-specific mutagenesis and heterologous expression. The present contribution summarizes these recent advances with emphasis on the part played by iron–sulfur centers in photosynthesis.

If the inorganic chemistry of iron–sulfur centers has evolved tremendously since 1962, the modern notion of photosynthesis equally has little to do with its early versions. We now know that plant-type photosynthesis occurred first in eubacteria, or more specifically in the ancestors of extant cyanobacteria, and was subsequently imported into eukaryotes via the events of endosymbiosis. The term "oxygenic photosynthesis" appears more appropriate than "plant photosynthesis," since it applies to plastids as well as to cyanobacteria (see Fig. 1a, scheme [3]). Since no photosynthetic mechanisms based on chlorophylls have so far been found in archaebacteria, the evolution of photosynthesis is considered to have exclusively occurred within the domain of eubacteria (Fig. 1b). In this domain, two further (anoxygenic) photosynthetic principles have been observed, each involving a cytochrome *bc* complex and only a single reaction center (RC), which resembles either photosystem I or photosystem II (except in the oxygen-evolving capacity) of oxygenic photosynthesis (see Fig. 1a, schemes [1] and [2]). The localization on the phylogenetic tree of life, based on comparisons of 16S r-RNA sequences (*7*), of the species performing the respective types of photosynthetic mechanism is shown in Fig. 1b. The iron–sulfur centers participating in the light reactions of the

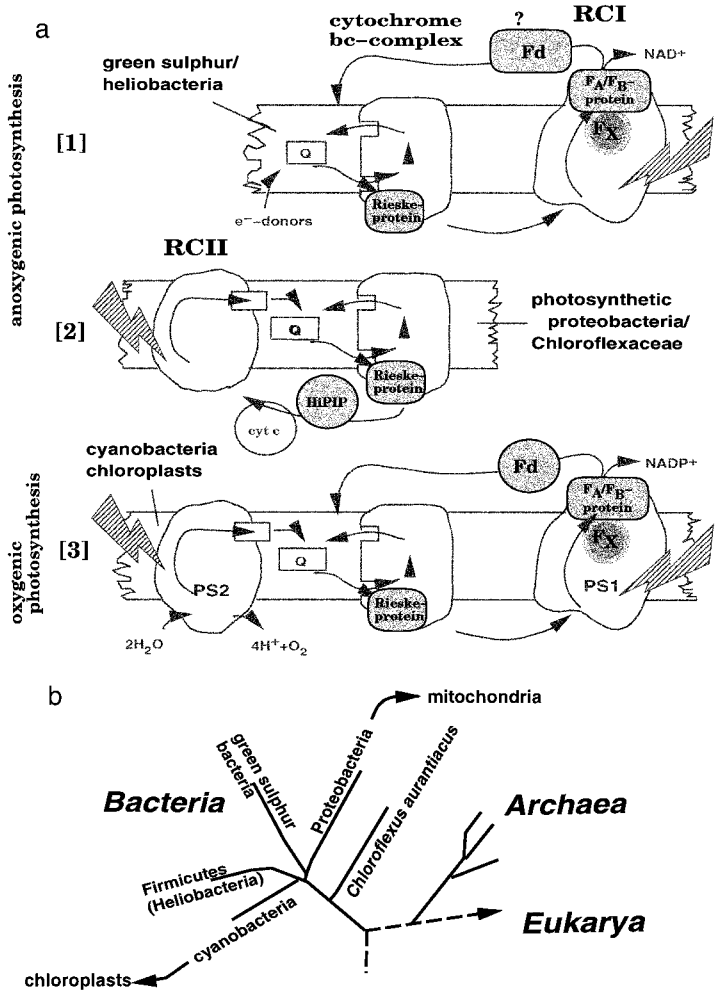

FIG. 1. (a) Schematic representation of the three types of anoxygenic ([1] and [2]) and oxygenic ([3]) photosynthesis found in plants and bacteria. (b) Phylogenetic tree based on 16S-rRNA sequence comparisons featuring only photosynthetic phyla.

three different photosynthetic principles are highlighted in the schemes of Fig. 1a, comprising (a) the water-soluble ferredoxins accepting electrons from RCI (i.e., PS1 and related photosystems), (b) the electron acceptors F_X, F_A, and F_B of the membrane-bound RCI, (c) the membrane-bound Rieske's cluster of the cytochrome *bc* complex, and (d) the HiPIP as soluble redox mediator between the cyto-

chrome bc_1 complex and the RCII-type photosystem in the majority of the photosynthetic proteobacteria (Fig. 1a, scheme [2]).

II. 2[4Fe–4S] Proteins

A. 2[4Fe–4S] Ferredoxins as Water-Soluble Electron Carriers

The 2[4Fe–4S] and [3Fe–4S][4Fe–4S] ferredoxins are components of virtually all eubacteria and archaebacteria (*3*). Several comprehensive reviews dealing with these small metalloproteins have appeared (*3*, *8–12*), but only those participating directly in the photosynthetic light reactions will be addressed here.

Water-soluble ferredoxins shuttle electrons from the reducing side of RCI-type photosystems toward ferredoxin-NADP-oxidoreductases (FNR). Whereas this role is fulfilled by the so-called plant-type [2Fe–2S] ferredoxin (*13*) in the oxygenic photosynthetic chain of cyanobacteria and chloroplasts (see Fig. 1a, scheme [3]), the anoxygenic photosynthetic chain of the green sulfur bacteria (Fig. 1a, scheme [1]) is generally considered to use the bacterial-type, that is, 2[4Fe–4S] ferredoxin (*14*). The presence of such a 2[4Fe–4S] ferredoxin in *Chlorobium limicola* (*15–17*) and more recently *Heliobacillus mobilis* (*18*) had been shown. The primary sequence of the chlorobial protein has been determined (*16*), and it has been shown by reconstitution experiments to potentially serve as electron acceptor to the chlorobial RCI. For the heliobacterial protein, apparent single cluster redox potentials of −500 and −530 mV have been obtained (*18*), in line with a possible role as electron acceptor to the photosystem. For a more critical discussion of the nature of the water-soluble ferredoxin involved in photosynthesis of green sulfur and heliobacteria, see Section IV.

B. The F_A/F_B-Binding Subunit of RCI-Type Photosystems

1. Global Structure and Differences between Species

Whereas the 2[4Fe–4S] ferredoxin may have been replaced by the [2Fe–2S] ferredoxins in oxygenic photosynthesis, another 2[4Fe–4S] protein, the so-called F_A/F_B-binding subunit (see Fig. 1), appears to be common to all RCI-type photosystems.

In 1987, the iron–sulfur clusters F_A and F_B acting as terminal electron acceptors in photosystem I have been shown to be located on a

small protein of MW_{app} of about 8 kDa (*19*, *20*), and the subsequent sequence determination (*21*) has suggested that the F_A/F_B-subunit is closely related to 2[4Fe–4S] ferredoxins. With this presumption, the structure of the protein has been modeled (*22–24*). The structure of PS1 that has been determined at 4 Å resolution (*25*) disagrees in a few structural details (see later discussion), but confirms the global similarity of the F_A/F_B-protein to 2[4Fe–4S] ferredoxins.

Clusters F_A and F_B of photosystem I from cyanobacteria and chloroplasts are distinguished by their EPR signatures (*26*, *27*) and their reduction potentials (-520 mV for F_A and -580 mV for F_B; Ref. (*28*). The assignment of cysteines in the primary sequence as ligands to individual clusters has been achieved by site-specific mutagenesis (*29*, Fig. 3), and structural information with regard to the environment of both clusters has been obtained by NMR (*24*).

EPR-studies suggested that the terminal iron–sulfur acceptors in the green sulfur bacterial RC (Fig. 1) strongly resemble those found in PS1 with respect to spectral parameters, orientations of *g*-tensor axes to the parent membrane, and intercluster distance (*30–32*). A major difference, however, is in the inverted order of reduction potentials, with F_B less reducing than F_A (*31*, *32*). The protein has subsequently been identified (*33*) and sequenced (*34*, Fig. 3). Unexpectedly, the F_A/F_B-subunit in green sulfur bacteria features a molecular mass of about 20 kDa. This was rationalized by the presence of additional domains in the primary sequence, such as a highly positively charged N-terminal part (133 residues) and a C-terminal extension (32 residues), in addition to the central domain which corresponds to a 2[4Fe–4S] ferredoxin (see Fig. 3). Büttner *et al.* (*34*) have speculated that the positively charged segment may participate in docking of the putative electron-transfer partner, i.e., the chlorobial 2[4Fe–4S] ferredoxin, which is a strongly negatively charged protein. It is of note, however, that N- and C-terminal extensions are not rare in 2[4Fe–4S] ferredoxins (see, e.g., the Zn-binding domain of the archaeal ferredoxin from *Sulfolobus* (*35*, *36*) or the C-terminal α-helical extension in the *Azotobacter* ferredoxin (*34*)), and they are generally assumed to serve in stabilizing the $(\beta\alpha\beta)_2$-core fold by providing bridging interactions between the otherwise noninteracting β-strands of the core structure. It therefore appears likely that, along with other possible functions, the N- and C-terminal extensions increase the stability of the F_A/F_B-subunit in the green sulfur bacterial RC. It is of note that the C-terminal stretch contains two histidines and several aspartic acids, which together with a histidine at the end of the N-terminal extension might even form an additional metal binding site reminis-

cent of that which has been discovered in the *Sulfolobus* ferredoxin. The green sulfur bacterial RC appears to be made up of only the homodimeric membrane-integral core, and the F_A/F_B-binding subunit (*34*). By contrast, photosystem I contains close to 10 additional small subunits, some of which appear to clamp the F_A/F_B-subunit to the RC core (*25*). This fact may explain why the F_A/F_B-protein in PS1 does not need additional structural elements in order to stabilize it.

A common feature of the F_A/F_B-proteins from both PS1 and the green sulfur bacterial RC is an insertion of 11 (PS1) or 12 (green sulfur bacteria) residues with respect to the model 2[4Fe–4S] ferredoxin, that from *Peptococcus aerogenes*, in the sequence stretch between the two cluster binding motifs (Fig. 3). This stretch corresponds to a loop represented on the bottom of the *Peptococcus* ferredoxin in Fig. 2a. In the previously published models (*22*, *23*), this stretch resembled a blister-like protrusion on the basic structure of the *Peptococcus* protein, whereas the structure proposed from the 4 Å electron density map merely extends the loop already present in the *Peptococcus* ferredoxin (denoted by the darker gray in Fig. 2b). Interestingly, a corresponding extension is present in the [3Fe–4S][4Fe–4S] ferredoxin from the archaebacterium *Sulfolobus acidocaldarius*. The 3D structure (*35*) of the *Sulfolobus* protein (Fig. 2c) corroborates the prediction put forward for the F_A/F_B-protein. One might even argue that the ancestral ferredoxin contained the extended loop, since the capture of the F_A/F_B-subunit most probably occurs close to the root of the phylogenetic tree of the eubacteria. The deletion of part of this loop much later in evolution would then have led to the *Peptococcus aerogenes*-type ferredoxins.

EPR studies on the heliobacterial RCI-type photosystem have again demonstrated the presence of terminal iron–sulfur cluster acceptors resembling F_A/F_B (*37*, *38*). An F_A/F_B-subunit had, however, escaped detection at this time. Detergent-solubilized RC preparations are devoid of such a subunit (and of light-reducible iron–sulfur centers in general). One might speculate that the heliobacterial RCI represents an evolutionary state prior to capture of the 2[4Fe–4S] ferredoxin as a fixed RC-subunit. In such a scenario, a water-soluble 2[4Fe–4S]-ferredoxin could pick up electrons directly from the RC core and shuttle them to FNR. As mentioned earlier, significant amounts of 2[4Fe–4S]-ferredoxin are indeed present in the soluble fraction of heliobacteria (*18*). The EPR spectral features of this 2[4Fe–4S]-ferredoxin are, however, quite different from those of the photoreducible centers (*18*), arguing against the mobile F_A/F_B-subunit hypothesis. It appears much more likely to us that a strong oxygen sensitivity of F_A/F_B in

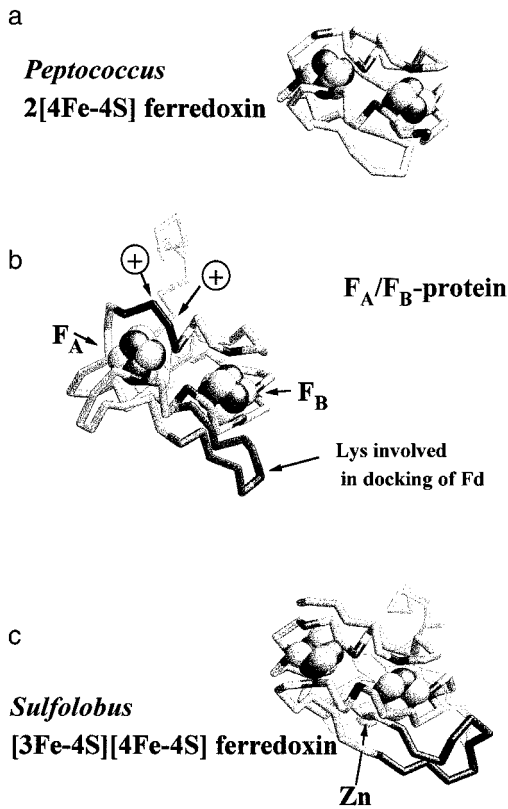

FIG. 2. Protein backbone representations of (a) the 2[4Fe–4S] ferredoxin from *Peptococcus aerogenes*, (b) the proposed structure of the F_A/F_B-binding protein of PS1 based on the 4 Å crystal structure (*25*), and (c) the [3Fe–4S][4Fe–4S] ferredoxin from *Sulfolobus acidocaldarius.* Ligands to clusters F_A and F_B, important residues as well as the loop extension (see text) are highlighted in darker gray.

the obligatorily anaerobic heliobacteria together with a weak association of the subunit to the RC core may have hampered detection of the protein.

2. Cluster Attribution, Redox Properties, and Electron Exchange

Clusters F_A and F_B can be (photo-)reduced by light-induced charge separation within the RC complex at cryogenic temperatures. Since, under these conditions, only one electron is injected into the F_A/F_B-protein, and since furthermore the EPR spectra of F_A and F_B are significantly different, a straightforward assignment of individual clusters to the cluster-binding motifs in the primary sequence was

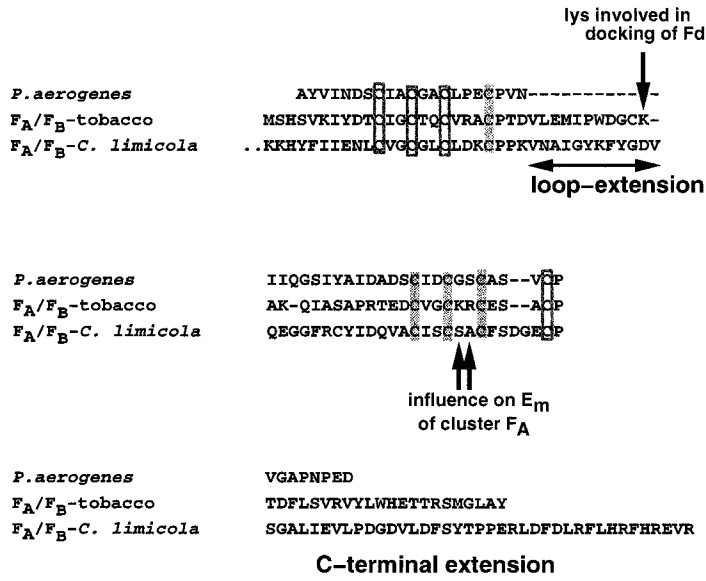

FIG. 3. Sequence comparison of the F_A/F_B-binding subunits of PS1 from tobacco and the RC of green sulfur bacteria with that of the 2[4Fe–4S] ferredoxin from *Peptococcus aerogenes.* Cysteine ligands to the right-hand cluster in the three structures of Fig. 2 (i.e., cluster F_B for the case of the F_A/F_B-protein) are marked by open boxes and residues ligating the left-hand cluster by hatched boxes.

achieved based on alterations induced by site-specific mutagenesis on PS1 from cyanobacteria (*29*). Cluster F_B could thus be shown to be ligated by cysteines 11, 14, 17, 58, whereas cysteines 21, 48, 51, 54 bind the F_A-cluster (Fig. 2b). A similar conclusion was arrived at based on sequence comparisons between the green sulfur bacterial and the plastidic F_A/F_B-binding subunits (*14*). In the green sulfur bacterial protein, cluster F_A is more negative than cluster F_B (*31*), whereas the reverse situation is encountered in PS1 (*28*). In the second cluster-binding motif of the green sulfur bacterial subunit (Fig. 3), and in close structural vicinity of cluster F_A (Fig. 2b), two positive charges conserved in all PS1-F_A/F_B-subunits are absent, suggesting an influence of these two residues on the reduction potential of the respective clusters. The second cysteine motif has therefore been proposed to ligate cluster F_B (*34*). In a site-specific mutagenesis study in *Chlamydomonas*, the two residues in question were converted into those present in *Chlorobium* (*39*), nicely confirming the proposal based on the sequence comparison. The mutated *Chlamydomonas* PS1 was found to behave just like green sulfur bacteria in several respects and in particular showed an inversed order of reduction po-

tentials for F_A and F_B. With this electrochemical and structural data available, the F_A/F_B-binding protein represents an ideal model to study the influence of electrostatic interactions on reduction potentials.

Since the early days of research on the terminal acceptors in PS1, a controversy has existed as to whether F_A and F_B transfer electrons in series or are part of two distinct electron-transfer pathways from PS1. The (still preliminary) structure determination of PS1 has provided important clues concerning this question, showing that the F_A/F_B-subunit is asymmetrically attached to the RC, yielding distances of 15 and 22 Å between each of the clusters and their presumable electron donor, the core-bound cluster F_X (*25*). From the structural data it appears clear that only the proximal cluster will accept electrons from F_X. This proximal cluster can then either directly reduce the soluble ferredoxin or transfer its electron over the 12.5 Å distance toward the distal cluster. In soluble 2[4Fe–4S] ferredoxins, examples showing high electron exchange rates between both clusters (e.g., *Clostridium pasteurianum*, Ref (*40*)) or absence thereof (e.g., *Chromatium vinosum*, Ref. (41)) have been described. The differences between these two cases have been rationalized invoking different localizations of the mixed-valence pairs on the respective clusters (*42*), which may result in significant variations in electron-transfer distances between the mixed-valence pairs. An NMR study of the cyanobacterial F_A/F_B-subunit expressed in *E. coli* has been carried out and provided evidence for electron exchange rate constants between the clusters faster than 100 μs (*24*). It therefore seems likely that the F_A/F_B-subunit in PS1 (and judging from the high similarity of *g*-tensor orientations, also that of the green sulfur bacterial RCI) serves as an electron wire from center F_X in the RC core toward the soluble ferredoxin.

At present, the assignment of the proximal and distal clusters to F_A or F_B is still a subject of debate (*25*, *27*, *43*, *44*). Whereas the group performing the structure determination of PS1 admit that the present resolution does not allow a definitive answer, they strongly favor the model attributing center F_B to the proximal and center F_A to the distal cluster (*25*). A large body of functional data, however, contradicts this model (for a review, see Ref. (27)). Rather compelling evidence for center F_B being the distal cluster has been provided by site-directed mutagenesis on a Lys residue situated on a loop extension close to center F_B (Fig. 2b). Since these data showed that the residue in question is directly involved in docking of ferredoxin to the F_A/F_B-binding protein (*45*), center F_B is most probably the electron donor to the ferredoxin.

III. The Bridging Cluster F_X

In 1975, Evans *et al.* (*46*, *47*) reported the EPR spectrum of a PS1-electron acceptor apparently preceding the terminal iron–sulfur cluster F_A/F_B. The EPR parameters of this center named "X" (g_z = 2.06, g_y = 1.86, and g_x = 1.76) and the wide linewidths on all three g-values only remotely resembled those of typical iron–sulfur clusters. Several hypotheses were put forward with respect to the chemical nature of X. The presence of two conserved cysteine residues on each of the two large PS1-subunits forming the heterodimeric core of the reaction center, together with biochemical evidence (for a review, see (26)) strongly suggested this acceptor to be an iron–sulfur cluster bridging the two halves of the dimeric core, very much like the situation encountered in the case of the nitrogenase Fe-protein (*48*). Center X thus became known as the F_X cluster. The likely cluster binding motifs were preceded by sequence segments resembling a leucine-zipper motif (*49*). Comparisons with the green sulfur (*34*) and heliobacterial (*50*) RC sequences as well as the 4Å-structure (*25*) did not, however, support the leucine-zipper hypothesis. Site-specific mutagenesis confirmed the conserved cysteine residues as ligands to the cluster (*51–53*), and the 3D structure of PS1 (*25*), although unable to identify the ligands, showed the cluster to be at the interface of the two large subunits.

Cluster F_X was also identified via its EPR spectral features in the RCI photosystem from green sulfur bacteria (*31*, *32*) and the cluster binding motif was subsequently found in the gene sequence (*34*) of the (single) subunit of the homodimeric reaction center core (for a review, see (*54*, *55*)). Whereas the same sequence motif is present in the RCI from heliobacteria (*50*), no EPR evidence for the presence of an iron–sulfur cluster related to F_X has been obtained. There are, however, indications from time-resolved optical spectroscopy for the involvement of an F_X-type center in electron transfer through the heliobacterial RC (*56*).

IV. [2Fe–2S] Ferredoxins

The prototype of this class of soluble ferredoxins was initially obtained from spinach chloroplasts and subsequently been shown to play a role in physiological electron shuttling between PS1 and a number of redox proteins, most prominently ferredoxin-NADP-reductase (*13*). Homologous proteins were purified from several cyanobac-

teria, yielding the first X-ray structures of the so-called plant-type ferredoxins (*57*). Many isoforms have been detected, on both the protein and the genome levels; however, specific functions can only be attributed to a small fraction of these iso-ferredoxins (for reviews, see (*3*, *8*)). Representatives of this family have meanwhile been detected in a wide variety of prokaryotes besides cyanobacteria, and including even archaebacteria (*3*), rendering the description "plant-type ferredoxin" even more obsolete.

The study of the [2Fe–2S] ferredoxin serving as an electron acceptor to PS1 was for a long time restricted to the determination of biochemical, biophysical, and structural characteristics. The examination of the electron-transfer reaction between PS1 and the ferredoxin was hampered by the low optical extinction coefficients and the closely similar spectra of the electron-donating [4Fe–4S] clusters and the [2Fe–2S] center on the ferredoxin. More recently, instrumental advances together with the application of molecular biology have allowed a breakthrough with respect to this question. The kinetics of electron transfer from PS1 to ferredoxin are now characterized to great detail (*44*, *58*, *59*) and first elements concerning the possible docking site for ferredoxin on PS1 have been obtained (*45*).

As mentioned in Section II,A, it is generally assumed that a 2[4Fe–4S] protein plays the role of the electron acceptor to the RCI-type reaction center in green sulfur bacteria (*14*). We suggest some caution concerning this hypothesis. In heliobacteria, in addition to an abundant 2[4Fe–4S] protein, a second soluble ferredoxin has been purified (following purification protocols described for the plant-type ferredoxin), the EPR characteristics of which correspond rather to [2Fe–2S] than to [4Fe–4S] centers (*18*). Its reduction potential has been determined as −520 mV (*18*), that is, in line with a possible function as electron acceptor to the RC. As long as there is no clear evidence for the absence of such a [2Fe–2S] ferredoxin in green sulfur bacteria, a scenario where [2Fe–2S] ferredoxins act as electron acceptors to all RCI-type photosystems cannot be discarded. In such a scenario, soluble 2[4Fe–4S] proteins would not be involved in the light reactions of photosynthesis.

V. High-Potential Iron–Sulfur Proteins

High-potential iron–sulfur proteins (HiPIP) form a family of small (∼6–10 kDa) soluble electron transport proteins originally only found in photosynthetic representatives of the proteobacteria (for reviews,

see (*60*, *61*). Subsequently, three species of nonphotosynthetic proteobacteria have been shown to contain HiPIP (*62–64*). HiPIP proteins from selected organisms have been studied in detail with respect to electrochemical properties (*65*, *66*), primary sequences (*67–71*), and 3D structure (*40*, *72–78*). The structure–function relationships of HiPIPs have been reviewed (*79*).

In many HiPIPs, heterogeneous EPR spectra have been observed, arguing for the presence of two populations differing in some electronic parameter (*77*, *78*, *80*, *81*). These heterogeneous populations are presently attributed to the existence of two different localizations of the mixed-valence pair within the cube (*40*, *76*). For the dominant population, an attribution of *g*-tensor to molecular axes was proposed (*81*) based on the study of spin–spin interaction within the dimeric form of HiPIP. In this model, the g_{max} direction was proposed to point out of the sulfur edge of the cube that is closest to the dimer interface. An ENDOR-study (*82*) arrives at a different conclusion on the HiPIP from *Ectothiorhodospira halophila* (iso II), putting g_{max} perpendicular to the face of the cubane formed by the acid-labile sulfur atoms S2 and S4 (PDB numbering) and the mixed-valence pair.

On the basis of their abundances and their appropriate reduction potentials, HiPIPs have previously been proposed as electron donor to the proteobacterial photosynthetic RC (*61*). Time-resolved optical spectroscopy performed on the purple bacteria *Rubrivivax gelatinosus*, *Rhodoferax fermentans*, and *Rhodocyclus tenuis* in fact demonstrated that under certain conditions HiPIP acts as the physiological electron shuttle between the cytochrome bc_1 complex and the RC-associated tetraheme cytochrome subunit in these bacteria (*83–86*). A subsequent screening of photosynthetic proteobacteria using this technique showed that HiPIP participates in photosynthetic electron transport in most species of purple bacteria containing a tetraheme subunit (*87*). In aerobically (i.e., nonphotosynthetically) grown cultures of the purple bacterium *Rhodoferax fermentans*, HiPIP appears to transport electrons from the cytochrome bc_1 complex to a *cb*-type oxidase (*84*). Osyczka *et al.* (*88*) and Menin *et al.* (*86*) have furthermore shown that both HiPIP and the low-potential cytochrome c_{551} (E_m about +50 mV) for the case of *Ru. gelatinosus* or the high-potential cytochrome c_8 for the case of *R. tenuis* are able to rapidly donate electrons to the tetraheme subunit, suggesting the presence of multiple binding sites on these tetraheme subunits.

An EPR study (*89*) on two-dimensionally ordered membranes has shown (a) a strong association of HiPIP to the photosynthetic membrane, and (b) that part of this membrane associated HiPIP forms a

complex with the RC and can therefore be photooxidized even in samples immobilized by partial dehydration. Based on the attribution of *g*-tensor axes to molecular axes (*82*), structural information with respect to the interaction between HiPIP and the RC can be deduced (*89*). The functional role of HiPIPs thus appears to be in the process of being understood at last.

VI. The Rieske Protein

A. Rieske Proteins from Photosynthetic and Respiratory Chains: The Wrong Dichotomy

A decade after the discovery of the Rieske protein in mitochondria (*90*), a similar FeS protein was identified in spinach chloroplasts (*91*) on the basis of its unique EPR spectrum and its unusually high reduction potential. In 1981, the Rieske protein was shown to be present in purified cytochrome b_6f complex from spinach (*92*) and cyanobacteria (*93*). In addition to the discovery in oxygenic photosynthesis, Rieske centers have been detected in both single-RC photosynthetic systems [2] (e.g., *R. sphaeroides* (*94*), *Chloroflexus* (*95*)) and [1] (*Chlorobium limicola* (*96*, *97*), *H. chlorum* (*98*)). They form the subject of a review in this volume.

In contrast to common usage, the distinction between "photosynthetic" and "respiratory" Rieske proteins does not seem to make sense. The mitochondrial Rieske protein is closely related to that of photosynthetic purple bacteria, which represent the endosymbiotic ancestors of mitochondria (for a review, see also (*99*)). Moreover, during its evolution Rieske's protein appears to have existed prior to photosynthesis (*100*, *101*), and the photosynthetic chain was probably built around a preexisting cytochrome *bc* complex (*99*). The evolution of Rieske proteins from photosynthetic electron transport chains is therefore intricately intertwined with that of respiration, and a discussion of the photosynthetic representatives necessarily has to include excursions into nonphotosynthetic systems.

B. The Rieske Center, an Unusual [2Fe–2S] Cluster

Rieske centers distinguish themselves from common [2Fe–2S] and [4Fe–4S] clusters (a) by an unusual EPR spectrum characterized by a low g_{av}-value of 1.91 as compared to 1.96 for most 2Fe2S and 4Fe4S ferredoxins (*102*) and (b) by an electrochemical potential that is al-

most 700 mV more positive than that of the bulk of "normal" iron–sulfur clusters. The extraordinarily high redox potential prompted Blumberg and Peisach (*103*) to invoke elements less electron-donating than sulfur, such as oxygen or nitrogen, as ligands to the cluster. In 1984, data on the Rieske proteins from *Thermus thermophilus* were presented as providing evidence for histidines occupying at least part of the ligand sphere of the cluster (*104*). The number of reducing equivalents needed to fully reduce the cluster, as well as the quantification of Fe and acid-labile sulfur, indicated the presence of two (spectroscopically fully identical) clusters within one protein. The amino acid composition, however, showed the presence of only four cysteines, that is, an insufficient number to ligate two clusters. Meanwhile, primary sequences of Rieske proteins (e.g., that of *C. limicola* (*105*)) functionally more closely related to the *Thermus* protein than those of plastids and mitochondria (see Section VI,E) have been determined, yielding amino acid composition patterns very similar to that of the *Thermus thermophilus* protein while containing the ligand motifs for only one cluster. This indicates that the two-cluster hypothesis for the *T. thermophilus* protein was based on insufficient accuracy of the chemical/biochemical determinations. At the same time, X-band ENDOR spectroscopy on several Rieske proteins (*106*, *107*) supposedly demonstrated the presence of histidine ligands because of the observation of strongly hyperfine coupled nitrogens (A = 26–28 MHz). The respective ENDOR spectra were subsequently shown to be misinterpreted and the presumable nitrogen resonances actually arose from protons coupling to the cluster (*108*, *109*). Q-band ENDOR and ESEEM data (*109–112*), by contrast, indeed provided evidence for hyperfine couplings arising from histidine nitrogens in the frequency range below 10 MHz. The fact that the A-tensor determined in the Q-band ENDOR study (*109*) showed a nonvanishing trace indicated a Fermi-contact contribution to this hyperfine coupling, that is, through-bond interactions between an N-nucleus on histidine and the unpaired spin. It is of note, however, that the data analysis yielding the hyperfine tensor was based on a correlation of g-tensor and molecular axes that has been rendered unlikely by the structure determination of the cytochrome bc_1 complex (*113*) (see later discussion). A site-specific mutagenesis study on a photosynthetic proteobacterium showed that exchange of one of the four cys-candidates in the sequence against serine resulted in the formation of about 5% of residual cluster (*114*). The conclusion that the respective residue therefore cannot be a ligand to the cluster, however, is not fully stringent, since serine has been shown to substitute cysteine in bacterial [2Fe–2S] ferredoxins.

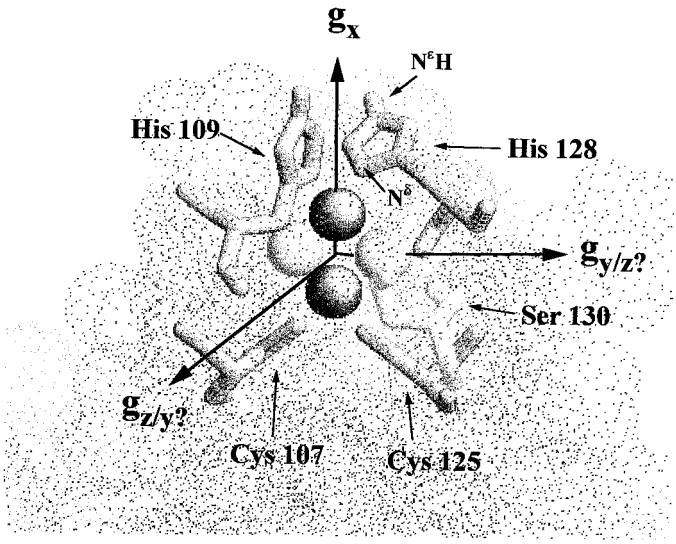

FIG. 4. Representation of the ligand sphere of the [2Fe–2S] cluster of the Rieske protein from spinach and the attribution of *g*-tensor to molecular axes as discussed in the text. Ser 130 has been observed to influence the redox potential of the cluster via hydrogen interactions with the acid-labile bridging sulfur.

It was thus not before the resolution of the 3D structures of proteolytic soluble fragments of the mitochondrial and plastidic Rieske proteins (*115*, *116*) that the ligands to the Rieske cluster were unambiguously assigned. These structures show the 2Fe2S cluster to be asymmetrically ligated by two cysteines to the redox inactive high-spin Fe^{3+} located toward the interior of the protein and by two surface-exposed histidines binding to the "outer" iron atom, which undergoes the change in valence from high-spin Fe^{3+} to high-spin Fe^{2+} (Fig. 4; see also (*102*, *117*)). A correlation of the X-ray crystallographic structure of mitochondrial cytochrome bc_1 complex (*113*) and two-dimensionally ordered EPR (*118*) indicates that g_x is collinear with the Fe–Fe vector (see Fig. 4), an attribution that has already been discussed by Bertrand *et al.* (*102*) and Link and Iwata (*119*), but that disagrees with the assumptions made in the Q-band ENDOR study by Gurbiel *et al.* (*109*).

C. Structure and Sequence Comparisons

Sequence comparisons of Rieske proteins from various species prior to the cystal structures (*120*, *121*) noted a high degree of conservation in the C-terminal part of the protein, that is, the segment including

the cluster binding motifs. Concerning the N-terminal two-thirds of the sequence, two classes represented by the plastidic/cyanobacterial and mitochondrial/proteobacterial proteins, respectively, could be distinguished with only scant homologies between the two families. Crystal structures of a mitochondrial (*115*) and a plastid (*116*) Rieske protein (or more specifically, the water-soluble domains thereof) have rationalized these findings. The Rieske proteins were seen to contain two domains; a cluster binding C-terminal subdomain, which is almost identical in the proteins from both families; and a large (mostly N-terminal) domain showing only low structural similarity (Fig. 5). Carrell *et al.* (*116*) have presented a sequence comparison between the two families based on the available structural information. A condensed version of this sequence comparison is represented in Fig. 6.

In addition to the b_6f and bc_1 Rieske proteins, we have included the available sequences from two other photosynthetic phyla (see phylogenetic tree in Fig. 1b); from green sulfur bacteria (*105*) and firmicutes (*122*) (note that the shown sequence is from a nonphotosynthetic representative of the firmicutes). The sequence comparison demonstrates that the green sulfur bacterial protein closely resembles the mitochondrial representative with respect to the folding pattern of the large N-terminal domain, whereas the firmicute Rieske protein appears to belong to the b_6f class (Fig. 6). These findings are in line with the topology of the phylogenetic tree shown in Fig. 1b. Considering only the photosynthetic species of the eubacteria, a divergence into the two different types of N-terminal domains seems to have occurred at the level of the branching-off of the cyanobacterial/firmicute phylum. Phylogenetically more distant Rieske proteins, such as those of the respiring eubacterium *Aquifex* (*123*) or the archaebacterium *Sulfolobus* (*100*), may well again have different folding patterns in this domain. From the available sequence information, we would not dare to attribute them to one of the two groups shown in Fig. 6.

D. A Unique Functional Mechanism Involving the Rieske Protein

X-ray structures of mitochondrial bc_1 complexes from three different sources (*113*, *124*, *125*) have found the *b*- and *c*-type hemes at roughly identical positions, whereas the Rieske protein was seen in different places as a function of crystal space group and presence or absence of inhibitors of the enzyme. This fact was interpreted to suggest a long-range conformational movement of the Rieske protein during turnover of the complex. The range of observed positions of the Rieske protein indicated that the soluble domain can move like a

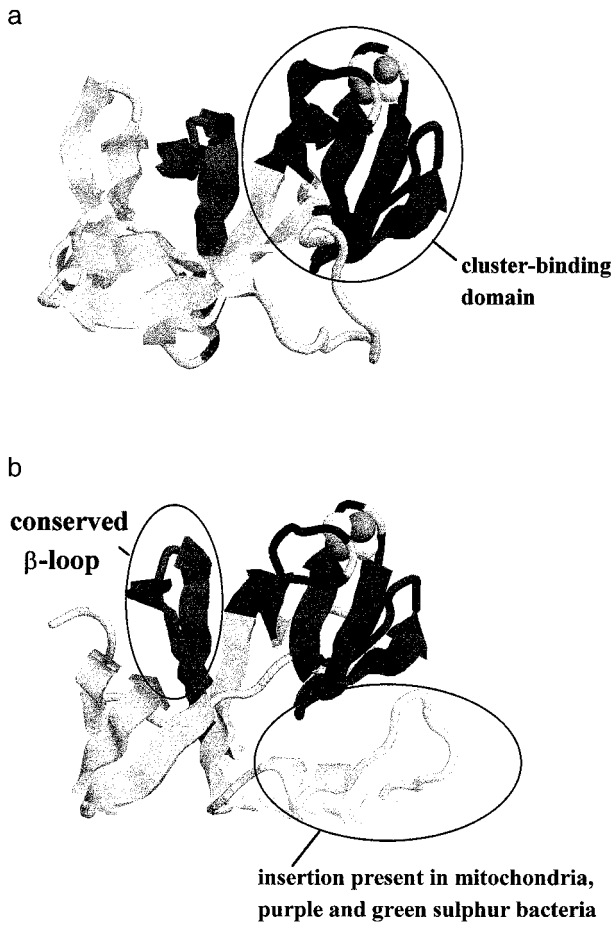

FIG. 5. Structural comparison of the water-soluble fragments of the Rieske proteins from (a) spinach chloroplasts and (b) beef heart mitochondria. Conserved and variable regions are highlighted and the conserved β-loop discussed in Fig. 6 is denoted by darker gray on the rear of the molecules.

pump head, shuttling electrons from the substrate-binding ("Q_o-") site close to the b_L-heme onto cytochrome c_1 (*113*, *125*). Stimulated by the crystallographic results, differing conformations of the Rieske protein have also been observed by EPR on two-dimensionally ordered samples (*118*), removing doubts as to whether the observed variability in positions might reflect stabilization of nonphysiological conformations due to crystal contacts.

The Rieske protein in the cytochrome bc_1 complex thus represents

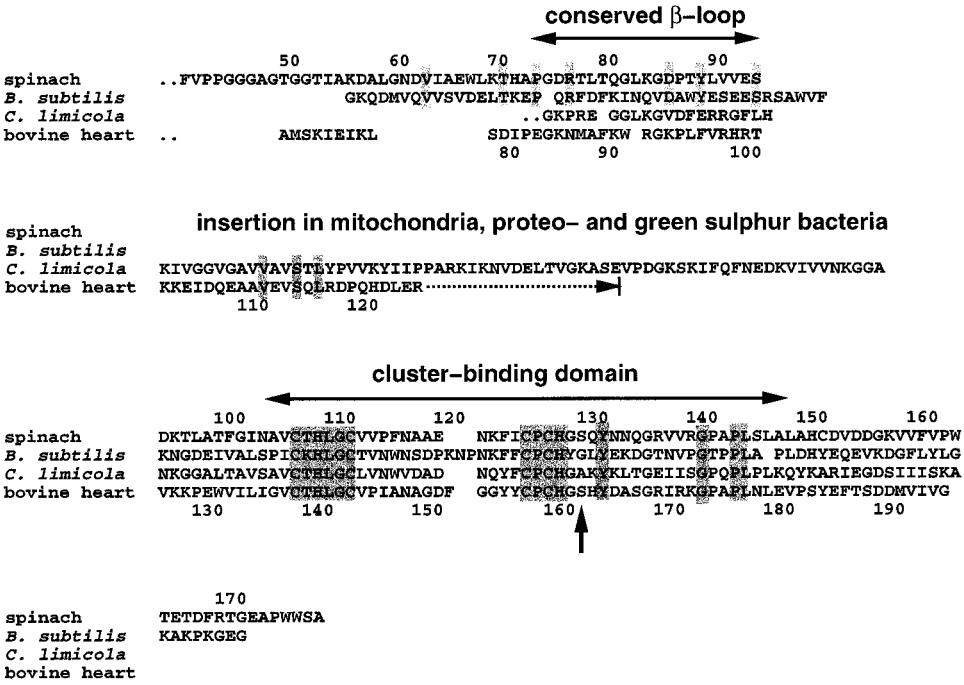

FIG. 6. Sequence comparisons of Rieske proteins from spinach chloroplasts, beef heart mitochondria, green sulfur bacteria, and firmicutes. The extended insertion of proteobacterial Rieske proteins as compared to the mitochondrial one is indicated by a dotted arrow. The redox-potential-influencing Ser residue is marked by a vertical arrow. The top and the bottom sequence numberings refer to the spinach and bovine proteins, respectively. Fully conserved residues are marked by dark shading, whereas the residues conserved in the b6f-group are denoted by lighter shading.

the first example of intracomplex electron shuttling based on domain movement rather than on outer-shell electron transfer through a fixed scaffolding of redox centers (*126*, *127*). EPR measurements on Rieske clusters from phylogenetically distant species (including archaebacteria) show that the movement of the Rieske protein is conserved through the evolution of cytochrome *bc* complexes (*128*), underscoring the functional importance of this mechanism for turnover of cytochrome *bc* complexes.

E. REDUCTION POTENTIALS AND THEIR pH DEPENDENCE

The Rieske clusters observed in cytochrome *bc* complexes from "traditional" sources (i.e., mitochondria, proteobacteria, plastids, and cy-

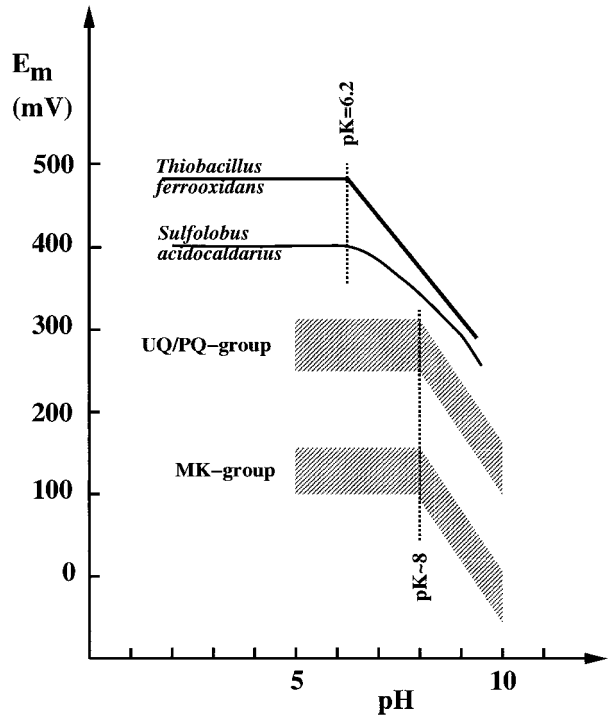

FIG. 7. Schematic comparison of the E_m–pH curves determined from various Rieske centers as described in the text.

anobacteria) titrate in the vicinity of 300 mV (vs SHE). Since the early 1980s, however, a number of Rieske centers with significantly lower E_m values have been reported, such as those from *Bacillus alkalophilus* (*129*), *Thermus thermophilus* (*130*), *Chloroflexus aurantiacus* (*95*), *Bacillus* PS3 (*131*), *Bacillus firmus* (*132*), *Heliobacterium chlorum* (*98*), and *Chlorobium limicola* (*96*, *97*).

All these latter centers were seen to titrate at around 150 mV, that is, some 150 mV lower than the "traditional" centers, and thus form a separate subclass of this type of redox proteins (see Fig. 7). Since similar downshifts were observed for almost all redox components in the mentioned species (for a compilation, see (*133*), it is generally assumed that the differences between the two groups represent an adaptation to the difference in E_m value of the quinone pool, which is plastoquinone(PQ)/ubiquinone(UQ) ($E_{m,7} \sim 100$ mV) in the "traditional" species and menaquinone (MK) ($E_{m,7} \sim -70$ mV) in the other organisms mentioned.

The difference in E_m values between the PQ/UQ and MK classes of Rieske centers represents a rare case in bioinorganic chemistry where such a shift in potential can be pinned down to a single amino acid residue. The high-resolution structure of the mitochondrial Rieske fragment showed the hydroxyl group of a serine residue two positions upstream from the second cluster-ligating histidine to form a hydrogen bridge with one of the bridging sulfur atoms of the cluster (Fig. 4). This hydrogen bridge can be expected to withdraw electron density from the cluster, that is, to raise its midpoint potential. Intriguingly, in all available sequences of Rieske proteins belonging to the MK class, this serine is replaced by a residue that will not support hydrogen-bond interactions (Fig. 6). The crucial influence of this hydrogen bond was subsequently confirmed via exchange of the serine by site-specific mutagenesis resulting in a drop of 130 mV in the E_m of the Rieske cluster (*134*, *135*).

As early as 1976, Prince and Dutton (*94*) showed that the E_m values of the mitochondrial and proteobacterial Rieske centers decrease above pH 8, indicating the involvement in the redox transition of a deprotonatable group on the oxidized form of the cluster. A similar p*K* value of about 8 was subsequently found for Rieske proteins from both the PQ/UQ and the MK classes (*97*, *130–132*, *136–138*). It was furthermore shown that the implication of two protons rather than one (*131*) with differing p*K* values (*138*) can be distinguished above pH 8.

These two redox-linked protons were tentatively attributed to the N^{ε}-protons of the cluster-ligating histidine residues (*130*, *131*, *137*). Although this attribution appears likely in the light of the structure, so far no experimental evidence substantiating this hypothesis is available.

To date, only two exceptions to the "p*K* of 8" rule have been found; the Rieske protein from *Sulfolobus acidocaldarius* (*139*) and that from *Thiobacillus ferrooxidans* (*140*). In both cases, a first p*K* is observed in the vicinity of 6 (Fig. 7). The fact that *Sulfolobus* and *Thiobacillus* are phylogenetically almost as distant as they can possibly be, but share acidophilic growth conditions (medium-pH of 2), indicates that the p*K*, which is lower by 2 pH units in *Sulfolobus* and *Thiobacillus*, reflects adaptation. In the absence of structural information for the two acidophilic Rieske proteins, the molecular modifications resulting in this p*K* shift are difficult to guess. The absence of sequence data for the *Thiobacillus* protein furthermore precludes a comparative approach. It seems likely, however, that the solvent-exposed histidine ligands to the cluster will become slightly more bur-

ied by aromatic residues as has been observed for a similarly exposed histidine (serving as a copper ligand) in the blue copper protein rusticyanin from *Thiobacillus* (*141*). These structural modifications are considered to induce strong shifts in p*K* value. The analogy with the small blue copper proteins may furthermore provide a rationale for the necessity of such a p*K* shift. Since in both UQ/PQ and MK systems, these p*K* values are well above the operating pH of the enzymes, a functional presure to downshift the p*K* values seems unlikely. However (in addition to the stability problem concerning the "acid-labile" bridging sulfurs), the partial histidine-ligation of the Rieske center may render this 2Fe2S cluster susceptible to breakage of the ligand–metal bond due to protonation of the histidine(s), just as had been demonstrated for the case of plastocyanin (*142*). Hampered access of solvent protons to the histidine ligands may stabilize the ligand–metal bond and render it tolerant to the low ambient pH. This strategy obviously allows rusticyanin to survive exposure to pH 2, that is, pH values where ordinary small blue copper proteins would have been entirely transformed to apoprotein.

VII. Evolutionary Remarks

Studies (see, e.g., (*101*)) indicate that photosynthesis originated after the development of respiratory electron transfer pathways (*99*, *143*). The photosynthetic reaction center, in this scenario, would have been created in order to enhance the efficiency of the already existing electron transport chains, that is, by adding a light-driven cycle around the cytochrome *bc* complex. The Rieske protein as the key subunit in cytochrome *bc* complexes would in this picture have contributed the first iron–sulfur center involved in photosynthetic mechanisms (since on the basis of the present data, it seems likely to us that the first photosynthetic RC resembled RCII, i.e., was devoid of iron–sulfur clusters).

RCII may subsequently have been transformed into RCI by formation of the F_x cluster and eventually the capturing of a soluble 2[4Fe–4S] protein as an RC-associated subunit. These additions would have allowed electrons to leave the space of the membrane and serve for reductive processes in the dark reactions of photosynthesis. Our present knowledge concerning distribution of HiPIPs among species indicate that this electron carrier would have been invented only lately within the branch of the proteobacteria. The evolutionary driving

forces favoring replacement of small blue copper proteins or cytochromes by HiPIP remains something of a mystery at present.

Acknowledgments

We thank P. Bertrand, M. Bruschi, F. Guerlesquin, B. Guigliarelli, R. Kappl, M. Hippler, J. Hüttermann, D. Lemesle-Meunier, U. Mühlenhoff, A. W. Rutherford, C. L. Schmidt, A. Schricker, and P. Sétif for stimulating discussions and for communicating results prior to publication.

References

1. Mortenson, L. E.; Valentine, R. C.; Carnahan, J. E. *Biochem. Biophys. Res. Commun.* **1962,** *7,* 448.
2. Tagawa, K.; Arnon, D. I. *Nature* **1962,** *195,* 537.
3. Matsubara, H.; Saeki, K. *Adv. Inorg. Chem.* **1992,** *38,* 223.
4. Malkin, R.; Bearden, A. J. *Proc. Natl. Acad. Sci USA* **1971,** *68,* 16.
5. Malkin, R.; Aparicio, P.-J. *Biochem. Biophys. Res. Commun.* **1975,** *63,* 1157.
6. Cammack, R.; Ryan, M. D.; Stewart, A. C. *FEBS Lett.* **1979,** *107,* 422.
7. Olsen, G. J.; Woese, C. R.; Overbeek, R. *J. Bact.* **1994,** *176,* 1.
8. Cammack, R. *Adv. Inorg. Chem.* **1992,** *38,* 281.
9. Bertini, I.; Ciurli, S.; Luchinat, C. *Structure and Bonding* **1995,** *83,* 1.
10. Paraskeva, E.; Hentze, M. W. *FEBS Letters* **1996,** *389,* 40.
11. Bruschi, M.; Guerlesquin, F. *FEMS Microbiol. Rev.* **1988,** *54,* 155.
12. Arendsen, A. F.; Schalk, J.; Van Dongen, W. M. A. M.; Hagen, W. R. *Eur. J. Biochem.* **1995,** *231,* 352.
13. Knaff, D. B.; Hirasawa, M. *Biochim. Biophys. Acta* **1991,** *1056,* 93.
14. Feiler, U.; Hauska, G. In "Anoxygenic Photosynthetic Bacteria"; Blankenship, R. E.; Madigan, M. M.; and Bauer, C. E., Eds.; Kluwer Acad. Publ.: Dordrecht, 1995; pp. 665–685.
15. Buchanan, B. B.; Evans, M. C. W. *Biochim. Biophys. Acta* **1969,** *180,* 123.
16. Buchanan, B. B.; Matsubara, H.; Evans, M. C. W. *Biochim. Biophys. Acta* **1969,** *189,* 46.
17. Rao, K. K.; Matsubara, H.; Buchanan, B. B.; Evans, M. C. W. *J. Bact.* **1969,** *100,* 1411.
18. Schricker, A. 1997, Soluble electron transport proteins in *Heliobacillus mobilis*, Diploma Thesis, University of Freiburg/FRG.
19. Høj, P. D.; Svendsen, I.; Scheller, H. V.; Møller, B. L. *J. Biol. Chem.* **1987,** *262,* 12676.
20. Wynn, R. M.; Malkin, R. *FEBS Lett.* **1988,** *229,* 193.
21. Oh-oka, H.; Itoh, S.; Sacki, K.; Takahashi, Y.; Matsubara, H. *Plant. Cell. Physiol.* **1991,** *32,* 11.
22. Oh-Oka, H.; Takahashi, Y.; Kuriyama, K.; Saeki, K.; Matsubara, H. *J. Biochem.* **1988,** *103,* 962.
23. Dunn, P. P. J.; Gray, J. C. *Plant Mol. Biol.* **1988,** *11,* 311.

24. Bentrop, D.; Bertini, I.; Luchinat, C.; Nitschke, W.; Mühlenhoff, U. *Biochemistry* **1997,** *36,* 13629.
25. Schubert, W.-D.; Klukas, O.; Krauss, N.; Saenger, W.; Fromme, P.; Witt, H. T. *J. Mol. Biol.* **1997,** *272,* 741.
26. Golbeck, J. H.; Bryant, D. A. In "Current topics in Bioenergetics"; Lee, C. P., Ed.; Academic Press: New York; 1992; Vol. 16, p. 83.
27. Brettel, K. *Biochim. Biophys. Acta* **1997,** *1318,* 322.
28. Heathcote, P.; William-Smith, D. L.; Sihra, C. K.; Evans, M. C. W. *Biochim. Biophys. Acta* **1978,** *503,* 333.
29. Zhao, J.; Li, N.; Warren, P. V.; Golbeck, J. H.; Bryant, D. A. *Biochemistry* **1992,** *31,* 5093.
30. Jennings, J. V.; Evans, M. C. W. *FEBS Lett.* **1977,** *75,* 33.
31. Nitschke, W.; Feiler, U.; Rutherford, A. W. *Biochemistry* **1990,** *29,* 3834.
32. Hager-Braun, C.; Jarosch, U.; Hauska, G.; Nitschke, W.; Riedel, A. *Photosynth. Res.* **1997,** *51,* 127.
33. Illinger, N.; Xie, D.-L.; Hauska, G.; Nelson, N. *Photosynth. Res.* **199 ,** *38,* 111.
34. Büttner, M.; Xie, D.-L.; Nelson, H.; Pinther, W.; Hauska G.; Nelson, N. *PNAS* **1992,** *89,* 8135.
35. Fujii, T.; Hata, Y.; Wakaji, I.; Tanaka, N.; Oshima, T. *Nature Structural Biology* **1996,** *3,* 834.
36. Kissinger, C. R.; Sieker, L. C.; Adman, E. T.; Jensen, L. H. *J. Mol. Biol.* **1991,** *219,* 693.
37. Prince, R. C; Gest, H.; Blankenship, R. E. *Biochim. Biophys. Acta* **1985,** *810,* 377.
38. Nitschke, W.; Sétif, P.; Liebl, U.; Feiler, U.; Rutherford, A. W. *Biochemistry* **1990,** *29,* 11079.
39. Fischer, N.; Setif, P.; Rochaix, J.-D. *Biochemistry* **1997,** *36,* 93.
40. Bertini, I.; Briganti, F.; Luchinat, C.; Messori, L.; Monnanni, R.; Scozzafava, A; Vallini, G. *Eur. J. Biochem.* **1992,** *204,* 831.
41. Huber, J. G.; Gaillard, J.; Moulis, J. M. *Biochemistry* **1995,** *34,* 194.
42. Moulis, J. M.; Sieker, L. C.; Wilson, K. S.; Dauter, Z. *Protein Sci.* **1996,** *5,* 1765.
43. Kamlowski, A.; van der Est, A.; Fromme, P.; Stehlik, D. *Biochim. Biophys. Acta* **1997,** *1319,* 185.
44. Diaz-Quintana, A.; Leibl, W.; Bottin, H.; Sétif, P. *Biochemistry* **1998,** *37,* 3429.
45. Fischer, N.; Hippler, M.; Sétif, P.; Jacquot, J.-P.; Rochaix, J.-D. *EMBO J.* **1998,** *17,* 849.
46. Evans, M. C. W.; Sihra, C. K.; Bolton, J. R.; Cammack, R. *Nature* **1975,** *259,* 668.
47. Evans, M. C. W.; Sihra, C. K.; Cammack, R. *Biochem. J.* **1977,** *162,* 75.
48. Georgiadis, M. M.; Komiya, H.; Chakrabatti, P.; Woo, D.; Kornne, J. J.; Rees, D. C. *Science* **1992,** *257,* 1653.
49. Webber, A. N.; Malkin, R. *FEBS Lett.* **1990,** *264,* 1.
50. Liebl, U.; Mockensturm-Wilson, M.; Trost, J. T.; Brune, D. C.; Blankenship, R. E.; Vermaas, W. F. J. *Proc. Natl. Acad. Sci. USA* **199 ,** *90,* 7124.
51. Smart, L. B.; Warren, P. V.; Golbeck, J. H.; McIntosh, L. *Proc. Natl. Acad. Sci. USA* **199 ,** *90,* 1132.
52. Warren, P. V.; Smart, L. B.; McIntosh, L.; Golbeck, J. H. *Biochemistry* **199 ,** *32,* 4411.
53. Webber, A. N.; Gibbs, P. B.; Ward, J. B.; Bingham, S. E. *J. Biol. Chem.* **199 ,** *268,* 12990.
54. Golbeck, J. H. *Proc. Natl. Acad. Sci USA* **199 ,** *90,* 1642.
55. Nitschke, W.; Mattioli, T. A.; Rutherford, W. A. In "Origins and Evolution of Bio-

logical Energy Conversion"; Baltscheffsky, H., Ed.; VCH Publishers: New York, 1996; pp. 177–203.
56. Kleinherenbrink, F. A. M.; Chiou, H.-C.; LoBrutto, R.; Blankenship, R. E. *Photosynth. Res.* **1994,** *41,* 115.
57. Tsukihara, T.; Fukuyama, K.; Nakamura, M.; Katsube, Y.; Tanaka, N.; Kakudo, M.; Wada, K.; Hase, T.; Matsubara, H. *J. Biochem.* (*Tokyo*) **1981,** *90,* 1763.
58. Sétif, P. Q. Y.; Bottin, H. *Biochemistry* **1994,** *33,* 8495.
59. Sétif, P. Q. Y.; Bottin, H. *Biochemistry* **1995,** *34,* 9059.
60. Bartsch, R. G. *Biochim. Biophys. Acta* **1991,** *1058,* 28.
61. Meyer, T. E. In "Anoxygenic Photosynthetic Bacteria"; Blankenship, R. E.; Madigan, M. T.; Bauer, C. E., Eds.; Kluwer Academic Publ.: Dordrecht, 1995; pp. 775–805.
62. Tedro, S. M.; Meyer, T. E.; Kamen, M. D. *J. Biol. Chem.* **1977,** *252,* 7826.
63. Peireira, M. M.; Antunes, A. M.; Nunes, O. C.; da Costa, M. S.; Teixeria, N. M. *FEBS. Lett.* **1994,** *352,* 327.
64. Cavazza, C.; Guigliarelli, B.; Bertrand, P.; Bruschi, M. *FEMS Microbiol. Lett.* **1995,** *130,* 193.
65. Meyer, T. E.; Przysiek, C. T.; Watkins, J. A.; Bhattacharyya, A.; Simondsen, R. P.; Cusanovich, M. A.; Tollin, G. *Proc. Natl. Acad. Sci. USA* **198 ,** *80,* 6740.
66. Mizrahi, I. A.; Meyer, T. E.; Cusanovich, M. A. *Biochemistry* **1980,** *19,* 4727.
67. Dus, K. J. *Biol. Chem* **197 ,** *248,* 7318.
68. Tedro, S. M.; Meyer, T. E.; Kamen, M. D. *Arch. Biochem. Biophys.* **1985,** *241,* 656.
69. Tedro, S. M.; Meyer, T. E.; Kamen, M. D. *J. Biol. Chem.* **1974,** *249,* 1182.
70. Tedro, S. M.; Meyer, T. E.; Kamen, M. D. *J. Biol. Chem.* **1976,** *251,* 129.
71. Tedro, S. M.; Meyer, T. E.; Kamen, M. D. *J. Biol. Chem.* **1979,** *254,* 1495.
72. Carter, C. W. Jr; Kraut, J.; Freer, S. T.; Xuong, N.-H.; Alden, R. A.; Bartsch, R. G. *J. Biol. Chem.* **1974,** *249,* 4212.
73. Rayment, I.; Wesenberg, G.; Meyer, T. E.; Cusanovich, M. A.; Holden, H. M. *J. Mol. Biol.* **1992,** *228,* 672.
74. Breiter, D. R.; Meyer, T. E.; Rayment, I.; Holden, H. M. *J. Biol. Chem.* **1991,** *266,* 18660.
75. Benning, M. M.; Meyer, T. E.; Rayment, I.; Holden, H. M. *Biochemistry* **1994,** *33,* 2476.
76. Banci, L.; Bertini, I.; Capozzi, F.; Carloni, P.; Ciurli, S.; Luchinat, C.; Piccioli, M. *J. Am. Chem. Soc.* **199 ,** *115,* 3431.
77. Bertini, I.; Ciurli, S.; Dikiy, A.; Luchinat, C. *J. Am. Chem. Soc.* **199 ,** *115,* 12020.
78. Bertini, I.; Campos, A. P.; Luchinat, C.; Teixeira, M. J. *J. Inorg. Biochem.* **199 ,** *52,* 227.
79. Cowan, J. A.; Lui, S. M. *Adv. Inorg. Chem.* **1998,** *45,* 313.
80. Antanaitis, B. C.; Moss, T. H. *Biochim. Biophys. Acta* **1975,** *405,* 262.
81. Dunham, W. R.; Hagen, W. R.; Fee, J. A.; Sands, R. H.; Dunbar, J. B.; Humblet, C. *Biochim. Biophys. Acta* **1991,** *1079,* 253.
82. Kappl, R.; Ciurli, S.; Luchinat, C.; Hüttermann, J. *J. Am. Chem. Soc.* **1998,** in press.
83. Schoepp, B.; Parot, P.; Menin, L.; Gaillard, J.; Richaud, P.; Verméglio, A. *Biochemistry* **1995,** *34,* 11736.
84. Hochkoeppler, A.; Kofod, P.; Zannoni, D. *FEBS Lett.* **1995,** *375,* 197.
85. Hochkoeppler, A.; Zannoni, D.; Ciurli, S.; Meyer, T. E.; Cusanovich, M. A.; Tollin, G. *Proc. Natl. Acad. Sci. USA* **1996,** *93,* 6998.
86. Menin, L.; Schoepp, B.; Parot, P.; Verméglio, A. *Biochemistry* **1997,** *36,* 12183.

87. Menin, L.; Gaillard, J.; Parot, P.; Schoepp, B.; Nitschke, W.; Verméglio, A. *Photosynth. Res.* **1998,** *55,* 343.
88. Osyczka, A.; Yoshida, M.; Nagashima, K. V. P., Shimada, K.; Matsuura, K. *Biochim. Biophys. Acta* **1997,** *1321,* 93.
89. Schoepp, B.; Riedel, A.; Verméglio, A.; Kappl, R.; Nitschke, N. Submitted.
90. Rieske, J. S.; Maclennan, D. H.; Coleman, R. *Biochem. Biophys. Res. Commun* **1964,** *15,* 338.
91. Malkin, R.; Aparicio, P.-J. *Biochem. Biophys. Res. Commun.* **1975,** *63,* 1157.
92. Hurt, E.; Hauska, G.; Malkin, R. *FEBS Lett.* **1981,** *134,* 1.
93. Krinner, M.; Hauska, G.; Hurt, E.; Lockau, W. *Biochim. Biophys. Acta* **1982,** *681,* 110.
94. Prince, R. C.; Dutton, P. L. *FEBS Lett.* **1976,** *65,* 117.
95. Zannoni, D.; Ingledew, W. J. *FEBS Lett.* **1985,** *193,* 93.
96. Knaff, D. B.; Malkin, R. *Biochim. Biophys. Acta.* **1976,** *430,* 244.
97. Brugna, M.; Albouy, D.; Nitschke, W. *J. Bact.* **1998,** *180,* 3719.
98. Liebl, U.; Rutherford, A. W.; Nitschke W. *FEBS Lett.* **1990,** *261,* 427.
99. Nitschke, W.; Mühlenhoff, U.; Liebl, U. In "Photosynthesis"; Raghavendra, A. S., Ed.; Cambridge Univ. Press: UK, 1998; pp. 285–304.
100. Schmidt, C. L.; Anemüller, S.; Schäfer, G. *FEBS Lett.* **1996,** *388,* 43.
101. Castresana, J.; Lübben, M.; Saraste, M. *J. Mol. Biol.* **1995,** *250,* 202.
102. Bertrand, P.; Guigliarelli, B.; Gayda, J.-P.; Beardwood, P.; Gibson, J. F. *Biochim. Biophys. Acta* **1985,** *831,* 261.
103. Blumberg, W. E.; Peisach, J. *Arch. Biochem. Biophys.* **1974,** *162,* 502.
104. Fee, J. A.; Findling, K. L.; Yoshida, T.; Hille, R.; Tarr, G. E.; Hearshen, D. O.; Dunham, W. R.; Day, E. P.; Kent, T. A.; Münck, E. *J. Biol. Chem.* **1984,** *259,* 124.
105. Schütz, M., Zirngibl, S.; le Coutre, J.; Büttner, M.; Xie, D.; Nelson, N.; Deutzmann, R.; Hauska, G. *Photosynth. Res.* **1994,** *39,* 163.
106. Cline, J. F.; Hoffman, B. M.; Mims, W. B.; La Haie, E.; Ballou, D.-P.; Fee, J. A. *J. Biol. Chem.* **1985,** *260,* 3251.
107. Telser, J.; Hoffman, B. M.; LoBrutto, R.; Ohnishi, T.; Tsai, A.-L.; Simpkin, D.; Palmer, G. *FEBS Lett.* **1987,** *214,* 117.
108. Nitschke, W.; Hauska, G. In "Progress in Photosynthesis Research"; Biggins, J., Ed.; Martinus Nijhoff Publishers: Dordrecht, The Netherlands, 1987; Vol. II, pp. 1–165.
109. Gurbiel, R. J.; Batie, C. J.; Sivaraja, M.; True, A. E.; Fee, J. A.; Hoffman, B. M.; Ballou, D. P. *Biochemistry* **1989,** *28,* 4861.
110. Britt, R. D.; Sauer, K.; Klein, M. P.; Knaff, D. B.; Kriauciunas, A.; Yu, C.-A.; Yu, L.; Malkin, R. *Biochemistry* **1991,** *30,* 1892.
111. Shergill, J. K.; Cammack, R. *Biochim. Biophys. Acta* **1994,** *1185,* 35.
112. Riedel, A.; Fetzner, S.; Rampp, M.; Lingens, F.; Liebl, U.; Zimmermann, J.-L.; Nitschke, W. *J. Biol. Chem.* **1995,** *270,* 30869.
113. Zhang, Z.; Huang, L.; Shumeister, V. M.; Chi, Y.-I.; Kim, K. K.; Hung, L.-W.; Crofts, A. R.; Berry, E. A.; Kim, S.-H. *Nature* **1998,** *392,* 677.
114. Davidson, E.; Ohnishi, T.; Atta-Asafo-Adjei, E.; Daldal, F. *Biochemistry* **1992,** *31,* 3342.
115. Iwata, S.; Saynovits, M.; Link, T. A.; Michel, H. *Structure* **1996,** *4,* 567.
116. Carrell, C. J.; Zhang, H.; Cramer, W. A.; Smith, J. L. *Structure* **1997,** *5,* 1613.
117. Guigliarelli, B.; Bertrand, P. This volume.
118. Brugna, M.; Rodgers, S.; Schricker, A.; Montoya, G.; Kazmeier, M.; Nitschke, W.; Sinning, I. **1998,** submitted.

119. Link, T. A.; Iwata, S. *Biochim. Biophys. Acta* **1996,** *1275,* 54.
120. Hauska, G.; Nitschke, W.; Hermann, R. G. *J. Bioenerg. Biomemb.* **1988,** *20,* 211.
121. Furbacher, P. N.; Tae, G.-S.; Cramer, W. In "Origin and Evolution of Biological Energy Conversion"; Baltscheffsky, H., Ed.; VCH Publishers: New York, 1996; p. 221.
122. Yu., J.; Hederstedt, L.; Piggot, P. J. *J. Bact.* **1995,** *177,* 6751.
123. Deckert, G.; Warren, P. V.; Gaasterland, T.; Young, W. G.; Lennox, A. L.; Graham, D. E.; Overbeek, R.; Snead, M. A.; Keller, M.; Aujay, M.; Huber, R.; Feldman, R. A.; Short, J. M.; Olsen, G. Y.; Swanson, R. V. *Nature* **1998,** *392,* 353.
124. Xia, D.; Yu, C.-A.; Kim, H.; Xia, J.-Z.; Kachurin, A. M.; Zhang, L.; Yu, L. Deisenhofer, J. *Science* **1997,** *277,* 60.
125. Iwata, S.; Lee, J. W.; Okada, K.; Lee, J. K.; Iwata, M.; Rasmussen, B.; Link, T. A.; Ramaswamy, S.; Jap, B. K. *Science* **1998,** *281,* 64.
126. Marcus, R. A.; Suttin, N. *Biochim. Biophys. Acta* **1985,** *811,* 265.
127. Moser, C. C.; Keske, J. N.; Warncke, K.; Farid, R. S.; Dutton, P. L. *Nature* **1992,** *355,* 796.
128. Schoepp, B.; Brugna, M.; Riedel, A.; Nitschke, W.; Kramer, D. M. *FEBS Lett.* submitted.
129. Lewis, R. J.; Prince, R. C.; Dutton, P. L.; Knaff, D. B.; Krulwich, T. A. *J. Biol. Chem.* **1981,** *256,* 10543.
130. Kuila, D.; Fee, J. A. *Biol. Chem.* **1986,** *261,* 2768.
131. Liebl, U.; Pezennec, S.; Riedel, A.; Kellner, E.; Nitschke, W. *J. Biol. Chem.* **1992,** *267,* 14068.
132. Riedel, A.; Kellner, E.; Grodzitzki, D.; Liebl, U.; Hauska, G.; Müller, A.; Rutherford, A. W.; Nitschke, W. *Biochim. Biophys. Acta* **199 ,** *1183,* 263.
133. Nitschke, W.; Kramer, D. M., Riedel, A.; Liebl, U. In "Photosynthesis: From Light to Biosphere"; Mathis, P., Ed.; Kluwer Acad. Publishers: Dordrecht, The Netherlands; Vol. I, p. 945.
134. Denke, E.; Merbitz-Zahradnik, T.; Hatzfeld, O. M.; Snyder, C. H.; Link, T.; Trumpower, B. L. *J. Biol. Chem.* **1998,** *273,* 9085.
135. Schröter, T.; Hatzfeld, O. M.; Gemeinhardt, S.; Korn, M.; Friedrich, T.; Ludwig, B.; Link, T. *Eur. J. Biochem* **1998,** *255,* 100.
136. Nitschke, W.; Joliot, P.; Liebl, U.; Rutherford, A. W.; Hauska, G.; Müller, A.; Riedel, A. *Biochim. Biophys. Acta* **1992,** *1102,* 266.
137. Link, T. A. *Biochim. Biophys. Acta* **1994,** *1185,* 81.
138. Link, T. A.; Hagen, W. R.; Pierik, A. J.; Assmann, C.; Von Jagow, G. *Eur. J. Biochem.* **1992,** *208,* 685.
139. Anemüller, S., Schmidt, C. L.; Schäfer, G.; Bill, E.; Trautwein, A. X.; Teixeira, M. *Biochem. Biophys. Res. Commun.* **1994,** *202,* 252.
140. Brugna, M.; Nitschke, W.; Lemesle-Meunier, D.; Schmidt, C. L. *J. Biol. Chem.* (submitted).
141. Botuyan, M. V.; Toy-Palmer, A.; Chung, J.; Blake II, R. C.; Beroza, P.; Case, D. A.; Dyson, H. J. *J. Mol. Biol.* **1996,** *263,* 752.
142. Guss, J. M.; Harrowell, P. R.; Murata, M.; Norris, V. A.; Freeman, H. C. *J. Mol. Biol.* **1986,** *192,* 361.
143. Castresana, J.; Saraste, M. *Trends Biochem. Sci.* **1995,** *20,* 443.

SIMPLE AND COMPLEX IRON–SULFUR PROTEINS IN SULFATE REDUCING BACTERIA

ISABEL MOURA, ALICE S. PEREIRA, PEDRO TAVARES, and JOSÉ J. G. MOURA

Departamento de Química e Centro de Química Fina e Biotecnologia, Faculdade de Ciências e Tecnologia, Universidade Nova de Lisboa, 2825-114 Monte de Caparica, Portugal

I. Introduction
II. Rubredoxin and Desulforedoxin
III. Desulfoferrodoxin
IV. Rubrerythrin
V. Ferredoxins
  A. Structures and Cluster Binding Motifs
  B. Electronic and Magnetic Properties of [3Fe–4S] and [4Fe–4S] Clusters
  C. Cluster Structural Interconversions and Synthesis of Heterometal Clusters
VI. Fuscoredoxin (Novel Fe–S Cluster)
VII. APS Reductase
VIII. Pyruvate–Ferredoxin Oxidoreductase
IX. Sulfite Reductase
X. Hydrogenase
  A. [Fe] Hydrogenases
  B. [NiFe] Hydrogenases
XI. Molybdopterin-Containing Enzymes in SRB
  A. Aldehyde Oxidoreductases
  B. Formate Dehydrogenase
  C. Nitrate Reductase
  D. Other Molybdenum-Containing Proteins in SRB
XII. Concluding Remarks
  A. Electron Transfer and Magnetic Interactions
References

I. Introduction

This chapter will focus on simple and complex iron–sulfur-containing proteins isolated from sulfate reducing bacteria (SRB), in order to review the following topics: types and distribution of proteins; metal clusters involved and their association with other centers and

Copyright 1999 by Academic Press.
All rights of reproduction in any form reserved.
0898-8838/99 $30.00

cofactors; cluster binding motifs; electronic and magnetic properties of the iron–sulfur clusters present; and cluster interconversions, including heterometal cluster formation. The text is organized starting from mononuclear to multinuclear Fe–S sites and then considers associations within these basic units, as well as with novel Fe–S structural arrangements. Finally, complex structures involving Fe–S basic units and other redox centers (flavin, heme, nickel, and molybdenum) are described. The basic units are indicated in Fig. 1.[1,2]

II. Rubredoxin and Desulforedoxin

Isolated from the cytoplasmic fractions of different *Desulfovibrio* strains (*1–4*), as well as other anaerobic bacteria (*5–8*), rubredoxins (Rd) are the simplest iron–sulfur proteins. Rubredoxins are small monomeric proteins (approx. 6 kDa) that contain a single iron atom per polypeptide chain. The iron atom is coordinated by four cysteine residues in a pattern common to all Rd proteins (see Fig. 1). This center can be stabilized in two redox states. In the oxidized form of the protein, the iron is in the paramagnetic high-spin ferric state. The UV/visible spectrum of the protein is dominated by cysteinyl-S $\rightarrow$ Fe(III) charge transfer transitions with absorption maxima at 493, 376, and 278 nm (typically $\varepsilon_{493} = 7$ $mM^{-1}cm^{-1}$/iron atom). In the oxidized state an EPR signal can be observed with resonances around $g = 4.3$ and 9.4, characteristic of a fully rhombic Kramer system with $S = \frac{5}{2}$. In accordance with this observation, the Mössbauer data show a magnetic spectrum that can be simulated with parameters typical of tetrahedral sulfur coordination ($E/D = \frac{1}{3}$) (*9*). The reduced state is obtained by treatment with weak reducing agents since the midpoint redox potential is reasonably high (-50 mV $< E_0 < 0$ mV). The Mössbauer spectrum of the reduced form is consistent with the presence of an iron atom in the high-spin ferrous state.

An exception to this coordination pattern is observed in *Desulfovibrio* (*D.*) *gigas* desulforedoxin (Dx). The protein is a 8-kDa homodimer where it was found that two of the coordinating cysteines were contiguous in the amino acid sequence (*10, 11*) (Fig. 2). This fact im-

[1] Most of the enzymes are built of homo or heteromultimeric structures. For the sake of simplification, in the figures only the structures of the monomeric unit of the homomultimer will be shown.

[2] Through the text *Desulfovibrio* will be referred to as *D.* and *Desulfovibrio desulfuricans* ATCC 27774 as *D. desulfuricans*.

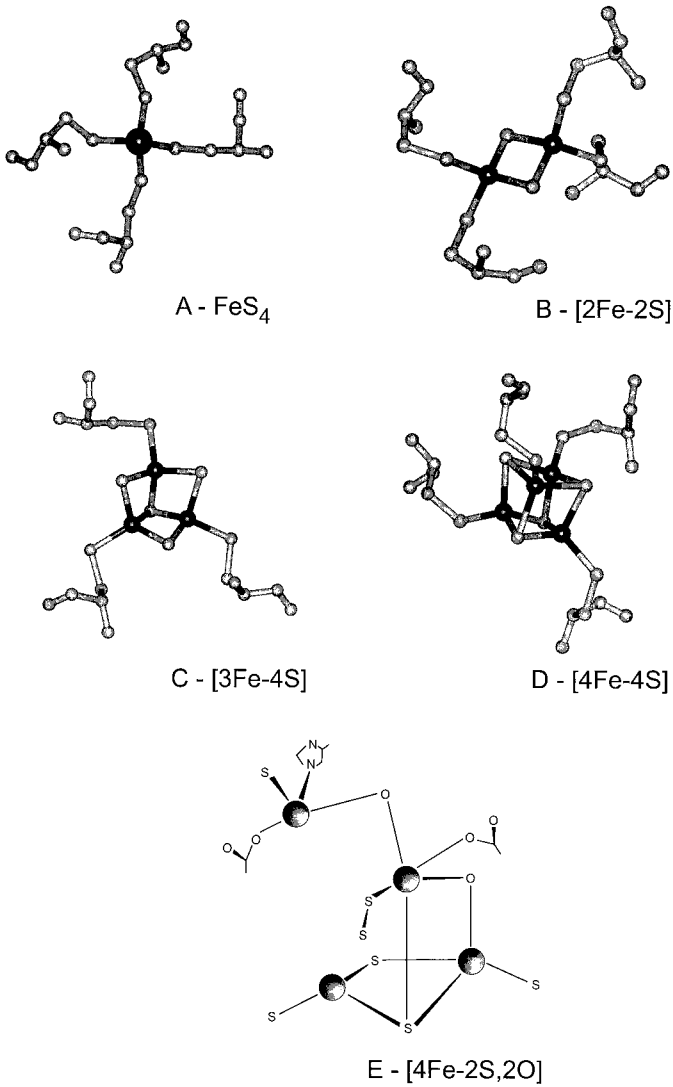

FIG. 1. Iron–sulfur clusters: basic building blocks. In most cases the iron is tetrahedrally coordinated by sulfur from cysteinyl residues (and labile sulfur). Variability on coordination is allowed (see text). A, Rubredoxin type FeS_4 (simplest cluster, no labile sulfur); B, plant-type ferredoxin [2Fe–2S]; C, bacterial ferredoxin [3Fe–4S]; D, bacterial ferredoxin and HiPIP [4Fe–4S]; E, novel cluster [4Fe–2S, 2O] ("hybrid cluster").

```
                        I  II      III IV
                        |  |       |  |
Rd D.v. M   X5-CTVCG-X28-CPICG-X9
Rd D.d.     X5-CNVCG-X21-CPVCG-X9
Rd D.g.     X5-CTVCG-X28-CPVCG-X9
Rd D.v. H   X5-CTVCG-X28-CPVCG-X9
Dx D.g.     X8-CELCG-X14-C--CG-X6
```

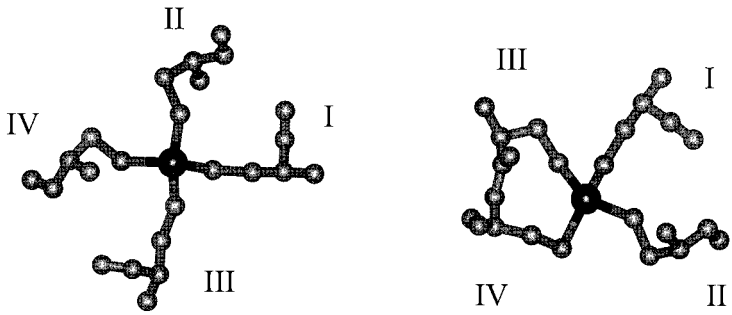

	I	II	III	IV
Rd				
I		111.4-114.8	110.9-112.8	104.7-106.2
II	111.4-114.8		100.8-104.5	109.2-114.1
III	110.9-112.8	100.8-104.5		111.8-113.4
IV	104.7-106.2	109.2-114.1	111.8-113.4	
Dx				
I		108.6-109.7	106.7-108.5	108.3-110.1
II	108.6-109.7		101.9-104.0	103.7-104.9
III	106.7-108.5	101.9-104.0		119.5-125.9
IV	108.3-110.1	103.7-104.9	119.5-125.9	

FIG. 2. Comparison of the metal site geometries and dihedral angles in rubredoxin and desulforedoxin. Sequence labels: *D.v.* M—*D. vulgaris* Miyazaki; *D.d.*—*Desulfovibrio desulfuricans* ATCC 27774; *D.g.*—*Desulfovibrio gigas*; *D.v.* H—*Desulfovibrio vulgaris* Hildenborough. In the table (*bottom*) are shown the dihedral angles (degrees) corresponding to ranges of values for both subunits of Dx and for three different Rd structures from the *Desulfovibrio* genus.

poses a distortion that changes the observed magnetic properties of the center. In the Dx case, the EPR spectrum shows resonances at $g = 1.8$, 4.1, 5.7, and 7.7 that are explained by a Kramers system with $E/D = 0.08$ (*12*). In this particular case Mössbauer spectroscopy proved to be an invaluable tool to determine the correct coordination (*13*). In both ferric and ferrous states, Mössbauer data are consistent with the distorted tetrahedral sulfur coordination. Because of the small size of the monomer, a total synthetic protein was prepared to produce a Dx-like polypeptide chain followed by chemical reconstitution of the iron center (*14*).

FIG. 3. The structure of *D. gigas* desulforedoxin monomer, showing the $Fe(RS)_4$ core and the tracing of the polypeptide chain.

While crystal structures of rubredoxins have been known since 1970 (for a full review on rubredoxins in the crystalline state, see Ref. (*15*)), only recently have both crystal and solution structures of Dx been reported (*16, 17*) (Fig. 3). The protein can be described as a 2-fold symmetric dimer, firmly hydrogen-bonded and folded as an incomplete β-barrel with the two iron centers placed on opposite poles of the molecule, 16 Å apart. Superimposition of Dx and Rd structures reveal that while some structural features are shared between these two proteins, significant differences in the metal environment and water structure exist. They can account for the spectroscopic differences described earlier.

Mutants of Dx were constructed, introducing Gly and Pro–Val sequences between Cys 28 and Cys 29 residues, altering the spacing between the adjacent coordinating cysteines. The properties of the mutated proteins are altered and the center became more close to that in rubredoxin (*18*).

Different metals are readily incorporated into rubredoxin-type centers after reconstitution of apoprotein with appropriate metal salts (*5*). Rd and Dx derivatives containing Ni and Co have been analyzed by UV-vis, NMR, EPR, electrochemistry, and MCD (*13, 19–22*). ^{57}Fe replacement has been used for Mössbauer studies and an indium de-

rivative used for phase resolution in X-ray structural determination of Dx (*13, 16*). Substitution of the native iron by ^{113}Cd, ^{199}Hg, and Zn has been carried out for NMR studies. In particular the Zn derivatives of Dx and Rd have been exploited by 2D NMR (*23–25*). The 3D solution structure of ^{113}Cd Dx has been completely solved and a comparison of the solution structures of Fe, Zn, and ^{113}Cd derivatives made (*26*). The main conclusion was that the geometry at the metal site and the overall folding was not too much affected, but the hydrogen bonding was altered. The NMR study of ^{113}Cd substituted Rd, Dx, and Dx mutants, as well as Dfx-N-terminal constructs, indicates that the ^{113}Cd chemical shift is a quite sensitive tool to probe subtle geometric differences at the site (*27*).

It has always been assumed that these simple proteins act as electron-transfer proteins. This is also a fair conclusion if we take in account that different proteins were isolated in which the $Fe(RS)_4$ center is in association with other non-heme, non-iron-sulfur centers. In these proteins the $Fe(RS)_4$ center may serve as electron donor/acceptor to the catalytic site, as in other iron–sulfur proteins where [2Fe–2S], [3Fe–4S], and [4Fe–4S] clusters are proposed to be involved in the intramolecular electron transfer pathway (see the following examples).

III. Desulfoferrodoxin

First isolated from *D. desulfuricans* (*28*), desulfoferrodoxin (Dfx) was also isolated from *D. vulgaris* (*29*). Dfx is a 28-kDa homodimer that contains two monomeric iron centers per protein. These iron centers were extensively characterized by UV/visible, EPR, resonance Raman, and Mössbauer spectroscopies (*30*). The data obtained were consistent with the presence of one Dx-like center (center I) and another monomeric iron center with higher coordination number (penta or hexacoordinate), with O/N ligands and one or two cysteine residues (center II). Comparison of known Dfx sequences led to the conclusion that only five cysteines were conserved, and that only one of them could be a ligand of center II (*31*).

The protein can be purified in two distinct redox states: the fully oxidized form, called the gray form, and the half-reduced form, called the pink form (*30*). In the gray form both iron centers are in the high-spin ferric state ($S = \frac{5}{2}$). In addition to the signals associated with the Dx-like center, the gray form of Dfx exhibits a signal at $g = 4.3$ and a shoulder at $g = 9.6$, indicating a high-spin ferric state with $E/D \approx$

$\frac{1}{3}$ attributed to the oxidized center II. The Dx-like center dominates the absorption spectrum. However, in the gray form additional peaks at 635 and 335 nm were observed. The visible band at 635 nm, responsible for the gray color of the protein, was assigned to a cysteinyl-S $\rightarrow$ Fe(III) charge transfer transition localized on center II. Upon one-electron reduction, center II becomes high-spin ferrous and the protein retains the pink color due to the oxidized center I.

Redox titrations of the gray form monitored by optical spectroscopy indicate midpoint potentials of approx. +4 and +240 mV for centers I and II, respectively.

The Dfx 3D structure has been determined by MAD phasing and refinement to 1.9 Å resolution (*32*). As expected, the structure shows a homodimer that contains two iron centers per monomer. The polypeptide chain is folded into two domains. Domain I is structurally similar to Dx and contains the $Fe(RS)_4$ center. Domain II has an iron center with square pyramidal coordination to four nitrogens from histidines as the equatorial ligands, and one sulfur from a cysteine as the axial ligand. Interestingly, a calcium atom (used in the crystallization process) was found at the dimer interface, possibly stabilizing the dimeric state. The function of Dfx is not known. However, this protein is not exclusive of the *Desulfovibrio* genus. DNA sequences have revealed that *Desulfoarculus baarsi* (*33, 34*), *Archaeoglobus fulgidus* (*35*), *Metanobacterium thermoautotrophicum* (*36*), and *Methanococcus jannaschii* (*37*) all contain Dfx.

IV. Rubrerythrin

Rubrerythrin (Rr) was first isolated in 1988 from cellular extracts of *D. vulgaris* Hildenborough (*38*), and later also found in *D. desulfuricans* (*39*). Rr is constituted by two identical subunits of 22 kDa and it was shown that each monomer contains one Rd-like center, $Fe(RS)_4$, and a diiron-oxo center similar to the ones found in methane monooxygenase (MMO) (*40, 41*) or ribonucleotide reductase (RNR-R2) (*42*). After aerobic purification, the UV-visible spectrum shows maxima at 492, 365, and 280 nm, and shoulders at 570 and 350 nm. This spectrum is similar to the ones observed for Rd proteins. From a simple subtraction of a typical Rd UV-vis spectrum (normalized to 492 nm) it is possible to show that the remainder of the spectrum (maxima at 365 nm and a shoulder at 460 nm) strongly resembles the spectrum of met-hemerythrin, another diiron-oxo containing protein.

The EPR spectrum of the as-isolated protein exhibits resonances at $g = 9.4$ and 4.3 as expected for a high-spin ferric Rd-like center. However, another rhombic signal can be observed with resonances at $g = 1.98$, 1.76 and 1.57. These g values, as well as the shape of the signals, are typical of diiron-oxo centers and can be attributed to a small percentage of half-reduced diiron centers. In this state one high-spin Fe(II) ($S = 2$) is antiferromagnetically coupled with a high-spin Fe(III) ($S = \frac{5}{2}$) to give rise to a system with $S = \frac{1}{2}$.

Strongly supporting this spectroscopic data, Mössbauer spectroscopy of the as-isolated Rr shows the presence of two types of iron centers: a magnetic component that can be well simulated by the parameters of Rd, and a diamagnetic component attributed to the diiron-oxo cluster and resulting from the antiferromagnetic coupling of the two irons.

Biochemical and spectroscopic studies performed on the native (*43*) and reconstituted (*44*) protein from *D. vulgaris* and on the *D. desulfuricans* native Rr (*39*) proved that each monomer contains one Rd-like center and one μ-oxo diiron center. From the analysis of the primary structure, a strong homology was found between the C-terminal of Rr and the *D. vulgaris* Rd sequence, suggesting that the $Fe(RS)_4$ center is, therefore, located in the C-terminal domain (*45, 46*). Also the N-terminal portion of the sequence contains two internally homologous sequences, each containing a Glu-X-X-His motif. Since these repetitive sequence motifs are found to provide carboxylate and histidine ligands to each diiron site in MMO and RNR-R2, it was suggested that these Glu-X-X-His motifs also provide ligands to the diiron-oxo cluster in Rr (*47*).

The midpoint redox potentials were estimated to be +230 mV (pH = 8.6) or +281 mV (pH = 7.0) for the Rd-like centers, and +339 and +246 mV (pH = 7.0) for the diiron-oxo center (*38, 43*). This is a surprising observation, since the normal redox potential of Rd centers is about 0 mV. All spectroscopic evidence points to the fact that the monomeric iron centers present in Rr are virtually identical to the ones found in Rd. Hence, it is reasonable to assume that the first coordination sphere of these centers cannot be held responsible for the 250 mV difference in the midpoint redox potentials.

In 1996, the 3D-structure of *D. vulgaris* Rr was published by deMaré and collaborators (*48*), and all the studies earlier published were proved to be correct. The protein is described as a tetramer of two-domain subunits (Fig. 4). Each subunit contains a domain characterized by a four-helix bundle surrounding a diiron-oxo site and a C-terminal rubredoxin-like $Fe(RS)_4$ domain (see Fig. 2). In this last do-

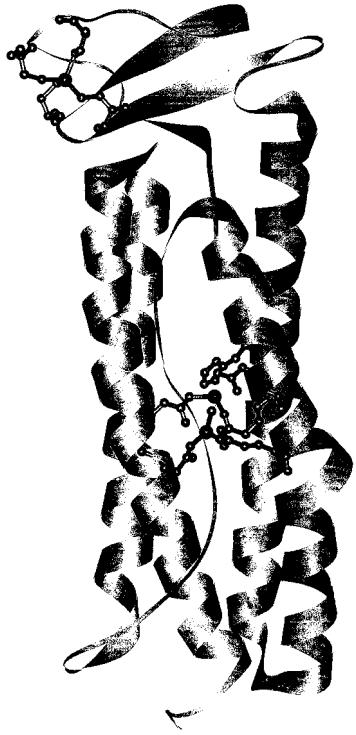

FIG. 4. The structure of *D. vulgaris* Rubrerythrin monomer, showing the $Fe(RS)_4$ core, the diiron-oxo cluster, and the tracing of the polypeptide chain. The presence of two distinct domains is striking.

main, some of the residues present in the vicinity of the $Fe(RS)_4$ center (Asn 160, His 179, and Ala 176) are nonconserved in Rd and appear to create a more polar and solvent-exposed environment around the center. This different environment is suggested to account for the unusually high midpoint redox potential observed. The diiron-oxo center is approximately octahedrally coordinated by two terminal carboxylates, one histidine, and three bridging carboxylates. Interestingly, the four-helix bundle of Rr closely resembles those found in ferritin (*49, 50*) and bacterioferritin subunits (*51*), suggesting a relationship among these proteins. This observation is even more relevant if we consider the fact that an *in vitro* ferroxidase activity was reported for Rr (*52*). It has been demonstrated that in human H-ferritin, diiron-oxo sites, similar to the one present in Rr, are intermediates in the mineralization process (*53*). However, ferritins are large protein mole-

cules composed of 24 subunits, forming a hollow sphere with a diameter of approximately 12 nm. This highly specialized structure can store up to 4500 iron atoms, an obvious contrast to the dimeric structure of Rr. So, unless more conclusive experimental data is obtained, it seems premature to attribute a role in the iron storage mechanism to Rr.

Finally, also isolated from *D. vulgaris* was another homodimeric protein (subunit molecular mass of 27 kDa) named nigerythrin (*43*). Spectroscopic characterization revealed that this protein is similar to Rr. The function of nigerythrin is also unknown. It should be noted that genes coding for two similar Rr proteins were also found in *Archaeoglobus fulgidus*.

V. Ferredoxins

Four distinct types of ferredoxins[3] are found in SRB, containing [3Fe–4S], [4Fe–4S], [3Fe–4S] + [4Fe–4S], and 2 × [4Fe–4S] clusters. A common structural feature shared by these centers is that each iron atom is tetrahedrally coordinated and contains bridging inorganic sulfur atoms. The terminal ligands for the clusters are in general cysteinyl sulfur (*54–58*) but other ligands containing O/N may be involved (i.e., aspartic acid or histidine can be a cluster ligand; see hydrogenase section). A close structural relationship is apparent between the [3Fe–4S] and the [4Fe–4S] clusters.

In particular, the study of SRB ferredoxins enables us to survey the different properties of simple iron–sulfur proteins, including electron transfer, flexibility in coordination chemistry, and ability to undergo cluster interconversions. Most of the observations can be extrapolated to more complex situations.

Seven ferredoxins are well characterized in SRB. Different SRB species have now been found to contain more than one type of ferre-

[3] Ferredoxins (Fd) are simple iron–sulfur proteins characterized by the presence of iron and sulfide (not necessarily in equimolar amounts), low molecular masses (≈6 kDa), preponderance of acidic and low content in aromatic amino acid residues, characteristic electronic spectra dominated by cysteinyl-S → Fe charge transfer transitions (300–400 nm region), and typical EPR signals observed in oxidized and/or reduced states. Three stable oxidation states, 3+, 2+, and 1+, have been observed for the [4Fe–4S] cluster. The 3+ and 2+ states are stable in high potential iron–sulfur proteins, while the 2+ and 1+ states are detected in bacterial ferredoxins and other 4Fe cluster-containing proteins (*59*). The clusters discovered in ferredoxins from SRB belong to this last category. Both the 3+ and 1+ states are paramagnetic with $S = \frac{1}{2}$. The 2+ state is diamagnetic.

doxin (*59*). Only [3Fe–4S] (1+, 0 oxidation states) and [4Fe–4S] (2+, 1+ oxidation states, bacterial ferredoxin-type) centers are found in the active sites of ferredoxins isolated from SRB.

The ferredoxins isolated from *D. gigas* have been quite extensively studied by different experimental approaches and spectroscopic techniques and will be used here as a reference system. Ferredoxin I (*D. gigas* FdI) and ferredoxin II (*D. gigas* FdII) (*60–62*) are composed of the same polypeptide chain (58 amino acids, 6 cysteines) (*63*). *D. gigas* FdI is a dimer and contains a single $[4Fe–4S]^{2+,1+}$, whereas the same monomeric unit of the tetrameric *D. gigas* FdII contains a single $[3Fe–4S]^{1+,0}$ cluster.

Two ferredoxins have been isolated from *Desulfomicrobium baculatum* (*Dsm. baculatum*) strain Norway 4 (*64, 65*). *Dsm. baculatum* ferredoxin I (59 amino acids, 6 cysteines) has one conventional $[4Fe–4S]^{2+,1+}$ cluster. *Dsm. baculatum* FdII, the most acidic, is very unstable toward oxygen exposure and contains $2 \times [4Fe–4S]^{2+,1+}$ cores in a polypeptide chain of 59 amino acids and 8 cysteines (*66, 67*).

Three ferredoxins were isolated and characterized from *D. africanus*. The proteins are dimers of subunits with a molecular mass of circa 6 kDa. *D. africanus* FdI contains a single $[4Fe–4S]^{2+,1+}$ center bound to a polypeptide structure of 60 amino acids with only 4 cysteines. This is the minimal requirement for [4Fe–4S] cluster binding. *D. africanus* FdII is a minor component, not so well characterized, and seems to contain a [4Fe–4S] center (*68, 69*). FdIII of this strain is a dimer containing 61 amino acids and 7 cysteine residues per subunit. The protein contains a $[3Fe–4S]^{1+,0}$ and a $[4Fe–4S]^{2+,1+}$ cluster (*70–72*).

Two ferredoxins were isolated and purified from *D. vulgaris* Miyazaki. FdI, the major form, contains two redox centers with distinct behavior and a high sequence homology to *D. africanus* FdIII (*73*). The protein is a dimer of a polypeptide chain of 61 amino acids with 7 cysteines. *D. vulgaris* Miyazaki FdII is a dimer of 63 amino acids, containing 7 cysteines but only one $[4Fe–4S]^{2+,1+}$ cluster (*73–75*).

From a related organism, *Desulforomonas acetoxidans*, a $2 \times [4Fe–4S]^{2+,1+}$ ferredoxin was isolated (*76*). Other ferredoxins are present, but not yet fully characterized, in the following SRB: *D. vulgaris* Hidenborough, *D. salexigens*, *D. desulfuricans*, *Dsm. baculatum* strain 9974, and *Desulfotomaculum* ((*77, 78*) and our unpublished results).

A. Structures and Cluster Binding Motifs

[3Fe–4S] *D. gigas* FdII structure is the only high-resolution crystallograph study performed in ferredoxins isolated from SRB (*56*)

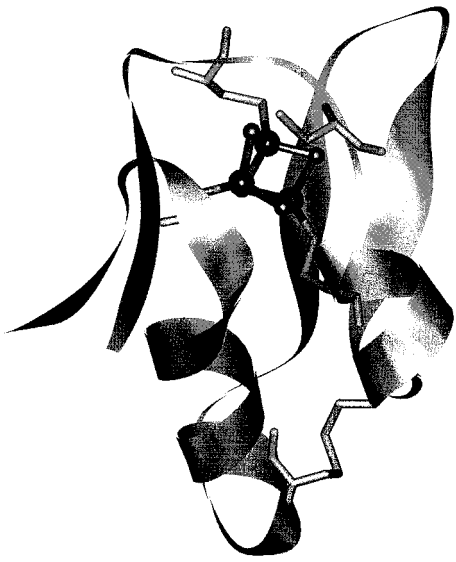

FIG. 5. The structure of *D. gigas* FdII monomer, showing the [3Fe–4S] core, the disulfide bridge, and the tracing of the polypeptide chain. Indicated in the lower part is Cys 11, not bound to the cluster, that is the ligand used for the structural switch from a tri- to a tetranuclear core (also involved in heterometal cluster formation).

(Fig. 5). There are no 3D-crystallographic data on [4Fe–4S] Fds isolated from this bacterial group. The X-ray structure analysis performed for *D. gigas* FdII (*56*) indicates that the cluster is bound to the polypeptide chain by three cysteinyl residues: Cys 8, Cys 14, and Cys 50. The residue Cys 11 (a potential ligand for a fourth site, if the cluster was a [4Fe–4S] cluster) is not bound and is tilted toward the solvent, away from the cluster. A disulfide bridge is present between Cys 18 and Cys 42 (connecting the remaining two cysteines of the four that bind a second iron sulfur core in two cluster containing Fd, i.e., *Peptococcus* (*P.*) *aerogenes* Fd). The lost of a second cluster is associated with the disappearance of Cys 41 and Cys 47. Since *Bacillus thermoproteolyticus* Fd does not have a disulfide bridge and has a folding similar to the *D. gigas* FdII, the disfulfide bridge does not seem to be a full requirement to maintain the overall structure. The 3D structure of FdII also revealed similarities to the general folding of that of 2 × [4Fe–4S] *P. aerogenes* Fd (*79*), [3Fe–4S] + [4Fe–4S] *Azotobacter vinelandii* FdI (*57, 80*), and [4Fe–4S] *Bacillus thermoproteolyticus* Fd (*54*). On the basis of sequence homology and secondary structure predictions, the chain fold in other [4Fe–4S] proteins was

predicted, including *D. gigas* FdI (*81*). An extended α-helix, found in *B. thermoproteolyticus* Fd, was proven to be present in *D. gigas* FdII and experimental evidence was given for its presence in *Dsm. baculatum* FdI, by 2D NMR (*82*). Preliminary crystallographic data were obtained for the [4Fe–4S] *Dsm. baculatum* FdI and a structural prediction made (*83*).

The [3Fe–4S] core is now considered an unique basic iron–sulfur core whose structure was determined in *D. gigas* FdII (*56, 84*) (as well as in aconitase (*85–87*) and *A. vinelandii* Fd (*57, 59, 80*)). The cluster in these proteins have Fe–Fe and Fe–S distances around 2.8 and 2.2 Å and the core described as a cuboidal geometry with one corner missing (Fe : S stoichiometry of 3 : 4).

The definitions of the cluster ligands of the [3Fe–4S] cluster and of the related structural features are quite useful to predict cluster types in other Fds of known sequence, as well as to determine the nature of the cluster coordinating atoms (and variability) and their control on the type and performances of the metal sites, in particular in terms of cluster stability, cluster interconversion capability, and acceptance of other metals at the cluster.

In *Desulfovibrio* ferredoxins a general binding motif can be outlined, taking into account the presence of only one [3Fe–4S], one or two [4Fe–4S] cores, the substitution of one cluster by a S–S bridge, or even the replacement of the second cysteinyl residue by an aspartic acid (as in *D. vulgaris* Miyazaki FdI and *D. africanus* FdIII), which can, in certain conditions, coordinate a fourth iron atom to build a [4Fe–4S] (*88*) (Fig. 6).

B. Electronic and Magnetic Properties of [3Fe–4S] and [4Fe–4S] Clusters

The magnetic and electronic properties of the *D. gigas* FdII [3Fe–4S] center were revealed by different and complementary spectroscopic techniques: EPR (*89*), Mössbauer (*90, 91*), resonance Raman (RR) (*92*), magnetic circular dichroism (*MCD*) (*93*), EXAFS (*94*), saturation magnetization (*95*), electrochemistry (*96*), and NMR (*97, 98*). The [4Fe–4S] center is also well characterized and surprising information has been obtained in relation to cluster interconversions and noncysteinyl coordination, as illustrated for *D. gigas* FdI and *D. africanus* FdIII, as well as the possibility of generating unusual reduced states.

The [3Fe–4S] cluster can be stabilized in two oxidation states, 1+ and 0. In the oxidized state the $[3Fe–4S]^{1+}$ cluster contains three

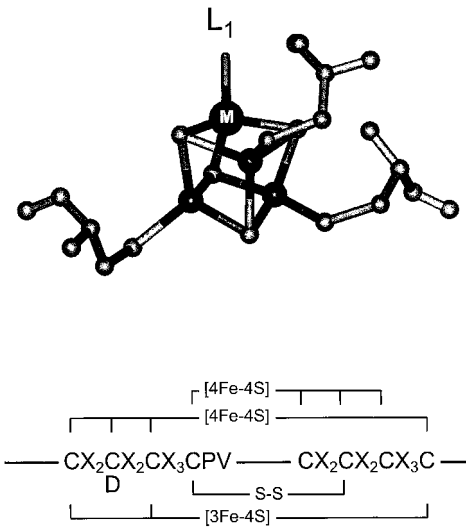

FIG. 6. A schematic view of the [3Fe–4S] and [4Fe–4S] cores, as versatile structures. The absence of one site leads to the formation of a [3Fe–4S] core. The cubane structure can incorporate different metals (in proteins, M = Fe, Co, Zn, Cd, Ni, Tl, Cs), and S, N, O may be coordinating atoms from ligands (L_1). The versatility can be extended to higher coordination number at the iron site and a water molecule can even be a ligand, exchangeable with substrate (as in the case of aconitase (*87*)). The most characteristic binding motifs are schematically indicated, for different situations: proteins accommodating [3Fe–4S], [4Fe–4S], [3Fe–4S] + [4Fe–4S], and [4Fe–4S] + [4Fe–4S] clusters. A disulfide bridge may replace a cluster site (see text).

high-spin ferric ions spin-coupled to form an $S = \frac{1}{2}$ state (*90, 99, 100*) and exhibits an isotropic EPR signal centered around $g = 2.02$ (*90*). Mössbauer spectra taken at $T > 40$ K exhibit one sharp quadrupole doublet with $\Delta E_Q = 0.54$ mm/s and $\delta = 0.27$ mm/s, typical of Fe^{3+} ions in a tetrahedral environment of thiolate ligands. The effective $S = \frac{1}{2}$ results from antiferromagnetic coupling of three high-spin ferric rubredoxin-type ions ($S_1 = S_2 = S_3 = \frac{5}{2}$) (*91*). Reduction by one electron yields a $[3Fe–4S]^0$ cluster ($E_m = -130$ mV, vs NHE) with integer spin ($S = 2$) (*68*) proved by MCD studies (*93*) and in agreement with the Mössbauer predictions leading to the detection of a $\Delta m_s = 4$ EPR transition, at around $g = 12$ (*91*). At 4.2 K and $H = 0$, the Mössbauer spectrum of the reduced cluster exhibits two quadrupole doublets with intensity ratios 2 : 1. The more intense doublet, representing two iron sites (site I), has $\Delta E_Q(I) = 1.47$ mm/s and $\delta(I) = 0.46$ mm/s. The second doublet (site II) has $\Delta E_Q(II) = 0.52$ mm/s and $\delta(II) = 0.32$ mm/s. The values obtained for site II suggest that the iron atom is in

the high-spin ferric state, similar to the iron sites in the oxidized FdII. The parameters of doublet I indicate a formal oxidation state between 2+ and 3+. The two iron atoms are in the oxidation level $Fe^{2.5+}$. The reduced core is an example of a mixed valence compound with one localized Fe^{3+} site (site II) and a delocalized iron pair. Spectroscopic evidence is consistent with the delocalized pair having a spin of $\frac{9}{2}$ coupled to the high-spin ferric ion forming a cluster spin of 2 (*91*). This is the simplest iron cluster to exhibit this equal sharing of an electron by more than one iron site: a feature in common with the [4Fe–4S] cluster.

A further two-electron reduction was indicated to occur in *D. gigas* FdII originating an all-ferrous trinuclear core (*96*), similar to the process previously studied by Armstrong and co-workers in *D. africanus* FdIII (*101, 102*). Electrochemical studies on this protein adsorbed with neomycin as an electroactive film on pyrolytic graphite edge showed that the $[3Fe–4S]^0$ can undergo a two-electron further reduction step at −720 mV, in a pH-dependent process. The observation of similar voltammetric waves in other 3Fe-containing proteins suggest that stabilization of an all-ferrous cluster may be a common feature of this cluster.

The redox potential of the $[3Fe–4S]^{+1,0}$ redox couple shows a wide variability (400 mV). These redox potentials are pH dependent (*103–106*), as are those linking lower oxidation levels, and so can be modulated by the medium. *D. africanus* FdIII is one of these examples where the conversion 0/−2 states is suggested to be a 2e-$3H^+$ process.

The [4Fe–4S] centers in *D. gigas* FdI (or reconstituted FdII or Fe^{2+} activated FdII; see later discussion) are indistinguishable (*107*). The center is diamagnetic in the oxidized state. Upon one-electron reduction, an EPR signal develops at $g = 1.91$, 1.94, and 2.07, typical of a [4Fe–4S] cluster in the 1+ state. The Mössbauer spectrum of the oxidized *D. gigas* FdI consists of two sharp quadrupole doublets (labeled I and II) with intensity 1:3, characteristics of a diamagnetic state ($S = 0$). The quadrupole splitting and isomer shift of doublet II are typical of a subsite of a [4Fe–4S] cluster in the 2+ state ($\Delta E_Q = 1.32$ mm/s, $\delta = 0.45$ mm/s). The doublets reflect inequivalent subsites of the $[4Fe–4S]^{2+}$ cluster. The reduced spectrum exhibits paramagnetic hyperfine structure (in agreement with the EPR active species detected, $S = \frac{1}{2}$). The Mössbauer data are almost identical to the one reported for [4Fe–4S] *B. polymyxa* Fd and could be fitted with the same set of parameters (*108*).

One-dimensional nuclear Overhauser effect (NOE), relaxation measurements in native *D. gigas* FdII, and analysis of temperature depen-

dence studies of the NMR signals due to one pair of β-CH_2 protons of cluster-bound cysteine were used to calculate the coupling constant between the iron sites (*97*). Moreover, the complementary use of the available X-ray crystallographic coordinates enabled specific assignment of Cys 50. A full structural assignment of the three cysteine ligands of the [3Fe–4S] core in *D. gigas* FdII was possible by 2D NMR methodology (*98*). In the absence of a crystallographic structure for *D. gigas* FdI, multidimensional NMR was used to identify the four cysteines that are cluster ligands. The presence of four pairs of geminal β-CH_2 protons for *D. gigas* FdI unambiguously proves the occupancy of the fourth site of the trinuclear complex and implied the coordination of Cys 11 at the Fe cluster (*98*).

^{1}H NMR 1D and 2D spectra on *D. gigas* FdII have allowed the determination of its solution structure (our unpublished results).

The two ferredoxins isolated from *Dsm. baculatum* were investigated by EPR spectroscopy (*67*). The $[4Fe–4S]^{2+,1+}$ center of FdI shows a well-defined rhombic EPR signal in the reduced form at low temperature with *g*-values at 1.902, 1.937, and 2.068. The as-isolated *Dsm. baculatum* FdII shows a weak contribution of a $[3Fe–4S]^{1+,0}$ cluster (5%, $E_0 = -115$ mV). Upon reduction a complex EPR signal appears, indicating an interaction between two $[4Fe–4S]^{2+,1+}$ clusters located in the same protein subunit. The midpoint redox potentials reported for the $[4Fe–4S]^{2+,1+}$ centers were circa -500 mV.

EPR spectra of the native *D. africanus* FdIII show an almost isotropic signal centered around $g = 2.01$ similar to the one observed in proteins containing $[3Fe–4S]^{1+}$ clusters (*72*). The temperature dependence of this signal and low-temperature MCD spectra and magnetization properties are identical to the ones reported for *D. gigas* FdII (*93*). Upon one-electron reduction a $g = 12$ signal develops, characteristic of the $[3Fe–4S]^0$ state. Two-electron reduction elicits an EPR active species with an axial properties and *g*-values of 1.93 and 2.05, consistent with the presence of a $[4Fe–4S]^{1+}$ center.

C. Cluster Structural Interconversions and Synthesis of Heterometal Clusters

The mimicking of the iron–sulfur clusters by synthetic chemistry has been quite successful over the years. One of the last synthetic clusters to be obtained was the [3Fe–4S] cluster (*109, 110*). This new synthetic compound was useful for the demonstration of interconversion pathways, as well as for the formation of different heterometal clusters beyond those produced in proteins (*111*). The [3Fe–4S] core

present in *D. gigas* FdII can be converted into a cubane of the [4Fe–4S] type. This facile transformation occurs upon incubation of the protein with an excess of Fe^{2+} in the presence of a reducing agent. A summary of the interconversion pathways as well as the potentialities of the method for specific labeling an iron–sulfur core was previously discussed (*107, 112*). Combination of ^{57}Fe isotopic enrichment and specific introduction of a fourth iron atom into the [3Fe–4S] core produces different isotopically labelled clusters.

Electrochemical studies performed in the 7 × Cys–Asp14 *D. africanus* FdIII indicate that the reduced [3Fe–4S] center can react rapidly with Fe^{2+} to form a [4Fe–4S] core that must include noncysteinyl coordination (*101*). The carboxylate side chain of Asp 14 was proposed as the most likely candidate, since this amino acid occupies the cysteine position in the typical sequence of a 8Fe protein as indicated before. The novel [4Fe–4S] cluster with mixed S and O coordination has a midpoint redox potential of −400 mV (*88*). This novel coordinated state with an oxygen coordination to the iron–sulfur core is a plausible model for a [4Fe–4S] core showing unusual spin states present in complex proteins (*113, 114*).

A number of proteins containing [3Fe–4S] centers form cubane-like clustes of the type [M,3Fe–4S] (*115–120*), which were prepared using this facile [3Fe–4S]/[4Fe–4S] conversion pathway. The [3Fe–4S] core present in *D. gigas* FdII was the first precursor used for the synthesis of heterometal cores inside a protein matrix, and the first derivative synthesized was the [Co,3Fe–4S] core (*121*). Similar synthetic products have also been derived in *D. africanus* FdIII (*118, 119*).

Cobalt(II) ion was introduced into a heterometal cluster, which assumed a paramagnetic configuration ($S = \frac{3}{2}$) at the fourth site of a cubane structure. The newly formed cluster was studied in the oxidized and reduced states. In the oxidized state the cluster exhibits an $S = \frac{1}{2}$ EPR signal with g-values at 1.82, 1.92, and 1.98 (g-values obtained after spectral simulation). The well-resolved ^{59}Co hyperfine at the g_z line ($A_z \approx 4.4$ mT) is also broadened by ^{57}Fe isotopic substitution, indicating that Fe and Co share a common unpaired electron. Upon one-electron reduction ($E_m = -220$ mV, vs NHE) the cluster has an integer spin ($S = 1$) as indicated by Mössbauer and MCD measurements. At 4.2 K, the Mössbauer spectrum of the oxidized cluster exhibits two distinct spectral subsites with an intensity ratio 2 : 1, indicating that the three iron atoms reside in the same cluster and suggesting the presence of a Fe^{3+} site and again a delocalized pair (*121*). Upon one-electron reduction the third iron is formally Fe^{2+}. The introduction of Cu^{1+}, Zn^{2+}, Cd^{2+}, and Ga^{3+} was anticipated with great

interest due to the possibility of introducing a diamagnetic site at the cubane (*115*). The zinc incubated product was shown to be EPR-active ($S = \frac{5}{2}$) with $E/D \approx 0.25$ and $D = -2.7$ cm^{-1} and shows ^{57}Fe hyperfine broadening (*116*). The Mössbauer spectrum performed at 4.2 K consists of two spectral components with an intensity ratio of 2:1, with parameters suggesting again a delocalized Fe^{2+}/Fe^{3+} pair, as observed for the reduced [3Fe–4S] core. The formal oxidation states involved were assigned: two Fe^{2+}, one Fe^{3+}, and being a Kramer system ($S = \frac{5}{2}$) the zinc site must be divalent. Incorporation of the zinc atom at the vacant site of the [3Fe–4S] core implies a previous reduction step of the cluster plus an extra electron for metal incorporation. There is also preliminary evidence for the incorporation of Cd^{2+}, which yields an $S = \frac{5}{2}$ system, as well, under reducing conditions (*122*). A similar $[Ni,3Fe–4S]^{1+}$ cluster was produced in *D. gigas* FdII (*123*). The dithionite reduction of Fd after anaerobic incubation with excess Ni(II) in the presence of dithiothreitol shows EPR spectral features dominated by the presence of an $S = \frac{3}{2}$ species.

The redox properties of a series of heterometal clusters were assessed by electrochemical and EPR measurements. The redox potentials of derivatives formed in *D. gigas* FdII were measured by direct square wave voltammetry promoted by Mg(II) at a vitreous carbon electrode, and the following values were determined: −495, −420, −360, and −245 mV (vs NHE) for the Cd, Fe, Ni, and Co complexes, respectively. The values agree well with independent measurements (*96, 123*). Similar derivatives generated in *D. africanus* FdIII measured by cyclic voltammetry in film and bulk solution yield −590 (Cd), −490 (Zn), and −400 (Fe) mV (*118*). A novel addition to this series was obtained by the introduction of a monovalent ion (*119*). The $[Tl,3Fe–4S]^{2+}$ core shows a redox transition at 80 mV.

VI. Fuscoredoxin (Novel Fe–S Cluster)

A preliminary characterization of a new iron–sulfur protein isolated from *Desulfovibrio vulgaris* Hildenborough was reported in 1989 (*124*). The protein contained approximately 6 iron and 6 inorganic sulfur atoms per molecule. The EPR spectrum of the dithionite reduced protein exhibited an $S = \frac{1}{2}$ signal similar to what was found for synthetic compounds with a $[6Fe–6S]^{3+}$ core (prismane core). No other EPR signals were reported at this time, and based on the observed similarity it was suggested that this peculiar iron–sulfur protein contained a [6Fe–6S] cluster. Because it had no known function, the pro-

tein was later named prismane protein. At the same time, an iron–sulfur protein with similar characteristics was isolated from *D. desulfuricans*, where a more detailed study, including EPR and Mössbauer characterization, was performed (*125*). From the Mössbauer data collected for the as-isolated form it was shown that the protein contained, not one, but two distinct multinuclear iron clusters, termed clusters I and II.[4] The low-temperature spectrum (1.5–4.2 K) displays two components of equal absorption. One of them is a diamagnetic quadrupole doublet, similar to those of $[4Fe–4S]^{2+}$ clusters, that was attributed to cluster 1. Cluster 2 was found to be paramagnetic and exhibited unique Mössbauer and EPR spectra consistent with a spin $S = \frac{9}{2}$ system. Four well-resolved spectral components, each accounting for 8% of the total absorption, could be deconvoluted from the spectrum. Each of these components represented one iron site of cluster 2, and since approximately 50% of the total absorption was attributed to this cluster, it was concluded that the cluster was composed of 6 iron atoms ($6 \times 8\% = 48\%$). Consequently, the spectrum was analyzed with six components, four of which were well resolved, plus two that overlapped with the diamagnetic spectrum of cluster 1. From this analysis it was possible to conclude that the iron atoms in cluster 2 had a mixed coordination (N, O, and S ligands). Also, one of the resolved iron atoms had parameters typical of high-spin ferrous ion with nitrogen and/or oxygen coordination. Finally, another conclusion was extracted from the analysis. Since cluster 2 was determined to be a 6Fe cluster and both clusters had the same absorption percentages, cluster 1 should have the same nuclearity as cluster 2.

Both clusters were found to be redox active, with cluster 1 accepting a single electron and cluster 2 undergoing a multiple-electron reduction. The EPR spectrum of the dithionite-reduced protein shows a "prismane"-like $S = \frac{1}{2}$ signal, as well as an $S = \frac{3}{2}$ signal at around $g = 4.7$. Based on Mössbauer data interpretation, the first EPR signal was attributed to cluster 1. The origin of the second signal was not determined.

Finally, a disagreement was noted between the iron determination results, which showed the existence of only 5 to 8 iron atoms/molecule, and the above analysis. As a solution to this discrepancy, it was proposed that the samples could contain a mixture of holo- and apoprotein.

[4] Based on recently obtained crystallographic data, cluster I and II were renamed cluster 2 and 1, respectively. In the following discussion the new nomenclature will be used.

The spectroscopic and biochemical properties of the *D. vulgaris* protein were shown to be very similar to the ones described for *D. desulfuricans* protein (*126, 127*). Hagen and collaborators performed a comprehensive spectroscopic study on the *D. vulgaris* protein. From the characterization done, it was shown that, in addition to the $S = \frac{9}{2}$ EPR signal observed in the as-purified samples, an integer-spin signal with a *g*-value around 16 could be observed for a more reduced form of the protein (*126*). Magnetic circular dichroism (MCD) studies on this redox state suggested that this signal arises from an $S = 4$ ground state (*128*). All these unusual spectroscopic properties were attributed to the presence of a [6Fe–6S] cluster. The authors found support for this interpretation in the fact that iron and sulfur quantitated to 6 atoms per molecule, and the EPR of the dithionite-reduced protein closely resembled that of the synthetic prismane cluster.

The genes encoding both the *D. vulgaris* and *D. desulfuricans* proteins have been cloned, sequenced, and overexpressed in *D. vulgaris* (*129–131*). A high degree of homology in amino acid sequence was observed for the two proteins, and 66% of the residues were found to be identical. There are nine conserved cysteine residues. Although no sequence homology is found with known sequence motifs that bind iron–sulfur clusters, four of these residues at the N-terminal region form a sequence motif ($CX_2CX_8CX_5C$) suggestive of binding of an iron–sulfur cluster. The recombinant proteins were found to be able to accommodate multiple redox states, which exhibited optical and EPR spectra similar to those of the wild-type proteins. This observation strongly indicates that the iron clusters in the recombinant and wild-type proteins are similar.

Resonance Raman studies of the recombinant proteins showed vibrational bands at the 200–430 cm^{-1} region characteristic of iron–sulfur clusters (*124*). Most interestingly, on Fe and O isotope sensitive band was detected at 801 cm^{-1}, which could be attributed to either a Fe(IV)=O species or a monobridged Fe–O–Fe structure. This observation, together with Mössbauer analysis, which indicated a mixed N, O, and S ligand environment for cluster 2, suggests a Fe–O–Fe or Fe=O unit as part of the structure for cluster 2.

The crystallographic structure of the *D. vulgaris* protein has been reported by Lindley and collaborators (*132*). The structure was solved to a resolution of 1.7 Å. The major findings are consistent with most of the conclusions derived from the Mössbauer work done in the *D. desulfuricans* protein. The protein was found to contain two distinct clusters of the same nuclearity. Also, one cluster has a mixed N, O, S ligand environment, while the other has a regular iron–sulfur core

structure (see Fig. 4). Nevertheless, the proposed nuclearity was incorrect. Both iron clusters are tetranuclear, not hexanuclear. Cluster 1 can be described as a [4Fe–4S] cluster and is located at the N-terminal region. Cluster 2 revealed the most interesting and unusual structure. Part of this cluster can be described as a pair of dinuclear iron centers. One of the pairs (Fe_5 and Fe_6) is bridged by two inorganic sulfide ions, and each iron is coordinated by one additional cysteine. The other pair (Fe_7 and Fe_8) is bridged by a single oxo group. The coordination sphere is completed by one cysteine, one histidine, and one glutamate for one of the irons (Fe_7), and one glutamate and a cysteine, through a persulfide group, for the other (Fe_8). Finally, the two pairs are connected by a sulfur and an oxo group.

Mössbauer spectroscopy has been used to characterize the iron clusters in fuscoredoxin isolated from *D. desulfuricans* (*133*). The authors explained why the iron nuclearity was incorrectly determined, and studied the protein in three different oxidation states: fully oxidized, one-electron reduced, and two-electron reduced. The error made in determining the iron cluster nuclearity was caused by the assumption that in the as-purified fuscoredoxin, cluster 2 is in a pure $S = \frac{9}{2}$ state. This assumption was proven to be false and unnecessary. In fact, the observation of four resolved, equal intensity (8% of total Fe absorption) spectral components associated with the $S = \frac{9}{2}$ species in the as-purified protein is consistent with cluster 2 being a tetranuclear Fe cluster. The $4 \times 8 = 32\%$ Fe absorption for the four components indicates that only 64% of clusters 2 are in the $S = \frac{9}{2}$ state (the total Fe absorption for cluster 2 is 50% of the total Fe absorption). The remaining clusters 2 are in a different oxidation state, the spectrum of which is unresolved from that of cluster 1.

The three samples studied included a sample of the as-purified protein and two poised at redox potentials of 40 mV and 320 mV. Cluster 1 was found to stay at the same oxidation state in all three samples. The Mössbauer parameters obtained for cluster 1 are typical of a cubane type [4Fe–4S] cluster in the 2+ oxidation state. Spectra recorded at strong fields indicate further that the cluster is diamagnetic, supporting the 2+ oxidation state assignment. These observations suggest that cluster 1 belongs to the class of ferredoxin-type [4Fe–4S] cluster, which generally has a relatively low midpoint redox potential in the range of -200 to -400 mV for the 2+/1+ couple. Since cluster 1 is diamagnetic, the previously observed $S = \frac{9}{2}$ EPR signal in the as-purified protein and an integer-spin EPR single detected in the 40-mV sample were attributed to cluster 2. Consistent with the EPR assignment, the Mössbauer data show that cluster 2

is redox-active in the potential range studied and exhibits different Mössbauer spectra in the three samples. Analysis of Mössbauer data, recorded over a wide range of experimental conditions, made it possible to determine the redox state of cluster 2 in each sample and to characterize cluster 2 in detail. In the as-purified and 320-mV sample, cluster 2 was found to be at a redox equilibrium between its fully oxidized (diamagnetic) and one-electron reduced ($S = \frac{9}{2}$) states. In the 40-mV sample, it is reduced to the two-electron reduced state. Four iron sites with different Mössbauer parameters were obtained, reflecting the different ligand environments surrounding the four iron atoms as revealed in the X-ray crystallographic structure. Based on the data described previously, the authors also propose a simple four-spin coupling model to explain the observed $S = \frac{9}{2}$ spin system. At the same time, the protein was named fuscoredoxin based on its brown color and on the fact that it can be stabilized in different redox states.

A similar study was also performed for the *D. vulgaris* fuscoredoxin (*134*). In accordance with the crystallographic data, the protein is described as containing two four-iron clusters (contrary to a previously reported Mössbauer study where the data was interpreted assuming the existence of a single hexanuclear cluster). Figure 7 summarizes the current knowledge of the structural and magnetic information available for the different redox states of the iron clusters present in fuscoredoxin.

VII. APS Reductase

The adenylylsulfate reductase (APS reductase, Ado*P*SO_4 reductase) catalyzes the following reversible reaction:

$$\mathrm{APS} + 2\,\mathrm{e}^- \leftrightarrow \mathrm{AMP} + \mathrm{SO}_3^{2-}$$

This key enzyme of the dissimilatory sulfate reduction was isolated from all *Desulfovibrio* strains studied until now (*135*), and from some sulfur oxidizing bacteria and thermophilic Archaea (*136, 137*). The enzymes isolated from sulfate-reducing bacteria contain two [4Fe–4S] clusters and a flavin group (FAD) as demonstrated by visible, EPR, and Mössbauer spectroscopies. With a total molecular mass ranging from 150 to 220 kDa, APS reductases have a subunit composition of the type $\alpha_2\beta_2$ or $\alpha_2\beta$. The subunit molecular mass is approximately 70 and 20 kDa for the α and β subunits, respectively. Amino-acid sequence data suggest that both iron–sulfur clusters are located in the β subunit

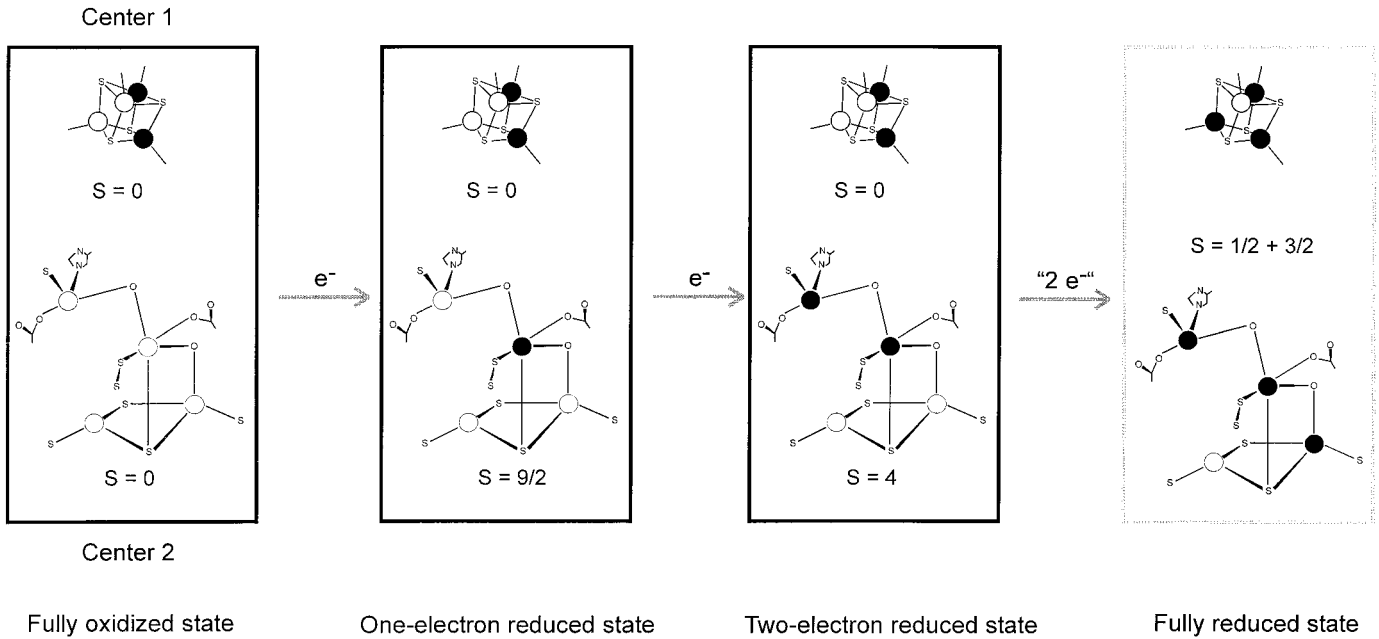

FIG. 7. Schematic representation of the redox and spin states attained by center 1 and center 2 of *D. desulfuricans* Fuscoredoxin as indicated by EPR and Mössbauer spectroscopies. The fully reduced state indicated in the figure remains to be completely understood. In particular, the numbers of electrons accepted are still under debate. Filled circles represent Fe(II).

(*138*). Redox titrations monitored by visible and EPR spectroscopies show that the clusters have very different midpoint redox potentials: approximately 0 mV for center I, and < -300 mV for center II (*139*).

The addition of sulfite to APS reductase results in changes of the flavin visible spectrum that are explained by the formation of an adduct between the sulfite and the FAD group (*135*). Addition of AMP to the as-isolated enzyme causes no change in the spectroscopic properties. Addition of AMP to the sulfite-reacted enzyme causes the reduction of center I. However, the formation of a semiquinone signal has never been observed either by EPR or visible spectroscopies. Also, Mössbauer and EPR data indicate that AMP closely interacts with center I (*139*).

EPR studies have been carried out extensively in a large number of different APS reductases, in the native form, in the presence of natural substrates (AMP and sulfite) and in the semi- and fully reduced states (*135*). The EPR spectrum of the native enzyme shows an almost isotropic signal with g-values centered around $g = 2.02$ and detectable at temperatures below 18 K and representing 0.1 to 0.25 spins/molecule. The EPR behavior and Mössbauer parameters of this isotropic-like signal is typical of a [3Fe–4S] and, since the signal quantitation is preparation-dependent, is explained as the result of a small degradation of the [4Fe–4S] clusters during the purification process. The addition of AMP or APS causes no changes in the EPR spectrum of the native enzyme. However, the addition of sulfite alone to the native reductase causes the appearance of a very weak "$g = 1.94$"-type signal that is attributed to the existence of residual and endogenous AMP (in contrast to what is observed in visible spectroscopy, where it is seen that sulfite produces a relatively strong decrease in absorbance). Addition of AMP to the sulfite-reacted enzyme causes major changes on the EPR: The isotropic signal decreases in intensity and a rhombic signal rises with g-values of 2.096, 1.940, and 1.890, characteristic of a reduced [4Fe–4S] (center I) that accounts for 0.35–0.5 spins/molecule. The addition of chemical reductants, such as sodium dithionite for a short incubation, or reduced methyl viologen, to the native APS reductase causes the total disappearance of the isotropic signal and the development of center I signal to its fully intensity (0.8–1.0 spins/molecule) at g-values equal to 2.079, 1.939, and 1.897. EPR and Mössbauer data reveal that in this state the sampleis in a half-reduced state, with 50% of the iron clusters reduced, indicating the presence of yet another [Fe–S] cluster. The full reduction of the reductase is accomplished only with a long incubation with dithionite (at least 30 min). The EPR spectrum of the fully reduced state is characterized by the presence of a complex signal similar to those describing interacting [4Fe–4S] cluster, confirming the existence

of a second [4Fe–4S] cluster (center II). The total signal accounts for 1.5 to 1.96 spins/molecule, depending on the samples (*139, 140*).

Although three different models were already proposed to explain the mechanism of adenylylsulfate reduction (*141–143*), a global model (taking in account the spectroscopic features discussed earlier) was not yet presented. In particular, the role of center II is still unknown.

VIII. Pyruvate–Ferredoxin Oxidoreductase

In *Desulfovibrio*, as in other strict anaerobes and some aerobic microorganisms, pyruvate is oxidatively decarboxylated by pyruvate oxidoreductase (POR) according to the following reaction:

$$\text{Pyruvate} + \text{CoA} + \text{Fd}_{ox} \rightarrow \text{Acetyl CoA} + \text{CO}_2 + \text{Fd}_{red}$$

Two attempts were made to purify POR from the *Desulfovibrio* genus. First Ogata and Yagi partially purified POR from *D. vulgaris* Miyazaki F (*144*). These researchers were only able to obtain a threefold purification of the enzyme. Further manipulations resulted in the total loss of the activity. However, Pieulle and collaborators were able to isolate POR from *Desulfovibrio africanus* (*145*). POR is a 256-kDa homodimer that contains one thiamine pyrophosphate (TPP) and three [4Fe–4S] clusters per subunit. The enzyme, aerobically purified, is highly stable to oxygen. Activation is achieved by incubation with dithioerythriol or 2-mercaptoethanol. After activation the enzyme becomes air sensitive, exhibiting an irreversible loss of activity accompanied by a bleaching of the protein solution. Both observations are probably due to oxidative damage of the iron–sulfur clusters.

The UV-visible spectrum of POR is typical of an iron–sulfur protein with a broad absorbance band around 400 nm (105 mM^{-1} cm^{-1}) and a shoulder in the 315-nm region. Midpoint redox potentials, as determined by reductive redox titrations, were found to be −390, −515, and −540 mV. Becaue of the differences in potentials, it was possible to isolate the EPR signal of one of the [4Fe–4S] centers. Below −330 mV a rhombic signal with *g*-values at 2.053, 1.947, and 1.881 was observed. Below −440 mV, the EPR signal becomes very complex because of the magnetic interaction of the centers, with features between $g = 2.093$ and 1.842 progressively replacing the rhombic signal. The same EPR spectrum could be obtained by photoreduction in the presence of 5-deazaflavin, and

quantification of this signal gave 2.9 ± 0.2 spins/POR monomer, further supporting the presence of three centers.

Incubation of both activated and as-isolated POR with pyruvate produced a free radical signal that was equimolar to the TPP content and showed a substrate-dependent hyperfine structure. The latter observation confirmed the delocalization of the spin density over the substrate. The radical signal appeared concomitantly with the rhombic signal of the highest potential [4Fe–4S] cluster. After addition of CoA the radical signal disappeared, and by incubation with excess of both substrates the EPR spectrum of the fully reduced protein was obtained. A mechanistic conclusion can be drawn from these observations. After binding of pyruvate to TPP, the substrate suffers decarboxylation transferring one electron to the TPP and another to an oxidized $[4Fe–4S]^{2+}$ cluster, thus forming the observed radical and the reduced $[4Fe–4S]^{1+}$. One important aspect of the proposed mechanism is that the formation of a free radical intermediate during the catalytic cycle rules out the tentative distinction between the bacterial and archeal POR mechanisms (*146, 147*).

Further studies have shown that *D. africanus* ferredoxins I and II are involved as physiological electron carriers of POR. Also, using immunogold labeling, it was possible to show that POR is located in the cytoplasm.

IX. Sulfite Reductase

Sulfite reductase catalyzes the six-electron reduction of sulfite to sulfide, an essential enzymatic reaction in the dissimilatory sulfate reduction process. Several different types of dissimilatory sulfite reductases were already isolated from sulfate reducers, namely desulfoviridin (*148–150*), desulforubidin (*151, 152*), P-582 (*153, 154*), and desulfofuscidin (*155*). In addition to these four enzymes, an assimilatory-type sulfite reductase was also isolated from *D. vulgaris*. Although all these enzymes have significantly different subunit composition and amino acid sequences, it is interesting to note that, as will be discussed later, all of them share a unique type of cofactor.

Desulfoviridin was found in *D. gigas*, *D. salexigens*, and *D. vulgaris* Hildenborough. Desulfoviridin is composed of three different subunits organized in a $\alpha_2\beta_2\gamma_2$ configuration with a total molecular mass of approximately 200 kDa. The molecular mass of the α, β, and γ subunits was calculated to be 50, 40, and 11 kDa, respectively (*156*).

The UV-visible spectrum of desulfoviridin is dominated by bands around 400, 540–580, and 628 nm, typical of the siroheme group. However, upon extraction with acetone–HCl, approximately two metal-free sirohydrochlorins are obtained (*157*). This finding is contrary to what was observed in all other sulfite reductases from which sirohemes could be extracted. The Mössbauer data shed light into the chemical composition of the desulfoviridin cofactors (*152*). Mössbauer data show that 80% of the iron in the sample is in the form of [4Fe–4S] uncoupled clusters, 10% in the form of exchanged-coupled ferric high-spin siroheme–$[4Fe–4S]^{2+}$, and 10% in the form of mononuclear Fe^{3+}. Since it was determined that the samples under study had 18 Fe/molecule, Mössbauer data clearly indicates that only 0.4 sirohemes/molecule should exist. In support of these findings, EPR spin quantitation yielded a substoichiometric amount of heme signal (0.2–0.4 spin/molecule). Furthermore, a resonance Raman study confirmed the presence of metal-free sirohydroclorin in desulfoviridin (*158*).

Desulforubidin was found in strains of the *Desulfomicrobium* genus and has been described as the sulfite reductase of this genus. The subunit composition and molecular mass are similar to what was observed for desulfoviridin. However, in desulforubidin all sirohydrochlorins are metalated as proved by Mössbauer spectroscopy (*152*). The as-isolated protein contains four $[4Fe–4S]^{2+}$ clusters; two of them are exchange-coupled to two paramagnetic sirohemes.

Desulfofuscidin is present only in the extreme thermophilic sulfate reducing bacteria of the genus *Thermodesulfobacterium*. The protein was described as a tetramer exhibiting a quaternary structure of $\alpha_2\beta_2$ type. The total molecular mass ranges from 167 to 190 kDa (subunit molecular mass of 44 to 48 kDa). N-terminal sequence analysis shows that both subunit types are similar, but not identical. The enzyme contains four sirohemes (twice the number obtained for desulforubidin) and, depending upon the strain, four (*T. commune*) (*159*) or eight (*T. mobile*) (*155*) [4Fe–4S] clusters. Although no Mössbauer data are available for desulfofuscidin, EPR data obtained for the CO-reacted reduced enzyme suggest the existence of an exchange-coupled system, as was found in the sulfite reductases discussed previously.

Low-spin sulfite reductase were isolated from *D. vulgaris* (*160*), *Desulfuromonas acetoxidans* (*161*), and *Methanosarcina barkeri* (DSM 800) (*162*). The *D. vulgaris* protein has a molecular mass of 27 kDa and contains a single [4Fe–4S] cluster and one siroheme. The EPR spectrum shows a rhombic signal with g values at 2.44, 2.36, and 1.77, characteristic of a ferriheme low-spin system. This is a unique

feature since in all other sulfite reductases the siroheme is in the high-spin state. By comparison with model complexes, this observation might be explained by the fact that in this new class of sulfite reductases the siroheme possesses two axial ligands. As in the other sulfite reductases the two cofactors are exchanged-coupled as proven by Mössbauer spectroscopy (*160*).

A detailed reaction pathway for the six-electron reduction of sulfite to sulfide was proposed by Tan and Cowan based on ^{35}S-labeled enzyme and the relative reaction rates of nitrogenous substrates (*163*). The ligand bridging the prosthetic [4Fe–4S]–siroheme center was exchanged by $^{35}S^{2-}$ in both oxidized and reduced enzyme. This bridging ligand is retained in the course of sulfite reduction, with the substrate binding to the nonbridging axial site of the siroheme. The mechanism suggests that sulfite binds to the ferrous siroheme iron through a sulfur atom followed by a series of two-electron reductive cleavages of S–O bonds. The protonation of the oxygen group facilitates the bond cleavage, producing hydroxide as the leaving group. The bridge between the siroheme and the iron–sulfur cluster remains intact during the catalytic cycle, providing an efficient coupling pathway for electron transfer between the cluster and the siroheme.

X. Hydrogenase

Molecular hydrogen plays a major role on the oxidation–reduction processes involved in bacterial energetics, as well as in the degradation and conversion of biomass related with all major elemental cycles. Hydrogenase has a key role on this process and catalyzes the reversible oxidation of dihydrogen, important in bacterial anaerobic metabolism:

$$2\,H^+ + 2\,e^- \leftrightarrow H_2$$

Sulfate reducing bacteria of the genus *Desulfovibrio* are one of the main sources of enzyme. Hydrogenases can be found in different sites in the bacterial cell: periplasm, cytoplasm, and membrane. A given species may have hydrogenases in one or in several of these cell sites.

The hydrogenases isolated can be broadly classified into two groups: [Fe–S]-only, and nickel–[Fe–S]-containing hydrogenases. The first group, the [Fe–S]-only or [Fe] hydrogenases, is characterized by the absence of nickel on the active site, and are rare in sulfate reducing bacteria. They contain [4Fe–4S] clusters and, in addition, a catalytic

iron cluster (designated as H-cluster) of unknown structure (*164*). The nickel–[Fe–S]-containing hydrogenases or [NiFe] hydrogenases are the most common and contain two [4Fe–4S] clusters, one [3Fe–4S] cluster, and a nickel site. A subdivision under this class can be made for nickel–selenium–[iron–sulfur]-containing hydrogenases that lack the [3Fe–4S] cluster and exhibit selenocysteine coordination to the nickel site (*152, 165*).

Especially for this latter class of hydrogenases, great effort has been devoted to the purification and the characterization of the metal centers involved, using biochemical, genetic, spectroscopic (IR, EPR, Mössbauer, MCD, EXAFS, and mass spectrometry), and crystallographic techniques (*152, 165, 166*).

A. [Fe] Hydrogenases

The *D. vulgaris* Hildenborough [Fe] hydrogenase is a periplasmic protein composed of two subunits with molecular masses of 45.8 and 10 kDa, respectively (*167, 168*). The reported iron content varies from 10 to 16 moles of iron per mole of protein (*169*). The type of iron clusters present has been difficult to establish because of the difficulty associated with the iron determination and complexity of the spectroscopic data available. Analysis of the aminoacid sequence of the protein suggests the presence of two Ferredoxin-type [4Fe–4S] clusters, accounting for eight iron atoms in the *D. vulgaris* [Fe] Hydrogenase (*170*). The remaining iron was proposed to belong to a cluster of unknown structure, named the H-cluster.

Most of the spectroscopic data obtained on this enzyme are from EPR. There are six EPR signals reported so far (*168, 171–173*): (*1*) the isotropic signal, observed in the native form of the enzyme and believed to be an artifact of the purification process (the signal accounts to 0.02–0.2 spins/molecule) and resembling that of a [3Fe–4S]$^{1+}$ cluster; (*2*) a complex signal that appears upon dithionite reduction of the enzyme, similar to the one resulting from the magnetic interaction of two [4Fe–4S]$^{1+}$ previously observed in 8 $\times$ Fe Ferredoxins; (*3*) the rhombic $g = 2.06$ signal (g at 2.06, 1.96, and 1.89), detected during reductive titrations, with a maximum intensity at around -110 mV and representing about 0.7 spins/molecule; (*4*) the rhombic $g = 2.10$ signal ($g = 2.10$, 2.04, and 2.00), believed to represent the active form of the H-cluster, and observable at $E_m < -160$ mV; (*5*) the axial 2.06 signal ($g = 2.06$, 2.00, and 2.00); and the high-spin $g = 5$ signal. Oxidative–reductive EPR titrations seems to indicate that the rhombic 2.06 and the 2.10 signals are interconvertible,

since the appearance of the last one is concomitant with the disappearance of the rhombic $g = 2.06$ EPR signal; the signals are suggested to represent the inactive and active form of the H-cluster, respectively.

The Mössbauer data performed on the as-isolated *D. vulgaris* [Fe] hydrogenase are in agreement with the EPR data, and further support the presence of two ferredoxin-type [4Fe–4S] clusters and that the H-cluster is in the diamagnetic state in the as-purified enzyme (*169*).

Recently, two 3D structures of Fe only hydrogenases were published: *Clostridium pasteurianum* at 1.8 Å (*245*) and *Desulfovibrio desulfuricans* ATCC 7757 at 1.6 Å (*246*). Several iron–sulfur clusters are present, involved in electron transfer ($3 \times$ [4Fe–4S] and $1 \times$ [2Fe–2S] cores in *Cp* and $2 \times$ [4Fe–4S] in *Dd* ATCC 7757). The catalytic site (H cluster) is the most remarkable feature of these hydrogenases. Six iron atoms are involved, rearranged as a thiocubane structure bridged by a sulfur atom of a cysteinyl residue to a novel type of binuclear cluster, a subsite of the H core. The di-iron core has an organometallic character with CO and CN^- ligands. Differences are found, at the moment in the bridging ligands of the di-iron cluster. The *Dd* structure clear indicates that a propane dithiol ligand is present. The *Cp* structure also points to the presence of two sulfur ligands and one additional CO/CN bridging ligand. The novelty of the structural arrangement found at the H cluster will be a challenge for the interpretation of the magnetic and spectroscopic features of the active site of Fe only hydrogenases.

B. [NiFe] Hydrogenases

The [NiFe] hydrogenase from *D. gigas* has been used as a prototype of the [NiFe] hydrogenases. The enzyme is a heterodimer (62 and 26 kDa subunits) and contains four redox active centers: one nickel site, one [3Fe–4S], and two [4Fe–4S] clusters, as proven by electron paramagnetic resonance (EPR) and Mössbauer spectroscopic studies (*174*). The enzyme has been isolated with different isotopic enrichments [^{61}Ni ($I = \frac{3}{2}$), ^{59,60}Ni ($I = 0$), ^{56}Fe ($I = 0$), and ^{57}Fe ($I = \frac{1}{2}$)] and studied after reaction with H and D. Isotopic substitutions are valuable tools for spectroscopic assignments and catalytic studies (*165, 166, 175*).

Most of the as-isolated [NiFe] hydrogenases are inactive, and the nickel center exhibits an intense rhombic EPR signal termed Ni-A ($g = 2.31$, 2.26, and 2.02) with variable amounts of a second nickel species, named Ni-B ($g = 2.33$, 2.16, and 2.02), with slightly different

rhombicity (*176*). Some hydrogenases may contain only Ni-B (*177*). Upon reaction with hydrogen, the natural substrate, and after a reductive activation step (lag phase), these signals disappear and are replaced by a transient nickel EPR signal termed Ni-C (g = 2.19, 2.14, and 2.02). The Ni-C state is considered a *key intermediate* (detected in all [NiFe] hydrogenases). These signals can be observed up to 100 K without noticeable line broadening. Ni-A signals in hydrogenases have been related to an unready state of the enzyme and to the reversible inactivation of hydrogenases. The minor amounts of Ni-B that are observed in the oxidized state can be enhanced by recycling the enzyme in the absence of oxygen (*178*). The increase in the amount of Ni-B has been pointed out as representing an enzyme state that is easy to activate and that does not require deoxygenation steps but just a reductive one (*178, 179*).

Oxidation–reduction titrations revealed the existence of two other oxidation–reduction states, EPR silent, designated as Ni-Si (Ni-Silent) and Ni-R (Ni-Reduced) (*178, 180*). A detailed study of the oxidation–reduction pattern involved enabled the following sequence of events (in the oxidation direction) to be written:

$$\text{Ni-R} \rightarrow \text{Ni-C} \rightarrow \text{Ni-Si} \rightarrow \text{Ni-B} \rightarrow (+\text{O}_2) \rightarrow \text{Ni-A}$$

Some controversy can be found in literature about the oxidation states involved (*165, 166, 175, 176, 181–183*).

Mössbauer and EPR spectroscopies were used as complementary tools for the characterization of the iron–sulfur centers of *D. gigas* hydrogenase for a complete understanding of the magnetic properties of these clusters in different redox states of the enzyme. Detailed characterization of all three clusters (one [3Fe–4S] and two [4Fe–4S] centers) have been obtained through Mössbauer measurements of the enzyme at different intermediate redox states, as well as in fully oxidized and fully reduced states (*174*). The Mössbauer data of the two $[4\text{Fe–4S}]^{2+}$ clusters in the oxidized state show a broad quadrupole doublet with parameters (apparent ΔE_Q = 1.10 mm/s and δ = 0.35 mm/s) typical for this type of cluster. Upon reduction, the two $[4\text{Fe–4S}]^{1+}$ clusters are spectroscopically distinguishable. Cluster I (with a midpoint potential of −340 mV) has an average ΔE_Q = 1.15 mm/s and δ = 0.525 mm/s. Cluster II (with a midpoint potential of −340 mV) has an average ΔE_Q = 1.35 mm/s and δ = 0.47 mm/s. The observed isomer shifts are typical of reduced cubane structures. However, unusually small hyperfine coupling constants were observed for site 1 of both reduced centers I and II. As for the [3Fe–4S], the Mössbauer

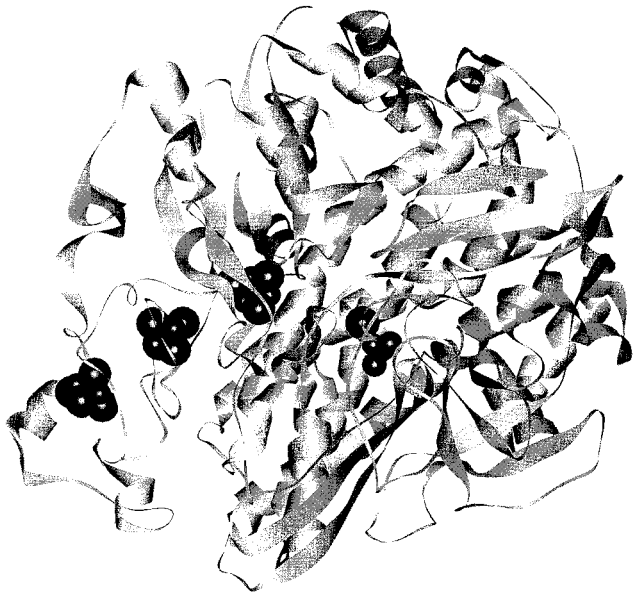

FIG. 8. The structure of *D. gigas* hydrogenase showing the novel heterodinuclear [NiFe] site, the three iron–sulfur clusters, and the tracing of the polypeptide chain (*164*).

parameters in the oxidized (+1) state are ΔE_Q = 1.67 mm/s and δ = 0.47 mm/s, and in the one-electron reduced (0 oxidation state) ΔE_Q = 0.38 mm/s and δ = 0.39 mm/s, similar to the ones observed in *D. gigas* FdII. However, in *D. gigas* hydrogenase the isomer shifts obtained for the ferric sites in both the +1 and 0 states of the [3Fe–4S] cluster are approx. 0.1 mm/s higher than those observed in other proteins.

1. 3D Structure of [NiFe] Hydrogenases

The three-dimensional structure of *D. gigas* hydrogenase was the first hydrogenase structure to be determined, revealing an unusual and unexpected Ni active center (*164*) (Fig. 8). The crystallographic studies obtained at 2.85 Å, and more recently at 2.54 Å resolution (*184*) have shown that the active site is a new heterobinuclear site, containing nickel and another transition metal, probably iron (*164*). This unexpected result challenges previous reported spectroscopic studies that failed to predict the existence of this second metal ion. The *D. gigas* [NiFe] hydrogenase is a heterodimer (26 and 62 kDa, respectively). The small subunit contains the [Fe–S] clusters, two

[4Fe–4S], and a [3Fe–4S], while the Ni catalytic center is present in the large subunit. The iron–sulfur clusters are disposed along an almost straight line; one of the [4Fe–4S] clusters is in the vicinity of the nickel center (and for that reason is named proximal), and the other [4Fe–4S] cluster, called distal, is localized near the protein surface, while the [3Fe–4S] cluster is located halfway between these two centers. This "linear" spatial arrangement of the [Fe–S] centers may provide a channel to transfer electrons between hydrogenase and its redox partners. The histidinyl coordination of one of the iron atoms of the distal [4Fe–4S] cluster is also new in biological systems and suggests a direct involvement of the imidazole ring from the histidine in the electron transfer (*164*).

The 3D crystal structure of *Dsm. baculatum* [NiSeFe] hydrogenase has been solved (*185*), and it was indicated that the enzyme contains three [4Fe–4S] centers. A cysteine (replacing a proline usually found near the [3Fe–4S] core) provides an extra ligand, enabling the acceptance of a fourth iron site at this cluster.

In addition, the [NiFe] hydrogenase from *D. fructosovorans* is very similar to *D. gigas* hydrogenase, and its structure has been solved (*185*). In order to understand the role of the [3Fe–4S] cluster, a Pro-432Cys mutant was produced. In this mutant the conversion of a [3Fe–4S] into a [4Fe–4S] center was proven by EPR and X-ray crystallography.

A crystallographic analysis of xenon binding to [NiFe] hydrogenase, together with a molecular dynamic simulation study of xenon and dihydrogen diffusion in the enzyme interior, suggests the existence of hydrophobic channels connecting the molecular surface with the active site (*184*).

2. The Novel Heterodinuclear Site Containing Ni, S, and Fe

The crystallographic analysis of the native *D. gigas* hydrogenase has shown that this center is a heterobinuclear center of the type $(Cys)_2$-Ni-μ-$(Cys)_2$-μ-$Fe(CO)(CN)_2$ consisting of nickel and a second metal ion, which by anomalous dispersion effects, EXAFS, and Q-band ENDOR studies has been assigned as an iron atom (*164, 186*) (Fig. 9). The nickel atom is coordinated by four cysteine residues: Cys 65, Cys 68, Cys 530, and Cys 533. Two of these cysteines (Cys 533 and Cys 68) serve as bridging ligands between the nickel and the iron atoms. Iron is also coordinated by three nonprotein ligands (diatomic molecules), that recently have been proposed, by FTIR measurements, to be one CO and two CN^-. A fourth nonprotein ligand, probably involving oxygen, could bridge Ni and Fe (*164, 187*). The surpris-

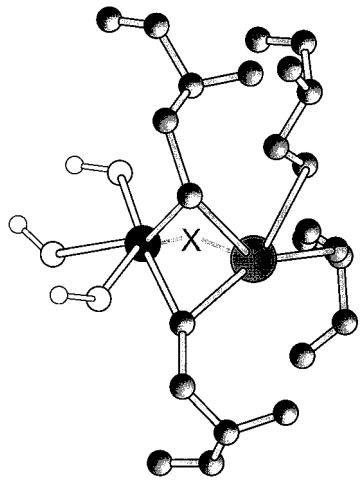

FIG. 9. The novel heterodinuclear [NiFe] site of *D. gigas* hydrogenase. The figure shows the complete heterodimer. The NiFe cluster is present in the larger subunit. Evidence is given to the diatomic ligands at the Fe site. Cysteinyl residues can act as monodentate ligands as well as bridging ligands between Fe and Ni sites. An extra bridging ligand has been pointed out (*164*, *190*).

ing nature of these three diatomic ligands puts hydrogenase in the small group of organometallic compounds used in biological systems, along with vitamin B_{12} and carbon monoxide dehydrogenase (*188, 189*).

^{57}Fe Q-band ENDOR study of the isotopically enriched Ni-C state of *D. gigas* and *D. desulfuricans* hydrogenases and Ni-B state of *D. desulfuricans* revealed a weak coupling between the ^{57}Fe and the nickel atoms when the enzyme was in the Ni-A forms while no coupling was observed for the Ni-B form (*186*). A careful analysis of linewidth of Ni-A and Ni-B EPR signals detected in ^{57}Fe enriched and nonenriched hydrogenase samples indicated that hyperfine interactions are lost in the spectral linewidth and, hence, nondetectable.

The crystal structure of *D. vulgaris* Miyazaki [NiFe] hydrogenase has been solved at 1.8 Å resolution by Higuchi and collaborators (*190*). The overall folding pattern and the spatial arrangement of the iron clusters are very similar to those of the *D. gigas* hydrogenase. The main difference is the fact that the ligands of the heterodinuclear NiFe center have been proposed to be diatomic S=O, C≡O, and C≡N molecules instead of the two C≡N and one C≡O found in the *D. gigas*

enzyme. The authors suggest that such unusual ligands could be involved in the electron transfer from the hydrogenase active site to its biological redox partners, or they could stabilize the redox state of the Fe(II) during the catalytic cycle of the enzyme.

3. Proposal of a Mechanism for the Catalytic Cycle

The discovery of a new heterodinuclear active site in [NiFe] hydrogenases opens the way for the proposal of catalytic cycles based on the available spectroscopic data on the different active site redox states, namely EXAFS studies that reveal that the Ni-edge energy upon reduction of the enzyme supports an increase in the charge density of the nickel (*191*).

The catalytic cycle for hydrogen production can involve a nickel-based redox chemistry, an iron-based redox chemistry, or a combination of these two possibilities, plus a role for the cysteinyl sulfur as a "non-innocent" ligand, based on mass spectrometric kinetic measurements (*192*) and model compound studies (*193*). Under this assumption, and considering that (*i*) the Ni-edge energy variation of the enzyme oxidation state supports a slight increase in the charge density of the nickel from Ni-A, Ni-B undergoing reduction (*191*); (*ii*) sulfur has a role as a "non-innocent" ligand (*193*); (*iii*) it has been suggested the iron atom at the heterodinuclear site must be in a ferrous low-spin configuration; and (*iv*) several pieces of evidence indicate that the nickel site is involved with substrate handling (*176, 177, 194, 195*)—given all this, a catalytic oxidation–reduction cycle has been proposed for the enzyme. This cycle is an alternative proposal to the one presented by Fontecilla (*196*) that suggested a possible alteration of iron oxidation–reduction state, keeping nickel unchanged during enzyme turnover. Several results clearly show a variability in the coordination of the heterodinuclear site of the *D. gigas* and *D. desulfuricans* hydrogenases and that the Ni-C signal in fact represents the active site where the substrate interacts.

XI. Molybdopterin-Containing Enzymes in SRB

The enzymes that utilize molybdenum can be grouped into two broad categories: (1) the nitrogenases, where Mo is part of a multinuclear metal center, or (2) the mononuclear molybdenum enzymes, such as xanthine oxidase (XO), dimethyl sulfoxide (DMSO) reductase, formate dehydrogenase (FDH), and sulfite oxidase (SO). The last

group catalyzes a diversity of two-electron oxidation/reduction reactions that involve the net transfer of an oxygen atom between the substrate and water (*197*). The mononuclear molybdenum (or tungsten) enzymes containing pterin cofactors are widely distributed and have important biological roles in a wide range of elemental cycles. The site containing molybdenum is coordinated to the *cis*-dithiolene group of one or two molybdopterins plus additional terminal oxo groups and/or sulfido groups or side chains of serine or cysteine residues. Molybdopterin-containing enzymes may be grouped into three broad families, a classification based on X-ray structural data and supported by spectroscopic and biochemical data as well as primary sequence alignments (*198*): (i) the xanthine-oxidase family ((MCD) Mo^{VI} =O, =S, $-H_2O$); (ii) the DMSO reductase family ((MGD)$_2$ Mo^{VI} =O, (–OSer, –SCys, or –SeCys)); and (iii) the sulfite oxidase family ((MPT) Mo^{VI} =O, =O, $-H_2O$, (–SCys)). Additionally, they can be subcategorized on the basis of whether the molydenum center of the active site possesses a MoO_2 or MoOS unit. Historically, these have been distinguished on the basis of the ability of cyanide to irreversibly inhibit the MoOS-containing enzymes, reacting with the Mo=S moiety to remove S by the release of thiocyanate.

The three known crystal structures of molybdopterin-containing enzymes are from members of the first two families: the aldehyde oxidoreductase from *D. gigas* (MOP) belongs to the xanthine oxidase family (*199*, *200*), whereas the DMSO reductases from *Rhodobacter* (*R.*) *capsulatus* (*201*) and from *R. sphaeroides* (*202*) and the formate dehydrogenase from *E. coli* (*203*) are all members of the second family of enzymes. There is a preliminary report of the X-ray structure for enzymes of the sulfite oxidase family (*204*).

These enzymes may contain other redox-active sites (iron–sulfur centers, hemes, and/or flavins), either in distinct domains of a single polypeptide or bound in separate subunits. These additional cofactors perform electron transfer from the molybdenum center to an external electron acceptor/donor.

Sulfate reducers can use a wide range of terminal electron acceptors, and sulfate can be replaced by nitrate as a respiratory substrate. Molybdenum-containing enzymes have been discovered in SRB (also see later discussion) and, in particular, *D. desulfuricans,* grown in the presence of nitrate, generates a complex enzymatic system containing the following molybdenum enzymes: (a) aldehyde oxidoreductase (AOR), which reduces adehydes to carboxylic acids; (b) formate dehydrogenase (FDH), which oxidizes formate to CO_2; and (c) nitrate reductase (the first isolated from a SRB), which completes the enzy-

TABLE I

MOLYBDENUM (AND TUNGSTEN)-CONTAINING ENZYMES IN SRB

Enzyme	Properties	*D. desulfuricans*	*D. gigas*
AOR	M_r (kDa) (subunits)	200 (dimer: 100)	200 (dimer: 100)
	Mo–pterin	1 MCD–Mo	1 MCD–Mo
	Other redox centers	2 × [2Fe–2S]	2 × [2Fe–2S]
FDH	M_r (kDa) (subunits)	150 (88, 29, and 16)	118 (88 and 30)
	Mo–pterin	2 MGD–Mo	2 MGD–W
	Other redox centers	2 × [4Fe–4S]	2 × [4Fe–4S]
		4 *c*-type hemes	
NAP	M_r (kDa) (subunits)	74 (no subunits)	
	Mo–pterin	2 MGD–Mo	Not found
	Other redox centers	1 × [4 Fe–4S]	

matic system required to convert nitrate (through nitrite) to ammonia. (See Table I).

The molybdopterin cofactor, as found in different enzymes, may be present either as the nucleoside monophosphate or in the dinucleotide form. In some cases the molybdenum atom binds one single cofactor molecule, while in others, two pterin cofactors coordinate the metal. Molybdopterin cytosine dinucleotide (MCD) is found in AORs from sulfate reducers, and molybdopterin adenine dinucleotide and molybdopterin hypoxanthine dinucleotide were reported for other enzymes (*205*). The first structural evidence for binding of the dithiolene group of the pterin tricyclic system to molybdenum was shown for the AOR from *Pyrococcus furiosus* and *D. gigas* (*199*). In the latter, one molybdopterin cytosine dinucleotide (MCD) is used for molybdenum ligation. Two molecules of MGD are present in the formate dehydrogenase and nitrate reductase.

A. ALDEHYDE OXIDOREDUCTASES

D. gigas AOR was the first Mo–pterin-containing protein whose 3D structure was solved. From *D. desulfuricans,* a homologous AOR (MOD) was purified, characterized, and crystallized. Both proteins are homodimers with-100 kDa subunits and contain one Mo-pterin site (MCD-cofactor) and two [2Fe–2S] clusters. Flavin moieties are not found. The visible absorption spectrum of the proteins (absorption wavelengths, extinction coefficients, and optical ratios at characteristic wavelengths) are similar to those observed for the deflavo-forms of

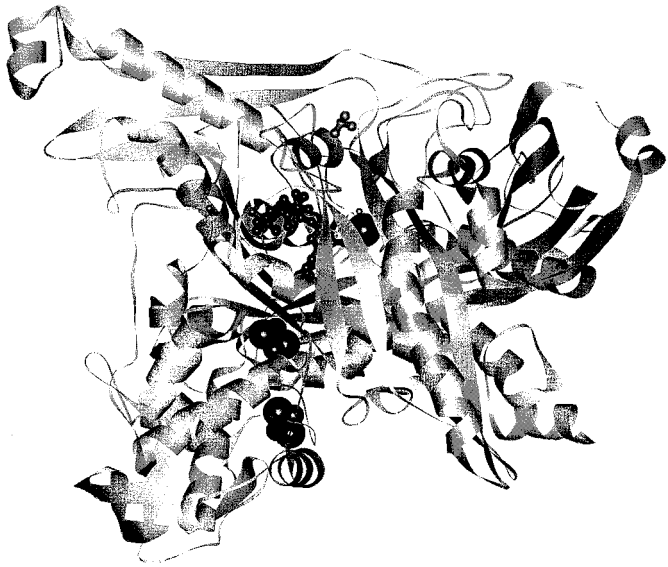

FIG. 10. The structure of *D. gigas* aldehyde oxidoreductase (AOR) monomer, showing the Mo-MCD site, the two [2Fe–2S] centers, and the tracing of the polypeptide chain. The Fe–S center most exposed is included in a protein domain whose folding is quite similar to the one found in plant-type ferredoxins (*199*).

xanthine and aldehyde oxidases (*206–210*) and reminiscent of the one observed for plant-type ferredoxins. The circular dichroism spectrum is intense and indicative of the presence of [2Fe–2S] centers, again similar to the spectra of plant ferredoxins and xanthine oxidase (*211*).

1. Three-Dimensional Structure of D. gigas AOR

The aldehyde oxidoreductase from *Desulfovibrio gigas* shows 52% sequence identity with xanthine oxidase (*199*, *212*) and is, so far, the single representative of the xanthine oxidase family. The 3D structure of MOP was analyzed at 1.8 Å resolution in several states: oxidized, reduced, "desulfo" and "sulfo" forms, and alcohol-bound (*200*), which has allowed more precise definition of the metal coordination site and contributed to the understanding of its role in catalysis. The overall structure, composed of a single polypeptide of 907 amino acid residues, is organized into four domains: two N-terminus smaller domains, which bind the two types of [2Fe–2S] centers and two much larger domains, which harbor the molybdopterin cofactor, deeply buried in the molecule (Fig. 10). The pterin cofactor is present as a cytosine dinucleotide (MCD) and is 15 Å away from the molecular surface,

with a shortest Mo–Fe distance of 14.9 Å for one of the iron atoms of center Fe–S II. This center is completely buried and inaccessible to solvent (≈15 Å away from the surface), while Fe–S I is exposed and may be the site for docking of an electron acceptor (physiologically unknown) (*213*). The closest distance between iron atoms of the two [2Fe–2S] clusters is ≈12.3 Å. The first domain (Fe–S I) (residues 1–76) exhibits a fold typical of plant-type ferredoxins, and the iron atoms are coordinated by cysteines 40, 45, 47, and 60. Domain Fe–S II (residues 84–156) is a four-helix bundle, with two central longer helices, flanked by shorter, peripheral ones. In this domain, the [2Fe–2S] center lies at the N-termini of the two larger helices and is bound by cysteines 100, 103, 137, and 139. This domain is connected to the first molybdopterin-binding domain (Mo1) via an extended segment that spans 50 Å across a concave region on the molecular surface. According to sequence homology of MOP with several xanthine dehydrogenases (~52% similarity) (*212*) in the Fe–S and Mo domains, it may be anticipated that the flavin domain of xanthine oxidases (and absent in MOP) must lie somewhere along the extended segment. The two large Mo domains, Mo1 and Mo2, lie across each other approximately perpendicularly and the molybdenum site is located at their interface. There is no protein ligand to the molybdenum atom, although Glu 869 is rather close, at 3.5 Å, and *trans* to the apical position, and it may play a role in the catalytic cycle coordinating to the metal by a minor change in the carboxylate position. The molybdenum adopts a distorted square-pyramidal coordination geometry with the metal ~0.5 Å displaced out of the equatorial plane. The pterin cofactor binds to the molybdenum via its dithiolene, defining one side of the equatorial plane of the coordination sphere. *Trans* to the dithiolene are two oxygen ligands: one at a shorter distance assigned to a Mo=O bond, *trans* to S8′ and one longer Mo–O bond (~2.4 Å) which was assigned as a bound water molecule. The apical position is a Mo=O bond in the "desulfo" form of MOP, replaced by Mo=S in crystals of the "sulfo" form. Resulfuration of the crystals was achieved by incubation with sulfide under turnover conditions. The water ligand is pointing in the direction of an extended, 15 Å deep, solvent channel that provides access to the active site of the enzyme. This channel is coated with hydrophobic residues from both Mo1 and Mo2 domains and is funnel-shaped, being wider at the surface of the molecule.

These structural data are in agreement and support EXAFS data for MOP (*214*) as well as for xanthine oxidase (in both oxidized and reduced forms) (*198*, *215*), but the coordinated water ligand was iden-

tified for the first time in the crystal structure of MOP. Two different samples of *D. gigas* AOR were studied by EXAFS. These measurements reflect that the enzyme is purified as a variable mixture of sulfo and desulfo forms. One of the samples contained mainly desulfo form (*214*). In the oxidized form the molybdenum environment is found to contain two terminal oxo groups and two long (2.47 Å) Mo–S bonds. Evidence was also found for an oxygen or nitrogen ligand at 1.90 Å. The behavior of both oxidized and dithionite-treated forms is similar to that observed previously with desulfo xanthine oxidase and resembles sulfite oxidase and nitrate reductase. A reanalysis of *D. gigas* and *D. desulfuricans* AORs suggests that the fitting of the experimental data improves when a mixture of sulfo and oxo (desulfo) species is considered. The data were fitted with similar atomic distances (here indicated for the *D. gigas* enzyme): Mo–S 2.44 Å, Mo=O 1.67 Å, Mo=S (or O) 2.14 Å (the analysis was made keeping S + O = 2, in the proportion 0.7 Mo=S and 1.3 Mo=O), and a longer Mo–O distance 1.83 Å (assigned to a water or hydroxyl group) (G. George, in preparation).

2. *Spectroscopic Data*

The set of Mo(V) EPR signals detected in *D. gigas* and *D. desulfuricans* AORs shows close homology with the molybdenum-containing hydroxylase group. Mössbauer and X/Q-band EPR spectroscopic studies (*208*, *216*) complemented the UV/visible and CD studies and the assignment of the [2Fe–2S] arrangement of the iron–sulfur cores.

The molybdenum cofactor was liberated from *D. gigas* AOR, and under appropriate conditions was transferred quantitatively to nitrate reductase in extracts of *Neurospora crassa* (*nit-1 mutant*) to yield active nitrate reductase (*217*). On the basis of molybdenum content, the activity observed for reconstitution with molybdenum cofactor of *D. gigas* was lower (25%) than the values observed for the procedure using extractable molybdenum cofactor of XO, used as reference. This result can now be put in the context of the difference in pterin present (MPT–XO and MCD–AOR) (*218*).

a. Molybdenum Center EPR has been used as a valuable tool for revealing the different aspects of Mo(V) coordination at the active site of molybdenum-containing hydroxylases. The work on xanthine oxidase and related enzymes established the nomenclature adopted (*197*, *198*, *206*, *219*). The catalytically active form of the enzyme contains a sulfido ligand at the Mo site. The conversion to an oxo ligand (desulfo form) results in the loss of catalytic activity. Molybdenum-containing

hydroxylases are mixtures of inactive desulfo forms (that originate after long exposure to dithionite, Mo(V) *slow type* EPR signals) and active species (yielding *rapid type* signals that are generated in the presence of substrates or short chemical reduction). Kinetics and thermodynamics of the reduction of Mo(VI) to Mo(V) and Mo(IV) differ markedly within these species. The midpoint redox potential determined associated with the slow type signal are −415 mV (Mo(VI)/Mo(V)) and −530 mV (Mo(V)/Mo(IV)) (*208*). Different catalytic competent forms have been detected. Mo(V) EPR *rapid type 2* signal shows two strongly coupled protons that can be exchanged. Mo(V) EPR *rapid type 1* signal has one strongly and one weakly coupled proton. The different EPR signals that can be generated and observed in *D. gigas* (and *D. desulfuricans*) AOR reflect the reactivity and coordination versatility of the Mo site and place the enzyme in the group of the molybdenum hydroxylases. This variability of metal coordination relates to the multiple "faces" shown by EPR Mo(V) signals and can now be discussed in conjunction with the 3D structural data of *D. gigas* AOR.

b. Iron–Sulfur Centers EPR studies (complemented with Mössbauer studies; see later discussion) reveal the presence of two types of [2Fe–2S] cores, named Fe–S I and Fe–S II centers (*217*, *220*, *221*). X- and Q-band EPR studies established the presence of two EPR signals in equal amounts (Fe–S I and Fe–S II centers), as determined by computer simulation using the same set of parameters at the two different frequencies and double integration performed at different powers and temperatures. The Fe–S I is observed at 77 K (g-values at 2.021, 1.938, and 1.919, g_{av} = 1.959). The Fe–S II is only observable below 65 K (g-values at 2.057, 1.970, and 1.900, g_{av} = 1.976). Variation of amplitude of Fe/S I and Fe–S II centers as a function of redox potential revealed midpoint potentials of −260 and −285 mV, respectively.

An important advance on these studies was the possibility of isolating AORs from ^{57}Fe enriched media with obvious interest for an iron–sulfur center site labeling, with enhanced sensitivity of the Mössbauer studies. The work developed with bacterial systems is advantageous as compared with mammalian systems for isotopic labeling and opens the possibility of a direct measurement of substrate binding. Spectra of the enzyme in oxidized, partially reduced, benzaldehyde-reacted, and fully reduced states were recorded at different temperatures and with variable externally applied magnetic fields (*222*). In the oxidized enzyme, the clusters are diamag-

netic and exhibit a single quadrupole doublet with parameters $\Delta E_Q = 0.62 \pm 0.02$ mm/s and $\delta = 0.27 \pm 0.01$ mm/s) typical of the +2 state (ferric–ferric). Mössbauer spectra of the reduced clusters also show characteristic parameters of the +1 state (ferric–ferrous). The spectra could be explained by the spin-coupling model proposed for the [2Fe–2S] cluster, where the high-spin ferrous site ($S = 2$) is antiferromagnetically coupled to a high-spin ferric site ($S = \frac{5}{2}$) to form an $S = \frac{1}{2}$ system (localized valences). Two ferrous sites with different ΔE_Q (3.42 and 2.93 mm/s) are observed at 85 K, indicating the presence of two spectroscopically distinguishable [2Fe–2S] centers.

A Mössbauer study of the protein reacted with benzaldehyde (in parallel with EPR detection of Mo(V) signals) shows partial reduction of the iron–sulfur centers, indicating the involvement of the clusters in the process of substrate oxidation and rapid intramolecular electron transfer from the molybdenum to the iron–sulfur sites.

The larger ΔE_Q values observed for the ferrous sites in reduced [2Fe–2S] clusters and the hyperfine parameters obtained for the Fe–S clusters in the *D. gigas* AOR are very similar to those of the [2Fe–2S] centers in plant ferredoxins.

Another Mössbauer study on molybdenum hydroxylases was performed on a nonenriched sample of milk xanthine oxidase (*219*), and an unusually large ΔE_Q (3.2 mm/s at 175 K) was also observed for the ferrous site of one of the clusters.

B. Formate Dehydrogenase

Formate dehydrogenases are a diverse group of enzymes found in both prokaryotes and eukaryotes, capable of converting formate to CO_2. Formate dehydrogenases from anaerobic microorganisms are, in most cases, Mo- or W- containing iron–sulfur proteins and additionally flavin or hemes. Selenium cysteine is a Mo- ligand.

Three formate dehydrogenases have been purified from three different strains of sulfate-reducing bacteria: *D. vulgaris* (*223*), *D. desulfuricans* (*224*), and *D. gigas* (*225*). The enzyme from *D. vulgaris* was partially purified by Yagi (*226*, *227*) in 1969 and was found to reduce the monoheme cytochrome c_{553} but not the tetraheme cytochrome c_3. The purification of the formate dehydrogenase from *D. vulgaris* has been reexamined and claimed to be oxygen sensitive. The enzyme is composed of three subunits and was proposed to contain a molybdenum cofactor (bound to the large subunit) iron–sulfur center, and heme *c*-type moieties (bound to the small subunit) (*224*).

In two sulfate-reducing bacteria we found oxygen-tolerant formate dehydrogenases with different subunit composition. The formate dehydrogenase from *D. desulfuricans* is an $\alpha\beta\gamma$ protein whereas the one from *D. gigas* is an $\alpha\beta$ protein. Both proteins contain two MGD cofactors but the protein from *D. desulfuricans* contains four heme *c* attached to the γ subunit (16 kDa).

The protein from *D. desulfuricans* has been characterized by Mössbauer and EPR spectroscopy (*224*). The enzyme has a molecular mass of approximately 150 kDa (three different subunits: 88, 29, and 16 kDa) and contains three different types of redox-active centers: four *c*-type hemes, nonheme iron arranged as two $[4Fe–4S]^{2+/1+}$ centers, and a molybdopterin site (Mo-bound to two MGD). Selenium was also chemically detected. The enzyme specific activity is 78 units per mg of protein.

Mo(V) EPR signals were observed in the native, reduced, and formate-reacted states. A rhombic signal, designated rhombic I, is observed in the native state of the enzyme with *g*-values at $g_{max} = 2.019$, $g_{med} = 1.988$, and $g_{min} = 1.963$. This signal does not change in intensity when the redox potential changes from +140 to −400 mV. At redox potentials around −162 mV, another rhombic EPR signal due to Mo (V) (rhombic II), with *g*-values at $g_{max} = 2.009$, $g_{med} = 1.984$, and $g_{min} = 1.951$, appears. This EPR signal is transient in nature, reaching a maximum intensity and then declining with a decrease of the redox potential. The redox potential could be estimated for the redox couples at pH 7.6 where Mo(VI)/Mo(V) = −160 ± 5 mV and Mo(V)/Mo(IV) = −330 ± 5 mV.

Another intense and complex Mo(V) EPR signal with hyperfine splitting is obtained in *D. desulfuricans* FDH after anaerobic reaction with sodium formate. This signal is very different from the one observed in other FDHs (*224*).

After reduction by dithionite or formate at low temperature, two types of iron–sulfur centers can be distinguished by EPR: an [Fe–S] center I ($g_{max} = 2.050, g_{med} = 1.947, g_{min} = 1.896$) and an [Fe–S] center II ($g_{max} = 2.071$, $g_{med} = 1.926$, $g_{min} = 1.865$). The two iron–sulfur centers have similar midpoint redox potentials (at pH 7.6, center I, −350 ± 5 mV and center II, −335 ± 5 mV) as determined by EPR redox titration.

In the native state FDH displays rhombic EPR signals, observable at low temperature (10 K), with *g* values typical or ferric low-spin hemes, around $g_{max} = 3$.

Mössbauer spectroscopy confirmed the presence of four low-spin hemes. The iron–sulfur centers were identified as two different $[4Fe–4S]^{2+,1+}$ centers. The [4Fe–4S] center II has an unusually small ^{57}Fe hy-

perfine coupling constant. There are examples of clusters like these, such as those found in *D. gigas* hydrogenase (*174*).

D. gigas formate dehydrogenase seems to be quite different in terms of subunit composition. It does not contain a γ subunit and no heme *c* was detected (*225*). Also, two MGD were identified, but surprisingly, the enzyme contains tungsten instead of molybdenum. Mössbauer and EPR studies confirmed the presence of two $[4Fe–4S]^{2+,1+}$ clusters with similar properties to the ones found in *D. desulfuricans* FDH (*247*).

C. Nitrate Reductase

D. desulfuricans is able to grow on nitrate, inducing two enzymes: that responsible for the steps of conversion of nitrate to nitrite (nitrate reductase–NAP), which is an iron–sulfur Mo-containing enzyme, and that for conversion of nitrite to ammonia (nitrite reductase–NIR), which is a heme-containing enzyme. Nitrate reductase from *D. desulfuricans* is the only characterized enzyme isolated from a sulfate reducer that has this function. The enzyme is a monomer of 74 kDa and contains two MGD bound to a molybdenum and one $[4Fe–4S]^{2+/+1}$ center (*228*, *229*) in a single polypeptide chain of 753 amino acids. EXAFS data on the native nitrate reductase show that besides the two pterins coordinated to the molybdenum, there is a cysteine and a nonsulfur ligand, probably a Mo–OH (G. N. George, personal communication).

Recently, the first 3D crystal structure of the nitrate reductase from *D. desulfuricans* NAP was determined at 1.9 Å resolution by MAD methods (*230*). The structure is composed of four domains that are all involved in the binding of the cofactors. The [4Fe–4S] center is located near the surface of the molecule. The $Mo(MGD)_2$ cofactor extends to the interior of the protein. A 15 Å deep crevice toward the Mo site gives access to the substrate molecule and the Fe–S cluster is 12 Å apart from the catalytic site. Besides the four sulfur atoms from the pterin cofactor, a cysteinyl residue and a water/hydroxyl ligand complete the Mo coordination sphere. An electron transfer pathway connects the Fe–S center to the Mo site. The polypeptide fold and the arrangement of the cofactors have strong homologies with those found in the 3D structure of *E. coli* formate dehydrogenase (in this case a selenum cysteinyl ligand is present) (*231*).

EPR studies at low temperature detect the presence of one iron–sulfur center and molybdenum. At low temperature a sample of nitrate reductase reduced by dithionite shows a rhombic signal (g_{max} = 2.04, g_{med} = 1.94, and g_{min} = 1.90). This signal accounts for 0.84 spins/

molecule and was assigned to a [4Fe–4S] cluster. Preliminary Mössbauer studies confirm this assignment (*229*).

In the region of $g \cong 2$, another signal is present that is better detected at high temperature and that increases its intensity in the presence of nitrate. This signal has g values of $g_{max} = 1.998$, $g_{med} = 1.988$, and $g_{min} = 1.981$, and A values of $A_{max} = 0.54$ mT, $A_{med} = 0.59$ mT, and $A_{min} = 0.51$ mT. Similar Mo(V) signals have also been observed for soluble enzymes isolated from *A. vinelandii* (*232*) and *T. pantotropha* (*233–235*).

There are four different classes of nitrate reductases (*234*). The nitrate reductases from *D. desulfuricans* show a strong homology to the α-subunit of the class of periplasmic respiratory nitrate reductases, and also to some of the enzymes that are included on the class of cytoplasmic assimilatory nitrate reductases. Because of this fact, a proposal was made for a new class of monomeric NAP, which contains the minimal arrangement of metal centers to perform nitrate reduction: one [4Fe–4S] cluster and a Mo bound to two MGD.

D. Other Molybdenum-Containing Proteins in SRB

Homologous proteins to *D. gigas* and *D. desulfuricans* AORs have been isolated and partially characterized from SRB strains Berre eau and Berre sol ((*236*) and our unpublished results). The molecular mass ranges within 110–130 kDa (monomer). The UV/visible spectra have analogies with the former enzymes with maxima at around 280, 300, 420, 460, and a shoulder at 520 nm. Mo(V) EPR signals (slow and rapid type 2) were detected, as well as two sets of Fe/S centers (*236*). Different, and less well characterized, molybdenum proteins have been isolated from other sulfate reducers, and it is difficult at this stage to classify them. A molybdenum-containing iron–sulfur protein has been isolated from *D. africanus* strain Benghazi (*237*). The protein appears to be a complex protein of high molecular mass (112 kDa) composed of 10 subunits (each subunit contains circa 106 amino acids and a molecular mass of 11.5 kDa, with 2 cysteines) and 5–6 Mo atoms, 20 iron atoms, and labile sulfur. The spectrum shows peaks around 615 (48.4), 410 (64.4), 325 (141), and 280 nm. The N-terminal sequence was determined up to 26 residues. From *D. salexigens,* a similar protein was isolated, and characterized by its blue-gray color with bands at 612, 410, 275, and a shoulder at 319, having a molecular mass of 110 kDa (13 kDa subunits) (*150*). At the moment no information

is available on the molybdenum site and the iron–sulfur center arrangement, but preliminary EPR data seem to indicate that they are of a new type.

XII. Concluding Remarks

A. Electron Transfer and Magnetic Interactions

Several 3D crystal structures of simple and complex iron–sulfur-containing proteins isolated from sulfate reducers have been solved. The main structural features have been thoroughly discussed in the text. They include the simple rubredoxin family (Rd, Dx, and Dfx), ferredoxins, hydrogenase, and AOR. In addition, structures of other electron carriers such as cytochromes and flavodoxins have been determined (for review, see Refs. (*238*, *239*)). The overall data indicate the wide range of structural solutions adopted in the construction of the metal-containing active sites and were inspiring motifs for the proposal of catalytic mechanisms. The ligands, the geometries, the distortions imposed at the active site, and their exposure to solvent are determinants for the overall enzymic performance. A step forward has already begun, since not only the as-isolated "unready" states have been analyzed: structural data on "ready" states (different poised redox states) and also states of the enzymes in interaction with substrates (and inhibitors and products) are becoming known. As anticipated, subtle conformational changes are detected between "unready" and "ready" forms preparing the active sites for action. The alterations in the primary coordination sphere of the metals are important in order that substrates can coordenate to metals at the active site for *a posteriori* processing.

We will use here the main results obtained for two complex and distinct situations: the structural and spectroscopic information gathered for *D. gigas* [NiFe] hydrogenase and AOR, in order to discuss relevant aspects related to magnetic interaction between the redox centers, intramolecular electron transfer, and, finally, interaction with other redox partners in direct relation with intermolecular electron transfer and processing of substrates to products.

It is clear that multiredox devices are built up in order to transfer electrons between electron donors and acceptors in a precise vectorial pathway.

The [NiFe] hydrogenase metal sites were completely defined by spectroscopy and X-ray diffraction studies, as discussed before. The

Mössbauer data on the native state of the enzyme revealed the presence of a $[3Fe–4S]^{1+}$ and two $[4Fe–4S]^{2+}$ clusters (*174*), results that were fully supported by 3D crystallographic studies (*164*). As-prepared [NiFe] hydrogenase is described as containing four noninteracting redox active centers, the three [Fe–S] clusters and the NiFe site. EPR and Mössbauer studies performed on the iron–sulfur clusters of the enzyme at different poised oxidation–reduction potentials and reacted with dihydrogen indicated that no cluster conversion occurs (*174*). However, after reaction with substrate, the enzyme shows a complex magnetic behavior. It is clear from the observation of the relaxation behavior of the sites, as well as from magnetic splittings of the EPR lines, that the NiFe site is affected by the proximity of the reduced [4Fe–4S] cluster, and the reduced [3Fe–4S] site ($S = 2$) is perturbed by the paramagnetism of the other reduced cubane site (most probably the "distal" one) (see Fig. 11A).

A complex interaction pattern is also detected in *D. gigas* and *D. desulfuricans* AORs (and in xanthine oxidase (*240*)) when the sites become paramagnetic. EPR data revealed that the Mo(V) site and the reduced [Fe–S] centers interact magnetically. The X-ray crystallographic determination of the structure of *D. gigas* AOR precisely indicates the localization of the metal centers and their relative position, and gives now support for the interpretation of magnetic interactions observed in the EPR spectra. As a result of EPR work, it has long been recognized that these enzymes contain two kinds of [2Fe–2S] centers, called Fe–S I and Fe–S II. As discussed before, Fe–S I has EPR parameters similar to those of spinach ferredoxin, whereas Fe/S II is unusual in having a larger g_{av}, not being observable at temperatures above 40 K. The 3D crystal structure indicates that one of the Fe–S centers is included in a protein domain with a similar fold to that in spinach ferredoxin (on the surface of the molecule) and the other, completely buried, is located in a domain with a unique fold (see Fig. 11B).

A few arguments can now be put forward in order to assign which Fe–S center seen in the X-ray structure corresponds to the spectroscopically distinct Fe–S center. Fe–S center II is close to the Mo site, in a bridging position to Fe–S center I (see Fig. 11). The Mo(V) slow signal is split at low temperature by a magnetic interaction with an iron–sulfur center. Fe–S center II is the candidate as the interacting partner. The Fe–S center I feature at g_{max} is clearly split below 40 K. The large splitting (circa 20 G) must be due to the paramagnetic Fe–S center II; the low quantitation of

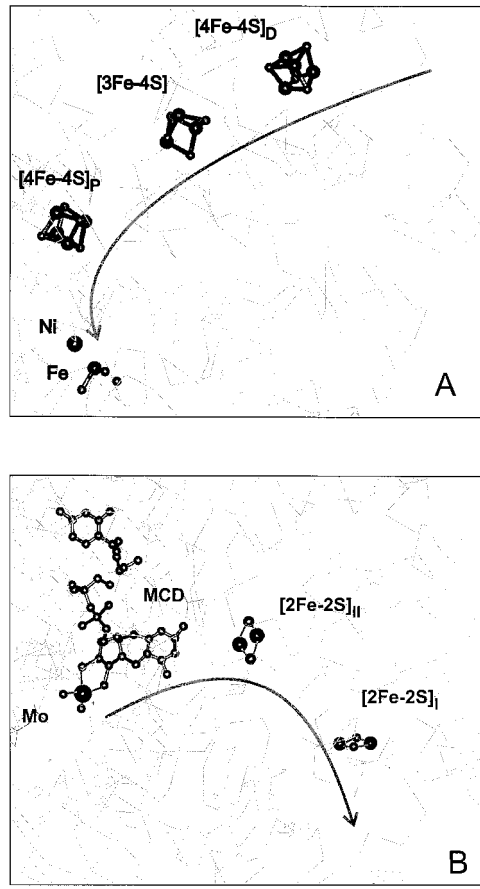

FIG. 11. The metal sites in *D. gigas* hydrogenase (Hase) (A) and aldehyde oxidoreductase (AOR) (B). The figure emphasizes the relative positioning of the metal sites and their proximity, suggesting an attractive electron transfer pathway. The arrows indicate electron transfer for hydrogen evolution requiring an electron donor (A) and aldehyde conversion to carboxylic acid, the electrons being transferred to an electron acceptor (B).

Mo(V) paramagnetic species is also an argument to exclude an interaction between the Mo site and Fe–S center I. These studies were further complemented by detailed study of the observable splitting and its temperature dependence, EPR saturation, and the effect of differential reduction of the Fe–S centers. A magnetic interaction was also seen in xanthine oxidase, between various Mo(V) EPR species and one of the Fe–S centers. A study on the

exchangeability of protons interacting with these Fe–S centers using ENDOR (ref) supports the idea that Fe–S I is more solvent-exposed than Fe–S II, consistent with the former having a typical spinach ferredoxin fold and spinach-ferredoxin-like EPR parameters. These assignments appear to be in conflict with the conclusions from previous work on the identity of the Fe–S centers in XO (*239*).

The EPR results agree with the crystallographic results, the Mo being ca. 15 Å from the buried Fe–S (center II—spinach atypical fold) and ca. 27 Å from the solvent-exposed Fe–S (center I—ferredoxin-like) and could help to advance the understanding of the possibly related intramolecular electron-transfer processes occuring during enzyme turnover. A detailed study on the magnetic interaction is underway using X- and Q-band EPR tools (J. Caldeira, J. J. G. Moura, in collaboration with P. Bertrand and co-workers, in preparation).

Another important outcome of the structural analysis is the relative positioning of the metal sites and their distances in order to define plausible electron transfer pathways between electron donors and acceptors. A common pattern starts to emerge (the same applies to cytochrome oxidase (*241*, *242*). Figure 11 gives a pictorial view of the electron transfer pathway:

$$\begin{aligned} &e \rightarrow [4Fe\text{–}4S]\ \text{“distal”} \rightarrow [3Fe\text{–}4S] \rightarrow [4Fe\text{–}4S]\ \text{“proximal”} \rightarrow [Ni\text{–}Fe]\ \textbf{HASE} \rightarrow H_2 \\ &\quad \text{Aldehydes} \rightarrow \text{Mo(MCD)–}\textbf{AO} \rightarrow [2Fe\text{–}2S]_{II} \rightarrow [2Fe\text{–}2S]_{I} \rightarrow \text{DCPIP } (e^- \text{ acceptor}). \end{aligned}$$

Moreover, an electron transfer chain could be reconstituted *in vitro* that is able to oxidize aldehydes to carboxylic acids with concomitant reduction of protons and net production of dihydrogen (*213*, *243*). The first enzyme in this chain is an aldehyde oxidoreductase (AOR), a homodimer (100 kDa) containing one Mo cofactor (MCD) and two [2Fe–2S] centers per subunit (*199*). The enzyme catalytic cycle can be regenerated by transferring electrons to flavodoxin, an FMN-containing protein of 16 kDa (and afterwards to a multiheme cytochrome and then to hydrogenase):

$$\text{Aldehydes} \rightarrow \text{AOR} \rightarrow \text{Flavodoxin} \rightarrow \text{Multiheme cytochrome} \rightarrow \text{Hase} \rightarrow H_2.$$

This study of such of an electron transfer chain is most timely, since the 3D structures of all the components involved are known (and related components can easily be obtained by homology molecular modeling). Proposals of structural models for the complexes formed between *D. gigas* AOR and flavodoxin, based on the available X-ray

structures of the two isolated proteins, is underway. Flavodoxin–cytochrome c_3 docking has been studied in detail (*244*). Hydrogenase–cytochrome c_3 is also under study. The model of the complexes is proposed with the aid of a macromolecular docking program developed in our laboratory (Krippahl, L., Palma, P. N., Wampler, J. E., and Moura, J. J. G., in preparation), which has been able to predict with success the geometry of a series of different protein–protein complexes. Cocrystallization and cross-linking between the partners is a prospective avenue for future experiments. The advantage of these models are their functional viability in terms of electron transfer, being supported by the known biochemical and spectroscopic data.

These two case studies also stress the importance of exploiting spectroscopic and crystallographic results in a complementary way. The coordination of Ni and Fe in the novel heterometal core is a challenge for inorganic chemistry: not only the atypical nonproteic terminal iron ligands, but the oxo bridge species. The need for a decrease in the coordination site of the nickel (assumed as the hydrogen binding site) may involve the removal of this extra ligand, giving a means for the oxo species to regulate "unready" and "ready" forms of the enzyme. The coordination of the dihydrogen shared between Ni and Fe is a tempting proposal.

The data gathered on different molybdenum proteins and the data available for AOR (and nitrate reductase, in preparation), together with the structures revealed for FDH dehydrogenases and DMSO reductases, enlarge our understanding of this enzyme group, and enable enzyme family grouping. It is now clear that a wide variability can be found in terms of type and number of pterins, as well as the presence (or not) of a direct ligand offered by the main polypeptide chain. Oxo or sulfur atom coordination is a structural and reactional determinant. The mechanistic implications, directly deduced from the 3D structural features, have been of obvious interest.

ACKNOWLEDGMENTS

This work supported by grants under the programs PRAXIS 2/2.1/BIO/05/94, Praxis 2/2.1/QUIM/3/94, and Bio4 CT96-0281. We would like to acknowledge the collaboration with Professor M. J. Romão and Professor R. Huber that have been "revealing" of several of the structures discussed; we are grateful for their enthusiasm and support. Also, we express our appreciation to the Mössbauer contribution of Professor B. H. Huynh, whose long collaboration has allowed the characterization of many Fe–S proteins from SRB. Finally, we thank our colleagues from the groups of Bioinorgânica and Bioquímica Física de Proteínas (CQFB) for their inputs in the several ongoing projects.

References

1. LeGall, J.; Fauque, G. "Biology of Anaerobic Microorganisms"; Zehnder, A. J. B., Ed.; Wiley: New York, pp. 587–639, 1988.
2. LeGall, J.; Peck, H. J. *FEMS Microbiol. Rev.* **1987,** *46,* 35.
3. Odom, J. M.; Peck, H. D., Jr. *Ann. Rev. Microbiol.* **1984,** *38,* 551.
4. LeGall, J.; Moura, J.; Peck, H.; Xavier, A. "Iron–Sulfur Proteins"; Spiro, T. G., Ed.; Wiley: New York, pp. 177–248. 1982; Vol. 4.
5. Probst, I.; Moura, J. J.; Moura, I.; Bruschi, M.; Le Gall, J. *Biochim. Biophys. Acta* **1978,** *502,* 38.
6. Papavassiliou, P.; Hatchikian, E. C. *Biochim. Biophys. Acta* **1985,** *810,* 1.
7. Lovenberg, W.; Williams, W. M. *Biochemistry* **1969,** *8,* 141.
8. Lovenberg, W.; Sobel, B. E. *Proc. Natl. Acad. Sci. USA* **1965,** *54,* 193.
9. Rao, K. K.; Evans, M. C.; Cammack, R.; Hall, D. O.; Thompson, C. L.; Jackson, P. J.; Johnson, C. E. *Biochem. J.* **1972,** *129,* 1063.
10. Bruschi, M.; Moura, I.; Le Gall, J.; Xavier, A. V.; Sieker, L. C.; Couchoud, P. *Biochem. Biophys. Res. Commun.* **1979,** *90,* 596.
11. Brumlik, M. J.; Leroy, G.; Bruschi, M.; Voordouw, G. *J. Bacteriol.* **1990,** *172,* 7289.
12. Moura, I.; Xavier, A. V.; Cammack, R.; Bruschi, M.; Le Gall, J. *Biochim. Biophys. Acta* **1978,** *533,* 156.
13. Moura, I.; Huynh, B. H.; Hausinger, R. P.; Le Gall, J.; Xavier, A. V.; Münck, E. *J. Biol. Chem.* **1980,** *255,* 2493.
14. Tavares, P.; Wunderlich, J. K.; Lloyd, S. G.; LeGall, J.; Moura, J. J.; Moura, I. *Biochem. Biophys. Res. Commun.* **1995,** *208,* 680.
15. Sieker, L. C.; Stenkamp, R. E.; LeGall, J. *Meth. Enzymol.* **1994,** *243,* 203.
16. Archer, M.; Huber, R.; Tavares, P.; Moura, I.; Moura, J. J.; Carrondo, M. A.; Sieker, L. C.; LeGall, J.; Romão, M. J. *J. Mol. Biol.* **1995,** *251,* 690.
17. Goodfellow, B.; Tavares, P.; Romão, M.; Czaja, C.; Rusnak, F.; LeGall, J.; Moura, I.; Moura, J. *J. Bioinorg. Chem.* **1996,** *1,* 341.
18. Yu, L.; Kennedy, M.; Czaja, C.; Tavares, P.; Moura, J. J.; Moura, I.; Rusnak, F. *Biochem. Biophys. Res. Commun.* **1997,** *231,* 679.
19. Moura, I.; Teixeira, M.; Xaviera, A. V.; Moura, J. J. G.; Lespinat, P. A.; LeGall, J.; Berlier, Y.; Saint-Martin, P.; Fauque, G. *Trav. Chim. Pays-bas* **1987,** *106,* 418.
20. Huang, Y. H.; Moura, I.; Moura, J. J. G.; LeGall, J.; Park, J. B., Adams, M. W.; Johnson, M. K. *Inorg. Chem.* **1993,** *32,* 406.
21. Yachandra, V. K.; Hare, J.; Moura, I.; Spiro, T. G. *J. Am. Chem. Soc.* **1983,** *105,* 6455.
22. Moura, I.; Teixeira, M.; LeGall, J.; Moura, J. J. G. *J. Inorg. Chem.* **1991,** *44,* 127.
23. Blake, P. R.; Park, J.-B.; Bryant, F. O.; Aono, S.; Magnuson, J. K.; Eccleston, E.; Howard, J. B.; Summers, M. F.; Adams, M. W. *Biochemistry* **1991,** *30,* 10885.
24. Blake, P. R.; Park, J.-B.; Zhou, Z. H.; Hare, D. R.; Adams, M. W. W.; Summers, M. F. *Protein Sci.* **1992,** *1,* 1508.
25. Goodfellow, B. J.; Tavares, P.; Romão, M. J.; Carrondo, M. A.; Czaja, C.; Rusnak, F.; LeGall, J.; Moura, I.; Moura, J. J. G. *J. Biol. Inorg. Chem.* **1996,** *1,* 341.
26. Goodfellow, B. J.; Rusnak, F.; Moura, I.; Domke, T.; Moura, J. J. G. *Protein Sci.* **1998,** *7,* 928.
27. Goodfellow, B. J.; Lima, M. J.; Ascenso, C.; Kennedy, M.; Sikkink, R.; Rusnak, F.; Moura, I.; Moura, J. J. G. *Inorg. Chem. Acta* **1998,** *273,* 279.
28. Moura, I.; Tavares, P.; Moura, J. J.; Ravi, N.; Huynh, B. H.; Liu, M. Y.; LeGall, J. *J. Biol. Chem.* **1990,** *265,* 21596.

29. Verhagen, M. F.; Voorhorst, W. G.; Kolkman, J. A.; Wolbert, R. B.; Hagen, W. R. *FEBS Lett.* **1993,** *336,* 13.

30. Tavares, P.; Ravi, N.; Moura, J. J.; LeGall, J.; Huang, Y. H.; Crouse, B. R.; Johnson, M. K.; Huynh, B. H.; Moura, I. *J. Biol. Chem.* **1994,** *269,* 10504.

31. Devreese, B.; Tavares, P.; Lampreia, J.; Van Damme, N.; Le Gall, J.; Moura, J. J.; Van Beeumen, J.; Moura, I. *FEBS Lett.* **1996,** *385,* 138.

32. Coelho, A. V.; Matias, P.; Fülöp, V.; Thompson, A.; Gonzalez, A.; Carrondo, M. A. *J. Bioinorg. Chem.* **1997,** *2,* 680.

33. Pianzzola, M. J.; Soubes, M.; Touati, D. *J. Bacteriol.* **1996,** *178,* 6736.

34. Liochev, S. I.; Fridovich, I. *J. Biol. Chem.* **1997,** *272,* 25573.

35. Klenk, H. P.; Clayton, R. A.; Tomb, J. F.; White, O.; Nelson, K. E.; Ketchum, K. A.; Dodson, R. J.; Gwinn, M.; Hickey, E. K.; Peterson, J. D.; Richardson, D. L.; Kerlavage, A. R.; Graham, D. E.; Kyrpides, N. C.; Fleischmann, R. D.; Quackenbush, J.; Lee, N. H.; Sutton, G. G.; Gill, S.; Kirkness, E. F.; Dougherty, B. A.; McKenney, K.; Adams, M. D.; Loftus, B.; Venter, J. C. *Nature* **1997,** *390,* 364.

36. Smith, D. R.; Doucette-Stamm, L. A.; Deloughery, C.; Lee, H.; Dubois, J.; Aldredge, T.; Bashirzadeh, R.; Blakely, D.; Cook, R.; Gilbert, K.; Harrison, D.; Hoang, L.; Keagle, P.; Lumm, W.; Pothier, B.; Qiu, D.; Spadafora, R.; Vicaire, R.; Wang, Y.; Wierzbowski, J.; Gibson, R.; Jiwani, N.; Caruso, A.; Bush, D.; Reeve, J. N. *J. Bacteriol.* **1997,** *179,* 7135.

37. Bult, C. J.; White, O.; Olsen, G. J.; Zhou, L.; Fleischmann, R. D.; Sutton, G. G.; Blake, J. A.; FitzGerald, L. M.; Clayton, R. A.; Gocayne, J. D.; Kerlavage, A. R.; Dougherty, B. A.; Tomb, J. F.; Adams, M. D.; Reich, C. I.; Overbeek, R.; Kirkness, E. F.; Weinstock, K. G.; Merrick, J. M.; Glodek, A.; Scott, J. L.; Geoghagen, N. S. M.; Venter, J. C. *Science* **1996,** *273,* 1058.

38. LeGall, J.; Prickril, B. C.; Moura, I.; Xavier, A. V.; Moura, J. J.; Huynh, B. H. *Biochemistry* **1988,** *27,* 1636.

39. Tavares, P. Ph.D. Thesis; Universidade Nova de Lisboa: Lisbon, 1994.

40. Elango, N.; Radhakrishnan, R.; Froland, W. A.; Wallar, B. J.; Earhart, C. A.; Lipscomb, J. D.; Ohlendorf, D. H. *Protein Sci.* **1997,** *6,* 556.

41. Nordlund, P.; Dalton, H.; Eklund, H. *FEBS Lett.* **1992,** *307,* 257.

42. Logan, D. T.; Su, X. D.; Aberg, A.; Regnstrom, K.; Hajdu, J.; Eklund, H.; Nordlund, P. *Structure* **1996,** *4,* 1053.

43. Pierik, A. J.; Wolbert, R. B.; Portier, G. L.; Verhagen, M. F.; Hagen, W. R. *Eur. J. Biochem.* **1993,** *212,* 237.

44. Ravi, N.; Prickril, B. C.; Kurtz, D. M., Jr.; Huynh, B. H. *Biochemistry* **1993,** *32,* 8487.

45. Prickril, B. C.; Kurtz, D. M., Jr.; LeGall, J.; Voordouw, G. *Biochemistry* **1991,** *30,* 11118.

46. Van Beeumen, J. J.; Van Driessche, G.; Liu, M.-Y.; LeGall, J. *J. Biol. Chem.* **1991,** *266,* 20645.

47. Kurtz, D. M., Jr.; Prickril, B. C. *Biochem. Biophys. Res. Commun.* **1991,** *181,* 337.

48. deMaré, F.; Kurtz, D. M., Jr.; Nordlund, P. *Nature Struct. Biol.* **1996,** *3,* 539.

49. Trikha, J.; Theil, E. C.; Allewell, N. M. *J. Mol. Biol.* **1995,** *248,* 949.

50. Lawson, D. M.; Artymiuk, P. J.; Yewdall, S. J.; Smith, J. M.; Livingstone, J. C.; Treffry, A.; Luzzago, A.; Levi, S.; Arosio, P.; Cesareni, G. *Nature* **1991,** *349,* 541.

51. Frolow, F.; Kalb, A. J.; Yariv, J. *Nature Struct. Biol.* **1994,** *1,* 453.

52. Bonomi, F.; Kurtz, D. M. J.; Cui, X. *J. Bioinorg. Chem.* **1996,** *1,* 69.

53. Pereira, A. S.; Tavares, P.; Lloyd, S. G.; Danger, D.; Edmondson, D. E.; Theil, E. C.; Huynh, B. H. *Biochemistry* **1997,** *36,* 7917.

54. Fukuyama, K.; Matsubara, H.; Tsukihara, T.; Katsube, Y. *J. Mol. Biol.* **1989,** *210,* 383.
55. Stout, C. D. *J. Mol. Biol.* **1989,** *205,* 545.
56. Kissinger, C. R.; Adman, E. T.; Sieker, L. C.; Jensen, L. H.; LeGall, J. *FEBS Lett.* **1989,** *244,* 447.
57. Stout, G. H.; Turley, S.; Sieker, L. C.; Jensen, L. H. *Proc. Natl. Acad. Sci. USA* **1988,** *85,* 1020.
58. Fukuyama, K.; Hase, T.; Matsumoto, S.; Tsukihara, T.; Katsube, Y.; Tanaka, N.; Kakudo, M.; Wada, K.; Matsubara, H. *Nature* **1980,** *286,* 522.
59. Matsubara, H.; Kazuhiko, S.; *Adv. Inorg. Chem.* **1992,** *38,* 223.
60. Hatchikian, E. C.; LeGall, J. *Ann. Inst. Pasteur* **1970,** *118,* 288.
61. LeGall, J.; Dragoni, N. *Biochem. Biophys. Res. Commun.* **1966,** *23,* 145.
62. Bruschi, M.; Hatchikian, C.; LeGall, J.; Moura, J. J.; Xavier, A. V. *Biochimica et Biophysica Acta* **1976,** *449,* 275.
63. Bruschi, M.; Couchoud, P. *Biochem. Biophys. Res. Commun.* **1979,** *91,* 623.
64. Bruschi, M.; Hatchikian, C. E.; Golovleva, L. A.; Gall, J. L. *J. Bacteriol.* **1977,** *129, 30.*
65. Guerlesquin, F.; Bruschi, M.; Bovier-Lapierre, G.; Fauque, G. *Biochim. Biophys. Acta* **1980,** *626,* 127.
66. Bruschi, M. H.; Guerlesquin, F. A.; Bovier-Lapierre, G. E., Bonicel, J. J.; Couchoud, P. M. *J. Biol. Chem.* **1985,** *260,* 8292.
67. Guerlesquin, F.; Moura, J. J.; Cammack, R. *Biochim. Biophys. Acta* **1982,** *679,* 422.
68. Hatchikian, C. E.; Jones, H. E.; Bruschi, M. *Biochim. Biophys. Acta* **1979,** *548,* 471.
69. Bruschi, M.; Hatchikian, E. C. *Biochimie* **1982,** *64,* 503.
70. Hatchikian, E. C.; Bruschi, M. *Biochim. Biophys. Acta* **1981,** *634,* 41.
71. Bovier-Lapierre, G.; Bruschi, M.; Bonicel, J.; Hatchikian, E. C. *Biochim. Biophys. Acta* **1987,** *913,* 20.
72. Armstrong, F. A.; George, S. J.; Cammack, R.; Hatchikian, E. C.; Thomson, A. J. *Biochem. J.* **1989,** *264,* 265.
73. Ogata, M.; Kondo, S.; Okawara, N.; Yagi, T. *J. Biochem.* **1988,** *103,* 121.
74. Okawara, N.; Ogata, M.; Yagi, T.; Wakabayashi, S.; Matsubara, H. *J. Biochem.* **1988,** *104,* 196.
75. Okawara, N.; Ogata, M.; Yagi, T.; Wakabayashi, S.; Matsubara, H. *Biochimie* **1988,** *70,* 1815.
76. Probst, I.; Moura, J. J. G.; Moura, I.; Bruschi, M.; LeGall, J. *Biochim. Biophys. Acta* **1978,** *502,* 38.
77. Postgate, J. R.; "Sulphate Reducing Bacteria"; 2nd ed.; Cambridge University Press: Cambridge, 1984.
78. LeGall, J.; Postgate, J. R. *Adv. Microb. Physiol.* **1973,** *20,* 81.
79. Adman, E. T.; Sieker, L. C.; Jensen, L. H. *J. Biol. Chem.* **1973,** *248,* 3987.
80. Stout, C. D. *J. Biol. Chem.* **1988,** *263,* 9256.
81. Fukuyama, K.; Nagahara, Y.; Tsukihara, T.; Katsube, Y.; Hase, T.; Matsubara, H. *J. Mol. Biol.* **1988,** *199,* 183.
82. Marion, D.; Guerlesquin, F. *Biochem. Biophys. Res. Commun.* **1989,** *159,* 592.
83. Cambillau, C.; Frey, M.; Mosse, J.; Guerlesquin, F.; Bruschi, M. *Proteins* **1988,** *4,* 63.
84. Sieker, L. C.; Adman, E. T.; Jensen, L. H.; LeGall, J. *J. Mol. Biol.* **1984,** *179,* 151.
85. Beinert, H.; Kennedy, M. C. *Eur. J. Biochem.* **1989,** *186,* 5.
86. Robbins, A. H.; Stout, C. D. *Proc. Natl. Acad. Sci. USA* **1989,** *86,* 3639.
87. Kennedy, M. C.; Stout, C. D.; *Adv. Inorg. Chem.* **1992,** *38,* 323.

88. George, S. J.; Armstrong, F. A.; Hatchikian, E. C.; Thomson, A. J. *Biochem. J.* **1989,** *264,* 275.
89. Cammack, R.; Rao, K. K.; Hall, D. O.; Moura, J. J. G.; Xavier, A. V.; Bruschi, M.; LeGall, J.; Deville, A.; Gayda, J. P. *Biochim. Biophys. Acta* **1977,** *490,* 311.
90. Huynh, B. H.; Moura, J. J.; Moura, I.; Kent, T. A.; LeGall, J.; Xavier, A. V.; Munck, E. *J. Biol. Chem.* **1980,** *255,* 3242.
91. Papaefthymiou, V.; Girerd, J.-J.; Moura, I.; Moura, J. J. G.; Münck, E. *J. Am. Chem. Soc.* **1987,** *109,* 4703.
92. Johnson, M. K.; Hare, J. W.; Spiro, T. G.; Moura, J. J.; Xavier, A. V.; LeGall, J. *J. Biol. Chem.* **1981,** *256,* 9806.
93. Thomson, A. J.; Robinson, A. E.; Johnson, M. K.; Moura, J. J.; Moura, I.; Xavier, A. V.; Legall, J. *Biochim. Biophys. Acta* **1981,** *670,* 93.
94. Antonio, M. R.; Averill, B. A.; Moura, I.; Moura, J. J.; Orme-Johnson, W. H.; Teo, B. K.; Xavier, A. V. *J. Biol. Chem.* **1982,** *257,* 6646.
95. Day, E. P.; Peterson, J.; Bonvoisin, J. J.; Moura, I.; Moura, J. J. *J. Biol. Chem.* **1988,** *263,* 3684.
96. Moreno, C.; Macedo, A. L.; Moura, I.; LeGall, J.; Moura, J. J. G. *J. Inorg. Biochem.* **1994,** *53,* 219.
97. Macedo, A. L.; Moura, I.; Moura, J. J. G.; LeGall, J.; Huynh, B. H. *Inorg. Chem.* **1993,** *32,* 1101.
98. Macedo, A. L.; Palma, P. N.; Moura, I.; LeGall, J.; Wray, V.; Moura, J. J. G. *Mag. Res. Chem.* **1993,** *31,* 559.
99. Kent, T. A.; Huynh, B. H.; Munck, E. *Proc. Natl. Acad. Sci. USA* **1980,** *77,* 6574.
100. Emptage, M. H.; Kent, T. A.; Huynh, B. H.; Rawlings, J.; Orme-Johnson, W. H.; Munck, E. *J. Biol. Chem.* **1980,** *255,* 1793.
101. Armstrong, F. A.; Butt, J. N.; George, S. J.; Hatchikian, E. C.; Thomson, A. J. *FEBS Lett.* **1989,** *259,* 15.
102. Armstrong, F. A. *Adv. Inorg. Chem.* **1992,** *38,* 117.
103. Iismaa, S. E.; Vazquez, A. E.; Jensen, G. M.; Stephens, P. J.; Butt, J. N.; Armstrong, F. A.; Burgess, B. K. *J. Biol. Chem.* **1991,** *266,* 21563.
104. Shen, B.; Martin, L. L.; Butt, J. N.; Armstrong, F. A.; Stout, C. D.; Jensen, G. M.; Stephens, P. J.; La Mar, G. N.; Gorst, C. M.; Burgess, B. K. *J. Biol. Chem.* **1993,** *268,* 25928.
105. Tong, J.; Feinberg, B. A. *J. Biol. Chem.* **1994,** *269,* 24920.
106. Armstrong, F. A.; George, S. J.; Thomson, A. J.; Yates, M. G. *FEBS Lett.* **1988,** *234,* 107.
107. Moura, J. J.; Moura, I.; Kent, T. A.; Lipscomb, J. D.; Huynh, B. H.; LeGall, J.; Xavier, A. V.; Munck, E. *J. Biol. Chem.* **1982,** *257,* 6259.
108. Middleton, P.; Dickson, D. P.; Johnson, C. E.; Rush, J. D. *Eur. J. Biochem.* **1978,** *88,* 135.
109. Zhou, J.; Holm, R. H. *J. Am. Chem. Soc.* **1995,** *117,* 11353.
110. Zhou, J.; Hu, Z.; Münck, E.; Holm, R. H. *J. Am. Chem. Soc.* **1996,** *118,* 1966.
111. Beinert, H.; Holm, R. H.; Munck, E. *Science* **1997,** *277,* 653.
112. Kent, T. A.; Moura, J. J. G.; Moura, I.; Lispcomb, J. D.; Huynh, B. H.; LeGall, J.; Xavier, A. V.; Münck, E. *FEBS Lett.* **1982,** *138,* 55.
113. Moura, I.; Macedo, A. L.; Moura, J. J. G. "Advanced EPR and Applications in Biology and Biochemistry"; Elsevier: Amsterdam, 1989.
114. Hagen, W. R. *Adv. Inorg. Chem.* **1992,** *38,* 165.
115. Conover, R. C.; Kowal, A. T.; Fu, W. G.; Park, J. B.; Aono, S.; Adams, M. W.; Johnson, M. K. *J. Biol. Chem.* **1990,** *265,* 8533.

116. Moura, I.; Moura, J. J. G.; Münck, E.; Papaefthymiou, V.; LeGall, J. *J. Am. Chem. Soc.* **1986,** *108,* 349.
117. Surerus, K. K.; Münck, E.; Moura, I.; Moura, J. J. G.; LeGall, J. *J. Am. Chem. Soc.* **1987,** *109,* 3805.
118. Butt, J. N.; Armstrong, F. A.; Breton, J.; George, S. J.; Thomson, A. J.; Hatchikian, E. C. *J. Am. Chem. Soc.* **1991,** *113,* 6663.
119. Butt, J. N.; Sucheta, A.; Armstrong, F. A.; Breton, J.; Thomson, A. J.; Hatchikian, E. C. *J. Am. Chem. Soc.* **1991,** *113,* 8948.
120. Conover, R. C.; Park, J.-B.; Adams, M. W. W.; Johnson, M. K. *J. Am. Chem. Soc.* **1990,** *112,* 4562.
121. Thomson, A. J.; Robinson, A. E.; Johnson, M. K.; Cammack, R.; Rao, K. K.; Hall, D. O. *Biochim. Biophys. Acta* **1981,** *637,* 423.
122. Münck, E.; Papaefthymiou, V.; Surerus, K. K.; Girerd, J.-J. "Metal Ions in Proteins"; Que, L., Ed.; ACS Symposium Series, *372,* Chap. 15, Washington, D.C.
123. Moreno, C.; Macedo, A. L.; Surerus, K. K.; Münck, E.; LeGall, J.; Moura, J. J. G. *Abstract, 3rd International Conference on Molecular Biology of Hydrogenases* **1991,** Tróia, Portugal.
124. Hagen, W. R.; Pierik, A. J.; Veeger, C. *J. Chem. Soc. Faraday Trans.* **1989,** *85,* 4083.
125. Moura, I.; Tavares, P.; Moura, J. J.; Ravi, N.; Huynh, B. H.; Liu, M. Y.; LeGall, J. *J. Biol. Chem.* **1992,** *267,* 4489.
126. Pierik, A. J.; Hagen, W. R.; Dunham, W. R.; Sands, R. H. *Eur. J. Biochem.* **1992,** *206,* 705.
127. Pierik, A. J.; Wolbert, R. B.; Mutsaers, P. H.; Hagen, W. R.; Veeger, C. *Eur. J. Biochem.* **1992,** *206,* 697.
128. Marritt, S. J.; Farrar, J. A.; Breton, J. L.; Hagen, W. R.; Thomson, A. J. *Eur. J. Biochem.* **1995,** *232,* 501.
129. van den Berg, W. A.; Stevens, A. A.; Verhagen, M. F.; van Dongen, W. M.; Hagen, W. R. *Biochim. Biophys. Acta* **1994,** *1206,* 240.
130. Stokkermans, J. P.; Houba, P. H.; Pierik, A. J.; Hagen, W. R.; van Dongen, W. M.; Veeger, C. *Eur. J. Biochem.* **1992,** *210,* 983.
131. Stokkermans, J. P.; Pierik, A. J.; Wolbert, R. B.; Hagen, W. R.; Van Dongen, W. M.; Veeger, C. *Eur. J. Biochem.* **1992,** *208,* 435.
132. Arendsen, A. F.; Hadden, J.; Card, G.; McAlpine, A. S.; Bailey, S.; Zaitsev, V.; Duke, E. H. M.; Lindley, P. F.; Kröckel, M.; Trautwein, A. X.; Feiters, M. C.; Charnock, J. M.; Garner, C. D.; Marrit, S. J.; Thomson, A. J.; Kooter, I. M.; Johnson, M. K.; van den Berg, W. A. M.; van Dongen, W. M. A. M.; Hagen, R. W. *J. Bioinorg. Chem.* **1998,** *3,* 81.
133. Tavares, P.; Pereira, A. S.; Krebs, C.; Ravi, N.; Moura, J. J.; Moura, I.; Huynh, B. H. *Biochemistry* **1998,** *37,* 2830.
134. Krockel, M.; Trautwein, A. X.; Arendsen, A. F.; Hagen, W. R. *Eur. J. Biochem.* **1998,** *251,* 454.
135. Lampreia, J.; Pereira, A. S.; Moura, J. J. G. *Meth. Enzymol.* **1994,** *243,* 241.
136. Lampreia, J.; Moura, I.; Xavier, A. V.; LeGall, J.; Peck, H. D. J.; Moura, J. J. G. "Chemistry and Biochemistry of Flavoenzymes"; CCR, Bocca Raton, Florida; p. 333. 1990; Vol. III.
137. Lampreia, J.; Fauque, G.; Speich, N.; Dahl, C.; Moura, I.; Truper, H. G.; Moura, J. J. *Biochem. Biophys. Res. Commun.* **1991,** *181,* 342.
138. Speich, N.; Dahl, C.; Heisig, P.; Klein, A.; Lottspeich, F.; Stetter, K. O.; Truper, H. G. *Microbiology* **1994,** *140,* 1273.

139. Lampreia, J.; Moura, I.; Teixeira, M.; Peck, H. D., Jr.; LeGall, J.; Huynh, B. H.; Moura, J. J. *Eur. J. Biochem.* **1990,** *188,* 653.
140. Pereira, A. S.; Franco, R.; Feio, M. J.; Pinto, C.; Lampreia, J.; Reis, M. A.; Calvete, J.; Moura, I.; Beech, I.; Lino, A. R.; Moura, J. J. *Biochem. Biophys. Res. Commun.* **1996,** *221,* 414.
141. Michaels, G. B.; Davidson, J. T.; Peck, H. D., Jr. *Biochem. Biophys. Res. Commun.* **1970,** *39,* 321.
142. Michaels, G. B.; Davidson, J. T.; Peck, H. D. J. "*Flavins and Flavoproteins*"; Kamin, H., Ed.; University Park Press: Baltimore, 1971.
143. Lampreia, J. "Estudos espectroscópicos da reductase do APS"; PhD Thesis, Universidade Nova de Lisboa: Lisbon, 1989.
144. Ogata, M.; Yagi, T. *J. Biochem.* **1986,** *100,* 311.
145. Pieulle, L.; Guigliarelli, B.; Asso, M.; Dole, F.; Bernadac, A.; Hatchikian, E. C. *Biochim. Biophys. Acta* **1995,** *1250,* 49.
146. Blamey, J. M.; Adams, M. W. *Biochemistry* **1994,** *33,* 1000.
147. Smith, E. T.; Blamey, J. M.; Adams, M. W. *Biochemistry* **1994,** *33,* 1008.
148. Lee, J. P.; LeGall, J.; Peck, H. D., Jr. *J. Bacteriol.* **1973,** *115,* 529.
149. Lee, J. P.; Peck, H. D., Jr. *Biochem. Biophys. Res. Commun.* **1971,** *45,* 583.
150. Czechowski, M.; Fauque, G.; Galliano, N.; Dimon, B.; Moura, I.; Moura, J. J. G.; Xavier, A. V.; Barata, B. A. S.; Lino, A. R.; LeGall, J. *J. Ind. Microbiol.* **1986,** *1,* 139.
151. Lee, J. P.; Yi, C. S.; LeGall, J.; Peck, H. D., Jr. *J. Bacteriol.* **1973,** *115,* 453.
152. Moura, I.; LeGall, J.; Lino, A. R.; Peck, H. D. J.; Fauque, G.; Xavier, A. V.; DerVartanian, D.; Moura, J. J. G.; Huynh, B. H. *J. Am. Chem. Soc.* **1988,** *110,* 1075.
153. Trudinger, P. A. *J. Bacteriol.* **1970,** *104,* 158.
154. Akagi, J. M.; Adams, V. *J. Bacteriol.* **1973,** *116,* 392.
155. Fauque, G.; Lino, A. R.; Czechowski, M.; Kang, L.; DerVartanian, D. V.; Moura, J. J.; LeGall, J.; Moura, I. *Biochim. Biophys. Acta* **1990,** *1040,* 112.
156. Pierik, A. J.; Duyvis, M. G.; van Helvoort, J. M.; Wolbert, R. B.; Hagen, W. R. *Eur. J. Biochem.* **1992,** *205,* 111.
157. Murphy, M. J.; Siegel, L. M.; Kamin, H.; DerVartanian, D. V.; Lee, J. P.; LeGall, J.; Peck, H. D., Jr. *Biochem. Biophys. Res. Commun.* **1973,** *54,* 82.
158. Lai, K. K.; Moura, I.; Liu, M. Y.; LeGall, J.; Yue, K. T. *Biochim. Biophys. Acta* **1991,** *1060,* 25.
159. Hatchikian, E. C.; Zeikus, J. G. *J. Bacteriol.* **1983,** *153,* 1211.
160. Huynh, B. H.; Kang, L.; DerVartanian, D. V.; Peck, H. D., Jr.; LeGall, J. *J. Biol. Chem.* **1984,** *259,* 15373.
161. Moura, I.; Lino, A. R.; Moura, J. J.; Xavier, A. V.; Fauque, G.; Peck, H. D., Jr.; LeGall, J. *Biochem. Biophys. Res. Commun.* **1986,** *141,* 1032.
162. Moura, J. J.; Moura, I.; Santos, H.; Xavier, A. V.; Scandellari, M.; LeGall, J. *Biochem. Biophys. Res. Commun.* **1982,** *108,* 1002.
163. Tan, J.; Cowan, J. A. *Biochemistry* **1991,** *30,* 8910.
164. Volbeda, A.; Charon, M. H.; Piras, C.; Hatchikian, E. C.; Frey, M.; Fontecilla-Camps, J. C. *Nature* **1995,** *373,* 580.
165. Cammack, R.; Fernandez, V. M.; Hatchikian, E. C. *Meth. Enzymol.* **1994,** *243,* 43.
166. Albracht, S. P. *Biochim. Biophys. Acta* **1994,** *1188,* 167.
167. Prickril, B. C.; Czechowski, M. H.; Przybyla, A. E.; Peck, H. D., Jr.; LeGall, J. *J. Bacteriol.* **1986,** *167,* 722.
168. Hagen, W. R.; van Berkel-Arts, A.; Kruse-Wolters, K. M.; Dunham, W. R.; Veeger, C. *FEBS Lett.* **1986,** *201,* 158.

169. Huynh, B. H.; Czechowski, M. H.; Kruger, H. J.; DerVartanian, D. V.; Peck, H. D., Jr.; LeGall, J. *Proc. Natl. Acad. Sci. USA* **1984,** *81,* 3728.
170. Voordouw, G.; Brenner, S. *Eur. J. Biochem.* **1985,** *148,* 515.
171. Grande, H. J.; Dunham, W. R.; Averill, B.; Van Dijk, C.; Sands, R. H. *Eur. J. Biochem.* **1983,** *136,* 201.
172. Patil, D. S.; Moura, J. J.; He, S. H.; Teixeira, M.; Prickril, B. C.; DerVartanian, D. V.; Peck, H. D., Jr.; LeGall, J.; Huynh, B. H. *J. Biol. Chem.* **1988,** *263,* 18732.
173. Pierik, A. J.; Hagen, W. R.; Redeker, J. S.; Wolbert, R. B.; Boersma, M.; Verhagen, M. F.; Grande, H. J.; Veeger, C.; Mutsaers, P. H.; Sands, R. H. *Eur. J. Biochem.* **1992,** *209,* 63.
174. Teixeira, M.; Moura, I.; Xavier, A. V.; Moura, J. J.; LeGall, J.; DerVartanian, D. V.; Peck, H. D., Jr.; Huynh, B. H. *J. Biol. Chem.* **1989,** *264,* 16435.
175. Cammack, R. "Bioinorganic Catalysis"; Marcel Dekker, Inc.: New York, 1992.
176. Moura, J. J. G.: Teixeira, M.; Moura, I.; LeGall, J. "The Bioinorganic Chemistry of Nickel"; VCH: New York, 1988.
177. Franco, R.; Moura, I.; LeGall, J.; Peck, H. D., Jr.; Huynh, B. H.; Moura, J. J. *Biochim. Biophys. Acta* **1993,** *1144,* 302.
178. Teixeira, M.; Moura, I.; Xavier, A. V.; Huynh, B. H.; DerVartanian, D. V.; Peck, H. D., Jr.; LeGall, J.; Moura, J. J. *J. Biol. Chem.* **1985,** *260,* 8942.
179. Cammack, R.; Patil, D. S.; Fernandez, V. M. *Biochem. Soc. Trans.* **1985,** *13,* 572.
180. Lindhal, P. A.; Kojima, N.; Hausinger, R. P.; Fox, J. A.; Teo, B. K.; Walsh, C. T.; Orme-Johnson, W. H. *J. Am. Chem. Soc.* **1984,** *106,* 3062.
181. Moura, J. J. G.; Moura, I.; Teixeira, M.; Xavier, A. V.; Fauque, G. D.; LeGall, J. "Metal Ions in Biological Systems"; Marcel Dekker, Inc.: New York, 1988; Vol. 23.
182. Coremans, J. M. C. C.; Van Garderen, C. J.; Albracht, S. P. J. *Biochim. Biophys. Acta* **1994,** *1119,* 148.
183. Wang, C. P.; Franco, R.; Moura, J. J.; Moura, I.; Day, E. P. *J. Biol. Chem.* **1992,** *267,* 7378.
184. Montet, Y.; Amara, P.; Volbeda, A.; Vernede, X.; Hatchikian, E. C.; Field, M. J.; Frey, M.; Fontecilla-Camps, J. C. *Nature Struct. Biol.* **1997,** *4,* 523.
185. Garcin, E.; Volbeda, A.; Vernede, X.; Hatchikian, E. C.; Frey, M.; Fontecilla-Camps, J. C. *Vth International Conference on the Molecular Biology of Hydrogenases,* Albertville, 1997.
186. Huyett, J.; Carepo, M.; Pamplona, A.; Franco, R.; Moura, I.; Moura, J. J. G.; Hoffman, B. *J. Am. Chem. Soc.* **1997,** *119,* 9291.
187. Happe, R. P.; Roseboom, W.; Bagley, K. A.; Pierik, A. J.; Albracht, S. P. J. *Nature* **1996,** *385,* 126.
188. Pratt, J. M. "Inorganic Chemistry of Vitamin B12"; Academic Press: New York, 1972.
189. Ragsdale, S. W.; Bauer, J. R.; Gorst, C. M.; Harder, S. R.; Lu, W. P.; Roberts, D. L.; Runquist, J. A.; Schiau, I. *FEMS Microbiol. Rev.* **1990,** *87,* 397.
190. Higuchi, Y.; Yagi, T.; Yasuoka, N. *Structure* **1997,** *5,* 1671.
191. Gu, Z.; Dong, J.; Choudhury, S. B.; Franco, R.; Moura, J. J. G.; Moura, I.; LeGall, J.; Przybyla, A. E.; Roseboom, W.; Albracht, S. P. J.; Axley, M. J.; Scott, R. A.; Maroney, M. J. *J. Am. Chem. Soc.* **1996,** *118*, 11155.
192. Fauque, G.; Czechowski, M.; Berlier, Y. M.; Lespinat, P. A.; LeGall, J.; Moura, J. J. *Biochem. Biophys. Res. Commun.* **1992,** *184,* 1256.
193. Krüger, H. J.; Holm, R. H. *J. Am. Chem. Soc.* **1990,** *112,* 2955.

194. Cammack, R.; Fernandez, V. M.; Schneider, K. "The Bioinorganic Chemistry of Nickel"; VCH: New York, 1988.
195. Fan, C.; Teixeira, M.; Moura, J. J. G.; Moura, I.; Huynh, B. H.; LeGall, J.; Peck, J., H. D.; Hoffman, B. M. *J. Am. Chem. Soc.* **1991,** *113,* 20.
196. Fontecilla-Camps, J. C. *J. Biol. Inorg. Chem.* **1996,** *1,* 91.
197. Coughlan, M., Ed.; "Molybdenum and Molybdenum Containing Enzymes"; Pergamon Press, Oxford, 1980.
198. Hille, R. *Chem. Rev.* **1996,** *96,* 2757.
199. Romao, M. J.; Archer, M.; Moura, I.; Moura, J. J.; LeGall, J.; Engh, R.; Schneider, M.; Hof, P.; Huber, R. *Science* **1995,** *270,* 1170.
200. Huber, R.; Hof, P.; Duarte, R. O.; Moura, J. J.; Moura, I.; Liu, M. Y.; LeGall, J.; Hille, R.; Archer, M.; Ramao, M. J. *Proc. Natl. Acad. Sci. USA* **1996,** *93,* 8846.
201. Schneider, F.; Lowe, J.; Huber, R.; Schindelin, H.; Kisker, C.; Knablein, J. *J. Mol. Biol.* **1996,** *263,* 53.
202. Schindelin, H.; Kisker, C.; Hilton, J.; Rajagopalan, K. V.; Rees, D. C. *Science* **1996,** *272,* 1615.
203. Boyington, J. C.; Gladyshev, V. N.; Khangulov, S. V.; Stadtman, T. C.; Sun, P. D. *Science* **1997,** *275,* 1305.
204. Kisker, C.; Schindelin, H.; Rees, D. C. *Molybdenum Enzymes Meeting,* University Sussex, 1997.
205. Börner, G.; Karrasch, M.; Thauer, R. K. *FEBS Lett.* **1991,** *290,* 31.
206. Bray, R. C. "The Enzymes"; Boyer, P. D., Ed.; Vol. 12, p. 299, Academic Press, NY, 1975.
207. Bray, R. C. "Advances in Enzymology"; Plenum Press: New York, 1980; Vol. 2.
208. Moura, J. J.; Xavier, A. V.; Bruschi, M.; LeGall, J.; Hall, D. O.; Cammack, R. *Biochem. Biophys. Res. Commun.* **1976,** *72,* 782.
209. Komai, H.; Massey, V.; Palmer, G. *J. Biol. Chem.* **1969,** *244,* 1692.
210. Rajagopalan, K. V.; Handler, P. *J. Biol. Chem.* **1964,** *239,* 2022.
211. Garbett, K.; Gillard, R. D.; Knowles, P. F.; Stangroom, J. E. *Nature* **1967,** *215,* 824.
212. Thoenes, U.; Flores, O. L.; Neves, A.; Devreese, B.; Van Beeumen, J. J.; Huber, R.; Romao, M. J.; LeGall, J.; Moura, J. J.; Rodrigues-Pousada, C. *Eur. J. Biochem.* **1994,** *220,* 901.
213. Barata, B. A.; LeGall, J.; Moura, J. J. *Biochemistry* **1993,** *32,* 11559.
214. Cramer, S. P.; Moura, J. J.; Xavier, A. V.; LeGall, J. *J. Inorg. Biochem.* **1984,** *20,* 275.
215. Cramer, S. P.; Hille, R. *J. Am. Chem. Soc.* **1985,** *107,* 8164.
216. Moura, J. J.; Xavier, A. V.; Cammack, R.; Hall, D. O.; Bruschi, M.; LeGall, J. *Biochem. J.* **1978,** *173,* 419.
217. Turner, N. A.; Barata, B. A. S.; Bray, R. C.; Deistung, J.; LeGall, J.; Moura, J. J. G. *Biochem. J.* **1987,** *243,* 755.
218. Caldeira, J.; Moura, I.; Romao, M. J.; Huber, R.; LeGall, J.; Moura, J. J. G. *J. Inorg. Biochem.* (*Abstracts of the 7th International Conference on Bioinorganic Chemistry*) **1995,** *59,* 739.
219. Hille, R.; Massey, V. "Molybdenum Enzymes—Metal Ions in Biology"; Wiley Interscience: New York, 1985; Vol. 7.
220. Moura, J. J.; Xavier, A. V.; Hatchikian, E. C.; LeGall, J. *FEBS Lett.* **1978,** *89,* 177.
221. Bray, R. C.; Turner, N. A.; LeGall, J.; Barata, B. A. S.; Moura, J. J. G. *Biochem. J.* **1991,** *280,* 817.
222. Barata, B. A.; Liang, J.; Moura, I.; LeGall, J.; Moura, J. J.; Huynh, B. H. *Eur. J. Biochem.* **1992,** *204,* 773.

223. Sebban, C.; Blanchard, L.; Bruschi, M.; Guerlesquin, F. *FEMS Microbiol. Lett.* **1995,** *133,* 143.
224. Costa, C.; Teixeira, M.; LeGall, J.; Moura, J. J. G.; Moura, I. *J. Biol. Inorg. Chem.* **1997,** *2,* 198.
225. Almendra, M. J.; Gavel, O.; Duarte, R. O.; Caldeira, J.; Bursakov, S.; Costa, C.; Moura, I.; Moura, J. J. G. *J. Inorg. Biochem.* **1997,** *67,* 16.
226. Yagi, T. *J. Biochem.* **1969,** *66,* 473.
227. Yagi, T. *Biochim. Biophys. Acta* **1979,** *548,* 96.
228. Bursakov, S. A.; Liu, M. Y.; Payne, W. J.; LeGall, J.; Moura, I.; Moura, J. J. G. *Anaerobe* **1995,** *1,* 55.
229. Bursakov, S. A.; Carneiro, C.; Almendra, M. J.; Duarte, R. O.; Caldeira, J.; Moura, I.; Moura, J. J. *Biochem. Biophys. Res. Commun.* **1997,** *239,* 816.
230. Dias, J. M.; Than, M. E.; Humm, A.; Huber, R.; Caldeira, J.; Carneiro, C.; J. J. G.; Moura I.; Romão, M. J. *Structure* **1999,** *7,* 65.
231. Boyington, J. C.; Gladishev, V. N.; Khangulov, S. V.; Stadman, T. C.; Sun, P. D. *Science* **1997,** *272,* 1615.
232. Gangeswaran, R.; Lowe, D. J.; Eady, R. R. *Biochem. J.* **1993,** *289,* 335.
233. Breton, J.; Berks, B. C.; Reilly, A.; Thomson, A. J.; Ferguson, S. J.; Richardson, D. J. *FEBS Lett.* **1994,** *345,* 76.
234. Bennett, B.; Berks, B. C.; Ferguson, S. J.; Thomson, A. J.; Richardson, D. J. *European J. Biochem.* **1994,** *226,* 789.
235. Moura, I.; Bursakov, S.; Costa, C.; Moura, J. J. G. *Anaerobe* **1997,** *3,* 279.
236. Moura, J. J. G.; Barata, B. A. S. *Meth. Enzymol.* **1994,** *243,* 24.
237. Hatchikian, E. C.; Bruschi, M. *Biochem. Biophys. Res. Commun.* **1979,** *86,* 725.
238. Coutinho, I. B.; Xavier, A. V. "Inorganic Microbial Sulfur Metabolism"; Academic Press: New York, 1994; Vol. 243.
239. Vervoort, J.; Heering, D.; Peelen, S.; van Berkel, W. "Inorganic Microbial Sulfur Metabolism"; Academic Press: New York, 1994; Vol. 243.
240. Lowe, D. J.; Lynden-Bell, R. M.; Bray, R. C. *Biochem. J.* **1972,** *130,* 239.
241. Tsukihara, T.; Aoyama, H.; Yamashita, E.; Tomizaki, T.; Yamaguchi, H.; Shinzawa-Itoh, K.; Nakashima, R.; Yaono, R.; Yoshikawa, S. *Science* **1995,** *269,* 1069.
242. Iwata, S.; Ostermeier, C.; Ludwig, B.; Michel, H. *Nature* **1995,** *376,* 660.
243. Moura, J. J.; Barata, B. A. *Meth. Enzymol.* **1994,** *243,* 24.
244. Palma, P. N.; Moura, I.; LeGall, J.; Van Beeumen, J.; Wampler, J. E.; Moura, J. J. *Biochemistry* **1994,** *33,* 6394.
245. Peters, J. W.; Lanzilotta, W. N.; Lemon, B. J.; Seefeldt, L. C. *Science* **1998,** *282,* 1853.
246. Nicolet, Y.; Piras, C.; Legrand, P.; Hatchikian, E. C.; Fontecilla-Camps, J. C. *Structure* **1999,** *7,* 13–23.
247. Almendra, M. J.; Brondino, C. D.; Gavel, O.; Pereira, A. S.; Tavares, P.; Bursakov, S.; Duarte, R.; Caldeira, J.; Moura, J. J. G.; Moura, I. (in preparation).

This Page Intentionally Left Blank

APPLICATION OF EPR SPECTROSCOPY TO THE STRUCTURAL AND FUNCTIONAL STUDY OF IRON–SULFUR PROTEINS

BRUNO GUIGLIARELLI and PATRICK BERTRAND

Laboratoire de Bioénergétique et Ingénierie des Protéins, IBSM, CNRS, 13402 Marseille Cedex 20, France, and Université de Provence, 13331 Marseille Cedex 3, France

I. Introduction
II. EPR Characteristics and Relaxation Properties of the Centers
  A. FeS_4 Centers
  B. $[2Fe–2S]^{1+}$ Centers
  C. $[3Fe–4S]^{1+,0}$ Centers
  D. $[4Fe–4S]^{1+}$ and $[4Fe–4S]^{3+}$ Centers
  E. Concluding Remarks: Identifying the Centers
III. Application of EPR to the Structural Study of Iron–Sulfur Proteins
  A. Site-Directed Mutagenesis Monitored by EPR
  B. Determining the Relative Arrangement of Centers Coupled by Spin–Spin Interactions
  C. EPR Studies on Oriented Iron–Sulfur Systems
IV. Application of EPR to the Functional Study of Iron–Sulfur Centers
  A. Electron Transfer
  B. Other Functions
V. Conclusion
Appendix: Spin–Lattice Relaxation Processes
References

I. Introduction

During the past 20 years, considerable progress has been made toward understanding the electronic properties of iron–sulfur centers thanks to the fruitful interplay between various approaches such as synthetic analog chemistry, theoretical modeling, and of course spectroscopic studies. Modeling studies have been strongly stimulated by the permanent supply of complementary data provided especially by EPR, Mössbauer, ENDOR, MCD, and NMR experiments. However,

Copyright 1999 by Academic Press.
All rights of reproduction in any form reserved.
0898-8838/99 $30.00

the basic technique for detecting, quantifying, and characterizing the redox properties of iron–sulfur centers in biological systems is undoubtedly continuous wave EPR. The application of EPR spectroscopy to iron–sulfur proteins is greatly facilitated by the fact that their frozen solution spectrum is generally characterized by a weak anisotropy and consequently by a relatively large amplitude. For example, at a given concentration, the amplitude of the spectrum exhibited by a $[2Fe–2S]^{1+}$ center characterized by $g_x = 1.88$, $g_y = 1.94$, $g_z = 2.05$ can be expected to be about 60 times larger than that displayed by a low-spin heme characterized by $g_x = 1.50$, $g_y = 2.20$, $g_z = 3.00$. It is therefore not surprising that this new type of metal center was discovered in 1960 by H. Beinert and R. H. Sands during an EPR study on mitochondrial membranes (*1*, *2*). Since then, low-temperature EPR studies on numerous biological systems have shown that iron–sulfur centers are present in all living organisms, from bacteria to plants and mammals. Thanks to its weak anisotropy, the spectrum obtained with some iron–sulfur proteins can even be investigated by high-field EPR, a technique that has been applied essentially to the study of radicals so far. Although EPR spectroscopy is well suited to studying iron–sulfur centers, the quantitative analysis of the complex spectra displayed by multicenter proteins and membrane-bound complexes often requires numerical simulations and multifrequency experiments. In addition, possible ways of interpreting the spectra obtained with some new types of centers are only just beginning to emerge.

In this chapter, the various applications of EPR spectroscopy developed in the field of iron–sulfur research are reviewed. Since the electronic structure of the centers has often been explicitly dealt with in these studies, the main characteristics of the EPR spectrum and the relaxation properties of the diverse types of centers are presented in Section II in relation to their electronic structure. To conclude this section, some of the issues raised by the identification of iron–sulfur centers by EPR are discussed. The various approaches involving EPR spectroscopy that have been used to obtain structural information about systems containing iron–sulfur centers are reviewed in Section III. These include elucidating their coordination scheme by site-directed mutagenesis, establishing the relative arrangement of centers coupled by spin–spin interactions, and determining their magnetic axes in oriented systems. Most of these structural investigations naturally have functional implications. However, those studies that focus directly on elucidating how these systems function are dealt with separately in Section IV. In the conclusion at the end of this chapter, the outlook for future research in this field is discussed.

II. EPR Characteristics and Relaxation Properties of the Centers

In this section, the characteristics of the spectra displayed by the different types of iron–sulfur centers are presented, with special emphasis on how they depend on the geometrical and electronic structure of the centers. The electronic structure is only briefly recalled here, however, and interested readers are referred to the excellent standard texts published on this topic (*3*, *4*). Likewise, the relaxation properties of the centers are described, but the nature of the underlying spin–lattice relaxation processes is not analyzed in detail. However, a short outline of these processes is given in the Appendix. The aim of this introductory section is therefore mainly to describe the tools used in the practical applications presented in Sections III and IV. It ends in a discussion about some of the issues that may arise when EPR spectroscopy is used to identify iron–sulfur centers.

A. FeS_4 Centers

The simplest iron–sulfur centers, which were first discovered in rubredoxins, consist of one iron ion coordinated by a distorted tetrahedron of cysteinyl sulfur atoms. This environment provides a weak ligand field giving a spin equal to $\frac{5}{2}$ and 2 when the ion is Fe(III) and Fe(II), respectively. It also determines the splitting of the ground spin manifold, and consequently the characteristics of the EPR spectrum. This splitting is generally described in the framework of the spin Hamiltonian:

$$H = \beta\vec{B}\cdot\tilde{g}\cdot\vec{S} + D(S_Z^2 - S(S+1)/3) + E(S_X^2 - S_Y^2) + \vec{S}\cdot\tilde{A}\cdot\vec{I}. \qquad (1)$$

The hyperfine terms are irrelevant to the EPR spectrum as long as the protein is not enriched with ^{57}Fe. The high-resolution crystal structures of several oxidized rubredoxins display Fe–S distances ranging between 2.27 and 2.31 Å and S–Fe–S angles ranging between 101° and 115° (*5*, *6*). The deviation from perfect tetrahedral geometry is sufficiently large for the zero-field splitting terms to be predominant in the Hamiltonian (1) at X-band. Under these conditions, the position of the EPR lines does not depend on E and D separately, but only on the ratio E/D, which can always be set between 0 and $\frac{1}{3}$ by suitably labeling the (X, Y, Z) axes. In the most general case, the position of the lines also depends on the g tensor components and on the relative orientation of the g tensor and zero-field splitting tensor axes.

1. Oxidized Form

In the oxidized form, rubredoxins exhibit EPR spectra characterized by strongly temperature-dependent features at g_{eff} = 9.5, 4.3 (*7–9*). In order to explain this finding, we first note that the g tensor components of a Fe(III) ion with tetrahedral-sulfur coordination can be expected in the 2.010–2.030 range (*10–12*). A good approximation therefore consists in assuming this tensor to be isotropic with g = 2.00, which makes it possible to calculate the effective values g_{eff} as a function of the parameter E/D alone (*13*). Under these conditions, the g_{eff} values measured in the rubredoxin spectrum were found to correspond to an E/D ratio having almost the maximum value of 1/3 (*7–9*). Positive D values in the +1.2 to +1.7 cm^{-1} range were deduced from a study on the temperature dependence of the line intensity and from Mössbauer experiments (*14*, *15*). EPR spectra very similar to those of rubredoxins are displayed by two rather different proteins of the bacterium *Desulfovibrio vulgaris* called rubrerythrin and nigerythrin, which contain an extra metal center of the hemerythrin type (*16*, *17*). In these three kinds of proteins, the cysteine residues ligating the iron center are arranged in the sequence according to the motif Cys–X_2–Cys–$(X)_n$–Cys–X_2–Cys. By contrast, the desulforedoxin from *D. gigas* (*18*) and the desulfoferrodoxins from *D. desulfuricans* (*19*) and *D. vulgaris* (*20*) contain a FeS_4 center ligated by the motif Cys–X_2–Cys–$(X)_n$–Cys–Cys. In the oxidized form, these proteins exhibit an EPR spectrum characterized by g_{eff} = 7.7, 5.7, 4.1, 1.8 corresponding to an E/D ratio of 0.08. Parameter D was estimated at +2.2 cm^{-1} in desulforedoxin (*18*). The significant difference observed in comparison with the zero-field splitting parameters of rubredoxins was attributed to the steric constraints imposed by the vicinity of the two last cysteine residues in the sequence (*18*, *19*). This hypothesis was subsequently confirmed by the resolution of the crystal structure of the desulforedoxin from *D. gigas* (*21*) and the desulfoferrodoxin from *D. desulfuricans* (*22*), which showed that although the Fe–S bond lengths are very similar to those measured in rubredoxins, the sulfur atoms of the adjacent cysteine residues form an S–Fe–S angle of about 126°, which differs significantly from the tetrahedral value of 109° (*21*, *22*). Besides, desulforedoxin mutants in which two residues were inserted between the two last cysteines have been constructed (*23*). These mutants were found to exhibit very similar EPR features to those of rubredoxins, with an E/D ratio of about 0.22 (*23*).

The ^{57}Fe hyperfine tensor components were determined by Mössbauer spectroscopy in the case of the rubredoxin from *Clostridium*

pasteurianum, $A_X = -23$ MHz, $A_Y = -22$ MHz, $A_Z = -23$ MHz (*15*), and that of the desulforedoxin from *D. gigas*, $A_X \approx A_Y \approx A_Z = -21$ MHz (*18*).

2. Reduced Form

Under some conditions, $S = 2$ systems give X-band EPR spectra that can be detected both in the conventional perpendicular ($\vec{B}_1 \perp \vec{B}$) mode and in the parallel ($\vec{B}_1 \| \vec{B}$) mode. Owing to the magnitude of the zero-field splitting parameters, this generally occurs when the splitting in zero field of the doublet originating from the $\{|2, \pm 2>\}$ states, which is equal to $2D[1-(1 + 3(E/D)^2)^{1/2}]$ for $D < 0$, is smaller than the microwave quantum $h\nu$ (0.3 cm^{-1} at X-band) (*24*). Since parameters D and E are distributed in protein samples, it may happen that this condition is satisfied only in a fraction of all the molecules, so that a broad asymmetric line beginning with a nonzero absorption at $B = 0$ is observed at very low fields (*25*). Contrary to what happens in the case of half-integer spin systems, the position of this line cannot be marked out by a frequency-independent number g_{eff}, and a quantitative interpretation of the spectrum requires a complete numerical simulation (*25*).

No EPR spectra have yet been reported to our knowledge in the case of a protein containing a well-characterized reduced FeS_4 center, although a spectrum has been observed in the case of a model complex (*24*). The lack of EPR signals in the case of proteins is apparently directly related to the D and E values, which are equal to $D = +7.5$ cm^{-1}, $E/D = 0.28$ in the case of *C. pasteurianum* rubredoxin (*15*), and $D = -6$ cm^{-1}, $E/D = 0.19$ in that of *D. gigas* desulforedoxin (*18*), based on Mössbauer experiments. These same experiments provided the ^{57}Fe hyperfine tensor components: $A_X = -27.4$ MHz, $A_Y = -11.4$ MHz, $A_Z = -31.5$ MHz for rubredoxin and $A_X = -27.4$ MHz, $A_Y = -27.4$ MHz, $A_Z = -9.2$ MHz for desulforedoxin (*15*, *18*). The differences between these two sets of spin Hamiltonian parameters were interpreted in terms of a ligand field model suggesting that they arise mainly from angular factors (*26*), in keeping with the differences observed in the crystal structures.

3. Relaxation Properties

In the oxidized form, the weak coupling of the high-spin Fe(III) ion to its surroundings and the very large ligand-field energy of about 10,000 cm^{-1} (*12*) are not liable to give rise to very efficient relaxation processes (see Appendix). However, the $S = 5/2$ manifold provides a set of transitions for multiple direct processes that may be efficient

at very low temperatures. Although no quantitative studies on the relaxation properties of oxidized FeS_4 centers in proteins have been published so far, the available data concerning the microwave saturation and the spectral broadening of the EPR spectrum are in line with these qualitative predictions: The signal is not easily saturated at low temperatures (*17*, *27*), but it remains detectable above 100 K (*16*, *17*, *20*, *27*). Mössbauer studies have shown that the relaxation process is still slow at 200 K (*18*). A quantitative study has been carried out on the spin–lattice relaxation of the reduced form of *C. pasteurianum* rubredoxin using Mössbauer spectroscopy (*28*).

B. $[2Fe–2S]^{1+}$ Centers

The FeS_4 unit of mononuclear centers is also present at the iron sites of [2Fe–2S] clusters and in polynuclear iron–sulfur centers in general. At these sites, the spin is therefore 5/2 and 2 when the ion is ferric and ferrous, respectively. This environment consisting of four sulfur atoms also determines the magnitude of the *local parameters* characterizing each iron site: g tensor, zero-field splitting tensor, and hyperfine tensors, the values of which can therefore be expected to be similar to those measured in mononuclear centers. However, the geometrical arrangement and even the chemical nature (cysteinyl or bridging) of the four sulfur ligands vary with the type of center, so that local parameters are not directly transferrable from one center to another (*29*, *30*). In polynuclear clusters, the interactions between the iron sites are much stronger than the local terms described by Hamiltonians of the type given in Eq. (1), so that the ladder of energy levels and the spin states of the clusters are mainly determined by these interactions. The characteristics of the EPR spectrum depend strongly on the local terms, however.

1. g Tensor Analysis

This general scheme was first applied to [2Fe–2S] centers by J. Gibson *et al*. (*31*). By postulating the existence of strong antiferromagnetic interactions due to a bridging structure between the two iron sites, these authors explained the diamagnetism of the ground state of the oxidized form [Fe(III), Fe(III)] and the $S = 1/2$ value of the ground state of the reduced form [Fe(III), Fe(III)] of spinach ferredoxin. This model yielded the following expression for the g tensor of the $S = 1/2$ state:

$$\tilde{g} = 7/3\tilde{g}_1 - 4/3\tilde{g}_2, \qquad (2)$$

where $\tilde{g}_1$ and $\tilde{g}_2$ are the local g tensors of the Fe(III) and Fe(II) sites, respectively. The experimental values $g_x = 1.88$, $g_y = 1.94$, $g_z = 2.04$ were accounted for by taking the first tensor to be isotropic with $g_1 = 2.019$, the value observed for a Fe(III) ion in ZnS, and by choosing appropriate ligand field parameters for a Fe(II) ion with distorted tetrahedral coordination (*31*). The validity of this model has been confirmed using other techniques such as Mössbauer and ENDOR spectroscopy (*32*, *33*). In addition, magnetic susceptibility experiments carried out on [2Fe–2S] ferredoxins from plants and cyanobacteria have shown that the exchange interactions can be described by a Heisenberg Hamiltonian $H_{ex} = -2J\vec{S}_1 \cdot \vec{S}_2$, where J is equal to about -180 cm^{-1} in the oxidized form and -90 cm^{-1} in the reduced form (*34–36*). Lastly, the existence of a bridging structure involving two inorganic sulfur atoms and the tetrahedral coordination of the two iron sites have been fully confirmed by the resolution of the X-ray crystal structure of several plant-type [2Fe–2S] ferredoxins (*37–40*). The cysteine residues ligating the reducible site of the cluster have been identified by NMR studies in the case of plant-type ferredoxins (*41*, *42*) and by site-directed mutagenesis experiments monitored by EPR in the case of other proteins (see Section III,A).

Dinuclear $[2Fe–2S]^{2+,1+}$ centers that in their reduced form give a similar EPR spectrum to that of plant-type ferredoxins with $g_{av} = (g_x + g_y + g_z)/3 \approx 1.96$ are found in a great variety of living organisms, from bacteria to mammals. Within this class of centers, large variations in the spectral shape are observed, from the rhombic spectrum of plant-type ferredoxins to the axial spectrum of adrenal ferredoxin, but the variations in the g tensor components appear to be correlated (Fig. 1). These variations can be rationalized by a ligand field model that is a generalized version of that proposed by Gibson *et al.*, in which the g tensor of the Fe(III) site is taken to be constant and anisotropic: $g_{1x} = 2.015$, $g_{1y} = 2.034$, $g_{1z} = 2.030$, and the Fe(II) site is assumed to undergo a rhombic distortion that varies while obeying an idealized C_{2v} symmetry (*43*). Under these conditions, the orbital part of the ground state of the Fe(II) ion can be written

$$|\varphi_0\rangle = \cos\,\theta\,|z^2\rangle + \sin\,\theta\,|x^2 - y^2\rangle$$

and the components of the ferrous g tensor take the form

$$g_{2x} = g_e - (8\lambda/\Delta_{yz})\sin^2(\theta + \pi/3)$$

$$g_{2y} = g_e - (8\lambda/\Delta_{xz})\sin^2(\theta - \pi/3)$$

$$g_{2z} = g_e - (8\lambda/\Delta_{xy})\sin^2\theta,$$

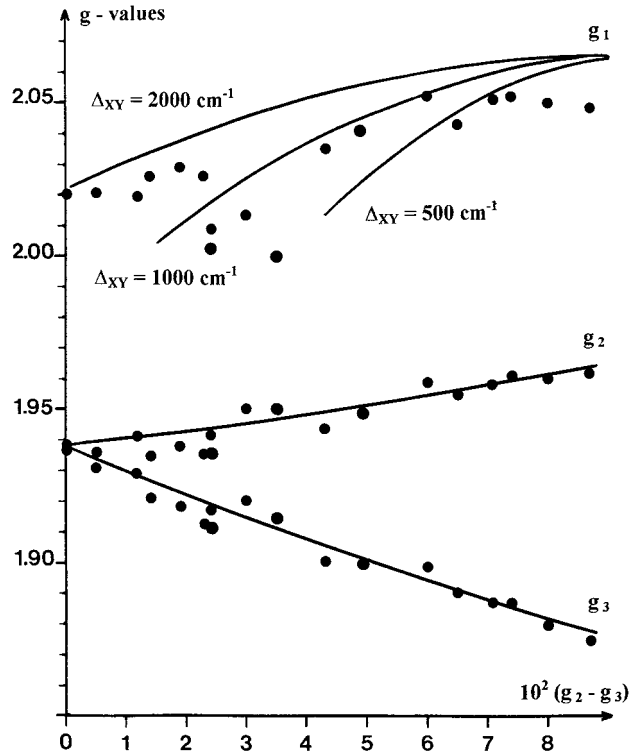

FIG. 1. g values of $[2Fe–2S]^{1+}$ centers in proteins displaying a $g \approx 1.96$ type EPR spectrum, plotted as a function of the difference $g_2 - g_3$ ($g_3 < g_2 < g_1$). Data from Refs. (*142*, *305*, *306*) have been added to those previously used in Fig. 3 in Ref. (*304*). The calculated lines are identical to those given in that figure.

where the Δ_{ij} are ligand field energies of the Fe(II) site. Taking the values $\Delta_{xz} = 6000$ cm^{-1} and $\Delta_{yz} = 4000$ cm^{-1} measured in adrenal and spinach ferredoxins by far infrared spectroscopy and taking the spin–orbit constant λ to be equal to -80 cm^{-1}, it is possible to account for the experimentally observed variations by varying the mixing parameter θ in the -20 to -5°C range (Fig. 1). This model provides a semiempirical description based on symmetry properties alone that tells us nothing about the structural significance of the mixing parameter θ. Information on this point has been provided, however, by LCAO–Xα valence bond calculations, which have shown that the θ value depends mainly on the Fe(II)–S–C (Cys) angle (*29*). In C_{2v} symmetry, the magnetic axes are oriented along the orthorhombic axes, and fitting the data led to assigning the axis corresponding to the

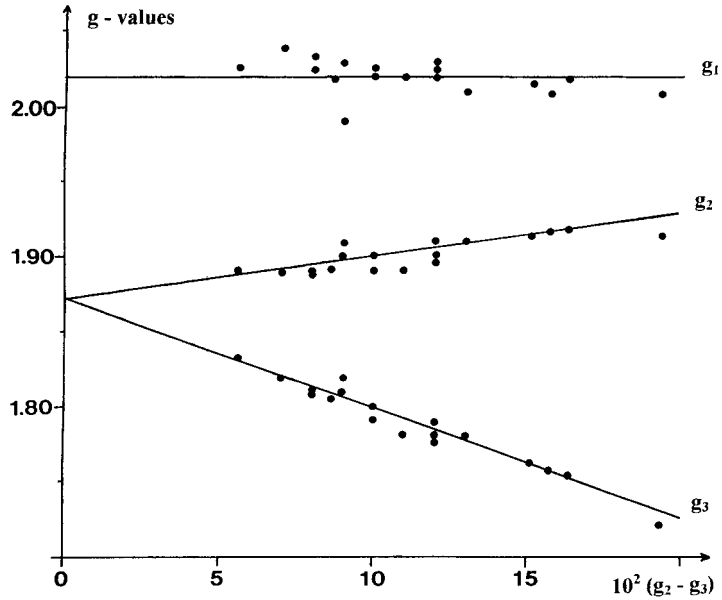

FIG. 2. g values of $[2Fe–2S]^{1+}$ centers in proteins displaying a $g \approx 1.91$ type EPR spectrum, plotted as a function of $g_2 - g_3$. Data from Refs. (*61*, *264*, *307*) have been added to those previously used in Fig. 6 in Ref. (*304*). The calculated lines are identical to those given in that figure.

largest g value to the iron-to-iron direction (*43*). The same model was found to account for the g-strain broadening of the spectra (*44*) and for the variations of the g tensor components of [2Fe–2S] proteins in which the bridging sulfides were replaced by selenium (*45*). More recently, it was used to interpet the polarized X-ray absorption spectrum obtained with the [2Fe–2S] ferredoxin from *Clostridium pasteurianum* (*46*).

In their reduced form, several proteins containing [2Fe–2S] centers display EPR spectra that are characterized by $g_{av} \approx 1.91$. These include on the one hand the Rieske proteins present in the bc_1 complex of mitochondria and bacteria and in the b_6f complex of chloroplasts and photosynthetic bacteria, and on the other hand some bacterial dioxygenases. In this class of [2Fe–2S] clusters, the variations of the g tensor components are also correlated (Fig. 2). These variations are satisfactorily described by a model involving a large ligand field splitting of about 15,000 cm^{-1} that was ascribed to the chemical inequivalence between the bridging sulfur and the terminal ligands of the Fe(II) site (*47*). Fitting the experimental data led to identifying the

iron-to-iron direction with the magnetic axis corresponding to either the smallest or the intermediate g value (*47*). Evidence for histidine nitrogen coordination of these centers was provided on the one hand by ENDOR experiments carried out on phthalate dioxygenase from *Pseudomonas cepacia* (*48*) and on the Rieske protein from *Rhodobacter capsulatus* (*49*), and on the other hand by ESEEM experiments carried out on several Rieske proteins (*50*). This coordination was fully confirmed by the resolution of the crystal structure of a soluble fragment of the beef heart bc_1 complex, in which the strong inequivalence between the bridging sulfurs and the terminal histidine nitrogens is reflected by a N–Fe–N angle of 90° (*51*). In addition, circular dichroism experiments carried out on the reduced form of several [2Fe–2S] proteins displaying a $g_{av} \approx 1.91$ type EPR spectrum have shown the existence of a d–d transition of energy amounting to 20,000 cm^{-1}, which is not detected in the reduced ferredoxins giving a $g_{av} \approx 1.96$ spectrum (*52*). Although the geometry of the reducible site displayed in the crystal structure departs significantly from idealized C_{2v} symmetry, these recent findings seem to confirm the validity of the ligand field model. In this class of [2Fe–2S] clusters, elucidating the nature of the variable distortion that modulates the g tensor anisotropy must await further structural determination and/or the development of ab initio theoretical models.

2. *Influence of Valence Delocalization on the EPR Spectrum*

Assuming the existence of a strong antiferromagnetic interaction between the two sites of [2Fe–2S] clusters makes it possible to account quite simply for the spin state of the different forms: $S = 0$ for [Fe(III), Fe(III)], $S = 1/2$ for [Fe(III), Fe(II)], and $S = 0$ for the superreduced [Fe(II), Fe(II)] form that has been generated under very specific conditions (*53–55*). However, in the case of the mixed-valence [Fe(III), Fe(II)] form, a more complex reality probably underlies this simplified picture. If the iron sites of the cluster are labeled A and B, the possibility that the two configurations a = [Fe_A(II), Fe_B(III)] and b = [Fe_A(III), Fe_B(II)] may participate in the spin states of the cluster must be in fact considered. These states and their energies are determined by the interplay between several factors, which are briefly recalled here. To begin with, it is convenient to consider the hypothetical case where sites A and B are independent, which would occur if they were located far apart. In this situation, configurations a and b would give rise to states Ψ_a and Ψ_b, respectively, whose energies E_a and E_b would vary with the geometry Q of the system as shown in Fig. 3. Note that the geometries Q_a and Q_b corresponding to the mini-

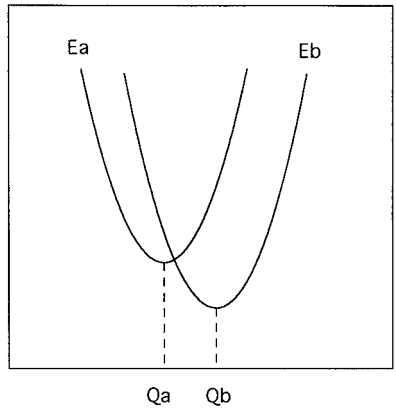

FIG. 3. Energy profile of the configurations a = [Fe_A(II), Fe_B(III)] and b = [Fe_A(III), Fe_B (II)] as a function of the geometry of the system when sites A and B are independent.

mum of E_a and E_b are necessarily different. For example, in state Ψ_a, the metal–ligand bond length is expected to be shorter in site B (ferric) than in site A (ferrous), whereas the opposite is expected to occur in state Ψ_b. These so-called vibronic coupling effects tend therefore to localize the valences. Besides, the minima of E_a and E_b may differ if the two sites are not equivalent, and this situation is likely to occur in a protein. In the situation depicted in Fig. 3, the smallest energy would therefore be obtained in configuration b = [Fe_A(III), Fe_B(II)] for the equilibrium geometry Q_b. When the two sites are allowed to interact, two kinds of interactions may take place, which can both be expressed in terms of the value of the total spin $\vec{S} = \vec{S}_A + \vec{S}_B$: an exchange interaction dominated by a large antiferromagnetic contribution mediated by the two bridging sulfurs, which is described by a Heisenberg Hamiltonian $-2J\vec{S}_A \cdot \vec{S}_B$, and a double exchange interaction due to the valence delocalization phenomenon that gives a $\pm B(S + 1/2)$ term (*56*). In the presence of valence delocalization, the states of the system become

$$\Psi_S = c_a \Psi_S^a \pm c_b \Psi_S^b, \tag{3}$$

where c_a and c_b are localization coefficients satisfying $c_a^2 + c_b^2 \approx 1$ if the overlap between Ψ_S^a and Ψ_S^b is weak. The energies $E_S = E(\Psi_S)$ are determined by the parameters J and B, which depend slightly on the geometry, and by the difference $U = (E_a - E_b)$, which is a sensitive function of the geometry of the system (Fig. 3). It follows that the spin

value, the energy, and the equilibrium geometry of the various states are determined by the interplay between these diverse factors. It has been established that the E_S values of the lowest energy set of spin states are given by (*56*)

$$E_S = -JS(S+1) - [U^2 + B^2(2S+1)^2]^{1/2}/2, \tag{4}$$

and that the localization coefficients depend only on the ratio $r = B/U$ and on S (*57*):

$$\begin{aligned} c_a^2 &= [1 - (1 + r^2(2S+1)^2)^{1/2}]^2/N \\ c_b^2 &= r^2(2S+1)^2/N \\ N &= [1 - (1 + r^2(2S+1)^2)^{1/2}]^2 + r^2(2S+1)^2. \end{aligned} \tag{5}$$

It should be noted that the values of all the parameters involved in Eqs. (4) and (5) correspond to the equilibrium geometry of the ground state. According to this analysis, the double exchange interaction gives rise to a departure of the ladder of energy levels from that predicted by the Heisenberg Hamiltonian [Eq. (4) and Fig. 4] and to a spin-dependent delocalization of the Ψ_S states [Eq. (5) and Fig. 5]. These two phenomena may affect the EPR properties of $[2Fe–2S]^{1+}$ centers to different extents. Owing to the delocalization process, the g tensor of the $S = 1/2$ state is given by Eq. (2), in which g_1 and g_2 are now averaged ferric and ferrous tensors defined by (*30*)

$$\begin{aligned} \tilde{g}_1 &= c_a^2 \tilde{g}_1^B + c_b^2 \tilde{g}_1^A \\ \tilde{g}_2 &= c_a^2 \tilde{g}_2^A + c_b^2 \tilde{g}_2^B, \end{aligned} \tag{6}$$

where $\tilde{g}_1^B$ and $\tilde{g}_1^A$ are the ferric g tensors corresponding to the a and b configurations, respectively, and a similar definition holds for $\tilde{g}_2^A$ and $\tilde{g}_2^B$. In general, the averaging process apparent in Eqs. (6) does not seem likely to significantly affect the g values in comparison with those observed in the case of trapped valences. More drastic effects may occur when a substantial value of the ratio B/J brings the first excited state $S = \frac{3}{2}$ close to the $S = \frac{1}{2}$ ground state (Fig. 4). In these circumstances, the mixing of the two states due to the local zero-field

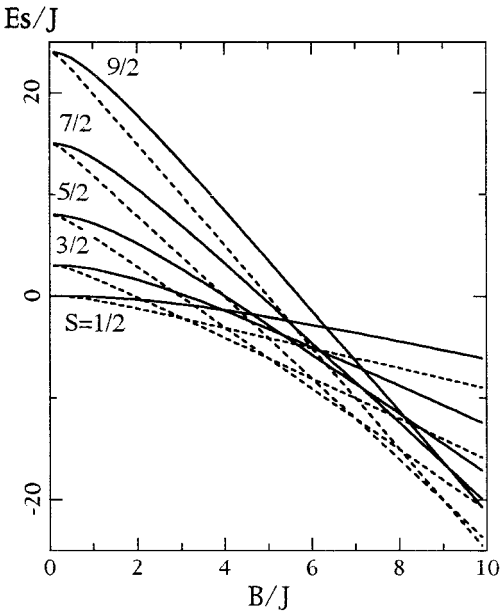

FIG. 4. Lowest energy set of spin states of a $[2Fe–2S]^{1+}$ center as a function of the ratio B/J, as calculated from Eq. (4) in the case of $U = 10J$ (full lines) and $U = 2J$ (dashed lines). In both cases, the energy of the $S = 1/2$ state when $B = 0$ was taken to be zero.

splitting terms may significantly shift the g tensor components from the values given by Eq. (2). In addition, the proximity of the excited states may accelerate the relaxation of the ground state (*58*).

Now, what do we know about the degree of valence delocalization occuring in $[2Fe–2S]^{1+}$ clusters? The answer has been provided by Mössbauer spectroscopy experiments, which have shown that the values of the isomer shift, the quadrupole splitting, and the ^{57}Fe hyperfine constants correspond to trapped valence Fe(III) and Fe(II) sites in both the $g_{av} \approx 1.96$ (*33*, *59*) and $g_{av} \approx 1.91$ (*60*, *61*) classes of centers. These experiments demonstrate that the B/U ratio is small in these centers (Fig. 5), but they give no information about the magnitude of the B/J ratio that is relevant to Fig. 4. In the case of plant-type and adrenal ferredoxins, it was established that the energy Δ between the ground state and the $S = \frac{3}{2}$ state determined by magnetic susceptibility experiments is sufficiently large for the corrections to Eq. (2) to be neglected (*62*). The relaxation properties of $[2Fe–2S]^{1+}$ centers giving an EPR spectrum character-

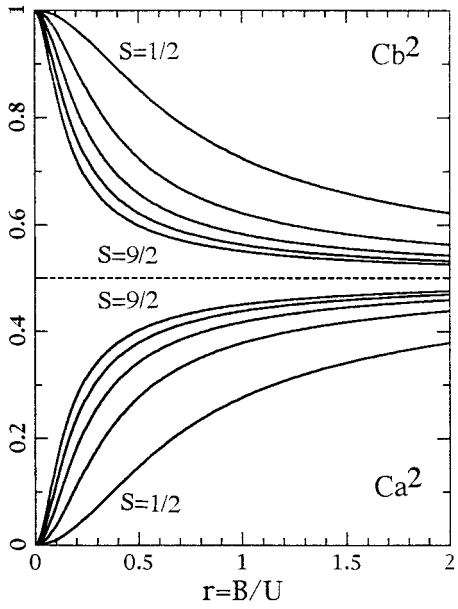

FIG. 5. Localization coefficients c_a^2 and c_b^2 of the various spin states of a $[2Fe–2S]^{1+}$ center as a function of the ratio B/U, as calculated from Eq. (5).

ized by $g_{av} \approx 1.91$ were found to be very similar to those of the $g_{av} \approx 1.96$ class (*63*), indicating that no low-lying excited level is present in these centers, either.

Although no double exchange effects have been detected in the EPR spectra obtained with the usual [2Fe–2S] proteins, processes of this kind might explain the anomalous properties displayed by some centers. The milk enzyme xanthine oxidase contains two [2Fe–2S] centers. Center 1 exhibits an EPR spectrum similar to those observed in the $g_{av} \approx 1.96$ class, whereas the spectrum of center 2 is characterized by anomalous g values: $g_x = 1.902$, $g_y = 1.991$, $g_z = 2.110$ ($g_{av} = 2.00$), very broad lines, and very efficient spin–lattice relaxation processes leading to the disappearance of the signal at temperatures above 35 K (*64*). Although a Mössbauer study has provided evidence that the valences are trapped in both centers (*64*), the peculiar properties of the center 2 signal might be explained by a similar model to that initially proposed for center F_X^- of photosystem I, which was based on the existence of a small Δ value (*58*). Finally, it may happen that the double exchange interaction is sufficiently large for the ground state

to be characterized by a spin $S > 1/2$ (Fig. 4). A situation of this kind has been described in the case of Cys-to-Ser mutants of *C. pasteurianum* ferredoxin (see Section III,A).

3. Relaxation Properties

As mentioned previously, magnetic susceptibility experiments have shown that the energy Δ of the $S = \frac{3}{2}$ state is equal to about 270 cm^{-1} in the case of $[2Fe–2S]^{1+}$ centers of plant-type ferredoxins (*34–36*). In view of the relative proximity of excited states and the strong coupling between the ferrous ion and the lattice, the relaxation processes are expected to be faster in these clusters than in mononuclear $Fe(III)S_4$ centers, except perhaps at very low temperatures, where several direct processes can accelerate the relaxation of the $S = \frac{5}{2}$ multiplet. $[2Fe–2S]^{1+}$ clusters are certainly the biological metal centers whose relaxation properties have been the most extensively investigated. Using a combination of techniques, the spin–lattice relaxation time T_1 of the $[2Fe–2S]^{1+}$ center of *Spirulina maxima* ferredoxin was found to vary from about 1 s at 1.2 K to 2×10^{-10} s at 133 K (*65*). Three relaxation processes have been identified, including an Orbach process, which was found to be predominant at temperatures above 30 K and to lead to the disappearance of the signal via relaxation broadening at about 150 K (*65*, *66*). This Orbach process involves an excited level of energy $\Delta = 250$ cm^{-1}, which is a very similar value to that deduced from magnetic susceptibility experiments. The relaxation broadening of other proteins giving a $g_{av} \approx 1.96$ type signal has also been studied, yielding Δ values ranging from 220 cm^{-1} in the case of *Halobacterium halobium* ferredoxin to 510 cm^{-1} in the case of adrenal gland ferredoxin (*67*). The large value obtained with the latter protein is consistent with the results of susceptibility experiments in which no departure from the Curie law was detected in the 4–250 K range (*68*). A still larger value of $\Delta \approx 900$ cm^{-1} has been estimated in the case of the $[2Fe–2S]^{1+}$ cluster of the mammalian enzyme ferrochelatase (*69*). The relaxation behavior of several [2Fe–2S] proteins giving a $g_{av} \approx 1.91$ type signal was found to be similar to that observed in the $g_{av} \approx 1.96$ class (*63*). Although large Δ values in the 600 to 900 cm^{-1} range have generally been deduced from the relaxation broadening of $[2Fe–2S]^{1+}$ model complexes (*70*, *71*), the value of $\Delta = 105$ cm^{-1} was inferred from both the relaxation broadening of the EPR spectrum and the temperature dependence of the Mössbauer spectrum of the complex $[Fe_2S_2(\text{dimethylmethanebisbenzimidazolate})_2]^{3-}$ (*57*). This small value of Δ and the anomalous Mössbauer parameters

have been convincingly explained in terms of a partially valence-delocalized [2Fe–2S]$^{1+}$ cluster (*57*).

C. [3Fe–4S]$^{1+,0}$ Centers

With trinuclear clusters, we are now dealing with systems whose electronic structure depends on multiple intersite interactions that may differ from one iron pair to another. As a result, the separation between adjacent energy levels depends, not on the magnitude of these interactions, but on their difference. This may give rise to low-lying excited levels, which may have far-reaching effects on both the EPR spectrum and the relaxation properties.

1. Oxidized Form

A priori, one might have expected a [3Fe–4S]$^{1+}$ center to give a particularly simple EPR spectrum. Contrary to what was suggested in Ref. (*13*), the electronic structure of this cluster, which possess three ferric sites, is not liable to be complicated by valence delocalization phenomena, so that the intersite interactions can be described by the Heisenberg Hamiltonian:

$$H = \sum_{i<j=1}^{3} -2J_{ij}\vec{S}_i \cdot \vec{S}_j,$$

with $S_1 = S_2 = S_3 = \frac{5}{2}$. The cuboidal arrangement displayed by the crystal structures (*72–74*) suggests that the J_{ij} are negative (antiferromagnetic) and of similar magnitude, so that a $S = \frac{1}{2}$ ground state can be expected to exist (*75*). Actually, two different $S = \frac{1}{2}$ states are possible, each of which is characterized by a particular set of spin coupling coefficients $\{K_i\}$. When the ground state is clearly separated from the excited states, its g tenor is simply given by a linear combination of the local ferric g tensors:

$$\tilde{g} = \sum K_i' \tilde{g}_i, \tag{7}$$

where the K_i' values depend on the spin coupling coefficients K_i and on the relative differences between the J_{ij} values (*76*). By using the g values of high-spin ferric centers with tetrahedral sulfur coordination, it can be shown that the g tensor components predicted by Eq. (7) fall in the 1.97–2.08 range (76). Moreover, since ferric $\tilde{g}_i$ tensors are

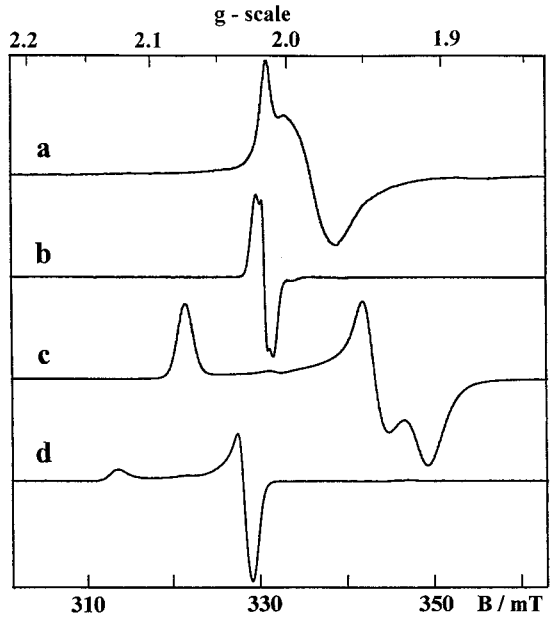

FIG. 6. Representative EPR spectra displayed by trinuclear and tetranuclear iron–sulfur centers. (a) and (b) $[3Fe–4S]^{1+}$ center in the NarH subunit of *Escherichia coli* nitrate reductase and the Ni–Fe hydrogenase from *D. gigas,* respectively. (c) $[4Fe–4S]^{1+}$ center in *D. desulfuricans* Norway ferredoxin I. (d) $[4Fe–4S]^{3+}$ center in *Thiobacillus ferrooxidans* ferredoxin. Experimental conditions: temperature, 15 K; microwave frequency, 9.330 GHz; microwave power, (a) 100 mW, (b) 0.04 mW, (c) and (d) 0.5 mW; modulation amplitude (a), (c), (d) 0.5 mT, (b) 0.1 mT.

generally not very sensitive to structural variations, these components can be expected to differ very little from one protein to another.

Proteins containing $[3Fe–4S]^{1+}$ centers display low-temperature EPR spectra centered at $g \approx 2.01$, which are characteristic of a $S = \frac{1}{2}$ state. The spectral shape is generally highly asymmetric, with a narrow peak at low-field and a broad featureless trough at high-field extending outside the range of g values predicted by Eq. (7) (Fig. 6a). Since multifrequency experiments have shown that the linewidth of these spectra is essentially determined by g-strain effects (*77*, *78*), it can be concluded that the smallest g value is distinctly smaller than 1.97 in a sizeable population of molecules. This is illustrated in Fig. 7 by the spectra of *D. gigas* ferredoxin II recorded at 9 and 285 GHz. In addition, the EPR signals displayed by $[3Fe–4S]^{1+}$ centers are characterized by fast relaxation properties, which is at first sight surprising for centers comprising only high-spin ferric sites. Actually, the

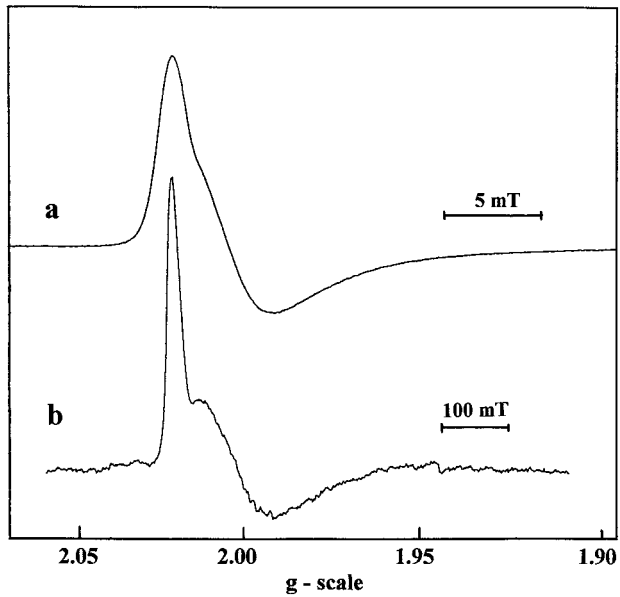

FIG. 7. EPR spectra of the $[3Fe–4S]^{1+}$ center of *D. gigas* ferredoxin II recorded at 5 K in nonsaturating conditions at (a) 9 GHz and (b) 285 GHz. The 285 GHz spectrum was recorded at the Laboratoire des Champs Magnétiques Intenses, CNRS, Grenoble.

overall anisotropy of the spectrum and the relaxation rates vary considerably among proteins containing [3Fe–4S] centers, but these variations appear to be correlated with each other. In this respect, the two limiting situations are probably on the one hand the signals displayed by the $[3Fe–4S]^{1+}$ centers of the Ni–Fe hydrogenases from *Desulfovibrio gigas* and *Desulfovibrio vulgaris* Miyazaki, which are characterized by a very weak anisotropy (Fig. 6b) and can be detected up to 100 K (*79*), and on the other hand the very anisotropic signal exhibited by the $[3Fe–4S]^{1+}$ center of *Azospirillum brasilense* glutamate synthase, in which the relaxation broadening is already observed at 9 K (*80*). Intermediate spectral shapes and relaxation behaviors have been observed in the case of *Azotobacter vinelandii* ferredoxin I and *D. gigas* ferredoxin II (Fig. 7a) (*76*, *81*). This correlation is also observed when the electronic properties of $[3Fe–4S]^{1+}$ centers are modified. For example, the $[3Fe–4S]^{1+}$ cluster of *Pyrococcus furiosus* ferredoxin can incorporate a diamagnetic Tl^{1+} ion to form a cubane $[TlFe_3S_4]^{2+}$ cluster, giving an EPR signal characterized by both a smaller anisotropy and a slower relaxation rate than those of the native center (*82*). Similarly, the EPR spectrum given by the center S_3 of succinate quinone reductase from *Bacillus subtilis* was found to

become more isotropic in the presence of methanol or when a neighbouring serine was replaced by a cysteine (*83*). In both cases, the narrowing of the signal was accompanied by a significant decrease in the spin–lattice relaxation rate (*83*).

The correlation between the anisotropy of the EPR spectrum and the spin–lattice relaxation properties of $[3Fe–4S]^{1+}$ centers, which has been pointed out by several authors (*77*, *84*), strongly suggests that the peculiar properties of EPR signals displayed by $[3Fe–4S]^{1+}$ centers are attributable to the existence of low-lying excited levels that invalidate Eq. (7). It was suggested some time ago that levels of this kind might explain the anomalous temperature dependence of the EPR signals given by *D. gigas* ferredoxin II and *A. vinelandii* ferredoxin I (*81*). A model based on the admixture of the $S = \frac{3}{2}$ states into the $S = \frac{1}{2}$ ground doublet via the local zero-field splitting terms was shown to account quantitatively for the main characteristics of the EPR signal, in terms of the g tensor anisotropy, the asymmetric shape of the spectrum, the temperature dependence, and the relaxation properties of the signal (*77*, *78*, *82*). Besides, this model was reported to provide a quantitative explanation for the anomalous anisotropy of the ^{57}Fe hyperfine tensors determined by ENDOR and Mössbauer spectroscopies (*78*, *85*). When zero-field splitting parameters appropriate for $Fe(III)S_4$ sites were used in this model, the value $J \approx -20$ cm^{-1} was obtained for the exchange parameter (*77*). This small value was initially taken to be consistent with the adamantane-type geometry displayed in the first X-ray crystal structure of *A. vinelandii* ferredoxin I, in which the distance between the iron atoms was about 4 Å (*86*). Subsequently, the cuboidal structure detected in other studies (*72–74*) raised an intriguing question as to the magnitude of the exchange interactions in $[3Fe–4S]^{1+}$ clusters, which was apparently solved when a large value $|J| = 150$ cm^{-1} was determined in magnetic susceptibility measurements (*87*) and NMR experiments (*88*) carried out on *D. gigas* ferredoxin II. With such a large J value, the admixture of the $S = \frac{3}{2}$ states into the $S = \frac{1}{2}$ ground doublets brought about by the local zero-field splitting terms does not suffice to explain the peculiar spectroscopic properties of $[3Fe–4S]^{1+}$ centers. It should, however, be noted that, in addition to the isotropic component represented by the Heisenberg Hamiltonian, the exchange interactions give rise to anisotropic components (*89*) and higher order contributions such as biquadratic terms (*90*). A more general exchange Hamiltonian should therefore be written:

$$H_{ex} = \Sigma\,(-2J_{ij}\vec{S}_c \cdot \vec{S}_j + \vec{S}_i \cdot \tilde{D}_{ij} \cdot \vec{S}_j + \vec{d}_{ij} \cdot \vec{S}_i \times \vec{S}_j + j_{ij}\vec{S}_i^2\vec{S}_j^2).$$

From the selection rules of the 6*j* coefficients (*89*), it follows that the biquadratic terms cannot mix the $S = \frac{1}{2}$ levels with higher spin states. By contrast, the anisotropic symmetric and antisymmetric terms, whose magnitude is related to that of the isotropic component (*89*), can give rise to a substantial mixing. However, a detailed quantitative model is needed to verify whether the peculiar magnetic properties of $[3Fe–4S]^{1+}$ centers can be explained by this mixing.

2. Reduced Forms

MCD experiments have shown that the ground manifold of $[3Fe–4S]^0$ centers is $S = 2$ in all the [3Fe–4S] proteins studied so far with this technique (*82*, *84*). A detailed Mössbauer study carried out on *D. gigas* ferredoxin II has demonstrated moreover that this spin state arises from the antiferromagnetic coupling of a [Fe(III), $S_C = \frac{5}{2}$] site to the two sites of a fully delocalized [Fe(III)–Fe(II), $S_{AB} = \frac{9}{2}$] mixed-valence pair (*85*) (Fig. 8A). This asymmetric electron distribution, which has also been observed in synthetic analogs (*91*), is apparently an intrinsic property of the $[3Fe–4S]^0$ unit (*92*). Actually, the interplay between double exchange interactions and vibronic coupling effects gives rise to fully delocalized [Fe(III)–Fe(II)] pairs in the majority of mixed-valence clusters with a nuclearity larger than 2, including the $[3Fe–4S]^{1+}$ fragment present in heterometallic $[MFe_3S_4]$ clusters and $[4Fe–4S]^{1+,2+,3+}$ clusters (see later discussion).

Like mononuclear $Fe(II)S_4$ centers, $[3Fe–4S]^0$ centers can give an EPR spectrum. Indeed, a broad, asymmetric line is often observed at very low field in the spectra obtained with proteins containing these centers, such as *D. gigas*, *T. thermophilus*, and *P. furiosus* ferredoxins (*85*, *93*, *94*) and Ni–Fe hydrogenases (*95*), as well as those obtained with synthetic analogs (*91*). The zero-field splitting parameters determined by Mössbauer and MCD spectroscopy were found to be $D \approx -2.5$ cm^{-1}, $E/D \approx 0.22$ in the case of all these $[3Fe–4S]^0$ centers, except for *T. thermophilus* ferredoxin, where $E = 0$ (*85*, *93*, *94*). Although the zero-field splitting parameters of the $[3Fe–4S]^0$ cluster of *A. vinelandii* ferredoxin I were found to be very similar (*96*), no EPR spectrum was observed, probably because the E/D ratio was slightly larger and/or these parameters were more widely distributed in this protein (*84*). Since the zero-field splitting parameters of the $S = 2$ state are determined both by the local parameters of the iron sites and by the anisotropic component of the intersite exchange interactions, it seems quite remarkable that they vary so little from one protein to another.

It is also worth mentioning the case of the $[3Fe–4S]^{-1}$ fragments

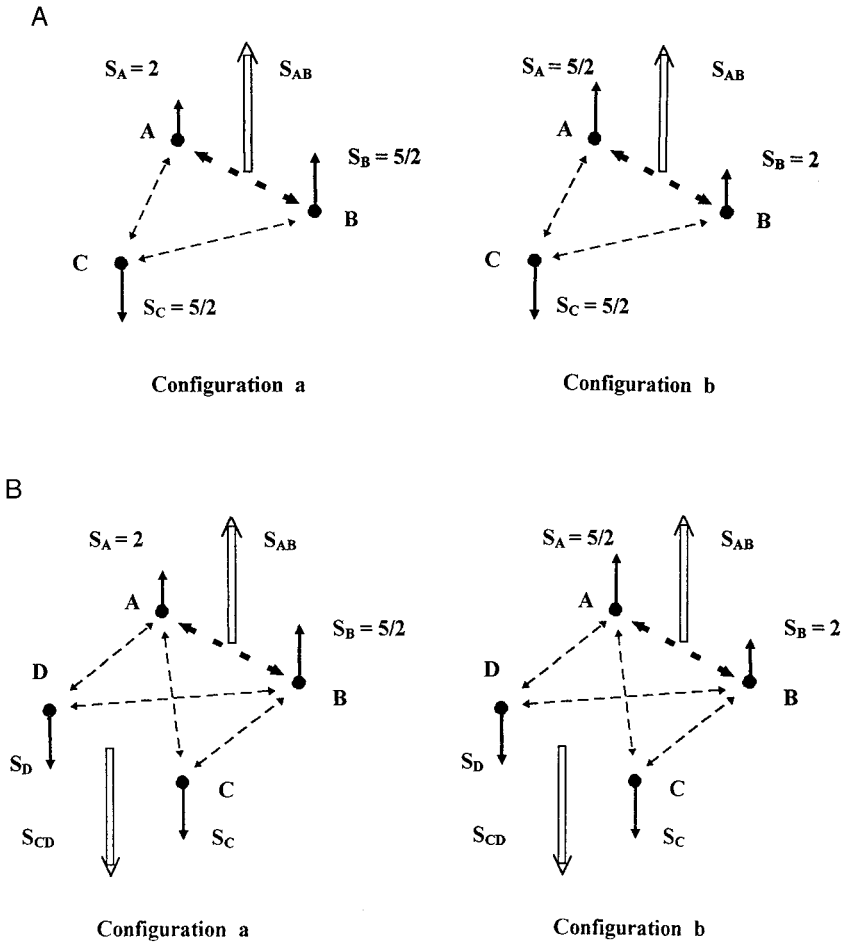

FIG. 8. Scheme of the electronic structure of (A) $[3Fe–4S]^0$ centers and (B) $[4Fe–4S]^{3+,1+}$ centers according to the standard model. The thin and thick dashed lines indicate the antiferromagnetic and double exchange coupling, respectively. Configurations a and b correspond to the two possible locations of the excess electron in the mixed-valence pair. In part (B), the local spin values are $S_C = S_D = 2$ in the case of $[4Fe–4S]^{1+}$ centers and $S_C = S_D = \frac{5}{2}$ in the case of $[4Fe–4S]^{3+}$ centers.

present in modified heterometallic $[MFe_3S_4]^{1+}$ clusters of proteins, in which M is a divalent diamagnetic metal ion. The $S = \frac{5}{2}$ ground state of these fragments results from the antiferromagnetic coupling between a [Fe(II), $S_1 = 2$] site and a fully delocalized [Fe(III)–Fe(II), $S_{23} = \frac{9}{2}$] mixed-valence pair (*97*). The EPR spectrum is characterized

by g_{eff} values ranging between 3.0 and 10, which were analyzed with a spin Hamiltonian similar to that given by Eq. (1) with $D \approx -2.5$ cm^{-1} and an E/D ratio equal to 0.25 and 0.18 in *D. gigas* ferredoxin II (*98*) and *P. furiosus* ferredoxin (*97*), respectively. Lastly, it should be mentioned that the $[3Fe–4S]^{-2}$ form recently generated electrochemically gives a diamagnetic ground state (*99–102*).

3. Relaxation Properties

Owing to the weak coupling of Fe(III) ions to the lattice, the relaxation of $[3Fe–4S]^{1+}$ centers might have been expected to be relatively slow. In fact, the spin–lattice relaxation rate of the $[3Fe–4S]^{1+}$ centers of *Azotobacter vinelandii* ferredoxin I and *D. gigas* ferredoxin II was found to be two orders of magnitude faster than that of the $[2Fe–2S]^{1+}$ center of *Spirulina maxima* ferredoxin between 4 and 50 K (*103*). In the 20 to 50 K range, the temperature dependence of the relaxation rate was satisfactorily described by an Orbach process involving an excited state of energy $\Delta = 88$ cm^{-1} (*81*). This value is in good agreement with the value $\Delta \approx 80$ cm^{-1} deduced from a MCD study carried out on *D. gigas* ferredoxin II (*104*). The relaxation rate of the $[3Fe–4S]^{1+}$ center of *D. desulfuricans* Miyazaki hydrogenase was found in contrast to be two orders of magnitude slower than that of the two previously cited ferredoxins in the 10 to 60 K range (*79*). Since the anisotropy of the EPR spectrum exhibited by this center is much smaller than that observed with the two ferredoxins, these findings are fully consistent with the idea that the anisotropy of the spectrum is due to a mixing with excited states.

In the reduced form, the set of energy levels provided by the $S = 2$ manifold may promote efficient relaxation processes at low temperatures. However, since no low-lying excited levels were detected in $[3Fe–4S]^{0}$ centers in magnetic susceptibility studies (*87*), the relaxation is not likely to be particularly fast at intermediate and high temperatures. To our knowledge, the only information available on this point was provided by a study on the temperature dependence of the EPR signal given by the center of *D. vulgaris* Miyazaki hydrogenase, which showed no evidence of relaxation broadening in the 20–50 K range (*79*).

D. $[4Fe–4S]^{1+}$ and $[4Fe–4S]^{3+}$ Centers

$[4Fe–4S]^{2+,1+}$ clusters are certainly the most ubiquitous iron–sulfur centers in biological systems. They play the role of low potential redox centers in ferredoxins, membrane-bound complexes of the respiratory

and photosynthetic electron transfer chains and a great variety of metalloenzymes. There is growing evidence that they can also perform nonredox functions [see Ref. (*105*) and Section IV,B].

1. EPR Spectrum

The characteristic derivative-shaped feature at $g \approx 1.94$ first observed in mitochondrial membranes has long been considered as the sole EPR fingerprint of iron–sulfur centers. The EPR spectrum exhibited by $[4Fe–4S]^{1+}$ centers generally reflects a ground state with $S = \frac{1}{2}$ and is characterized by g values and a spectral shape similar to those displayed by $[2Fe–2S]^{1+}$ centers (Fig. 6c). Proteins containing $[4Fe–4S]^{3+}$ centers, which are sometimes called HIPIP, essentially act as electron carriers in the photoinduced cyclic electron transfer of purple bacteria (*106*), although they have also been discovered in nonphotosynthetic bacteria (*107*). Their EPR spectrum exhibits an axial shape that varies little from one protein to another with $g_{//} \approx 2.11–2.14$ and $g_{\perp} \approx 2.03–2.04$ (*106–108*), plus extra features indicative of some heterogeneous characteristics (Fig. 6d).

The electronic structure of tetranuclear clusters is determined by the interplay between numerous exchange and double exchange intersite interactions and between vibronic coupling effects. However, the ground state of $[4Fe–4S]^{1+}$ and $[4Fe–4S]^{3+}$ clusters is generally an $S = \frac{1}{2}$ state, which suggests that it depends on factors that are not very sensitive to structural variations. Actually, a clue about the nature of this ground state has been provided by the low-temperature Mössbauer spectrum of these centers, in which the four iron sites generally form two internally equivalent pairs: In the case of two sites A and B, the parameters are those of a fully delocalized mixed-valance [Fe(III), Fe(II)] pair and the ^{57}Fe hyperfine coupling constants are negative, whereas in that of the other sites C and D, the parameters correspond to ferrous sites in $[4Fe–4S]^{1+}$ clusters and ferric sites in $[4Fe–4S]^{3+}$ clusters, and the hyperfine constants are positive (*109*, *110*). Since the isotropic component of the hyperfine interactions is proportional to the spin density at the corresponding iron nucleus, this pattern directly reflects the orientation of the local spins with respect to the total spin $\vec{S}$ of the cluster. These orientations are suitably described by a phenomenological pairwise model, which can be currently considered as the standard model for polynuclear iron–sulfur centers with a nuclearity greater than 2 (Fig. 8B): Within the pair (A,B), the double exchange interactions force the spins $\vec{S}_A$ and $\vec{S}_B$ into a parallel alignment. In turn, the antiferromagnetic interactions between these sites and sites C and D force $\vec{S}_C$ and $\vec{S}_D$ to be

parallel despite their antiferromagnetic coupling, giving a net spin $S = \frac{1}{2}$ (Fig. 8B). When all the exchange parameters are equal, the antiferromagnetic interactions between the (A,B) and (C,D) pairs can be written $-2J\vec{S}_{AB}\cdot\vec{S}_{CD}$, where $\vec{S}_{AB} = \vec{S}_A + \vec{S}_B$, $\vec{S}_{CD} = \vec{S}_C + \vec{S}_D$, so that S_{AB} and S_{CD} are good quantum numbers. This remains true even if three different values are used for J[Fe(III), Fe(III)], J[Fe(III), Fe(II)], and J[Fe(II), Fe(II)] (*111*). Under these conditions, if we note $S_3 = \frac{5}{2}$, $S_4 = 2$ as the spins of the mixed-valence pair and $S_1 = S_2$ as those of the localized pair, equal to $\frac{5}{2}$ and 2 in $[4Fe–4S]^{3+}$ and $[4Fe–4S]^{+}$ centers, respectively, the four hyperfine tensors $\tilde{A}_i$ are related to the local hyperfine tensors $\tilde{a}_i$ by $\tilde{A}_i = K_i\tilde{a}_i$, where K_i is a spin coupling coefficient depending on S_i, S_{12}, and S_{34} (*111*). Upon taking the two configurations a and b shown in Fig. 8B, this relation can be generalized to take into account the valence delocalization between A and B (*112*). The isotropic components of the values A_{ix}, A_{iy}, A_{iz} measured by Mössbauer and ENDOR experiments performed on $[4Fe–4S]^{1+}$ and $[4Fe–4S]^{3+}$ clusters were satisfactorily reproduced by using the isotropic components measured in mononuclear FeS_4 centers as local hyperfine constants and the set $K_1 = K_2 = -\frac{4}{3}$, $K_3 = \frac{55}{27}$, $K_4 = \frac{44}{27}$ corresponding to $S_{12} = 4$, $S_{34} = \frac{9}{2}$ (*109*, *111*). As established in the case of $[3Fe–4S]^{0}$ clusters, the asymmetric electron distribution apparent in Fig. 8B results essentially from the interplay between valence delocalization and vibronic coupling effects (*113*).

In the framework of this standard model, the g tensor of the $S = \frac{1}{2}$ state is given by the simple expression

$$\tilde{g} = \sum_{i=1}^{4} K_i\tilde{g}_i, \tag{8}$$

where $\tilde{g}_1$ and $\tilde{g}_2$ are the local g tensors of sites D and C, respectively, and $\tilde{g}_3$ and $\tilde{g}_4$ are average g tensors given by expressions such as Eq. (6):

$$\begin{aligned}\tilde{g}_3 &= c_a^2\tilde{g}_3^B + c_b^2\tilde{g}_3^A\\ \tilde{g}_4 &= c_a^2\tilde{g}_4^A + c_b^2\tilde{g}_4^B\end{aligned} \tag{9}$$

According to Eqs. (8) and (9), the g tensor of $[4Fe–4S]^{1+}$ clusters depends on four ferrous ($\tilde{g}_1$, $\tilde{g}_2$, $\tilde{g}_4^A$, $\tilde{g}_4^B$) and two ferric ($\tilde{g}_3^A$,$\tilde{g}_3^B$) local g tensors. This holds true even if the mixed-valence pair is fully delocalized: $c_a^2 = c_b^2 = \frac{1}{2}$. Owing to the low-lying excitation energies of the

ferrous sites (*114*), the ferrous g tensors are expected to be highly sensitive to variations in the structure and the environment of the $[4Fe–4S]^{1+}$ cluster in the protein. This cause of variability, together with the large number of parameters determining the g tensor of these clusters, may explain why the variations in their principal components from one protein to another do not appear to be correlated, contrary to what is observed in the case of $[2Fe–2S]^{1+}$ clusters. In the case of $[4Fe–4S]^{3+}$ clusters, C and D are ferric sites and two ferrous g tensors and four ferric local g tensors are therefore involved in Eq. (8). This may explain why less variability has been observed experimentally.

The range of g values predicted by the standard model can be roughly estimated by assuming that all the local g tensors are isotopic and take only two different g values: $g(\mathrm{Fe(III)}) = 2.02$ and $g(\mathrm{Fe(II)}) = 2.00 + \Delta g$, with $\Delta g \geq 0$. One obtains

$$[4Fe–4S]^{1+} \text{ clusters: } g = 2.04 - 1.03\,\Delta g$$

$$[4Fe–4S]^{3+} \text{ clusters: } g = 1.99 - 1.63\,\Delta g$$

By comparison, the same approximation yields $g = 2.05 - 1.33\,\Delta g$ in the case of a $[2Fe–2S]^{1+}$ cluster. Although these simple expressions account approximately for the values observed experimentally, they should not be taken too seriously because of the tensorial character of the quantities involved in Eqs. (8) and (9). Actually, a general model for the interpretation of the g tensors of $[4Fe–4S]^{1+}$ and $[4Fe–4S]^{3+}$ clusters has been proposed (*115*). An important prediction made by this model concerns the orientation of the magnetic axis corresponding to the largest g value with respect to the cubane structure: with $[4Fe–4S]^{3+}$ clusters, this magnetic axis was predicted to be close to the common perpendicular to the directions defined by the $[Fe_C(III), Fe_D(III)]$ and mixed-valence $[Fe_A(III), Fe_B(II)]$ pairs, whereas with $[4Fe–4S]^{1+}$ clusters, a similar orientation was predicted to occur only in the case of a symmetric structure in which the ferrous sites C and D are practically equivalent. These predictions were largely confirmed by the results of single-crystal EPR studies carried out on model compounds (*115*, *116*) and by an ENDOR study on the $[4Fe–4S]^{3+}$ center in *Ectothiorhodospira halophila* HIPIP (*117*).

The above-mentioned set of K_i values are deduced from analyses based on the hyperfine constants of mononuclear FeS_4 centers. However, we have already stressed that local parameter values are not necessarily transferable from one type of iron–sulfur center to an-

other. An attempt to overcome this difficulty has been presented in a study in which free ion constants and estimated covalency factors were used to define "site values" for the isotropic components of the hyperfine interactions in the various types of iron–sulfur clusters (*118*). In the case of $[4Fe–4S]^{1+}$ clusters, the semiempirical K_i values deduced from this study were generally found to be intermediate between those corresponding to ($S_{12} = 3$, $S_{34} = \frac{7}{2}$) and ($S_{12} = 2$, $S_{34} = \frac{5}{2}$), but the aconitase cluster, where oxygen ligands are present at one iron site, had coefficients intermediate between those corresponding to ($S_{12} = 4$, $S_{34} = \frac{9}{2}$) and ($S_{12} = 3$, $S_{34} = \frac{7}{2}$) (*118*). In the case of $[4Fe–4S]^{3+}$ clusters, the best description was found to be ($S_{12} = 3$, $S_{34} = \frac{7}{2}$) (*118*). These conclusions are consistent with the results of EPR and ENDOR single-crystal experiments carried out on synthetic analog by Lamotte and co-workers (*118*). All these findings show that S_{12} and S_{34} are not always good quantum numbers and call for a refinement of the standard model. A further complication may arise when the complex pattern of intersite interactions brings excited states sufficiently close to the ground state for its magnetic properties to be affected. This situation is probably encountered in the case of very fast-relaxing $[4Fe–4S]^{1+}$ centers exhibiting broad, anisotropic EPR spectra extending beyond the range of g values predicted by Eq. (8), such as center F_X^- of photosystem I (PSI) with $g_x = 1.75$, $g_y = 1.88$, $g_z = 2.14$ (*119*), and the $S = \frac{1}{2}$ $[4Fe–54S]^{1+}$ center of *Pyrococcus furiosus* ferredoxin with $g_x = 1.80$, $g_y = 1.87$, $g_z = 2.10$ (*120*).

The heterogeneous character of the EPR spectra given by some HIPIP is probably due to the heterogeneous location of the mixed-valence pair in the $[4Fe–4S]^{3+}$ centers, which was established in detailed NMR studies (*121*, *122*). Since a heterogeneous location of the mixed-valence pair was also observed in the case of the $[4Fe–4S]^{1+}$ centers of *Chromatium vinosum* ferredoxin (*123*), the same phenomenon may account for the complex EPR spectra displayed by these centers in some proteins (*124–126*).

Lastly, $[4Fe–4S]^{1+}$ centers display EPR spectra resulting from spin states with $S > \frac{1}{2}$ in some proteins. This was first observed in the case of the selenium derivative of *C. pasteurianum* ferredoxin, in which EPR features at $g_{\text{eff}} \approx 4.5$, 3.5, 2 and $g_{\text{eff}} \approx 5.2$ were observed in addition to the usual $S = \frac{1}{2}$ EPR signal, which were assigned to $S = \frac{3}{2}$ and $S = \frac{7}{2}$ spin states, respectively (*127*). Likewise, the $[4Fe–4S]^{1+}$ center of the Fe protein of the *Azotobacter vinelandii* nitrogenase was reported to exist in a form exhibiting an $S = \frac{1}{2}$ ground state and in a form giving an $S = \frac{3}{2}$ state characterized by strongly temperature-dependent EPR features at $g_{\text{eff}} \approx 5.9$ and 4.7 (*128*). Since then, $[4Fe–4S]^{1+}$ centers giving EPR signals arising from $S = \frac{3}{2}$ and even $S = \frac{5}{2}$

spin states have been identified in a variety of iron–sulfur proteins, some of which show a noncysteinyl ligation to one iron atom, such as *Pyrococcus furiousus* ferredoxin (*120*) and *E. coli* dihydroxy-acid dehydratase (*129*).

In the light of the growing body of data showing that the electronic structure of $[4Fe–4S]^{1+}$ centers may depart significantly from that described by the standard model, $[4Fe–4S]^{2+}$ centers having nondiamagnetic ground states will predictably be discovered in the near future. In this context, it is worth noting that an all-ferrous $[4Fe–4S]^{0}$ form with an $S = 4$ ground state displaying an EPR feature at $g_{\text{eff}} \approx 16$ has been observed in the Fe protein of nitrogenase (*130*).

2. Relaxation Properties

Owing to their markedly "ferrous" character, $[4Fe–4S]^{1+}$ clusters are likely to be more strongly coupled to their environment than $[4Fe–4S]^{3+}$ clusters. However, as observed in the case of $[3Fe–4S]^{1+}$ clusters, one of the main factors determining the spin–lattice relaxation rate of these $S = \frac{1}{2}$ states is the energy of the closest excited states. This energy, which depends on many intersite interactions, can vary considerably from one protein to another, and various patterns of relaxation behavior can therefore be observed. The temperature dependence of the spin–lattice relaxation rate of the $[4Fe–4S]^{1+}$ center of *Bacillus stearothermophilus* ferredoxin was studied in the 1.2 to 40 K range and was interpreted in terms of the same relaxation processes as in the case of the $[2Fe–2S]^{1+}$ center of *S. maxima* ferredoxin (*131*). In particular, the relaxation broadening was attributed to an Orbach process involving an excited state of energy $\Delta = 110$ cm^{-1} (*131*). In a study on the relaxation broadening of other proteins containing $[4Fe–4S]^{1+}$ centers, Δ values in the 110–300 cm^{-1} range were obtained (*132*), which significantly overlap those observed for $[2Fe–2S]^{1+}$ centers. In contrast, the relaxation broadening of center F_X^- of PSI, which begins at 10 K, was attributed to the presence of a very close excited level of energy $\Delta = 50$ cm^{-1} (*58*).

The spin–lattice relaxation rate of *Chromatium vinosum* HIPIP was measured between 5 and 50 K (*103*). In comparison with the $[4Fe–4S]^{1+}$ cluster of *B. stearothermophilus* ferredoxin, the relaxation was found to be faster below 15 K and slower above this temperature.

E. Concluding Remarks: Identifying the Centers

The dream of any bioinorganic chemist working on biological systems is to have a sensitive, selective technique with which it is possi-

ble to unambiguously identify the various types of metal centers. In the case of iron–sulfur centers, EPR spectroscopy can play this role to a large extent, although complementary techniques are sometimes needed. In what follows, the various types of iron–sulfur clusters are examined from this standpoint.

1. Mononuclear FeS_4 Centers

As we saw in Section II,A, the E/D ratio that determines the main features of the spectrum given by oxidized FeS_4 centers differs in the case of rubredoxin-like and desulforedoxin-like proteins because the four cysteines ligating the center are differently arranged in these two classes of proteins. Conversely, ferric centers having different patterns of coordination can have the same E/D ratio and consequently give very similar EPR spectra. It has been previously pointed out that the EPR spectrum exhibited by the iron center of protocatechuate 3,4-dioxygenase is very similar to that of rubredoxin (*16*). Moreover, the EPR spectrum of rubredoxin was not significantly affected when a cysteine ligand was replaced by a serine (*133*). These findings simply reflect the fact that the E/D ratio is close to the maximum rhombicity value in all these centers. At the other extremity of the E/D scale, an identical E/D ratio equal to 0.08 has been obtained for desulfoferrodoxin and a pentagonal bipyramidally coordinated ferric complex, which gave rise to a misinterpretation (*20*). These few examples show that any EPR study of these centers should be completed by at least a UV-visible absorption spectrum.

2. [3Fe–4S]$^{1+,0}$ Centers

In retrospect, it may seem surprising that the EPR signature of $[3Fe–4S]^{1+}$ centers was authenticated as late as 1980. Actually, this spectrum centered at $g \approx 2.01$, which was detected in the oxidized form, had long been assigned to a radical or to a $[4Fe–4S]^{1+}$ center. Moreover, owing to the substoichiometric amounts present in several systems, these centers were initially taken to be artifacts produced by oxidative degradation, which delayed closer investigations on these centers. Since 1980, the weak anisotropy of their EPR signal has greatly facilited the detection of these centers in membrane-bound complexes of the respiratory chains and in a number of metalloenzymes, including *in vivo* systems, which confirms that they play a functional role (*134*). The typical shape of the spectrum and the redox state at which it is observed now provide reliable fingerprints for identifying $[3Fe–4S]^{1+,0}$ centers.

3. $[4Fe–4S]^{3+,2+}$ *Centers*

Like [3Fe–4S] centers, these centers display an EPR spectrum centered at $g \approx 2$ in the oxidized form. However, the g values and the spectral shapes differ sufficiently between the two types of centers to preclude any confusion between them (Fig. 6). Both types of centers are characterized by fast relaxation properties, although this can vary from one protein to another.

4. $[2Fe–2S]^{2+,1+}$ *and* $[4Fe–4S]^{2+,1+}$ *Centers*

Discriminating between these two types of centers, which have mostly been identified in biological systems, often presents EPR spectroscopists with a serious challenge. The great majority of properly identified $[2Fe–2S]^{1+}$ centers of proteins give EPR spectra characterized by $g_{av} \approx 1.96$ or 1.91, with g values around those given in Figs. 1 and 2. In particular, the largest g value rarely exceeds 2.05, which is not true in the case of $[4Fe–4S]^{1+}$ centers. However, some dinuclear centers, such as center 2 of xanthine oxidase and that of *D. gigas* aldehyde oxidoreductase, can exhibit anomalous g values, probably due to low-lying excited levels (see Section II,B). The g values alone do not therefore always suffice to discriminate between these two types of iron–sulfur centers. Owing to their "ferrous" character and to the possibility that low-lying excited levels may be present, $[4Fe–4S]^{1+}$ clusters often exhibit fast relaxation rates. It can be seen from several examples, however, that this relaxation is not always much faster than that of $[2Fe–2S]^{1+}$ centers. In the 1.2 to 40 K range, the relaxation rate of the $[4Fe–4S]^{1+}$ center of *B. stearothermophilus* ferredoxin is faster than that of the $[2Fe–2S]^{1+}$ center of *S. maxima* ferredoxin, but the difference amounts to only a factor of 3 between 5 and 12 K (*131*). Likewise, the relaxation rate of the $[4Fe–4S]^{1+}$ center of the superreduced HIPIP from *C. vinosum* is equal to that of the $[2Fe–2S]^{1+}$ center of *S. maxima* ferredoxin between 50 and 100 K, and the relaxation rate of the $[4Fe–4S]^{1+}$ center of *D. gigas* ferredoxin I is practically equal to that of the $[2Fe–2S]^{1+}$ center of *Halobacterium halobium* ferredoxin between 50 and 80 K (*67*, *132*). Conversely, as mentioned in Section II,B, the $[2Fe–2S]^{1+}$ center 2 of xanthine oxidase is characterized by very fast relaxation rates. These few examples show that attempts to identify iron–sulfur centers based on the sole relaxation characteristics can give unreliable results. This is especially true in the case of multicenter systems in which spin–spin interactions can accelerate the relaxation of interacting centers. Lastly, it should be noted that the half-saturation power at a given tempera-

ture and the temperature at which the EPR spectrum disappears due to relaxation broadening are only semiquantitative indicators that cannot be substituted for a T_1 measurement. In practice, recording a UV-visible absorption spectrum can often help to discriminate between the two types of centers.

III. Application of EPR to the Structural Study of Iron–Sulfur Proteins

The structural relationships between an iron–sulfur center and its coordinating polypeptide can be approached from two points of view: On the one hand, the center binds to three or four residues spaced out in the primary sequence, thus contributing to the protein folding and stability. On the other hand, the polypeptide chain keeps the iron–sulfur centers and other prosthetic groups in an appropriate arrangement to ensure that the protein remains functional. To obtain further insights into these two aspects, two complementary strategies have been developed. The first one, which has been widely used over the past few years, has yielded some useful information about the folding of the protein. This strategy consists in mutating some residues that are expected to ligate the center and in monitoring the concomitant changes in its electronic structure by EPR. The aim of the second approach is to determine the relative arrangement of the prosthetic groups in multicenter proteins, based on the quantitative analysis of intercenter spin–spin interactions. This strategy constitutes a useful alternative to X-ray crystallography and structural NMR, especially in the case of high molecular weight complexes (*135*).

Despite its weakness, the anisotropy of the g tensor of iron–sulfur centers can be used to determine the orientation of these centers or that of the accommodating polypeptide in relation to a more complex system such as a membrane-bound complex. For this purpose, the EPR study has to be carried out on either partially or fully oriented systems (oriented membranes or monocrystals, respectively). Lastly, the sensitivity of the EPR spectra of iron–sulfur centers to structural changes can be utilized to monitor the conformational changes induced in the protein by different factors, such as the pH and the ionic strength of the solvent or the binding of substrates and inhibitors. We return to the latter point in Section IV.

A. Site-Directed Mutagenesis Monitored by EPR

A general picture of the coordination of the various types of iron–sulfur centers was first outlined on the basis of the three-dimensional

structure of small proteins such as ferredoxins (*136*). Consensus Cys motifs of this kind have been widely used to predict the presence of iron–sulfur centers in complex enzymatic systems on the basis of their primary structure, which has generally been deduced from the nucleotide sequencing of the structural genes (*137*, *138*). The concept of consensus motif became somewhat looser after the discovery of new coordinating Cys arrangements (*139*) and the possible existence of noncysteinyl ligands (*140*). Under these conditions, SDM experiments monitored by EPR have proved to be a valuable means of assessing the coordination scheme of iron–sulfur centers in various proteins. However, attempts at selectively removing a center by substituting a noncoordinating residue (Ala or Gly) for Cys have often led to the loss of all the metal cofactors and to protein denaturation (*141*). Milder modifications have therefore been devised that require either altering the center environment or directly exchanging a ligand, or even converting the center into another one. Despite these precautions, only a few studies have yielded proteins that were stable enough to be studied by EPR. In the case of multicenter proteins, these techniques are useful only on condition that the various centers can be distinguished spectroscopically and that the properties of the unmodified centers are not too markedly affected by the mutations.

1. [*2Fe–2S*] *Centers*

Among the numerous SDM studies carried out on [2Fe–2S]-containing proteins, those based on Cys-to-Ser substitutions have yielded the most interesting results. As mentioned in Section II,B, the variations in the g tensors of $[2Fe–2S]^{1+}$ centers essentially reflect the variations in the rhombic distortion at the ferrous site. The weak sensitivity of the ferric g tensor to structural changes has been confirmed by spectroscopic data published on the [2Fe–2S] centers of human and mouse ferrochelatases. A combination of site-directed mutagenesis, resonance Raman, and MCD experiments carried out on the human enzyme have suggested that the center is ligated by three cysteine residues and one oxygenic ligand (*142*). The MCD study furthermore provided evidence that the oxygenic ligand could be bound at the nonreducible Fe(III) site (*142*). This assignment is consistent with the results of a Mössbauer study on the dithionite-reduced ferrochelatase of mouse liver, which showed that the electronic structure of the Fe(II) site is well described by the ligand field model applicable to [2Fe–2S] centers with pure cysteinyl coordination (*69*). Despite the probable presence of an oxygenic ligand at the Fe(III) site, the g values of this $[2Fe–2S]^{1+}$

center, which are equal to 1.912, 1.936, 2.002, are similar to those observed in the $g_{av} \approx 1.96$ class (Fig. 1).

The example of ferrochelatase shows that the EPR spectra of [2Fe–2S]$^{1+}$ centers of proteins are probably only weakly affected by the substitution of a serine for a cysteine ligating the nonreducible site. When the substitution takes place at the reducible site, however, the loss of symmetry is likely to shift the g values significantly. In this analysis, it is implicitly assumed that the serinate coordination is effective and that the magnetic properties of the unmodified site are not affected by the mutation. Although the latter assumption is only a working hypothesis, evidence supporting the former one can be provided by the occurrence of a blue shift in the UV-visible absorption bands and a significant negative shift of the redox potential that occurs when the modified site is the reducible one, as in the case of model compounds (*143*, *144*) and that of the C42S mutant of rubredoxin (*133*). Despite the similarities existing between cysteine and serine residues, Cys-to-Ser substitutions made it possible to assemble [2Fe–2S] centers (*141*) and to study them using EPR techniques in only a limited number of cases. In what follows, the results obtained with the Frd B subunit of *E. coli* fumarate reductase, the [2Fe–2S] human ferredoxin and the ferredoxins from *C. pasteurianum* and *Anabaena* 7120 will be analyzed. The cysteine residues involved in these studies are given in Fig. 9, and the apparent g values measured on

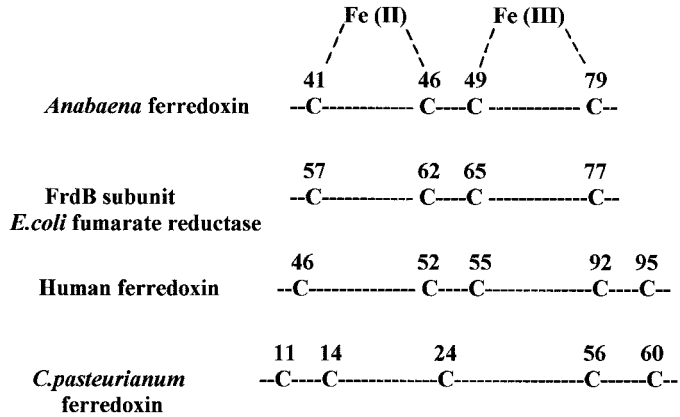

FIG. 9. Cysteine residues involved in the Cys-to-Ser substitutions carried out on [2Fe–2S] proteins. The reducible site of the center was identified by NMR in the case of *Anabaena* ferredoxin (*42*).

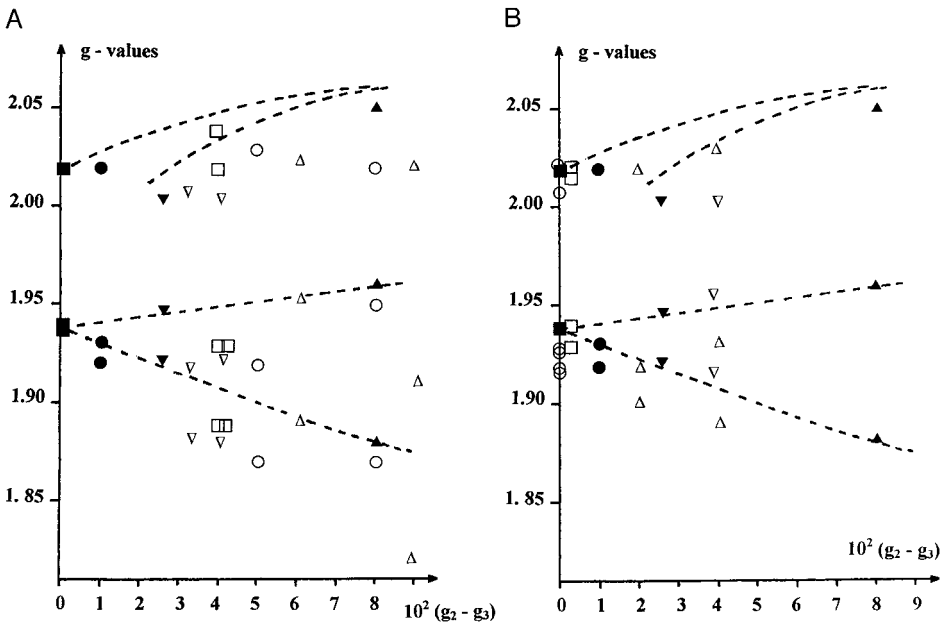

FIG. 10. Comparison between the g values of Cys-to-Ser mutants and wild-type [2Fe–2S] proteins, in cases where the substitution takes place at (A) the reducible site and (B) the nonreducible site. The following symbols indicate the various proteins: ▲, *Anabaena* 7120 vegetative ferredoxin; ■, human ferredoxin; ●, Frd B subunit in *E. coli* fumarate reductase; ▼, *Clostridium pasteurianum* ferredoxin. Filled and empty symbols indicate the wild-type and mutant proteins, respectively.

the EPR spectra of the wild-type and mutant proteins are plotted in Fig. 10.

The first protein in which the cysteine residues expected to coordinate a [2Fe–2S] center were systematically replaced by Ser was the Frd B subunit of *E. coli* fumarate reductase (*145*). The N-terminal part of the sequence contains a very similar cysteine motif to that coordinating the [2Fe–2S] centers of plant-type ferredoxins such as that of *Anabaena* (Fig. 9). In these ferredoxins, NMR studies have established that the reducible site is coordinated by Cys41 and Cys46 (*41*, *42*). When the four Cys of Frd B were individually changed to Ser, a considerable decrease in the redox potential of 100 and 240 mV was observed in the case of the C57S and C62S mutants, while moderate changes of +30 and −30 mV occurred in the case of the C65S and C77S variants, respectively (*145*). These results strongly suggest that the reducible iron site is coordinated by the first two cysteines in

the motif, as observed in the case of plant-type ferredoxins. The EPR data are fully consistent with this assignment, since the spectra of the C65S and C77S mutants were found to be practically identical to that given by the wild-type protein, while those of the C57S and C62S mutants are markedly different (*145*). Actually, several findings suggest that Cys65 might not be directly involved as a ligand (*140*). The [2Fe–2S] ferredoxin from *C. pasteurianum* contains five cysteine residues in positions 11, 14, 24, 56, and 60, an arrangement that differs from all the Cys motifs known to coordinate [2Fe–2S] centers (Fig. 9). Among the numerous site-directed mutations that were carried out on this protein, the individual Cys-to-Ser replacement of the five cysteine residues gave [2Fe–2S] centers that could be characterized spectroscopically (*146*). The spectroscopic and potentiometric properties of the C14S and C24S mutants were found to be identical to those of the wild-type protein, which was attributed to the exchange of a ligand (*147*), whereas the UV-visible absorption spectra of the three other mutants exhibited the blue shift characteristic of an effective serinate coordination (*146*). In the case of the C56S and C60S mutants, this coordination was borne out by detailed resonance Raman and MCD studies (*146*, *148*). Besides, the fact that the redox potentials of these two mutants were found to be 100 mV negatively shifted compared to the wild-type protein suggested that the serinate coordination occurred at the reducible iron site (*149*). In agreement with this assignment, the EPR spectra of the C56S and C60S mutants were found to differ conspicuously from that of the wild-type protein, while that of the C11S mutant remained practically unchanged (*146*).

The [2Fe–2S] center of human ferredoxin, the human equivalent of bovine adrenodoxin, is coordinated by cysteines 46, 52, 55, and 92 (*150*). In order to prevent ligand exchange from occuring, the fifth cysteine, Cys 95, was systematically replaced by an alanine in the four serine mutants (*151*). The blue shift of the UV-visible absorption bands typical of a serinate coordination was clearly observed only in the case of the C52S and C92S mutants. The EPR spectra of the C55S and C92S mutants were found to be identical to that of the wild-type protein, while the spectra of the C46S and C52S mutants were markedly different. In particular, the spectrum of the C46S variant shown in Fig. 3 of Ref. (*151*) was more anisotropic and much broader than that of the wild-type protein, a finding that was initially overlooked by the authors of that study (*151*). The EPR data are therefore fully consistent with the reducible iron site being ligated by Cys46 and Cys52. This assignment was confirmed by recent MCD data indicating that the charge transfer bands involving the ferric site of the di-

thionite-reduced C55S variant are strongly affected by the mutation (*142*).

Let us now look at the case of *Anabaena* 7120 vegetative ferredoxin. Among the four cysteines present in this plant-type ferredoxin, Cys41 and Cys46 have been shown to coordinate the reducible site (*42*) (Fig. 9). When the four cysteine residues were individually replaced by a serine, a blue shift was clearly observed in the UV-visible absorption spectrum of the C41S and C49S variants (*152*). The 422- and 466-nm bands shifted in opposite directions in the case of the C46S variant, whereas they collapsed at 440 nm in the case of the C79S variant (*152*). Changing Cys to Ser at position 46 did not affect the redox potential of the [2Fe–2S] center (*153*). This result was unexpected, since the authors had previously concluded on the basis of NMR data that this residue ligates the reducible site in the C46S mutant (*152*). The EPR spectra of the C46S and C41S mutants were found to differ significantly from that of the wild-type protein, with a complex shape indicative of some heterogeneity. This has been ascribed to components arising from two species differing in the location of the excess electron (*153*). Substituting Ser for a Cys coordinating the reducible site of the [2Fe–2S] center therefore gives rise to some complex and unpredictable effects in the case of *Anabaena* ferredoxin. A similar phenomenon was observed when the mutations were directed toward the nonreducible site: Upon mutation of Cys49, a positive shift of the redox potential equal to +55 mV was observed (*153*). Besides, the EPR spectra of the C49S and C79S mutants were found to differ strongly from that of the wild-type protein, suggesting that the magnetic properties of the reducible site were altered by the mutation in both cases. No large structural change could be detected, however, in the X-ray crystal structure of the C49S mutant, apart from the shorter Fe–O bond distance of 2.0 Å as compared with the Fe–S bond of 2.3 Å measured in the wild-type protein (*153*).

The case of *Anabaena* ferredoxin provides a good example of the difficulties liable to be encountered when interpreting the results of site-directed mutagenesis experiments. Why is the behavior of this particular protein so complex? Although a definite answer would require more detailed studies, it is worth noting that the EPR spectra given by plant-type ferredoxins are characterized by relatively broad lines, reflecting a significant degree of structural flexibility at the ferrous site (*44*). It can be speculated that this flexibility, which is possibly due to the high degree of solvent exposure of this site (*154*), may be responsible for the wide range of potentiometric and spectroscopic properties exhibited by the Cys-to-Ser mutants.

Detailed MCD experiments carried out on the dithionite-reduced forms of the C56S and C60S mutants of *C. pasteurianum* ferredoxin have shown that a large fraction of the $[2Fe–2S]^{1+}$ centers have an $S = 9/2$ ground state (*148*). These centers exhibit temperature-dependent features at $g_{eff} = 10.1$, 9.25, 6.00, and 3.00, corresponding to $E/D = 0.16$ with $D = -1.1$ cm^{-1} (*148*). According to the model presented in Section II,B, $[2Fe–2S]^{1+}$ centers with $S = 9/2$ are liable to have delocalized valences (Fig. 5). This was confirmed by a Mössbauer study on the C56S mutant, which also showed that the valences are trapped in those centers having $S = 1/2$ (*155*). Elucidating the molecular mechanism whereby the electronic structure of these centers is switched in the protein from a fully localized $S = 1/2$ state to a fully delocalized $S = 9/2$ state constitutes a most exciting challenge for theoreticians.

2. [*4Fe–4S*] *and* [*3Fe–4S*] *Centers*

a. Naturally Occurring Coordination Schemes The three-dimensional structure of ferredoxins has shown that the structures and coordinating motifs of [4Fe–4S] and [3Fe–4S] centers are closely related (*72*, *73*). Indeed, although the $CX_2CX_2CX_3C$ arrangement has long been thought to be the typical binding motif of [4Fe–4S] centers (*136*), it can also bind [3Fe–4S] centers either when the second Cys is absent, as observed in the case of 7Fe ferredoxins (*156*), or when it is present and oriented in such a way that the ligation of a fourth iron atom is not possible, as observed in *Azotobacter vinelandii* ferredoxin I (*72*, *157*). Conversely, the coordination of [4Fe–4S] centers may mobilize only three cysteine residues. In *Desulfovibrio africanus* ferredoxin III (*158*), *Desulfovibrio vulgaris* Miyazaki ferredoxin I (*159*), and *Pyrococcus furiosus* ferredoxin (*120*), the second Cys of the consensus motif is replaced by Asp, and a $[3Fe–4S]^{1+}$ center is present in the as-prepared form. After incubation with Fe^{2+} salts under reducing conditions, these centers were found to have been converted into $[4Fe–4S]^{1+}$ centers displaying unusual EPR properties: in the case of *D. africanus* and *D. vulgaris* Miyazaki ferredoxins, a resonance at $g_{eff} \approx 5$ arising from an $S = \frac{3}{2}$ ground state was observed (*158*, *159*), whereas a mixture of signals arising from $S = \frac{1}{2}$ and $S = \frac{3}{2}$ states was observed in the case of *P. furiosus* ferredoxin (*94*). As mentioned in Section II,D, the minor $S = \frac{1}{2}$ species of *P. furiosus* ferredoxin exhibited a broad anisotropic spectrum and fast relaxation properties, suggesting the presence of low-lying excited levels. In this ferredoxin, the direct binding of Asp to the $[4Fe–4S]^{1+}$ center was assessed in a detailed NMR study (*160*). The peculiar magnetic properties of these

centers are apparently due to the noncysteinyl ligation of one iron atom, since a $[4Fe–4S]^{1+}$ center with an $S = \frac{1}{2}$ ground state and usual EPR characteristics was recovered upon substituting Cys for Asp in *D. africanus* ferredoxin III (*161*). However, the presence of a noncysteinyl coordination does not necessarily show up in the EPR spectrum, as shown by the case of active aconitase, which exhibits a ferredoxin-type spectrum despite the presence of an oxygenic ligand (*162*, *163*).

Another example of noncysteinyl coordination of a [4Fe–4S] center was provided by the resolution of the X-ray structure of *D. gigas* hydrogenase, which revealed that one iron atom of the distal [4Fe–4S] center was ligated by the N_δ atom of a histidine residue (*164*). Unfortunately, the EPR signature of this center could not be determined because of intercenter spin–spin interactions with other iron–sulfur centers (*95*).

The above analysis shows that the presence of a [4Fe–4S] or [3Fe–4S] center cannot be inferred from the sole examination of the cysteine arrangement and that spectroscopic investigations are needed to obtain more reliable information.

b. Results of Site-Directed Mutagenesis Experiments The cysteine residues coordinating [4Fe–4S] and [3Fe–4S] centers are apparently less amenable to genetic manipulations than those of [2Fe–2S] centers. Even in the case of small proteins such as clostridial 2 × [4Fe–4S] ferredoxins, replacing the coordinating Cys by other residues did not result in stable proteins (*141*). Those mutations of the polypeptide chain that made it possible to assemble the iron–sulfur centers were accompanied only by weak variations in their redox and spectroscopic properties (*165–167*), and comparing the EPR signals of the centers was difficult because of intercenter spin–spin interactions. In *Azotobacter vinelandii* ferredoxin I, replacing Cys 20, the fourth coordinating Cys of the [4Fe–4S] center, by Ala or Ser led to a rearrangement of the protein structure and to the binding of Cys 24 to the center (*168*, *169*). The EPR characterization of this center was precluded by the large negative shift of the redox potential of about 100 mV (*170*).

Similar difficulties have been encountered in the case of complex enzymes such as fumarate reductase and nitrate reductase from *E. coli*, in which substituting certain Cys ligands led to the loss of several if not all the iron–sulfur centers (*171*, *172*). However, in the case of nitrate reductase, which possesses one [3Fe–4S] and three [4Fe–4S] centers, it was possible to remove selectively one [4Fe–4S]

center without significantly altering the properties of the other centers: Mutations C16A,S, C19A,S, and C263A led to the disappearance of the highest potential center, whereas the C26A substitution was found to abolish the lowest potential one (*173*, *174*). These results, which have made it possible to elucidate the coordination scheme of the four iron–sulfur centers of the enzyme, demonstrate that the binding properties of the various Cys motifs of a protein can be very differently affected by Cys-to-Ala and Cys-to-Ser substitutions.

Contrary to what was achieved with the Cys ligands of [2Fe–2S] centers, it has rarely been possible to replace those of [4Fe–4S] and [3Fe–4S] centers by Ser. Upon substituting the Cys565 and Cys556 coordinating center F_X of PSI, a mixture of [3Fe–4S] centers and [4Fe–4S] centers with serinate coordination was observed (*175*, *176*). This coordination gave rise to a substantial decrease in the g tensor anisotropy, from g values of 1.75, 1.85, 2.14 to 1.811, 1.941, 2.015, and to a concomitant decrease in the relaxation rate, which suggested that the excited-state energies had increased (see Section II,D). In *E. coli* fumarate reductase, systematically substituting Ser for the Cys expected to coordinate the [4Fe–4S] and [3Fe–4S] centers led to the loss of both centers, except in the case of the C148S and C151S mutants in which the [4Fe–4S] center could be assembled with a serinate coordination (*171*). The redox potential decreased by 60–70 mV, and the ground state was found to be $S = \frac{1}{2}$ and $S = \frac{3}{2}$ in the C148S and C151S reduced mutants, respectively. The individual EPR characteristics of this center could not be determined owing to the spin–spin interactions with the neighboring $[2Fe–2S]^{1+}$ and $[3Fe–4S]^{0}$ centers. The same problem was encountered in *E. coli* nitrate reductase, in which the serinate coordination of a low potential [4Fe–4S] center could not be assessed by EPR in the C184S mutant. Although the spectroscopic and redox properties of this variant were found to be similar to those of the wild-type protein, a significant decrease in the enzymatic activity was observed (*172*). The coordination of a [4Fe–4S] cluster by oxygen was clearly established, however, by NMR in the case of the C77S variant of *Chromatium vinosum* HIPIP (*177*, *178*). This mutation was found to induce a slight decrease of 25 mV in the redox potential and a partial reorganization of the iron valences in the oxidized $[4Fe–4S]^{3+}$ cluster, since the iron ion bound to residue 77 changed from the mixed-valence state in the wild-type protein to the ferric state in the mutant. Unfortunately, no EPR experiments were performed on this mutated protein.

Actually, one of the most fruitful SDM approaches consists in interconverting [3Fe–4S] and [4Fe–4S] centers by modifying the residue

TABLE I

INTERCONVERSIONS BETWEEN [3Fe–4S] AND [4Fe–4S] CLUSTERS INDUCED BY SITE-DIRECTED MUTAGENESIS

Enzyme	Mutation	3Fe → 4Fe Conversion	ΔE (mV)[a]	Refs.
E. coli fumarate reductase	FrdB: V207C	+	−420	*181*
D. africanus FdIII	D14C	+	~−300	*161*
D. fructosovorans Ni–Fe hydrogenase	P238C	+	−315	*182*
E. coli nitrate reductase A	NarH: W220C	−		*172*
		4Fe → 3Fe Conversion		
E. coli DMSO reductase	DmsB: C102(W,S,T,F)	+	+270 to +310	*179, 183*
Synechococcus elongatus photosystem I	Unbound PsaC: C14(D,A,S)	+	+400 to +500	*185*
	C51(D,A,S)	+	+400 to +500	*186*
	C21D	+	nd	*186*
	C58D	+	nd	*186*
Synechocystis 6803 photosystem I	PsaB: C565S	+	nd	*175*
	C556S	+	nd	*176*
C. thermoaceticum corrinoid iron–sulfur protein	AcsC: C20A	+	+490	*184*
E. coli nitrate reductase A	NarH: C247D	+	+500	[b]
	C187D	−		[b]
	C19(A,S)	−		*173*

[a] Difference between the midpoint potential of the cluster generated by the mutation and that of the native cluster.

[b] E. Valay, B. Guigliarelli, M. Asso, P. Bertrand, F. Blasco, unpublished results, 1998.

located at the position of the second Cys in the consensus motif, when this motif is present. This transformation, which preserves the structural role of the cluster, can be easily detected since the two kinds of centers are EPR-active in different redox forms and display very different spectra. Besides, it gives rise to a large change in the redox potential of several hundred millivolts (Table I), which makes it possible to study the functional role of the modified center (*179*, *180*).

The conversion of a [3Fe–4S] into a [4Fe–4S] center was achieved by restoring the second residue of the consensus motif in *E. coli* fumarate reductase (*181*) and in *D. africanus* ferredoxin III (*161*). However, the coordination scheme of the iron–sulfur centers of *A. vinelan-*

dii ferredoxin I suggests that restoring the second Cys of the consensus motif does not always suffice to ensure the coordination of a [4Fe–4S] center, as occurred in the case of the W220C mutant of *E. coli* nitrate reductase (*164*). A [3Fe–4S] into [4Fe–4S] conversion has been assessed by a combined EPR and X-ray crystal study on a variant of the Ni–Fe hydrogenase from *Desulfovibrio fructosovorans* in which the Pro238 oriented toward the [3Fe–4S] center was replaced by Cys (*182*).

In some proteins, the opposite [4Fe–4S] into [3Fe–4S] conversion was achieved by replacing the second Cys of a ferredoxin-type motif by other residues able (Ser, Asp, Tyr) or not (Ala, Trp, Phe) to coordinate an iron atom. In the case of *E. coli* DMSO reductase, the conversion was complete whatever residue was substituted (*183*) (Table I). The same conversion has been observed upon substituting Ala for the second Cys of the Cys motif liable to bind the [4Fe–4S] center of the *Clostridium thermoaceticum* corrinoid iron–sulfur protein (*184*). By contrast, in the case of the PsaC polypeptide accommodating the [4Fe–4S] centers F_A and F_B, a conversion was observed only after PsaC had been removed from PSI, and only with some substitutive residues (*185*, *186*). Replacing Cys14 and Cys51 by Asp therefore led to conversion of F_B and F_A, respectively, into [3Fe–4S] centers, whereas replacing them by Ala or Ser led to a mixture of [3Fe–4S] centers and [4Fe–4S] centers having an $S = \frac{3}{2}$ ground state in the reduced form (*186*). The redox potentials of the [3Fe–4S] centers were found to be positively shifted by up to 500 mV in comparison with the native [4Fe–4S] centers, while the redox and spectroscopic characteristics of the unmodified center remained practically unchanged. The formation of [3Fe–4S] centers was also observed when the fourth Cys of the motifs (Cys21 and Cys58) were replaced by Asp (Table I). The double mutation C14D/C51D failed to produce a pair of [3Fe–4S] centers, and a mixture of [3Fe–4S] and [4Fe–4S] centers having an $S = \frac{1}{2}$ ground state was observed instead (*186*). When the mutated PsaC polypeptides were inserted into the PSI complex, the modified centers were found to be converted back into [4Fe–4S] centers displaying $S = \frac{1}{2}$ signals (*180*, *187–189*). In those mutants in which Cys14 had been modified, center F_B^- exhibited an EPR spectrum with g values of 1.852, 1.899, 2.115 that did not depend on the substituted residue, and this was observed even with noncoordinating amino acids. This spectrum was ascribed to centers in which the fourth coordination was brought about by exogeneous thiolates present in the medium used to reconstitute the iron–sulfur centers (*180*). This finding shows that the results of SDM studies in which the reconstitution of iron–

sulfur centers has been carried out *in vitro* should be handled with caution.

Although the second Cys of the three groups of cysteine residues expected to coordinate the [4Fe–4S] centers of *E. coli* nitrate reductase were systematically mutated to induce their conversion into [3Fe–4S] centers, this conversion was achieved only in the case of the C247D mutation affecting the lowest potential [4Fe–4S] center (E. Valay, B. Guigliarelli, M. Asso, P. Bertrand, and F. Blasco, unpublished results, 1998). This result, which confirms the proposed coordination scheme (*174*), shows once again that the coordination capacity of the various Cys motifs of a protein can be differently affected by amino acid substitutions.

The large body of data already provided by SDM experiments shows that the stability, structure, and magnetic properties of the centers generated by substituting the Cys residues coordinating [4Fe–4S] and [3Fe–4S] are hardly predictable. The only ligand substitution that has been achieved so far is the sulfur-to-oxygen one. This substitution does not necessarily show up in the EPR spectrum, since it can give $S = \frac{1}{2}$ as well as $S = \frac{3}{2}$ spin states in the $[4Fe–4S]^{1+}$ form. Spin quantitation and complementary spectroscopic studies are therefore often needed to confirm the existence of a substitution and to rule out the occurrence of artifacts resulting from the reorganization of the protein or the binding of adventitious ligands.

B. Determining the Relative Arrangement of Centers Coupled by Spin–Spin Interactions

1. Background

Prosthetic groups separated by about 10 to 20 Å commonly occur in biological electron transfer systems and in a great variety of redox enzymes. At these distances, significant dipolar and exchange intercenter interactions can take place when the redox state of the system is such that two neighboring centers are simultaneously paramagnetic. These spin–spin interactions give rise to a splitting δB of the resonance lines of a given center if the spin–lattice relaxation time T_1 of the other center is larger than $\hbar/g\beta\delta B$ (*190*). When this condition is met, the effects of the spin–spin interactions show up in the spectrum in the form of either a broadening or a resolved splitting, depending upon the linewidth. Owing to the anisotropy of the interactions, a complex spectrum is then observed, the shape of which is determined by these interactions and by the microwave frequency value.

TABLE II

IRON–SULFUR PROTEINS SHOWING STATIC EFFECTS OF SPIN–SPIN INTERACTIONS ON THE EPR SPECTRUM

Interacting centers	Proteins	Quantitative study	Refs.
$[2Fe–2S]^{1+}$, Mo(V)	Milk xanthine oxidase	*	*192*
	D. gigas aldehyde oxidoreductase		*202*
$2 \times [2Fe–2S]^{1+}$	*D. gigas* aldehyde oxidoreductase		*202*
	P. diminuta isoquinoline 1-oxidoreductase		*308*
$[4Fe–4S]^{1+}$, $FMN^{\bullet}$	*M. methylotrophus* trimethylamine dehydrogenase	*	*210*
$[4Fe–4S]^{1+}$, Ni center	*D. gigas* Ni–Fe hydrogenase	*	*112*
$[4Fe–4S]^{1+}$, $TPP^{\bullet}$	*H. halobium* pyruvate : ferredoxin oxidoreductase		*300*
$[4Fe–4S]^{1+}$, $UQ^{\bullet}$	Bovine heart complex I		*301*
$[4Fe–4S]^{1+}$, $[3Fe–4S]^{0}$	*E. coli* fumarate reductase		*302*
	7Fe ferredoxins		*93*, *102*
$2 \times [4Fe–4S]^{1+}$	Clostridial ferredoxins	*	*135*
	D. africanus pyruvate : ferredoxin oxidoreductase	*	*135*
	Photosystem I	*	*119*
$2 \times [4Fe–4S]^{1+}$	*C. vinosum* HiPIP	*	*108*

The first evidence for intercenter spin–spin interactions in biological systems came from the xanthine oxidase enzyme, in which a distinct splitting of the Mo(V) center spectrum and a broadening of a [2Fe–2S] center spectrum were observed when both centers were paramagnetic (*191*). Since then, interaction spectra involving iron–sulfur centers have been observed in many systems (Table II). Since the shape of these spectra depends on the relative arrangement of the interacting centers, the quantitative interpretation of intercenter spin–spin interactions based on the numerical simulation of spectra recorded at several microwave frequencies provides a useful method of obtaining structural information. This method has been generally used in the framework of a simplified description of the magnetic dipolar interactions, where each interacting center is represented by one magnetic moment. Although this so-called point dipole approximation is reasonably valid in the case of mononuclear centers in which the spin density is mainly localized on the metal ions, it may be more questionable in the case of organic radicals in which the spin density is often widely delocalized over the paramagnetic center (*89*, *192*). The situation is conceptually different when the system contains polynuclear metal clusters, because in that case the magnetic mo-

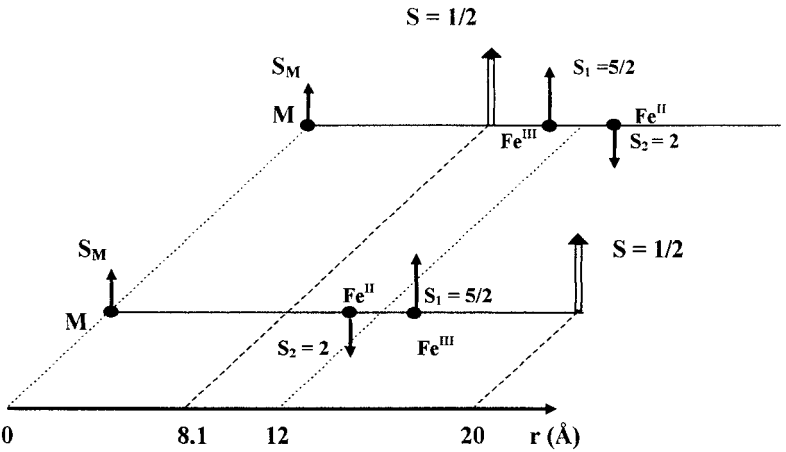

FIG. 11. Scheme of the two possible colinear arrangements in the case of a $[2Fe–2S]^{1+}$ center interacting magnetically with a mononuclear center M. The iron-to-iron distance was taken equal to 2.7 Å and the center-to-center distance was assumed to be equal to 12 Å. The open arrows indicate the location of the equivalent magnetic moment that can be used to describe the dipolar interactions between M and both the ferric and ferrous sites of the $[2Fe–2S]^{1+}$ center.

ments $\vec{\mu}_i$ carried by all the metal sites in the system can interact magnetically. Within a cluster, the local spins $\vec{S}_i$ are strongly coupled by the internal antiferromagnetic and double exchange interactions, so that the magnetic moments can be written $\vec{\mu}_i = -\beta K_i \tilde{g}_i \cdot \vec{S}_i$, where $\vec{S}$ is the total spin of the cluster and the K_i terms are the usual spin projection coefficients. Because of the antiferromagnetic coupling, some of these coefficients have opposite signs (Fig. 8). It follows that, as far as the intercenter dipolar interactions are concerned, the set of magnetic moments carried by a cluster cannot be replaced by a single moment located *within* the cluster. In order to illustrate this important point, consider a system comprising a $[2Fe–2S]^{1+}$ cluster and a mononuclear center M in a colinear arrangement (Fig. 11). To further simplify the problem, the g tensors of the three metal sites are assumed to be equal. In this particular situation, the sum of the dipolar terms describing the interactions between M and the two iron sites in the cluster can be put in the form of a single dipolar term corresponding to the interactions between M and an equivalent magnetic moment $\vec{\mu}_S = -\beta \tilde{g} \cdot \vec{S}$ located at the distance r_{eff} given by

$$r_{eff}^{-3} = \tfrac{7}{3} r_{M1}^{-3} - \tfrac{4}{3} r_{M2}^{-3}, \tag{10}$$

where r_{M1} and r_{M2} are the distances between M and the ferric and ferrous site, respectively (*192*). The *effective distance* given by Eq. (10) is generally very different from the center-to-center distance r (*192*). For example, for $r = 12$ Å, $|r_{eff}|$ is equal to 8.1 and 20 Å when M is on the side of the ferric and ferrous site, respectively (Fig. 11). In the latter case, r_{eff} is negative. Although the sign of r_{eff} is meaningless in the case of purely dipolar interactions, it is important when the exchange and dipolar contributions of the spin–spin interactions are both considered. According to Eq. (10), the effective distance becomes infinite when the intercenter distance r is equal to 14.5 Å. In the case of this particular arrangement, the two dipolar terms cancel out exactly, giving rise to a "magic configuration."

This example shows that dipolar interactions can produce unexpected effects in systems containing polynuclear clusters, so that their complete quantitative description requires a model in which the dipolar interactions between all the paramagnetic sites of the system are explicitly taken into account. *Local spin* models of this kind can provide a description of the relative arrangement of the interacting centers at atomic resolution and have been worked out for systems containing $[2Fe–2S]^{1+}$ and $[4Fe–4S]^{1+}$ clusters (*112*, *192*). In the latter case, an additional complication arises due to the delocalized character of the [Fe(III), Fe(II)] mixed-valence pair, so that the magnetic moments carried by the two sites A and B of Fig. 8B must be written

$$\vec{\mu}_A = -\beta(c_a^2 K_4 \tilde{g}_4^A + c_b^2 K_3 \tilde{g}_3^A) \cdot \vec{S}$$

$$\vec{\mu}_B = -\beta(c_a^2 K_3 \tilde{g}_3^B + c_b^2 K_4 \tilde{g}_4^B) \cdot \vec{S},$$

where $\tilde{g}_3^A, \tilde{g}_3^B$ and $\tilde{g}_4^A, \tilde{g}_4^B$ are the ferric and ferrous g tensors defined in Eq. (9). Systematic comparisons between the EPR spectra calculated using the point dipole and local spin models have shown that the point dipole model is often able to approximately simulate the spectral shape given by the local spin treatment, provided an *effective* distance is used (*112*, *192*). This is an important advantage from the methodological point of view, because it means that some of the numerous parameters involved in the numerical simulation of interaction spectra can be evaluated by performing preliminary simulations based on the simpler point dipole model.

Up to now, we have dealt only with the *static* effects of the spin–spin interactions. These effects are no longer observed when the splitting δB of the resonance lines due to these interactions is much smaller than the spectral linewidth or when the spin–lattice relax-

ation time is much shorter than $\hbar/g\beta\delta B$. In the latter case, however, a *dynamic* effect arising from both the dipolar and exchange contributions gives rise to a shortening of the relaxation times T_1 and T_2 of the interacting species (*190*, *193*). Since iron–sulfur centers are generally characterized by short relaxation times, these dynamic effects often give rise to the shortening of the relaxation times of nearby slowly relaxing species. In principle, the quantitative study of these effects should yield the same structural information as that given by the static effects. However, the anisotropy of the g tensors and that of the dipolar interactions give rise to powder distributions of T_1 and T_2 values that can spread over several orders of magnitude. In the case of frozen solution spectra, quantitative studies on these distributions are very difficult or even impossible, so that only an estimate of the intercenter distance can be obtained (*193*, *194*). The contribution to the anisotropy for which the g tensor is responsible can be partly eliminated by measuring the relaxation rates at the extreme turning points of the spectrum, which often involves recording the spectrum at high frequencies in the case of radicals (*195*). Examples of studies carried out on systems containing iron–sulfur centers can be found in Refs. (*194*, *196*).

2. Application to Specific Systems

a. $[2Fe–2S]^{1+}$ *Centers Interacting with a Mononuclear Center or a Radical* Since 1972, the interaction EPR spectra given by different forms of xanthine oxidase have attracted the attention of several groups (*191*, *197–199*). This enzyme contains one molybdenum center, one FAD, and two [2Fe–2S] clusters. As mentioned in Section II,B, center 1 gives an EPR spectrum of the $g_{av} \approx 1.96$ type, while the spectrum of center 2 is characterized by several anomalous properties. In the so-called desulfo-inhibited form, the effects of the spin–spin interactions between center 1 and the Mo(V) center can be clearly observed in both spectra, and these effects disappear when the center 1 signal broadens because of the shortening of its spin–lattice relaxation time (*200*). Using the point dipole model and assuming that the magnetic axes are colinear, an exchange parameter $J = 1.1 \times 10^{-3}$ cm^{-1} and an intercenter distance equal to 15 Å were deduced from a numerical simulation of the X-band and Q-band spectra obtained with the desulfo-inhibited form (*199*). In a more recent study, the effective nature of the distance yielded by the point dipole approximation was recognized, and numerical simulations of spectra recorded at S-band, X-band, and Q-band based on the local spin model were carried out to obtain a detailed description of the relative ar-

rangement of the centers, including the intercenter distance, which was found to be equal to 19 Å (*192*). No other structural information is currently available for xanthine oxidase, but the X-ray crystal structure of the related enzyme aldehyde oxido-reductase (AOR) from *D. gigas* has been solved at 2.25-Å resolution (*201*). This structure displays a quasi-linear arrangement of the metal centers, giving distances between the Mo atom and the centers of the two [2Fe–2S] clusters equal to 16 and 26 Å (*201*). Preliminary EPR experiments have suggested that the [2Fe–2S] cluster interacting with the Mo(V) center in AOR is not center 1, but center 2 (J. Caldeira, M. Asso, B. Guigliarelli, C. More, I. Moura, J. Moura, and P. Bertrand, unpublished results, 1998). Besides, the static effects of the spin–spin interactions between center 1 and center 2 are clearly visible in the EPR spectrum displayed by AOR (*202*), whereas only a weak dynamic effect is observed in the case of xanthine oxidase (*198*). All these findings suggest that the pattern of spin–spin interactions differs between the two enzymes, despite the great similarity between the amino acid sequences of the segments associated with the iron–sulfur centers and the molybdopterin (*203*). A more detailed comparison must await the quantitative study of the full pattern of spin–spin interactions in AOR, based on the local spin model and the crystal structure.

Although the spin–spin interactions between center 1 and the molybdenum center of xanthine oxidase are dominated by the exchange contribution, the effects of the dipolar interactions can be clearly observed in the Mo(V) EPR spectrum despite the large intercenter distance of 19 Å. This is due to the very narrow lines given by this center, as well as to its location on the side of the Fe(III) site, which gives rise to a shorter effective distance equal to 16 Å (*192*). Actually, if it had been located on the side of the Fe(II), the effective distance would have been much larger or a magic configuration might even have occured, leading to the disappearance of the dipolar effects. One may wonder whether a situation of this kind has ever been observed previously in a protein. This is apparently so in the case of the phthalate dioxygenase reductase (PDR) enzyme of *Pseudomonas cepacia*, in which a [2Fe–2S] cluster and an FMN group are separated by a center-to-center distance of about 12 Å according to the X-ray crystal structure (*204*), and where no effects of the spin–spin interactions are observed in the EPR spectrum when both centers are paramagnetic (*205*). In a study of this system based on the local spin model, it has been established that the vanishing of the dipolar effects in PDR is due both to the peculiar arrangement of the two prosthetic

groups in the protein and to the location of the reducible site of the $[2Fe–2S]^{1+}$ cluster on the side of the FMN group (*206*). The fact that no effects of the exchange interactions were observed either is probably due to the presence of an unfavorable superexchange pathway (*135*).

b. $[4Fe–4S]^{1+}$ *Centers Interacting with a Mononuclear Center or a Radical* Although spin–spin interactions between the Ni center and the iron–sulfur centers of Ni–Fe hydrogenases have been observed for a long time in the active Ni–C form of the enzyme (*207*), they have been studied quantitatively only since the mid-1990s. In the first step, the point dipole model was used to demonstrate that the so-called split Ni–C spectrum recorded at S-band, X-band, and Q-band could be simulated by assuming that the Ni center interacts magnetically with a single $[4Fe–4S]^{1+}$ cluster (*194*). The effective distance deduced from this study was found to be equal to 8.6 Å, which is a much smaller value than the center-to-center distance of 12 Å obtained in an X-ray crystal study carried out at 2.85-Å resolution on the inactive form of the enzyme (*164*). In the second step, the spectral simulations were improved by using a local spin description of the dipolar interactions, providing a detailed picture of the relative arrangement of the two centers (*112*). This arrangement was found to be very similar to that given by the crystal structure, with the intercenter axis close to a diagonal of the cubane structure and the center-to-center distance equal to 11.7 Å (*112*). It was therefore established in this study that activating the enzyme does not appreciably modify the respective positions of the two centers in the protein. The results showed in addition that the iron site closest to the Ni center belongs to the mixed-valence pair of the $[4Fe–4S]^{1+}$ cluster. This information may be necessary to be able to define the electron transfer pathway connecting the two centers (*112*). Another finding made in this study concerns the orientation of the magnetic axes of the $[4Fe–4S]^{1+}$ center with respect to the cubane structure: As observed in the case of model compounds, one of the magnetic axes was found to be practically oriented along the common perpendicular to the directions defined by the mixed-valence and ferrous pairs (see Section II,D). However, this axis was associated, not with the largest g value, but with the intermediate one. Still another assignment has been proposed for the $[4Fe–4S]^{1+}$ center of the enzyme enoate reductase (*208*).

Like PDR, trimethylamine dehydrogenase (TMADH) from *Methylophilus methylotrophus* W_3A_1 provides an example of a system in which an iron–sulfur center, in this case a $[4Fe–4S]^{1+}$ cluster, interacts

magnetically with an $FMN^{\cdot}$ radical. Indeed, the relative arrangements of the interacting centers displayed by the crystal structures of these two enzymes is very similar: in both cases the center-to-center distance is about 12 Å and the most favorable superexchange pathway between the two centers seems to involve the 8-methyl group of the FMN, which is separated by a 4-Å gap (4.7 Å in PDR) from the sulfur atom ligating the closest iron atom in the cluster (*204*, *209*). Despite these striking structural similarities, the effects of the spin–spin interactions on the X-band EPR spectrum differ dramatically between the two systems: as mentioned earlier, no effect at all is detected in the case of PDR, while a signal characteristic of a triplet state is observed in the case of TMADH (*210*). Since the absence of any dipolar effects in PDR is due to a magic configuration, one may wonder whether the strong effects observed in the case of TMADH may arise from an enhancement of the dipolar interactions due to the particular location of the mixed-valence pair in the $[4Fe–4S]^{1+}$ cluster. Numerous spectra have been calculated using the local spin model and the relative arrangement of the two centers observed in the crystal structure, but no acceptable simulation of the triplet state spectrum could be obtained by taking values smaller than 10^{-2} cm^{-1} for the exchange parameter, which are those usually found with these intercenter distances (*211*). It can be therefore concluded that the magnitude of the exchange interactions is unusually large in TMADH. A recent high-field EPR study carried out on this enzyme yielded the value $J = -0.36$ cm^{-1} (*212*).

c. Two Interacting [4Fe–4S]$^{1+}$ Centers Systems consisting of two $[4Fe–4S]^{1+}$ clusters coupled by spin–spin interactions are commonly found in ferredoxins as well as in metalloenzymes and membrane-bound complexes (Table II). These systems exhibit a variety of interaction EPR spectra, some of which have been simulated using the point dipole model (*135*). In the case of *Clostridium pasteurianum* ferredoxin and PsaC from *Synechocystis*, the distances deduced from these simulations were found to be 7.9 and 9.8 Å, respectively (*135*). These values are distinctly smaller than the center-to-center distance of 12 Å obtained in the X-ray crystal studies (*213*, *214*), which once again illustrates their effective nature. In the case of PsaC, the relative orientation of the magnetic axes of centers F_A^- and F_B^- determined by simulating the interaction spectrum was found to be consistent with that deduced independently from oriented multilayer experiments (*119*). This result, together with comparisons between the sets of parameters deduced from numerical simulations based on the point

dipole and local spin models, indicates that the angular parameters given by the former model constitute a useful first approximation. However, a local spin description of the dipolar interactions is now needed in order to be able to assign a valence to the various metal ions of the clusters and to determine the orientation of the magnetic axes with respect to the cubane structure.

Lastly, proteins containing a single paramagnetic species per subunit or per molecule can give interaction EPR spectra. This phenomenon was first observed in the case of *C. vinosum* HIPIP, which was found to dimerize and give an interaction spectrum upon freezing in the presence of high NaCl concentrations (*108*). On the basis of the point dipole model, the interaction EPR spectrum was interpreted as arising from two different dimeric structures with a relative arrangement of the $[4Fe–4S]^{3+}$ centers such that the intercenter axis is parallel to the z magnetic axis and the intercenter distances are equal to 13 and 16 Å, respectively (*108*). A computer-generated model accounting for this arrangement has also been described (*215*). Owing to the effective nature of the distances deduced from numerical simulations based on the point dipole approximation, this arrangement and the results of the molecular modeling study should be treated with caution. A similar polymerization phenomenon has been observed, based on the emergence of an interaction spectrum at high protein concentrations, in the case of benzene dioxygenase ferredoxin (*216*), which contains a single [2Fe–2S] cluster per molecule (R. Cammack, P. Unalkat, B. Guigliarelli, and P. Bertrand, unpublished results, 1997). Finally, the dimeric ferredoxin II from *D. vulgaris* Miyazaki, which contains a single [4Fe–4S] cluster per subunit, was found to exhibit an interaction spectrum in the fully reduced state (*159*).

d. Concluding Remarks The exchange parameter $|J|$ has been found to be roughly equal to or smaller than 5×10^{-3} cm^{-1} in all the systems containing iron–sulfur clusters where intercenter magnetic interactions have been studied, except in the case of TMADH (*135*). This raises the question as to whether this limit is imposed either by some particular physical reason or by the method that consists in simulating spectra recorded with microwave frequencies ranging from some gigahertz to some tens of gigahertz. Recall that when two centers A and B are coupled by an exchange interaction described by the Hamiltonian $-2J\tilde{S}_A \cdot \tilde{S}_B$, a line splitting is observed in the EPR spectrum only when $|2J|$ is smaller than $\Delta g\ \beta B$, where $\Delta g = |g_{\text{effA}} - g_{\text{effB}}|$ is the difference between the effective g values for a given orientation of the magnetic field. When $|2J|$ is comparable to or larger than Δg

βB, the two central lines of the splitting pattern collapse at the mean position defined by $(g_{effA} + g_{effB})/2$, while the outer lines vanish because of the decrease in their amplitude. In particular, the exchange interaction has no effects on the EPR spectrum when the two centers have identical or very similar g tensors. Since the g tensors of iron–sulfur centers are anisotropic, the value of $\Delta g\ \beta B$ depends strongly on the orientation of the magnetic field with respect to the magnetic axes of the two centers. The line splitting will therefore be visible in those parts of the powder spectrum where the condition $\Delta g\ \beta B \gg |2J|$ is satisfied, whereas the lines will collapse in those parts where $\Delta g\ \beta B \leq |2J|$ (*135*). When $|2J|$ is larger than the maximum value of $\Delta g\ \beta B$, no line splittings will be observed in the spectrum and the spin–spin interaction will escape detection. This phenomenon can be illustrated by the example of a system comprising two identical centers with g values equal to 2.07, 1.96, 1.89, and rotated magnetic axes. In the absence of any spin–spin interactions, this system will exhibit the spectrum given in Fig. 12a. When the two centers are coupled by a strong exchange interaction giving $|J| = 25 \times 10^{-3}$ cm^{-1}, the interaction spectrum calculated at X-band (9 GHz) has an axial shape, and no effects attributable to the spin–spin interactions are apparent

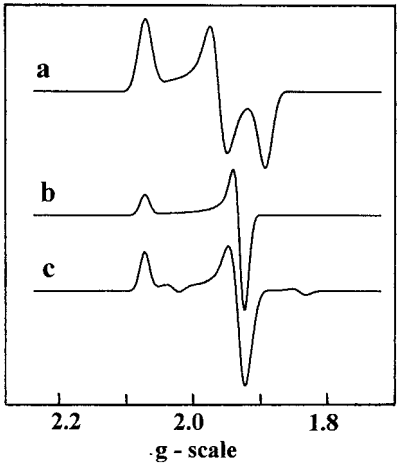

FIG. 12. Effect of a strong exchange interaction on the shape of the EPR spectrum displayed by a pair of centers A and B having identical g values, $g_x = 1.89$, $g_y = 1.96$, $g_z = 2.07$, and rotated magnetic axes according to $x_A//y_B$, $y_A//x_B$, $z_A//z_B$. (a) 9 GHz spectrum calculated with $J = 0$; (b) and (c) spectra calculated with $J = 25 \times 10^{-3}$ cm^{-1} at 9 and 35 GHz, respectively. The spectra were calculated as described in Ref. (*192*) without including any dipolar terms, with the linewidths $\sigma_x = \sigma_y = \sigma_z = 0.01$.

(Fig. 12b). Since practically the same spectral shape is obtained at Q-band (35 GHz) (Fig. 12c), the commonly used criterion stating that the shape of an interaction spectrum is frequency-dependent fails to apply in this case. Actually, outer lines arising from the exchange interaction are visible on the spectrum calculated at Q-band (Fig. 12c), but these lines would be hardly detectable in an experimental spectrum, because of their weak intensity and to the small signal-to-noise ratio inherent in Q-band experiments. In these circumstances, spectra recorded at higher frequency would be needed to allow detection and study of the spin–spin interactions.

C. EPR Studies on Oriented Iron–Sulfur Systems

The EPR spectrum displayed by a frozen solution of molecules containing $S = \frac{1}{2}$ paramagnetic species can yield the g values, but it tells us nothing about the directions of the magnetic axes. In order to determine these directions, it is necessary to study spectra obtained with samples in which the molecules are partly or completely oriented. In the case of biological systems, one of the methods most commonly used for this purpose consists in preparing samples having a one-dimensional order. When the magnetic susceptibility is sufficiently anisotropic (*217*), this can be achieved by freezing a protein solution placed in a strong magnetic field (*218*, *219*). In the case of membrane-bound systems, oriented multilayers can be prepared by partially dehydrating membrane vesicles spread on a Mylar sheet, and the redox state of the system can be controlled by briefly incubating the Mylar sheet with a reducing or oxidizing solution. In samples of this kind, the one-dimensional order is not perfect, however, since the direction of the normal to the membrane is necessarily spread about a mean direction. This so-called *mosaic spread* can be modeled by a Gaussian distribution characterized by a half-width ranging between 20° and 30° in the case of biological samples (*220*, *221*). The EPR spectrum displayed by these samples therefore looks like a powder spectrum, but the amplitude of the peaks g_x, g_y, and g_z depends strongly on the angle ω between the normal to the Mylar sheet and the direction of the applied magnetic field. Since the amplitude of a given peak reaches the maximum value when the mean direction of the corresponding magnetic axis is parallel to the magnetic field, the orientation of the magnetic axes relative to the normal to the membrane plane can be determined by studying the variations in this amplitude as a function of ω.

This method has been widely used to determine the orientation of

paramagnetic centers in membrane-bound complexes of respiratory and photosynthetic systems. In the case of heme groups, the g_z magnetic axis was known at an early stage to be nearly perpendicular to the heme plane, so that the results could be interpreted directly in structural terms (*221–225*). The situation was different in the case of iron–sulfur centers, in which no simple relations between the magnetic axes and the molecular structure were known, at least in the case of [3Fe–4S] and [4Fe–4S] centers. At first, the results of these studies were therefore interpreted in qualitative terms and were either taken to show that iron–sulfur centers were not randomly oriented in membrane-bound oxidoreductases such as nitrate reductase (*226*) and fumarate reductase from *E. coli* (*227*), or used to make comparisons between the orientations of some centers in various systems, such as the [4Fe–4S] centers F_X, F_A, F_B in photosystem I from higher plants (*218*, *219*, *228*), algae (*229*), and cyanobacteria (*119*) and in the reaction center of green sulfur bacteria (*230*).

According to the ligand field model, the g_z magnetic axis ($g_x < g_y < g_z$) of ferredoxin-type [2Fe–2S] centers is oriented in the iron-to-iron direction (see Section II,B). Based on this attribution, the iron-to-iron direction of center S_1 of succinate dehydrogenase was proposed to be parallel to the membrane plane (*231*). Likewise, the g_y and g_x magnetic axes of the Rieske center of the mitochondrial bc_1 complex were found to be parallel and perpendicular to the membrane plane, respectively, but the above-mentioned attribution of the g_z axis, which does not apply to Rieske-type centers (see Section II,B), was mistakenly used to deduce the iron-to-iron direction (*222*). In the case of the Rieske center of the b_6f complex, the g_y axis was initially found to be perpendicular to the membrane plane, which was interpreted as indicating that the orientation of the [2Fe–2S] center was different in this complex (*228*). This unexpected result was later found to be an artifact due to saturation effects, and a more detailed study showed that the orientation of the magnetic axes of the Rieske center is in fact the same in both complexes (*232*). Assuming that the g_x magnetic axis corresponds to the iron-to-iron direction, this orientation was used to position a structurally defined fragment of the Rieske protein (*51*) in the bc_1 complex (*233*). More recently, the fact that the orientation of the magnetic axes of the Rieske center of the bc_1 complex reduced at cryogenic temperatures by the products of radiolysis was found to differ strongly from that observed in a sample chemically reduced at room temperature provided evidence in favor of a redox-linked conformational change. Upon comparing these two sets of axes with the two positions of the Rieske protein observed in an X-ray

study on this complex (*234*), it has emerged that the g_x axis is actually oriented in the iron-to-iron direction (see the chapter by W. Nitschke and co-workers).

Structural information about the organization of the [4Fe–4S] centers F_A and F_B in *Synechocystis* PCC 6803 PSI was obtained via a combination of EPR studies on oriented multilayers and on a solution of particles prepared in a redox state giving an EPR spectrum displaying intercenter spin–spin interactions (*119*). The numerical simulation of interaction spectra recorded at different microwave frequencies yielded the values of the Euler angles defining the relative orientation of the magnetic axes of F_A^- and F_B^- as well as the direction of the intercenter vector in the frame of the F_A^- magnetic axes. In addition, the orientation of the magnetic axes of F_A^- and F_B^- relative to the normal to the membrane plane was deduced independently from the study of oriented multilayers. By combining these data, it was established that the angle between the intercenter vector and the normal to the membrane plane is equal to about 30°, a small value that is consistent with a sequential electron transfer mechanism between the iron–sulfur centers in PSI (*119*).

A priori, the best method of determining the orientation of the magnetic axes of a paramagnetic center undoubtely consists in studying the EPR spectrum displayed by a monocrystal. Experiments of this kind were carried out by Brettel *et al.* (*235*) on a monocrystal of PSI from *Synechococcus elongatus* that had been photoreduced at low temperature. By analyzing the position of the six resonance lines displayed by the center F_A^- of the six PSI complexes present in the unit cell, it was possible to accurately determine the g values and the magnetic axes of these centers relative to the crystallographic axes. The results of this study are in excellent agreement with those deduced from oriented multilayer experiments, taking the $\vec{c}$ crystal axis to be perpendicular to the membrane plane. Extending this study to center F_B^- was difficult because of the need to monitor the positions of 12 resonance lines as a function of the crystal orientation (*236*). Moreover, a nontrivial problem arose as to how to form pairwise associations between the tensors of the centers F_A^- and F_B^- belonging to the same complex. Surprisingly enough, the solution to this problem that the authors of this study preferred corresponds to a relative orientation of the F_A^- and F_B^- g tensors that differs markedly from that deduced from the analysis of the spin–spin interactions in particles (*119*). This discrepancy is not likely to arise from structural differences between the PSI complexes of *Synechocystis* and *Synechococcus* sp., since these complexes were observed to display identical interac-

tion EPR spectra in solution (*237*). Lastly, it should be noted that the angle between the intercenter axis and the normal to the membrane plane provided by the X-ray crystal structure is equal to 54° (*213*), which is significantly larger than the value of about 30° given by the analysis of the spin–spin interactions between F_A^- and F_B^- (*119*). These various points call on the one hand for a refinement of the analysis of the spin–spin interactions based on a local spin description of the dipolar interactions, and on the other hand for a reexamination of the various ways of forming pairwise associations between the six F_A^- *g* tensors and the six F_B^- *g* tensors deduced from the EPR crystal study. It is worth noting, however, that the occurrence of a small structural change in the PSI complex in the crystal cannot be ruled out, since the *g* values and the directions of the magnetic axes of the F_B^- center determined in the crystal and in oriented multilayers differ significantly (*238*). Owing to the low resolution (4 Å) of the X-ray structure of the PSI complex, it is not yet possible to locate the iron and sulfur atoms of the clusters (*213*). Several attempts to position the clusters and their coordinating polypeptide have therefore been made based on the orientations of the magnetic axes of F_A^- (*235*) and F_B^- (239) determined in the crystal. Since several orientations of the magnetic axes relative to the $[4Fe–4S]^{1+}$ cubane structure have been observed in model compounds (*115*, *116*, *240*, *241*) as well as in proteins (*112*, *208*), the results obtained using this method will have to be confirmed using other approaches.

IV. Application of EPR to the Functional Study of Iron–Sulfur Centers

A. Electron Transfer

1. Midpoint Potentials

The redox potentials of iron–sulfur centers vary considerably, depending on the type of center (*242*) and its environment in the protein (*243*), ranging from about −700 mV in the case of some $[4Fe–4S]^{2+,1+}$ centers (*244*, *245*) to about +450 mV in the case of some $[4Fe–4S]^{3+,2+}$ centers (*246*). Iron–sulfur centers therefore act as redox centers in numerous electron transfer systems, including the respiratory and photosynthetic bioenergetic chains as well as a wide variety of redox enzymes. Among the many studies that have dealt with these systems, some have yielded structural information of the kind described in Section III. Most of them were designed, however, to measure the

midpoint potential of the centers by performing potentiometric titrations monitored by low-temperature EPR. In these studies, it was implicitly assumed that the redox equilibrium probed by EPR at cryogenic temperature does not differ significantly from that reached at room temperature. This assumption is fully justified in the case of a solution of proteins containing a single center, in which the intermolecular electron exchanges ensuring the redox equilibrium are blocked when the solution is frozen. In the case of multicenter molecules, however, intramolecular exchanges may shift the redox equilibrium during the freezing process when the parameters governing this equilibrium are temperature dependent. A situation of this kind was encountered in the case of xanthine oxidase, in which the results of potentiometric titrations monitored by EPR and UV-visible absorption spectroscopy were observed to differ significantly (*247*). It is liable to occur when the midpoint potentials of the centers are pH-dependent and the titration is performed in a buffer characterized by a strongly temperature-dependent pK_a value (*248*).

Midpoint potential values are useful quantitites for defining the role of the various centers in the system. In some instances, these values have even been used to predict the location of the centers in the electron transfer chain, assuming that the potential increases along the chain from the electron donor to the electron acceptor. In several oxidoreductases, however, the measured potential of some centers was found to be clearly outside the range defined by the donor and the acceptor, which raised an intriguing question as to their function. This was observed, for instance, in the case of the $[4Fe–4S]^{2+,1+}$ ($E_m = -320$ mV) center in *E. coli* fumarate reductase (*249*), the $[3Fe–4S]^{1+,0}$ ($E_m = -30$ mV) center in *D. gigas* hydrogenase (*207*), and the low-potential $[4Fe–4S]^{2+,1+}$ ($E_m = -200$ and -400 mV) centers in *E. coli* nitrate reductase (*124*). These findings raise the question as to whether midpoint potentials are relevant quantities for describing dynamic processes such as intramolecular electron transfers. The following points are worth considering in this connection. On the one hand, contrary to what occurs in a solution in which small molecules undergo random collisions, redox centers embedded in a redox enzyme are structurally organized in such a way that only some electron transfers are kinetically possible. On the other hand, when analyzing the redox properties of a multicenter system, it is necessary to distinguish between the microscopic potential of each center and the macroscopic potentials of the systems and to consider the possibility of intercenter redox cooperativity. The concept of cooperativity has been commonly used in the fields of protein–protein interactions, ligand

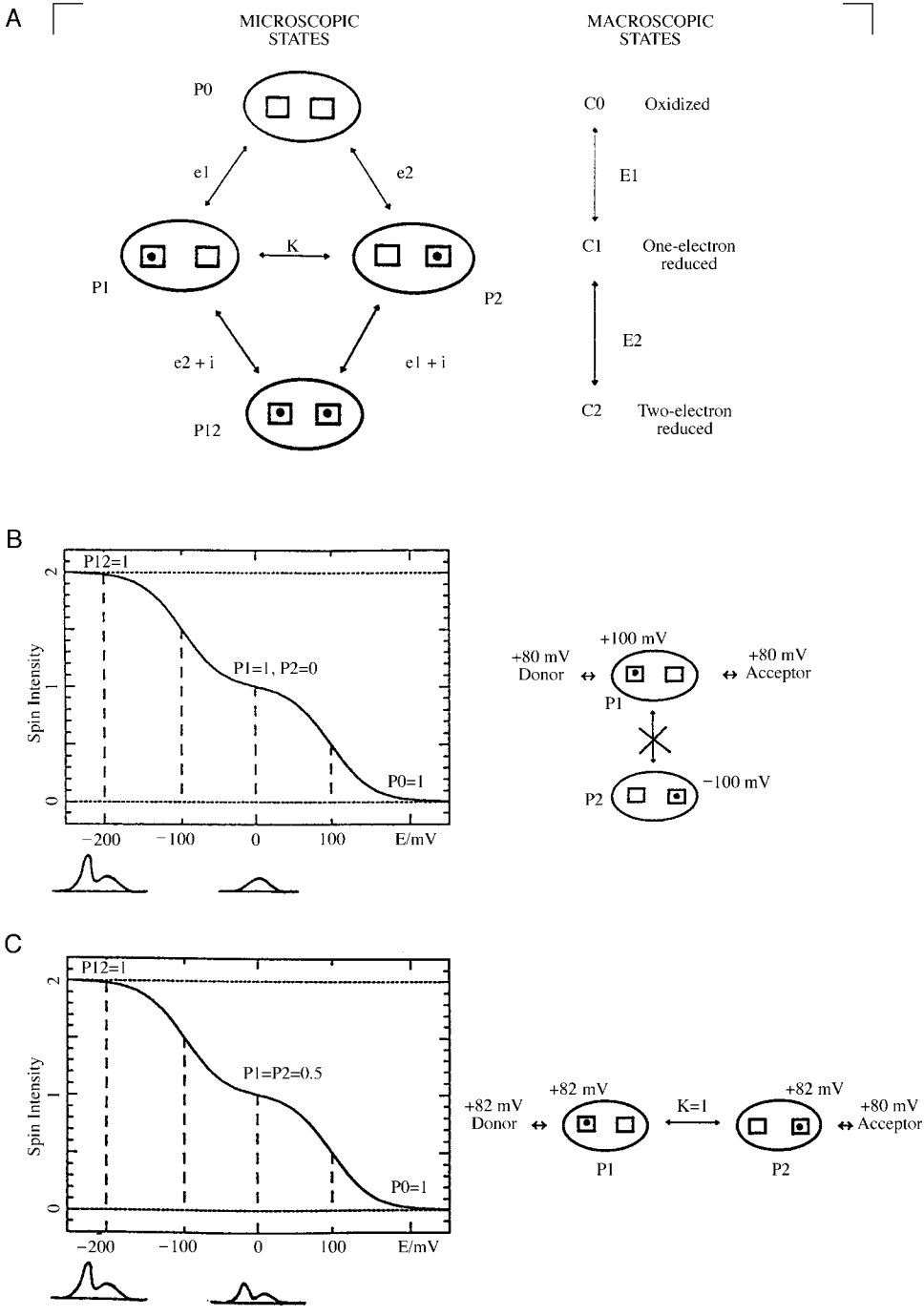
A
MICROSCOPIC STATES
MACROSCOPIC STATES
P0
e1
e2
K
P1
P2
e2 + i
e1 + i
P12
C0
Oxidized
E1
C1
One-electron reduced
E2
C2
Two-electron reduced
B
P12=1
P1=1, P2=0
P0=1
Spin Intensity
2
1
0
−200
−100
0
100
E/mV
+100 mV
+80 mV Donor
+80 mV Acceptor
P1
P2
−100 mV
C
P12=1
P1=P2=0.5
P0=1
Spin Intensity
2
1
0
−200
−100
0
100
E/mV
+82 mV
+82 mV Donor
+82 mV
K=1
+82 mV
+80 mV Acceptor
P1
P2

binding, and acid–base processes (*250*). It has seldom been applied, however, in the field of biological redox processes, except in the case of multiheme cytochromes (*251–254*) and cytochrome *c* oxidase (*255*, *256*). In order to illustrate its relevance to the functional analysis of electron transfer systems, take a hypothetical protein containing two redox centers, say two $[4Fe–4S]^{2+,1+}$ centers, that catalyzes the electron exchange between a donor and an acceptor characterized by the same potential of +80 mV. The redox behavior of this system can be described in terms of either the microscopic potentials (e_1, e_2) of the centers and the interaction potential i_{12}, or the two macroscopic potentials (E_1, E_2) characterizing the two successive one-electron redox processes at work in the protein (Fig. 13a). The macroscopic quantities can be deduced from the microscopic ones using the following expressions:

$$E_1 = e_1 + (1/\alpha)\ln[1 + \exp(\alpha(e_2 - e_1))]$$
$$E_2 = e_2 + i_{12} - (1/\alpha)\ln[1 + \exp(\alpha(e_2 - e_1))],$$

where $\alpha = F/RT$. Different sets of microscopic parameters can give the same E_1 and E_2 values. For example, the values ($E_1 = +100$ mV, $E_2 = -100$ mV) can be obtained in two limiting situations: In the first one, the two centers have very different potentials, $e_1 = +100$ mV, $e_2 = -100$ mV, and there are no redox interactions: $i_{12} = 0$ (Fig. 13b), whereas in the second one, the two centers have the same redox potential $e_1 = e_2 = +82$ mV and are coupled by a large anticooperative redox interaction i_{12} equal to -164 mV (Fig. 13c). The way the system functions differs greatly between these two situations, since in the first case, only center 1 can be expected to participate in the electron exchange between the donor and the acceptor, whereas in the second case, both centers may be involved in a sequential electron transfer (Fig. 13b,c). Although these two situations are undistinguishable when only the macroscopic potentials are determined by measuring the spin intensity of the whole EPR spectrum (or the UV-visible absorbance) as a function of the solution potential, they can be easily distinguished during a reducing redox titration in which the EPR signal of each center is monitored: in the first case, center 1 will be re-

FIG. 13. Redox behavior of a protein containing two redox centers. (a) Definition of the microscopic and macroscopic potentials; (b) and (c) two limiting situations giving $E_1 = +100$ mV, $E_2 = -100$ mV. In case (b), $e_1 = +100$ mV, $e_2 = -100$ mV, $i = 0$, whereas in case (c), $e_1 = e_2 = +82$ mV and $i = -164$ mV. The variations of the shape of the EPR spectrum as a function of the solution potential are schematically pictured.

duced first and its EPR signal will reach a maximum at about 0 mV (Fig. 13b), whereas in the second case, the two centers will be concomitantly reduced and will both contribute equally to the intensity of the whole spectrum at 0 mV (Fig. 13c).

When the amplitude of the EPR signals displayed by the various centers can be measured, by numerically simulating the spectrum for instance, it is possible to elucidate the redox behavior of every center in the protein and therefore to determine the microscopic parameters of the system. Using an approach of this kind, the $[3Fe–4S]^{1+,0}$ and $[4Fe–4S]^{2+,1+}$ high-potential centers in *E. coli* nitrate reductase were found to be coupled by an anticooperative redox interaction equal to −45 mV (*124*), and the $[4Fe–4S]^{3+,2+}$ centers present in the tetrameric HIPIP from *Thiobacillus ferrooxidans* were found to be coupled by a cooperative interaction equal to about +100 mV (*107*). No redox interactions were detected, however, in the case of clostridial 2 × [4Fe–4S] ferredoxins (*257*). Going back to the previously mentioned oxidases, the fact that anomalous potentials have been measured in the case of some iron–sulfur centers does not necessarily mean that these centers are not involved in intramolecular electron transfers. For example, assuming the existence of intercenter redox interactions of about 100 mV, it can be shown that the high-potential [3Fe–4S] center in Ni–Fe hydrogenases can play a redox role in some microscopic states of these enzymes (B. Guigliarelli, unpublished results, 1998). In a site-directed mutagenesis study on the *D. fructosovorans* enzyme, it has been established that converting this $[3Fe–4S]^{1+,0}$ center into a $[4Fe–4S]^{2+,1+}$ center caused a negative shift of about −300 mV in the redox potential without significantly affecting the enzymatic activity (*182*), which illustrates the fact that the functional role of this center cannot be assessed on the basis of its midpoint potential value alone.

2. *Kinetic Aspects*

EPR studies on electron transfer systems where neighboring centers are coupled by spin–spin interactions can yield useful data for analyzing the electron transfer kinetics. In the framework of the Condon approximation, the electron transfer rate constant predicted by electron transfer theories can be expressed as the product of an electronic factor T_{ab} by a nuclear factor that depends explicitly on temperature (*258*). On the one hand, since iron–sulfur clusters are spatially extended redox centers, the electronic factor strongly depends on how the various sites of the cluster are affected by the variation in the electronic structure between the oxidized and reduced forms. Theoret-

ical calculations have shown that when an iron–sulfur center is reduced, the excess electron is mainly accepted by the bridging and terminal sulfur ligands (*29*). The spatial distribution of the excess charge is governed, however, by the distribution of the valences of the Fe ions in the cluster, which can be determined by studying the intercenter magnetic dipolar interactions in the framework of the local spin model (see Section III,B). On the other hand, T_{ab} depends on the superexchange pathways between neighboring redox centers, which also determine the magnitude of the exchange coupling constant J when both centers are paramagnetic (*259*). Up to now, the relationships between kinetic quantities and data obtained by studying intercenter spin–spin interactions have been used only qualitatively in systems containing iron–sulfur centers (*112*, *206*, *212*).

B. Other Functions

Although the presence of iron–sulfur centers in systems the function of which is obviously not to transfer electrons has by now been clearly established, detailed information about the role of these centers is only just beginning to emerge. Since this new field in iron–sulfur research has been reviewed (*105*, *260*), we focus here on those systems on which important information has been obtained by performing EPR studies.

1. Catalytic Activity

The only reactions in which the ability of iron–sulfur centers to activate a substrate has been demonstrated so far are hydration/dehydration processes. In reactions of this kind, iron–sulfur centers act as Lewis acids, catalyzing the formation of a double bond via the reversible elimination of a water molecule. The enzyme in which this mechanism has been the most thoroughly studied in undoubtedly mammalian mitochondrial aconitase (*261*). The $[3Fe–4S]^{1+}$ center present in the inactive form of the enzyme can be converted into a $[4Fe–4S]^{2+}$ center, yielding an active form. This [4Fe–4S] center is coordinated by three cysteine residues, and one iron atom Fe_a is ligated by an oxygen atom arising from either a water molecule or the substrate. Since a significant level of activity persists when the center is in the paramagnetic $[4Fe–4S]^{1+}$ state, EPR and ENDOR spectroscopy have been extensively used to characterize the interactions of the enzyme with its substrate and its inhibitors (*261*). In aconitase, the spin state of the $[4Fe–4S]^{1+}$ center is always $S = \frac{1}{2}$, but the g values shift from (1.86, 1.93, 2.06) in the free form to (1.78, 1.85, 2.04)

in the citrate-bound form (*162*, *163*). From the data obtained on the one hand in ENDOR experiments carried out on ^{57}Fe, ^{33}S, ^{17}O, ^{1}H, and ^{2}H nuclei and on the other hand in Mössbauer studies, it was deduced that the substrate binds at the Fe_a atom of the center and that the coordination number of this atom varies between 4 and 6 during the catalytic cycle (*261*). The mechanism found to occur in the case of aconitase may apply as well to other dehydratases in which a [4Fe–4S] center is present (*105*). In *E. coli* dihydroxy-acid dehydratase, a $[4Fe–4S]^{1+}$ center exists, forming a mixture of $S = \frac{1}{2}, \frac{3}{2}, \frac{5}{2}$ spin states, with a major proportion of $S = \frac{3}{2}$ states. In this enzyme, the presence of a noncysteinyl ligand has been demonstrated by resonance Raman studies (*129*). Likewise, it has been suggested that a [4Fe–4S] center may be involved in the catalytic cycle of the 4-hydroxybutyryl-CoA dehydratase from *Clostridium aminobutyricum* (*262*) and the L-serine dehydratase from *Peptostreptococcus asaccharolyticus* (*263*). In the former case, the presence of a $[4Fe–4S]^{1+}$ center with g values equal to 1.844, 1.895, 2.037 was established by photoreducing the enzyme, whereas in the latter case a signal typical of a $[3Fe–4S]^{1+}$ center was observed, the intensity of which was found to decrease as the enzymatic activity increased. The great sensitivity of this signal to the nature of the buffer and to the presence of the substrate has been taken to indicate that the [4Fe–4S] center might be involved in the catalytic mechanism (*263*).

Lastly, it is worth mentioning the case of the dihydroxy-acid dehydratase from spinach, in which the reduced form of a [2Fe–2S] center was found to exhibit a heterogeneous EPR spectrum of the $g_{av} \approx 1.91$ type, indicating the presence of noncysteinyl ligands at the reducible site. This signal was converted into a $g_{av} \approx 1.96$ type spectrum upon addition of the substrate, which suggests that this center may be involved in the catalytic cycle (*264*).

2. *Regulation Role*

Iron–sulfur centers can participate in regulation mechanisms either directly, when they control the activity of an enzyme, or at a more integrated level, when they modulate the expression of some genes. The regulation mechanisms that have been elucidated so far involve either a change in the redox state or the interconversion of iron–sulfur centers.

a. Redox Regulation The best example of this kind of mechanism is provided by the SoxR protein, a transcription factor that governs a regulon of oxidative stress resistance genes in *E. coli*. This homodi-

meric protein contains one [2Fe–2S] center per monomer, and this center is essential to activating the transcription of the *soxS* gene, whereas the protein SoxS in turn activates the transcription of other genes (*265*). The SoxR protein is only active under oxidizing conditions where the iron–sulfur center is in the state $[2Fe–2S]^{2+}$. The reduction of the center, which can be monitored by looking for an EPR signal characterized by g values at 1.90, 1.92, 2.01 (*266*) ($E'_0 = -285$ mV), inhibits the transcription (*267*). The physiological relevance of this redox-linked mechanism has been confirmed by EPR studies carried out on whole cells (*268*). These experiments ruled out the hypothesis that a regulation mechanism based on the reversible disassembly of the iron–sulfur center might be involved, as proposed by previous authors (*269*). In this regulation process, the iron–sulfur center therefore acts as a direct sensor of the oxidative agents inducing the expression of the resistance genes. Since the affinity of the protein SoxR for the *soxS* promoter of the DNA is almost identical in both the oxidized and reduced states (*267*), the conformational changes induced by the reduction of the iron–sulfur center are probably small.

A relationship between the redox state of an iron–sulfur center and the conformation of the host protein was furthermore established in an X-ray crystal study on center P in *Azotobacter vinelandii* nitrogenase (*270*). In this enzyme, the two-electron oxidation of center P was found to be accompanied by a significant displacement of about 1 Å of two iron atoms. In both cases, this displacement was associated with an additional ligation provided by a serine residue and the amide nitrogen of a cysteine residue, respectively. Since these two residues are protonable, it has been suggested that this structural change might help to synchronize the transfer of electrons and protons to the Fe–Mo cofactor of the enzyme (*270*).

b. Regulation Based on Cluster Conversions The interconversion between [3Fe–4S] and [4Fe–4S] centers, which can be easily monitored by EPR (*162*, *271–273*), was observed soon after the discovery of [3Fe–4S] centers (*274*). The [4Fe–4S] into [3Fe–4S] conversion occurs under oxidizing conditions and is reversible either under reducing conditions or in the presence of Fe^{2+} and S^{2-} ions and thiols. It was therefore soon proposed that these transformations may play a physiological role consisting either in protecting some proteins from oxidative degradation, or in controlling the activity of some enzymes (*275*, *276*). Nowadays, these functions are still hypothetical, although the latter possibility seems quite plausible in the case of aconitase, in which the [4Fe–4S] form of the center is active whereas the [3Fe–4S]

one is not (*261*). A regulation mechanism based on the transformation of an iron–sulfur center seems to occur, however, in the case of the iron-regulatory protein (IRP), which controls the metabolism of intracellular iron at a translational level by binding to a consensus sequence of mRNA called the iron responsive element (IRE). The IRP protein corresponds to the cytosolic aconitase, which is homologous to mitochondrial aconitase (*277*) and can take the form of either a holoprotein containing a [4Fe–4S] center that can be easily converted into a [3Fe–4S] form, or an apoprotein in which the iron–sulfur center is disassembled. When the cells are iron-replete, the IRP protein functions in the same way as active aconitase, whereas the apoprotein binds to mRNA and controls the iron uptake and storage when the cells are iron-depleted (*278*). The assembly/disassembly of the iron–sulfur center may therefore be a key feature in the response to levels of iron in the control of iron homeostasis (*261*).

A similar mechanism has been proposed in the case of the FNR protein, a transcriptional activator that controls several genes essential to the anaerobic respiratory metabolism in *E. coli*. Under anaerobic conditions, the protein is present in a dimeric form that contains one $[4Fe–4S]^{2+}$ center per subunit and can bind to the DNA, thus activating the transcription. After exposure to dioxygen, the protein is converted into a monomeric form with no iron–sulfur centers, which possess a lower affinity for the DNA (*279*). The first phase in the protein inactivation process has been found to consist in the fast conversion of $[4Fe–4S]^{2+}$ centers into $[2Fe–2S]^{2+}$ centers, giving a new form of the protein that is relatively stable toward dioxygen. The [2Fe–2S] centers can be converted back into [4Fe–4S] centers under reducing conditions (*280*). Since the iron–sulfur centers remain diamagnetic during the interconversion between [4Fe–4S] and [2Fe–2S] centers, this process, which may constitute the basis of the FNR regulation mechanism, was monitored by Mössbauer spectroscopy.

Using a combination of techniques such as EPR, resonance Raman, and MCD spectroscopy, the conversion of $[2Fe–2S]^{2+}$ into $[4Fe–4S]^{2+}$ centers has been found to take place under reducing conditions in *E. coli* biotin synthase (*281*). The as-prepared form of this enzyme has been thought to contain one [2Fe–2S] center per monomer, coordinated by the three cysteine residues of the motif $Cys–X_3–Cys–X_2–Cys$ and by a fourth, noncysteinyl ligand. Upon reduction, a [4Fe–4S] cluster bridging two monomers may be formed in the active enzyme. In the reduced state, the $[4Fe–4S]^{1+}$ center is characterized by a mixture of $S = \frac{3}{2}$ and $S = \frac{1}{2}$ spin states giving EPR features at $g \sim 5.6$ and

g = 2.004, 1.944, 1.914, respectively. A [2Fe–2S] to [4Fe–4S] cluster conversion of this kind was proposed to occur in other enzymes showing homologies with biotin synthase, such as the anaerobic ribonucleotide reductase (*282*), the pyruvate formate lyase activating enzyme (*283*), and the lysine 2,3-aminomutase (*284*).

3. Radical Stabilization

Some enzymes in which the regulation mechanism involves a stable protein-based radical require an activation system consisting of an iron–sulfur subunit and a cofactor, *S*-adenosylmethionine. Detailed EPR studies on the anaerobic ribonucleotide reductase (*285*), the pyruvate formate lyase activating enzyme (*283*, *286*), and the lysine 2,3-aminomutase (*284*) have suggested that the same activating mechanism occurs in all three enzymes. A $[4Fe–4S]^{2+,1+}$ center bridging two subunits may initiate the radical mechanism by facilitating the reductive one-electron cleavage of *S*-adenosylmethionine into methionine and the 5′-deoxyadenosyl radical. The details of this mechanism, which is also thought to take place in biotin synthase (*281*), are not yet known. However, since the presence of *S*-adenosylmethionine was found to significantly affect either the EPR signal (*284–286*) or the redox properties (*283*, *285*) of the $[4Fe–4S]^{1+}$ center, its binding site is probably located close to the iron–sulfur center.

It has been suggested that an iron–sulfur center may directly stabilize a radical species in the ferredoxin thioredoxin reductase enzyme, which serves to reduce the disulfide bridge of thioredoxin (*287*). The active site of this enzyme is a disulfide bridge located in the close vicinity of a $[4Fe–4S]^{2+}$ center. This center could not be reduced even by using very strong reductants. The substoichiometric, fast-relaxing $S = \frac{1}{2}$ EPR signal with g values of 2.01, 2.04, 2.09 that was recorded when the enzyme was oxidized by ferricyanide was attributed to a $[4Fe–4S]^{3+}$ state. These findings strongly suggest that the $[4Fe–4S]^{2+,1+}$ center cannot play a redox role in mediating the electron transfer between the ferredoxin and the disulfide bridge of the enzyme. A stoichiometric, slowly relaxing $S = \frac{1}{2}$ signal with g values of 1.98, 2.00, 2.11 was recorded with a form of the enzyme in which the disulfide bridge had been broken by selectively modifying one of the cysteines with *N*-ethylmaleimide. Although the corresponding paramagnetic species can be broadly defined as a $[4Fe–4S]^{3+}$ center, it was tenatively identified as a $[4Fe–4S]^{2+}$ cluster covalently bound to a cysteine-based thiyl radical via a μ_3–S^{2-} bridge on the basis of several spectroscopic studies (*287*). Since its redox potential was found to be consistent with the reduction of a disulfide bridge, this species was

taken to be a one-electron reduced intermediate stabilized by the Fe–S cluster in the two-electron catalytic reaction.

A mechanism involving the stabilization of a radical species via the ligand of a metal center was also proposed in the case of the Ni–Fe center that constitutes the active site in Ni–Fe hydrogenases (*288*). In the active form of the enzyme, the nickel center exhibits a typical EPR signal called Ni–C with g values of 2.01, 2.14, 2.19, which is characterized by a slow relaxation and can be observed up to room temperature. EPR studies (*288*) and ENDOR experiments on ^{57}Fe nuclei (*289*) have established that the iron ion is diamagnetic in the Ni–C species. From a detailed analysis of the available data, it was furthermore concluded that the spin density, which was initially assumed on the basis of experiments on samples enriched with ^{61}Ni to be mainly centered on the Ni atom (*290*), is actually largely delocalized onto the sulfur atom of a terminal cysteine ligand. Based on the results of this study, the Ni–C species should therefore be classified as a Fe(II)–Ni(II)–$S^{+\cdot}$–Cys entity (*288*). The finding that a radical intermediate stabilizes on the sulfur ligand of the metal site argues strongly in favor of the idea that a ligand-based mechanism may be involved in the activation of molecular hydrogen. Generally speaking, sulfur-based radicals such as thiyl and perthiyl radicals exhibit anisotropic EPR signals with $g_{av} > 2.0$ (*291*) that are hardly distinguishable from those displayed by some mononuclear and polynuclear metal centers. By analogy with the Ni–C species, it is therefore conceivable that the well-known, slowly relaxing EPR signal with g values of 2.00, 2.04, 2.10 displayed by active Fe-only hydrogenases (*292*) may arise from a radical species stabilized on a cysteine ligand of the H-cluster, which would mean that the same catalytic mechanism may be at work in both Ni–Fe and Fe-only hydrogenases.

V. Conclusion

The applications of EPR spectroscopy reviewed in the present chapter are based on the sensitivity of the spectrum displayed by iron–sulfur centers to various characteristics, such as the redox state of the center, the distribution of the valences on the iron ions, the nature and the geometry of the ligands, and the presence of nearby paramagnetic species. Although considerable progress has been made during the past few years in the quantitative analysis of these various effects in the case of the conventional iron–sulfur centers described in Section II, the discovery of centers exhibiting unusual EPR properties as

well as new types of centers constitutes a new challenge for spectroscopists. As mentioned in Section II,D, $[4Fe–4S]^{2+,1+}$centers with $S = \frac{1}{2}$ can exhibit very fast relaxation rates and very anisotropic spectra probably arising from the admixture of low-lying excited states, and these centers can even display spin states with $S > \frac{1}{2}$. These unusual properties are often observed in the case of centers having anomalous coordinating Cys motifs. For instance, the X-ray structure of the "putative prismane" protein from *Desulfovibrio vulgaris* solved at 1.7 Å resolution has shown the existence of an unexpected $[4Fe–4S]^{2+,1+}$ center bound by an unusual, sequential arrangement of four cysteine residues (*293*). In the reduced state, this center exhibits an EPR spectrum with features at $g_{\text{eff}} \approx 1.5, 1.8, 4.5$, which were interpreted as arising from the quantum admixture of an $S = \frac{1}{2}$ state into an $S = \frac{3}{2}$ state (*293*).

A further level of complexity is reached in the case of some new types of centers consisting of a [4Fe–4S] cluster in which one iron atom shares a ligand with a mononuclear center. A structure of this kind, which had been initially described on the basis of spectroscopic data (*294*), has been confirmed by the results of an X-ray crystal study performed on *E. coli* sulfite reductase, in which the mononuclear center is a siroheme (*295*). The C-cluster of *Rhodospirillum rubrum* carbon monoxide dehydrogenase, in which the mononuclear center is a Ni center, is probably of the same type (*296*). The unusual spectroscopic properties of these centers were explained using a perturbation approach in which the difference in energy between the ground state and the excited states of the [4Fe–4S] entity was assumed to be much larger than the coupling with the mononuclear center (*294*, *296*). In these clusters, the electronic structure of the iron–sulfur center therefore seems to be preserved.

More recently, polynuclear centers having similar structural motifs to those observed in conventional iron–sulfur centers, such as Fe atoms coordinated by inorganic or cysteinyl sulfur, together with other types of metal sites, have been discovered in a number of metalloproteins. These include the Fe–Mo cofactor and the P cluster in nitrogenase (*270*), the dinuclear Ni–Fe center in Ni–Fe hydrogenases (*164*, *297*), the "hybrid" cluster 2 present in the "putative prismane" protein from *D. vulgaris* (*293*) and in the closely related protein from *D. desulfuricans* called fuscoredoxin (*298*). The H-cluster of iron-only hydrogenases, in which one iron site is apparently coordinated by CO and/or CN^- ligands (*299*), probably belongs to this category. Since these polynuclear centers contain metal sites and bridging ligands that differ from those present in conventional iron–sulfur centers,

they can be expected to exhibit a still wider variety of spectroscopic properties.

Appendix: Spin–Lattice Relaxation Processes

The thermal equilibration of a system of paramagnetic centers is ensured by the exchange of energy between the lattice vibrations and the spin system: The vibrations modulate the potential energy of the paramagnetic centers, thus stimulating transitions between their spin states through spin–orbit coupling. This may involve various relaxation processes that can be identified by determining the temperature dependence of the relaxation rate (*303*).

1. The *direct* process is a resonant process involving low-frequency vibrational modes of energy $\hbar\omega = \delta E$, where δE is the transition energy, which gives rise to the temperature dependence $1/T_1 \propto T$. This process generally predominates at very low temperatures, although it is sometimes masked by a phonon bottleneck phenomenon giving a T^2 temperature dependence.
2. In the *Raman* process, two vibrational modes of energy $\hbar\omega_1$ and $\hbar\omega_2$ such that $\hbar\omega_1 - \hbar\omega_2 = \delta E$ are needed. In the case of paramagnetic centers with half-integer spins coupled to long-wavelength phonons, this process is characterized by the temperature dependence $1/T_1 \propto T^9 I_8\,(\theta_D/T)$, where θ_D is the Debye temperature characterizing the cutoff of the phonon spectrum and $I_8(x)$ is a transport integral. This gives a T^9 and T^2 temperature dependence when $T \ll \theta_D$ and $T \gg \theta_D$, respectively.
3. A resonant *Orbach* process occurs when the energy of the coupled vibrational modes is equal to the energy Δ of the first excited level of the paramagnetic center. This leads to the temperature dependence $1/T_1 \propto (\exp(\Delta/k_B T) - 1)^{-1} \approx \exp(-\Delta/k_B T)$ when $k_B T \ll \Delta$.

Generally speaking, the spin–lattice relaxation properties of a given paramagnetic center depend on several factors:

- The number of possible electronic transitions: The relaxation can be expected to be more efficient in the case of centers with $S > \frac{1}{2}$ than in that of $S = \frac{1}{2}$ centers. Note that in the former case, no single relaxation time can be defined.
- The strength of the coupling of the paramagnetic center to its surroundings, which is determined by the orbital part of the

wavefunction: A high-spin Fe(III) ion with $L = 0$ is much less strongly coupled than a high-spin Fe(II) ion with $L = 2$.

- The presence of low-lying excited levels can greatly increase the efficiency of the relaxation processes, especially in the case of paramagnetic centers with half-integer spins.
- The intrinsic relaxation rate of a paramagnetic center can be enhanced by spin–spin coupling with a nearby fast-relaxing species.

References

1. Beinert, H.; Sands, R. H. *Biochem. Biophys. Res. Commun.* **1 60,** *3,* 41.
2. Sands, R. H.; Beinert, H. *Biochem. Biophys. Res. Commun.* **1 60,** *3,* 47.
3. Noodleman, L.; Case, D. A. *Adv. Inorg. Chem.* **1 2,** *38,* 423.
4. Noodleman, L.; Peng, C. Y.; Case, D. A.; Mouesca, J.-M. *Coord. Chem. Rev.* **1 5,** *144,* 199.
5. Sieker, L. C.; Stenkamp, R. E.; LeGall, J. *Methods Enzymol.* **1 4,** *243,* 203.
6. Frey, M.; Sieker, L.; Payan, F.; Haser, R.; Bruschi, M.; Pepe, G.; LeGall, J. *J. Mol. Biol.* **1 87,** *197,* 25.
7. Peterson, J. A.; Coon, M. J. *J. Biol. Chem.* **1 68,** *243,* 329.
8. Peisach, J.; Blumberg, W. E.; Lode, E. T.; Coon, M. J. *J. Biol. Chem.* **1 71,** *246,* 5877.
9. Moura, I.; Xavier, A. V.; Cammack, R.; Bruschi, M.; Legall, J. *Biochim. Biophys. Acta* **1 78,** *533,* 156.
10. Schneider, J.; Dischler, B.; Raüber, A. *J. Phys. Chem. Solids* **1 68,** *29,* 451.
11. Sweeney, W. V.; Coffman, R. E. *Biochim. Biophys. Acta* **1 72,** *286,* 26.
12. Gebhard, M. S.; Deaton, J. C.; Koch, S. A.; Millar, M.; Solomon, E. I. *J. Am. Chem. Soc.* **1 0,** *112,* 2217.
13. Hagen, W. R. *Adv. Inorg. Chem.* **1 2,** *38,* 165.
14. Debrunner, W. E.; Münck, E.; Que, L.; Schulz, C. E. In "Iron–Sulfur Proteins"; Lovenberg, W., Ed.; Academic Press: New York, 1977, Vol. 3, 381–417.
15. Schulz, C.; Debrunner, W. E. *J. Phys. Colloq.* **1 76,** *C6,* 153.
16. LeGall, J.; Prickril, B. C.; Moura, I.; Xavier, A.; Moura, J. J. G.; Huynh B.-H. *Biochemistry* **1 88,** *27,* 1636.
17. Pierik, A.; Wolbert, R. B. G.; Portier, G. L.; Verhagen, M. F. J. M.; Hagen, W. R. *Eur. J. Biochem.* **1 3,** *212,* 237.
18. Moura, I.; Huynh, B. H.; Hausinger, R. P.; LeGall, J.; Xavier, A.; Münck, E. *J. Biol. Chem.* **1 80,** *255,* 2493.
19. Moura, I.; Tavares, P.; Moura, J. J. G.; Ravi, N.; Huynh, B. H.; Liu, M. Y.; LeGall, J. *J. Biol. Chem.* **1 0,** *265,* 21596.
20. Verhagen, M. F. J. M.; Voorhorst, W. G. B.; Kolkman, J. A. K.; Wolbert, R. B. G.; Hagen, W. R. *FEBS Lett.* **1 3,** *336,* 13.
21. Archer, M.; Huber, R.; Tavares, P.; Moura, I.; Moura, J. J. G.; Carrondo, M. A.; Sieker, L. C.; LeGall, J.; Ramao, M. J. *J. Mol. Biol.* **1 5,** *251,* 690.
22. Coelho, A. V.; Matias, P.; Fülöp, V.; Thompson, A.; Gonzales, A.; Carrondo, M. A. *J. Biol. Inorg. Chem.* **1 7,** *2,* 680.
23. Yu, L.; Kennedy, M.; Czaja, C.; Tavares, P.; Moura, J. J. G.; Moura, I.; Rusnak, F. *Biochem. Biophys. Res. Commun.* **1 7,** *231,* 679.

24. Werth, M. T.; Kurtz, D. M.; Howes, B. D.; Huynh, B. H. *Inorg. Chem.* **1 8 ,** *28,* 1357.
25. Hendrich, M. P.; Debrunner, P. G. *Biophys. J.* **1 8 ,** *56,* 489.
26. Bertrand, P.; Gayda, J. P. *Biochim. Biophys. Acta* **1 88,** *954,* 347.
27. Rupp, H.; Rao, K. K.; Hall, D. O.; Cammack, R. *Biochim. Biophys. Acta* **1 78,** *537,* 255.
28. Winkler, H.; Schulz, C.; Debrunner, P. G. *Phys. Lett.* **1 7 ,** *69A,* 360.
29. Noodleman, L.; Norman, J. G.; Osborne, J. H.; Aizman, A.; Case, D. *J. Am. Chem. Soc.* **1 85,** *107,* 3418.
30. Bertrand, P. *Inorg. Chem.* **1 3,** *32,* 741.
31. Gibson, J.; Hall, J. O.; Thornley, J. H. M.; Whatley, F. R. *Proc. Natl. Acad. Sci. USA* **1 66,** *56,* 987.
32. Fritz, J.; Anderson, R.; Fee, J.; Palmer, G.; Sands, R. H.; Tsibris, J. C. M.; Gunsalus, I. C.; Orme-Johnson, W. H.; Beinert, H. *Biochim. Biophys. Acta* **1 71,** *253,* 110.
33. Dunham, W. R.; Bearden, A.; Salmeen, I. T.; Palmer, G.; Sands, R. H.; Orme-Johnson, W. H.; Beinert, H. *Biochim. Biophys. Acta* **1 71,** *253,* 134.
34. Palmer, G.; Dunham, W. R.; Fee, J. A.; Sands, R. H.; Iizuka, T.; Yonetani, T. *Biochim. Biophys. Acta* **1 71,** *245,* 201.
35. Anderson, R. E.; Dunham, W. R.; Sands, R. H.; Bearden, A. J.; Crespi, H. L. *Biochim. Biophys. Acta* **1 75,** *408,* 306.
36. Peterson, L.; Cammack, R.; Rao, K. K. *Biochim. Biophys. Acta* **1 80,** *622,* 18.
37. Tsukihara, T.; Fukuyama, K.; Nakamura, M.; Katsube, Y.; Tanaka, N.; Kakudo, M.; Wada, K.; Hase, T.; Matsubara, H. *J. Biochem.* **1 81,** *90,* 1760.
38. Tsutsui, T.; Tsukihara, T.; Fukuyama, K.; Katsube, Y.; Hase, T.; Matsubara, H.; Nishikikawa, Y.; Tanaka, N. *J. Biochem.* **1 83,** *94,* 299.
39. Rypniewski, W. R.; Breiter, D. R.; Benning, M. M.; Wesenberg, G.; Oh, B.-H.; Markley, J. L.; Rayment, I.; Holden, H. M. *Biochemistry* **1 1,** *30,* 4126.
40. Tsukihara, T.; Fukuyama, K.; Mizushima, M.; Harioka, T.; Kusunoki, M.; Katsube, Y.; Hase, T.; Matsubara, H. *J. Mol. Biol.* **1 0,** *216,* 399.
41. Dugad, L. B.; LaMar, G. N.; Banci, L.; Bertini, I. *Biochemistry* **1 0,** *29,* 2263.
42. Skjeldal, L.; Westler, W. M.; Oh, B.-H.; Krezel, A. M.; Holden, H. M.; Jacobson, B. L.; Rayment, I.; Markley, J. L. *Biochemistry* **1 1,** *30,* 7363.
43. Bertrand, P.; Gayda, J.-P. *Biochim. Biophys Acta* **1 7 ,** *579,* 107.
44. More, C.; Bertrand, P.; Gayda, J. P. *J. Magn. Reson.* **1 87,** *73,* 13.
45. Bertrand, P.; Gayda, J. P. *Biochim. Biophys. Acta* **1 80,** *625,* 337.
46. Lovesey, S. W.; Allenspach, P. *Physica Scripta* **1 8,** *57,* 657.
47. Bertrand, P.; Guigliarelli, B.; Gayda, J. P.; Beardwood, P.; Gibson, J. F. *Biochim. Biophys. Acta* **1 85,** *831,* 261.
48. Gurbiel, R.; Batie, C. J.; Sivaraja, M.; True, A. E.; Fee, J. A.; Hoffman, B. M.; Ballou, D. P. *Biochemistry* **1 8 ,** *28,* 4861.
49. Gurbiel, R.; Ohnishi, T.; Robertson, D. E.; Daldal, F.; Hoffman, B. M. *Biochemistry* **1 1,** *30,* 11579.
50. Britt, R. D.; Sauer, K.; Klein, M.; Knaff, D. B.; Kriauciunas, A.; Yu, C. A.; Yu, L.; Malkin, R. *Biochemistry* **1 1,** *30,* 1892.
51. Iwata, S.; Saynovits, M.; Link, T. A.; Michel, H. *Structure* **1 6,** *4,* 567.
52. Link, T.; Hatzfeld, O. M.; Unalkat, P.; Shergill, J.; Cammack, R.; Mason, J. R. *Biochemistry* **1 6,** *35,* 7546.
53. Verhagen, M. F. J. M.; Link, T. A.; Hagen, W. R. *FEBS Lett.* **1 5,** *361,* 75.
54. Im, S.-C.; Lam, M.-C.; Ooi, B.-L.; Sykes, A. G. *J. Am. Chem. Soc.* **1 5,** *117,* 3635.

55. Im, S.-C.; Kohzuma, T.; McFarlane, W.; Gaillard, J.; Sykes, A. G. *Inorg. Chem.* **1 7,** *36,* 1388.
56. Blondin, G.; Girerd, J. J. *Chem. Rev.* **1 0,** *90,* 1359.
57. Ding, X.-Q.; Bill, E.; Trautwein, A. X.; Winkler, H.; Kostikas, A.; Papaefthymiou, V.; Simopoulos, A.; Beardwood, P.; Gibson, J. F. *J. Chem. Phys.* **1 3,** *99,* 6421.
58. Bertrand, P.; Guigliarelli, B.; Gayda, J. P.; Setif, P.; Mathis, P. *Biochim. Biophys. Acta* **1 88,** *933,* 393.
59. Münck, E.; Debrunner, P. G.; Tsibris, J. C. M.; Gunsalus, I. C. *Biochemistry* **1 72,** *11,* 855.
60. Fee, J.; Findling, K. L.; Yoshida, T.; Hille, R.; Tarr, G. E.; Hearshen, D. O.; Dunham, W. R.; Day, E. P.; Kent, T. A.; Münck, E. *J. Biol. Chem.* **1 84,** *259,* 124.
61. Pikus, J. D.; Studts, J. M.; Achim, C.; Kauffman, K. E.; Münck, E.; Steffan, R. J.; McClay, K.; Fox, B. G. *Biochemistry* **1 6,** *35,* 9106.
62. Guigliarelli, B.; Bertrand, P.; Gayda, J. P. *J. Chem. Phys.* **1 86,** *85,* 1689.
63. Bertrand, P.; Gayda, J. P.; Fee, J. A.; Kuila, D.; Cammack, R. *Biochim. Biophys. Acta* **1 87,** *916,* 24.
64. Hille, R.; Hagen, W. R.; Dunham, W. R. *J. Biol. Chem.* **1 85,** *260,* 10569.
65. Gayda, J. P.; Bertrand, P.; Deville, A.; More, C.; Roger, G.; Gibson, J. F.; Cammack, R. *Biochim. Biophys. Acta* **1 7 ,** *581,* 15.
66. Bertrand, P.; Roger, G.; Gayda, J. P. *J. Magn. Reson.* **1 80,** *40,* 539.
67. Gayda, J. P.; Bertrand, P.; More, C.; Cammack, R. *Biochimie* **1 81,** *63,* 847.
68. Kimura, T.; Tasaki, A.; Watari, H. *J. Biol. Chem.* **1 70,** *245,* 4450.
69. Lloyd, S. G.; Franco, R.; Moura, J. J. G.; Moura, I.; Ferreira, G. C.; Huynh, B. H. *J. Am. Chem. Soc.* **1 6,** *118,* 9892.
70. Beardwood, P.; Gibson, J. F. *J. Chem. Soc. Dalton* **1 83,** 737.
71. Beardwood, P.; Gibson, J. F.; Bertrand, P.; Gayda, J. P. *Biochim. Biophys. Acta* **1 83,** *742,* 426.
72. Stout, C. D. *J. Mol. Biol.* **1 8 ,** *205,* 545.
73. Kissinger, C. R.; Sieker, L. C.; Adman, E. T.; Jensen, L. H. *J. Mol. Biol.* **1 1,** *219,* 693.
74. Robbins, A. H.; Stout, C. D. *Proteins* **1 8 ,** *5,* 289.
75. Kent, T. A.; Huynh, B. H.; Münck, E. *Proc. Natl. Acad. Sci. USA* **1 80,** *77,* 6574.
76. Guigliarelli, B.; More, C.; Bertrand, P.; Gayda, J. P. *J. Chem. Phys.* **1 86,** *85,* 2774.
77. Guigliarelli, B.; Gayda, J. P.; Bertrand, P.; More, C. *Biochim. Biophys. Acta* **1 86,** *871,* 149.
78. Fan, C.; Houseman; A. L. P.; Doan, P.; Hoffman, B. M. *J. Phys. Chem.* **1 3,** *97,* 3017.
79. Asso, M.; Guigliarelli, B.; Yagi, T.; Bertrand, P. *Biochim. Biophys. Acta* **1 2,** *1122,* 50.
80. Vanoni, M. A.; Fischer, F.; Ravasio, S.; Verzotti, E.; Edmondson, D. E.; Hagen, W. R.; Zanetti, G.; Curti, B. *Biochemistry* **1 8,** *37,* 1828.
81. Gayda, J. P.; Bertrand, P.; Guigliarelli, B.; Meyer, J. *J. Chem. Phys.* **1 83,** *79,* 5732.
82. Fu, W.; Telser, J.; Hoffman, B. M.; Smith, E. T.; Adams, M. W. W.; Finnegan, M. G.; Conover, R. C.; Johnson, M. K. *J. Am. Chem. Soc.* **1 4,** *116,* 5722.
83. Hägerhäll, C.; Sled, V.; Hederstedt, L.; Ohnishi, T. *Biochim. Biophys. Acta* **1 5,** *1229,* 356.
84. Johnson, M. K.; Bennett, D. E.; Fee, J. A.; Sweeney, W. V. *Biochim. Biophys. Acta* **1 87,** *911,* 81.

85. Papaefthymiou, V.; Girerd, J.-J.; Moura, I.; Moura, J. J. G.; Münck, E. *J. Am. Chem. Soc.* **1 87,** *109,* 4703.
86. Ghosh, D.; Furey, W.; O'Donnell, S.; Stout, C. D. *J. Biol. Chem.* **1 81,** *256,* 4185.
87. Day, E. P.; Peterson, J.; Bonvoisin, J. J.; Moura, I.; Moura, J. J. G. *J. Biol. Chem.* **1 88,** *263,* 3684.
88. Macedo, A. L.; Moura, I.; Moura, J. J. G.; LeGall, J.; Huynh, B. H. *Inorg. Chem.* **1 3,** *32,* 1101.
89. Bencini, A.; Gatteschi, D.; "EPR of Exchange Coupled Systems"; Springer: Berlin, 1990.
90. Griffith, J. S. *Structure and Bonding* **1 72,** *10,* 87.
91. Zhou, J.; Hu, Z.; Münck, E.; Holm, R. H. *J. Am. Chem. Soc.* **1 6,** *118,* 1966.
92. Broshch, S. A.; Bominaar, E. L.; Blondin, G.; Girerd, J.-J. *J. Am. Chem. Soc.* **1 3,** *115,* 5155.
93. Hagen, W. R.; Dunham, W. R.; Johnson, M. K.; Fee, J. A. *Biochim. Biophys. Acta* **1 85,** *828,* 369.
94. Adams, M. W. W. *Adv. Inorg. Chem.* **1 2,** *38,* 341.
95. Teixeira, M.; Moura, I.; Xavier, A. V.; Moura, J. J. G.; LeGall, J.; DerVartanian, D. V.; Peck, H. D.; Huynh, B. H. *J. Biol. Chem.* **1 8 ,** *264,* 16435.
96. Hu, Z.; Jollie, D.; Burgess, B.; Stephens, P. J.; Münck, E. *Biochemistry* **1 4,** *33,* 14475.
97. Finnegan, M. G.; Conover, R. C.; Park, J.-B.; Zhou, Z. H.; Adams, M. W. W.; Johnson, M. K. *Inorg. Chem.* **1 5,** *34,* 5358.
98. Surerus, K. K.; Münck, E.; Moura, I.; Moura, J. J. G.; LeGall, J. *J. Am. Chem. Soc.* **1 87,** *109,* 3805.
99. Armstrong, F. A.; Butt, J. N.; George, S. J.; Hatchikian, E. C.; Thomson, A. J. *FEBS Lett.* **1 8 ,** *259,* 15.
100. Moreno, C.; Macedo, A. L.; Moura, I.; LeGall, J.; Moura, J. J. G. *J. Inorg. Biochem.* **1 4,** *53,* 219.
101. Tong, J.; Feinberg, B. A. *J. Biol. Chem.* **1 4,** *269,* 24920.
102. Duff, J. L. C.; Breton, J. L. J.; Butt, J. N.; Armstrong, F. A.; Thomson, A. J. *J. Am. Chem. Soc.* **1 6,** *118,* 8593.
103. Bertrand, P.; Guigliarelli, B.; Meyer, J.; Gayda, J. P. *Biochimie* **1 84,** *66,* 77.
104. Thomson, A. J.; Robinson, A. E.; Johnson, M. K.; Moura, J. J. G.; Moura, I.; Xavier, A. V.; LeGall, J. *Biochim. Biophys. Acta* **1 81,** *670,* 93.
105. Flint, D. H.; Allen, R. M. *Chem. Rev.* **1 6,** *96,* 2315.
106. Schoepp, B.; Parot, P.; Menin, L.; Gaillard, J.; Richaud, P.; Vermeglio, A. *Biochemistry* **1 5,** *34,* 11736.
107. Cavazza, C.; Guigliarelli, B.; Bertrand, P.; Bruschi, M. *FEMS Microbiol. Lett.* **1 5,** *130,* 193.
108. Dunham, W. R.; Hagen, W. R.; Fee, J. A.; Sands, R. H.; Dunbar, J. B.; Humblet, C. *Biochim. Biochim. Acta* **1 1,** *1079,* 253.
109. Middleton, P.; Dickson, D. P. E.; Johnson, C. E.; Rush, J. D. *Eur. J. Biochem.* **1 78,** *88,* 135.
110. Middleton, P.; Dickson, D. P. E.; Johnson, C. E.; Rush, J. D. *Eur. J. Biochem.* **1 80,** *104,* 289.
111. Noodleman, L. *Inorg. Chem.* **1 88,** *27,* 3677.
112. Bertrand, P.; Camensuli, P.; More, C.; Guigliarelli, B. *J. Am. Chem. Soc.* **1 6,** *118,* 1426.
113. Boominar, E. I.; Borshch, S. A.; Girerd, J. J. *J. Am. Chem. Soc.* **1 4,** *116,* 5362.
114. Noodleman, L.; Case, D. A. *Adv. Inorg. Chem.* **1 2,** *38,* 423.

115. Le Pape, L.; Lamotte, B.; Mouesca, J. M.; Rius, G. *J. Am. Chem. Soc.* **1 7,** *119,* 9757.
116. Le Pape, L.; Lamotte, B.; Mouesca, J. M.; Rius, G. *J. Am. Chem. Soc.* **1 7,** *119,* 9771.
117. Kappl, R.; Ciurli, S.; Luchinat, C.; Hüttermann, J. *J. Am. Chem. Soc.* **1 ,** in press.
118. Mouesca, J. M.; Noodleman, L.; Case, D. A.; Lamotte, B. *Inorg. Chem.* **1 5,** *34,* 4347.
119. Guigliarelli, B.; Guillaussier, J.; More, C.; Setif, P.; Bottin, H.; Bertrand, P. *J. Biol. Chem.* **1 3,** *268,* 900.
120. Conover, R. C.; Kowal, A. T.; Fu, W.; Park, S.; Aono, S.; Adams, M. W. W.; Johnson, M. K. *J. Biol. Chem.* **1 0,** *265,* 8533.
121. Banci, L.; Bertini, I.; Ciurli, S.; Ferretti, S.; Luchinat, C.; Piccioli, M. *Biochemistry* **1 3,** *32,* 9387.
122. Bertini, I.; Ciurli, S.; Luchinat, C. *Structure and Bonding* **1 5,** *83,* 1.
123. Huber, J. G.; Moulis, J. M.; Gaillard, J. *Biochemistry* **1 6,** *35,* 12705.
124. Guigliarelli, B.; Asso, M.; More, C.; Augier, V.; Blasco, F.; Giordano, G.; Bertrand, P. *Eur. J. Biochem.* **1 2,** *207,* 61.
125. Hatchikian, E. C.; Cammack, R.; Patil, D. S.; Robinson, A. E.; Richards, A. J. M.; George, S.; Thomson, A. J. *Biochim. Biophys. Acta* **1 84,** *784,* 40.
126. Ragsdale, S. W.; Lindhal, P. A.; Münck, E. *J. Biol. Chem.* **1 87,** *262,* 14289.
127. Moulis, J.-M.; Auric, P.; Gaillard, J.; Meyer, J. *J. Biol. Chem.* **1 84,** *259,* 11396.
128. Lindhal, P. A.; Day, E. P.; Kent, T. A.; Orme-Johnson, W. H.; Münck, E. *J. Biol. Chem.* **1 85,** *260,* 11160.
129. Flint, D. H.; Emptage, M. H.; Finnegan, M. G.; Fu, W.; Johnson, M. K. *J. Biol. Chem.* **1 3,** *268,* 14732.
130. Angove, H.; Yoo, S. J.; Burgess, B. K.; Münck, E. *J. Am. Chem. Soc.* **1 7,** *119,* 8730.
131. Bertrand, P.; Gayda, J.-P.; Rao, K. K. *J. Chem. Phys.* **1 82,** *76,* 4715.
132. Gayda, J.-P.; Bertrand, P.; More, C.; LeGall, J.; Cammack, R. *Biochem. Biophys. Res. Commun.* **1 81,** *99,* 1265.
133. Meyer, J.; Gaillard, J.; Lutz, M. *Biochem. Biophys. Res. Commun.* **1 5,** *212,* 827.
134. Johnson, M. K.; Morningstar, J. E.; Cecchini, G.; Ackrell, B. A. C. *Biochem. Biophys. Res. Commun.* **1 85,** *131, 653.*
135. More, C.; Camensuli, P.; Dole, F.; Guigliarelli, B.; Asso, M.; Fournel, A.; Bertrand, P. *J. Biol. Inorg. Chem.* **1 6,** *1,* 152.
136. Bruschi, M.; Guerlesquin, F. *FEMS Microbiol. Rev.* **1 88,** *54,* 155.
137. Blasco, F.; Iobbi, C.; Giordano, G.; Chippaux, M.; Bonnefoy, V. *Mol. Gen. Genet.* **1 8 ,** *218,* 249.
138. Albracht, S. P. J.; Mariette, A.; De jong, Ph. *Biochim. Biophys. Acta* **1 7,** *1318,* 92.
139. Vordow, G. *Adv. Inorg. Chem.* **1 2,** *38,* 397.
140. Werth, M. T.; Sices, H.; Cecchini, G.; Schröder, I.; Lasage, S.; Gunsalus, R. P.; Johnson, M. K. *FEBS Lett.* **1 2,** *299,* 1.
141. Moulis, J.-M.; Davasse, V.; Golinelli, M.-P.; Meyer, J.; Quinkal, I. *J. Biol. Inorg. Chem.* **1 6,** *1,* 2.
142. Crouse, B. R.; Sellers, V. M.; Finnegan, M. G.; Dailey, H. A.; Johnson, M. K. *Biochemistry* **1 6,** *35,* 16222.
143. Cleland, W. E.; Averill, B. A. *Inorg. Chem.* **1 84,** *23,* 4192.
144. Beardwood, P.; Gibson, J. F. *J. Chem. Soc. Chem. Commun.* **1 85,** 102.

145. Werth, M. T.; Cecchini, G.; Manodori, A.; Ackrell, B. A. C.; Schröder, I.; Gunsalus, R. P.; Johnson, M. K. *Proc. Natl. Acad. Sci. USA* **1 0,** *87,* 8965.
146. Meyer, J.; Fujinaka, J.; Gaillard, J.; Lutz, M. *Biochemistry* **1 4, 33,** 13642.
147. Golinelli, M.-P.; Akin, L. A.; Crouse, B. R.; Johnson, M. K.; Meyer, J. *Biochemistry* **1 6,** *35,* 8995.
148. Crouse, B. R.; Meyer, J.; Johnson, M. K. *J. Am. Chem. Soc.* **1 5,** *117,* 9612.
149. Golinelli, M.-P. Ph.D. Thesis, 1997, Universite J. Fourier, Grenoble, France.
150. Cupp, J. R.; Vickery, L. E. *J. Biol. Chem.* **1 88,** *263,* 17418.
151. Xia, H. C.; Bandarian, V.; Reed, G. H.; Markley, J. L. *Biochemistry* **1 6,** *35,* 9488.
152. Cheng, H.; Xia, B.; Reed, G. H.; Markley, J. L. *Biochemistry* **1 4,** *33,* 3155.
153. Hurley, J. K.; Weber-Main, A. M.; Hodges, A. E.; Stankovich, M.; Benning, M. M.; Holden, H. M.; Cheng, H.; Xia, B.; Markley, J. L.; Genzor, C.; Gomez-Moreno, C.; Hazefi, R.; Tollin, G. *Biochemistry* **1 7,** *36,* 15109.
154. Holden, H. M.; Jacobson, B. L.; Hurley, J. K.; Tollin, G.; Oh, B.-H.; Skjeldal, L.; Chae, Y. K.; Cheng, H.; Xia, B.; Markley, J. *J. Bioenerg. Biomembr.* **1 4,** *26,* 67.
155. Achim, C.; Golinelli, M.-P.; Bominaar, E. L.; Meyer, J.; Münck, E. *J. Am. Chem. Soc.* **1 6,** *118,* 8168.
156. Matsubara, H.; Saeki, K. *Adv. Inorg. Chem.* **1 2,** *38,* 223.
157. Stout, C. D. *J. Biol. Chem.* **1 88,** *263,* 9256.
158. George, S. J.; Armstrong, F. A.; Hatchikian, E. C.; Thomson, A. J. *Biochem. J.* **1 8 ,** *264,* 275.
159. Asso, M.; Mbarki, O.; Guigliarelli, B.; Yagi, T.; Bertrand, P. *Biochem. Biophys. Res. Commun.* **1 5,** *211,* 198.
160. Calzolai, L.; Gorst, C. M.; Zhao, Z. H.; Teng, Q.; Adams, M. W. W.; La Mar, G. *Biochemistry* **1 5,** *34,* 11373.
161. Bush, J. L.; Breton, J. L.; Barlett, B. M.; Armstrong, F. A.; James, R.; Thomson, A. J. *Biochem. J.* **1 7,** *323,* 95.
162. Emptage, M. H.; Dreyer, J. L.; Kennedy, M. C.; Beinert, H. *J. Biol. Chem.* **1 83,** *258,* 11106.
163. Emptage, M. H.; Kent, T. A.; Kennedy, M. C.; Beinert, H.; Münck, E. *Proc. Natl. Acad. Sci. USA* **1 83,** *80,* 4674.
164. Volbeda, A.; Charon, M. H.; Piras, C.; Hatchikian, E. C.; Frey, M.; Fontecilla-Camps, J. C. *Nature* **1 5,** *373,* 580.
165. Gaillard, J.; Quinkal, I.; Moulis, J. M. *Biochemistry* **1 3,** *32,* 9881.
166. Quinkal, I.; Davasse, V.; Gaillard, J.; Moulis, J. M. *Protein Engineering* **1 4,** *7,* 681.
167. Quinkal, I. Ph.D. Thesis, 1995, Universite J. Fourier, Grenoble, France.
168. Martin, A. E.; Burgess, B. K.; Stout, C. D.; Cash, V. L.; Dean, D. R.; Jensen, G. M.; Stephens, P. J. *Proc. Natl. Acad. Sci. USA* **1 0,** *87,* 598.
169. Shen, B.; Jollie, D. R.; Diller, T. C.; Stout, C. D.; Stephens, P. J.; Burgess, B. K. *Proc. Natl. Acad. Sci. USA* **1 5,** *92,* 10064.
170. Isma, S. E.; Vasquez, A. E.; Jensen, G. M.; Stephens, P. J.; Butt, J. N.; Armstrong, F. A.; Burgess, B. K. *J. Biol. Chem.* **1 1,** *266,* 21563.
171. Kowal, A. J.; Werth, M. T.; Manodori, A.; Cecchini, G.; Schröder, I.; Gunsalus, R. P.; Johnson, M. K. *Biochemistry* **1 5,** *34,* 12284.
172. Augier, V.; Guigliarelli, B.; Asso, M.; Bertrand, P.; Frixon, C.; Giordano, G.; Chippaux, M.; Blasco, F. *Biochemistry* **1 3,** *32,* 2013.
173. Augier, V.; Asso, M.; Guigliarelli, B.; More, C.; Bertrand, P.; Santini, C. L.; Blasco, F.; Chippaux, M.; Giordano, G. *Biochemistry* **1 3,** *32,* 5099.

174. Guigliarelli, B.; Magalon, A.; Asso, M.; Bertrand, P.; Frixon, C.; Giordano, G.; Blasco, F. *Biochemistry* **1 6,** *35,* 4828.
175. Warren, P. V.; Smart, L. B.; McIntosh, L.; Golbeck, J. H. *Biochemistry* **1 3,** *32,* 4411.
176. Vassiliev, I. R.; Jung, Y.-S.; Smart, L. B.; Schulz, R.; McIntosh, L.; Golbeck, J. H. *Biophys. J.* **1 5,** *69,* 1544.
177. Babini, E.; Bertini, I.; Borsari, M.; Capozzi, F.; Dikiy, A.; Eltis, L. D.; Luchinat, C. *J. Am. Chem. Soc.* **1 6,** *118,* 75.
178. Bentrop, D.; Bertini, I.; Capozzi, F.; Dikiy, A.; Eltis, L.; Luchinat, C. *Biochemistry* **1 6,** *35,* 5928.
179. Rothery, R. A.; Weiner, J. H. *Biochemistry* **1 6,** *35,* 3247.
180. Jung, Y.-S.; Vassiliev, I. R.; Qiao, F.; Bryant, D.; Golbeck, J. H. *J. Biol. Chem.* **1 6,** *271,* 31135.
181. Manodori, A.; Cecchini, G.; Schröder, I.; Gunsalus, R. P.; Werth, M. T.; Johnson, M. K. *Biochemistry* **1 2,** *31,* 2703.
182. Rousset, M.; Montet, Y.; Guigliarelli, B.; Forget, N.; Asso, M.; Bertrand, P.; Fontecilla-Camps, J. C.; Hatchikian, E. C. *Proc. Natl. Acad. Sci. USA* **1 8,** *95,* 11625.
183. Rothery, R. A.; Weiner, J. H. Biochemistry **1 1,** *30,* 8296.
184. Menon, S.; Ragsdale, S. W. *Biochemistry* **1 8,** *37,* 5689.
185. Yu, L.; Zhao, J.; Lu, W.; Bryant, D. A.; Golbeck, J. H. *Biochemistry* **1 3,** *32,* 8251.
186. Mehari, T.; Qiao, F.; Scott, M. P.; Nellis, D. F.; Zhao, J.; Bryant, D. A.; Golbeck, J. H. *J. Biol. Chem.* **1 5,** *270,* 28108.
187. Yu, L.; Vassiliev, I. R.; Jung, Y.-S.; Bryant, D. A.; Golbeck, J. H. *J. Biol. Chem.* **1 5,** *270,* 28118.
188. Yu, L.; Bryant, D. A.; Golbeck, J. H. *Biochemistry* **1 5,** *34,* 7861.
189. Mannan, R. M.; He, W.-Z.; Metzger, S.; Whitmarsh, J.; Malkin, R.; Paksari, H. B. *EMBO J.* **1 6,** *15,* 1826.
190. Goodman, G.; Leigh, J. S. *Biochemistry* **1 85,** *24,* 2310.
191. Lowe, D. J.; Lynden-Bell, R. M.; Bray, R. C. *Biochem. J.* **1 72,** *130,* 239.
192. Bertrand, P.; More, C.; Guigliarelli, B.; Fournel, A.; Bennett, B.; Howes, B. *J. Am. Chem. Soc.* **1 4,** *116,* 3078.
193. Hirsh, D. J.; Beck, W. F.; Innes, J. B.; Brudvig, G. W. *Biochemistry* **1 2,** *31,* 532.
194. Guigliarelli, B.; More, C.; Fournel, A.; Asso, M.; Hatchikian, C. E.; Williams, R.; Cammack, R.; Bertrand, P. *Biochemistry* **1 5,** *34,* 4781.
195. Un, S.; Brunel, L. C.; Brill, T.; Zimmermann, J. L.; Rutherford, A. W. *Proc. Natl. Acad. Sci. USA* **1 4,** *91,* 5262.
196. Berry, M.; Bratt, P. J.; Evans, M. C. W. *Biochim. Biophys. Acta* **1 7,** *1319,* 163.
197. Coffman, R. E.; Buettner, G. R. *J. Phys. Chem.* **1 7 ,** *83,* 2392.
198. Barber, M. J.; Salerno, J. C.; Siegel, L. M. *Biochemistry* **1 82,** *21,* 1648.
199. George, G. N. In "Flavins and Flavoproteins"; Bray, R. C.; Engel, P. C.; Mayhew, S. G., eds.; pp. 325–330; de Gruyter: Berlin, 1984.
200. Lowe, D. J.; Bray, R. C. *Biochem. J.* **1 78,** *169,* 471.
201. Romao, M. J.; Archer, M.; Moura, I.; Moura, J. J. G.; LeGall, J.; Engh, R.; Schneider, M.; Hof, P.; Huber, R. *Science* **1 5,** *270,* 1170.
202. Bray, R. C.; Turner, N. A.; LeGall, J.; Barata, B. A. S.; Moura, J. J. G. *Biochem. J.* **1 1,** *280,* 817.
203. Hille, R. *Chem. Rev.* **1 6,** *96,* 2757.
204. Correl, C.; Batie, C. J.; Ballou, D. P.; Ludwig, M. L. *Science* **1 2,** *258,* 1604.
205. Batie, C. J.; Ballou, D. P.; Correl, C. C. In "Chemistry and Biochemistry of Flavoenzymes"; Muller, F., ed.; Vol. 3, 543–556, CRC Press: Boca Raton, FL, 1991.

206. Bertrand, P.; More, C.; Camensuli, P. *J. Am. Chem. Soc.* **1 5,** *117,* 1807.
207. Cammack, R.; Patil, D. S.; Hatchikian, E. C.; Fernandez, V. *Biochim. Biophys. Acta* **1 87,** *912,* 98.
208. Hüttermann, J.; Däges, G. P.; Reinhard, H.; Schmidt, G. In "Nuclear Magnetic Resonance of Paramagnetic Molecules" LaMar, G. N., ed.; pp. 165–192. Kluwer: Dordrecht, 1996.
209. Lim, L. W.; Shamala, N.; Mathews, F. S.; Steenkamp, D. J.; Hamlin, R.; Xuong, N. H. *J. Biol. Chem.* **1 86,** *261,* 15140.
210. Stevenson, R. C.; Dunham, W. R.; Sands, R. H.; Singer, T. P.; Beinert, H. *Biochim. Biophys. Acta* **1 86,** *869,* 81.
211. Camensuli, P. Ph.D. Thesis, 1995, Université de Provence, Marseille, France.
212. Fournel, A.; Gambarelli, S.; Guigliarelli, B.; More, C.; Asso, M.; Chouteau, G.; Hille, R.; Bertrand, P. *J. Chem. Phys.* **1 8,** *109,* 10905.
213. Krauss, N.; Schubert, W.-D.; Klukas, O.; Fromme, P.; Witt, H. T.; Saenger, W. *Nature Struct. Biol.* **1 6,** *3,* 965.
214. Dauter, Z.; Wilson, K. S.; Sieker, L. C.; Meyer, J.; Moulis, J.-M. *Biochemistry* **1 7,** *36,* 16065.
215. Adman, E. T.; Mather, M. W.; Fee, J. A. *Biochim. Biophys. Acta* **1 3,** *1142,* 93.
216. Mason, J.; Cammack, R. *Ann. Rev. Microbiol.* **1 2,** 1.
217. Torbet, J. *TIBS* **1 87,** *12,* 327.
218. Dismukes, G. C.; Sauer, K. *Biochim. Biophys. Acta* **1 78,** *504,* 431.
219. Aasa, R.; Bergström, J.; Vänngard, T. *Biochim. Biophys. Acta* **1 81,** *637,* 118.
220. Blum, H.; Salerno, J. C.; Leigh, J. S. *J. Magn. Reson.* **1 78,** *30,* 385.
221. Blum, H.; Harmon, H. J.; Leigh, J. S.; Salerno, J. C.; Chance, B. *Biochim. Biophys Acta* **1 78,** *502,* 1.
222. Erecinska, M.; Wilson, D. F. *Arch. Biochem. Biophys.* **1 7 ,** *192,* 80.
223. Blasie, J. K.; Erecinska, M.; Samuels, S.; Leigh, J. S. *Biochim. Biophys. Acta* **1 78,** *501,* 33.
224. Nitschke, W.; Jubault-Bregler, M.; Rutherford, A. W. *Biochemistry* **1 3,** *32,* 8871.
225. Nitschke, W.; Schoepp, B.; Floss, B.; Schriker, A.; Rutherford, A. W.; Liebl, U. *Eur. J. Biochem.* **1 6,** *242,* 695.
226. Blum, H.; Poole, R. K. *Biochem. Biophys. Res. Commun.* **1 82,** *107,* 903.
227. Simpkin, D.; Ingledew, J. W. *Biochem. Soc. Trans.* **1 85,** *13,* 603.
228. Prince, R. C.; Crowder, M. S.; Bearden, A. J. *Biochim. Biophys. Acta* **1 80,** *592,* 323.
229. Hootkins, R.; Bearden, A. *Biochim. Biophys. Acta* **1 83,** *723,* 16.
230. Nitschke, W.; Feiler, U.; Rutherford, A. W. *Biochemistry* **1 0,** *29,* 3834.
231. Salerno, J. C.; Blum, H.; Ohnishi, T. *Biochim. Biophys. Acta* **1 7 ,** *547,* 270.
232. Reidel, A.; Rutherford, A. W.; Hauska, G.; Müller, A.; Nitschke, W. *J. Biol. Chem.* **1 1,** *266,* 17838.
233. Link, T.; Iwata, S. *Biochim. Biophys. Acta* **1 6,** *1275,* 54.
234. Zhang, Z.; Huang, L.; Shulmeister, V. M.; Chi, Y. I.; Kim, K. K.; Hung, L. W.; Crofts, A. R.; Berry, E. A.; Kim, S. H. *Nature* **1 8,** *392,* 677.
235. Brettel, K.; Sieckmann, I.; Fromme, P.; Van der Est, A.; Stehlik, D. *Biochim. Biophys. Acta* **1 2,** *1098,* 266.
236. Kamlowski, A.; Van der Est, A.; Fromme, P.; Stehlik, D. *Biochim. Biophys. Acta* **1 7,** *1319,* 185.
237. Li, N.; Zhao, J.; Warren, P.; Warden, J. T.; Bryant, D. A.; Golbeck, J. *Biochemistry* **1 1,** *30,* 7863.
238. Brettel, K. *Biochim. Biophys. Acta* **1 7,** *1318,* 322.

239. Kamlowski, A.; Van der Est, A.; Fromme, P.; Krauss, N.; Schubert, W. D.; Klukas, O.; Stehlik, D. *Biochim. Biophys. Acta* **1 7,** *1319,* 199.
240. Gloux, J.; Gloux, P.; Hendriks, H.; Rius, G. *J. Am. Chem. Soc.* **1 87,** *109,* 3220.
241. Gloux, J.; Gloux, P.; Lamotte, B.; Mouesca, J. M.; Rius, G. *J. Am. Chem. Soc.* **1 4,** *116,* 1953.
242. Mouesca, J.-M.; Chen, J. L.; Noodleman, L.; Bashford, D.; Case, D. A. *J. Am. Chem. Soc.* **1 4,** *116,* 11898.
243. Stephens, P. J.; Jollie, D. R.; Warshell, A. *Chem. Rev.* **1 6,** *96,* 2491.
244. Chamorowski, S. K.; Cammack, R. *Photobiochem. Photobiophys.* **1 82,** *4,* 195.
245. Kyritsis, P.; Hatzfeld, O. M.; Link, T.; Moulis, J. M. *J. Biol. Chem.* **1 8,** *273,* 15404.
246. Menin, L.; Gaillard, J.; Parot, P.; Shoepp, B.; Nitschke, W.; Vermeglio, A. *Photosynth. Res.* **1 8,** *55,* 343.
247. Porras, A. T.; Palmer, G. *J. Biol. Chem.* **1 82,** *257,* 11617.
248. Williams-Smith, D. L.; Bray, R. C.; Barber, M. J.; Tsopanakis, A. D.; Vincent, S. P. *Biochem. J.* **1 77,** *167,* 593.
249. Hederstedt, L., Ohnishi, T. In "Molecular Mechanisms in Bioenergetics"; Ernster, L., ed.; pp. 163–198; Elsevier: New York, 1992.
250. Neet, K. E. *Methods Enzymol.* **1 5,** *249,* 519.
251. Sokol, W. F.; Evans, D. H.; Niki, K.; Yagi, T. *Electroanal. Chem.* **1 80,** *108,* 107.
252. Santos, H.; Moura, J. J. G.; Moura, I.; LeGall, J.; Xavier, A. V. *Eur. J. Biochem.* **1 84,** *141,* 283.
253. Gayda, J. P.; Benosman, H.; Bertrand, P.; More, C.; Asso, M. *Eur. J. Biochem.* **1 88,** *177,* 199.
254. Turner, D. L.; Salgueiro, C. A.; Catarino, T.; LeGall, J.; Xavier, A. V. *Eur. J. Biochem.* **1 6,** *241,* 723.
255. Wang, H.; Blair, F.; Ellis, W. R.; Gray, H. B.; Chan, S. I. *Biochemistry* **1 86,** *25,* 167.
256. Salerno, J. C.; Bolgiano, B.; Poole, R. K.; Gennis, R. B.; Ingledew, W. J. I. *J. Biol. Chem.* **1 0,** *265,* 4364.
257. Sweeney, W. V.; McIntosh, B. A. *J. Biol. Chem.* **1 7 ,** *254,* 4499.
258. Marcus, R. A.; Sutin, N. *Biochim. Biophys. Acta* **1 85,** *811,* 265.
259. Bertrand, P. *Structure and Bonding* **1 1,** *75,* 1.
260. Beinert, H.; Holm, R. H.; Münck, E. *Science* **1 7,** *277,* 653.
261. Beinert, H.; Kennedy, M. C.; Stout, C. D. *Chem. Rev.* **1 6,** *96,* 2335.
262. Müh, U.; Cinkaya, I.; Albracht, S. P. J.; Buckel, W. *Biochemistry* **1 6,** *35,* 11710.
263. Hofmeister, A. E. M.; Albracht, S. P. J.; Buckel, W. *FEBS Lett.* **1 4,** *351,* 416.
264. Flint, D. H.; Emptage, M. H. *J. Biol. Chem.* **1 88,** *263,* 3558.
265. Hidaldo, H.; Demple, B. *EMBO J.* **1 4,** *13,* 138.
266. Wu, J.; Dunham, W. R.; Weiss, B. *J. Biol. Chem.* **1 5,** *270,* 10323.
267. Gaudu, P.; Weiss, B. *Proc. Natl. Acad. Sci. USA* **1 6,** *93,* 10094.
268. Gaudu, P.; Moon, N.; Weiss, B. *J. Biol. Chem.* **1 7,** *272,* 5082.
269. Hidalgo, E.; Demple, B. *J. Biol. Chem.* **1 6,** *271,* 7269.
270. Peters, J. W.; Stowell, M. H. B.; Soltis, M.; Finnegan, M. G.; Johnson, M. K., Rees, D. C. *Biochemistry* **1 7,** *36,* 1181.
271. Moura, J. J. G.; Moura, I.; Kent, T. A.; Lipscomb, J. D.; Huynh, B. H.; LeGall, J.; Xavier, A. V.; Münck, E. *J. Biol. Chem.* **1 82,** *257,* 6259.
272. Morgan, T. V.; Stephens, P. J.; Burgess, B. K.; Stout, C. D. *FEBS Lett.* **1 84,** *167,* 137.

273. Guigliarelli, B.; Bertrand, P.; More, C.; Papavassiliou, P.; Hatchikian, E. C.; Gayda, J. P. *Biochim. Biophys. Acta* **1 85,** *810,* 319.
274. Emptage, M. A.; Kent, T. A.; Huynh, B. H.; Rawlings, J.; Orme-Johnson, W. H.; Münck, E. *J. Biol. Chem.* **1 80,** *255,* 1793.
275. Cammack, R. *Nature* **1 82,** *298,* 792.
276. Beinert, H.; Thomson, A. J. *Arch. Biochem. Biophys.* **1 83,** *222,* 333.
277. Kennedy, M. C.; Mende-Mueller, L.; Blondin, G. A.; Beinert, H. *Proc. Natl. Acad. Sci. USA* **1 2,** *89,* 11730.
278. Haile, D. J.; Rouault, T. A.; Harford, J. B.; Kennedy, M. C.; Blondin, G. A.; Beinert, H.; Klausner, R. D. *Proc. Natl. Acad. Sci. USA* **1 2,** *89,* 11735.
279. Lazazzera, B. A.; Beinert, H.; Khoroshilova, N.; Kennedy, M. C.; Kiley, P. J. *J. Biol. Chem.* **1 6,** *271,* 2762.
280. Khoroshilova, N.; Popescu, C.; Münck, E.; Beinert, H.; Kiley, P. J. *Proc. Natl. Acad. Sci. USA* **1 7,** *94,* 6087.
281. Duin, E. C.; Lafferty, M. E.; Crouse, B. R.; Allen, R. M.; Sanyal, I.; Flint, D. E.; Johnson, M. K. *Biochemistry* **1 7,** *36,* 11811.
282. Ollagnier, S.; Mulliez, E.; Gaillard, J.; Eliasson, R.; Fontecave, M.; Reichard, P. *J. Biol. Chem.* **1 6,** *271,* 9410.
283. Broderick, J. B.; Duderstad, R. E.; Fernandez, D. C.; Wojtuszewski, K.; Henshaw, T. F.; Johnson, M. K. *J. Am. Chem. Soc.* **1 7,** *119,* 7396.
284. Lieder, K. W.; Booker, S.; Ruzicka, F. J.; Beinert, H.; Reed, G. H.; Frey, P. A. *Biochemistry* **1 8,** *37,* 2578.
285. Ollagnier, S.; Mulliez, E.; Schmidt, P. P.; Eliasson, R.; Gaillard, J.; Deronzier, C.; Bergman, T.; Gräslund, A.; Reichard, P.; Fontecave, M. *J. Biol. Chem.* **1 7,** *272,* 24216.
286. Külzer, R.; Pils, T.; Kappl, R.; Hüttermann, J.; Knappe, J. *J. Biol. Chem.* **1 8,** *273,* 4897.
287. Staples, C. R.; Ameyibor, E.; Fu, W.; Gardet-Salvi, L.; Stritt-Etter, A. L.; Schürmann, P.; Knaff, D. B.; Johnson, M. K. *Biochemistry* **1 6,** *35,* 11425.
288. Dole, F.; Fournel, A.; Magro, V.; Hatchikian, E. C.; Bertrand, P.; Guigliarelli, B. *Biochemistry* **1 7,** *36,* 7847.
289. Huyett, J. E.; Carepo, M.; Pamplona, A.; Franco, R.; Moura, I.; Moura, J. J. G.; Hoffman, B. M. *J. Am. Chem. Soc.* **1 7,** *119,* 9291.
290. Albracht, S. P. J. *Biochim. Biophys. Acta* **1 4,** *1188,* 167.
291. Coves, J.; Le Hir de Fallois, L.; Le Pape, L.; Decout, J. L.; Fontecave, M. *Biochemistry* **1 6,** *35,* 8595.
292. Adams, M. W. W. *Biochim. Biophys. Acta* **1 0,** *1020,* 115.
293. Arendsen, A. F.; Hadden, J.; Card, G.; McAlpine, A. S.; Bailey, S.; Zaitsev, V.; Duke, E. H. M.; Lindley, P. F.; Kröckel, M.; Trautwein, A. X.; Feiters, M. C.; Charnok, J. M.; Garner, C. D.; Marritt, S. J.; Thomson, A. J.; Kooter, I. M.; Johnson, M. K.; Van der Berg, W. A. M.; Van Dongen, W. M.; Hagen, W. R. *J. Biol. Inorg. Chem.* **1 8,** *3,* 81.
294. Christner, J. A.; Münck, E.; Kent, T. A.; Janick, P. A.; Salerno, J. C.; Siegel, L. M. *J. Am. Chem. Soc.* **1 84,** *106,* 6786.
295. Crane, B. R.; Siegel, L. M.; Getzoff, E. D. *Science* **1 5,** *270,* 59.
296. Hu, Z.; Spangler, N. J.; Anderson, M. E.; Xia, J.; Ludden, P. W.; Lindhal, P. A.; Münck, E. *J. Am. Chem. Soc.* **1 6,** *118,* 830.
297. Volbeda, A.; Garcin, E.; Piras, C.; De Lacey, A. L.; Fernandez, V. M.; Hatchikian, E. C.; Frey, M.; Fontecilla-Camps, J. C. *J. Am. Chem. Soc.* **1 6,** *118,* 12989.

298. Tavares, P.; Pereira, A. S.; Krebs, C., Ravi, N.; Moura, J. J. G.; Moura, I.; Huynh, B. H. *Biochemistry* **1 8,** *37,* 2830.
299. Van der Spek, T. M.; Arendsen, A. F.; Happe, R. P.; Yun, S.; Bagley, K. A.; Stufkens, D. J.; Hagen, W. R.; Albracht, S. P. J. *Eur. J. Biochem.* **1 6,** *237,* 629.
300. Cammack, R.; Kerscher, L.; Oesterhelt, D. *FEBS Lett.* **1 80,** *118,* 271.
301. Vinogradov, A. D.; Sled, V. D.; Burbaev, D. S.; Gnivennikova, V. G.; Moroz, I. A.; Ohnishi, T. *FEBS Lett.* **1 5,** *370,* 83.
302. Maguire, J. J.; Johnson, M. K.; Morningstar, J. E.; Ackrell, B. A.; Kearney, E. B. *J. Biol. Chem.* **1 85,** *260,* 10909.
303. Orbach, R.; Stapleton, H. J. In "Electron Paramagnetic Resonance"; Geschwind, S., ed.; pp. 121–216; Plenum: New York, 1972.
304. Bertrand, P.; Guigliarelli, B.; More, C. *New J. Chem.* **1 1,** *15,* 445.
305. De Luca, G.; Asso, M.; Belaich, J. P.; Dermoun, *Z. Biochemistry* **1 8,** *37,* 2660.
306. Correll, C. C.; Batie, C. J.; Ballou, D. P.; Ludwig, M. L. *J. Biol. Chem.* **1 85;** *260,* 14633.
307. Liebl, U.; Rutherford, A. W.; Nitschke, W., *FEBS Lett.* **1 0,** *261,* 427.
308. Canne, C.; Stephan, I.; Finsterbush, J.; Lingens, F.; Kappl, F.; Fetzner, S.; Hüttermann, J. *Biochemistry* **1 7,** *36,* 9780.

This Page Intentionally Left Blank

INDEX

A

Absorption spectra, Rieske and Rieske-type proteins, 113–114
Acetogenic bacteria, 306
Acetyl-CoA pathway, 24
Acetyl-CoA synthase (ACS), 284, 295, 305
  biomedical role, 306, 307
  synthesis, 314, 320–322, 325–326
A cluster, 322
Aconitase, 3
  catalytic activity, 479
  cluster conversions, 4, 57
  EXAFS, 3
  ground-state properties, 23, 27, 35
  IRP, 482
  spectroscopy, 27
  structure, 17–18
  vibrational properties, 32, 33
ACS. *See* Acetyl-CoA synthase
S-Adenosylmethionine, 483
Adenylylsulfate reductase (APS reductase), in sulfate-reducing bacteria, 382–385
Aldehyde oxidoreductase (AOR)
  spin–spin interactions, 462
  structure, 465–466
  in sulfate-reducing bacteria, 396, 397–402, 406–408
anfA gene, 203
AOR. *See* Aldehyde oxidoreductase
Apo MoFe protein, 176, 180–181, 182
Apo VFe protein, 204
APS reductase. *See* Adenylylsulfate reductase

B

BLAST (software), 85

C

Carbon monoxide dehydrogenase (CODH), 229, 284–285, 305
  acetyl-CoA synthesis, 314, 320–322, 325–326
  A cluster, 322
  activity, 307, 309
  biomedical role, 306, 307
  carbon monoxide oxidation, 314–315, 317–319
  C cluster, 314–316, 319–320, 485
  genetics, 311–313
  history, 306–307
Carbon monoxide dehydrogenase/acetyl-CoA synthase (CODH/ACS), 284–285, 305–326
  biomedical importance, 306
  genetic structure, 309, 312, 313
  history, 307, 308
  isolated subunits, 325–326
  properties, 307, 308–310
C cluster, 314–316, 319–320, 485
Circular dichroism (CD), Rieske and Rieske-type proteins, 113, 115–116
ClustalW (software), 86
Cluster conversions, 4, 55–58, 376, 459, 481
Clusters
  A cluster, 322
  C cluster, 314–316, 319–320
  cubane cluster, 239
  H cluster, 485
  heterometallic cubane clusters, 63
  "hybrid" cluster, 240, 244, 245, 485
  iron–sulfur clusters. *See* Iron–sulfur clusters
  nickel–iron–sulfur clusters, 283
  P clusters, 169–170, 171, 205
  protein-bound clusters, 63, 68

Rieske center, 347–349, 472
Rieske-type, 142–144, 146
synthetic MFe_3S_4 clusters, 68–72
CODH. *See* Carbon monoxide dehydrogenase
Concensus motif, 451
cooF gene, 290
cooH gene, 290
Crystallography
fuscoredoxin, 380
"prismane" protein, 232–233
Rieske and Rieske-type proteins, 92–109
Cubane cluster, 239
Cuboidal clusters. *See* Trinuclear iron–sulfur clusters
"Cupredoxin fold," 95
Cyclic voltammetry, Rieske proteins, 138, 139
Cytochrome b_6f complexes
Rieske proteins, 88
EPR spectra, 131
g values and rhombicity, 125
redox potential, 136, 137
structure, 96, 100, 102
Cytochrome bc_1 complexes, 83
Rieske proteins, 86–88, 350–352
EPR spectra, 131
function, 146–149
g values and rhombicity, 125
mutational studies, 109–112
redox potential, 136, 137–140
structure, 96, 104, 107–109

D

DALI (software), 94
Delocalization. *See* Valence delocalization
Desulfoferrodoxin (Dfx), in sulfate-reducing bacteria, 366–367
Desulfofuscidin, 387
Desulforedoxin, 362–363, 424, 425, 448
Desulforubidin, 387
Desulfoviridin, 386–387
Dfx. *See* Desulfoferrodoxin
Dinuclear iron–sulfur clusters, 219, 426
EPR spectra, 426–435, 449
interconversions, 482–483
site-directed mutagenesis, 451–456
spin-lattice relaxation, 435–436
Dioxygenase, 149–151, 429
naphthalene dioxygenase (NDO), 150
phthalate dioxygenase (PDO), 119, 132
site-directed mutagenesis, 112–113

E

Electron nuclear double resonance spectroscopy (ENDOR)
aconitase, 479
HiPIP, 443
hydrogenases, 394
NiFe hydrogenase, 300
Rieske and Rieske-type proteins, 132–134, 430
Electron paramagnetic resonance spectroscopy (EPR)
aconitase, 479
APS reductase, 384
CODH/ACS, 314, 317
Fe hydrogenase, 389
FeMoco, 200
ferredoxins, 427–428, 429, 430, 439–440, 442, 446–447, 449, 452–456, 468
formate dehydrogenase, 402
fuscoredoxin, 379
glutamate synthase, 438
HiPIP, 443, 446, 469, 478
iron–sulfur proteins, 400, 421–487
NiFe hydrogenase, 26–27, 294–295, 298–299, 300, 391, 438
nitrogenase, 446–447
oriented iron–sulfur systems, 471–472
"prismane" protein, 224–227
RCI-type photosystem, 339, 340
Rieske and Rieske-type proteins, 122–131, 429
valence delocalization, 257, 259, 261–265, 430–432
vanadium nitrogenases, 206
xanthine oxidase, 434, 465–466, 475
Electron relaxation times, iron–sulfur proteins, 252–257
Electron transfer
iron–sulfur proteins, 405, 474–479
in MoFe proteins, 191–192
nitrogenases, 160–161
Electron transport, NiFe hydrogenase, 16–17

ENDOR. *See* Electron nuclear double resonance spectroscopy
Enzymes
  iron-containing, 284
  iron–sulfur proteins, 1–73, 421–487
  iron uptake, 285
  molybdopterin-containing, 395–405
  nickel-containing, 284–285
  nickel–iron proteins, 286–305
  nickel–iron–sulfur proteins, 284–285, 305–326
  nickel uptake by organism, 285–286
  siroheme-containing, 92
  tungsten-containing enzymes, 401
EPR. *See* Electron paramagnetic resonance spectroscopy
ESEEM, Rieske and Rieske-type proteins, 133–134
EXAFS. *See* X-ray absorption fine structure

F

FeFe protein, 209
Fe hydrogenase, 389–390
FeMoco (FeMo cofactor)
  apo-MoFe protein and, 182
  biosynthesis, 176–180
  EXAFS, 199, 200
  site-directed mutagenesis, 195–199
  structure, 167–169, 221
  substrate binding, 195
Fepr genes, 228, 247
Fepr protein, 245–247
  crystallography, 232–233
  from *Desulfovibrio desulfuricans*, 227–228, 229, 232
  from *Desulfovibrio vulgaris*, 221–226, 228, 229, 232, 235, 239
  domain organization, 238–239
  EPR spectra, 224–227
  EXAFS, 231–232
  history, 221–224
  MCD studies, 230
  molecular structure, 238–245
  resonance Raman spectroscopy, 230–231
  sequence determination, 228–229
  site-directed mutagenesis, 229–230
  structure, 233–238
  X-ray diffraction, 233
Ferredoxins, 2, 3, 5, 6–11
  defined, 370
  history, 335–336
  interconversions, 4, 376–378
  iron–sulfur center, 265
  photosynthetic reactions, 337, 338, 344–345
  properties, 6–11
    electronic properties, 22–29, 35–50, 261–262, 373–376
    excited-state properties, 27–29, 40–50
    ground-state properties, 22–27, 35–40
    magnetic properties, 373–376
    relaxation properties, 433, 435
    vibrational properties, 29, 31–35, 50–52
  spectroscopy
    EPR, 427–428, 429, 430, 439–440, 442, 446–447, 449, 452–456, 468
    EXAFS, 3
  structure, 2, 3, 17–21, 371–373
  in sulfate-reducing bacteria, 370–378
  types, 6–11
    Anabaena, 455
    Azotobacter chroococcum, 8, 9, 38, 53
    Azotobacter vinelandii FdI, 2, 3, 6, 7–9, 17, 19–20, 22, 23, 29–33, 35, 38, 39, 42, 49, 54, 372, 373, 438–440, 442, 449, 456, 457, 459–460
    Bacillus schlegelii, 8, 9, 36, 38
    Bacillus thermoproteolyticus, 372
    C. pasteurianum, 29, 32, 44, 50, 56, 456
    Desulfolobus ambivalens, 8, 9–10, 36
    Desulfomicrobium baculatum, 371, 376
    Desulfonomonas acetoxidans, 371
    Desulfovibrio africanus Fd III, 4, 8–20, 53, 63–68, 64, 65, 68, 371, 375, 377, 378, 456, 457, 459
    Desulfovibrio gigas FdII, 2, 3, 6, 18, 20–23, 29–32, 34, 35, 42, 49, 53, 55–56, 63, 371, 377, 437, 438–440, 442
    Desulfovibrio spp., 373
    Desulfovibrio vulgaris Miyazaki FdI, 6, 8–10, 371, 456, 468, 469
    Mycobacterium smegmatis, 8, 9, 29

Pseudomonas ovalis, 8, 29
Pyrobaculum islandicum, 8, 10–11
Pyrococcus furiosus Fd, 4, 6, 17, 21, 23–25, 27–30, 33–36, 38, 40, 42, 43, 47, 49–52, 54, 58, 63, 65–68, 456
Rhodobacter capsulatus, 8, 9
Rieske-type, 89, 113, 125, 143
Streptomyces griseolus, 7, 9
Sulfolobus acidocaldarius, 8, 9–10, 36, 38, 42, 54, 55, 59
Sulfolobus spp., 8, 9–10, 17, 54
Thermococcus litoralis, 26
Thermoplasma acidophilum, 8, 9–10
Thermus thermophilus, 8, 23, 29–31, 33, 36, 42
Ferredoxin thioredoxin reductase, 483
Ferrochelatase, site-directed mutagenesis, 452–453
Fe–Ni–S proteins. *See* Iron–nickel–sulfur proteins
Fe–S proteins. *See* Iron–sulfur proteins
FeVaco, 206
Formate dehydrogenase, in sulfate-reducing bacteria, 396, 402–403
Fourier transform infrared spectroscopy (FTIR), NiFe hydrogenase, 295–298, 299, 303
Freeze quench EPR spectroscopy (FQ-EPR), CODH/ACS, 318
FTIR. *See* Fourier transform infrared spectroscopy
Fumarate reductase
  EPR, 452–456
  ground-state properties, 23
  oriented systems, 472
  properties, 6, 11–13
  spin–spin interactions, 462
Fuscoredoxin, 485
  in sulfur-reducing bacteria, 378–382

G

Glutamate synthase
  EPR, 438
  ground-state properties, 23
  properties, 3, 5, 14–15
GroEL, 182–183
g tensor, iron–sulfur centers, 426–430, 450

H

H cluster, 485
Heterometallic cubane clusters, 63
HiPIP (high-potential iron–sulfur proteins), 336
  iron–sulfur center, 265
  photosynthesis, 337–338, 345–347
  relaxation rate, 449
  spectroscopy, 261, 263
    ENDOR, 443
    EPR, 443, 446, 469, 478
    NMR, 272–275, 458
  spin-lattice relaxation, 447
  spin–spin interactions, 462
HoxN protein, 287
HoxW protein, 288
HoxX protein, 290
HupU protein, 289
HupUV proteins, 190
"Hybrid" cluster, 240, 244, 245, 485
HycE protein, 288
Hydrogenase-like proteins, 290
Hydrogenases
  from *Desulfovibrio* spp., 286–305
  Fe hydrogenase, 389–390
  NiFe hydrogenase, 286–305, 390–396
  from sulfate-reducing bacteria, 388–396
Hydrogenotrophic bacteria, 306
Hydrogen sensor proteins, 289
HypB protein, 289
HypC protein, 289
Hyperfine shift, iron–sulfur proteins, 261–265, 268–271
HypF protein, 289
HypX protein, 290

I

Interconversions. *See* Cluster conversions
IRE. *See* Iron responsive element
Iron
  isotopes, 284
  oxidation states, 284
  in proteins, 284
  uptake of extracellular iron, 285–286
Iron-containing enzymes, 284
  CODH/ACS, 284–295, 305–326

hydrogenase, 286–305
iron uptake by organism, 285
Iron hydrogenase, 389–390
Iron–nickel–sulfur proteins. *See* Nickel–iron–sulfur proteins
Iron-only nitrogenase
biosynthesis, 203, 208
properties, 209–210
in sulfate-reducing bacteria, 389–390
Iron proteins, 161
nucleotides, interaction with, 165–166
redox properties, 164–165
self-oxidization, 165
site-directed mutagenesis, 188
spectroscopy, 164–165
structure, 162–164
Iron-regulatory protein (IRP), 482
Iron responsive element (IRE), 482
Iron–sulfur clusters, 4–5, 219, 363
biological activity, 220–221
catalytic activity, 479–480
dinuclear. *See* Dinuclear iron–sulfur clusters
electron transfer, 474–479
EPR spectra, 423–450, 484–486
FeMoco-cofactor, 221
g tensor, 426–430, 450
history, 335–336
interconversions, 55–58, 376, 459, 481
mononuclear. *See* Mononuclear iron–sulfur clusters
in nitrogenase, 221
oriented iron–sulfur systems, 471–474
in photosynthetic reactions, 335–356
radical stabilization, 483–484
Raman spectroscopy, 31–34
regulation role, 480–483
site-directed mutagenesis, 450–461
spin-lattice relaxation, 425–426, 435–436, 442, 447, 486–487
spin–spin interactions, 461–471
tetranuclear. *See* Tetranuclear iron–sulfur clusters
trinuclear. *See* Trinuclear iron–sulfur clusters
types, 219–220
VTMCD, 28–30, 41, 46, 48–50
Iron–sulfur proteins
aldehyde oxidoreductase, 396, 397–402, 406–408, 462, 465–466
electron transfer, 405, 474–479
EPR, 400
ferredoxins, 2, 3, 5, 6–11
fumarate reductase, 6, 11–13, 23, 452–456, 462, 472
glutamate synthase, 14–15
NiFe hydrogenase. *See* NiFe hydrogenase
nitrate reductase, 3, 5, 13–14, 396, 403–406, 472, 475
NMR studies, 251–277
electron relaxation times, 252–257
polypeptide folding, 271–276
reduction potential, 265–266
solution structure, 266–271
valence delocalization, 257, 259, 261–265
oriented systems, 471–472
in photosynthetic reactions, 335–336
"prismane" iron–sulfur protein, 219–247
Rieske and Rieske-type proteins, 83–151
succinate dehydrogenase, 3, 5, 11–13, 23
in sulfate-reducing bacteria (SRB), 361–362
adenylylsulfate reductase, 382–385
aldehyde oxidoreductases, 396, 397–402, 406–408
desulfoferredoxin, 366–367
desulforedoxin, 362–363
electron transfer, 405–410
ferredoxins, 370–378
formate dehydrogenase, 396, 402–403
fuscoredoxin, 378–382
hydrogenases, 388–395
molybdopterin-containing enzymes, 396–405
nitrate reductase, 396, 403–406
pyruvate-ferredoxin oxidoreductase, 385–386
rubredoxin, 362–366
rubrerythrin, 367–370
sulfite reductase, 386–388
valence delocalization, 257, 259, 261–265, 430–432
IRP. *See* Iron-regulatory protein

L

Lowe–Thorneley mechanism, 183–186, 198, 211

M

Metalloenzymes. *See* Enzymes
Methanogenic archaea, 306
MgATP hydrolysis, nitrogenase turnover and, 189–191
Midpoint potential, iron–sulfur centers, 474–478
MoFe proteins
  active MoFe protein, 176, 182
  apo-MoFe protein, 176, 180–181, 182
  biosynthesis, 176–183
  electron transfer in, 191–192
  FeMoco (FeMo cofactors), 167–169, 176–180, 182, 195–199, 221
  P clusters, 169–170, 171
  redox properties, 170, 172–173
  spectroscopy, 170, 172–173
  structure, 166–170
  substrate interactions, 173–174
  X-ray crystal structure, 201
Molybdenum nitrogenase, 161–162, 202–203
  biosynthesis, 174–183
  iron proteins of, 161, 162–166, 176
  mechanisms, 183–202
    electron transfer, 191–192
    Lowe–Thorneley mechanism, 183–186, 198, 211
    MgATP hydrolysis and, 189–191
    nitrogenase complex, 186–189
    substrates, 192–202
  molybdenum iron proteins, 161, 166–174, 176–183, 191–192
  structure, 162–164, 166–170
Molybdopterin cofactor, 396
Molybdopterin-containing enzymes, 396–405
  aldehyde oxidoreductase, 396, 397–402, 406–408, 462, 465–466
  formate dehydrogenase, 396, 402–403
  nitrate reductase, 3, 5, 13–14, 396, 403–405, 472, 475
Molybdopterin cytosine dinucleotide (MCD), 230, 396
Mononuclear iron–sulfur clusters, 219
  EPR spectra, 423–425, 448
  ferredoxins, 6–7
  spin-lattice relaxation, 425–426
  spin–spin interactions, 462, 465–467
Mosaic spread, 471
Mössbauer spectroscopy
  formate dehydrogenase, 402
  fuscoredoxin, 379, 381
  molybdenum hydroxylases, 402, 403
  NiFe hydrogenase, 26–27, 391
  "prismane" protein, 226–227, 245
  Rieske and Rieske-type proteins, 118–119
  valence delocalization, 21
  vanadium nitrogenase, 205–206
Multalin (software), 86

N

Naphthalene dioxygenase (NDO), 150
NDO. *See* Naphthalene dioxygenase
Nickel
  isotopes, 284
  oxidation states, 284
  in proteins, 284–285
  uptake of extracellular nickel, 285–286
Nickel-containing enzymes, 284–285, 285–286
  CODH/ACS, 284–295, 305–326
  hydrogenase, 286–305
  nickel uptake by organism, 285–286
Nickel–iron proteins, hydrogenase, 286–305
Nickel–iron–sulfur clusters, 283
Nickel–iron–sulfur proteins, CODH/ACS, 284–295, 305–326
Nickel transport, hydrogenase, 286–287
Nickel transporters, 285–286
nifA gene, 203
nifA gene product, 175
nifB gene, 177, 178, 203, 204
nifB gene product, 175, 176, 178
nifD gene, 178
nifD gene product, 175
nifE gene product, 175, 176
NiFe hydrogenase, 284
  active site, 290–298
  catalytic cycle, 394–395
  catalytic mechanism, 298–305

crystal structure, 391–393, 457
electron transport, 16–17
expression, 289–290
forms
Ni-A form, 300
Ni-B form, 300
Ni-B species, 298
Ni-C form, 295, 298, 300, 304
Ni-R species, 298
Ni-SI species, 298
heterodinuclear site, 393–394
maturation, 288–289, 290
properties, 5, 15–17
ground-state properties, 23, 26, 35
vibrational properties, 31–32
radical stabilization, 484
spectroscopy
EPR, 26–27, 294–295, 298–299, 300, 391, 438
FTIR, 295–298, 299, 303
Mssbauer spectroscopy, 26–27, 391
X-ray absorption spectroscopy (XAS), 292–293
spin–spin interactions, 462, 467
structure, 15–17, 18
in sulfate-reducing bacteria, 390–396
synthesis, 286–287
nifF gene product, 175
nif gene, 203
nif genes, molybdenum nitrogenase biosynthesis and, 174–183, 203
nifH gene, 176, 178, 179–180, 209
nifH gene product, 175, 176, 182
nifJ gene product, 175
nifKD gene, 204
nifK gene, 178
nifK gene product, 175
nifL gene product, 175
nifM gene, 203
nifM gene product, 175, 176, 204
nifN_2E_2 gene, 177–178
nifN gene product, 175, 176
nifQ gene, 177
nifQ gene product, 175, 176
nifS gene, 203
nifS gene product, 175, 176
nifT gene product, 175
nifU gene, 203
nifU gene product, 175, 176
nifV gene, 178–179, 203
nifV gene product, 175, 176
nifW gene product, 175
nifX gene product, 175
nifY gene product, 175
nifZ gene product, 175
Nigerythrin, 370, 424
nikA protein, 286–287
nikB protein, 287
nikC protein, 287
nikD protein, 287
nikE protein, 287
Nitrate reductase
classes, 404
oriented systems, 472
properties, 3, 5, 13–14
midpoint potential, 475
in sulfate-reducing bacteria, 396, 403–405
Nitrogenase complex, 186–189
Nitrogenases, 160–162, 202, 211–212
electron transfer, 160–161
EPR, 446–447
iron-only nitrogenase
biosynthesis, 203, 208
properties, 209–210
molybdenum nitrogenase, 161–162, 202–203
biosynthesis, 174–183
iron proteins of, 161, 162–166, 176
mechanisms, 183–202
molybdenum iron proteins, 161, 166–174, 176–183, 191–192
structure, 162–164, 166–170, 481
pH dependence, 193–194
from *Streptomyces thermoautotrophicus*, 210–211
substrates, 192–202
vanadium nitrogenases, 203
activity, 207–208
biosynthesis, 203–204
structure, 204–207
NMR
FeMoco, 200
HiPIP, 458
Rieske and Rieske-type proteins, 134–137
Nuclear relaxation rates, iron–sulfur proteins, 267–268
Nucleotide binding proteins, iron protein and, 165–166
Nucleotides, MoFe proteins and, 174

O

Oxygenases, Rieske-type, 89–90, 125

P

P clusters, structure, 169–170, 171, 205
PDO. *See* Phthalate dioxygenase
Photosynthesis
  anoxygenic, 336–337
  bridging cluster Fx, 344
  evolution, 355
  ferredoxins, 337, 338, 344–345
  HiPIP, 337–338, 345–347
  RCI-type photosystems, 337, 338–343, 344
  Rieke proteins, 337, 347–355
Phthalate dioxygenase (PDO), 119
  ENDOR and ESEEM studies, 132
  spin–spin interactions, 466
Phthalate dioxygenase reductase, structure, 150
Polypeptide folding, iron–sulfur proteins, 271–276
"Prismane" protein, 245–247
  crystallography, 232–233
  from *Desulfovibrio desulfuricans*, 227–228, 229, 232
  from *Desulfovibrio vulgaris*, 221–226, 228, 229, 232, 235, 239
  domain organization, 238–239
  EPR spectra, 224–227
  EXAFS, 231–232
  history, 221–224
  MCD studies, 230
  molecular structure, 238–245
  resonance Raman spectroscopy, 230–231
  sequence determination, 228–229
  site-directed mutagenesis, 229–230
  structure, 233–238
  X-ray diffraction, 233
Protein-bound clusters, 63, 68
Proteins
  hydrogen sensor proteins, 289
  iron–sulfur proteins, 1–73, 421–487
  nickel–iron proteins, 286–305
  nickel–iron–sulfur proteins, 284–285, 305–326
  Rieske and Rieske-type proteins, 83–151
PSI, 473–474
"Putative prismane," 485
Putidaredoxin, 118
Pyruvate-ferredoxin oxidoreductase, in sulfate-reducing bacteria, 385–386

R

Raman spectroscopy
  Fepr protein, 230–231
  iron–sulfur cluster, 31–34
RCII, 355
RCI-type photosystems, 337, 338–343
Rd. *See* Rubredoxin
Redox chemistry
  hydrogenase catalysis, 298
  iron–sulfur centers, 480–481
Redox potential, Rieske and Rieske-type proteins, 136, 137–140
Reduction potential
  iron–sulfur proteins, 265–266
  Rieske proteins, 352–355
Resonance Raman spectroscopy
  fuscoredoxin, 380
  "prismane" protein, 230–231, 246
  Rieske and Rieske-type proteins, 119–121
Rieske center, 347–349, 472
"Rieske fold," 93–96, 100, 105
Rieske proteins, 83–85
  biosynthesis, 144–146
  crystallography, 94
  electrochemistry, 137–142
  function, 146–149
  occurrence, 347, 350
  photosynthetic reactions, 337, 347–355
  reduction potentials, 352–355
  Rieske center, 347–349, 472
  sequence comparison, 349–350
  spectroscopy, 113
    absorption spectra, 113–114
    circular dichroism, 113, 115–118
    ENDOR, 132–134, 430
    EPR spectroscopy, 122–131, 429
    ESEEM, 133–134
    EXAFS, 121
    Mössbauer spectroscopy, 118–119

NMR spectroscopy, 134–137
resonance Raman spectroscopy, 119–121
XANES, 122
X-ray absorption spectroscopy, 121–122
structure, 349–351
amino acid sequences, 85–89
mutational studies, 109–113
X-ray structure, 92–93, 100–109
types
from cytochrome b_6f complexes, 88, 96, 100, 102, 131, 136, 137
from cytochrome bc_1 complexes, 86–88, 96, 104, 107–112, 125, 131, 136, 137–148, 350–362
SoxF and SoxL, 88–89
from *Thermus thermophilus*, 88, 118, 119, 132, 348
TRP, 88, 118, 119, 132
Rieske-type clusters, 142–144, 146
Rieske-type proteins
bacterial Rieske-type ferredoxins, 89
bacterial Rieske-type oxygenases, 89–90
biosynthesis, 144, 145
dioxygenase, 112–113, 132, 149–151
electrochemistry, 142–144
from eukaryotes, 90–92
function, 149–151
redox potential, 136, 142–143
spectroscopy
absorption spectra, 113
circular dichroism, 115
structure
amino acid sequences, 89–92
mutational studies, 113
X-ray structure, 92–99, 105–109
Rubredoxin (Rd), 423–424, 425, 448
electron relaxation time, 253–254
spin-lattice relaxation, 426
in sulfate-reducing bacteria, 362–366
X-ray structure, 105–106
Rubrerythrin (Rr), 367–370, 424

S

SDD. *See* Spin-dependent delocalization
SDM. *See* Site-directed mutagenesis
S-F FTIR. *See* Stopped-flow Fourier transform infrared spectroscopy
Siderophores, 285
Siroheme-containing enzymes, 92
Site-directed mutagenesis (SDM)
dioxygenase, 112–113
EPR, 450–461
FeMoco, 195–199
iron protein, 188
"prismane" protein, 229–230
Rieske proteins, 109–112
SoxF protein, 89–90
SoxL protein, 89–90
SoxR protein, 480–481
Spectroscopy, *See also* individual types of spectroscopy
iron proteins, 164–165
MoFe proteins, 170, 172–173
Rieske and Rieske-type proteins, 113–137
Spin-dependent delocalization (SDD), 39
Spin-lattice relaxation
iron–sulfur centers, 486–487
dinuclear clusters, 435–436
HiPIP, 447
mononuclear clusters, 425–426
tetranuclear clusters, 447
trinuclear clusters, 442
Spin–spin interactions, iron–sulfur clusters, 461–471
SRB. *See* Sulfate-reducing bacteria
Stigmatellin, binding, 130
Stopped-flow Fourier transform infrared spectroscopy (S-F FTIR), nitrogenase, 194–195
Streptomyces thermoautotrophicus, nitrogenase from, 210–211
Succinate dehydrogenase
magnetic axes, 472
properties, 3, 5, 11–13
ground-state properties, 23
Sulfate-reducing bacteria (SRB), 306
iron–sulfur proteins, 361–362
adenylylsulfate reductase, 382–385
aldehyde oxidoreductases, 396, 397–402, 406–408
desulfoferredoxin, 366–367
desulforedoxin, 362–363
electron transfer, 405–410

ferredoxins, 370–378
formate dehydrogenase, 396, 402–403
fuscoredoxin, 378–382
hydrogenases, 388–395
molybdopterin-containing enzymes, 396–405
nitrate reductase, 396, 403–405
pyruvate-ferredoxin oxidoreductase, 385–386
rubredoxin, 362–366
rubrerythrin, 367–370
sulfite reductase, 386–388
Sulfite reductase, in sulfate-reducing bacteria, 386–388
Sulfur-containing enzymes, CODH/ACS, 284–295, 305–326
Sulfur–iron clusters. *See* Iron–sulfur clusters
Sulfur–iron proteins. *See* Iron–sulfur proteins
Sulfur–nickel–iron proteins. *See* Nickel–iron–sulfur clusters
Sulredoxin, 119

T

Tetranuclear iron–sulfur clusters, 219, 442–443
EPR spectra, 443–447, 449–450
interconversions, 459, 481–483
site-directed mutagenesis, 456–461
spin-lattice relaxation, 447
spin–spin interactions, 462, 467–469, 473
TFIIS, 105–106
Thermus thermophilus Rieske protein. *See* TRP
Trimethylamine dehydrogenase (TMADH), spin–spin interactions, 467–468
Trinuclear iron–sulfur clusters, 1–2, 72–73, 219, 436
discovery, 2, 448
early studies, 2–4
electronic properties, 3, 21–55
EPR spectra, 436–442, 448
interconversions, 3, 4, 55–58, 459, 481
magnetic properties, 3, 21–55
mixed metal clusters, 63–72
occurrence, 3, 5–17
site-directed mutagenesis, 456–461
spin-lattice relaxation, 442
structures, 2–3, 17–21
synthetic model compounds, 58–63
vibrational properties, 3, 21–55
TRP, 88, 118, 119, 132, 348
Tungsten-containing enzymes, in sulfate-reducing bacteria, 401

V

Valence delocalization, 39
iron–sulfur proteins, 257, 259, 261–265, 430–432
Mössbauer spectroscopy, 21
NMR, 257, 259, 261–265
Vanadium nitrogenases, 203
activities, 207–208
biosynthesis, 203–204
structure, 204–207
Variable-temperature magnetic circular dichroism (VTMCD)
ferredoxins, 2
iron–sulfur cluster, 28–30, 41, 46, 48–50
VFe protein, 205
vnfA gene, 203
vnfD gene, 204
vnfEN gene, 204
vnfG gene, 204
vnfH gene, 204
VnFH protein, 182
vnfK gene, 204
VTMCD. *See* Variable-temperature magnetic circular dichroism

W

Walker A nucleotide binding motifs, 165
Wood–Ljungdahl pathway, 306, 308, 312

X

XANES. *See* X-ray absorption near-edge spectroscopy
Xanthine oxidase
EPR, 434, 465–466, 475
spin–spin interaction, 462, 466

XAS. *See* X-ray absorption spectroscopy
X-ray absorption fine structure (EXAFS)
  aconitase, 3
  FeMoco, 199, 200
  ferredoxin, 3
  NiFe hydrogenase, 291
  "prismane" protein, 231–232
  Rieske and Rieske-type proteins, 121
  vanadium nitrogenases, 206
X-ray absorption near-edge spectroscopy (XANES)
  NiFe nitrogenase, 293
  Rieske proteins, 122
X-ray absorption spectroscopy (XAS)
  NiFe hydrogenase, 292–293
  Rieske and Rieske-type proteins, 121–122
  vanadium nitrogenases, 206
X-ray crystallography, Rieske and Rieske-type proteins, 92–109
X-ray diffraction, "prismane" protein, 233

This Page Intentionally Left Blank

CONTENTS OF PREVIOUS VOLUMES

VOLUME 37

On the Coordination Number of the Metal Crystalline Halogenocuprates(I) and Halogenoargentates(I)
Susan Jagner and Göran Helgesson

Structures of Organonitrogen-Lithium Compounds: Recent Patterns and Perspectives in Organolithium Chemistry
Karina Gregory, Paul von Ragué Schleyer, and Ronald Snaith

Cubane and Incomplete Cubane-Type Molybdenum and Tungsten Oxo/Sulfido Clusters
Takashi Shibahara

Interactions of Platinum Amine Compounds with Sulfur-Containing Biomolecules and DNA Fragments
Edwin L. M. Lempers and Jan Reedijk

Recent Advances in Osmium Chemistry
Peter A. Lay and W. Dean Harman

Oxidation of Coordinated Diimine Ligands in Basic Solutions of Tris(diimine)iron(III),-ruthenium(III), and -osmium(III)
O. Mønsted and G. Nord

INDEX

VOLUME 38

Trinuclear Cuboidal and Heterometallic Cubane-Type Iron-Sulfur Clusters: New Structural and Reacticity Themes in Chemistry and Biology
R. H. Holm

Replacement of Sulfur by Selenium in Iron Sulfur Proteins
Jacques Meyer, Jean-Marc Moulis, Jacques Gaillard, and Marc Lutz

Dynamic Electrochemistry of Iron-Sulfur Proteins
Fraser A. Armstrong

EPR Spectroscopy of Iron-Sulfur Proteins
Wilfred R. Hagen

Structural and Functional Diversity of Ferredoxins and Related Proteins
Hiroshi Matsubara and Kazuhiko Saeki

Iron-Sulfur Clusters in Enzymes: Themes and Variations
Richard Cammack

Aconitase: An Iron-Sulfur Enzyme
Mary Claire Kennedy and C. David Stout

Novel Iron-Sulfur Centers in Metalloenzymes and Redox Proteins from Extremely Thermophilic Bacteria
Michael W. W. Adams

Evolution of Hydrogenase Genes
Gerrit Voordoww

Density-Functional Theory of Spin Polarization and Spin Coupling in Iron-Sulfur Clusters
Louis Noodleman and David A. Case

INDEX

VOLUME 39

Synthetic Approach to the Structure and Function of Copper Proteins
Nobumasa Kitajima

Transition Metal and Organic Redox-Active Macrocycles Designed to Electrochemically Recognize Charged and Neutral Guest Species
Paul D. Beer

Structure of Complexes in Solution Derived from X-Ray Diffraction Measurements
Georg Johansson

High-Valent Complexes of Ruthenium and Osmium
Chi-Ming Che and Vivian Wing-Wah Yam

Heteronuclear Gold Cluster Compounds
D. Michael P. Mingos and Michael J. Watson

Molecular Aspects on the Dissolution and Nucleation of Ionic Crystals in Water
Hitoshi Ohtaki

INDEX

VOLUME 40

Bioinorganic Chemistry of Pterin-Containing Molybdenum and Tungsten Enzymes
John H. Enemark and Charles G. Young

Structure and Function of Nitrogenase
Douglas C. Rees, Michael K. Chan, and Jongsun Kim

Blue Copper Oxidases
A. Messerschmidt

Quadruply Bridged Dinuclear Complexes of Platinum, Palladium, and Nickel
Keisuke Umakoshi and Yoichi Sasaki

Octacyano and Oxo- and Nitridotetracyano Complexes of Second and Third Series Early Transition Metals
Johann G. Leipoldt, Stephen S. Basson, and Andreas Roodt

Macrocyclic Complexes as Models for Nonporphine Metalloproteins
Vickie McKee

Complexes of Sterically Hindered Thiolate Ligands
J. R. Dilworth and J. Hu

INDEX

VOLUME 41

The Coordination Chemistry of Technetium
John Baldas

Chemistry of Pentafluorosulfanyl Compounds
R. D. Verma, Robert L. Kirchmeier, and Jean'ne M. Shreeve

The Hunting of the Gallium Hydrides
Anthony J. Downs and Colin R. Pulham

The Structures of the Group 15 Element(III) Halides and Halogenoanions
George A. Fisher and Nicholas C. Norman

Intervalence Charge Transfer and Electron Exchange Studies of Dinuclear Ruthenium Complexes
Robert J. Crutchley

Recent Synthetic, Structral, Spectroscopic, and Theoretical Studies on Molecular Phosphorus Oxides and Oxide Sulfides
J. Clade, F. Frick, and M. Jansen

Structure and Reactivity of Transferrins
E. N. Baker

INDEX

VOLUME 42

Substitution Reactions of Solvated Metal Ions
Stephen F. Lincoln and André E. Merbach

Lewis Acid–Base Behavior in Aqueous Solution: Some Implications for Metal Ions in Biology
Robert D. Hancock and Arthur E. Martell

The Synthesis and Structure of Organosilanols
Paul D. Lickiss

Studies of the Soluble Methane Monooxygenase Protein System: Structure, Component Interactions, and Hydroxylation Mechanism
Katherine E. Liu and Stephen J. Lippard

Alkyl, Hydride, and Hydroxide Derivatives in the *s*- and *p*-Block Elements Supported by Poly(pyrazolyl)borato Ligation: Models for Carbonic Anhydrase, Receptors for Anions, and the Study of Controlled Crystallographic Disorder
Gerard Parkin

INDEX

VOLUME 43

Advances in Thallium Aqueous Solution Chemistry
Julius Glaser

Catalytic Structure–Function Relationships in Heme Peroxidases
Ann M. English and George Tsaprailis

Electron-, Energy-, and Atom-Transfer Reactions between Metal Complexes and DNA
H. Holden Thorp

Magnetism of Heterobimetallics: Toward Molecular-Based Magnets
Olivier Kahn

The Magnetochemistry of Homo- and Hetero-Tetranuclear First-Row *d*-Block Complexes
Keith S. Murray

Diiron–Oxygen Proteins
K. Kristoffer Andersson and Astrid Gräslund

Carbon Dioxide Fixation Catalyzed by Metal Complexes
Koji Tanaka

INDEX

VOLUME 44

Organometallic Complexes of Fullerenes
Adam H. H. Stephens and Malcolm L. H. Green

Group 6 Metal Chalcogenide Cluster Complexes and Their Relationships to Solid-State Cluster Compounds
Taro Saito

Macrocyclic Chemistry of Nickel
Myunghyun Paik Suh

Arsenic and Marine Organisms
Kevin A. Francesconi and John S. Edmonds

The Biochemical Action of Arsonic Acids Especially as Phosphate Analogues
Henry B. F. Dixon

Intrinsic Properties of Zinc(II) Ion Pertinent to Zinc Enzymes
Eiichi Kimura and Tohru Koike

Activation of Dioxygen by Cobalt Group Metal Complexes
Claudio Bianchini and Robert W. Zoellner

Recent Developments in Chromium Chemistry
Donald A. House

INDEX

VOLUME 45

Syntheses, Structures, and Reactions of Binary and Tertiary Thiomolybdate Complexes Containing the (O)Mo(S_x) and (S)Mo(S_x) Functional Groups (x = 1, 2, 4)
Dimitri Coucouvanis

The Transition Metal Ion Chemistry of Linked Macrocyclic Ligands
Leonard F. Lindoy

Structure and Properties of Copper–Zinc Superoxide Dismutases
Ivano Bertini, Stefano Mangani, and Maria Silvia Viezzoli

DNA and RNA Cleavage by Metal Complexes
Genevieve Pratviel, Jean Bernadou, and Bernard Meunier

Structure–Function Correlations in High Potential Iron Problems
J. A. Cowan and Siu Man Lui

The Methylamine Dehydrogenase Electron Transfer Chain
C. Dennison, G. W. Canters, S. de Vries, E. Vijgenboom, and R. J. van Spanning

INDEX

VOLUME 46

The Octahedral M_6Y_6 and M_6Y_{12} Clusters of Group 4 and 5 Transition Metals
Nicholas Prokopuk and D. F. Shriver

Recent Advances in Noble–Gas Chemistry
John H. Holloway and Eric G. Hope

Coming to Grips with Reactive Intermediates
Anthony J. Downs and Timothy M. Greene

Toward the Construction of Functional Solid-State Supramolecular Metal Complexes Containing Copper(I) and Silver(I)
Megumu Munakata, Liang Ping Wu, and Takayoshi Kuroda-Sowa

Manganese Redox Enzymes and Model Systems: Properties, Structures, and Reactivity
Neil A. Law, M. Tyler Caudle, and Vincent L. Pecoraro

Calcium-Binding Proteins
Bryan E. Finn and Torbjörn Drakenberg

Leghemoglobin: Properties and Reactions
Michael J. Davies, Christel Mathieu, and Alain Puppo

INDEX